TSUNAMIS - HARBOR OSCILLATIONS INDUCED BY NONLINEAR TRANSIENT LONG WAVES

Thesis by

Thierry Georges Lepelletier

In Partial Fulfillment of the Requirements

for the Degree of

Doctor of Philosophy

California Institute of Technology

Pasadena, California

1981

(Submitted October 14, 1980)

ACKNOWLEDGMENTS

Several people have contributed to this work in many vital ways and it is with deep gratitude that I acknowledge the help, time and patience they offered me throughout this study.

I am especially grateful to my thesis advisor, Professor Fredric Raichlen, who suggested the topic and offered the most valuable guidance and encouragement throughout this project.

I would like to sincerely thank Professor Theodore Wu for some very helpful discussions during the development of the theoretical analysis. I am also particularly indebted to Professor Thomas Hughes who gave advice and encouragement in the development of the finite element technique extensively used in this project. Dr. Robert C.Y. Koh has been most helpful in many aspects of the data reduction process. His MAGIC program helped remove a considerable burden and saved me many hours of programming.

Mr. Elton F. Daly, Supervisor of the Shop and Laboratory, provided invaluable assistance in every aspect of the design, construction and maintenance of the experimental equipment. His ideas always proved to be the best and I shall never be able to thank him enough for his help and concern. Mr. Joseph J. Fontana and Mr. Richard Eastvedt constructed the laboratory equipment.

I would like to thank Clement Tam whose much appreciated assistance has been vital during some critical stages of this project. In particular, he carried out entirely the rather awesome task of data implementation for the finite element programs. Several others provided friendship and advice. In particular, I would like to thank

Gregory Gartrell, Derek Goring and Jing-Chang Chen.

Mrs. Joan Mathews typed a large portion of this thesis and co-ordinated the whole typing process. She provided friendship and encouragement throughout all these years, especially toward the last few weeks when pressure became rather acute. The help of Mrs. Ruth Stratton, Mrs. Linda Malaby, Mrs. Pat Houseworth, Mrs. Mary Ann Gray and Mrs. Adelaide Massengale, who typed parts of the manuscript, is also appreciated. Mrs. Cecilia Lin and Mr. Phil Dubé did a nice job in drafting the figures.

My wife, Maite, encouraged me and provided strong moral support through her love and patience throughout these years.

I thank the International Rotary Foundation for providing me with a scholarship during my first year of graduate studies at Caltech. I also thank the California Institute of Technology for providing me with financial support through Graduate Teaching and Research Assistantships during the subsequent years. The research was supported by National Science Foundation Grant Numbers ENV72-03587 and ENV77-20499. Experiments were conducted at the W. M. Keck Laboratory of Hydraulics and Water Resources.

This report is essentially the thesis of the same title submitted by the writer on October 14, 1980 to the California Institute of Technology in partial fulfillment of the requirements for the degree of Doctor of Philosophy in Civil Engineering.

Gregory Gartrell, Derek Goring and Jing-Chang Chen.

Mrs. Joan Mathews typed a large portion of this thesis and co-ordinated the whole typing process. She provided friendship and encouragement throughout all these years, especially toward the last few weeks when pressure became rather acute. The help of Mrs. Ruth Stratton, Mrs. Linda Malaby, Mrs. Pat Houseworth, Mrs. Mary Ann Gray and Mrs. Adelaide Massengale, who typed parts of the manuscript, is also appreciated. Mrs. Cecilia Lin and Mr. Phil Dubé did a nice job in drafting the figures.

My wife, Maite, encouraged me and provided strong moral support through her love and patience throughout these years.

I thank the International Rotary Foundation for providing me with a scholarship during my first year of graduate studies at Caltech. I also thank the California Institute of Technology for providing me with financial support through Graduate Teaching and Research Assistantships during the subsequent years. The research was supported by National Science Foundation Grant Numbers ENV72-03587 and ENV77-20499. Experiments were conducted at the W. M. Keck Laboratory of Hydraulics and Water Resources.

ABSTRACT

The process of excitation of harbors and bays by transient nonlinear long waves is investigated theoretically and experimentally. In addition, nonlinear shallow water waves generated in a closed rectangular basin by the motion of the basin are also examined.

Two numerical methods based on finite element techniques are used to solve the weakly nonlinear-dispersive-dissipative equations of motion and are applied to the basin excitation problem and the transient harbor oscillation problem, respectively. In the latter case, the open sea conditions are simulated by including a radiative boundary condition in time at a finite distance from the harbor entrance. Various dissipative effects are also included. In addition to the numerical results, analytical solutions are presented to investigate certain particular aspects of basin and harbor oscillations (e.g., the effects of viscous dissipation in a harbor with simple geometry).

Experiments conducted in the closed rectangular basin indicate that for a continuous excitation at or near a resonant mode of oscillation the linear theory becomes inadequate and the nonlinear-dispersive-dissipative theory must be used. For a transient excitation the validity of the linear theory depends on the value of the Stokes parameter. Indeed, some features not predicted by the linear theory can be directly inferred from the magnitude of this parameter.

Experiments on the continuous wave induced oscillations of a narrow rectangular harbor with constant depth show that at the first resonant mode convective nonlinearities can be neglected and a linear dissipative solution is sufficient to describe the waves inside the harbor. At the

second resonant mode which corresponds to a longer harbor relative to the length of the incident wave, nonlinear convective effects become important and must be incorporated into the numerical model. Also the characteristics of various sources of dissipation which reduce resonance in the harbor are investigated experimentally. The sources considered include, among others, laminar boundary friction, leakage losses underneath the harbor walls, and energy dissipation due to flow separation at the entrance of the harbor.

The good agreement obtained between the experiments and the nonlinear numerical model developed in this study suggests that this model could be used with some confidence to predict the response characteristics of prototype harbors. As an example, the results of this study have been applied to the response of Ofunato Bay (Japan) to the tsunami generated by the Tokachi-Oki earthquake of May 16,1968. The model has been used to investigate the effects of convective nonlinearities on the bay oscillations and also to determine the efficiency of the breakwater which was built to reduce the effects of tsunamis at Ofunato.

TABLE OF CONTENTS

Chapter | Page

Chapter | Page

LIST OF TABLES

CHAPTER 1

INTRODUCTION

The word tsunami is used to designate the sea waves which are generated by a geophysical mechanism such as an under-sea landslide or earthquake. It is taken from the Japanese and translates literally to "harbor wave". This is quite descriptive of one of the major aspects of the problems associated with tsunamis, namely the interaction of the waves with harbors and bays.

The propagation of tsunamis from their source to the coastline can be divided into three major aspects:

(i) Generation and deep ocean propagation where the tsunami is typically tens to hundreds of kilometers long, with wave speeds of several hundreds of kilometers per hour and a maximum wave height of order of perhaps a meter.

(ii) Nearshore propagation where the tsunami approaches the coast and undergoes some transformation as it propagates past the continental shelf break and onto the shelf, with a reduction in depth in a ratio of three or four going from the open sea to the offshore coastal regions.

(iii) The interaction with the coastline which combines refraction, shoaling, geometric energy focusing, and dynamic resonance effects which may result in significantly increasing the wave height. These resultant waves which strike the shoreline can present significant hazards to life and property in populated regions.

An important coastal effect of tsunamis is the dynamic excitation of harbors and bays which can be greatly enhanced by the local characteristics of the embayment and may result in large wave heights

and associated currents. The currents can cause damage to floating and fixed structures inside the bay and harbor. Of course it is the wave runup at the lateral boundaries of a harbor or bay which can bring about considerable damage through the inundation of coastal areas.

As an illustration of harbor oscillations induced by tsunamis the tide gage recordings at Honolulu (Hawaii) and Mokuoloe Island (near Oahu Island, Hawaii) are presented in Fig. 1.1 for both the 1960 Chile Tsunami and the 1964 Alaska Tsunami. Those records show that for a given tsunami, the wave response at two rather closely spaced stations (less than 50 km apart) can be widely different in both the wave amplitude and the apparent frequency distribution of the energy. They also show that, for a given location, the shape of the oscillations tends to be similar for different tsunamis suggesting that the response of the local waters is of prime importance in defining the wave characteristics.

A better understanding of the wave dynamics inside a bay is motivated in two ways. First, it can lead to better protection of the coastal communities against tsunami action. Second, it may provide a means to determine in a reliable manner the incident wave outside the harbor or bay. This may in turn yield useful information concerning the deep water wave signature of the tsunami which is still largely unknown.

1.1 Objectives and Scope

The objective of this study is to investigate both theoretically and experimentally the process of excitation of harbors by transient nonlinear long waves which may result in nonlinear oscillations. The emphasis is placed on some interactive affects usually neglected

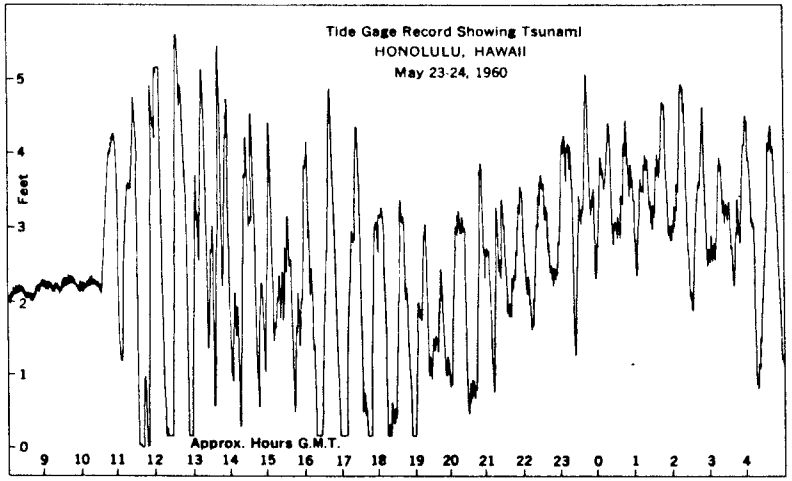

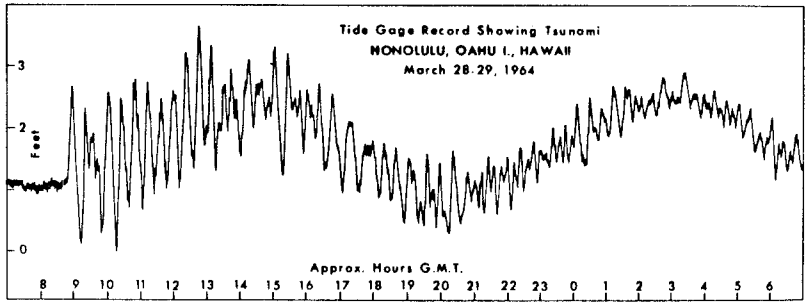

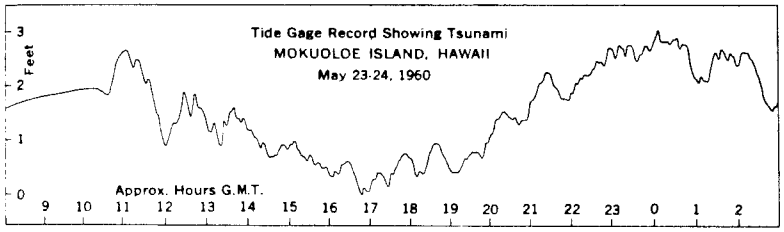

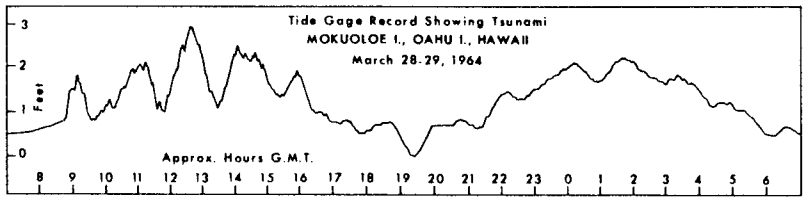

Fig. 2.1 Tide gage record at Honolulu and Mokuoloe Island, Oahu I., Hawaii, for the 1960 Chile Tsunami and the 1964 Alaska Tsunami.

in the linear inviscid approach; these include: convective nonlinearities, frequency dispersion, and viscous dissipation. Two major aspects of this investigation have evolved:

(i) The first deals with the waves induced in a closed rectangular basin, partially filled with water, by horizontal motions. A wide range of experiments and complementary theoretical results were obtained primarily to study various aspects of boundary friction in a controlled environment where the results could be applied directly to the harbor problem. It became apparent when these studies began that certain nonlinear effects which applied to the oscillations in a closed basin in the shallow water range also could be applied to the waves induced in a harbor. Therefore, these characteristics were studied theoretically and experimentally in some detail.

(ii) The continuous and transient excitations of a harbor is the second (and the most important) aspect investigated. A numerical model was constructed to incorporate the various effects mentioned previously. The experimental investigation of a harbor excited by continuous trains of waves (starting from rest) was restricted to a planform of a simple geometry, namely a long and narrow rectangular harbor with a constant depth. It was felt that a detailed experimental study for this harbor shape could yield information which would lead to fairly general conclusions applicable to more complicated shaped harbors. In this connection, certain dissipation mechanisms peculiar to the harbor problem were investigated experimentally. Most important of these in view of tsunamis is the energy loss at the entrance of the harbor for both a fully open and a partially closed harbor. The transient excitation

of a harbor was also investigated experimentally and extended to other harbor geometries.

In Chapter 2 previous studies of the long wave dynamics in closed basins and harbors are surveyed. A theoretical analysis is presented in Chapter 3. It consists of the derivation of the long wave equations applied to the present study, the development of various solutions for waves in a closed rectangular basin caused by a to-and-fro motion of the basin, a linear analytical solution including various forms of dissipation for the wave-induced oscillations in a rectangular harbor and the development of a general numerical solution for the transient wave dynamics in a harbor with arbitrary planform and variable depth and nonlinear wave excitation and response. The experimental equipment and procedures are described in Chapter 4. The results of the investigation for the closed basin and for the harbor are presented in Chapters 5 and 6, respectively. Applications of the study to prototype situations are discussed in Chapter 7 and major conclusions are presented in Chapter 8.

(THIS PAGE IS BLANK, DUE TO ERROR IN PAGINATION)

CHAPTER 2

LITERATURE SURVEY

In this chapter the literature which pertains to this study will be reviewed. It is divided into two major parts: the first deals with nonlinear oscillations in closed basins, and the second deals with the response of bays and harbors to transient waves.

2.1. Nonlinear Oscillations in Closed Basins

In this section only investigations related to nonlinear features which are associated with long waves induced in a closed basin by horizontal motions are reviewed.

Verhagen and Wijngaarden (1965) performed a theoretical and an experimental study of the steady state finite amplitude forced oscillations of a fluid in a shallow rectangular container. They used the nonlinear, nondispersive shallow water wave equations and derived their solution from the method of characteristics and by allowing a discontinuity to occur somewhere along the wave profile at resonance and applying shock relationships across it. The experiments showed differences with the results of their analysis due perhaps to important effects which were neglected, such as frequency dispersion and dissipation.

Chester (1968) recognized the importance of these factors and derived a steady state solution for the waves induced in a closed basin by horizontal motions including the effects of dispersion and dissipation. The method of solution was based on the representation of the unknown quantities by Fourier series which were substituted into the equations and truncated for the numerical calculations. This led to an algebraic

system of nonlinear equations to be solved for the Fourier components. Chester found that, although nonlinear effects remained important near resonance, dispersion introduced higher harmonics in the spectrum of the solution. When combined with viscous dissipation these effects tended to smooth the shape of the shock predicted by the nonlinear shallow water wave theory. Chester and Bones (1968) performed a series of experiments with a tank moved horizontally with a sinusoidal excursion near resonant frequencies. They found reasonably good agreement with the theoretical results of Chester (1968). In particular they were able to characterize and quantify to some extent the effects of each mechanism: nonlinearities, dispersion and dissipation. This study is important in the context of long wave excitation of harbors because the three effects observed in closed basins are expected to have similar characteristics (at least qualitatively) for the harbor problem.

Finally, Rogers and Mei (1975) derived an analytical expression for one dimensional standing gravity waves in a shallow basin from the equations of Boussinesq. They showed that as the Stokes parameter increased the standing wave changed from one with the usual sinusoidal shape to a solitary wave moving to-and-fro within the basin.

None of these studies investigated the transient features associated with the excitation of the basin. This aspect is important in the context of the tsunami problem and will be studied in some detail in this investigation.

2.2 The Response of Bays and Harbors to Transient Waves

In this section only the more recent studies of wave induced oscillations in harbors and bays are discussed. For a complete survey

of the work done in this area the reader is referred to Raichlen (1966), Wilson (1972), Miles (1974) and Raichlen (1976). Various aspects of the tsunami problem, including some coastal effects, have been reviewed by Van Dorn (1965). A recent survey can also be found in Hwang (1979).

The following discussion is divided into three parts. The linear inviscid approach is discussed first in Section 2.3.1. A few papers which specifically discuss viscous effects associated with harbor oscillations are presented in Section 2.3.2. Finally, the nonlinear approach is discussed in Section 2.3.3.

2.2.1 Linear Inviscid Solutions

A significant amount of work has been done in the past on the steady state characteristics of the linear inviscid response of harbors to harmonic incident waves. In all of these studies the flow is assumed to be irrotational and the boundary conditions at the water surface are linearized. These simplifications lead to the Helmholtz equation which must be solved in the region of interest.

An important contribution to the dynamics of harbor oscillations was introduced by Miles and Munk (1961) who treated the problem of a rectangular harbor connected directly to the open sea by including the effect of energy radiation from the harbor mouth to the open sea. This effect limits the maximum wave amplitude within the harbor for the inviscid case to a finite value even at resonance. They found that in the absence of viscous dissipation the narrowing of the harbor entrance leads to an enhancement in harbor surging of resonance. This result, termed "harbor paradox" by the authors, was found later to become invalid if viscous dissipation is introduced.

Ippen and Raichlen (1962) investigated both analytically and experimentally the wave induced oscillations in a smaller rectangular harbor connected to a larger highly reflective rectangular wave basin. Because of the high degree of coupling between the two basins the response characteristics of the harbor as a function of incident wave period were radically different from a similar prototype harbor connected to the open sea. The former was characterized by a large number of closely spaced spikes as opposed to the latter that would have discrete resonant modes of oscillations. This study emphasized the need for efficient wave filters and wave absorbers in a wave basin for the proper simulation of the open sea conditions in laboratory.

Ippen and Goda (1963) also studied, both theoretically and experimentally, the problem of a rectangular harbor connected to the open sea. Fairly good agreement was found between the theory and the experiments conducted in a wave basin (2.75 m wide and 3.35 m long) where satisfactory wave energy dissipators were installed around the boundary to simulate the open sea.

Hwang and Tuck (1970) and Lee (1971) independently developed analytical methods to solve the harbor resonance problem for harbors of arbitrary shape and constant depth connected to the open sea and excited by continuous wave trains. They both used integral techniques, but the former investigators considered only one fluid domain while the latter considered two regions, the outside ocean and the inside harbor with a matching procedure used at the harbor entrance. In addition, Lee (1971) performed careful experiments in the laboratory for various simple geometric shapes as well as for a more complicated configuration (Long Beach Harbor). For all cases the agreement between the theory and the

experiments was good. All the experiments were done in deep water using small amplitude incident waves. A subsequent theoretical and experimental study was conducted by Lee and Raichlen (1972) extending the results of Lee (1971) to harbors composed of connected basins. It was found in some cases that the coupling of the main basin in a harbor to smaller ones can aggravate the resonance problem instead of improving it.

Olsen and Hwang (1971) considered a harbor with arbitrary planform and variable depth. They used a finite difference model for the harbor and at some distance outside the entrance this model was matched to an open sea integral solution to determine the response defined in terms of the power density. They applied their model to a harbor in Hawaii where field measurements were available and reproduced reasonably well the trend of the distribution of energy.

Chen and Mei (1974) developed a hybrid finite-element model applicable to general linear diffraction problems. Two regions were considered. A finite element formulation was used in the interior region. The solution in the outer region was represented as the superposition of the incident wave system and the radiated wave system. The latter was represented as a series solution which satisfied the radiation condition automatically. A matching procedure, integrated into the variational formulation of the global problem, was applied at the boundary between the two regions.

Miles and Lee (1975) presented an approximate analytical method to determine the characteristics of the oscillations in a harbor at the Helmholtz mode for the case of an arbitrary planform and variable

depth. Their method applies reasonably well for cases where most of the kinetic energy of the wave oscillation remains concentrated mainly near the mouth.

Once the transfer function of the harbor at a particular location has been computed by one of the previously mentioned methods the transient response of the harbor at that location can be obtained for any incident transient wave using Fourier techniques, assuming the process to be entirely linear. This approach was chosen by various investigators to study the transient aspects related to harbor oscillation.

Carrier and Shaw (1969) used this method to investigate theoretically the response of a narrow mouthed rectangular harbor, with and without an entrance channel, to an incident wave which had the form of a pulse. They found oscillations with a relatively long duration compared to the duration of the incident wave; this shows the effect of resonance where a part of the energy is radiated out of the harbor while a part remains trapped inside for some time. An entrance channel coupled to the harbor in this inviscid treatment increased the energy trapping.

Lepelletier (1978) performed a set of transient experiments in deep water and intermediate depths for a fully open rectangular harbor and compared the experimental results with the linear inviscid theory. The incident wave looked like an impulse followed by several small oscillatory waves. Good agreement was obtained between the experiments and the linear theory except for the decay rate; this was larger for the experiments indicating effects of viscous dissipation. In particular the energy spectra for the experiments obtained from measurements at the backwall of the harbor agreed reasonably well with the corresponding

spectra obtained from the linear theory and were quite different from the spectra of the incident waves. The good agreement between linear theory and experiments even for large finite amplitude incident waves suggests that the response of the harbor, under certain conditions, may remain linear even in extreme cases.

Houston (1978) used a finite element numerical model based upon the method developed by Chen and Mei (1974) to calculate the interaction of tsunamis with the Hawaiian Islands. Using a numerical model for the generation and deep ocean propagation of the tsunami and data of ground uplift for the 1960 Chilean tsunami and for the 1964 Alaskan tsunami, Houston (1978) determined deep ocean wave shapes for these two tsunamis. These waves were used as input to the finite element model and the tsunamis were propagated to shore. Good agreement was found with tide gage records of these tsunamis at several locations around the Hawaiian Islands. Such good agreement indicates the possible good behavior, under certain conditions, of a linear theory to predict the interactions of a tsunami with coastal regions.

Very few studies have tackled the direct transient harbor problem in which the equations are solved with a time marching procedure. One difficulty stems from the semi-infinite domain in the outer region. For purposes of computation this outer region must be limited by an artificial boundary at some finite distance from the harbor. This in turn introduces numerical reflections of the radiated wave at the boundary which may affect the response in the bay. Mungal and Reid (1978) circumvented this problem by applying a condition at this boundary which becomes valid far enough from the radiation source.

They were able, using this method, to solve the direct linear transient problem of diffraction of a tsunami by an island or a group of islands.

2.2.2 Effects of Viscous Dissipation on Harbor Oscillations

An important aspect of the study of the interaction of tsunamis with bays and harbors is the role of dissipation in mitigating the response. It is of interest in this section to review the various studies which pertain to the influence of dissipation on resonance in harbors and bays. The main emphasis in this section will be the effect of a restricted entrance on the response. This is because it has been recognized that this form of dissipation is most effective in reducing the harbor and bay response in some situations.

Ito (1970) investigated numerically the effect of a narrow passage between two breakwaters in reducing the response of Ofunato Bay in Japan to tsunamis. He employed the linear nondispersive long wave equations and assumed the existence of the quadratic head loss across the narrow passage of the form:

$$\Delta\eta = \frac{1}{2}\frac{f_e}{g}\, u|u| \qquad (2.1)$$

where g is the acceleration of gravity, u is the velocity at the entrance and f_e is the separation loss coefficient which he assumed equal to 1.5 from the results of one dimensional hydraulics. The outer sea was replaced by a channel of constant width and depth. This computation indicated that a breakwater built in 1967 at Ofunato to mitigate tsunami hazards had contributed to reducing the tsunami of May 16, 1968 at the bay head to less than half the value it would have been without the breakwater.

Horikawa and Nishimura (1970) performed some laboratory experiments to investigate the efficiency of breakwaters in reducing wave induced oscillations in bays. They found that the reduction of the overall bay response increased with smaller openings at the bay mouth. They also analyzed tsunami records from Ofunato Bay before and after the construction of the breakwater mentioned previously. The frequency response curves they obtained from these records showed a significant attenuation of the wave inside the bay for the lowest mode of oscillation ($T \simeq 37$ min) of the bay whereas the amplitude of the second mode ($T \simeq 15$ min) was hardly affected by the presence of the breakwater.

Using analytical arguments Mei, Liu and Ippen (1976) modified the form of Equation (2.1) for the case of unsteady flow. They added an inertia term on the right hand side of Equation 2.1. They showed that when the entrance loss coefficient associated with the incoming flow differs from that associated with the outgoing flow a nonzero mean velocity is induced through the opening.

Ünlüata and Mei (1975) performed an analytical study on the effect of entrance dissipation on the steady state response of a partially closed rectangular harbor. Assuming a constant entrance loss coefficient f_e they derived an analytical solution which showed the effectiveness of entrance dissipation for small entrance gaps.

Miles and Lee (1975) compared the relative effects of entrance dissipation and turbulent boundary friction for the Helmholtz mode and concluded that the efficiency of the former dissipative source in reducing amplification is higher by several orders of magnitude than the latter.

In all of these studies the value of the separation loss coefficient f_e was assumed. One of the purposes of this present investigation is to measure this coefficient experimentally and to study the relative importance of several other sources of dissipation in the harbor, both in laboratory and prototype situations.

2.2.3 Nonlinear Solutions

Leendertse (1967) developed a finite difference numerical model for the propagation of nonlinear nondispersive long-period waves in an arbitrary shaped basin including nonlinear boundary friction. The results agreed well with certain field measurements; however, the water surface time history at a given location must be specified. Similar models were developed by Houston and Garcia (1978), Kawahara et al. (1978) and Chen et al. (1978) to investigate the interaction of tsunamis with coastal regions. Houston and Butler (1979) developed a model which in addition calculates land inundation of a tsunami with reasonably good agreement with some available field data.

Chwang and Wu (1976) investigated in detail the effects of nonlinearities and dispersion associated with the propagation of a cylindrical weakly nonlinear dispersive wave towards a cylindrical island followed by a reflection from the island and propagation away from it. They showed, by comparing their numerical results to experiments, that the wave evolution for the conditions they considered was best described by a nonlinear dispersive theory. Their results could conceivably be applied to the case of an incoming wave propagating along a long trapezoidal bay with a nonzero depth at the bay head.

Rogers and Mei (1978) reported the results of an investigation of the nonlinear resonant excitation of a long and narrow bay for steady

state conditions. The primary purpose was to investigate the importance of the effects of convective nonlinearities in the equation of motion in affecting the response of this simple geometric shape at resonance. They used the weakly nonlinear Boussinesq equations inside the bay and assumed that the wave system outside the bay was governed by linear equations. Their numerical results showed that near resonance higher harmonics are generated with a corresponding reduction in the magnitude of the first harmonic. They also found that nonlinear interaction could generate "secondary" resonant features not predicted by the linear theory. They suggested from their study that the effect of nonlinearities could result in an enhancement of resonance due to the generation of these closely spaced "secondary" resonant peaks. Experiments were performed by Rogers and Mei (1978) for three different bay lengths (corresponding to the first three resonant modes). The relative importance of entrance loss for the fully open harbors and boundary layer dissipation was estimated. They found that for short bay lengths, nonlinearities remained small and entrance dissipation was the most important source of damping. The reverse was found for longer bay lengths with the relative importance of nonlinearities increasing with the harbor length. However, their experiments were performed in the intermediate depth range and the conditions were outside the range of validity of the Boussinesq model: this tends to invalidate certain comparisons made between their experiments and their numerical results. Nevertheless, this appears to be the only past study where the importance of the effects of nonlinearities and dispersion in the harbor oscillation problem was investigated in some detail.

(THIS PAGE IS BLANK, DUE TO ERROR IN PAGINATION)

CHAPTER 3

THEORETICAL ANALYSIS

The analysis of the transient excitation of a rectangular basin and the transient wave-induced oscillations of an arbitrary shaped harbor with variable depth are presented in this chapter. The main features of this analysis are the inclusion of the convective nonlinearities, dispersion and various sources of dissipation to assess their relative importance in prototype and laboratory situations.

The viscous long wave equations in two horizontal dimensions for a variable depth are derived in Section 3.1. These equations are used in Section 3.2 for the analysis of the transient excitation of a rectangular basin, including a numerical solution of the nonlinear transient problem, an analytical solution of the corresponding linearized problem and a first order analytical nonlinear solution for the free steady state oscillations. Special attention is given in Section 3.3 to the various sources of dissipation affecting harbor oscillations in the laboratory, as well as in the field, by using a simple geometrical shape and a linearized model; this model will be used later for the experimental determination of the entrance loss and leakage coefficients and as a basis of comparison with the experiments. Finally, a numerical model for the treatment of the transient wave-induced oscillations of an arbitrary shaped harbor with variable depth is presented in Section 4. This model includes the effects of convective nonlinearities, dispersion and also some of the sources of dissipation discussed in Section 3.3.

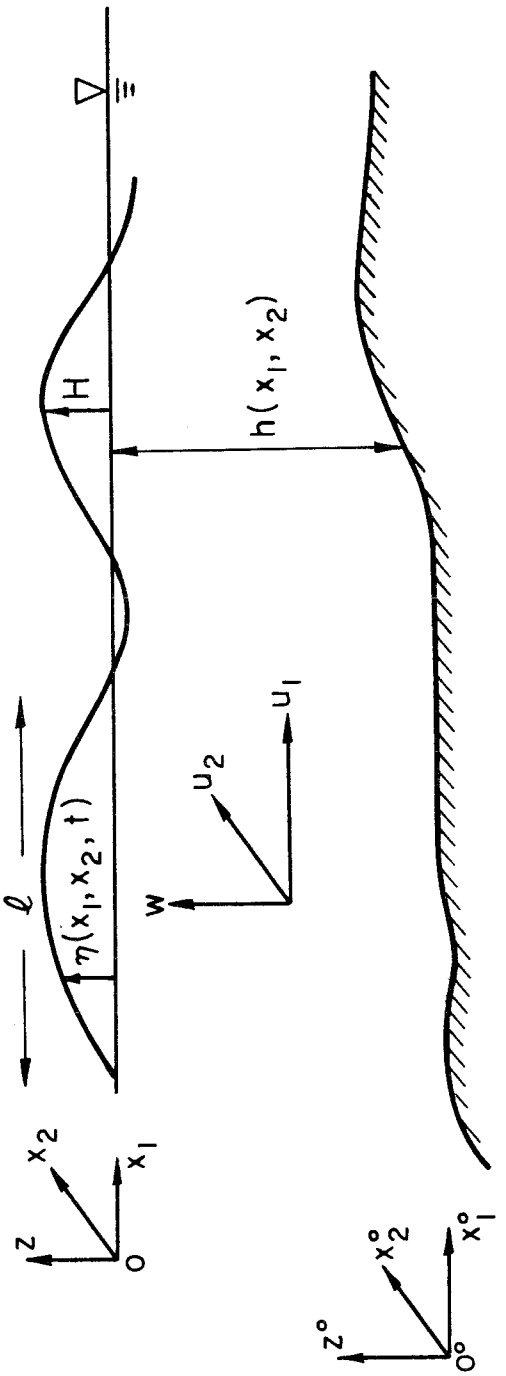

Fig. 3.1.1 Definition sketch for the coordinate system.

3.1 Derivation of the Long Wave Equations in Two Horizontal Dimensions and for Variable Depth Including the Effect of Viscous Bottom Friction

A definition sketch for the coordinate systems is presented in Figure 3.1.1. The unknown quantities are the wave amplitude $\eta(x_1,x_2,z,t)$, the pressure $p(x_1,x_2,z,t)$ and the velocity components $u_1(x_1,x_2,z,t)$, $u_2(x_1,x_2,z,t)$, $w(x_1,x_2,z,t)$ in the two horizontal x_1 and x_2 directions and in the vertical z direction, respectively, in the coordinate system $(0,x_1,x_2,z)$. The following assumptions are made:

(i) The fluid density ρ is constant.

(ii) The kinematic viscosity ν of the fluid is small (but not negligible everywhere).

(iii) The characteristic length ℓ of the wave in the x_1 direction is of the same order of magnitude as in the x_2 direction and is large compared to the depth.

(iv) The characteristic height H of the wave elevation is small (although not infinitesimal) compared to the depth.

(v) The rate of change of the depth h with x_1 and x_2 is small.

The last four assumptions will be stated more precisely later. In addition, it is assumed that the frame of reference $(0,x_1,x_2,z)$ is non-Newtonian and moves in a translational motion which is defined by the velocity components $[V_1^\circ(t),V_2^\circ(t),0]$ in the Newtonian frame $[0^\circ,x_1^\circ,x_2^\circ,z^\circ]$. (This slightly more general feature has direct application to the closed basin excitation problem).

Most of the previous studies have used the potential theory to derive the inviscid long wave equations (e.g., Whitham, 1974). In the present case, however, the presence of viscous forces introduces rotationality into the flow and a different formulation must be used.

The continuity and momentum equations are given by:

$$\frac{\partial u_j}{\partial x_j} + \frac{\partial w}{\partial z} = 0 \tag{3.1.1}$$

$$\frac{\partial u_i}{\partial t} + u_j \frac{\partial u_i}{\partial x_j} + w \frac{\partial u_i}{\partial z} = -\frac{1}{\rho}\frac{\partial p}{\partial x_i} - \frac{\partial V_i^{\circ}}{\partial t} + \nu\left(\frac{\partial^2 u_i}{\partial x_j \partial x_j} + \frac{\partial^2 u_i}{\partial z^2}\right) \quad i=1,2 \tag{3.1.2}$$

$$\frac{\partial w}{\partial t} + u_j \frac{\partial w}{\partial x_j} + w \frac{\partial w}{\partial z} = -\frac{1}{\rho}\frac{\partial p}{\partial z} - g + \nu\left(\frac{\partial^2 w}{\partial x_j \partial x_j} + \frac{\partial^2 w}{\partial z^2}\right) \tag{3.1.3}$$

where g is the acceleration of gravity and t the time; all the other quantities have been defined previously. In order to abbreviate the notations in such equations, the Einstein summation convention for indices 1 and 2 has been used; it will be employed throughout this subsection.

The boundary conditions are:

(i) zero velocity at the bottom:

$$u_i = 0, \quad i = 1,2 \qquad z = -h \tag{3.1.4}$$

$$w = 0 \qquad z = -h \tag{3.1.5}$$

(ii) kinematic boundary condition at the surface:

$$\frac{\partial \eta}{\partial t} + \frac{\partial \eta}{\partial x_j} u_j = w \qquad z = \eta \tag{3.1.6}$$

(iii) dynamic boundary conditions at the surface:

$$p = 0 \qquad z = \eta \tag{3.1.7}$$

$$\frac{\partial u_i}{\partial z} = 0 \qquad z = \eta \qquad i=1,2 \tag{3.1.8}$$

Eq. (3.1.8) expresses the fact that no shear force takes place at the free surface.

At this point it is anticipated (to be confirmed later) that the viscous forces are negligible except near the solid boundary $z = -h$. Therefore, two regions are defined: an interior region near $z = -h$ (also termed the boundary layer region) in which the viscous forces are considered, and an exterior region (also termed the free region) in which the viscous terms are neglected. The analytical procedure consists of deriving the velocity distributions in the exterior region and the interior layer region and, using them along with boundary conditions (3.1.4) through (3.1.8), to simplify the form of Eqs. (3.1.1) through (3.1.3).

The velocity distribution in the boundary layer region in the presence of an unsteady flow has been derived by several authors, e.g., Keulegan (1948), Lin (1957). The derivation of the solution is presented in Appendix A and only the main results are summarized here. Assuming a laminar boundary layer and neglecting the convective non-linearities, the relevant boundary layer equation in the i^{th} direction can be written as:

$$\frac{\partial(u_i^{\ell} - u_i)}{\partial t} = \nu \frac{\partial^2(u_i^{\ell} - u_i)}{\partial z^2} \tag{3.1.9}$$

where $u_i^{\ell}(x_1, x_2, z, t)$ is the i^{th} component of velocity in the interior

region, $u_i(x_1,x_2,-h+\delta_e,t)$ is the i^{th} component of the velocity in the exterior region just outside the boundary layer, and δ_e denotes the boundary layer thickness (see Figure 3.1.2). Considering Eq. (3.1.9) the pertinent boundary conditions are:

$$u_i^{\ell} - u_i = 0 \quad , \quad z \to \infty \tag{3.1.10}$$

$$u_i^{\ell} = 0 \quad , \quad z = -h \tag{3.1.11}$$

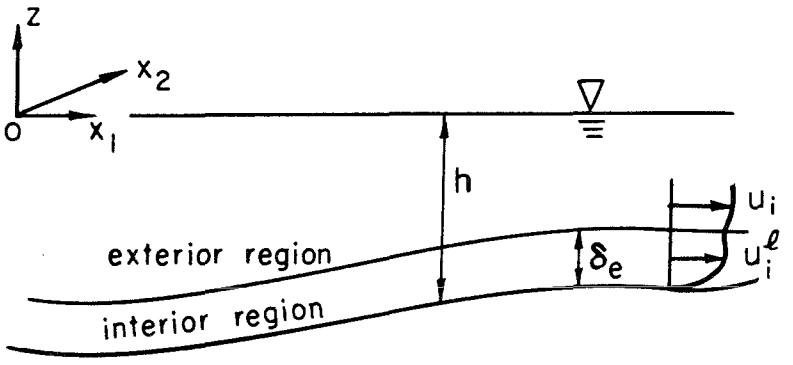

Figure 3.1.2 Definition sketch for the boundary layer in an unsteady flow.

Equation (3.1.9), along with boundary conditions (3.1.10) and (3.1.11), can be solved analytically and the expression for the velocity gradient in the z direction at the bottom is found as:

$$\frac{\partial u_i^{\ell}}{\partial z}(x_1,x_2,-h,t) = \sqrt{\frac{1}{\nu\pi}} \int_0^{\infty} \frac{\frac{\partial}{\partial t} u_i(t-t')}{\sqrt{t'}} \, dt' \tag{3.1.12}$$

where π is 3.14159... and u_i is computed at $z = -h+\delta_e$. An order of magnitude for δ_e can be estimated by considering Eq. (3.1.9) with $z \approx \delta_e$, $t \approx \ell/\sqrt{gh}$. Substituting these values for z and t into Eq. (3.1.9) the expression for δ_e is obtained as:

$$\delta_e \simeq \left(\frac{\nu\ell}{\sqrt{gh}}\right)^{1/2} \tag{3.1.13}$$

In most laboratory conditions $\frac{\delta_e}{h} < 0.01$, so that little error is introduced if the velocity component u_i in Eq. (3.1.12) is computed at $z = -h$ instead of $z = -h+\delta_e$. The validity of the present solution inside the boundary layer, as the wave height ratio H/h becomes finite, can be questioned since the convective terms may no longer be neglected and the flow may become turbulent. These considerations will be further discussed in Section 5.1.

The velocity distribution in the free region is derived as follows: neglecting the viscous terms in Eq. (3.1.2) and (3.1.3) yields the Euler equations. It is well known that the flow derived from these equations remains irrotational if it has been irrotational at some previous time. Therefore, a potential function $\Phi(x_1,x_2,z,t)$ exists such that:

$$u_i = \frac{\partial \Phi}{\partial x_i} \qquad i = 1,2 \tag{3.1.14}$$

$$w = \frac{\partial \Phi}{\partial z} \tag{3.1.15}$$

The proper boundary condition at the bottom for the exterior solution is zero velocity normal to the boundary expressed by:

$$w = -u_i \frac{\partial h}{\partial x_i} \qquad \text{at} \quad z = -h(x,y) \tag{3.1.16}$$

The crucial step consists of normalizing each variable by a characteristic quantity:

$$x_i = \frac{x_i^*}{\ell} \qquad z = \frac{z^*}{h_o} \qquad h = \frac{h^*}{h_o} \qquad t = t^* \frac{\sqrt{gh_o}}{\ell}$$

$$\eta = \frac{\eta^*}{H} \qquad \Phi = \frac{\Phi^*}{\ell\sqrt{gh_o}} \frac{h_o}{H} \qquad p = \frac{p^*}{\rho g h_o}$$

$$V_i^o = \frac{V_i^{o*}}{\sqrt{gh_o}} \frac{h_o}{H} \qquad u_i = \frac{u_i^*}{\sqrt{gh_o}} \frac{h_o}{H} \qquad w = \frac{w^*}{\sqrt{gh_o}} \frac{\ell}{H}$$

where starred symbols represent the original dimensional variables. The parameters H, ℓ and h_o refer to a characteristic wave height, wave length and depth, respectively. The scaling, based on the linear non-dispersive wave theory, is such that all the previously defined dimensionless variables are of order unity (henceforth all the equations will be dimensionless unless specifically stated otherwise).

Three dimensionless parameters emerge from the dimensionless equations:

(i) The nonlinear parameter $\alpha = H/h_o$

(ii) The dispersion parameter $\beta = (h_o/\ell)^2$

(iii) The dissipation parameter $\gamma = \left(1/h_o\right)\left(\frac{\nu\ell}{\pi\sqrt{gh_o}}\right)^{1/2}$

As usual in dealing with long waves it is assumed that $\beta \ll 1$.

The relative importance of the nonlinearities is best measured by the Ursell number $\underline{Ur} = \alpha/\beta$ (after Ursell, 1953); when $\underline{Ur} < 0(1)$ nonlinear effects can be omitted and the linear dispersive dissipative theory (α=0) can be used; when $\underline{Ur} > 0(1)$ the equations are dominated by nonlinearities and the nonlinear nondispersive dissipative theory (β=0)

can be used. When $\underline{Ur} = O(1)$, both nonlinearities and dispersion are important and the weakly nonlinear dispersive dissipative theory must be used.

Rewriting the relevant equations and boundary conditions in dimensionless form one obtains:

(i) The continuity equation:

$$\frac{\partial u_j}{\partial x_j} + \frac{\partial w}{\partial z} = 0 \tag{3.1.17}$$

(ii) The dynamic boundary condition at the free surface:

$$p = 0 \qquad z = \alpha\eta \tag{3.1.18}$$

(iii) The kinematic boundary conditions at the free surface and at the bottom in the exterior region:

$$w = \frac{\partial \eta}{\partial t} + \alpha u_j \frac{\partial \eta}{x_j} \tag{3.1.19}$$

$$w = -u_j \frac{\partial h}{\partial x_j} \qquad z = -h(x,y) \tag{3.1.20}$$

where it is assumed that $\partial h/\partial x_j = O(1)$, or equivalently, that the rate of change of depth h^* with x_i^* is $O(h_o/\ell)$

(iv) The integrated momentum equation in the x_i direction averaged through the depth:

$$\int_{-h}^{\alpha\eta} \left[\frac{\partial u_i}{\partial t} + \alpha u_j \frac{\partial u_i}{\partial x_j} + \alpha w \frac{\partial u_i}{\partial z} + \frac{1}{\alpha}\frac{\partial p}{\partial x} + \frac{\partial V_i^o}{\partial t} - \pi\gamma^2\beta \frac{\partial^2 u_i}{\partial x_j \partial x_j}\right] dz$$

$$= -\gamma \int_0^\infty \frac{\frac{\partial}{\partial t} u_i(x_1, x_2, -h, t-t')dt'}{\sqrt{t'}} \tag{3.1.21}$$

where Eqs. (3.1.8) and (3.1.12) have been used.

(v) The momentum equation in the z direction:

$$\frac{1}{\alpha}\frac{\partial p}{\partial z} + \frac{1}{\alpha} = -\beta\frac{\partial w}{\partial t} - \alpha\beta\, u_j\frac{\partial w}{\partial x_j} - \alpha\beta\, w\frac{\partial w}{\partial z} + \pi\gamma^2\beta\left(\beta\frac{\partial^2 w}{\partial x_j \partial x_j} + \frac{\partial^2 w}{\partial z^2}\right) \tag{3.1.22}$$

(vi) The relationship between the velocity components and the velocity potential:

$$u_i = \frac{\partial \Phi}{\partial x_i} \qquad i = 1,2 \tag{3.1.23}$$

$$w = \frac{1}{\beta}\frac{\partial \Phi}{\partial z} \tag{3.1.24}$$

The assumptions made initially can now be stated more precisely by imposing that the three parameters α, β, γ be of the same small order of magnitude:

$$O(\alpha) = O(\beta) = O(\gamma) < O(1) \tag{3.1.25}$$

In the subsequent algebraic manipulations only terms of the order of magnitude α, β, γ will be retained. It can be first noticed that, by inspection of Eqs. (3.1.19) and (3.1.20) the viscous terms arising outside the boundary layer are at most $O(\gamma^2)$ and thus can be neglected when compared to the viscous term arising from the boundary layer region which is $O(\gamma)$. A differential equation for Φ alone is obtained by substituting Eq. (3.1.23) and (3.1.24) into Eq. (3.1.17) as:

$$\beta\frac{\partial^2 \Phi}{\partial x_j \partial x_j} + \frac{\partial^2 \Phi}{\partial z^2} = 0 \tag{3.1.26}$$

An expansion for Φ , suggested by the form of Eq. (3.1.26), is assumed in the form:

$$\Phi = \Phi_o(x_1,x_2,z,t) + \beta\Phi_1(x_1,x_2,z,t) + O(\beta^2) \tag{3.1.27}$$

from Eq. (3.1.24) $\partial\Phi/\partial z = O(\beta)$ since $w = O(1)$ from the previous choice on the nondimensionalization of the vertical velocity component. This implies:

$$\Phi_o(x_1,x_2,z,t) = \Phi_o(x_1,x_2,t) \tag{3.1.28}$$

Substituting Eq. (3.1.27) into (3.1.26) and using boundary condition at the bottom (3.1.20) a proper form for Φ results in:

$$\Phi = \Phi_o(x_1,x_2,t) + \beta[\tilde{\Phi}_1(x_1,x_2,t) - z\frac{\partial}{\partial x_j}(h\frac{\partial\Phi_o}{\partial x_j}) - \frac{z^2}{2}\frac{\partial^2\Phi_o}{\partial x_j\partial x_j}] + O(\beta^2) \tag{3.1.29}$$

The expressions for the velocity components are as follows:

$$u_i = \frac{\partial\Phi}{\partial x_i} = \frac{\partial\Phi_o}{\partial x_i} + \beta[\frac{\partial\tilde{\Phi}_1}{\partial x_i} - z\frac{\partial^2}{\partial x_j\partial x_i}(h\frac{\partial\Phi_o}{\partial x_j}) - \frac{z^2}{2}\frac{\partial^3\Phi_o}{\partial x_j\partial x_j\partial x_i}] + O(\beta^2) \tag{3.1.30}$$

$$w = \frac{1}{\beta}\frac{\partial\Phi}{\partial z} = -[\frac{\partial}{\partial x_j}(h\frac{\partial\Phi_o}{\partial x_j}) + z\frac{\partial^2\Phi_o}{\partial x_j\partial x_j}] + O(\beta^2) \tag{3.1.31}$$

Defining the average horizontal velocity component $\bar{u}_i$ as:

$$\bar{u}_i = \frac{1}{(h+\alpha\eta)}\int_{-h}^{\alpha\eta} u_i dz = \frac{\partial\Phi_o}{\partial x_i} + O(\beta) \quad , \tag{3.1.32}$$

the continuity equation (3.1.17) can be integrated through the depth and becomes, after using the kinematic boundary conditions (3.1.19) and (3.1.20):

$$\frac{\partial\eta}{\partial t} + \frac{\partial}{\partial x_j}[(h+\alpha\eta)\frac{\partial\bar{u}_j}{\partial x_j}] = 0 \tag{3.1.33}$$

One notices that Eq. (3.1.33) is exact and does not require for its derivation a knowledge of the depthwise velocity profile.

The integration of Eq. (3.1.21) must be performed in two steps. First, the pressure distribution is found by integrating Eq. (3.1.22) in the vertical direction from $z_1 = z$ to $z_2 = \alpha\eta$ and using dynamic boundary condition (3.1.18) along with Eqs. (3.1.30) and (3.1.31).

$$\frac{p}{\alpha} = \eta - \frac{z}{\alpha} - \beta\left[z \frac{\partial^2(h\bar{u}_j)}{\partial t\, \partial x_j} - \frac{z^2}{2} \frac{\partial^2 \bar{u}_j}{\partial t \partial x_j}\right] + O(\beta^2, \alpha\beta, \gamma^2) \qquad (3.1.34)$$

Finally, the depth-averaged momentum equation is obtained by integrating Eq. (3.1.21) using Eqs. (3.1.30), (3.1.31), (3.1.32), and (3.1.34), and by noticing from Eq. (3.1.32) that $\partial\bar{u}_i/\partial x_j = \partial\bar{u}_j/\partial x_i + O(\beta)$:

$$\begin{aligned} &\frac{\partial \bar{u}_i}{\partial t} + \alpha \bar{u}_j \frac{\partial \bar{u}_i}{\partial x_j} + \frac{\partial \eta}{\partial x_i} + \frac{\partial V_i^o}{\partial t} \\ &\quad + \beta\left[-\frac{h}{2} \frac{\partial^3(h\bar{u}_j)}{\partial t\, \partial x_j \partial x_i} + \frac{h^2}{6} \frac{\partial^3 \bar{u}_i}{\partial t\, \partial x_j \partial x_j}\right] \\ &\quad + \frac{\gamma}{h} \int_0^\infty \frac{\partial}{\partial t} \frac{\bar{u}_i(t-t')}{\sqrt{t'}}\, dt' = O(\alpha\beta, \beta^2, \gamma\beta, \gamma^2) \qquad i = 1,2 \qquad (3.1.35) \end{aligned}$$

Equations (3.1.33) and (3.1.35) are the primary equations used in the viscous modeling of long wave dynamics in two horizontal dimensions in a translating frame of reference. The unknown quantities are the wave elevation $\eta(x_1, x_2, t)$ and the averaged potential velocities in the horizontal directions $\bar{u}_1(x_1, x_2, t)$ and $\bar{u}_2(x_1, x_2, t)$. One would like to find an approximate form for the viscous term in Eq. (3.1.35) which would be more amenable to numerical treatment. Equation (3.1.35) is first rewritten in dimensional form as:

$$\frac{\partial \bar{u}_i^*}{\partial t^*} + \bar{u}_j^* \frac{\partial \bar{u}_i^*}{\partial x_j^*} + g \frac{\partial \eta^*}{\partial x_i^*} + \frac{\partial V_i^{**}}{\partial t^*}$$

$$+ \left[- \frac{h^*}{2} \frac{\partial^3 (h^* \bar{u}_j^*)}{\partial t^* \partial x_j^* \partial x_i^*} + \frac{h^{*2}}{6} \frac{\partial^3 \bar{u}_j^*}{\partial t^* \partial x_j^* \partial x_j^*} \right] + \frac{\tau_i^*}{\rho h^*} = 0 \qquad i = 1,2 \tag{3.1.36}$$

where τ_i^* is the component of the shear stress force in the x_i direction at the bottom, and, in the case of shear laminar friction, is equal to:

$$\frac{\tau_i^*}{\rho h^*} = \frac{1}{h^*} \left(\frac{\nu}{\pi}\right)^{1/2} \int_0^\infty \frac{\partial}{\partial t^*} \frac{\bar{u}_i^*(t^* - t'^*)}{\sqrt{t'^*}} \, dt'^* \tag{3.1.37}$$

In order to simplify Eq. (3.1.37), a functional form for the velocity must be assumed. Since the equations are to be applied to oscillation problems, the velocity can be chosen sinusoidal in time with circular frequency σ:

$$\bar{u}_i^* = U_i^* \cos \sigma t^* \qquad i = 1,2$$

An equivalent expression for the laminar shear term is sought in the form:

$$\frac{\tau_i^*}{\rho h^*} = C^* \bar{u}_i^* \tag{3.1.38}$$

The constant C^* is found by equating the mean rate of energy dissipated through laminar friction using Eqs. (3.1.37) and (3.1.38), respectively. (See Appendix A for details of this derivation.) The result gives:

$$\frac{\tau_i^*}{\rho h^*} = \frac{1}{h^*} \left(\frac{\nu\sigma}{2}\right)^{1/2} \bar{u}_i^* \tag{3.1.39}$$

From Eqs. (3.1.33), (3.1.36), and (3.1.39), the simplified form for the viscous long wave equations can be written in dimensionless form as:

$$\frac{\partial \eta}{\partial t} + \frac{\partial}{\partial x_j}\left[(h+\alpha\eta)\,\bar{u}_j\right] = 0 \tag{3.1.40}$$

$$\frac{\partial \bar{u}_i}{\partial t} + \alpha\,\bar{u}_j\frac{\partial \bar{u}_i}{\partial x_j} + \frac{\partial \eta}{\partial x_i} + \frac{\partial V_i^o}{\partial t} + \beta\left[-\frac{h}{2}\frac{\partial^3 (h\,\bar{u}_j)}{\partial t\,\partial x_j \partial x_i} + \frac{h^2}{6}\frac{\partial^3 \bar{u}_i}{\partial t\,\partial x_j \partial x_j}\right] + \frac{\gamma_s}{h}\bar{u}_i = O(\alpha\beta,\beta^2,\gamma\beta,\gamma^2),$$

$$i = 1,2 \tag{3.1.41}$$

where $\alpha = \frac{H}{h_o}$, $\beta = \left(\frac{h_o}{\ell}\right)^2$, $\gamma_s = \left(\frac{\nu\sigma}{2}\right)^{1/2}\frac{\ell}{h_o\sqrt{gh_o}}$

The form of the dissipation term in Eq. (3.1.41) is accurate for a sinusoidal motion. It is expected to yield a good approximation to the exact dissipation term in the case of an oscillatory flow dominated by a single harmonic with frequency σ. If the wave energy is distributed over a wide range of frequencies, then the dissipation term in Eq. (3.1.41) can only yield an order of magnitude for the actual dissipation; fortunately, as seen in the expression for γ_s, the dissipation coefficient γ_s varies like the square root of the frequency.

Equations (3.1.40) and (3.1.41) will be used to solve the basin excitation problem in Section 3.2.

In the following derivation it is assumed that the frame of reference is again Newtonian, i.e., $\underset{\sim}{V}^o = 0$. Wu (1979) proposed an alternative form for Eqs. (3.1.40) and (3.1.41) to enhance their numerical treatment.

Following Wu's derivation the average velocity potential function $\overline{\Phi}$ is defined as:

$$\overline{\Phi} \equiv \frac{1}{(h+\alpha\eta)} \int_{-h}^{\alpha\eta} \Phi \, dz \tag{3.1.42}$$

Also, the pseudo-velocity component $\tilde{u}_i$ is defined as:

$$\tilde{u}_i \equiv \frac{\partial \overline{\Phi}}{\partial x_i} \qquad i = 1,2 \tag{3.1.43}$$

The difference between $\tilde{u}_i$ and $\overline{u}_i$ is obtained using Eqs. (3.1.29), (3.1.30), (3.1.42), and (3.1.43) as:

$$\tilde{u}_i - \overline{u}_i = \beta\left[\frac{1}{2}\frac{\partial h}{\partial x_i}\frac{\partial}{\partial x_k}\left(h\frac{\partial \Phi_o}{\partial x_k}\right) - \frac{h}{3}\frac{\partial h}{\partial x_i}\frac{\partial^2 \Phi_o}{\partial x_k \partial x_k}\right] + O(\alpha\beta,\beta^2) \tag{3.1.44}$$

Or, since $\partial\Phi_o/\partial x_i = \overline{u}_i + O(\beta)$ from Eq. (3.1.32):

$$\overline{u}_i = \frac{\partial \overline{\Phi}}{\partial x_i} - \beta\left[\frac{1}{2}\frac{\partial h}{\partial x_i}\frac{\partial}{\partial x_k}\left(h\frac{\partial \overline{\Phi}}{\partial x_k}\right) - \frac{h}{3}\frac{\partial h}{\partial x_i}\frac{\partial^2 \overline{\Phi}}{\partial x_k \partial x_k}\right] + O(\alpha\beta,\beta^2) \tag{3.1.45}$$

Substituting Eq. (3.1.45) into Eqs. (3.1.40) and (3.1.41), an equivalent form for the continuity equation, valid up to order α, β, is obtained as:

$$\frac{\partial \eta}{\partial t} + \frac{\partial}{\partial x_j}\left[(h+\alpha\eta)\,\frac{\partial \bar{\Phi}}{\partial x_j}\right]$$

$$= \beta\,\frac{\partial}{\partial x_j}\left[\frac{h}{2}\,\frac{\partial h}{\partial x_j}\,\frac{\partial}{\partial x_k}\left(h\,\frac{\partial \bar{\Phi}}{\partial x_k}\right) - \frac{h^2}{3}\,\frac{\partial h}{\partial x_j}\,\frac{\partial^2 \bar{\Phi}}{\partial x_k \partial x_k}\right] + O(\alpha\beta, \beta^2) \qquad (3.1.46)$$

Or, in vector notation:

$$\frac{\partial \eta}{\partial t} + \nabla\cdot\left[(h+\alpha\eta)\nabla\bar{\Phi}\right] = \beta\nabla\cdot\left[\left\{\frac{h}{2}\,\nabla\cdot(h\nabla\bar{\Phi}) - \frac{h^2}{3}\,\nabla^2\Phi\right\}\nabla h\right] + O(\alpha\beta, \beta^2) \qquad (3.1.47)$$

where ∇ denotes the gradient operator. Similar evaluations for each momentum equation (3.1.41) leads to:

$$\frac{\partial \bar{\Phi}}{\partial t} + \frac{\alpha}{2}\,\frac{\partial \bar{\Phi}}{\partial x_j}\,\frac{\partial \bar{\Phi}}{\partial x_j} + \eta - \beta\,\frac{\partial}{\partial t}\left\{\frac{h}{2}\,\frac{\partial}{\partial x_j}\left(h\,\frac{\partial \bar{\Phi}}{\partial x_j}\right) - \frac{h^2}{6}\,\frac{\partial^2 \bar{\Phi}}{\partial x_j \partial x_j}\right\}$$

$$+ \frac{\gamma_s}{h}\,\bar{\Phi} = O(\alpha\beta, \beta^2, \beta\gamma, \gamma^2) \qquad (3.1.48)$$

Or, in vector notations:

$$\frac{\partial \bar{\Phi}}{\partial t} + \frac{\alpha}{2}\,(\nabla\bar{\Phi})^2 + \eta - \beta\,\frac{\partial}{\partial t}\left\{\frac{h}{2}\,\nabla\cdot(h\nabla\bar{\Phi}) - \frac{h^2}{6}\,\nabla^2\bar{\Phi}\right\}$$

$$+ \frac{\gamma_s}{h}\,\bar{\Phi} = O(\alpha\beta, \beta^2, \beta\gamma, \gamma^2) \qquad (3.1.49)$$

Equations (3.1.47) and (3.1.49) without the viscous term were first derived by Wu (1979). Combining further those two equations, one equation for $\bar{\Phi}$ alone is obtained as:

$$\bar{\Phi}_{tt} - \nabla\cdot(h\nabla\bar{\Phi}) + \frac{\gamma_s}{h}\bar{\Phi}_t$$

$$- \beta\left[\frac{h}{2}\nabla\cdot(h\nabla\bar{\Phi}_{tt}) - \frac{h^2}{6}\nabla^2\bar{\Phi}_{tt}\right] + \beta\nabla\cdot\left\{\left(\frac{h}{6}\bar{\Phi}_{tt} + \frac{h}{3}\nabla h\cdot\nabla\bar{\Phi}\right)\nabla h\right\}$$

$$= -\alpha[\nabla\bar{\Phi}\cdot\nabla\bar{\Phi}_t + \nabla\cdot(\bar{\Phi}_t\nabla\bar{\Phi})] + \frac{\alpha^2}{2}\nabla\cdot[(\nabla\bar{\Phi})^2\nabla\bar{\Phi}]$$

$$+ O(\alpha\beta,\beta^2,\beta\gamma,\gamma^2) \qquad (3.1.50)$$

Mathematically, Eq. (3.1.50) is equivalent to Eqs. (3.1.40) and (3.1.41). Numerically, however, the use of Eq. (3.1.50) is more advantageous, since only one equation with one unknown, $\bar{\Phi}$, needs to be solved. Once the velocity potential $\bar{\Phi}$ is known, the wave amplitude η can be computed using Eq. (3.1.48). At the lowest order:

$$\eta = -\bar{\Phi}_t + O(\alpha,\beta,\gamma_s) \qquad (3.1.51)$$

Equation (3.1.50) forms an alternative theoretical basis for long wave dynamics in variable depth and will be applied to the harbor oscillation problem in Section 3.4.

3.2 The Excitation of a Closed Rectangular Basin

In this section several methods are presented to investigate the shallow water oscillations of a liquid in a narrow rigid rectangular basin subjected to a horizontal translational motion. The emphasis is put on the transient as well as on the steady state aspects of this problem.

A numerical solution based on the nonlinear dispersive and dissipative long wave equations is derived in subsection 3.2.1. A linear analytical transient solution which only includes dispersive and dissipative effects is presented in subsection 3.2.2. A first order analytical nonlinear standing wave solution is presented in subsection 3.2.3 with the primary purpose of gaining some physical understanding of the nature of the finite oscillations in a closed basin. Finally, the range of validity of the linear and nonlinear dispersive theories for closed basin excitation problems is discussed in subsection 3.2.4.

3.2.1 A Numerical Solution for Nonlinear Response Due to a Transient Excitation

3.2.1.1 The Analytical Formulation of the Problem

The rigid rectangular basin shown in Fig. 3.2.1 has a length L and a still water depth h. It is submitted to a translational motion in the x° direction defined by the velocity $V^\circ(t)$. The system $(O^\circ x^\bullet z^\bullet)$ denotes a Newtonian coordinate system in which the velocity $V^\circ(t)$ is defined while (Oxz) is the coordinate system attached to the basin.

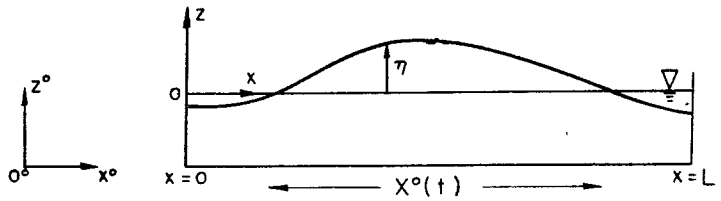

Fig. 3.2.1 Definition sketch for the Basin Excitation Problem.

Since the following analysis is restricted to long period oscillation it is assumed that $0(\frac{h}{L}) \ll 1$. Also the water particle motion is assumed to develop in the xz plane only, i.e., no variations are permitted in the direction perpendicular to the xz plane.

The equations used for this problem are the nonlinear dispersive, dissipative long wave equations developed in Section 3.1, applied here to the unidirectional case in dimensional form:

$$\eta_t + \{(h+\eta)\ \bar{u}\}_x = 0 \tag{3.2.1}$$

$$\bar{u}_t + \bar{u}\,\bar{u}_x + g\eta_x - \frac{1}{3}h^2\,\bar{u}_{xxt} + \frac{1}{h}\left(\frac{\nu\sigma}{2}\right)^{1/2}\bar{u} + V_t^o = 0 \tag{3.2.2}$$

where $\eta(x,t)$ is the wave elevation, $\bar{u}(x,t)$ is the velocity averaged in the z direction in the Oxz frame of reference, ν is the kinematic viscosity, and σ is a characteristic frequency of the fluid motion. In this section the averaged velocity $\bar{u}(x,t)$, for simplificity of notation, will be denoted as $u(x,t)$.

In order to account for dissipation due to wall friction and surface effects, the coefficient of the dissipation term in Eq. 3.2.2 can be multiplied by $(1 + \frac{2h}{b} + C)$ where b is the basin width and C a "surface contamination" factor which, according to Miles (1967), can vary between 0 and 2; for details of the discussion on these dissipation mechanisms, see Section 3.3. The end walls of the basin are assumed to be perfectly reflective and at time t = 0 the fluid is at rest. Thus, the initial

and boundary conditions are prescribed as:

$$\eta(x,0) = 0 \tag{3.2.3}$$

$$u(x,0) = 0 \tag{3.2.4}$$

$$u(0,t) = 0 \tag{3.2.5}$$

$$u(L,t) = 0 \tag{3.2.6}$$

The variables are nondimensionalized as follows:

$$\eta^* = H\eta \qquad x^* = Lx \qquad t^* = \frac{L}{\sqrt{gh}}\, t$$

$$u^* = \frac{H}{h}\sqrt{gh}\, u \qquad V_t^{o*} = A_c f^o(\sigma t^*)$$

where the starred symbols represent the original dimensional variables. (Henceforth all the variables will be dimensionless in the remainder of this subsection unless specifically stated otherwise.) The characteristic wave height H can be determined from the following consideration: when a basin with length L is moved in the x direction with a constant acceleration A_c, then the water surface elevation at either end of the basin is $O(A_cL/g)$. Therefore, for normalization, it seems reasonable to choose $H = A_cL/g$, so that the dimensionless water surface elevation η is $O(1)$. The characteristic frequency σ of the wave motion usually can be taken equal to the forcing frequency of the basin motion. Therefore, Eqs. (3.2.1) and (3.2.2) are rewritten in a dimensionless form as:

$$\eta_t + \{u(1+\alpha\eta)\}_x = 0 \tag{3.2.7}$$

$$u_t + \eta_x + \alpha u u_x - \frac{1}{3}\beta u_{xxt} + f^o(\delta t) + \gamma_s u = 0 \tag{3.2.8}$$

with the initial conditions:

$$\eta(x,0) = u(x,0) = 0 \tag{3.2.9}$$

and the boundary conditions:

$$u(0,t) = u(1,t) = 0 \tag{3.2.10}$$

Four nondimensional parameters appear in Eqs. (3.2.7) and (3.2.8):

(i) a nonlinear parameter $\alpha = A_c L/gh$

(ii) a dispersion parameter $\beta = h^2/L^2$ (3.2.12)

(iii) a dissipation parameter $\gamma_s = (\frac{\nu\sigma}{2})^{1/2} (1 + C + \frac{2h}{b}) \frac{L}{h\sqrt{gh}}$ (3.2.13)

(iv) a frequency parameter $\delta = \sigma L/\sqrt{gh}$ (3.2.14)

The first three parameters have been derived in the last section. The fourth parameter δ serves as an indicator of resonant conditions (and thus nonlinearities) in the basin. The relative importance of these four parameters for the basin excitation problem will be examined in detail in Section 3.2.2 and in Section 5.2.

3.2.1.2 A Finite Element Solution

The Strong form (S) is:

(S) Find the amplitude $\eta(x,t)$ and the velocity $u(x,t)$ in the interval $0 \leq x \leq 1$ and $0 \leq t \leq t'$ satisfying Eqs. (3.2.7) and (3.2.8) along with the initial conditions (3.2.9) and boundary conditions (3.2.10).

A weak form (W) of (S) is:

(W) Find the amplitude $\eta(x,t)$ in the function space H' and $u(x,t)$ in H_o' such that for all functions $\tilde{\eta}$ in H' and for all functions $\tilde{u}$ in H_o':

$$(\dot{\eta},\tilde{\eta}) + \int_0^1 \{u(1+\alpha\eta)\}_x \tilde{\eta}\, dx = 0 \tag{3.2.15}$$

$$(\dot{u},\tilde{u}) + \frac{1}{3}\beta(\dot{u}_x,\tilde{u}_x) + \gamma_s(u,\tilde{u}) =$$

$$- (\eta_x,\tilde{u}) - \int_0^1 f^o(\delta t)\tilde{u}\, dx - \alpha \int_0^1 u u_x \tilde{u}\, dx \tag{3.2.16}$$

and

$$(u(x,0),\ \tilde{u}(x,0)) = 0 \tag{3.2.17}$$

$$(\eta(x,0),\ \tilde{\eta}(x,0)) = 0 \tag{3.2.18}$$

where:

$$H' = \{f(x,t): \int_0^1 f_x\, dx \text{ is bounded for all } t \text{ in } [0,t']\}$$

$$H_o' = \{f(x,t): \ f(x,t) \text{ is in } H' \text{ and } f(0,t) = f(1,t) = 0\}$$

$$(f,g) = \int_0^1 fg\, dx$$

and the dot above the symbols denotes partial differentiation with respect to time. Under appropriate smoothness hypotheses, the solution of the weak formulation can be easily shown to be identical to the solution of (S).

The Galerkin form (G) of (W) is:

Find $\eta^h(x,t)$ in the function space S' and $u^h(x,t)$ in the function space S_o' such that for all functions $\tilde{\eta}^h(x,t)$ in S' and $\tilde{u}^h(x,t)$ in S_o':

$$(\mathring{\eta}^h, \tilde{\eta}^h) + \int_0^1 \{u^h(1+\alpha\eta^h)\}_x \tilde{\eta}^h dx = 0 \tag{3.2.19}$$

$$(G) \quad \left\{ \begin{array}{l} (\mathring{u}^h, \tilde{u}^h) + \frac{1}{3}\beta\,(\mathring{u}_x^h, \tilde{u}_x^h) + \gamma_s(u^h, \tilde{u}^h) = \\ -(\eta_x^h, \tilde{u}^h) - \int_0^1 f^\circ(\delta t)\tilde{u}^h dx - \alpha\int_0^1 u^h u_x^h \tilde{u}^h dx \end{array} \right. \tag{3.2.20}$$

and

$$(u^h(x,0),\ \tilde{u}^h(x,0)) = 0 \tag{3.2.21}$$

$$(\eta^h(x,0),\ \tilde{\eta}^h(x,0)) = 0 \tag{3.2.22}$$

where S' is a subspace of H'

and S_o' is a subspace of H_o'.

The finite element discretization consists of choosing the subspace S' in a simple manner in order to transform the Galerkin formulation into a matrix formulation with a finite number of unknowns. S' can be defined as:

$$S' = \{f^h : f^h = \sum_{i=1}^{N} f_i(t)\ \phi_i(x)\}$$

where $f_i(t)$ denotes any arbitrary continuously differentiable function in the time interval $[0,t']$ and $\phi_i(x)$ is a piecewise linear function defined as:

$$\phi_i(x_i) = 1 \qquad i=1,2,\ldots.N$$

$$\phi_i(x) = 0 \quad \text{for} \quad x > x_{i+1} \quad \text{or} \quad x < x_{i-1}$$

The functions $\phi_i(x)$ are called shape functions and are represented schematically on Fig. 3.2.2.

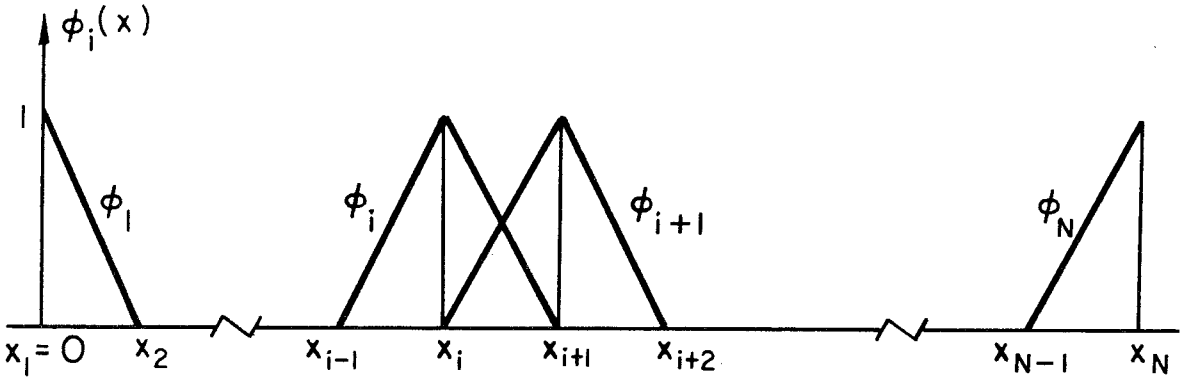

Fig. 3.2.2 Definition sketch for the shape functions.

The location x_i where the shape function is defined is called a node.

From the definition of the functions ϕ_i it follows that $f_i(t)$ is the value of the function f^h at the node i.

Therefore, the functions $\eta^h(x,t)$, $\tilde{\eta}^h(x,t)$, $u^h(x,t)$, $\tilde{u}^h(x,t)$ can be written as:

$$\left.\begin{aligned} \eta^h(x,t) &= \sum_{i=1}^{N} \eta_i(t)\ \phi_i(x) \\ \tilde{\eta}^h(x,t) &= \sum_{i=1}^{N} \tilde{\eta}_i(t)\ \phi_i(x) \end{aligned}\right\} \qquad \left.\begin{aligned} u^h(x,t) &= \sum_{i=2}^{N-1} u_i(t)\ \phi_i(x) \\ \tilde{u}^h(x,t) &= \sum_{i=2}^{N-1} \tilde{u}_i(t)\ \phi_i(x) \end{aligned}\right\} \qquad (3.2.23)$$

The unknowns are the functions $\eta_i(t)$ and $u_i(t)$ at each node. (Note that $u_1 = u_N = 0$ in accordance with the requirement that u^h belongs to S_o'. The next step is to substitute Eqs. (3.2.23) into Eqs. (3.2.19) through (3.2.22). Since the Galerkin equations must be checked for all functions $\tilde{\eta}_i$ ($i\varepsilon[1,N]$) and $\tilde{u}_i$($i\varepsilon[2,N-1]$), the coefficients of each function $\tilde{\eta}_i$ and $\tilde{u}_i$ must be zero and the following matrical system is obtained:

$$\sum_{j=1}^{N} (\phi_i,\phi_j)\dot{\eta}_i = -\int_o^1 \phi_i \left\{\left(\sum_{j=2}^{N-1} u_j\phi_j\right)\left(1+\alpha\sum_{k=1}^{N}\eta_k\phi_k\right)\right\}_x dx \quad , \qquad i=1,N \tag{3.2.24}$$

$$\sum_{j=2}^{N-1}\left\{(\phi_i,\phi_j) + \frac{1}{3}\beta\ (\phi_{i,x},\phi_{j,x})\right\}\dot{u}_j =$$
$$-\sum_{j=1}^{N}(\phi_i,\phi_{j,x})\eta_j - \gamma_s\sum_{j=2}^{N-1}(\phi_i,\phi_j)\ u_j - \int_o^1 f^\circ(\delta t)\phi_i dx$$
$$-\alpha\int_o^1\left(\sum_{k=2}^{N-1} u_k\phi_k\right)\left(\sum_{j=2}^{N-1} u_j\phi_{j,x}\right)\phi_i dx, \qquad i=2,N-1 \tag{3.2.25}$$

$$\left.\begin{aligned} \eta_j(0) &= 0 \qquad j=1,N \\ u_j(0) &= 0 \qquad j=2,N-1 \end{aligned}\right\} \tag{3.2.26}$$

Or, in matrix form:

$$M^\eta\ \dot{\underset{\sim}{\eta}} = \underset{\sim}{f}^\eta \tag{3.2.27}$$

$$M^u \underset{\sim}{\dot{u}} = \underset{\sim}{f}^u \tag{3.2.28}$$

with:

$$M^\eta_{ij} = (\phi_i, \phi_j) \qquad i,j=1,N \tag{3.2.29}$$

$$M^u_{ij} = (\phi_i, \phi_j) + \frac{1}{3}\beta \ (\phi_{i,x}, \phi_{j,x}) \qquad i,j=2,N-1 \tag{3.2.30}$$

$$f_i^\eta = -\int_o^1 \phi_i \left\{ \left(\sum_{j=2}^{N-1} u_j \phi_j \right) \left(1 + \alpha \sum_{k=1}^{N} \eta_k \phi_k \right) \right\}_x dx \qquad i=1,N \tag{3.2.31}$$

$$f_i^u = -\sum_{j=1}^{N} \left(\phi_i, \phi_{j,x} \right) \eta_j - \gamma_s \sum_{j=2}^{N-1} (\phi_i, \phi_j) u_j - \int_o^1 f^\circ(\delta t) \phi_i dx$$
$$- \alpha \int_o^1 \left(\sum_{k=2}^{N-1} u_k \phi_k \right) \left(\sum_{j=2}^{N-1} u_j \phi_{j,x} \right) \phi_i dx \ , \qquad i=2,N-1 \tag{3.2.32}$$

Eqs. (3.2.27) and (3.2.28) are coupled through the vectors $\underset{\sim}{f}^\eta$ and $\underset{\sim}{f}^u$. The matrix $\underset{\sim}{M}^\eta$ and $\underset{\sim}{M}^u$ are tridiagonal, symmetric, positive, which provides computational efficiency, and exact integration is performed on all the terms.

3.2.1.3 The Integration Algorithm

Equations (3.2.27) and (3.2.28) form a first order nonlinear differential system which can be solved using the generalized midpoint rule:

$$\underset{\sim}{M}^\eta (\underset{\sim}{\eta}_{n+1} - \underset{\sim}{\eta}_n) = \Delta t \ \underset{\sim}{f}^\eta (\underset{\sim}{u}_{n+\beta_*}, \underset{\sim}{\eta}_{n+\beta_*}) \tag{3.2.33}$$

$$M^u (\underset{\sim}{u}_{n+1} - \underset{\sim}{u}_n) = \Delta t \, \underset{\sim}{f}^u(\underset{\sim}{u}_{n+\beta_*}, \underset{\sim}{\eta}_{n+\beta_*}, t_{n+\beta_*}) \quad (3.2.34)$$

where $\Delta t = t_{n+1} - t_n$

$$t_{n+\beta_*} = \beta_* \, t_{n+1} + (1 - \beta_*) t_n$$

$$\underset{\sim}{u}_{n+\beta_*} = \beta_* \, \underset{\sim}{u}_{n+1} + (1 - \beta_*) \underset{\sim}{u}_n$$

where

β_* is a numerical parameter which can vary between 0 and 1. At time t_{n+1}, the unknown vectors $\underset{\sim}{\eta}_{n+1}$ and $\underset{\sim}{u}_{n+1}$ are found by solving Eqs. (3.2.33) and (3.2.34) using the following iterative procedure:

1. First iteration:
   - Compute $\underset{\sim}{f}^u(\underset{\sim}{u}_n, \underset{\sim}{\eta}_n, t_{n+\beta_*})$
   - Solve Eq. (3.2.34) for $\underset{\sim}{u}^{(1)}_{n+1}$
   - Compute $\underset{\sim}{f}^{\eta}(u^{(1)}_{n+\beta_*}, \underset{\sim}{\eta}_n)$
   - Solve Eq. (3.2.33) for $\underset{\sim}{\eta}^{(1)}_{n+1}$
2. Subsequent iterations:
   - Compute $\underset{\sim}{f}^u(\underset{\sim}{u}^{(k)}_{n+\beta_*}, \underset{\sim}{\eta}^{(k)}_{n+\beta_*}, t_{n+\beta_*})$

     where $\underset{\sim}{u}^{(k)}_{n+\beta_*} = \beta_* \, \underset{\sim}{u}^{(k)}_{n+1} + (1 - \beta_*) \underset{\sim}{u}_n$

     and $\underset{\sim}{\eta}^{(k)}_{n+\beta_*} = \beta_* \, \underset{\sim}{\eta}^{(k)}_{n+1} + (1 - \beta_*) \underset{\sim}{\eta}_n$
   - Solve Eq. (3.2.34) for $\underset{\sim}{u}^{(k+1)}_{n+1}$

- Compute $\underset{\sim}{f}^{\eta}\left(\underset{\sim}{u}_{n+\beta_*}^{(k+1)}, \underset{\sim}{\eta}_{n+\beta_*}^{(k)}\right)$

- Solve Eq. (3.2.33) for $\underset{\sim}{\eta}_{n+1}^{(k+1)}$

3.2.1.4 The Convergence and Accuracy of the Algorithm

The scheme presented previously belongs to the class of one-step integration schemes for nonlinear first order differential equations. It is considered specific to the problem of interest, and thus it may not be relevant to more general situations. A local truncation error analysis shows that the scheme is first order accurate except if $\beta_* = 1/2$, for which it is second order accurate. Stability analysis proved difficult owing to the form of the nonlinear terms and could not be carried out successfully. Instead, numerical experiments were performed with $\beta_* = 1/2$ and the results can be summarized as follows:

(i) The condition

$$\Delta t \leq \Delta x$$

where $\Delta x = x_{i+1} - x_i$ and $\Delta t = t_{n+1} - t_n$ must be fulfilled for all segments. Otherwise the scheme does not converge.

(ii) The number of iterations required per time step must not be less than 3, when $\Delta x \approx \Delta t$.

(iii) The number $N_x (=1/\Delta x)$ of segments discretizing the basin must be large enough to describe the wave profile accurately; if the wave is linear N_x can be related conveniently to a particular mode

shape by

$$N_x = 20\ n$$

where the integer n is equal to the number of nodes in the basin.

If finite amplitude effects are important, N_x must be increased in order to describe the secondary oscillations accurately, otherwise numerical damping occurs. When those three conditions are met, the scheme yields quite satisfactory results as will be shown in Section 5.2. In particular, numerical dissipation does not take place and a high degree of accuracy is achieved, allowing to perform integrations with a number of time steps up to 10,000.

Using $\Delta x = \Delta t$, the number of time steps per period of oscillations is about twice the number of elements for the sloshing mode (n=1). For instance, if $N_x = 20$ then 4,000 time steps are required to compute the solution for 100 cycles of oscillations.

All the calculations for the closed basin problem have been performed on a PDP11/60 computer in single precision (32 bits per word) and the results of the numerical runs will be presented in Section 5.2.

3.2.2 The Analytical Solution for the Linear Response Due to a Transient Excitation

In this section the linear dispersive dissipative theory is applied to the excitation of a closed basin. Two approaches are available. The first method involves computing the transfer function of a basin forced by an harmonic excitation. Based on the derived transfer function, numerical Fourier techniques can be used to compute

the basin response to a given transient excitation. The second method consists of using integral transform techniques when the expression for the transfer function can be obtained in an analytical form simple enough to allow an explicit analytical computation of the transient solution; this is the method which was followed.

The statement of the problem and the notation used are the same as in Section 3.2.1. Linearizing Eqs. (3.2.1) and (3.2.2) yields:

$$\eta_t + h\, u_x = 0 \tag{3.2.35}$$

$$u_t + g\,\eta_x - \frac{1}{3} h^2\, u_{xxt} + X^{\circ}_{tt} + \frac{1}{h}\left(1 + \frac{2h}{b} + C\right)\left(\frac{\nu\sigma}{2}\right)^{1/2} u = 0 \tag{3.2.36}$$

(The walls and surface friction are accounted for by multiplying the friction coefficient by $\left(1 + \frac{2h}{b} + C\right)$.

The initial conditions and boundary conditions are:

$$\eta(x,0) = u(x,0) = 0 \tag{3.2.37}$$

$$u(0,t) = u(L,t) = 0 \tag{3.2.38}$$

In dimensionless units Eqs. 3.2.35 through 3.2.38 can be rewritten as:

$$\eta_t + u_x = 0 \tag{3.2.39}$$

$$u_t + \eta_x - \frac{1}{3}\beta\, u_{xxt} + f^{\circ}(\delta t) + \gamma_s u = 0 \qquad (3.2.40)$$

$$\eta(x,0) = u(x,0) = 0 \qquad (3.2.41)$$

$$u(0,t) = u(1,t) = 0 \qquad (3.2.42)$$

where $\alpha = \dfrac{A_c L}{gh}$ $\qquad \beta = \dfrac{h^2}{L^2}$

$$\gamma_s = \frac{L}{h\sqrt{gh}} \left(\frac{\nu\sigma}{2}\right)^{1/2} (1 + C + \frac{2h}{b}) \qquad \delta = \frac{\sigma L}{\sqrt{gh}}$$

and $\dfrac{\eta^*}{h} = \alpha\eta$, $\qquad x^* = Lx$, $\qquad t^* = \dfrac{L}{\sqrt{gh}}\, t$,

$$\frac{u^*}{\sqrt{gh}} = \alpha u \ , \qquad X^{\circ}_{tt} = A_c f^{\circ\circ}(\sigma t^*) \ .$$

The starred quantities refer to dimensional variables. It is noted the nonlinear parameter, α, does not appear in the equations; it merely acts now as a scaling parameter for η^*/h and $u^*/\sqrt{gh}$.

The variable $u(x,t)$ is eliminated between Eq. (3.2.39) and Eq. (3.2.40); this yields an equation in terms of $\eta(x,t)$ alone:

$$-\eta_{tt} + \eta_{xx} + \frac{1}{3}\beta\, \eta_{xxtt} - \gamma_s \eta_t = 0 \qquad (3.2.43)$$

with the following initial conditions and boundary conditions:

$$\eta(x,0) = \eta_t(x,0) = 0 \qquad (3.2.44)$$

$$\eta_x(0,t) = \eta_x(1,t) = -f^\circ(\delta t) \tag{3.2.45}$$

Equations (3.2.43) through (3.2.45) are conveniently solved using integral transform techniques. Laplace transform is chosen because of the initial conditions:

$$\tilde{\eta}(x,s) = \int_0^\infty \eta(x,t)\ e^{-st}\ dt \tag{3.2.46}$$

Multiplying both sides of Eq. (3.2.43) by the kernel e^{-st} and using the initial conditions (3.2.44) yields a differential equation for $\tilde{\eta}$:

$$(1 + \frac{\beta}{3}\, s^2)\ \tilde{\eta}_{xx} - (s^2 + s\gamma_s)\tilde{\eta} = 0 \tag{3.2.47}$$

with the transformed boundary conditions:

$$\tilde{\eta}_x(0,s) = \tilde{\eta}_x(1,s) = -\tilde{f}^\circ(s) \tag{3.2.48}$$

where $$\tilde{f}^\circ(s) = \int_0^\infty f^\circ(\delta t)e^{-st}dt \tag{3.2.49}$$

The solution for $\tilde{\eta}$ is:

$$\tilde{\eta}(x,s) = -\tilde{f}^\circ(s)\ \frac{\sinh\kappa_o(x - \frac{1}{2})}{\kappa_o \cosh(\frac{\kappa_o}{2})} \tag{3.2.50}$$

where $$\kappa_o = \frac{s^{1/2}(s + \gamma_s)^{1/2}}{\sqrt{\frac{\beta}{3}}\left(s + i\sqrt{\frac{3}{\beta}}\right)^{1/2}\left(s - i\sqrt{\frac{3}{\beta}}\right)^{1/2}} \tag{3.2.51}$$

and i denotes the imaginary number $\sqrt{-1}$.

Using the inversion integral for the Laplace transform, the solution for $\eta(x,t)$ is obtained as:

$$\eta(x,t) = -\frac{1}{2\pi i}\int_{B_r} e^{st}\tilde{f}^{\circ}(s)\,\frac{\sinh\,\kappa_o(x-\frac{1}{2})}{\kappa_o\cosh(\frac{\kappa_o}{2})}\,ds \qquad (3.2.52)$$

where $\int_{B_r} \equiv \lim_{\Gamma\to\infty}\int_{\mu-i\Gamma}^{\mu+i\Gamma}$ is the Bromwich contour integral.

The time displacement history of the basin is defined dimensionally as:

$$X^{*}(t^{*}) = \begin{cases} -d & \text{if } t^{*} \le 0 \\ -d\cos\sigma t^{*} & \text{if } 0 \le t^{*} \le \frac{m\pi}{\sigma} \\ -(-1)^{m}d & \text{if } t^{*} \ge \frac{m\pi}{\sigma} \quad m=1,2,3\ldots \end{cases} \qquad (3.2.53)$$

where d is the amplitude of the basin displacement.

From Eq. 3.2.53 it is seen that the acceleration number A_c for this motion is $d\sigma^2$, and:

$$f^{\circ}(\delta t) = \begin{cases} 0 & \text{if } t \le 0 \text{ or } t \ge \frac{m\pi}{\delta} \\ \cos \delta t & \text{if } 0 \le t \le \frac{m\pi}{\delta} \end{cases} \tag{3.2.54}$$

The transform function $\tilde{f}_o(s)$ becomes:

$$\tilde{f}^{\circ}(s) = \frac{s}{s^2 + \delta^2} \left[1 + (-1)^{m+1} \exp \left[-s(\tfrac{m\pi}{\delta}) \right] \right] \tag{3.2.55}$$

and from Eq. (3.2.52) the integral solution for the surface elevation is

$$\eta(x,t) = -\frac{1}{2\pi i} \int_{B_r} \frac{s}{s^2 + \delta^2} \frac{\sinh \kappa_o (x - \frac{1}{2})}{\kappa_o \cosh(\frac{\kappa_o}{2})} \left[\exp(st) + (-1)^{m+1} \exp(s(t - \tfrac{m\pi}{\delta})) \right] ds \tag{3.2.56}$$

Eq. (3.2.56) can be evaluated explicitly using the Residue theorem. For details of the calculations the interested reader is directed to Appendix B; the final result is as follows:

<u>if $t \le \frac{m\pi}{\delta}$:</u>

$$\eta(x,t) = -\mathrm{Re}\left\{ \frac{1}{\kappa} \frac{\sin\left[\kappa(x - \frac{1}{2})\right]}{\cos(\frac{\kappa}{2})} \quad e^{i\delta t} \right\} \tag{3.2.57}$$

$$-2 \sum_{n=0}^{\infty} (-1)^n \sin[a_n (x - \tfrac{1}{2})] \; \mathrm{Re}[f_n \, e^{s_n t}]$$

<u>if $t > \frac{m\pi}{\delta}$:</u>

$$\eta(x,t) = -2 \sum_{n=0}^{\infty} (-1)^n \sin[a_n (x - \tfrac{1}{2})] \; \mathrm{Re}[f_n' \, e^{s_n t}] \tag{3.2.58}$$

where:

$$a_n = (2n+1)\pi$$

$$\kappa = \frac{\delta}{(1 - \frac{1}{3}\beta\,\delta^2)^{1/2}}\left(1 - \frac{i\gamma_s}{2\delta}\right) \tag{3.2.59}$$

$$\delta < \sqrt{\frac{3}{\beta}} \tag{3.2.60}$$

$$f_n = 4\,\frac{s_n}{(s_n^2+\delta^2)}\;\frac{1 + \frac{1}{3}\beta s_n^2}{[2s_n+\gamma_s(1-\frac{1}{3}\beta s_n^2)]} \tag{3.2.61}$$

$$f_n' = f_n\left[1 + (-1)^{m+1}\exp\left(\frac{-m\pi s_n}{\delta}\right)\right] \tag{3.2.62}$$

$$s_n = \frac{-\gamma_s - 2ia_n(1 + \frac{\beta}{3}a_n^2)^{1/2}}{2(1 + \frac{\beta}{3}a_n^2)} \tag{3.2.63}$$

The inequality shown in Eq. (3.2.60) validates this form of the solution mathematically. Physically this condition must always be met as will be seen in Section 3.2.4.

Equations (3.2.51) through (3.2.58) will be used in Chapter 5 as a basis of comparison with the nonlinear dispersive dissipative theory and with the experiments. A physical discussion of the linear solution and a derivation of several useful relationships follow in the remainder of that section. It is understood that $\beta \ll 1$ and $\gamma_s \ll 1$ in accordance with the assumptions underlying the derivation of the dissipative long wave equations in Section 3.1.

The solution closely parallels that for the motion of a damped

single degree of freedom oscillator. During the excitation phase ($t < \frac{m\pi}{\delta}$ two groups of terms contribute to the solution: a linear combination of all the free modes of oscillation of the basin representing the transients and a harmonic function with the frequency of the exciting motion corresponding to the steady state. During the initial stage of the excitation the transients play the dominant role and may induce a maximum amplitude greater than the steady state amplitude. As time progresses, however, the transients decay due to the presence of the exponential viscous term approximately equal to $\exp\left(-\frac{\gamma_s t}{2}\right)$ in each term of the series in Eq. (3.2.57) and after a time $t_\gamma = 0(\frac{1}{\gamma_s})$ only the steady state solution remains. When $t > \frac{m\pi}{\delta}$, the basin is no longer excited and the expression for the forced solution does not appear any more. Only the transient terms are present and they decay at the same rate as during the excitation phase. It can be noted from Eqs. (3.2.57) and (3.2.58) that because of the manner in which the basin is excited, only the modes of oscillation corresponding to an odd number of nodes are excited. Also, the water elevation at the middle of the basin is zero for all times. Specializing to the harmonic problem, the steady state response can be derived from Eqs. (3.2.57) and (3.2.59) and is written down for clarity:

$$\eta(x,t) = -\mathrm{Re}\left\{ \frac{1}{\kappa} \frac{\sin\left[\kappa(x - \frac{1}{2})\right]}{\cos(\frac{\kappa}{2})} e^{i\delta t} \right\} \tag{3.2.64}$$

$$\kappa = \frac{\delta}{(1 - \frac{1}{3}\beta\delta^2)^{1/2}} \left(1 - \frac{i\gamma_s}{2\delta}\right) \tag{3.2.65}$$

Equation (3.2.65) can be interpreted as the dispersion relation for this problem. It is seen from Eq. (3.2.64) that wave amplitude $||\eta(x,t)||$ is $0(\frac{1}{\kappa})$ except at resonance when $\cos(\frac{\kappa}{2}) \to 0$.

Thus maximum excitation is achieved when $\mathrm{Re}[\cos(\frac{\kappa}{2})] = 0$, that is:

$$\mathrm{Re}(\kappa) \approx \frac{\delta}{(1-\frac{1}{3}\beta\delta^2)^{1/2}} = (2n+1)\pi = a_n \ , \tag{3.2.66}$$

where γ_s and $\beta\delta^2$ are considered to be much less than unity:

Equation (3.2.66) can be rewritten as:

$$\delta \approx \frac{a_n}{(1+\frac{\beta}{3}a_n{}^2)^{1/2}} = |\mathrm{Im}(s_n)| \tag{3.2.67}$$

Thus, at resonance the excitation frequency is equal to one of the natural frequencies of oscillation of the basin, as expected.

The corresponding steady state wave amplitude at either end of the basin is computed at resonance from Eq. (3.2.64) through Eq. (3.2.66) as:

$$\frac{||\eta^*(0,t)||}{h\alpha} = \frac{4}{\gamma_s} \frac{1}{(2n+1)\pi} \tag{3.2.68}$$

Or, since $\alpha = d\delta^2/L$ and $\delta \approx (2n+1)\pi$ from Eq. (3.2.67):

$$\left|\left|\frac{\eta^*(0,t)}{h}\right|\right| \approx 4\frac{(2n+1)\pi}{\gamma_s}\frac{d}{L} \tag{3.2.69}$$

In typical laboratory conditions, $O(\gamma_s) \approx 10^{-2}$ and $d/L \approx 10^{-3}$ so that $||\eta^*(0,t)||/h \simeq 0.4$, which tends to invalidate the application of the linear theory near resonance. A detailed discussion on the range of validity of the linearized theory will be postponed until Section 3.2.4.

Assuming for the moment that the linear theory remains valid for all ranges of amplitude, the characteristic number of oscillations required for steady state to be achieved near a resonant frequency, starting the excitation of the basin from rest, is controlled by the exponential decay terms in Eq. (3.2.57), i.e., $\exp\left[-\frac{\gamma_s}{2} t\right]$ or in dimensional units:

$$\exp[-\frac{\gamma_s}{2n+1} \frac{t^*}{T}] \tag{3.2.70}$$

where T denotes the excitation period. The transients are reduced to 5% of their original value for:

$$\frac{t^*}{T} \approx \frac{\pi(2n+1)}{\gamma_s} = \frac{a_n}{\gamma_s} \tag{3.2.71}$$

Finally, from expression (3.2.70) and Eq. (3.2.69) an estimation of growth of the wave amplitude with time at either end wall at resonance can be made when, starting from rest, the basin is continuously excited at a period equal to one of its natural periods of oscillation, as:

$$\left\|\frac{\eta^*(0,t)}{h}\right\| = \frac{d}{L} \frac{4(2n+1)\pi}{\gamma_s} (1 - \exp[-\frac{\gamma_s}{2n+1} \frac{t^*}{T}]) \tag{3.2.72}$$

In particular, during the initial stages of the excitation the wave amplitude grows linearly with time:

$$\left|\left|\frac{\eta^*(0,t)}{h}\right|\right| = 4\pi \frac{d}{L} \frac{t^*}{T} \tag{3.2.73}$$

All of these results obtained from the linear theory will be used as a basis of reference in Section 5.2.

3.2.3 The First Order Solution for Nonlinear Standing Waves

It is a well known result, e.g., Ippen (1966), that the linear unidirectional natural modes of oscillations in a rectangular basin are formed by the superposition of two sinusoidal waves which have the same amplitude and travel in opposite directions. The relationships, for a long dispersive wave, using dimensional notations, are:

$$\eta(x,t) = \frac{H}{2} \cos\left(\frac{2\pi t}{T} + \frac{2\pi}{\lambda}x\right) + \frac{H}{2} \cos\left(\frac{2\pi t}{T} - \frac{2\pi}{\lambda}x\right) = H \cos\left(\frac{2\pi}{\lambda}x\right) \cos\left(\frac{2\pi t}{T}\right) \tag{3.2.74}$$

$$\frac{\lambda}{T} = C_o = \sqrt{gh}\left[1 - \frac{1}{6}\left(\frac{2\pi}{\lambda}h\right)^2\right] \tag{3.2.75}$$

$$\frac{L}{\lambda} = \frac{n}{2} \tag{3.2.76}$$

where L is the basin length, h is the still water depth, η is the wave elevation, H is the wave height, g is the acceleration of gravity,

T is the period, C_o is the wave celerity, λ is the wave length of the two progressive waves and n is an integer referring to the particular mode and equal to the number of nodes in the basin. This result is valid only for infinitesimal waves.

Rogers and Mei (1975, unpublished report) showed that in the case of a rectangular closed basin the finite wave amplitude could be represented as the sum of two nonlinear waves propagating in opposite directions, each being a solution of the Korteweg-de Vries equation corresponding to its direction of propagation. From that result, the natural modes of oscillations including the nonlinear and dispersion features can be defined analytically.

First, the derivation of the aforementioned basic result using the approach of Rogers and Mei (1975) based on the multiple scales method, e.g. see Cole (1969), is presented. The inviscid one-dimensional nonlinear dispersive long wave equations applied to a constant depth can be written in dimensionless form as (see Eqs. (3.1.50), (3.1.51)):

$$\Phi_{tt} - \Phi_{xx} = \frac{1}{3}\beta\Phi_{xxtt} - \alpha(2\Phi_x\Phi_{xt} + \Phi_t\Phi_{xx}) + O(\alpha\beta,\beta^2) \qquad (3.2.77)$$

$$\eta = -\Phi_t + O(\alpha,\beta) \qquad (3.2.78)$$

where:

$$\eta = \frac{H}{h}\eta^* \qquad x = \frac{x^*}{\ell} \qquad t = \frac{\sqrt{gh}}{\ell}t^*$$

$$\Phi = \frac{h}{H}\frac{1}{\ell\sqrt{gh}}\Phi^* \qquad \alpha = \frac{H}{h} \qquad \beta = \left(\frac{h}{\ell}\right)^2$$

and Φ is the depth-averaged velocity potential, H is a characteristic wave amplitude, ℓ is a characteristic wavelength. The starred quantities denote the dimensional variables. All the dimensionless variables are of order unity and $O(\alpha) = O(\beta) < 1$.

Equation (3.2.77) can be transformed with the same degree of accuracy into:

$$\Phi_{tt} - \Phi_{xx} = \frac{1}{3}\beta\,\Phi_{xxtt} - \alpha(2\Phi_x\Phi_{xt} + \Phi_t\Phi_{tt}) + O(\alpha\beta,\beta^2) \qquad (3.2.79)$$

The method of multiple scales is based on the assumption that the system is governed by rapid changes in time and space modulated by slow variations in both time and space. Mathematically this can be expressed by assuming a solution of the form:

$$\Phi(x,t) = \Phi^{(0)}(x,t,x',t') + \alpha\Phi^{(1)}(x,t,x',t') + O(\alpha^2) \qquad (3.2.80)$$

where $$x' = \alpha x \qquad t' = \alpha t \qquad (3.2.81)$$

x,t,x',t' are considered as independent variables in $\Phi^{(0)}$ and $\Phi^{(1)}$. Substituting Eq. (3.2.80) into Eq. (3.2.79) a zeroth and a first order equation are obtained as:

$$O(1): \quad \Phi^{(0)}_{tt} - \Phi^{(0)}_{xx} = 0 \qquad (3.2.82)$$

$$O(\alpha): \quad \Phi^{(1)}_{tt} - \Phi^{(1)}_{xx} = \frac{1}{3}\frac{\beta}{\alpha}\Phi^{(0)}_{xxtt} - \left[2\,\Phi^{(0)}_x\Phi^{(0)}_{xt} + \Phi^{(0)}_t\Phi^{(0)}_{tt}\right]$$

$$+ 2\left(\Phi^{(0)}_{xx'} - \Phi^{(0)}_{tt'}\right) \qquad (3.2.83)$$

The general solution to Eq. (3.2.82) is:

$$\Phi^{(0)} = \Phi^{+}(t+x,x',t') + \Phi^{-}(t-x,x',t') \tag{3.2.84}$$

Substituting Eq. (3.2.84) into the right-hand side of Eq. (3.2.83) two sets of terms are obtained, those which are functions of (t+x) or (t-x) alone, and hence secular, and those which are mixed. Thus, Eq. (3.2.83) can be rewritten as:

$$\Phi^{(1)}_{z_+z_-} = F^{+}(z_+) + F^{-}(z_-) + G(z_+,z_-) \tag{3.2.85}$$

where $z_+ = t+x$, $z_- = t-x$

The integration of Eq. (3.2.85) yields a solution of the form:

$$\Phi^{(1)}(z_+,z_-) = z_-F_1^{+}(z_+) + z_+F_1^{-}(z_-) + G_1(z_+,z_-) \tag{3.2.86}$$

Since a bounded solution is desired at all times, the function $F^{+}(z_+)$ and $F^{-}(z_-)$ must be set to zero. This gives:

$$\Phi^{+}_{xx'} - \Phi^{+}_{tt'} + \frac{1}{6}\frac{\beta}{\alpha}\Phi^{+}_{xxtt} - (\Phi^{+}_{x}\Phi^{+}_{xt} + \frac{1}{2}\Phi^{+}_{t}\Phi^{+}_{tt}) = 0 \tag{3.2.87}$$

$$\Phi^{-}_{xx'} - \Phi^{-}_{tt'} + \frac{1}{6}\frac{\beta}{\alpha}\Phi^{-}_{xxtt} - (\Phi^{-}_{x}\Phi^{-}_{tt} + \frac{1}{2}\Phi^{-}_{t}\Phi^{-}_{tt}) = 0 \tag{3.2.88}$$

Now define η^{+} and η^{-} as:

$$\eta^{+} = -\Phi^{+}_{t} \tag{3.2.89}$$

$$\eta^{-} = -\Phi^{-}_{t} \tag{3.2.90}$$

using Eq. (3.2.78) along with Eq. (3.2.84):

$$\eta = -\Phi_t + O(\alpha,\beta) = -\overset{(0)}{\Phi}_t + O(\alpha,\beta) = \eta^+ + \eta^- + O(\alpha,\beta) \qquad (3.2.91)$$

Thus, at the zeroth order:

$$\eta = \eta^+(t+x,x',t') + \eta^-(t-x\ ,x',t') \qquad (3.2.92)$$

From Eqs. (3.2.89)-(3.2.90) and the form of the functions Φ^+ and Φ^- in Eq. (3.2.84), it follows that:

$$\eta^+ = -\frac{\partial\Phi^+}{\partial x} = -\frac{\partial\Phi^+}{\partial z_+} \qquad (3.2.93)$$

$$\eta^- = \frac{\partial\Phi^-}{\partial x} = -\frac{\partial\Phi^-}{\partial z_-} \qquad (3.2.94)$$

Substituting Eq. (3.2.93) and (3.2.94) into Eqs. (3.2.87) and (3.2.88), two uncoupled equations for η^+ and η^- are obtained:

$$-\eta^+_{x'} + \eta^+_{t'} - \frac{1}{6}\frac{\beta}{\alpha}\eta^+_{z_+z_+z_+} - \frac{3}{2}\eta^+\eta^+_{z_+} = 0 \qquad (3.2.95)$$

$$+\eta^-_{x'} + \eta^-_{t'} - \frac{1}{6}\frac{\beta}{\alpha}\eta^-_{z_-z_-z_-} - \frac{3}{2}\eta^-\eta^-_{z_-} = 0 \qquad (3.2.96)$$

Equations (3.2.95) and (3.2.96) are now applied to the wave motion in a rectangular tank with length L. It appears reasonable to assume that $O(\frac{L}{\ell}) = 1$. Thus, the abscissa $x = O(\frac{L}{\ell}) = O(1)$ and the

dependence on the variable x' can be neglected in Eq. (3.2.95) and (3.2.96). Thus:

$$\eta^{+} = \eta^{+}(z_{+},t') \tag{3.2.97}$$

$$\eta^{-} = \eta^{-}(z_{-},t') \tag{3.2.98}$$

Reverting back to the initial variables x and t, Eqs. (3.2.95) and (3.2.96) can be expressed as:

$$\eta_x^{+} - \eta_t^{+} + \frac{1}{6}\beta\,\eta_{xxx}^{+} + \frac{3}{2}\alpha\,\eta^{+}\eta_x^{+} = 0 \tag{3.2.99}$$

$$\eta_x^{-} + \eta_t^{-} + \frac{1}{6}\beta\,\eta_{xxx}^{-} + \frac{3}{2}\alpha\,\eta^{-}\eta_x^{-} = 0 \tag{3.2.100}$$

It is noted that these are simply the KdV equations (after Korteweg and de Vries (1895)) for waves moving to the left and to the right, respectively.

The following basic result based on Eqs. (3.2.92), (3.2.99) and (3.2.100) can now be stated: in a narrow, closed rectangular basin the wave amplitude in shallow water can be described by the linear superposition of two nonlinear waves traveling in opposite directions, each satisfying its own KdV equation. Note that the approximation leading to that result is of the same order of magnitude as that which leads to the KdV equation from the nonlinear dispersive equations. Thus, to the same order of approximation, two waves propagating in the same direction do interact in a nonlinear fashion (e.g., Whitham (1974), p. 580) but two waves propagating in opposite directions do not! This can be understood

physically on the basis that as two waves propagate in the same direction their interaction time is relatively long while when they propagate in opposite directions their interaction time is much shorter, too short in fact to allow nonlinear interaction to take place.

The next step is to look for a solution represented as:

$$\eta(x,t) = \eta^{+}(Ct+x) + \eta^{-}(Ct-x) \tag{3.2.101}$$

where C is the wave speed and $\eta^{+}(Ct-x)$ and $\eta^{-}(Ct+x)$ are solutions of Eqs. (3.2.99) and (3.2.100), respectively, which satisfy the zero velocity boundary conditions at either end of the basin:

$$\Phi_x^{(0)}(0,t) = \Phi_x^{(0)}(\tfrac{L}{\ell},\ t) = 0 \tag{3.2.102}$$

Using Eqs. (3.2.84), (3.2.93) and (3.2.94), and choosing $\ell = L$ one obtains:

$$\eta^{+}(Ct) - \eta^{-}(Ct) = 0 \tag{3.2.103}$$

$$\eta^{+}(Ct+1) - \eta^{-}(Ct-1) = 0 \tag{3.2.104}$$

and from Eq. (3.2.103):

$$\eta^{+}(Ct) = \eta^{-}(Ct) = F(Ct) \tag{3.2.105}$$

Applying this relation to Eq. (3.2.104) the following results:

$$F(Ct+1) = F(Ct-1) \tag{3.2.106}$$

Thus, the particular solution must be periodic and of the form:

$$\eta(x,t) = F(Ct+x) + F(Ct-x)$$

Equation (3.2.106) is satisfied if, in dimensional units, the basin length L is an integral multiple of half the wave length λ.

An obvious solution for F is the cnoidal wave which is a periodic solution of the KdV equation. In dimensional notations the solution is written as:

$$\frac{\eta(x,t)}{H} = 2\left(\frac{d^t}{H} - \frac{h}{H}\right) + cn^2\left\{2K\left(\frac{t}{T} - \frac{x}{\lambda}\right) \middle| m\right\} + cn^2\left\{2K\left(\frac{x}{\lambda} + \frac{t}{T}\right) \middle| m\right\} \quad (3.2.107)$$

$$\frac{H\lambda^2}{h^3} = \frac{16}{3} mK^2 \quad (3.2.108)$$

$$d^t = h - H + \frac{H(K-E)}{mK} \quad (3.2.109)$$

$$C = \frac{\lambda}{T} = \sqrt{gh}\left[1 + \frac{H}{2hm}\left(2 - m - \frac{3E}{K}\right)\right] \quad (3.2.110)$$

$$\lambda = \frac{2L}{n} \quad (3.2.111)$$

where h is the depth, H is the wave height, d^t is the distance to the wave trough from the bottom, λ is the wave length, T is the period, C is the wave celerity, m is the elliptic parameter, K = K(m) and E = E(m) are the first and second complete elliptic integrals, respectively, and cn is the cnoidal Jacobian elliptic function. The integer n refers to a particular mode of free oscillation of the rectangular basin. A definition sketch for the various parameters is presented in Fig. 3.2.3.

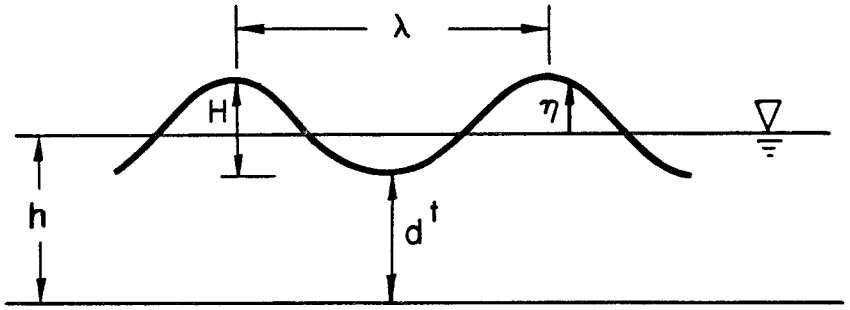

Fig. 3.2.3 Definition sketch for the cnoidal wave parameters.

Equations (3.2.107) to (3.2.111) define the finite amplitude unidirectional natural modes of oscillations in a rectangular basin. Two familiar features characterize those nonlinear modes. First, since a cnoidal wave is not symmetric with respect to the mean water level, fixed nodes do not exist. Second, the period of the oscillations varies with the amplitude as can be seen from Eq. (3.2.110) where the wave celerity can be expressed as:

$$\frac{C}{\sqrt{gh}} = f(\frac{H}{h}, \frac{h}{\lambda})$$

It is noted that those two features also characterize finite amplitude oscillation in the intermediate and the deep water range.

At the two extreme values of m:

(i) as $m \to 0$, $\frac{H\lambda^2}{h^3} \to 0$, $K \to \frac{\pi}{2}$, $E \to \frac{\pi}{2}$ and:

$$\frac{\eta(x,t)}{H} = 2 + \cos^2[\pi(\frac{t}{T} - \frac{x}{\lambda})] + \cos^2[\pi(\frac{x}{\lambda} + \frac{t}{T})]$$

or $$\frac{\eta(x,t)}{H} = \cos\frac{2\pi t}{T}\cos\frac{2\pi x}{\lambda}$$

$$\frac{C}{\sqrt{gh}} = \left[1 - \frac{1}{6}\left(\frac{2\pi h}{\lambda}\right)^2\right] = \frac{C_o}{\sqrt{gh}}$$

(This is the linearized result stated at the beginning of Sec. 3.3.3.)

(ii) as $m \to 1$ $\quad \frac{H\lambda^2}{h^3} \to \infty$, $K \to \infty$, $E \to 0$ and

$$\frac{\eta(x,t)}{H} = \operatorname{sech}^2\sqrt{\frac{3}{4}\frac{H}{h^3}}(x-Ct) + \operatorname{sech}^2\sqrt{\frac{3}{4}\frac{H}{h^3}}(x+Ct)$$

$$\frac{C}{\sqrt{gh}} = \left(1 + \frac{1}{2}\frac{H}{h}\right)$$

For this limiting case solitary waves will travel back and forth in the basin.

The ratio C/C_o, where C_o denotes the wave celerity computed from the linear dispersive theory, is plotted as a function of H/h in Fig. 3.2.4 for several values of h/λ. It is seen that for a fixed value of h/λ, C/C_o is an increasing function of H/h and for a fixed value of H/h it is a decreasing function of h/λ; the application of this property will appear clearly in Section 5.2. It can be noted that for a given basin length and a given mode of oscillation the ratio C/C_o is also equal to σ/σ_o, where σ_o denotes the frequency of the fundamental mode of oscillation as computed from the linear dispersive theory.

An important parameter in the study of long wave oscillations in

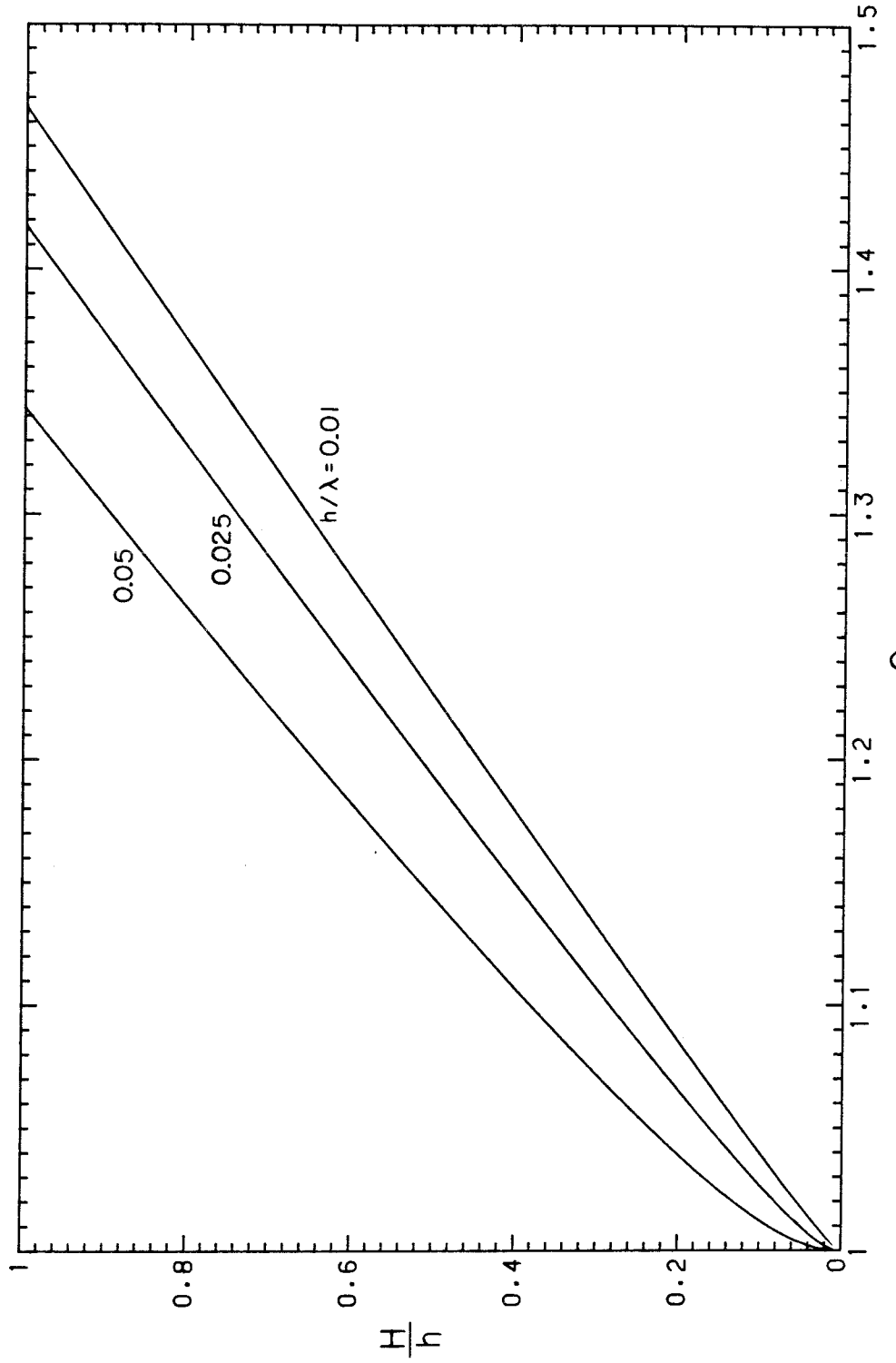

Fig. 3.2.4 Variation of the relative wave celerity C/C_o with H/h and h/λ for a cnoidal wave.

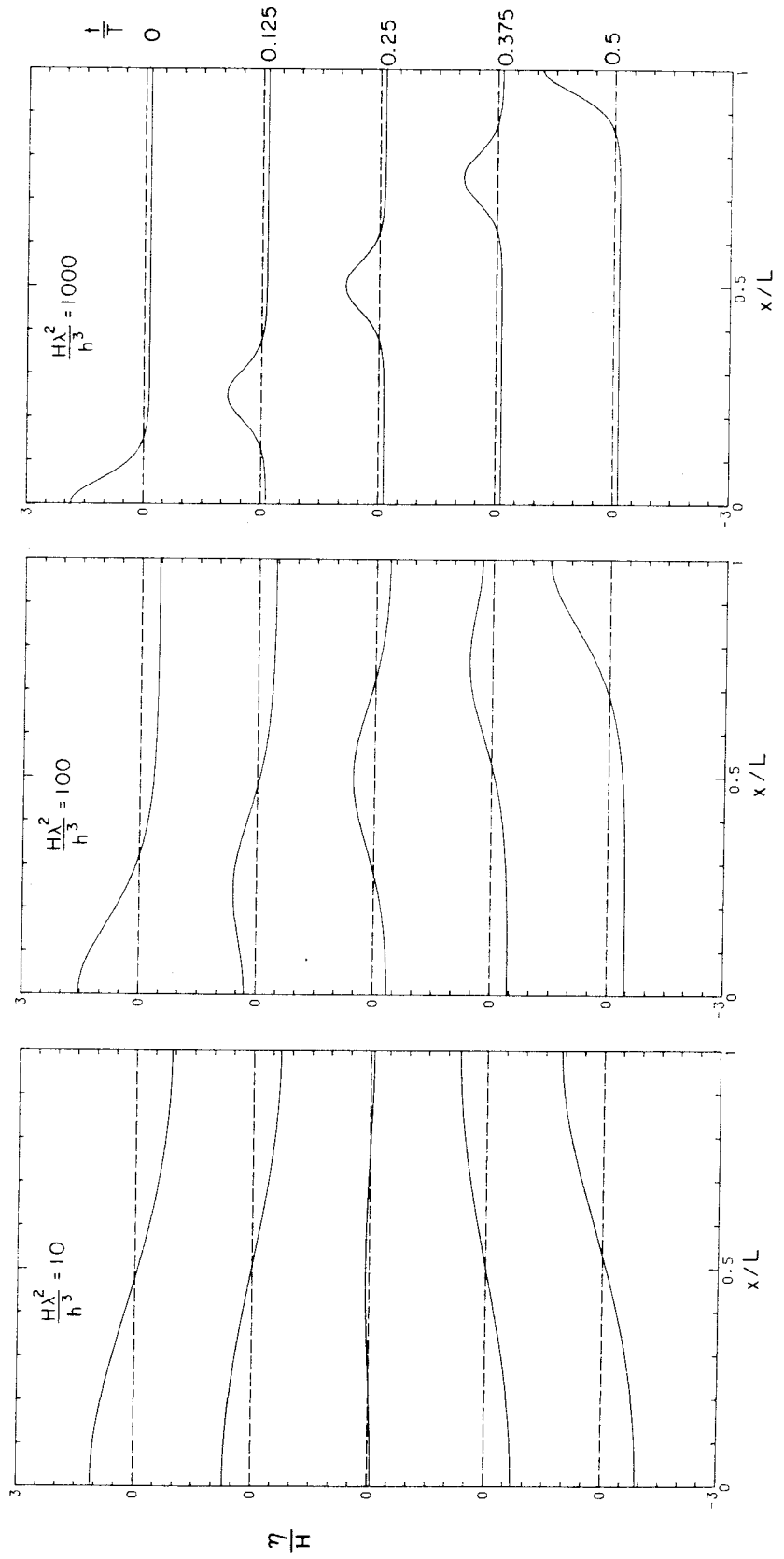

Fig. 3.2.5 Computed free surface profiles of standing waves in a closed basin at various times, for three values of the Stokes parameters, for the sloshing mode (λ = 2L).

closed basins is the Stokes parameter $H\lambda^2/h^3$. Inspection of Eqs. (3.2.107) to (3.2.109) shows that the shape of the curve $\eta(x,t)/H$ depends only on the value of $H\lambda^2/h^3$ at a given time t/T. The evolution in time of the wave in the basin has been plotted in Fig. 3.2.5 for three different values of $H\lambda^2/h^3$. For $H\lambda^2/h^3 = 10$ the profiles are similar to those predicted by the linear theory. However, no fixed node exists at x/L = 0.5 although the surface elevation remains small at all times at that location. For $H\lambda^2/h^3 = 100$ the comparison with the linear theory becomes poor; the standing wave pattern becomes a progressive wave pattern and the envelope of maximum surface elevations has constant height different from zero along the basin away from the walls. This nonlinear feature pertains only to the long wave range and is not observed in the intermediate or deep water range. For $H\lambda^2/h^3 = 1000$ the traveling wave pattern is even more apparent, actually the wave looks very much like a single "hump" traveling back and forth in the basin almost entirely above the still water level.

A comparison of these analytical results with experiments will be presented in Section 5.2. One major advantage of this analysis is that, although restricted to natural modes of oscillations, it provides insight into the characteristics of the finite amplitude oscillations. Using this approach it is also possible to delineate quantitatively the limits of validity of the linearized theory.

3.2.4 The Range of Validity of the Linear and Nonlinear Dispersive Theories

In this subsection all the variables are expressed in dimensional form. One common assumption to both the linear and

nonlinear dispersive theories is that $O(\frac{h}{\ell}) < O(1)$ where ℓ is a characteristic wavelength and h is the still water depth. Mathematically this assumption is expressed by the approximation of the classical linear dispersion relation by:

$$\sigma^2 = kg\left[kh - \frac{1}{3}(kh)^3\right] \tag{3.2.112}$$

This approximation is valid within 2% error if:

$$kh < 0.6 \tag{3.2.113}$$

or

$$\sigma\sqrt{h/g} < 0.6 \tag{3.2.114}$$

For the problems of the basin excitation or the wave-induced harbor oscillations, σ denotes some characteristic frequency of the excitation function.

Both linear and nonlinear long wave theories are applicable only if Eq. (3.2.113) is verified. If not, higher order dispersion terms should be introduced into the equations.

The second limitation concerns the effects of nonlinearities neglected in the linear theory. A relevant parameter indicating the importance of nonlinearities relative to dispersion is the Stokes parameter defined in Subsection 3.2.3 for the case of standing waves in a closed rectangular basin:

$$\underline{U}_s = \frac{H\lambda^2}{h^3} \tag{3.2.115}$$

where H and λ denote the cnoidal wave height and cnoidal wave length, respectively, associated with the standing wave oscillations.

It has been seen (Fig. 3.2.5) that if $\underline{U}_s$ is less than ten, finite amplitude effects remain small if not negligible for all modes of oscillation, but as $\underline{U}_s$ increases, the standing wave pattern changes into a wave pattern which is quite different from what the linear theory predicts. The critical value $\underline{U}_s = 10$ presumably can be chosen to define the upper limit at which finite amplitude effects can be neglected. For $\underline{U}_s < 10$ little error is introduced by replacing λ by $2\pi\sqrt{gh}/\sigma$. Furthermore, although the criterion has been established for the free oscillation of a standing wave system, it seems reasonable that it could also be extended for more general wave systems developing in the basin as well. Therefore, it is proposed to express the range of validity of the linear theory for long waves by:

$$\underline{U}_s = \left(\frac{\eta_+ - \eta_-}{2h}\right)\left(\frac{\sqrt{gh}\,2\pi}{\sigma h}\right)^2 \leq O(10) \qquad (3.2.116)$$

For a basin continuously excited with the motion described in Section 3.2.2 a resonant frequency is given by:

$$\frac{\sigma L}{\sqrt{gh}} \simeq (2n+1)\pi \qquad n = 0,1,2\cdots \qquad (3.2.117)$$

Using Eqs. (3.2.72), (3.2.116), and (3.2.117), an estimate of the evolution of the Stokes number with time when the basin is continuously excited at a resonant frequency can be derived as:

$$\underline{U}_s \simeq \frac{40}{(2n+1)\pi}\,\frac{d/L}{(h/L)^2}\,\frac{4}{\gamma_s}\left(1 - \exp\left[\frac{-\gamma_s}{2n+1}\,\frac{t}{T}\right]\right) \qquad (3.2.118)$$

In particular, during the first few oscillations:

$$\underline{U}_s \simeq \frac{160}{(2n+1)^2\pi} \frac{d/L}{(h/L)^2} \frac{t}{T} \qquad (3.2.119)$$

The significance of Eqs. (3.2.116), (3.2.118), and (3.2.119) will appear clearly in Section 5.2.

It is useful, at this point, to stress the difference between the Stokes number, defined specifically for the excitation of a closed basin, and the Ursell number, mentioned in Section 3.1 and used in a more general context to describe the evolution of a long wave system. The characteristic wave height H and the depth h are the same for the two parameters, but the characteristic length ℓ is different. For the Stokes number the length λ is the usual wavelength, related to the frequency σ by $\lambda \simeq 2\pi\sqrt{gh}/\sigma$, and it is independent of the local shape of the wave in the basin. In the Ursell number, the length ℓ refers to the local wave shape independent of the exciting conditions. A more quantitative definition of ℓ has been given by Hammack (1972) as $\ell = \eta_o / |\eta_x|$ where η_o is the maximum wave amplitude in the region of the wave under consideration and η_x is defined as the maximum value of the shape of the profile in that region. One important property of long waves, pointed out by Hammack (1972), is that they tend to evolve during their propagation in the absence of friction and geometric spreading effects towards a wave state characterized by a local Ursell number of order unity. An application of this consideration will be discussed in some detail in Section 5.2.

3.3 The Effects of Energy Dissipation on the Wave Induced Oscillations of a Narrow Rectangular Harbor

This aspect of the investigation presented here was motivated in the following ways. The initial purpose was to use a linearized analytical model for a harbor configuration with a simple geometry to determine the energy dissipation due to the entrance of a harbor. It turned out, however, that this method only yielded reliable results if the other sources of dissipation present in laboratory experiments were considered, such as boundary friction, surface tension, and leakage underneath harbor walls (for a harbor just sitting on the floor of a larger wave basin). Once the various sources of dissipation had been properly scaled, the results of the linear model could be used as a basis of comparison with the experiments for the investigation of the finite amplitude effects in both steady and transient wave induced oscillations. Since most of the experiments were performed for a narrow, rectangular harbor, a rectangular configuration was chosen for the analysis.

The incident waves generated in the laboratory are never sinusoidal, but contain higher harmonics. These harmonics may affect the harbor response significantly and since they are not necessarily in the shallow water range, the use of a fully dispersive linear theory is necessary.

The various sources of dissipation which may affect the wave dynamics in the present experimental harbor study are described in Section 3.3.1. The analytical formulation of the harmonic problem and the derivation of the dispersive, fully-dissipative solution are

presented in Section 3.3.2. A physical discussion of the solution and a correction for the sources of dissipation not included in the model, such as surface tension, is presented in Section 3.3.3. Finally, the application of the dissipative steady state solution to transient problems is presented in Section 3.3.4.

3.3.1 The Various Sources of Dissipation

In this section only the sources of dissipation affecting the present experimental harbor study are discussed.

(i) Laminar bottom friction

This source of dissipation has been included in the dissipative long wave equations derived in Section 3.1. It is caused by the laminar shear stress of the fluid against the bottom resulting in a velocity gradient at the bottom which can be approximated by (see Eqs. A.19 and A.23 in Appendix A):

$$\frac{\partial u_i}{\partial n} = \left(\frac{\sigma}{2\nu}\right)^{1/2} u_i \qquad (3.3.1)$$

where $\underset{\sim}{n}$ is the normal vector to the solid boundary, pointing toward the fluid domain, u_i is one of the velocity components parallel to the boundary, just outside the boundary layer, ν is the kinematic viscosity and σ is a characteristic frequency of the wave motion.

(ii) Laminar wall friction

When the fluid domain is bounded laterally by vertical walls, shear stress of the fluid against the lateral boundaries takes place, causing additional dissipation, and the resulting velocity gradient at the wall is also given by Eq. (3.3.1).

(iii) Laminar surface friction

In laboratory conditions a laminar shear stress often occurs at the water surface. It is caused by the formation of a thin film resulting from surface contamination. When the film is insoluble and becomes fully contaminated it acts as a solid boundary in the horizontal direction and the resulting velocity gradient at the surface can be expressed as:

$$\frac{\partial u_i}{\partial n} = C \left(\frac{\sigma}{2\nu}\right)^{1/2} u_i \qquad (3.3.2)$$

where C denotes the surface contamination factor which can, in principle, vary from 0 to 2 (Miles, 1967). In practice, for initially clean liquid surface in contact with ambient atmosphere experiments by Van Dorn (1966) indicate that C rapidly approaches a limiting value of unity. This value corresponds to the establishment of the fully contaminated surface film.

(iv) Dry friction from meniscus action

For a solid surface not wetted by a liquid, "Coulomb-like" frictional forces take place, according to Miles (1967), when the meniscus moves along the solid surface and can be expressed by:

$$F = \bar{\kappa}\, \Gamma_e \qquad (3.3.3)$$

per unit length of meniscus, where Γ_e is the surface tension at the air-water interface and $\bar{\kappa}$ a constant approximately equal to 0.31 for a distilled water-air-lucite contact (Miles, 1967). More precisely, according to Miles (1967), $\bar{\kappa}$ is equal to $\frac{1}{2}[\cos\theta_R - \cos\theta_A]$ where θ_A and θ_R

denote the contact angles of advance and recession, respectively, of the meniscus moving along the solid surface, which have unequal, but constant values. In the case of a distilled water-air-glass contact $\bar{\kappa}$ is nearly zero; this is reflected in the fact that distilled water wets glass but not lucite. In order to drastically reduce this friction force in the case of lucite (which was used in the present investigation) it is sufficient to add a small quantity of detergent in the water, e.g.,see Keulegan (1959).

(v) Residual dissipative source related to surface tension

An additional damping mechanism related to surface tension was apparently first measured by Keulegan (1959) in a special case and involves some "obscure surface activity phenomena" as expressed by Keulegan, apparently independent of surface film shear stress or dry meniscus friction. It becomes significant only for narrow vessels. One way to characterize this mechanism is to consider the surface as a membrane with a uniform tensile force Γ_e per unit length acting parallel to the water surface and connected to the walls (see definition sketch in Fig. 3.3.1).

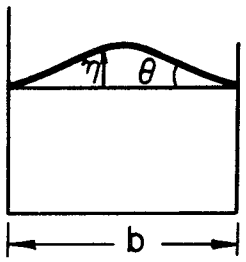

Fig. 3.3.1 Definition sketch for the additional surface dissipation mechanism.

The force F per unit length required to pull the membrane to an elevation η is given by:

$$F \sim \Gamma_e \sin \theta \sim \frac{\Gamma_e \eta}{b} \tag{3.3.4}$$

where Γ_e is the surface tension at the air-water interface, b is distance between the two walls and η is the wave height. One way to render this force dissipative is to assume the existence of a slight phase shift between F and η.

It can be noted that this dissipation mechanism and the four others previously mentioned affect the experimental study of the closed basin excitation as well as the experimental study of harbor oscillations.

(vi) Leakage losses

Many of the harbor experiments presented in Section 5.3 were performed with the harbor just sitting on the floor of the wave basin without seals. It was realized later in the program that this procedure introduced additional damping due to a small gap underneath the walls of the harbor. Thus, an analysis of this source of dissipation was necessary; this analysis is presented in Appendix D. The results can be expressed in the following way. First, the expressions for the horizontal component of the velocity vector and for the wave elevation are assumed to be of the form:

$$u_n(x_1,x_2,z,t) = \mathrm{Re}\left\{\hat{u}_n(x_1,x_2) \frac{\cosh k(z+h)}{\cosh kh} e^{-i\sigma t}\right\} \tag{3.3.5}$$

$$\eta(x_1,x_2,t) = \mathrm{Re}\left\{\hat{\eta}(x_1,x_2)\, e^{-i\sigma t}\right\} \tag{3.3.6}$$

where u_n denotes the outward normal component of the horizontal velocity vector at the wall, η is the wave elevation, h is the still water depth, σ is the circular frequency of the harmonic motion and k the corresponding wave number. The "leaking" boundary condition can be expressed as:

$$\hat{u}_n = \frac{e^3}{3\nu t_e} \frac{gk}{2kh + \sinh 2kh} \hat{\eta} \tag{3.3.7}$$

where e is the width of the gap between the wall and the floor, t_e is the wall thickness, g is the acceleration of gravity, and ν is the kinematic viscosity. One of these parameters, the gap e, is undefined and it will have to be found from the experiments presented in Section 6.2. Considering shallow water waves, the dependence of the leakage velocity on k in Eq. (3.3.7) disappears and $\hat{u}_n$ is related to $\hat{\eta}$ by:

$$\hat{u}_n = \frac{e^3}{12\nu t_e} \frac{g}{h} \hat{\eta} \tag{3.3.8}$$

It can be noticed that since Eq. (3.3.8) does not contain the frequency σ or the wave number k it applies equally well to the transient case for long waves.

(vii) Entrance separation loss

Similar to the approach of Ito (1970) and Ünlüata and Mei (1975), at the harbor mouth a head loss is assumed to exist such that the amplitude difference across the entrance is expressed as:

$$\overline{\Delta\eta(x_1,x_2,t)} = \frac{f_e}{2g} \overline{u_n(x_1,x_2,0,t)} \; \overline{|u_n(x_1,x_2,0,t)|} \tag{3.3.9}$$

where u_n denotes the velocity across the entrance, the horizontal bars denote the average along the entrance and the vertical

bars denote the absolute value for a real expression and the modulus for a complex expression. The friction factor f_e is ill defined for the unsteady case and will be investigated from experiments which will be described in Section 6.2. In addition, a discussion of the dependence of f_e on certain relevant physical parameters will be postponed also until Section 6.2.

If Eq. (3.3.9) is applied to the harmonic problem, higher harmonics are generated due to the quadratic terms. However, as a first approximation in Eq. (3.3.9) the quadratic entrance loss can be replaced by an equivalent linearized expression:

$$\overline{\Delta\eta(x_1,x_2,t)} = \frac{8}{3\pi}\frac{f_e}{2g}|\hat{u}_n|\,\overline{u_n(x_1,x_2,0,t)} \qquad (3.3.10)$$

where $\hat{u}_n$ is defined by Eq. (3.3.5). Equation (3.3.10) is obtained from Eq. (3.3.9) in the case of a sinusoidal wave by computing the loss of energy in one period at the entrance for a quadratic and a linear dissipation term and equating the results.

3.3.2 The Solution of the Harmonic Problem

The harbor under study has a rectangular shape and is partially closed at the mouth by a thin breakwater as shown by the definition sketch in Fig. 3.3.2. Several assumptions are made:

(i) The still water depth h is constant throughout the fluid domain.

(ii) The coastline AE,BF is straight.

(iii) The direction of the incident wave is perpendicular to the coastline.

ELEVATION VIEW

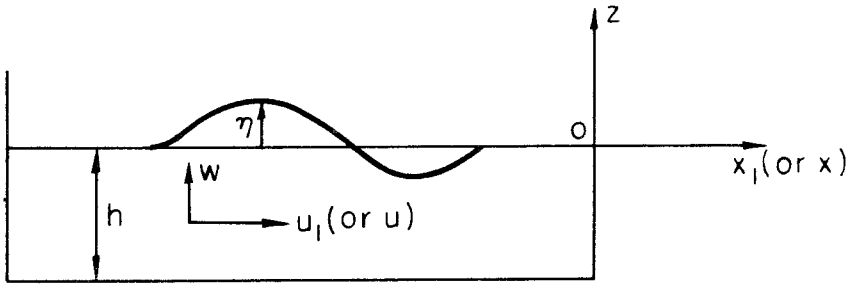

PLAN VIEW

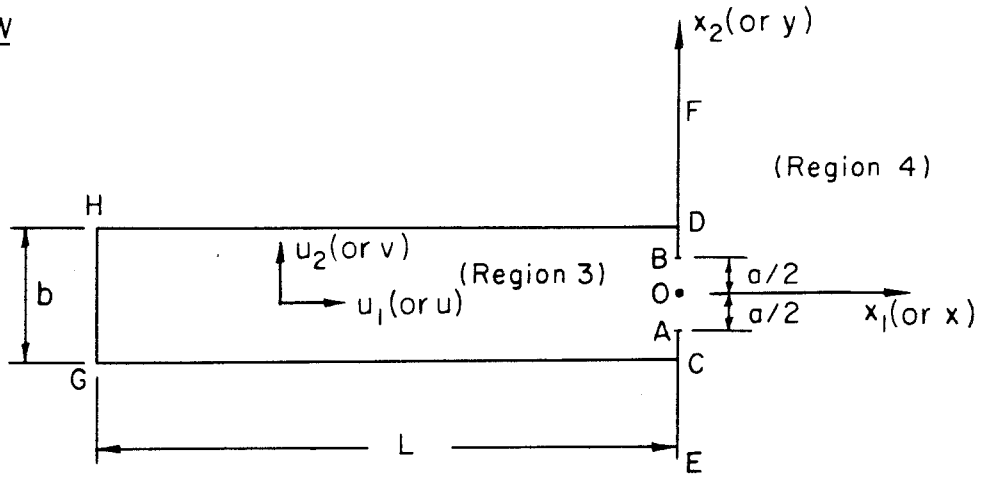

Fig. 3.3.2 Definition sketch of a rectangular harbor.

(iv) Finite amplitude effects are neglected. This implies the wave amplitude is small compared to the depth.

(v) The following dissipation sources, among those discussed in Section 3.3.1 are included in the present formulation: laminar boundary friction at the bottom, the walls, and at the surface inside the harbor, leakage losses under the walls DH, HG, and GC, separation losses across the entrance AB. A correction for the remaining sources of dissipation listed in Section 3.3.1 but not included in the formulation, namely the two dissipative sources related to surface tension, will be presented in Section 3.3.3.

(vi) The harbor width b is small compared to the harbor length ($b/L \leq 0.4$, say). Also, the ratio of b/λ, where λ is the wavelength of the incident wave, is small compared to unity (say, $b/\lambda \leq .2$).

The assumptions listed in (vi), which are consistent with the range of the experiments presented in Section 6.2, greatly simplify the derivation of the analytical solution as will be seen later. The solution will be obtained in four successive steps: derivation of a simplified form for the equations of motion including the effects of laminar boundary friction, representation of the solution inside the harbor, representation of the solution outside the harbor, and matching between the two regions at the harbor mouth.

Using the Einstein summation convention, the linearized continuity and momentum equations are:

$$\frac{\partial u_j}{\partial x_j} + \frac{\partial w}{\partial z} = 0 \tag{3.3.11}$$

$$\frac{\partial u_i}{\partial t} = -\frac{1}{\rho}\frac{\partial p_d}{\partial x_i} + \nu\left(\frac{\partial^2 u_i}{\partial x_j \partial x_j} + \frac{\partial^2 u_i}{\partial z^2}\right) \qquad i=1,2 \tag{3.3.12}$$

$$\frac{\partial w}{\partial t} = -\frac{1}{\rho}\frac{\partial p_d}{\partial z} + \nu\left(\frac{\partial^2 w}{\partial x_j \partial x_j} + \frac{\partial^2 w}{\partial z^2}\right) \tag{3.3.13}$$

where $u_i(x_1,x_2,z,t)$ is the component of the velocity vector in the horizontal x_i direction, $w(x_1,x_2,z,t)$ is the component of the velocity vector in the z direction, ρ is the fluid density, ν is the kinematic viscosity, t is the time, and p_d is the dynamic pressure defined as:

$$p_d = p + \rho g z \tag{3.3.14}$$

where g is the acceleration of gravity and p the static pressure. Internal dissipation is neglected throughout this analysis for the reason discussed in Section 3.1, and the only viscous terms retained are associated with the velocity gradients near the bottom and at the surface in a direction perpendicular to the bottom and surface boundaries.

The boundary conditions are:

$$p_d = \rho g \eta \qquad \text{at} \quad z = 0 \tag{3.3.15}$$

$$w = \partial\eta/\partial t \qquad \text{at} \quad z = 0 \tag{3.3.16}$$

$$w = 0 \qquad \text{at} \quad z = -h \tag{3.3.17}$$

$$\frac{\partial u_i}{\partial z} = \left(\frac{\sigma}{2\nu}\right)^{1/2} u_i \qquad \text{at} \quad z = -h \tag{3.3.18}$$

$$\frac{\partial u_i}{\partial z} = -C\left(\frac{\sigma}{2\nu}\right)^{1/2} u_i \qquad \text{at} \quad z = 0 \tag{3.3.19}$$

where $\eta(x_1,x_2,t)$ is the surface elevation, σ is a characteristic frequency of the fluid motion and C the surface contamination factor. Equations (3.3.18) and (3.3.19) are directly derived from Eqs. (3.3.1) and (3.3.2), respectively.

The analysis is now restricted to the harmonic problem. Since the effects of friction are only important near the solid boundaries, one could expect that the velocity and pressure fields in the fluid domain away from the boundaries have the same structure as in the frictionless case. That is, u_i, w, p_d and η are assumed to be of the form:

$$u_i = \mathrm{Re}\left\{ \hat{u}_i(x_1,x_2) \frac{\cosh k(h+z)}{\cosh kh} e^{-i\sigma t} \right\} \qquad i=1,2 \tag{3.3.20}$$

$$w = \mathrm{Re}\left\{ \hat{w}(x_1,x_2) \frac{\sinh k(h+z)}{\cosh kh} e^{-i\sigma t} \right\} \tag{3.3.21}$$

$$p_d = \mathrm{Re}\left\{ \hat{p}_d(x_1,x_2) \frac{\cosh k(h+z)}{\cosh kh} e^{-i\sigma t} \right\} \tag{3.3.22}$$

$$\eta = \mathrm{Re}\left\{ \hat{\eta}(x_1,x_2) e^{-i\sigma t} \right\} \tag{3.3.23}$$

where i denotes the imaginary number $\sqrt{-1}$ and k is a wave parameter to be found from the equations and boundary conditions.

Substituting expressions (3.3.20) and (3.3.21) into Eq. (3.3.11) yields

$$\frac{\partial \hat{u}_i}{\partial x_i} + k\hat{w} = 0 \tag{3.3.24}$$

Multiplying Eqs. (3.3.12) and (3.3.13) by u_i and w, respectively, and integrating through the depth yields:

$$[-i\sigma + \frac{1}{h}(\frac{\nu\sigma}{2})^{1/2} \frac{4kh(1+C\cosh^2 kh)}{2kh+\sinh 2kh}]\hat{u}_i = -\frac{1}{\rho}\frac{\hat{p}_d}{\partial x_i} + 0(\nu) \tag{3.3.25}$$

$$-\frac{i\sigma\hat{w}}{k} = -\frac{1}{\rho}\hat{p}_d + 0(\nu) \qquad i = 1,2 \tag{3.3.26}$$

The boundary condition (3.3.15) implies:

$$\hat{p}_d = \rho g \hat{\eta} \tag{3.3.27}$$

Combining Eqs. (3.3.26) and (3.3.27) one obtains:

$$-\frac{i\sigma\hat{w}}{k} = -g\hat{\eta} \tag{3.3.28}$$

The elimination of $\hat{w}$ between Eqs. (3.3.28) and (3.4.24) yields:

$$\frac{\partial \hat{u}_i}{\partial x_i} - \frac{ik^2 g}{\sigma}\hat{\eta} = 0 \tag{3.3.29}$$

Finally, after eliminating $\hat{u}_i$ and $\hat{p}_d$ between Eqs. (3.3.25), (3.3.27) and (3.3.29), an equation for η alone is obtained as:

$$\frac{\partial^2 \hat{\eta}}{\partial x_j \partial x_j} + k^2(1 + i\mu_{bs})\hat{\eta} = 0(\nu) \tag{3.3.30}$$

where μ_{bs} is the boundary dissipation factor equal to:

$$\mu_{bs} = \frac{1}{h} \left(\frac{\nu}{2\sigma}\right)^{1/2} \frac{2 \sinh 2kh}{2kh + \sinh 2kh} \left[\frac{2kh}{\sinh 2kh} + C \frac{kh}{\tanh kh}\right] \qquad (3.3.31)$$

The boundary condition (3.3.16) has still to be satisfied. Using Eq. (3.3.28), the classical dispersion relation between σ and the wave number k is obtained as:

$$\sigma^2 = kg \tanh kh \qquad (3.3.32)$$

The equations of motion have now been reduced to the modified Helmholtz equation (3.4.30). The relationship between $\hat{\eta}$ and the other variables can be rewritten using the various relations derived so far:

$$\hat{u}_i = -i \frac{g}{\sigma} (1 - i\mu_{bs}) \frac{\partial \hat{\eta}}{\partial x_i} \qquad i = 1,2 \qquad (3.3.33)$$

$$\hat{w} = -i \frac{kg}{\sigma} \hat{\eta} \qquad (3.3.34)$$

$$\hat{p}_d = \rho g \hat{\eta} \qquad (3.3.35)$$

It is noted that wall friction effects are not included in the damping coefficient μ_{bs} in Eq. (3.4.30), since the integration was only over the depth, not along the boundaries. Assuming momentarily that there is no variation of the wave motion in the x_2 direction, the momentum Equation (3.3.12) and (3.3.13) can be integrated first along the width so that the contribution of boundary friction at the walls can be obtained. Then, following the same procedure as in the previous derivation, the final equation is obtained as:

$$\frac{d^2\hat{\eta}}{dx_1^2} + k^2(1+i\mu_t)\hat{\eta} = 0(\nu) \tag{3.3.36}$$

with the following expression for μ_t:

$$\mu_t = \frac{1}{h}\left(\frac{\nu}{2\sigma}\right)^{1/2}\left[\frac{2\sinh 2kh}{2kh+\sinh 2kh}\right]\left[\frac{2kh}{\sinh 2kh} + \frac{Ckh}{\tanh kh} + \frac{2h}{b}\right] \tag{3.3.37}$$

For a small aspect ratio b/L one can expect the motion to remain one-dimensional except near the mouth. As a result, a reasonable way to include the effects of wall friction in Eq. (3.3.30) is to replace μ_{bs} by μ_t.

For purposes of clarity the coordinates x_1 and x_2 are replaced by x and y and the velocity components u_1, u_2 become u and v in the remainder of this section.

(ii) Representation of the solution inside the harbor (Region 3)

The variables are referenced by the subscript 3 in the interior harbor region, limited on Fig. 3.3.1 by the boundaries DH, HG, GC, and CD.

The problem consists in deriving a proper representation for $\hat{\eta}_3(x,y)$ satisfying the Helmholtz equation:

$$\frac{\partial^2\hat{\eta}_3}{\partial x^2} + \frac{\partial^2\hat{\eta}_3}{\partial y^2} + \tilde{k}^2\,\hat{\eta}_3 = 0 \tag{3.3.38}$$

$$\tilde{k} = k\left(1 + i\,\frac{\mu_t}{2}\right)$$

The proper boundary condition at the "leaking" boundary can be obtained by substituting Eq. (3.3.7) into Eq. (3.3.33):

$$\frac{\partial \hat{\eta}}{\partial x} = i\,\varepsilon\,k\hat{\eta} + 0(\varepsilon\mu_t) \tag{3.3.39}$$

where

$$\varepsilon = \frac{e^3}{3\nu t_e}\,\frac{\sigma}{2kh + \sinh\,2kh} \tag{3.3.40}$$

Typically $0(\varepsilon) = 0(\mu_t) = 0.01$, so that terms of order $\varepsilon\mu_t$, ε^2, and μ_t^2 will be neglected throughout the analysis. The boundary conditions are:

$$\frac{\partial \hat{\eta}_3}{\partial x}(-L,y) = 0 \quad , \; |y| < \frac{b}{2} \tag{3.3.41}$$

$$\frac{\partial \hat{\eta}_3}{\partial y}(x, \tfrac{b}{2}) = i\,\varepsilon\,\tilde{k}\,\hat{\eta}_3\,(x, \tfrac{b}{2}) \tag{3.3.42}$$

$$\frac{\partial \hat{\eta}_3}{\partial y}(x,-\tfrac{b}{2}) = -i\,\varepsilon\,\tilde{k}\,\hat{\eta}_3(x, -\tfrac{b}{2}) \tag{3.3.43}$$

$$\frac{\partial \hat{\eta}_3}{\partial x}(0,y) = c_3(y) \tag{3.3.44}$$

where $c_3(y) = 0$ for $|y| > \frac{a}{2}$

Following Miles and Munk (1961), a Green function representation of the solution is sought of the form:

$$\hat{\eta}_3(x,y) = \int_{-b/2}^{b/2} c_3(y')\ G(x,y,y')dy' \qquad (3.3.45)$$

where the Green function $G(x,y,\eta)$ must satisfy Eq. (3.3.38) to (3.3.43) (where $\hat{\eta}_3$ is replaced by G) and

$$\frac{\partial G}{\partial x}(0,y,y') = \delta(y-y') \qquad |y'| < b/2 \qquad (3.3.46)$$

where $\delta(y-y')$ denotes the Dirac function.

An elementary solution of Eq. (3.3.38) for G satisfying boundary conditions (3.3.41) to (3.3.43) is found as:

$$\cos(\tilde{\beta}_n y)\ \cos[\tilde{\alpha}_n(x+L) + i\varepsilon] \qquad (3.3.47)$$

where

$$\tilde{\alpha}_n = (\tilde{k}^2 - \tilde{\beta}_n^2)^{1/2}$$

$$\tilde{\beta}_n = \begin{cases} \dfrac{2\pi n}{b} - \dfrac{i\varepsilon}{\pi n b} & n=1,2,3\ldots \\ (i-1)\sqrt{\dfrac{\varepsilon}{kb}}\,k & n=0 \end{cases}$$

The general solution for G can be expressed in a series expansion:

$$G(x,y,y') = \sum_{n=0}^{\infty} d_n(y')\ \cos(\tilde{\beta}_n y)\ \cos[\tilde{\alpha}_n(x+L) + i\varepsilon] \qquad (3.3.48)$$

Each coefficient $d_n(y')$ is found by applying boundary condition (3.3.46) and integrating across the harbor width after multiplying each side of Eq. (3.3.46) by $\cos(\tilde{\beta}_n y)$:

$$d_n(y') = \begin{cases} -\dfrac{\cos(\tilde{\beta}_n y')}{\frac{b}{2}\tilde{\alpha}_n\left[1+\frac{2(-1)^n \varepsilon kb}{2(\pi n)^2}\right]\sin(\tilde{\alpha}_n L + i\varepsilon)} & n=1,2,3 \\ -\dfrac{\cos(\tilde{\beta}_o y')}{b\tilde{\alpha}_o \sin(\tilde{\alpha}_o L + i\varepsilon)} & n=0 \end{cases} \tag{3.3.49}$$

It has been assumed previously that $b/L \leq 0.4$. Thus, the wave for those situations can be considered unidirectional except near the mouth, and most of the wave energy remains concentrated in the first mode of oscillation (corresponding to n=0). Hence, the effect of dissipation will be retained only in the first term of the series in Eq. (3.3.48). Furthermore, it has been assumed that $b/\lambda << 1$; this implies that $kb < 2\pi$ and, thus, the final form of Green's function is obtained from Eq. (3.3.49) as:

$$G(x,y,y') = \frac{-\cos(\tilde{\beta}_o y')\cos(\tilde{\beta}_o y)\cos(\tilde{\alpha}_o(x+L)+i\varepsilon)}{b\tilde{\alpha}_o \sin(\tilde{\alpha}_o L + i\varepsilon)} + \sum_{n=1}^{\infty} \frac{\cos(\beta_n y')\cos(\beta_n y)\cosh[\alpha_n(x+L)]}{\frac{b}{2}\alpha_n \sinh(\alpha_n L)} \tag{3.3.50}$$

where

$$\beta_n = \frac{2\pi n}{b}, \quad \alpha_n = (\beta_n^2 - k^2)^{1/2}$$

A uniform velocity distribution is assumed across the mouth. This implies from Eq. (3.3.33) a constant value for $c_3(y)$:

$$\overline{c}_3 = c_3(y) = \frac{i\sigma}{g}(1+i\mu_t)\,\overline{\hat{u}_3(0,y)} \qquad \text{for} \quad |y| < \frac{a}{2} \tag{3.3.51}$$

From Eq. (3.3.45), an average amplitude across the entrance can be computed as:

$$\overline{\hat{\eta}_3(0,y)} = \frac{\overline{c_3}}{a}\int_{-a/2}^{a/2}\int_{-a/2}^{a/2} G(0,y,y')\,dy'\,dy \tag{3.3.52}$$

and the result can be put in the form:

$$\overline{\hat{\eta}_3(0,y)} = \overline{c_3}(E + a\overline{S_1}) \tag{3.3.53}$$

where

$$E = -\frac{a}{b}\frac{1}{\tilde{\alpha}_o}\frac{1}{\tan(\tilde{\alpha}_o L + i\varepsilon)} \tag{3.3.55}$$

$$\overline{S}_1 = \sum_{n=1}^{\infty} 2\left(\frac{b}{a}\right)^2 \left(\frac{1}{\pi n}\right)^2 \frac{1}{b\alpha_n}\frac{\cosh\,\alpha_n L}{\sinh\,\alpha_n L}\sin^2\left(\frac{\pi n a}{b}\right) \tag{3.3.56}$$

E can be expanded to the first order in μ_t and ε:

$$E = -\frac{a}{b}\frac{1}{k}\frac{1}{\tan\,kL} + i(I_\mu + I_\varepsilon) \tag{3.3.57}$$

where

$$I_\mu = \frac{\mu_t}{2}\left(\frac{a}{kb\,\tan\,kL} + \frac{L}{b}\frac{a}{\sin^2 kL}\right) \tag{3.3.58}$$

$$I_\varepsilon = \varepsilon\frac{a}{kb}\left[\frac{1}{kb\,\tan\,kL} + \left(1+\frac{L}{b}\right)\frac{1}{\sin^2 kL}\right] \tag{3.3.59}$$

The unknown $\bar{c}_3$ is to be found by matching the solution at the mouth as described by Eq. (3.3.53) with the form of solution outside the harbor, which will be derived next. Once $\bar{c}_3$ is known, the solution inside the harbor is given by Eq. (3.3.45). More explicitly, using Eq. (3.3.50) and expanding $G(x,y,y')$ to the first order in μ_t and ε, the amplitude function $\hat{\eta}_3$ is expressed as:

$$\hat{\eta}_3(x,y) = \frac{\bar{c}_3}{k}\left[-\frac{a}{b}\frac{\cos k(x+L)}{\sin kL} + i(J_\mu + J_\varepsilon) + \overline{S_2}(x,y)\right] \tag{3.3.60}$$

where

$$J_\mu = \frac{a}{b}\frac{\mu_t}{2}\frac{1}{\sin kL}\left[1 + \frac{kL}{\tan kL}\right] \tag{3.3.61}$$

$$J_\varepsilon = \frac{a}{b}\frac{\varepsilon}{\sin kL}\left[\frac{1}{kb} + \frac{(1 + L/b)}{\tan kL}\right] \tag{3.3.62}$$

$$\overline{S}_2(x,y) = \sum_{n=1}^{\infty} \frac{4kb \sin(\frac{\beta_n b}{2}) \cos(\beta_n y) \cosh[\alpha_n(x+L)]}{b^2\alpha_n\beta_n \sinh(\alpha_n L)} \tag{3.3.63}$$

(ii) Representation of the solution outside the harbor (Region 4)

The subscript 4 will be used to denote the variables in the region outside the harbor. In the outer region viscous and leakage effects are neglected. The amplitude function $\hat{\eta}_4$ must satisfy the Helmholtz equation:

$$\frac{\partial^2\hat{\eta}_4}{\partial x^2} + \frac{\partial\hat{\eta}_4}{\partial y^2} + k^2\hat{\eta}_4 = 0 \tag{3.3.64}$$

with the boundary condition:

$$\frac{\partial \hat{\eta}_4}{\partial y}(0,y) = 0 \qquad |y| > \frac{a}{2} \tag{3.3.65}$$

The amplitude can be conveniently divided into two parts:

$$\hat{\eta}_4 = \hat{\eta}_I + \hat{\eta}_s \tag{3.3.66}$$

where $\hat{\eta}_I$ denotes the amplitude function of the normally incident and reflected wave system in the absence of harbor:

$$\hat{\eta}_I = A_I \cos kx \tag{3.3.67}$$

and $\hat{\eta}_s$ is the amplitude function of the radiated wave produced by the presence of the harbor. A proper representation of the solution for $\hat{\eta}_s$ satisfying Eqs. (3.3.64) and (3.3.65) and the Sommerfeld radiation condition at infinity, i.e., $\hat{\eta}_s \to 0$ as $x^2+y^2 \to \infty$, can be obtained along the mouth (e.g.,Lamb (1932, §305) as:

$$\hat{\eta}_s(0,y) = -\frac{i}{2}\int_{-a/2}^{a/2} H_o'[k|y-y'|]c_4(y')dy' \tag{3.3.68}$$

where H_o' is the Hankel function of the first kind of zeroth order and c_4 is the normal derivative of $\hat{\eta}_s$ across the harbor entrance, i.e.,

$$c_4(y) = \frac{\partial \hat{\eta}_s}{\partial x}(0,y) \qquad |y| < \frac{a}{2} \tag{3.3.69}$$

From Eqs. (3.3.67) and (3.3.68) the wave amplitude in the outer region at the harbor mouth can be represented as:

$$\hat{\eta}_4(0,y) = A_I - \frac{i}{2}\int_{-a/2}^{a/2} H_o'[k|y-y'|]\, c_4(y')dy' \tag{3.3.70}$$

Since $\frac{\partial \hat{\eta}_I}{\partial y} \neq 0$ at $x = 0$ for all values of y, $c_4(y)$ also represents the normal derivative of $\hat{\eta}_4$ at the entrance:

$$c_4(y) = \frac{\partial \hat{\eta}_4}{\partial x}(0,y) \quad , \quad |y| < \frac{a}{2} \tag{3.3.71}$$

A uniform velocity distribution has been assumed across the mouth. This implies from Eq. (3.3.65) a constant value for $c_4(y)$

$$\overline{c_4} = c_4(y) = \frac{i\sigma}{g}\hat{u}_4(0,y) = \frac{i\sigma}{g}\overline{\hat{u}_4(0,y)} \tag{3.3.72}$$

An average amplitude can be computed across the entrance (see Lee (1971)) as:

$$\overline{\eta_4(0,y)} = A_I - \frac{i}{2}\overline{c}_4\, a(J_c + i\,\frac{2}{\pi}Y_c) \tag{3.3.73}$$

where $$J_c = 1 + 0(k^2a^2) \tag{3.3.74}$$

$$Y_c = \ln(0.1987\ ka) + 0(k^2a^2) \tag{3.3.75}$$

(iii) Matching the solution of each region at the harbor entrance

The existence of a head loss across the mouth has previously been assumed defined by Eq. (3.3.10). With the present notations and using Eqs. (3.3.20) to (3.3.23), Eq. (3.3.10) can also be written as:

$$\overline{\hat{\eta}_3(0,y)} - \overline{\hat{\eta}_4(0,y)} = \frac{8}{3\pi} \frac{f_e}{2g} \overline{|\hat{u}_3(0,y)|\, \hat{u}_3(0,y)} \tag{3.3.76}$$

where the vertical bars denote the modulus of the complex quantity $\hat{u}_3$. The continuity requirement at the entrance implies:

$$\overline{\hat{u}_3(0,y)} = \overline{\hat{u}_4(0,y)} \tag{3.3.77}$$

where the assumption of small wave amplitude compared to the depth has been used.

The remainder of the derivation follows directly. Substituting Eqs. (3.3.53) and (3.3.73) into Eq. (3.3.76) and using relations (3.3.77), (3.3.72) and (3.3.51) yields, after some manipulation, the following expression:

$$Y = \frac{i\sigma \overline{\hat{u}_3(0,y)}}{kgA_I} = \frac{\overline{c}_3}{kA_I} = \frac{1}{B + i(\chi_r + \chi_\mu + \chi_\varepsilon + \chi_f)} \tag{3.3.78}$$

where $$B = -\frac{ka}{\pi} \ln(0.1987\, ka) - \frac{a}{b} \operatorname{cotg}\, kL + ak\overline{S}_1 \tag{3.3.79}$$

$\overline{S_1}$ is the real quantity given by Eq. (3.3.56) and:

$$\chi_r = \frac{ak}{2} \tag{3.3.80}$$

$$\chi_\mu = \frac{\mu_t}{2} \frac{a}{b} \left[\frac{1}{\tan\, kL} + \frac{kL}{\sin^2 kL}\right] \tag{3.3.81}$$

$$\chi_\varepsilon = \varepsilon \frac{a}{b} \left[\frac{1}{kb\, \tan\, kL} + \left(1 + \frac{L}{b}\right) \frac{1}{\sin^2 kL}\right] \tag{3.3.82}$$

$$\chi_f = \frac{f_e}{2} \left(\frac{8}{3\pi}\right) \frac{A_I k^2 g}{\sigma^2} |Y| \tag{3.3.83}$$

The term χ_r comes about from the communication of the harbor with the open sea and is directly related to the imaginary part of Eq. (3.3.73). The physical significance of the four terms χ_r, χ_μ, χ_ε and χ_f will be discussed in Section 3.3.3.

Once the Eq. (3.3.78) has been solved for the unknown quantity $\overline{c}_3$ the wave amplitude can be computed at any location inside the harbor from Eq. (3.3.60). In particular, the series $\overline{S}_2(x,y)$ can be neglected at the backwall for $b/L < 1$ and a simple expression is obtained for $\hat{\eta}_3(-L,y)$:

$$\frac{\hat{\eta}_3(-L,y)}{A_I} = -Y\left[\frac{a}{b} \frac{1}{\sin kL} + i(J_\mu + J_\varepsilon)\right] \tag{3.3.84}$$

where J_μ and J_ε are defined by Eq. (3.3.61) and (3.3.62) respectively.

This concludes the analytical derivation of the solution for the wave-induced oscillations in a rectangular harbor with laminar boundary friction, entrance losses, and the effect of leakage incorporated (as mentioned, the primary application of the latter is in connection with the laboratory studies presented in Chapter 6).

The application of these results for the indirect experimental determination of the entrance friction coefficient f_e can be seen from Eqs.(3.3.84) and (3.3.78). The value of $|Y|$ can be determined from the measurement of the wave amplitude at the backwall of the harbor and from

Eq. (3.3.84). The coefficient f_e is derived from Eq. (3.3.78), assuming that χ_μ and χ_ε are known. A physical interpretation of the solution and its applications to the evaluation of the effects of other sources of dissipation not included in the present formulation are presented next in Section 3.3.3.

3.3.3 The Physical Interpretation of the Solution

The structure of the solution is best characterized by Eq. (3.3.78) which is similar to that which defines the amplification factor for the harmonic oscillator. The denominator consists of a real part B which becomes zero for some values of the incident wave number k, and an imaginary part composed of four terms, each generally less than order unity. These terms represent the effects of the four dissipative sources described earlier on the dynamics of the harbor.

The radiative damping term, χ_r, is produced by the communication of the harbor with the open sea which creates a leakage of energy away from the harbor. Since χ_r is proportional to ka the radiative damping decreases as the harbor opening gets smaller leading to the so-called harbor paradox (Miles and Munk (1961)). The boundary friction term, χ_μ, in this section is due to laminar friction along the bottom, lateral and surface boundaries. Equation (3.3.81) shows that χ_μ increases with kL, i.e., with higher modes of oscillation. The term χ_ε stems from the possible existence of a small gap beneath the harbor walls in the laboratory model, corresponding to a loss due to leakage. It is noted, from Eq. (3.3.82), that the importance of leakage damping increases as the ratio $\frac{L}{b}$ increases. Finally, entrance friction is represented by the

term χ_f and is produced by the head loss across the harbor entrance. From Eqs. (3.3.83) and (3.3.84) χ_f increases with $\frac{b}{a}$ and $\hat{\eta}_3$ so that the importance of entrance loss increases as the width of the entrance decreases and as the wave amplitude inside the harbor increases. If in Eq. (3.3.78) B = 0 for some wave number and $\chi_r \ll 1$, the quantity Y still remains finite because of the presence of the terms associated with viscous dissipation, i.e., χ_μ, χ_ε, χ_f.

The amplification factor R(x,y) is defined as:

$$R(x,y) = \left| \frac{\hat{\eta}_3(x,y)}{A_I} \right| \tag{3.3.85}$$

Specializing to the situation where $0(\chi_r + \chi_\mu + \chi_\varepsilon + \chi_f) < 1$, the reasonant conditions corresponding to a maximum velocity at the entrance are realized for B = 0 and the corresponding amplification factor is given at the backwall by:

$$R(-L,0) = \left[\frac{a}{b} \frac{1}{\sin|kL|} \right] \frac{1}{\chi_r + \chi_\mu + \chi_\varepsilon + \chi_f} + 0(\varepsilon,\mu) \tag{3.3.86}$$

At resonance, the value of kL for which B = 0 in Eq. (3.3.79) depends both on $\frac{a}{b}$ and $\frac{b}{L}$. However, if b/L remains sufficiently small, a zeroth order approximation for kL is:

$$kL \approx (2n+1)\frac{\pi}{2} \qquad n=0,1,2... \tag{3.3.87}$$

(In actual fact, these values of (kL) correspond to the limiting case where $\frac{b}{L} = 0$.) The corresponding mode shapes can be defined approximately

from Eq. (3.3.60) as:

$$\frac{\hat{\eta}_3(x,y)}{A_I} \sim \cos k(x+L) \tag{3.3.88}$$

In order to evaluate the effects of dissipative sources not included in the present model it is useful to define at resonance the factor Q_i associated with the dissipative source S_i as:

$$\frac{1}{Q_i} = \frac{1}{\sigma} \frac{dW_i/dt}{E_n} \tag{3.3.89}$$

where dW_i/dt is the mean power dissipated by the source S_i, and E_n is the mean wave energy in the harbor at resonance. From the resonant characteristics defined by Eqs. (3.3.87) and (3.3.88) E_n is given by (see e.g., Ippen (1966)):

$$E_n = \frac{1}{4} A^2 \rho g LB$$

where A denotes the wave amplitude at the backwall.

An alternative parameter measuring the effect of the dissipative source S_i is the decay coefficient $\bar{\alpha}_i$ which measures the damping rate of a freely oscillating wave system. It can be directly related to Q_i as follows. From the energy conservation principle the rate of energy loss in a system in free oscillation must be exactly balanced by the mean power dissipated by the source S_i:

$$\frac{dE_n}{dt} = - \frac{dW_i}{dt} \tag{3.3.90}$$

since $E_n \sim A^2$ it follows that:

$$\frac{dE_n}{dt} = 2 \frac{E_n}{A} \frac{dA}{dt} \tag{3.3.91}$$

Using Eq. (3.3.89) and (3.3.91), Eq. (3.3.90) becomes:

$$\frac{dA}{A} = \frac{-\sigma}{2} \frac{dt}{Q_i} \tag{3.3.92}$$

Or, integrating

$$\frac{A}{A_o} = \exp[- \bar{\alpha}_i \frac{t}{T}] \tag{3.3.93}$$

where the decay rate α_i is related to Q_i by:

$$\bar{\alpha}_i = \frac{\pi}{Q_i} \tag{3.3.94}$$

In case of n sources of dissipation, the same reasoning leads to an overall decay rate $\bar{\alpha}$ given by:

$$\bar{\alpha} = \sum_{i=1}^{n} \bar{\alpha}_i = \sum_{i=1}^{n} \frac{\pi}{Q_i} \tag{3.3.95}$$

The relationship (3.3.95) will be used in Section 5.1 for the experimental investigation of the sources of dissipation related to viscous boundary friction and surface tension dissipation.

The determination of the Q_i factor corresponding to radiation damping, laminar bottom, wall and surface friction, leakage losses and entrance dissipation is presented in detail in Appendix E; only the results will be summarized here as:

$$\frac{1}{Q_i} = \frac{4}{\pi}\frac{b}{a}\frac{1}{(2n+1)}\left[\frac{1}{2} + \frac{kh}{\sinh 2kh}\right]\chi_i \qquad i = 1,2,3,4 \qquad (3.3.96)$$

where $\chi_1 = \chi_r$, $\chi_2 = \chi_\mu$, $\chi_3 = \chi_\varepsilon$, $\chi_4 = \chi_f$. In other words, the product $\chi_i Q_i$ does not depend on the particular source of dissipation S_i. Combining Eqs. (3.3.86) and (3.3.96) yields:

$$\frac{1}{R} = \sum_{i=1}^{4}\frac{1}{R_i} \qquad (3.3.97)$$

$$\frac{1}{Q} = \sum_{i=1}^{4}\frac{1}{Q_i} \qquad (3.3.98)$$

$$R_i = \frac{4}{\pi}\frac{1}{(2n+1)}\left(\frac{1}{2} + \frac{kh}{\sinh 2kh}\right)Q_i \qquad (3.3.99)$$

$$R = \frac{4}{\pi}\frac{1}{(2n+1)}\left(\frac{1}{2} + \frac{kh}{\sinh 2kh}\right)Q \qquad (3.3.100)$$

R_i can be defined as the amplification factor at resonance corresponding to the dissipative source S_i. Physically it would be the value taken by the amplification factor at the backwall of the harbor if only the source S_i was present. These results suggest that the reduction of the amplification factor at (or close to) resonance resulting from any other source of dissipation can be derived simply from the Q_i factor corresponding to that source by using Eqs. (3.3.97) and (3.3.99).

If a source of dissipation introduces too much damping, e.g., leading to a value of R less than 2, the results from (3.3.97) can only be considered qualitative, because in that case maximum amplification may no longer correspond to values of k which cancel the expression for B in Eq. (3.3.79).

Several applications of these considerations are mentioned in the remainder of this section.

(i) Correction for surface tension effects

The effects of surface tension not included in the analytical solution derived in Section 3.3.3 can be estimated by computing the Q_i factors corresponding to this dissipative source. The details of the derivation are presented in Appendix E. Then the correction for the amplification factor R at resonance can be obtained from Eq. (3.3.97) and (3.3.99). This correction procedure will be used in particular in Section 6.2.2 and 6.2.3 for the experimental determination of the leakage coefficient ε and the entrance loss coefficient f_e, respectively.

(ii) Energy dissipation in the model and in the prototype

Hydraulic models are usually constructed to predict the wave dynamics in a prototype; however, the nature of dissipation in those two situations may be different. For instance, the boundary friction is likely to be turbulent in prototype, while it is usually laminar in a model. A comparison of the Q_i factors corresponding to those sources of dissipation can give an estimate of what their relative effects are in the case of a harbor with $b/L << 1$. This aspect will be investigated in Chapter 7.

(iii) Time required to reach steady state

The number of oscillations required to reach steady state (or within 5% of its limits) is, from Eq. (3.3.93), approximately equal to $3/\bar{\alpha}$, that is, using Eq. (3.3.94) equal to Q. In practice, the amplification factor R at the first resonant mode ($n = 0$) is less than eight when radiation damping and viscous losses are considered. Therefore, from Eq. (3.3.100), Q is at most equal to six and thus at most six oscillations are required for the steady state to establish. One conclusion may be

drawn from this. In practice, it takes only a few oscillations to achieve steady state in a long and narrow harbor excited with a narrow banded frequency; therefore, in the case of transient waves such as tsunami waves, there may be enough excitation time for normal mode oscillations to fully develop. (This is one reason why the investigation of the steady state oscillations of a harbor remains important.) Another conclusion concerns the basin space required for the simulation of steady state harbor oscillations in a laboratory, and this will be discussed in Section 6.1.

3.3.4 The Transient Linear Problem

Once the response of a linear system to a sinusoidal excitation is known, the linear superposition method allows the response of the system to any transient input excitation to be computed. The procedure is as follows: let $F(x,y,\sigma)$ represent the response in amplitude (which can be complex in the mathematical sense) at a given location (x,y) inside the harbor to a plane harmonic wave with frequency σ and a unit amplitude at the coastline. If the incident wave amplitude at the harbor entrance, with the entrance closed, is represented by the integral:

$$\eta_i(t) = \int_{-\infty}^{\infty} A_i(\sigma)\, e^{-i\sigma t}\, \frac{d\sigma}{2\pi} \qquad (3.3.101)$$

then the transient response of the harbor can be expressed simply as:

$$\eta(x,y,t) = \int_{-\infty}^{\infty} A_i(\sigma)\ F(x,y,\sigma)\ e^{-i\sigma t}\ \frac{d\sigma}{2\pi} \qquad (3.3.102)$$

This derivation is valid as long as there is no energy transfer between Fourier components.

Mathematically $\eta(x,y,t)$ is the product of convolution of $f(x,y,t)$ with $\eta_i(t)$:

$$\eta(x,y,t) = \int_{-\infty}^{\infty} \eta_i(t')f(x,y,t-t')dt' \qquad (3.3.103)$$

where $f(x,y,t)$ is the response of the harbor to a unit impulse, or equivalently represents the inverse Fourier transform of $F(x,y,\sigma)$.

The most efficient way to perform the operations involved in expression (3.3.103) consists in using the Discrete Fourier Transform (DFT) (e.g. Brigham (1974)). The practical computation procedure can be stated as follows:

-- Discretize the time record $\eta_i(t)$ into N equispaced values from t=0 to t=T. The time step Δt is defined as:

$$\Delta t = \frac{T}{N} \qquad (3.3.104)$$

-- Compute the Fourier transform of $\eta_i(t)$ with the DFT:

$$A_i(n\Delta f) = \frac{T}{N} \sum_{k=0}^{N-1} \eta_i(k\Delta t)[\exp(\frac{i2\pi}{N})]^{kn} \qquad n=0,1,2,\ldots N \qquad (3.3.105)$$

where

$$\Delta f = \frac{1}{T} \qquad (3.3.106)$$

-- Compute

$$B(x,y,n\Delta f) = A_i(n\Delta f)\ F(x,y,n\Delta f), \quad n=0,1,2,\ldots N/2 \qquad (3.3.107)$$

-- Complete the array B as:

$$B[(x,y,(\frac{N}{2}+1+i)\Delta f)] = B^*[(x,y,(\frac{N}{2}+1-i)\Delta f)] \quad i=1,2\ldots\frac{N}{2}-2 \qquad (3.3.108)$$

where the star denotes the complex conjugate.

-- Compute the inverse Fourier transform of B as:

$$\eta(x,y,k\Delta t) = \frac{1}{T}\sum_{k=0}^{N-1} B(x,y,n\Delta f)\,[\exp(-\frac{i2\pi}{N})]^{kn} \quad n=0,1,\ldots N \qquad (3.3.109)$$

Computations corresponding to Eqs. (3.3.105), (3.3.109) are most efficiently performed using the Fast Fourier Transform (FFT) algorithm. In order for this procedure to yield satisfactory results, two conditions must be respected: the time step Δt should be chosen such that the incident wave does not contain any energy for a frequency greater than $\frac{1}{2\Delta t}$ (Nyquist frequency) and the number N of discretization points should satisfy:

$$N \geq P + Q - 1 \ ,$$

such that $P\Delta t$ is the time during which the incident signal is not zero and $Q\Delta t$ is the time response of the system to an impulse signal. These Fourier methods will be used in Section 6.4 to compare the transient experiments with the linear dissipative theory. It should be mentioned

that this method remains valid only for a linear process. In particular, the effects of leakage and boundary friction included in the harmonic solution of Section 3.3.3 can be treated using this method. On the other hand, entrance dissipation which is nonlinear cannot be adequately treated for the transient oscillations using this technique. Another method must be used for the transient problem if entrance friction is introduced, such as the one to be presented in Section 3.4.

3.4 Nonlinear Transient Wave-Induced Oscillations of Harbors with Arbitrary Shape

The main purpose of Section 3.3 was to provide an analytical tool to investigate various sources of dissipation affecting wave-induced harbor oscillations by deriving analytically the linear response of a harbor with a simple geometry to a harmonic incident wave. In the present section a numerical finite element model is presented to solve the problem of nonlinear oscillations induced by plane incident transient long waves in a variable depth harbor with arbitrary planform. A "radiative" boundary is included in the model at some finite distance from the harbor entrance to allow smooth transmission of the wave radiated away from the harbor entrance. Incorporation of this feature in the numerical model allows the computations to be carried on as long as desired in a finite discretized domain without numerical reflection problems. This capability renders the model particularly suitable for the study of the buildup of nonlinearities inside the harbor for resonance conditions and for the investigation of steady state conditions in the harbor.

The numerical model is based on the potential function formulation of the nonlinear dispersive dissipative long wave theory discussed in Section 3.1. It includes three viscous dissipative effects, namely, laminar boundary function, leakage losses through lateral boundaries, and quadratic separation losses due to sudden changes in boundary geometry inside the harbor.

The analytical formulation of the problem is derived in Section 3.4.1. A finite element solving procedure is presented in Section 3.4.2 followed by a presentation of the transient algorithm in Section 3.4.3 and a discussion of its convergence and stability characteristics in Section 3.4.4. Finally, an example of implementation of the numerical method is given in Section 3.4.5.

3.4.1 Analytical formulation

The harbor configuration and the coordinate system are defined by the sketch in Fig. 3.4.1. The analysis is restricted to the fluid domain bounded by the semicircle Γ_R and the curve EDF. The origin of the coordinate system lies on the entrance of the harbor at $x = 0$. The problem consists of computing the wave system in the harbor induced by plane transient incident waves with a direction of propagation normal to the coastline whose incident wave characteristics are known. Two regions are considered:

(i) The harbor region, denoted by Ω_N is the fluid domain bounded laterally by the curve AGBDA, and at the bottom by the curve agbda, where the water depth can be slowly varying. The sources of energy dissipation considered are: the laminar boundary friction at the bottom and the

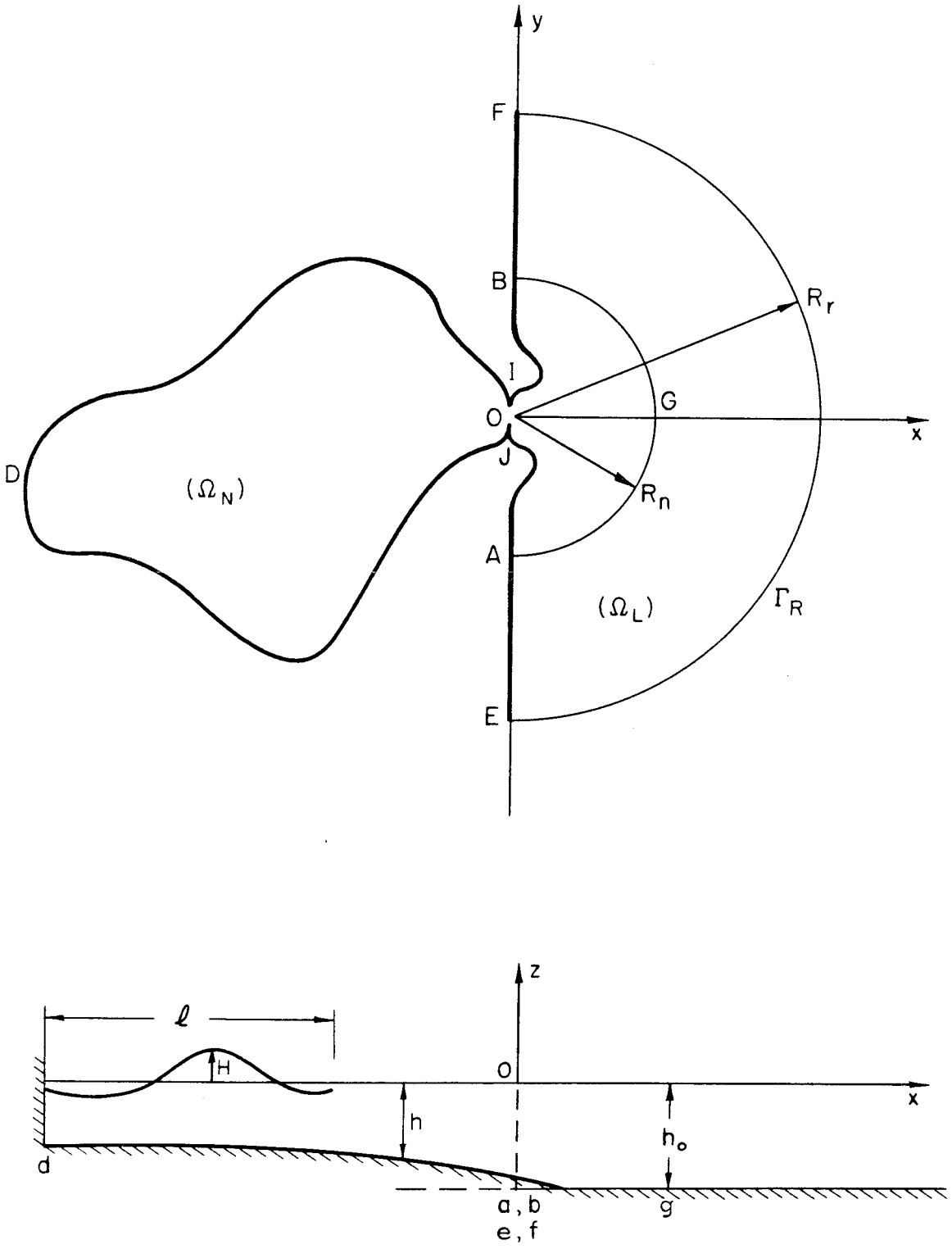

Fig. 3.4.1 Definition sketch of an arbitrary shaped harbor.

water surface, quadratic separation losses across narrow passages inside the harbor region, and leakage due to losses and laminar flow underneath the lateral vertical boundaries. Some additional losses, such as turbulent boundary friction, could be included in the formulation without great complication. However, since the present analytical model was constructed as a basis of comparison with laboratory experiments, only the treatment of the three mentioned viscous dissipative sources will be discussed here. The equations used in this harbor region are the weakly nonlinear dispersive and dissipative long wave equations derived in Section 3.1.

(ii) The outer region, denoted by Ω_L is the fluid domain bounded laterally by the curve EAGBF and the semicircle Γ_R. The water depth is assumed to be constant and is denoted by h_o, the portions of the coastline BF and AE are assumed to be straight and perfectly reflective. The effects of viscous dissipation, convective nonlinearities, and dispersion are neglected in this region. The justification of this assumption as well as the proper location of the boundaries AGB and Γ_R away from the harbor mouth will be discussed later in this section. As a consequence, the wave system is considered as resulting from the linear superposition of the known incident reflected wave system (supposed to be plane and moving normally to the coastline) and the radiated wave system emanating from the harbor mouth. Finally, a proper boundary condition is applied on the semicircle, Γ_R, to allow smooth transmission of the radiated wave through it. A matching procedure must be applied to connect the two regions. This is done by imposing continuity of the

flow rate and the wave amplitude across the boundary AGB.

In the remainder of Section 3.4, the physical variables are expressed in the same dimensionless form as in Section 3.1:

$$x = \frac{x^*}{\ell} \qquad y = \frac{y^*}{\ell} \qquad h = \frac{h^*}{h_o} \qquad t = \frac{t^*\sqrt{gh_o}}{\ell}$$

$$z = \frac{z^*}{h_o} \qquad \Phi = \frac{h_o}{H}\frac{\Phi^*}{\ell\sqrt{gh_o}} \qquad \underset{\sim}{u} = \frac{h_o}{H}\frac{\underset{\sim}{u}^*}{\sqrt{gh_o}} \qquad \eta = \frac{\eta^*}{H}$$

where h_o denotes the still water depth outside the harbor region, g is the acceleration of gravity, H is a characteristic wave height, ℓ is a characteristic wavelength, and the starred symbols refer to the dimensional variables: t^* is the time, x^* and y^* are the coordinates in the horizontal plane, η^* is the wave elevation, Φ^* denotes the depth averaged velocity potential function, and $\underset{\sim}{u}^*$ is the depth averaged velocity vector. Henceforth, all the equations will be dimensionless unless specifically stated otherwise. It is recalled that with the above nondimensional equations, all dimensionless terms are of order unity.

The mathematical formulation of the equations and boundary conditions and a detailed discussion of the simplifications stated above follow next.

3.4.1.1 The Harbor Region

Nonlinear, dispersive, as well as dissipative effects are considered in that region. Therefore the "pseudo" potential function, noted as Φ in that region (instead of $\bar{\phi}$ for simplicity in the notations), is set to satisfy Eq. (3.1.50) up to the first order in α, β, γ_s:

$$\Phi_{tt} - \nabla\cdot(h\nabla\Phi) + \frac{\gamma_s}{h}\Phi_t$$

$$- \beta[\frac{h}{2}\nabla\cdot(h\nabla\Phi_{tt}) - \frac{h^2}{6}\nabla^2\Phi_{tt}] + \beta\nabla\cdot\{(\frac{h}{6}\Phi_{tt} + \frac{h}{3}\nabla h\cdot\nabla\Phi)\nabla h\}$$

$$= -\alpha[\nabla\Phi\cdot\nabla\Phi_t + \nabla\cdot(\Phi_t\nabla\Phi)] \qquad (3.4.1)$$

where the nonlinear parameter α, the dispersive parameter β, and the dissipation parameter γ_s, are assumed small compared to unity, and are defined as:

$$\alpha = \frac{H}{h_o} \qquad \beta = (\frac{h_o}{\ell})^2 \qquad \gamma_s = (\frac{\nu\sigma}{2})^{1/2}(1+C)\frac{\ell}{h_o\sqrt{gh_o}} \qquad (3.4.2)$$

where ν denotes the kinematic viscosity of the fluid, C is the surface contamination factor, and σ denotes a characteristic frequency of the wave motion.

Equation (3.4.1) is exact up to the first order in α,β,γ_s. Once $\Phi(x,y,t)$ is known, the wave elevation $\eta(x,y,t)$ and the depth averaged velocity vector $\underset{\sim}{u}(x,y,t)$ can be derived simply from Φ at the lowest order as:

$$\eta = -\Phi_t + O(\alpha,\beta,\gamma_s) \qquad (3.4.3)$$

$$\underset{\sim}{u} = \underset{\sim}{\nabla}\Phi + O(\beta) \qquad (3.4.4)$$

In a hydraulic model it is possible that due to the presence of a small gap underneath the walls ADB energy can be lost "through" the boundaries of the model. Combining Eq. (3.3.88) with Eqs. (3.4.3) and (3.4.4),

the leakage condition is expressed in dimensionless form as

$$\frac{\partial \Phi}{\partial n} = - \frac{\varepsilon}{h} \Phi_t \qquad \text{on ADB} \tag{3.4.5}$$

where

$$\varepsilon = \frac{e^3}{12 \nu t_e} \sqrt{\frac{g}{h_o}} \tag{3.4.6}$$

where e and t_e denote the gap width under the walls and the wall thickness, respectively. It is recalled that h_o denotes the constant water depth outside the harbor region. One notices that expression (3.4.6) is identical to expression (3.3.40) for the leakage coefficient ε in the limit of the shallow water range.

Flow separation can take place in the harbor at locations where sudden expansions and combined contractions and expansions of the lateral boundaries occur, e.g., at narrow passages between two breakwaters at a harbor entrance. Using Eqs. (3.3.9), (3.4.3), and (3.4.4), the resulting loss is expressed as an amplitude difference across the gap in the following dimensionless form:

$$\Delta \Phi_t = - \frac{\alpha f_e}{2} \frac{\overline{\partial \Phi}}{\partial n} \left| \frac{\overline{\partial \Phi}}{\partial n} \right| \tag{3.4.7}$$

where $\frac{\overline{\partial \Phi}}{\partial n}$ denotes the averaged velocity (assumed continuous) across the gap, $\Delta \Phi_t$ denotes the jump in the value of Φ_t across the gap, and f_e denotes the separation loss coefficient. For purposes of clarity in the subsequent presentation, it will be assumed that only one contraction-expansion exists in a harbor, e.g., IJ in Fig. 3.3.1.

3.4.1.2 The Outer Region

Formally the wave dynamics outside the harbor region are also governed by the nonlinear-dispersive wave equation (3.4.1). Physically, the overall wave system in the outer region can be interpreted as being composed of two parts: (i) the plane incident-reflected wave system, assumed to be known at all times, which describes the wave evolution in the absence of harbor, i.e., in the case of a straight coastline and constant water depth everywhere, and (ii) the radiated wave system which emanates from the harbor entrance.

In general, these two wave systems (i and ii) interact in a nonlinear manner due to the presence of the nonlinear terms in Eq. (3.4.1) so that they cannot be linearly superimposed. However, this simplification of linear superposition constitutes a reasonable approximation if the radiated wave amplitude becomes much smaller than that of the incident-reflected wave system.

The wave height of the radiated wave at some distance from the harbor mouth can be estimated from the derivation presented in Appendix F2 based on the linear harmonic solution, as:

$$\left(\frac{H_s}{H_I}\right) \simeq ka\left|H_o^1(kr^*)\right| \tag{3.4.8}$$

where H_s and H_I denote the characteristic wave height of the radiated wave and incident-reflected wave, respectively, r^* is the dimensional distance from the mouth, k denotes the wave number associated with the harmonic wave, and H_o^1 denotes the Hankel function of the first kind and zeroth order. Based on the linear harmonic analysis, the characteristic

horizontal length ℓ is set equal to the wavelength λ related to the dominant frequency of the wave motion; this gives:

$$\ell \simeq 2\pi/k \tag{3.4.9}$$

Combining Eqs. (3.4.8) and (3.4.9), the nonlinear interaction between the incident-reflected wave and the radiated wave reasonably can be neglected if:

$$\frac{2\pi a}{\ell} \left| H_o^1\left(\frac{2\pi r^*}{\ell}\right) \right| < O(1) \tag{3.4.10}$$

The inequality (3.4.10) provides a means of determining the location of the boundary AGB at some distance R_n^* away from the harbor mouth, such that the nonlinear interaction between the incident-reflected and radiated wave systems can be neglected beyond that boundary. In particular, for small relative harbor openings (say $ka < 0.1$), the boundary AGB can approach the mouth quite closely, since for small values of kr^*, $H_o^1(kr^*)$ varies only as $\ell n(kr^*)$. (It is noted that this case corresponds to most tsunami situations.) For instance, the value $r^*/\ell = 0.1$ reasonably can be chosen. For moderate values of ka, however, the boundary AGB must be located further away from the mouth. $H_o^1(kr^*)$ varies thus only like $1/\sqrt{r^*}$, which implies that a rather large portion outside the harbor mouth must be incorporated in region Ω_N in order for inequality (3.4.10) to be fulfilled.

Provided that inequality (3.4.10) is met at $r^* = R_n^*$, the potential wave function in the outside region, denoted as Φ_L, may be written as:

$$\Phi_L = \Phi_I + \psi \tag{3.4.11}$$

with

$$O(\psi) < O(\Phi_I)$$

where Φ_I and ψ denote the potential function of the incident-reflected and radiated wave, respectively.

The potential function Φ_L must satisfy Eq. (3.4.1) with Φ replaced by Φ_L. Neglecting terms of order $\psi\Phi_I$, ψ^2, recalling that the depth is assumed constant ($h = 1$) in region Ω_L, and substituting Eq. (3.4.11) into Eq. (3.4.1), an uncoupled system for Φ_I and ψ is obtained as:

$$\Phi_{I_{tt}} - \nabla^2\Phi_I + \gamma_s\Phi_{I_t} - \frac{\beta}{3}\nabla^2\Phi_{I_{tt}}$$

$$= -\alpha(\nabla\Phi_I\cdot\nabla\Phi_{I_t} + \nabla\cdot(\Phi_{I_t}\nabla\Phi_I)) \qquad (3.4.12)$$

$$\psi_{tt} - \nabla^2\psi + \gamma_s\psi_t - \frac{\beta}{3}\nabla^2\psi_{tt} = 0 \qquad (3.4.13)$$

At the coastline perfect reflection is assumed. This implies

$$\frac{\partial\Phi_L}{\partial n} = 0 \qquad \text{on AE,BF} \qquad (3.4.14)$$

or, since $\partial\Phi_I/\partial n = 0$ on EF:

$$\frac{\partial\psi}{\partial n} = 0 \qquad \text{on AE,BF} \qquad (3.4.15)$$

Neglecting dispersion and dissipation effects for the radiated wave

as it spreads away from the harbor in region Ω_L ($\beta = \alpha = 0$ in Eq. 3.4.13, to be justified later), the proper boundary condition on the semicircle Γ_R, which allows smooth transmission of the radiated wave through Γ_R, has been derived in Appendix F1 and is expressed in dimensionless form as:

$$\frac{\partial \psi}{\partial n} = -\psi_t - \frac{1}{2R_r}\psi \qquad \text{at } (x^2+y^2)^{1/2} = R_r \tag{3.4.16}$$

If $R_r \to \infty$,

equation (3.4.16) is similar, in the time domain, to the asymptotic Sommerfeld radiation condition derived for the harmonic case. The relative error in using Eq. (3.4.16) at some finite distance from the harbor entrance has been computed in Appendix F.1 and yields

$$Er^o/o = \text{Max}\left(\frac{1}{8(kr^*)^2}, \frac{ka}{4(kr^*)^2}, 0\left[\frac{(ka)^2}{6}\right]\right) \tag{3.4.17}$$

For small relative harbor openings ($ka < 0(1)$) the accuracy of the radiative boundary conditions is only a function of the dimensionless distance kr^*. In particular, Eq. (3.4.16) is verified within a small percentage error for values of ak less than 0.5 if

$$R_r^*/\ell = 0.6 \tag{3.4.18}$$

where R_r^* denotes the dimensional radius of the boundary Γ_R.

For larger relative harbor openings and the same accuracy, the radius R_r^* becomes an increasing function of ak as the trend in Eq. (3.4.17) shows, and the present method, although still valid, becomes inefficient for $ak \geq 0(1)$ because of the large region Ω_L to consider in the computations.

The reason why dispersion and dissipation terms can be neglected in Eq. (3.4.13) stems from the relatively short distance between the radiative boundary and the harbor mouth; the radiated wave does not propagate far enough from the harbor entrance to the boundary Γ_R for the dispersion and dissipation terms in Eq. (3.4.13) to have time to affect the wave evolution.

In summary, the present treatment of the outer region applies well to narrow mouthed harbors (say, $ak \leq 0.5$). It can still be applied for wider entrances at the expense of computational efficiency, since for that case the distance of the boundaries AGB and Γ_R must increase with the harbor width to keep the same degree of accuracy.

A final simplification of the analysis is introduced concerning the incident-reflected wave system. As will be seen subsequently, its characteristics are needed in the present formulation on the boundary AGB only. In laboratory conditions the incident-reflected wave system can be characterized by the wave elevation at the coastline in the absence of harbor $\eta_I(t)$. Since the boundary AGB lies fairly close to the harbor mouth, as seen previously, first order effects do not have time to manifest as the incident wave propagates from the coastline to point G. Therefore, the potential function Φ_I can be analytically derived at the boundary AGB from the wave elevation $\eta_I(t)$ as:

$$\Phi_I(x,y,t) = -F_I(t+x) - F_I(t-x) \tag{3.4.19}$$

where

$$F_I(\theta) = \frac{1}{2}\int_0^{\theta} \eta_I(t')dt' \tag{3.4.20}$$

where the first order terms have been neglected in Eqs. (3.4.3) and

(3.4.12). This simplification has been used throughout the present study.

3.4.1.3 Matching Between Harbor and Outer Regions

Smooth transmission of the flow characteristics through the boundary AGB between regions Ω_N and Ω_L is ensured by equating the wave elevation and the flow rate between the two regions at the boundary between the regions. Using Eqs. (3.4.3) and (3.4.4), the continuity requirement is also expressed in terms of the velocity potentials as:

$$\phi = \phi_I + \psi \qquad \text{on AGB} \qquad (3.4.21)$$

$$\frac{\partial \Phi}{\partial n} = -\frac{\partial \Phi_I}{\partial n} - \frac{\partial \psi}{\partial n} \qquad \text{on AGB} \qquad (3.4.22)$$

where, by convention, the positive normal derivative of a function defined in a region is directed outward. This convention will hold throughout the remainder of this section, unless specifically stated otherwise.

A related boundary condition more amenable to numerical treatment is written as:

$$\frac{\partial \Phi}{\partial n} = \lambda_* (\Phi - \Phi_I - \psi) \qquad \text{on AGB} \qquad (3.4.23)$$

$$\frac{\partial \Phi_I}{\partial n} + \frac{\partial \psi}{\partial n} = -\lambda_* (\Phi - \Phi_I - \psi) \qquad \text{on AGB} \qquad (3.4.24)$$

where λ_* is a large fixed number typically chosen equal to 10^6, called the penalty parameter. It can be checked that in the limit where $\lambda_* \to \infty$, Eqs. (3.4.23) and (3.4.24) become equivalent to Eqs. (3.4.21) and (3.4.22).

3.4.2 A Finite Element Solution

As mentioned previously only one narrow gap with separation loss (in region Ω_N) is considered in the subsequent analysis for the sake of clarity in the presentation and in the notation. This gap is represented by the segment IJ in Fig. 3.4.1. For the subsequent treatment of the equations, the harbor region Ω_N is subdivided into two non-overlapping subregions Ω_N^1 and Ω_N^2 in each of which the solution is differentiable and such that

$$\Omega_N^1 \cup \Omega_N^2 = \Omega_N$$

Region Ω_N^2 is, by definition, the fluid domain bounded laterally by the curve IJD in Fig. 3.4.1 and subregion Ω_N^1 refers to the fluid domain bounded laterally by the curve IBGAJ. The first step in the derivation of the finite element solution consists in stating the strong form (S) of the solution:

Find the functions $\Phi^1(x,y,t)$, $\Phi^2(x,y,t)$, $\psi(x,y,t)$ differentiable in the domains Ω_N^1, Ω_N^2, Ω_L, respectively, and in the time interval $0 \leq t \leq t'$ such that:

$$\Phi_{tt}^i - \nabla\cdot(h\nabla\Phi^i) + \frac{\gamma_s}{h}\Phi_t^i$$

$$-\beta\left[\frac{h}{2}\nabla\cdot(h\nabla\Phi_{tt}^i) - \frac{h^2}{6}\nabla^2\Phi_{tt}^i\right] + \beta\nabla\cdot\left\{\left(\frac{h}{6}\Phi_{tt}^i + \frac{h}{3}\nabla h\cdot\nabla\Phi^i\right)\nabla h\right\}$$

$$= -\alpha[\nabla\Phi^i\cdot\nabla\Phi_t^i + \nabla\cdot(\Phi_t^i\nabla\Phi^i)] \qquad \text{in } \Omega_N^i,\ i = 1,2 \qquad (3.4.25)$$

$$\psi_{tt} - \nabla^2\psi = 0 \qquad \text{in } \Omega_L \qquad (3.4.26)$$

with the following boundary conditions:

$$\frac{\partial \Phi^1}{\partial n} = -\frac{\varepsilon}{h}\Phi_t^1 \qquad \text{on JA,IB}$$

$$\frac{\partial \Phi^2}{\partial n} = -\frac{\varepsilon}{h}\Phi_t^2 \qquad \text{on IDJ}$$

$$\frac{\partial \psi}{\partial n} = 0 \qquad \text{on AE,BF}$$

$$\frac{\partial \psi}{\partial n} = -\psi_t - \frac{1}{2R_r}\psi \qquad \text{on } \Gamma_R \qquad (3.4.27)$$

$$\frac{\partial \Phi^1}{\partial n} = -\frac{\partial \Phi^2}{\partial n} = -\left(\frac{2}{\alpha f_e}\right)^{1/2} \left|\Phi_t^1 - \Phi_t^2\right|^{1/2} \operatorname{sign}(\Phi_t^1 - \Phi_t^2) \qquad \text{on IJ}$$

$$\frac{\partial \Phi^1}{\partial n} = \lambda_*(\Phi^1 - \Phi_I - \psi)$$

$$\text{on AGB}$$

$$\frac{\partial \psi}{\partial n} = -\lambda_*(\Phi^1 - \Phi_I - \psi) - \frac{\partial \Phi_I}{\partial n}$$

And the initial conditions:

$$\Phi^i(x,y,0) = 0 \qquad \text{in } \Omega_N^i \ , \ i = 1,2$$

$$\psi(x,y,0) = 0 \qquad \text{in } \Omega_L \qquad (3.4.28)$$

Φ_I is the given potential function of the incident-reflected wave. Inspection of Eqs. (3.4.25) through (3.4.28) shows that only the knowledge of Φ_I and $\frac{\partial \Phi_I}{\partial n}$ on AGB is required, as mentioned previously. In order to insure a smooth solution initially, the computation must start before the first incident wave reaches the point where radiation begins,

i.e., point G in the case of Fig. 3.3.1. The weak formulation (W) is derived from the strong form (S) by multiplying both sides of Eq. (3.4.25) and (3.4.26) by a trial(or test)function and by integrating each equation in its respective domain, using the following Green's identity for all the integrals which involve spatial second derivatives:

$$\iint_{\Omega} f\nabla\cdot\nabla g \; d\Omega = \int_{\partial\Omega} f \frac{\partial g}{\partial n} \, d(\partial\Omega) - \iint_{\Omega} \nabla f\cdot\nabla g \; d\Omega \tag{3.4.29}$$

where $\partial\Omega$ denotes the boundary of the domain Ω. The last step consists of substituting the boundary conditions (3.4.27) into the line integrals resulting from the use of Green's identity.

Performing these steps, the weak form (W) of (S) is stated as:

Find $\Phi^i(x,y,t)$ in the function space $H'(\Omega_N^i)$, $i = 1,2$, and $\psi(x,y,t)$ in the function space $H'(\Omega_L)$ such that for all functions $\tilde{\Phi}^i \in H'(\Omega_N^i)$, $i = 1,2$ and for all functions $\tilde{\psi} \in H'(\Omega_L)$, respectively:

$$\sum_{i=1}^{2} \iint_{\Omega_N^i} [\Phi_{tt}^i \tilde{\Phi}^i + h\nabla\Phi^i \cdot \nabla\tilde{\Phi}^i] \, d\Omega$$

$$+ \iint_{\Omega_L} \psi_{tt}\tilde{\psi} \, d\Omega + \iint_{\Omega_L} \nabla\psi \cdot \nabla\tilde{\psi} \; d\Omega$$

$$+ \beta \sum_{i=1}^{2} \iint_{\Omega_N^i} (\frac{h^2}{3} \nabla\Phi_{tt}^i \cdot \nabla\tilde{\Phi}^i + \frac{h}{6} \tilde{\Phi}^i \nabla\Phi_{tt}^i \cdot \nabla h) \; d\Omega$$

$$- \beta \sum_{i=1}^{2} \iint_{\Omega_N^i} [\frac{h}{6} \Phi_{tt}^i \nabla\tilde{\Phi}^i \cdot \nabla h + \frac{h}{3} (\nabla h \cdot \nabla\Phi^i)(\nabla h \cdot \nabla\tilde{\Phi}^i)] \; d\Omega$$

$$+ \sum_{i=1}^{2} \frac{\gamma_s}{h} \iint_{\Omega_N^i} \Phi_t^i \, \tilde{\Phi}^i \, d\Omega$$

$$+ \varepsilon \int_{JA} \Phi_t^1 \, \tilde{\Phi}^1 \, d(\partial\Omega) + \varepsilon \int_{IB} \Phi_t^1 \, \tilde{\Phi}^1 \, d(\partial\Omega) + \varepsilon \int_{IDJ} \Phi_t^2 \, \tilde{\Phi}^2 \, d(\partial\Omega)$$

$$+ \int_{\Gamma_R} \psi_t \, \tilde{\psi} \, d(\partial\Omega) + \frac{1}{2R_r} \int_{\Gamma_R} \psi \, \tilde{\psi} \, d(\partial\Omega)$$

$$+ \lambda_* \int_{AGB} (\Phi^1 - \psi)(\tilde{\psi} - \tilde{\Phi}^1) \, d(\partial\Omega)$$

$$= \int_{AGB} \left[\lambda_* \phi_I (\tilde{\psi} - \tilde{\Phi}^1) - \frac{\partial \Phi_I}{\partial n} \tilde{\psi}\right] d(\partial\Omega)$$

$$+ \alpha \sum_{i=1}^{2} \int_{\Omega_N^i} \left[(\nabla\Phi^i \cdot \nabla\tilde{\Phi}^i)\Phi_t^i - (\nabla\Phi^i \cdot \nabla\Phi_t^i)\tilde{\Phi}^i\right] d\Omega$$

$$- \left(\frac{2}{\alpha f_e}\right)^{1/2} \int_{IJ} h \left|\Phi_t^1 - \Phi_t^2\right|^{1/2} (\tilde{\Phi}^1 - \tilde{\Phi}^2) \, \mathrm{sign}(\Phi_t^1 - \Phi_t^2) \, d(\partial\Omega) \qquad (3.4.30)$$

with the initial conditions:

$$\iint_{\Omega_L} \psi\tilde{\psi} \, d\Omega + \sum_{i=1}^{2} \iint_{\Omega_N^i} \Phi^i \tilde{\Phi}^i \, d\Omega = 0 \qquad \text{at} \quad t = 0$$

$$\iint_{\Omega_L} \psi_t \tilde{\psi} \, d\Omega + \sum_{i=1}^{2} \iint_{\Omega_N^i} \Phi_t^i \, \tilde{\Phi}^i \, d\Omega = 0 \qquad \text{at} \quad t = 0 \qquad (3.4.31)$$

where

$$H'(\Omega) = \{f(x,y,t): \iint_{\Omega} [(\frac{\partial f}{\partial x})^2 + (\frac{\partial f}{\partial y})^2] \, d\Omega \quad \text{bounded for } 0 \leq t \leq t'\}$$

Under appropriate smoothness hypotheses the solution of the weak formulations can be shown straightforwardly to be identical to the solution of (S). In order to retain consistency, second order terms in deriving Eq. (3.4.30) have been neglected.

The Galerkin form (G) of (S) is:

Find Φ^{ih} in the function space $S'(\Omega_N^i)$, $i = 1,2$, and ψ^h in the function space $S'(\Omega_L)$ such that for all functions $\tilde{\Phi}^{ih} \in S'(\Omega_N^i)$, $i = 1,2$, and all functions $\tilde{\psi}^h \in S'(\Omega_L)$, Eqs. (3.4.30) and (3.4.31) hold with Φ^i, $\tilde{\phi}^i$, ψ and $\tilde{\psi}$ replaced by Φ^{ih}, $\tilde{\Phi}^{ih}$, ψ^h, $\tilde{\psi}^h$, respectively.

The finite element discretization consists of choosing $S'(\Omega_N^i)$ and $S'(\Omega_L)$ in a simple manner in order to transform the weak formulation into a matrix formulation with a finite number of unknowns. Each domain Ω_N^i $(i = 1,2)$ and Ω_L is discretized into small non-overlapping regions called elements. Associated with the discretization is a set of "nodal points." Each function space is defined as

$$S'(\Omega) = \{f^h: \; f^h = \sum_{i=1}^{N_\Omega} f_i(t) \; N_i(x,y)\} \tag{3.4.32}$$

where $f_i(t)$ denotes any arbitrary differentiable function in the time interval $[0,t']$ and $N_i(x,y)$ is the shape function associated with node i and satisfies by definition:

$$N_i(x_j,y_j) = \delta_{ij} \tag{3.4.33}$$

where (x_j,y_j) is the location of the node j, and δ_{ij} denotes the

Kronecker delta symbol.

Thus, $f_i(t)$ represents the value of f^h at the location (x_i,y_i). The basic element used for this study is the four-node, bilinear, isoparametric quadrilateral element. Within an element f^h can be expressed as:

$$f^h = \sum_{a=1}^{4} f_a(t)\, N_a(\xi,\eta) \tag{3.4.34}$$

where

$$N_a(\xi,\eta) = \frac{1}{4}(1+\xi_a\xi)(1+\eta_a\eta) \ , \quad |\eta| \leq 1 \ , \quad |\xi| \leq 1 \tag{3.4.35}$$

$$x = \sum_{a=1}^{4} x_a N_a(\xi,\eta) \tag{3.4.36}$$

$$y = \sum_{a=1}^{4} y_a N_a(\xi,\eta) \tag{3.4.37}$$

The values of ξ_a,η_a are indicated as follows:

a	ξ_a	η_a
1	-1	-1
2	1	-1
3	1	1
4	-1	1

The shape function associated with node i and the variation of f^h within an element are represented in Fig. 3.4.2. An important remark is that the choice of the shape function N_i ensures continuity along the boundary of two adjacent elements within a subdomain Ω, which is in accordance with the requirement that each function f in the function space $S'(\Omega)$ must be continuous over Ω.

At the interface between two subdomains, namely along IJ and AGB,

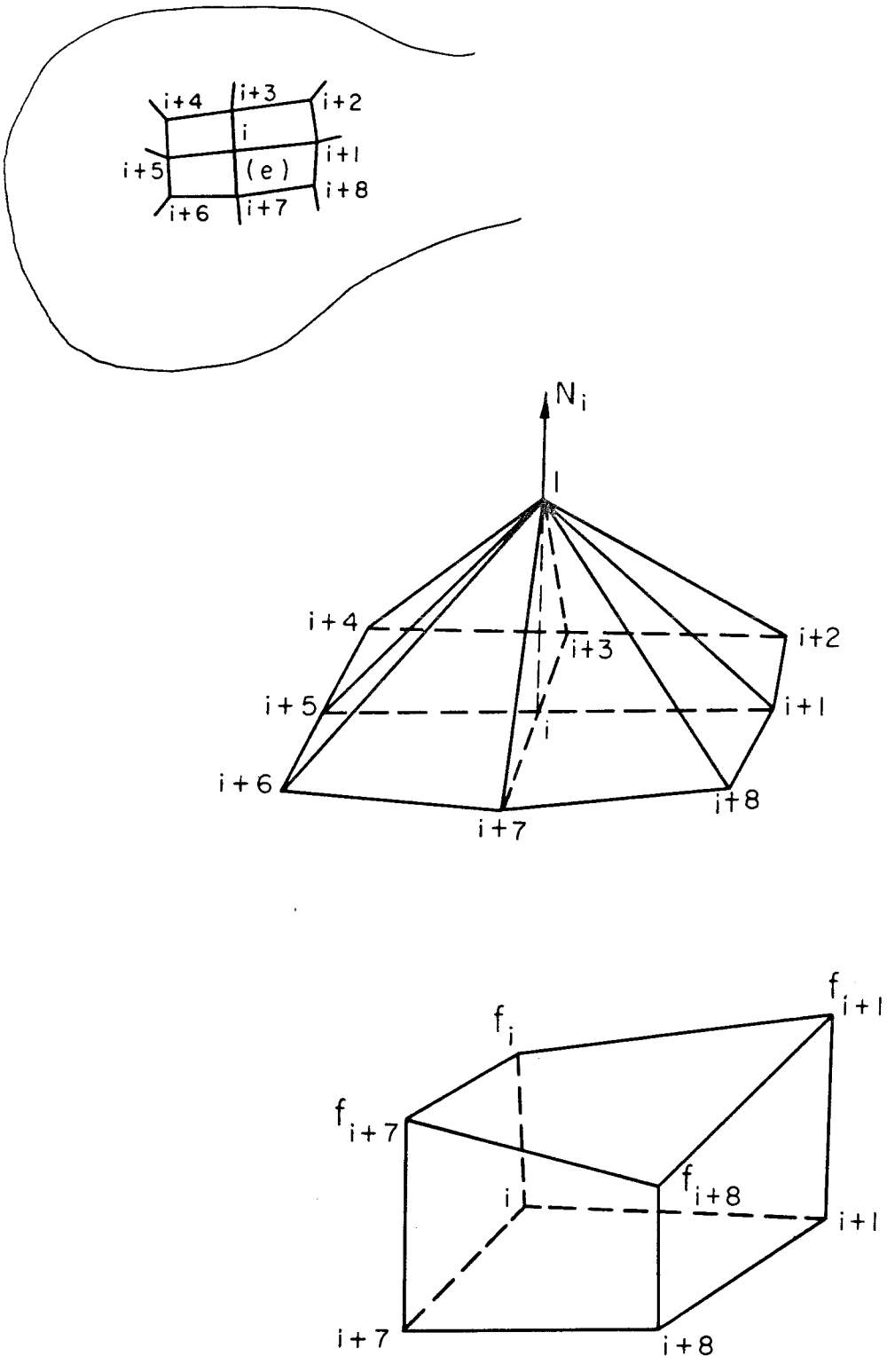

Fig. 3.4.2 Finite element discretization, shape function associated with node i and variation of f^h within element e.

two nodes must be present for each discretization point, one for each region.

The functions $\Phi^{k^h}, \tilde{\Phi}^{k^h}$ $(k = 1,2)$, $\psi^h, \tilde{\psi}^h$ are written as

$$\Phi^{k^h} = \sum_{i=1}^{N_k} \Phi_i^k(t)\, N_i(x,y) \qquad \tilde{\Phi}^{k^h} = \sum_{i=1}^{N_k} \tilde{\Phi}_i^k(t)\, N_i(x,y)$$

$$\psi^h = \sum_{i=1}^{N_3} \psi_i(t)\, N_i(x,y) \qquad \tilde{\psi}^h = \sum_{i=1}^{N_3} \tilde{\psi}_i(t)\, N_i(x,y) \tag{3.4.38}$$

where N_1, N_2, N_3 denote the number of nodes in region $\Omega_N^1, \Omega_N^2, \Omega_L$, respectively. The next step is to substitute Eq. (3.4.38) into Eqs. (3.4.30) and (3.4.31). The resulting scalar equations are obtained in matrix form as:

$$\tilde{\underset{\sim}{d}}^T \{ M \ddot{\underset{\sim}{d}} + C \dot{\underset{\sim}{d}} + K \underset{\sim}{d} = \underset{\sim}{f}_I(t) + \underset{\sim}{g}_1(\underset{\sim}{d}, \dot{\underset{\sim}{d}}) + \underset{\sim}{g}_2(\dot{\underset{\sim}{d}}) \} \tag{3.4.39}$$

$$\tilde{\underset{\sim}{d}}^T N \underset{\sim}{d}(0) = \tilde{\underset{\sim}{d}}^T N \dot{\underset{\sim}{d}}(0) = 0 \tag{3.4.40}$$

where the dots above the symbols denote differentiation with respect to time. The vector $\underset{\sim}{d}$ includes all the unknown nodal quantities $\Phi_i^1(t)$, $\Phi_i^2(t)$, and $\psi_i(t)$ in the whole fluid domain. The matrices M, C, K, and N are symmetric positive except in the case of variable depth, where matrices M and K become unsymmetric. They are most efficiently formed using the standard finite element assembly procedure by working on the element level and adding together the contributions from each element. $\underset{\sim}{f}_I(t)$ is a known force vector associated with the incident reflected wave data, $\underset{\sim}{g}_1$ includes the nonlinear convection terms, and $\underset{\sim}{g}_2$ accounts for the quadratic head loss across the segment IJ. All the integrations were performed using the 2×2 point Gauss quadrature rule.

Since Eqs. (3.4.39) and (3.4.40) must be checked for all vectors $\tilde{\underset{\sim}{d}}(t)$, the coefficients associated with each $\tilde{d}_i(t)$ in Eqs. (3.4.39) and (3.4.40) must vanish, and the following matrix system is obtained as:

$$M\overset{\infty}{\underset{\sim}{d}} + C\overset{\circ}{\underset{\sim}{d}} + K\underset{\sim}{d} = \underset{\sim}{f}_I(t) + \underset{\sim}{g}_1(\underset{\sim}{d},\overset{\circ}{\underset{\sim}{d}}) + \underset{\sim}{g}_2(\overset{\circ}{\underset{\sim}{d}}) \tag{3.4.41}$$

$$\underset{\sim}{d}(0) = \overset{\circ}{\underset{\sim}{d}}(0) = 0 \tag{3.4.42}$$

3.4.3 Time Integration Algorithm

An algorithm is presented in this section to solve the nonlinear second order differential equation (3.4.41). It has features similar to the "implicit-explicit operator splitting" technique (Hughes, et al, 1978) where all linear terms are treated implicitly and some of the nonlinear terms are treated explicitly, using a predictor-multicorrector algorithm. Stability problems were encountered when the nonlinear term $\underset{\sim}{g}_2(\overset{\circ}{\underset{\sim}{d}})$, which ensures a nonlinear contact between region Ω_N^1 and Ω_N^2, was treated explicitly. This term was subsequently treated implicitly and the stability problem disappeared.

Equation (3.4.41) is discretized in time as:

$$M\,\underset{\sim}{a}_{n+1}^{(i+1)} + C\,\underset{\sim}{v}_{n+1}^{(i+1)} + K\,\underset{\sim}{d}_{n+1}^{(i+1)} = \underset{\sim}{f}_I(t_{n+1}) + \underset{\sim}{g}_1(\underset{\sim}{d}_{n+1}^{(i)},\underset{\sim}{v}_{n+1}^{(i)}) + \underset{\sim}{g}_2(\underset{\sim}{v}_{n+1}^{(i+1)}) \tag{3.4.43}$$

$$
\begin{aligned}
\underset{\sim}{d}_{n+1}^{(i+1)} &= \underset{\sim}{\tilde{d}}_{n+1} + \Delta t^2 \beta_* \underset{\sim}{a}_{n+1}^{(i+1)} \\
\underset{\sim}{v}_{n+1}^{(i+1)} &= \underset{\sim}{\tilde{v}}_{n+1} + \Delta t \gamma_* \underset{\sim}{a}_{n+1}^{(i+1)} \\
\underset{\sim}{\tilde{d}}_{n+1} &= \underset{\sim}{d}_n + \Delta t \underset{\sim}{v}_n + \frac{\Delta t^2}{2}(1-2\beta_*)\underset{\sim}{a}_n \\
\underset{\sim}{\tilde{v}}_{n+1} &= \underset{\sim}{v}_n + \Delta t(1-\gamma_*)\underset{\sim}{a}_n
\end{aligned}
\tag{3.4.44}
$$

where Δt denotes the time step and β_* and γ_* are two numerical parameters governing the stability and accuracy of the linear scheme corresponding to $\underset{\sim}{g}_1 = \underset{\sim}{g}_2 = 0$. $\underset{\sim}{d}_{n+1}$, $\underset{\sim}{v}_{n+1}$, $\underset{\sim}{a}_{n+1}$ are the discretized values of $\underset{\sim}{d}(t_{n+1})$, $\overset{\circ}{\underset{\sim}{d}}(t_{n+1})$, $\overset{\infty}{\underset{\sim}{d}}(t_{n+1})$, respectively, and i is the iteration counter.

The implicit treatment of the nonlinear term $\underset{\sim}{g}_2(\overset{(i+1)}{\underset{\sim}{v}}_{n+1})$ implies the use of a tangent stiffness matrix C_{g_2} such that:

$$
\underset{\sim}{g}_2(\overset{(i+1)}{\underset{\sim}{v}}_{n+1}) = \underset{\sim}{g}_2(\overset{(i)}{\underset{\sim}{v}}_{n+1}) + C_{g_2}^{(i)}[\overset{(i+1)}{\underset{\sim}{v}}_{n+1} - \overset{(i)}{\underset{\sim}{v}}_{n+1}] \tag{3.4.45}
$$

where $C_{g_2}^{(i)}$ is defined at the i^{th} iteration by:

$$
C_{g_2}^{(i)} = \partial \underset{\sim}{g}_2 / \partial \overset{(i)}{\underset{\sim}{v}}_{n+1}
$$

Substituting Eqs. (3.4.44) and (3.4.45) into Eq. (3.4.43) yields:

$$K^{*(i)}\ \underset{\sim}{v}_{n+1}^{(i+1)} = \underset{\sim}{f}^{*}_{n+1} + \underset{\sim}{g}_1(\underset{\sim}{d}_{n+1}^{(i)}, \underset{\sim}{v}_{n+1}^{(i)}) + \underset{\sim}{g}_2(\underset{\sim}{v}_{n+1}^{(i)}) - C_{g_2}^{(i)}[\underset{\sim}{v}_{n+1}^{(i)}] \qquad (3.4.46)$$

where

$$K^{*(i)} = \frac{1}{\gamma_* \Delta t} M + C + \frac{\beta_* \Delta t}{\gamma_*} K - C_{g_2}^{(i)}$$

$$\underset{\sim}{f}^{*}_{n+1} = \underset{\sim}{f}_I(t_{n+1}) + \frac{M}{\Delta t \gamma_*} \underset{\sim}{\tilde{v}}_{n+1} - K[\underset{\sim}{\tilde{d}}_{n+1} - \frac{\Delta t \beta_*}{\gamma_*} \underset{\sim}{\tilde{v}}_{n+1}]$$

The procedure to perform I+1 iterations per time step (where i varies from 0 to I) is as follows:

(i) Compute $\underset{\sim}{\tilde{d}}_{n+1}$, $\underset{\sim}{\tilde{v}}_{n+1}$ from Eqs. (3.4.44)

(ii) Set $\underset{\sim}{d}_{n+1}^{(0)} = \underset{\sim}{\tilde{d}}_{n+1}$, $\underset{\sim}{v}_{n+1}^{(0)} = \underset{\sim}{\tilde{v}}_{n+1}$ at the beginning of time step t_{n+1}

(iii) Form the matrix $K^{*(i)}$ and the right hand side of Eq. (3.4.46),

(iv) Solve Eq. (3.4.46) for $\underset{\sim}{v}_{n+1}^{(i+1)}$

(v) Compute $\underset{\sim}{d}_{n+1}^{(i+1)}$ from Eqs. (3.4.44)

(vi) Continue the procedure until i = I

(vii) Set $\underset{\sim}{a}_{n+1} = \underset{\sim}{a}_{n+1}^{(I+1)}$, $\underset{\sim}{v}_{n+1} = \underset{\sim}{v}_{n+1}^{(I+1)}$, $\underset{\sim}{d}_{n+1} = \underset{\sim}{d}_{n+1}^{(I+1)}$

and proceed in the same manner for the next time step.

In order to reduce the computational cost, the tangent stiffness matrix C_{g_2} is only formed in practice at the beginning of every three or four time steps. Therefore, the matrix K* needs only be reformed and factorized every three or four time steps. Its structure can be fully exploited by the so-called "compacted column" equation solver in which zeros outside the profile are neither stored or operated upon (e.g., Bathe and Wilson, 1976).

The resulting main computational cost comes from the formation of the nonlinear vector at the right hand side of Eq. (3.4.46) and the equation solving procedure at each iteration.

3.4.4 Convergence and Accuracy of the Algorithm

Assuming in a first step that the nonlinear terms vanish everywhere at any time, the numerical scheme reduces to the well known Newmark family of algorithms used extensively in linear structural dynamics (after Newmark, 1959). Some of their properties can be summed up as follows:

-- Unconditional stability is achieved if:

$$\beta_* \geq \frac{\gamma_*}{2} \tag{3.4.47}$$

$$\gamma_* \geq \frac{1}{2} \tag{3.4.48}$$

-- The additional restriction

$$\beta_* = (\gamma_* + \frac{1}{2})^2 /4 \tag{3.4.49}$$

maximizes the high frequency numerical dissipation which is usually desirable.

-- The Newmark schemes are first order accurate except if $\gamma_* = \frac{1}{2}$, for which second order accuracy is achieved. When $\underset{\sim}{g}_1$ is considered in Eq. (3.3.46), the stability analysis of the resulting scheme becomes more involved. Hughes et al. (1978) showed that if the tangent stiffness matrices

$$K_T = \partial \underset{\sim}{g}_1 / \partial \underset{\sim}{d}$$

and $$C_T = \partial \underset{\sim}{g}_1 / \partial \overset{\circ}{\underset{\sim}{d}}$$

are symmetric positive-definite, the implicit-explicit algorithm becomes conditionally stable, depending on the value of a critical time step and on the characteristics of the tangent stiffness matrices. In the present case, however, the matrices K_T, C_T are not symmetric, and the conclusions of Hughes' stability study cannot be applied.

Based on the results of numerical tests, the following observations can be made:

-- It is best to retain unconditional stability for the linear terms by choosing β_* and γ_* in accordance with inequalities (3.4.47) and (3.4.48).

-- Two iterations per time step are required to achieve convergence when nonlinear terms are included in the formulation. It is not clear, when only one iteration is used, whether nonconvergence results from instability or accumulation of round-off errors.

-- For all cases solved with this numerical scheme, the time step was chosen as $\Delta t \simeq \Delta x_i$, where Δx_i denotes the length of element i in the direction of wave propagation. No stability or convergence problems were uncovered using this criterion.

3.4.5 Example of Implementation of the Numerical Method

It is felt useful at this point to illustrate the application of the previous analysis by an example for which comparison between theory and experiment is available. The harbor configuration has a trapezoidal plan form shape, constant depth, and partially closed harbor entrance.

The conditions chosen for this numerical example are: a = 2.5 cm, b = 20 cm, b_1 = 4 cm, L = 122 cm, where a,b,b_1,L denote the entrance width, harbor width near the mouth, backwall width, and harbor length, respectively and the water depth h is equal to 8 cm. The incident wave consists mainly of two cnoidal oscillations; the period of each oscillation is 1.92 sec.

The first step in implementing the computer program consists of choosing a characteristic wavelength ℓ. Since the incident wave has a dominant period T, ℓ is chosen as $\ell = T\sqrt{gh}$ which gives $\ell = 170$ cm. The incident wave at the coastline is given as a numerical input in the form of the discretized relative wave elevation η/h versus dimensional time. The time must be nondimensionalized by dividing it by the quantity $\ell/\sqrt{gh}$, that is, the characteristic period T; as a matter of convenience for the numerical computations, the characteristic height H is chosen equal to the depth h. In this manner the dimensionless given wave elevation η_I/h need not be rescaled for this computation.

The resulting values of the nonlinear parameter and dispersion parameters are for this choice of the scaling, $\alpha = 1.0$, $\beta = 0.0024$, respectively. The laminar boundary friction parameter γ_s is computed from Eq. (3.4.2) as equal to 0.10, leakage parameter ε is zero (the base of the harbor was sealed off for this experiment) and the separation loss coefficient f_e is taken equal to 1.15 from the results of the experimental study performed in Section 6.2.

(The reader should note these dimensions are those of an experiment which was conducted to investigate the validity of this numerical model.

The experimental and numerical results for this trapezoidal harbor will be given in Section 6.4.3.)

Of major importance is the determination of the locations of the boundaries AGB and Γ_R outside the harbor. As discussed previously, they depend on the value of the dimensionless parameter ak, where k denotes a typical wave number of the wave system related to ℓ by $k \simeq 2\pi/\ell$. In the present case ak = 0.09. Therefore, from the previous discussion, the boundaries AGB and Γ_R can be located at a relative distance from the mouth equal to $r/\ell = 0.1$ and $R_r/\ell = 0.6$, respectively.

The finite element mesh configuration where the coordinates are normalized with respect to ℓ, is shown in Fig. 3.4.3. Because of the symmetry of this problem, just half the total configuration is considered for the numerical computations. The location of the boundary IJ at the entrance, and of AGB can be readily recognized by the double node feature along them. In order to capture the evolution of secondary waves stemming from nonlinear interactions inside the harbor, the relative length of each element in the direction of wave propagation was set for most of the cases investigated in this study equal to 0.02. The resulting fine mesh configuration inside the harbor is noted. In contrast, the mesh becomes quite loose in the outer region, which renders computations economical.

The last step before running the program is to choose the dimensionless time step. In order to ensure stability, it is chosen equal to 0.02, i.e., equal to the element length in the direction of wave propagation inside the harbor. All the computations associated with this finite element scheme were performed on an IBM 370/3032 digital computer. In

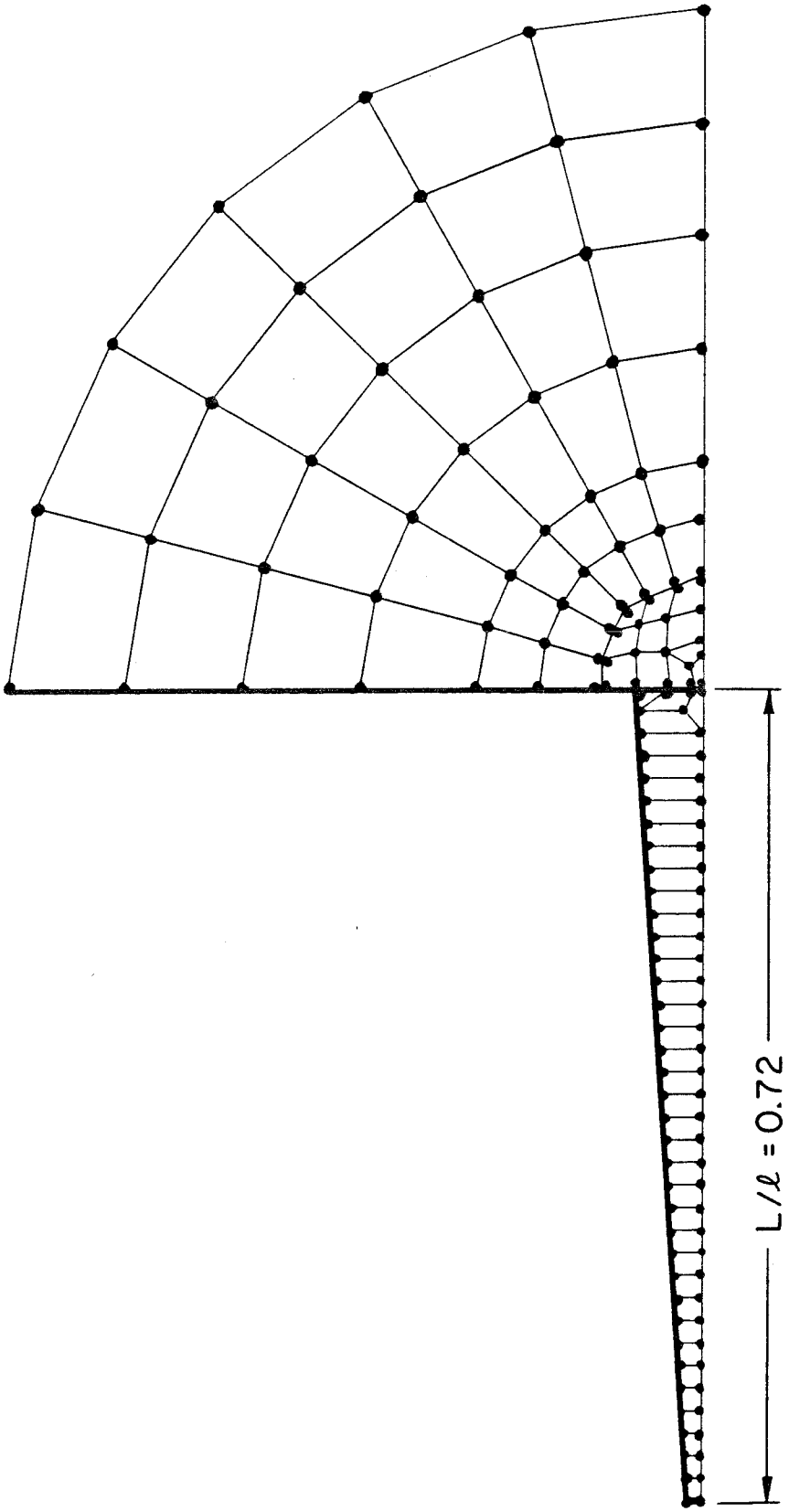

Fig. 3.4.3 Finite element mesh for a trapezoidal harbor.

the present example about 20,000 single precision words of data storage were required. The program was run for 380 time steps and required 90 sec of CPU time.

CHAPTER 4

EXPERIMENTAL EQUIPMENT AND PROCEDURES

4.1 The Wave Basin

The wave basin used for the experiments and shown in Figs. 4.1 and 4.2 was 58 cm deep, 4.73 m wide and 9.60 m long. The vertical walls and the floor were constructed of 1.91 cm (3/4 in.) marine plywood and 2.54 cm (1 in.) marine plywood, respectively. The basin floor rested 25.4 cm (10 in.) above the laboratory floor on a substructure consisting of wood sills and joists, which was built mainly to allow for proper leveling of the basin floor. (For additional details of the construction of the basin, see Raichlen, 1965.) In order to ensure water tightness and to provide a leveled bottom, a layer of polyester resin approximately 0.64 cm (1/4 in.) thick was poured into the basin. The resulting bottom was horizontal within ±0.05 cm (0.02 in.)

The wave absorbers placed along the sidewalls are also shown in Figs. 4.1 and 4.2. They were built to partially absorb the wave emanating from the harbor entrance; this aspect of the study will be discussed in more detail in Section 6.1. Each absorber was 48 cm high, 33 cm thick, 9.15 m long and consisted of 50 layers of fiberglass window screen cloth. The wire diameter of the screens was 0.03 cm with 18 wires per inch in one direction and 16 wires per inch in the other direction. Each unit consisting of ten screens spaced 0.95 cm (3/8 in.) apart was held together by brackets at each end, and it was stretched taut by 0.95 cm (3/8 in.) diameter stainless steel rods

(THIS PAGE IS BLANK, DUE TO ERROR IN PAGINATION)

which were connected from the brackets to a structural frame located outside the basin. Fittings with "O" ring seals were mounted in the walls to prevent the leakage around the rods. Five identical units were stretched along each side of the basin as shown in Fig. 4.1.

4.2 The Wave Generator

The wave generator which was designed and constructed for this study consisted of a vertical plate which was moved horizontally in a prescribed manner by means of an hydraulic servo-system. Three parts are considered in the discussion: the wave plate and carriage, the hydraulic system, and the servo-system. For details of the latter two the reader is referred to Goring (1978); only a summary will be presented here.

4.2.1 The Wave Plate and Carriage

The wave generator consisted of a piston-type wave machine. Photographs of the wave plate, overhead support frame and carriage can be seen in Figs. 4.1 and 4.2. The vertical wave generating surface was an aluminum plate 3.60 m long, 61 cm high and 0.64 cm (1/4 in.) thick which was attached to a structural aluminum angle frame to provide rigidity. An aluminum plate 2.98 m long, 64 cm wide and 0.64 cm (1/4 in.) thick was fastened on top of the structural frame to increase its stiffness. As shown in Fig. 4.2 this assembly was suspended from an overhead structure by three pairs of linear ball bushings (Pacific Bearings Model SPB-20-OPN) which traveled on 3.18 cm (1/4 in.) diameter hardened steel rails (Pacific Bearings Model SA-20-120). Each rail was connected to two vertical channels which were fastened to the overhead structure using slotted holes to

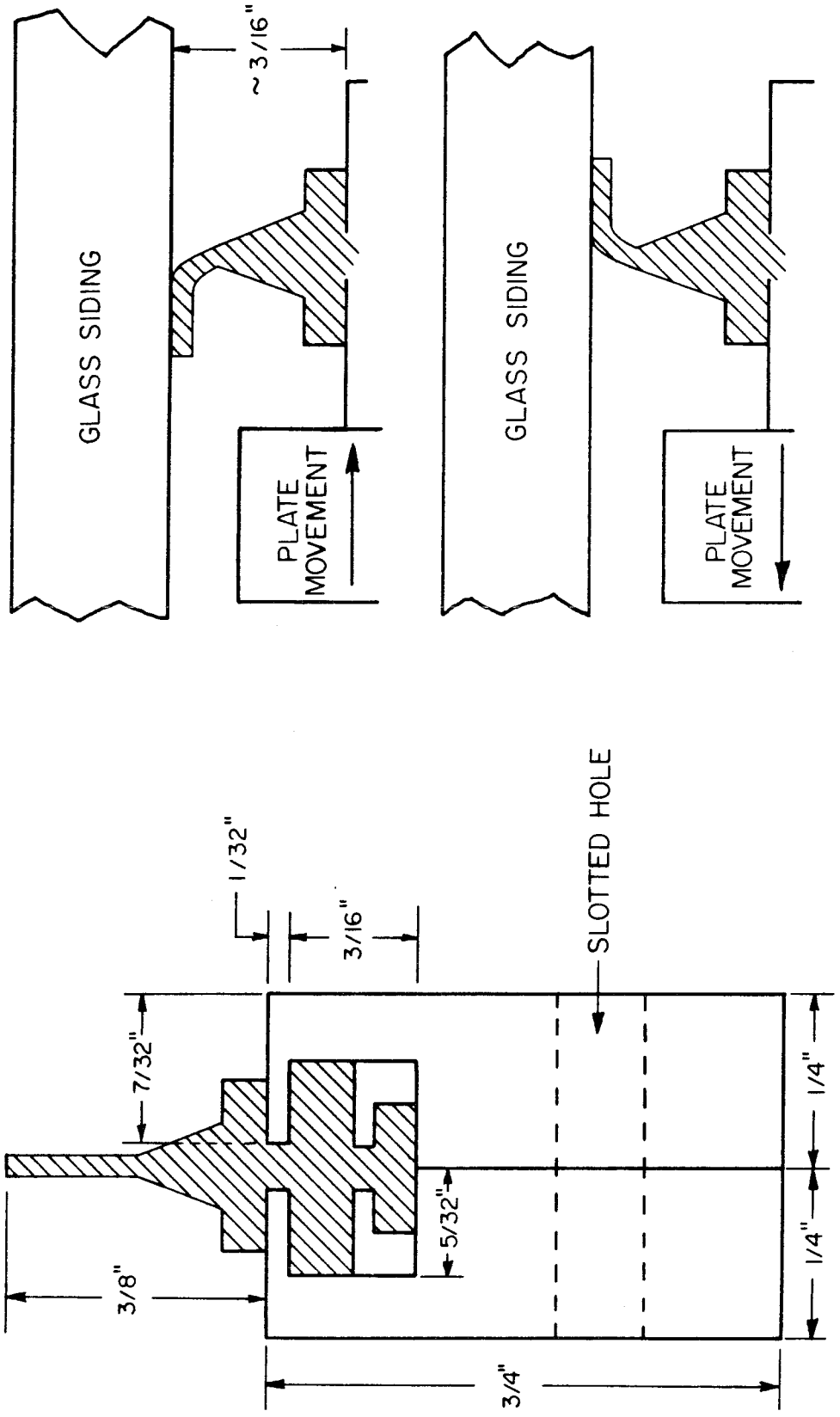

Fig. 4.3 Drawing of the blade holder (after Goring, 1978).

allow for vertical alignment of the rails. The overhead structure in turn was fixed to a reinforced concrete ceiling beam.

To reduce leakage around the wave plate two aluminum guide walls 60 cm high, 3.30 m long and 0.95 cm (3/8 in.) thick were placed parallel to the sidewalls of the basin and between the wave absorbers and the wave plate; these can be seen in Fig. 4.1 and 4.2. One end of the guide plates was connected to the backwall of the basin, and each plate was maintained in vertical position by three braces fastened between the top of the plate and the sidewalls of the basin. The wave plate itself was sealed against the aluminum guide walls and the bottom of the wave basin by windshield wiper blades. The arrangement for mounting the wiper blades is shown in Fig. 4.3. It consisted of two identical aluminum bars with grooves cut out to accept the body of the wiper blade; the blade was held in place by tightly bolting the two bars together.

As shown in Fig. 4.2 and 4.4, the plate assembly was connected to the rod of the hydraulic cylinder through three arms which were constructed of aluminum tube 6.37 cm (2-1/2 in.) diameter and 2.25 mm (1/8 in.) thick. A safety device was designed and constructed to connect the cylinder rod to the arm system to prevent the system from being exposed to excessive forces in case of a malfunction of the electro-hydraulic system. A drawing of this is shown in Fig. 4.5. The connection was made using a shear plate 0.03 cm thick, made out of Phosphor Bronze, which was designed to break if the shear load exceeded 13240 N (3000 pounds). (This was the maximum load which could be taken safely by the ball bearing and plate assembly.) In

(THIS PAGE IS BLANK, DUE TO ERROR IN PAGINATION)

case of shear plate rupture the piston arm could slide freely inside the central arm with the load transmitted to the plate decreasing to zero. During this study the shear plate never broke. The hydraulic cylinder was mounted to a 81 cm (32 in.) "I" beam used as a base, see Figs. 4.2 and 4.4. With that support no vibrations were observed during the motion of the wave generator. To eliminate any bending moment on the piston rod a nylon support bearing which was nylon lined, through which the central arm could slide, was installed inside a support block placed near the front edge of the base; this can be seen to the right in Fig. 4.4.

4.2.2 The Hydraulic System

The various components of the hydraulic system are shown schematically in Fig. 4.6. The reservoir had a capacity of 0.152 m^3 (40 gals.) of hydraulic oil. The pump, used to fill the accumulators with oil, was a Denison constant volume, axial-piston-type pump, rated at 0.012 m^3/min (2.9 gpm) at 20,000 kN/m^2 (3000 psi). It was powered by a 5.6 kW (7.5 hp) 1800 rpm electric motor. Immediately downstream of the pump was a filter with a nominal particle diameter rating of 5 microns, followed by an unloading valve and a check valve. The by-pass pressure valve of the unloading valve was adjusted to 17000 kN/m^2 (2500 psi), the check valve prevented a reverse flow through the pump from the pressurized system when the pump was turned off. Two 0.038 m^3 (10 gal.) accumulators provided operating conditions between 20,000 kN/m^3 (3000 psi) for which the accumulators were nearly full of oil, and 3000 kN/m^3 (450 psi) when the accumulators

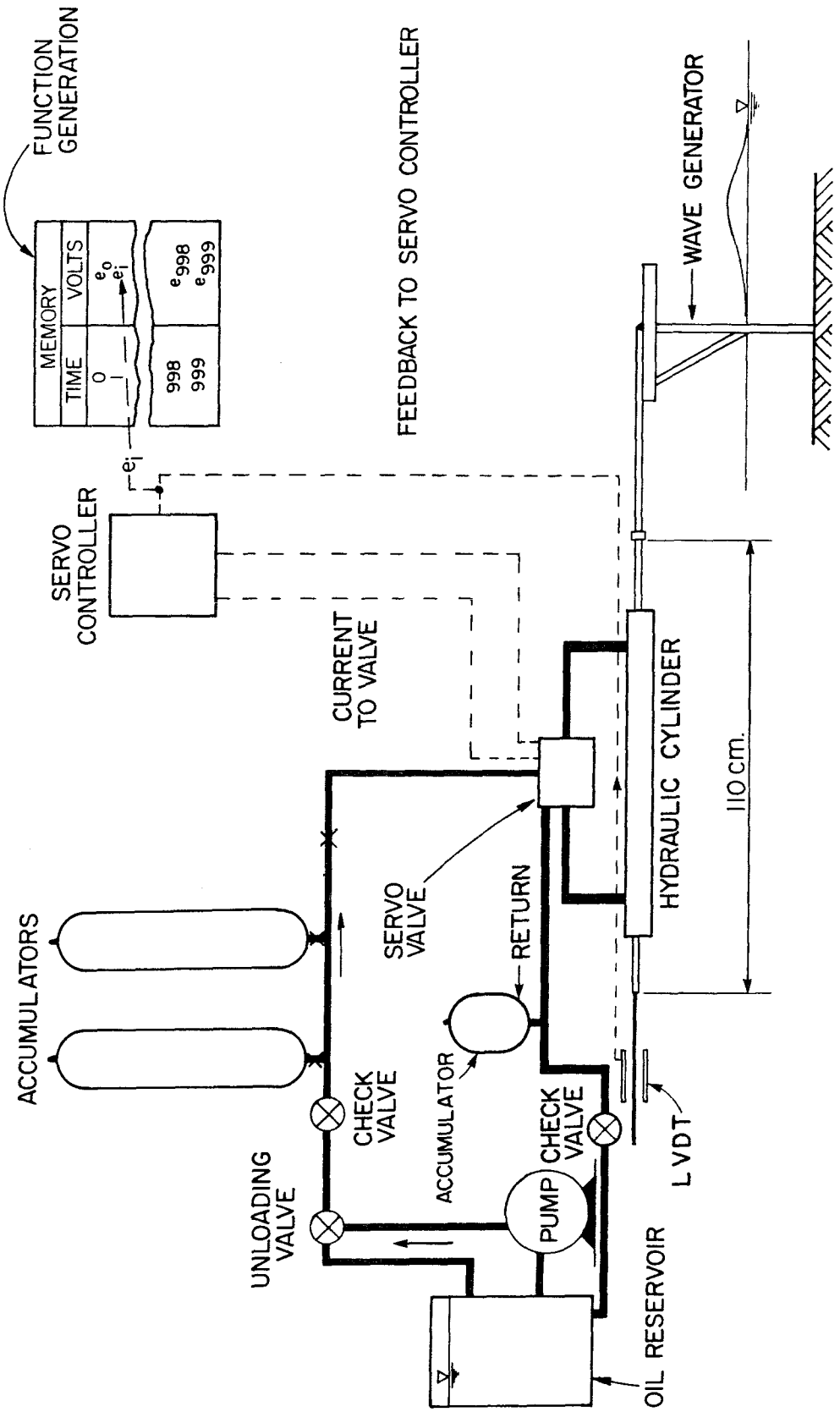

Fig. 4.6 Schematic drawing of the hydraulic system (modified from Goring, 1978)

were empty corresponding to the precharge pressure of each accumulator. The servo-valve (Moog Model 71-103) provided for the variation in direction of the flow of oil in direct proportion to the current it received from the electronic servo controller. It had a rated flow of 0.24 m^3/min (60 gpm) at 40 ma current. The double ended cylinder (Miller Model OH77B) had a 10.2 cm (4 in.) bore 4.45 cm (1-3/4 in.) rod with a stroke of 40.64 cm (16 in.). The seals between the piston and the piston rod had a small contact area to reduce static friction to a minimum (Shamban lip seals). One 0.0057 m^3 (1.5 gal.) accumulator was installed immediately downstream of the servo-valve to reduce pressure fluctuations in case of rapid changes in the servo-valve settings. Finally, a check valve, which opened at 96 kN/m^3 (14 psi) was placed just before the reservoir to keep the return line full of oil. (It should be mentioned that the hydraulic supply system was located one floor below the wave basin so the hydraulic cylinder for the wave machine drive was about 5 m above the oil reservoir.) The cylinder, the servo-valve just above it, and the small accumulator are shown in the photograph presented in Fig. 4.4.

4.2.3 The Servo-System

The servo-system consisted of a function generator, a feedback device and a servo-controller. The principle of operation is as follows: the voltage from the function generator and the voltage from the feedback device are of opposite signs and are added

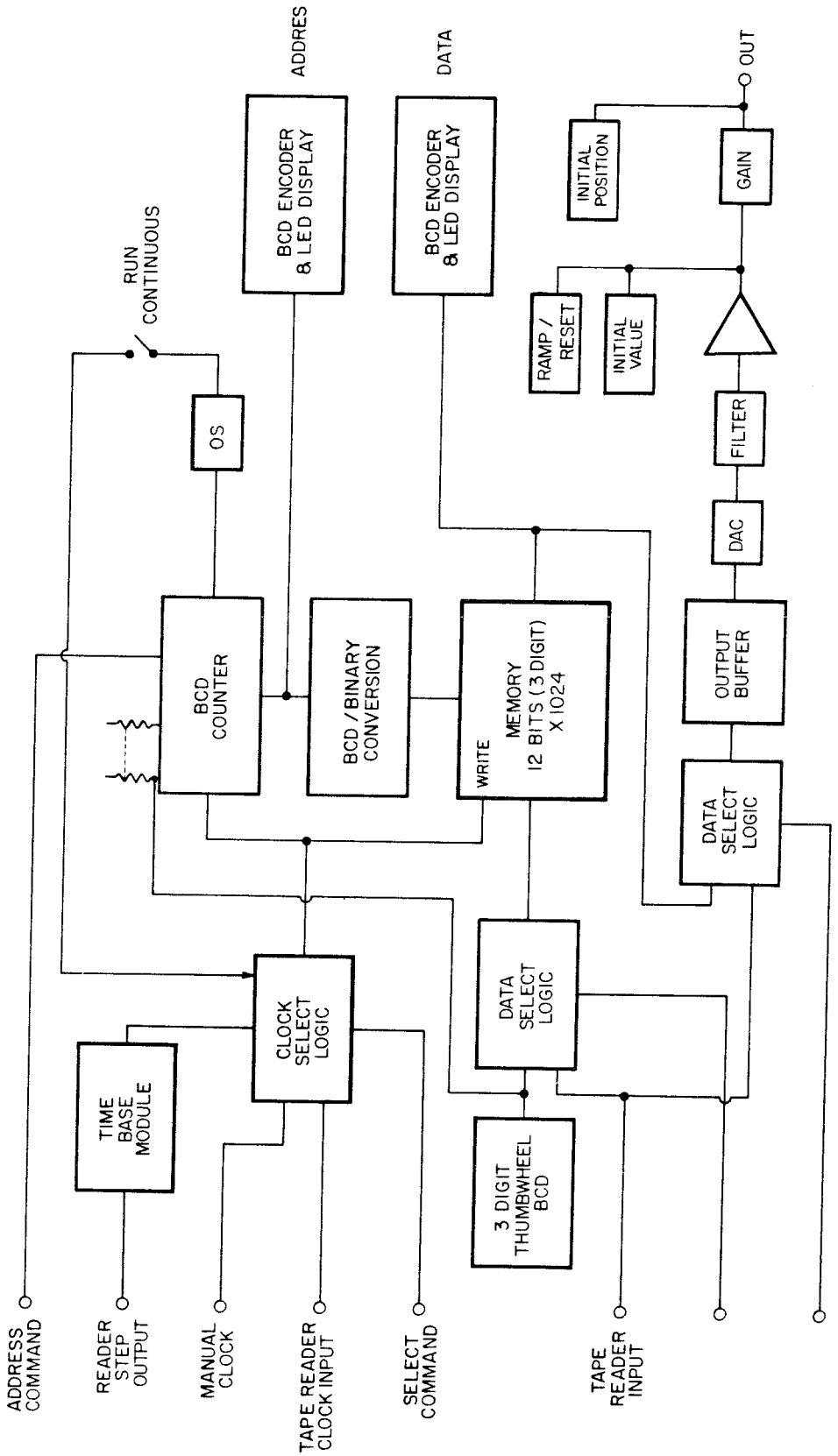

Fig. 4.7 Block circuit diagram of the function generator (after Goring, 1978).

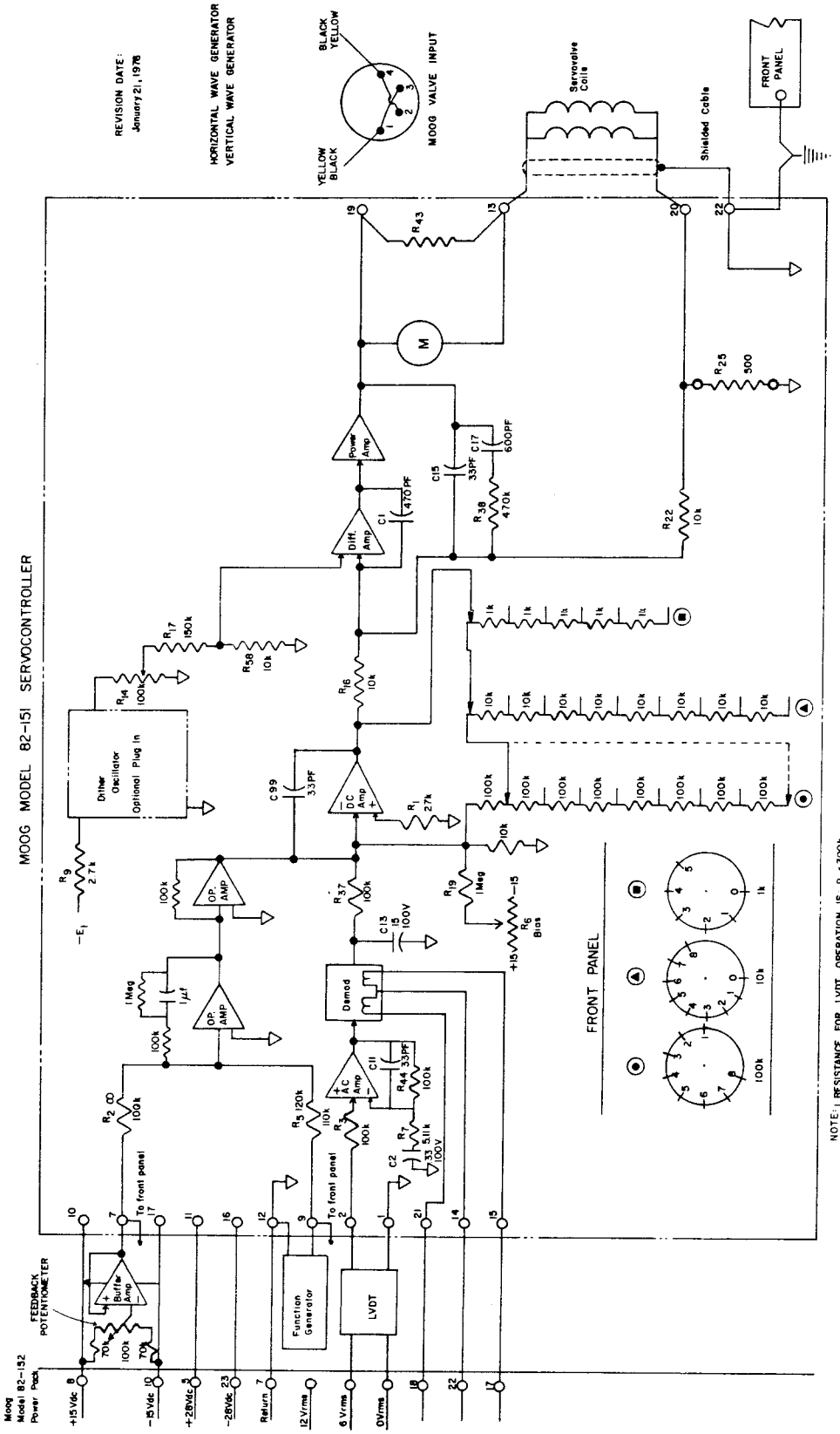

Fig. 4.8 Block circuit diagram of the servo controller (after Goring, 1978).

by the servo-controller which amplifies the resulting signal and transmits the corresponding current to the servo-valve. The quantity of flow through the servo-valve, and, thus, the velocity of the piston is proportional to the magnitude of the current generated in the servo-controller.

The block circuit diagram of the function generator is presented in Fig. 4.7. The time history of the desired motion is loaded into memory of the function generator through punched paper tape and an associated punched paper tape reader (manual loading is also possible). The input data consist of 1000 integer values, equispaced in time, which vary from 0 to 999. At the time of execution of the programmed motion the amplitude of the motion is scaled by the total stroke (the value of which was entered externally in the function generator) and the time duration controlled to 0.001 second (which was also entered separately).

The motion feedback device consists of an LVDT (linear variable differential transformer), Collins Model LMT 711 P38, shown in Fig. 4.4 along the side of the cylinder. The position of the carriage was converted into an electrical current by the LVDT which consisted of primary and secondary coils mounted in the form of a tube inside which a ferro-magnetic core moved. The primary coil was supplied with a 6 VAC from the servo-controller and the output of the secondary coil was returned to the servo-controller where it was demodulated into direct current. As the piston moved, the core which was attached

(THIS PAGE IS BLANK, DUE TO ERROR IN PAGINATION)

to the piston rod moved inside the coils and the demodulated voltage from the secondary coils varied linearly with the position of the carriage.

The servo-controller was a Moog AC/DC servo-controller (Model 82 151) and power pack (Model 82-152). Its circuit diagram is presented in Fig. 4.8. (The connection of the function generator and the LVDT can be seen in that figure.) A photograph of the function generator and servo-controller is presented in Fig. 4.9.

Examples of the response of the wave generator are presented in Fig. 4.10 where the solid curves are the programmed motion from the function generator and the dashed lines represent the actual motion of the plate. Figure 4.10(a) shows the response to a hyperbolic tangent time-displacement history which would be used to generate a solitary wave, and Fig. 4.10(b) shows the response to the function which would be used to generate a series of cnoidal waves. A time lag of approximately 0.05 sec between the programmed and actual motion is observed for the two examples and constitutes a feature of the servo-controller. (The "roughness" of the curves is attributed to the precision of the generated motion which is divided into one part per thousand.) Otherwise, good agreement is seen between the two curves in each figure.

4.3 The Closed Basins and Harbor Models

4.3.1 The Closed Basin Models

Two lucite basins were constructed for the experiments presented in Chapter 5. The first one, made of lucite 1.27 cm (1/2 in.) thick

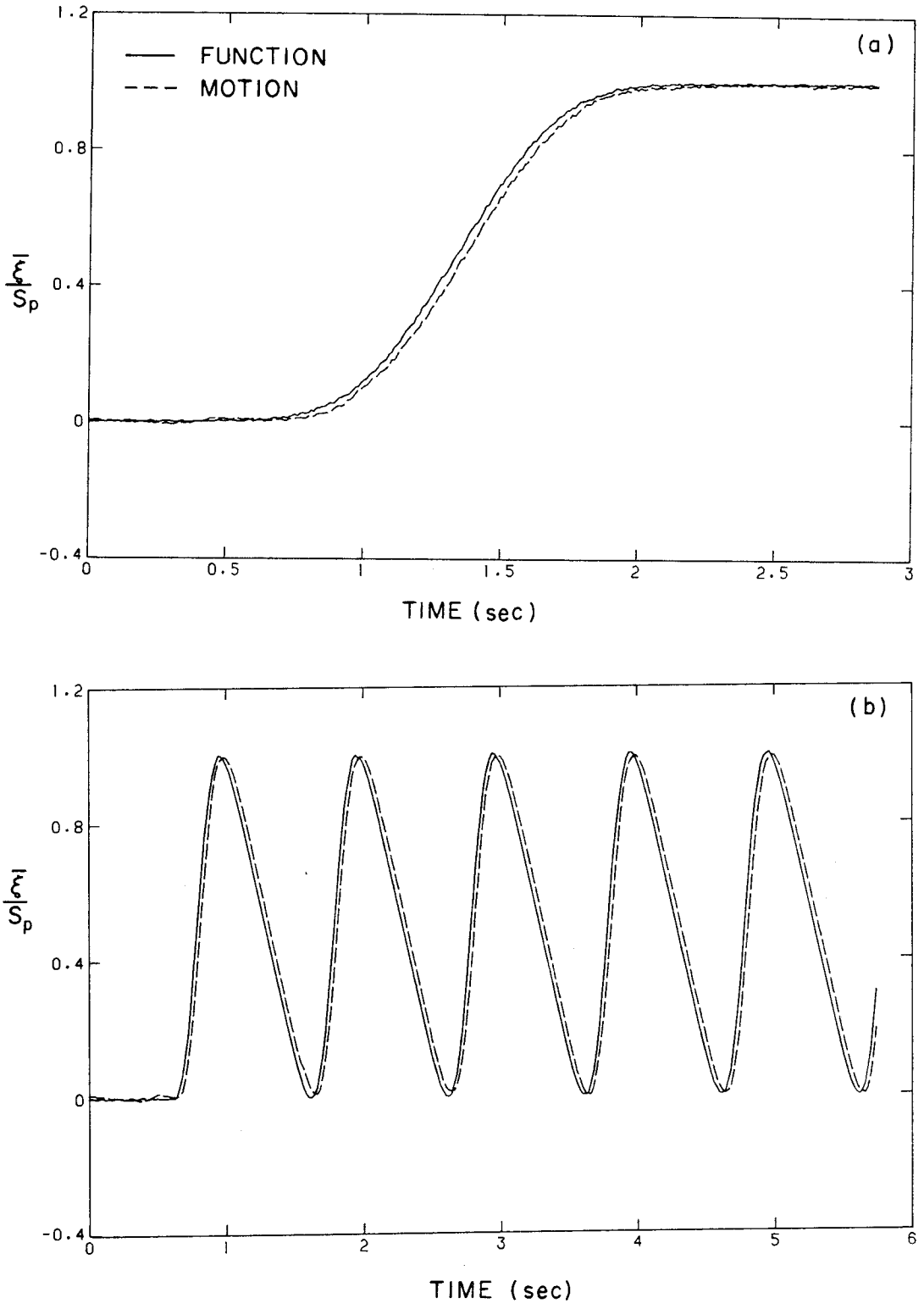

Fig. 4.10 Examples of the actual and programmed wave plate displacements for (a) solitary wave generation and (b) cnoidal generation.

was 60.95 cm long, 47 cm high and 30.5 cm wide. It could be partitioned in smaller widths by means of removable lucite walls 1.27 cm (1/2 in.) thick which were fastened at each end of the basin. The sealant was applied on the outside face of this wall at the joints to eliminate leaks. Experiments were performed using six different widths: 23 cm, 13.8 cm, 8 cm, 6.15 cm, 5 cm and 4 cm. This basin was used for the wave damping experiments and some experiments on the nonlinear resonant oscillations. The second basin, shown in Fig. 4.11 was 117.4 cm long, 13 cm wide and 40 cm high and was also made of lucite 1.27 cm (1/2 in.) thick. It was used to extend the experimental results dealing with nonlinear resonant oscillations to small depth to basin length ratios.

The two basins were fastened to the top of the wave generator wave plate assembly, as shown in Fig. 4.11. Therefore, they could be moved with a programmed horizontal back and forth motion in a precise manner using the hydraulic-electro-servo system. The structural angles seen in Fig. 4.11 attached to the upper edge of the basin were used to mount the wave recording device which, therefore, moved with the basin.

4.3.2 The Harbor Models

Two different harbor planforms were investigated experimentally: a rectangular harbor with variable width, length and entrance width and a trapezoidal harbor with fixed dimensions. The harbor models were designed so that each would fit into a false wall simulating a perfectly reflective "coastline" which was installed seven meters from, and parallel to, the wave plate. The false walls were made of lucite 0.95 cm (3/8 in.) thick and 40 cm high mounted to a frame

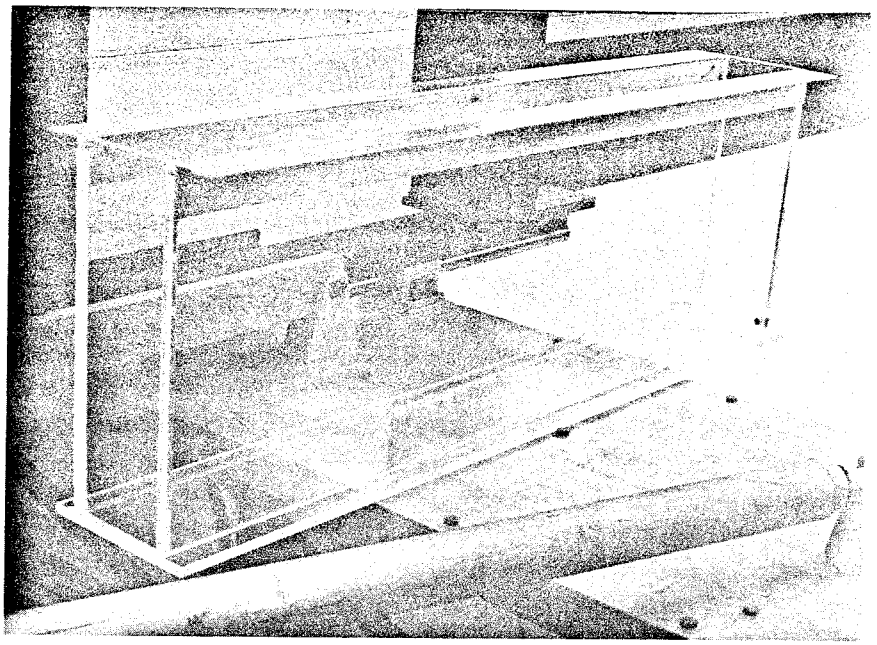

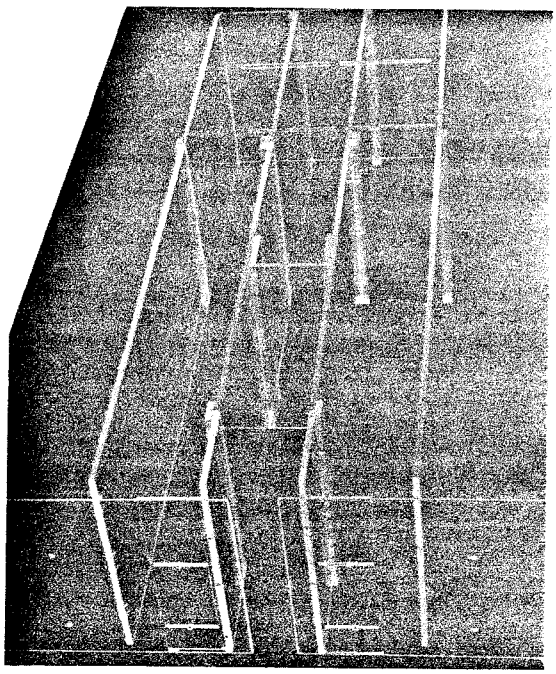

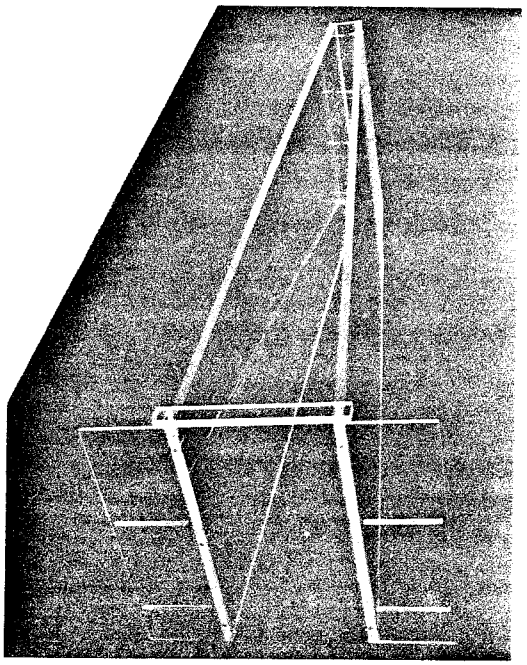

Fig. 4.11 Long rectangular closed basin, rectangular and trapezoidal harbors.

composed of galvanized iron angles constructed in two identical pieces: the east wing and the west wing. Each wing extended 145 cm from 30 cm off the center of the basin to the beginning of the wave absorbers screens. The supporting frames and the walls can be seen in Fig. 4.1. The walls were weighted to hold them in place. In line with the false walls, lucite spacers, 0.95 cm (3/8 in.) thick, 2.54 cm (1 in.) wide and 45 cm high were placed between each screen of the absorbers in order to prevent wave energy from penetrating the absorbers into the still water region behind the "coastline."

The variable size rectangular harbor, made of lucite, is shown in Fig. 4.11. A "U" shaped outer frame composed of three lucite walls connected to the false walls. This frame was built to reinforce the rigidity of the harbor itself. The harbor, made of lucite 1.27 cm (1/2 in.) thick, consisted of two parallel walls 178 cm long and 44 cm high connected to the backwall of the outer frame. This system of four walls can be seen clearly in Fig. 4.11; the distance between the two inner walls could be varied continuously. The backwall of the harbor consisted of rectangular lucite pieces 40 cm high, 1.27 cm (1/2 in.) thick of different widths. Each piece was held vertical by two other rectangular lucite pieces 10 cm long, 40 cm high, 1.27 cm (1/2 in.) thick, which were connected to it at right angles so that the assembly formed a "U" shape able to stand vertically by itself. (This can be seen in Fig. 4.11 midway back into the harbor.) With this arrangement the harbor width could only be varied incrementally by changing from one piece of lucite to another thereby maintaining

an approximately constant width-to-length ratio as the harbor length was adjusted. In the experiments twelve pieces of lucite were used, varying from 3 cm to 20 cm wide. The backwall of the harbor was held in place by clamps. The entrance width of the harbor was adjusted using two pieces of lucite 0.64 cm (1/4 in.) thick, 43 cm high, 116 cm long and rounded at the edges. These pieces could slide parallel to the false walls and were connected to these walls and to vertical plates shown near the harbor entrance in Fig. 4.11.

For some of the experiments presented in Section 6.4 a linear varying depth inside the harbor was created using a ramp with an aluminum plate on top of it and by pressing the sidewalls against it after it had been placed inside the harbor.

The trapezoidal harbor, used in some of the transient experiments presented in Section 6.4, had fixed dimensions. It was made of lucite walls 1.28 cm (1/2 in.) thick and was 122 cm long, 40 cm high, 20 cm and 4 cm wide at the entrance and the backwall, respectively. It could be partially closed in the same manner as for the rectangular harbor. Leakage at the bottom was eliminated by gluing the bottom edges of the walls to a thin lucite sheet 0.18 cm thick.

4.4 The Measurement of Water Surface Elevation

The only physical wave characteristic measured in this study was the water surface elevation. The measurement of the time history of the surface elevation at a given position is discussed first, followed by the measurement of the wave profile along the closed basin or harbor

at a given time (the spatial profile).

4.4.1 The Eulerian Measurement of Wave Amplitude

Resistance wave gages were used in conjunction with the Sanborn (150 series) recorder (shown in Fig. 4.9) for the measurement of the water surface elevation as a function of time at a specific location. A drawing of a typical wave gage is shown in Fig. 4.12. The wave gage consisted of two stainless steel wires 8.25 cm (3.25 in.) long with a diameter of 0.025 cm (0.01 in.) and spaced 0.4 cm (0.16 in.) apart. The wires were stretched taut and parallel in a frame constructed of 0.32 cm (1/8 in.) diameter stainless steel rod, and were insulated electrically from each other in the frame. For small depths ($h \leq 4$ cm) a special wave gage was constructed. It consisted of two stainless steel tubes 0.08 cm (1/32 in.) outside diameter, 0.01 cm (0.02 in.) wall thickness and 6 cm long which were slightly bent at the lower end mounted without the clamp shown in Fig. 4.12; using that gage the maximum depth of immersion of the tubes was equal to the water depth. A Sanborn Carrier Preamplifier (Model 150-1100 AS) supplied the 2400 cps, 4.5 volt excitation for the gages and also received the output signal from the wave gage which, after demodification and amplification was displayed on the recording unit. The circuit diagram for the wave gages is presented in Fig. 4.13. The immersion of the wave gage in water causes an imbalance in the full bridge circuit and induces an output voltage proportional to the change of depth of immersion relative to the balanced position.

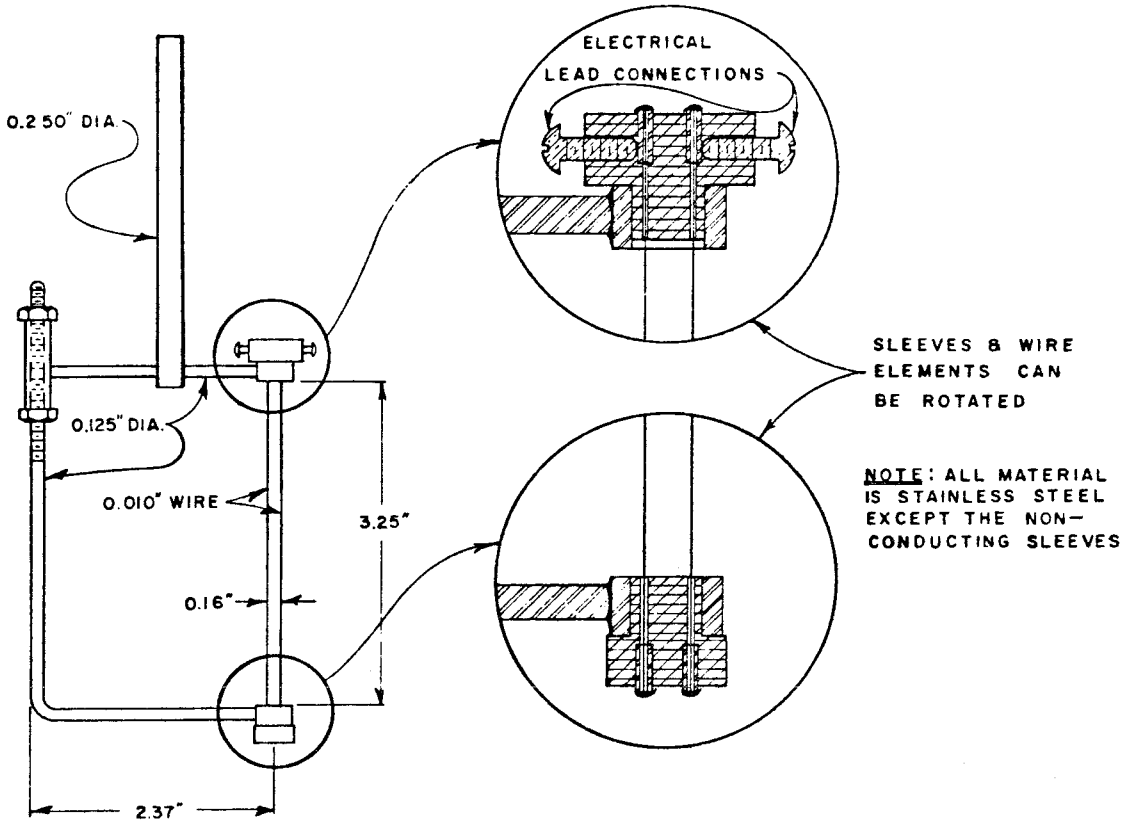

Fig. 4.12 Drawing of a typical wave gage (after Raichlen, 1965).

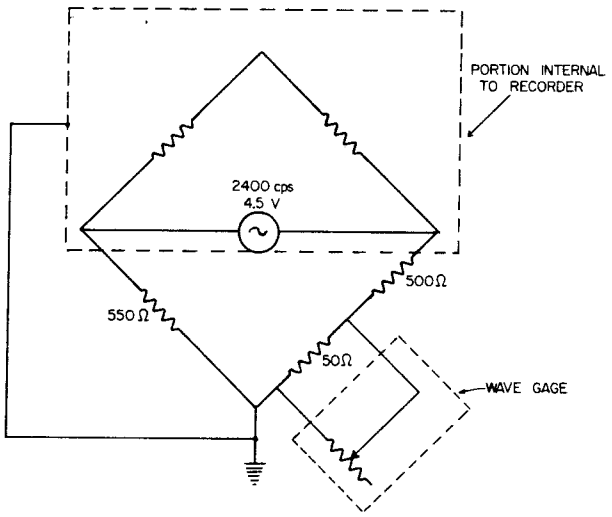

Fig. 4.13 Circuit diagram for wave gages (after Raichlen, 1965).

In addition to the display unit a voltage proportional to the wave amplitude is obtained from each amplifier of the recorder. Since the signal was not completely demodulated the output still retained some of the 2400 cps excitation voltage modulated by the wave signal and amplified to several hundred volts to drive the stylus of the display unit. This signal was to be used for purposes of automatic data acquisition; thus, the voltage had to be reduced and the signal had to be filtered to eliminate noise. The circuit diagrams shown in Figs. 4.14(a) and 4.14(b) were constructed to reduce the output voltage from the Sanborn recording system to be compatible with the laboratory data acquisition system and to reduce noise in the signal. The voltage divider and first stage filter (Fig. 4.14(a)) reduced the voltage to an acceptable ±5 volts range for the output signal. To reduce the noise level of several tens of millivolts with a dominant frequency of 120 Hz the signal was further processed by a low pass filter (4 Pole Butterworth filter) with a cutoff frequency of 60 Hz (Fig. 4.14(b)). The final output signal contained a noise level of 8 mv (r.m.s. value) or less.

Each wave gage was attached to a remotely controlled calibration device shown in Fig. 4.15, which consisted of a rack and pinion driven by a synchronous motor. The wave gage was attached to the rack with its weight counterbalanced. The synchronous motors (GE Model S-6 101) were connected parallel to the master control shown in the left part of Fig. 4.16, which consisted of a synchronous generator (GE Model SF 142) driven by a pinion and the rack of a point gage. Therefore, when the point gage was moved, a current was generated and relayed to the

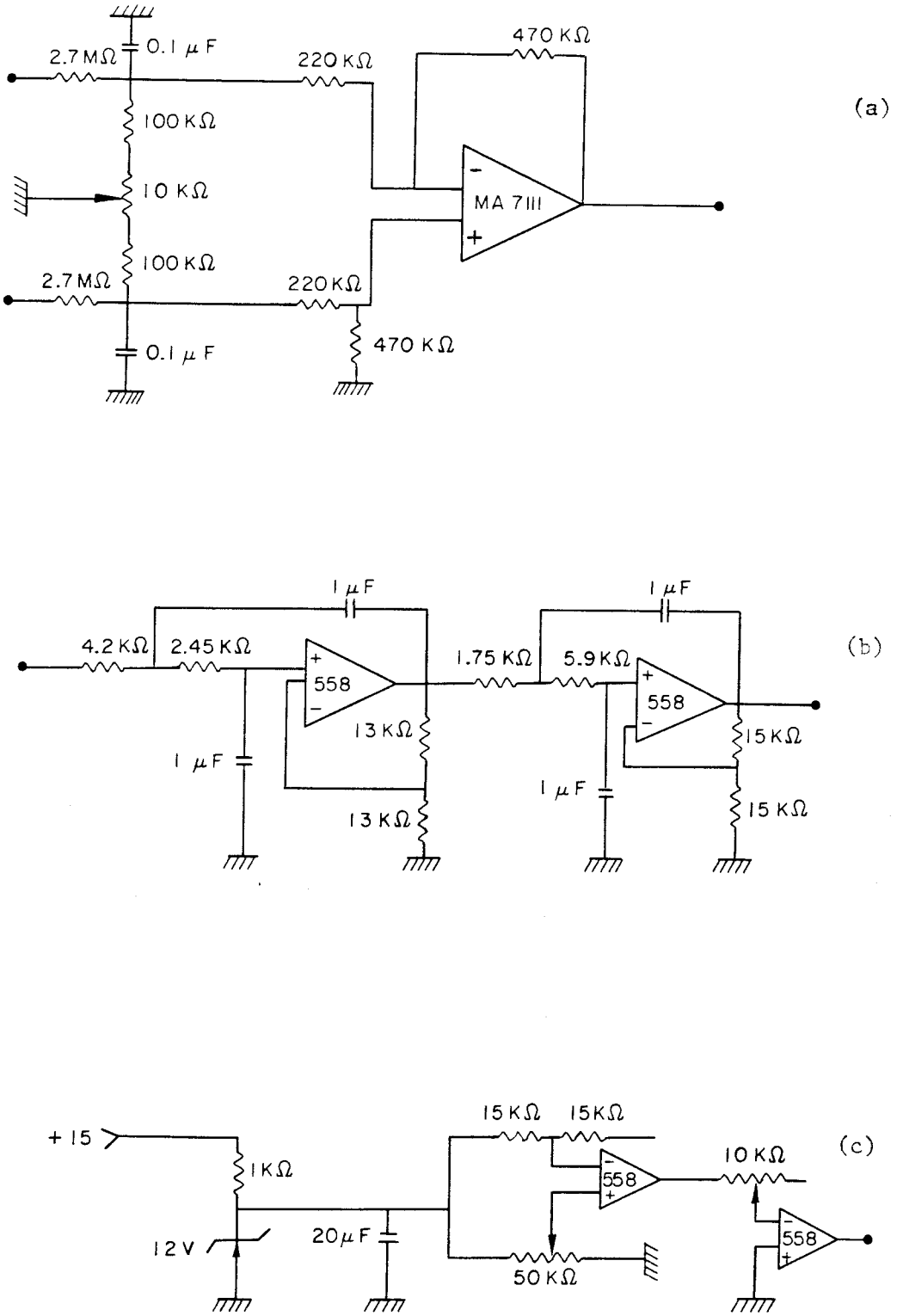

Fig. 4.14 Circuitry used in conjunction with A/D data acquisition system (a) filtering and voltage reduction of the signal from the Sanborn unit; (b) noise filtering; (c) potentiometer.

(THIS PAGE IS BLANK, DUE TO ERROR IN PAGINATION)

motors which moved the wave gages vertically in a one to one ratio. This arrangement allowed a quick calibration of the wave gages before each run. To record the calibration data with an analog-to-digital converter the motion of the rack of the point gage was converted to an electrical signal by a potentiometer and constant voltage signal. The circuit to scale and offset the voltage across the potentiometer within ±5 volts is shown in Fig. 4.16(c).

4.4.2 The Measurement of Spatial Wave Profiles

Two methods of measurements were used. For the closed basin, the water surface profiles were obtained photographically using the following procedure. Horizontal and vertical scales were mounted on the side of the basin which faced the camera. A 16 mm Bolex movie camera was mounted on a tripod about 1.50 m from the basin and a clock placed in the field of view of the camera next to the basin. The camera clutch and the clock remote control switch were engaged and the motion of the wave generator which moved the closed basin was started. To retrieve the wave profiles the film, after being processed, was projected frame by frame on a 40 cm by 40 cm screen and the selected wave profiles were copied. This method, although straightforward, yielded a fairly low degree of accuracy and the relative uncertainty in the wave height could reach 20% for small wave amplitude profiles.

The second method, used for the harbor, consisted of retrieving the spatial wave profiles from closely spaced interior water surface time histories obtained at various locations. This technique, although more involved and more time consuming than the previous one yielded far more accurate results. The description of the detailed procedure is

postponed until Chapter 6.

4.5 The Data Acquisition System

All voltage measurements were discretized with the Analog-to Digital (A/D) data acquisition system built into the PDP 11/60 computer installed in the laboratory. This system can accept eight analog voltage inputs in differential mode (16 in single-ended mode), digitize the signals and store the data on a disk. The digitized values are stored as integer numbers between 0 and 2048 corresponding to a ±5 volts range. The precision of the system was therefore ±0.005 volts. The data acquisition process was monitored through a Fortran routine which was run from a CRT interactive terminal next to the basin and shown in Fig. 4.16. The command program for data acquisition requires prior knowledge of the data rate, the number of channels to be processed, the total number of data to be taken and the data file name for the data storage.

The A/D converter of the PDP 11/60 computer was located several hundred feet away from the recording device. This situation significantly alters the quality of the data transmitted between the user's instrument and the A/D converter because of the noisy environment inside the building. The noise frequency ranged from 60 Hz to several kHz so that the use of a numerical filter was impractical. Therefore, the following alternative solution was chosen to eliminate the noise in the transmission lines. A circuit diagram of the arrangement is shown in Fig. 4.17. It consists of three parts:

(i) An input box (located at user's experiment) which transforms the signal coming from the user's instrument into a differential signal.

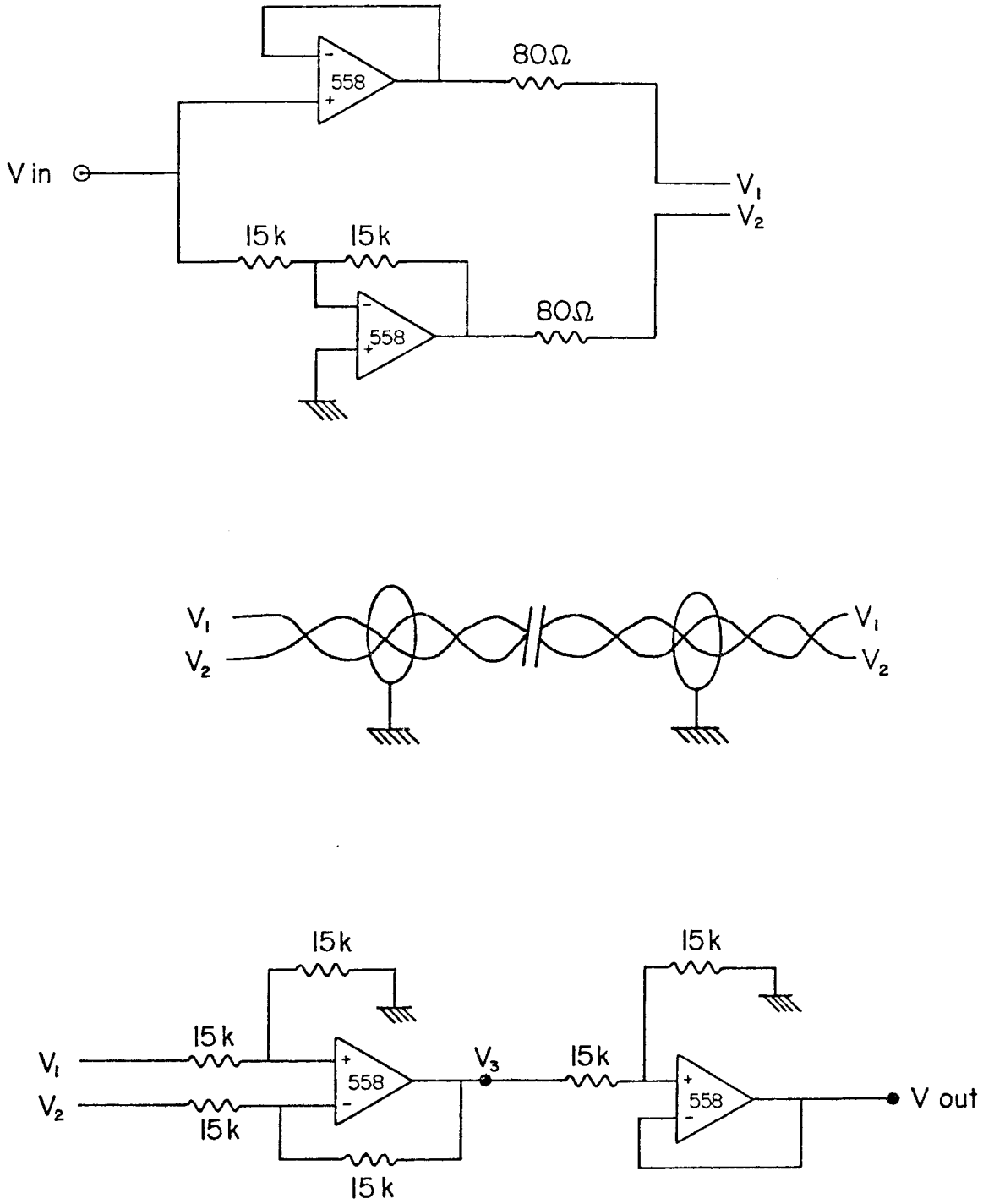

Fig. 4.17 Circuitry for the transmission of analog data towards A/D converter.

(ii) A twisted pair of cables which is used to transmit the signal to the A/D converter.

(iii) An output box located next to the A/D system which transforms the differential signal back into a signal referenced with respect to the user's ground potential. In this manner the noise picked up during transmission is automatically canceled by the differential signal. Tests performed with that circuitry showed that the amount of noise picked up by the whole system was less than 2 mV, which is below the detection level of the A/D.

4.6 The Experimental Procedure Using the Data Acquisition System

The use of the A/D converter in connection with the PDP 11/60 mini computer made it possible to reduce the wave data of each channel and obtain the calibrated wave heights in a matter of seconds after the end of the data collection. Calibration of the wave gages had to be performed before each experiment because of the variability of the resistivity of the water in the basin with time. Each experiment consisted of three consecutive steps:

(i) In the calibration phase, each wave gage, after balancing the corresponding circuit, was immersed a positive vertical distance from its equilibrium position which was larger than the maximum positive wave height to be measured. The A/D was activated and each gage was raised by turning the wheel on the point gage of the master unit until the negative vertical distance of the wave gage from its balance position became larger than the maximum negative wave height to be measured. At the end of the sweep the point gage was placed back in the equilibrium position. During that phase both the voltage from the

potentiometer and the voltages from the wave gages were acquired and digitized.

(ii) In the run phase, the wave was generated and the A/D was activated manually. This time only the voltage signals from the wave gages were discretized with the A/D converter.

(iii) At the end of the sweep a data reduction program was run to calibrate the wave data. For each wave record the basic operation consisted of fitting a fourth order polynomial to the corresponding calibration curve. The resulting coefficients were applied to calibrate the wave data obtained in the second step. To eliminate the influence of the end points, only points corresponding to a wave gage deflection within values prescribed to the Fortran program were considered for the calibration process. A typical calibration curve is presented in Fig. 4.18. Good agreement is obtained between the original calibration curve and the fitted one.

Usually these three steps took less than three minutes to be performed for the harbor experiments presented in Chapter 6. With this procedure the relative error on the wave height was estimated to be about 1%. Other Fortran programs were written to analyze the discretized data; they include curve plotting, searching for wave extrema, Fourier analysis. Sometimes the wave height to be measured in the harbor was larger than the depth; for these cases the experiments were carried in two steps. In a first run only the positive part of the wave was recorded and calibrated. The same run was repeated and this time only the negative part of the wave was recorded and calibrated. For each run, the complete wave was recorded with a wave gage outside the harbor for a time reference. A Fortran program was run to connect the

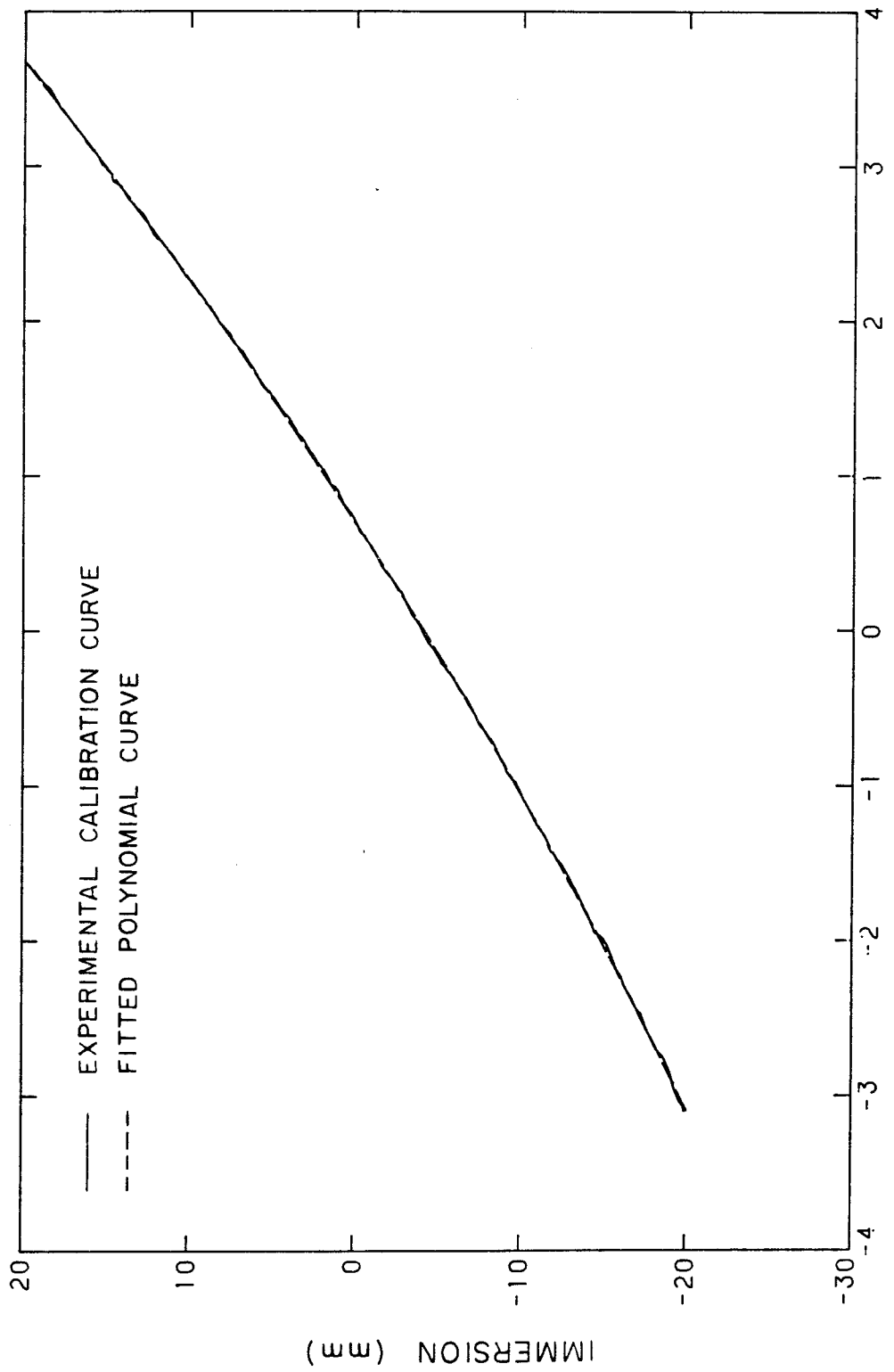

Fig. 4.18 Typical wave gage calibration curve using A/D data acquisition system.

positive and negative parts of the wave record together so that the complete wave could be reconstructed.

(THIS PAGE IS BLANK, DUE TO ERROR IN PAGINATION)

CHAPTER 5

PRESENTATION AND DISCUSSION OF THE RESULTS FOR THE CLOSED BASIN

Two sets of results related to the problem of wave dynamics in a closed rectangular basin are presented in this chapter. Section 5.1 deals with the damping characteristics of a standing wave in a closed rectangular lucite basin which result from dissipation related to laminar boundary friction and surface tension effects. In Section 5.2 experimental results on the wave dynamics resulting from the transient and steady state excitation of a closed rectangular basin in shallow water are presented and compared to the theory. It is recalled that this closed basin study was carried out to help elucidate some of the features pertaining to long wave oscillations in harbors and bays.

5.1 Experiments on Energy Dissipation in Standing Waves in Rectangular Lucite Basins

5.1.1 Introduction

Experiments were constructed to determine the damping characteristics of a standing wave in a rectangular lucite basin which result from dissipation related to laminar boundary friction and surface tension effects.

The main reason underlying this study stemmed from the necessity of knowing accurately the amount of dissipation resulting from the two aforementioned damping sources in order to investigate experimentally the other dissipation mechanims, such as leakage losses and entrance separation, affecting the harbor experiments presented in Chapter 6. Since the shapes of the modes of oscillations are similar for a rectangular basin and a narrow rectangular harbor (which was used mostly in the experimental study described in Chapter 6), the characteristics of laminar boundary friction and dissipation related to surface tension in the harbor can, therefore, be directly inferred from the closed basin experiments.

A convenient parameter to characterize the amount of dissipation is the decay coefficient $\bar{\alpha}$ defined as

$$\frac{A}{A_o} = e^{-\bar{\alpha}\frac{t}{T}} \tag{5.1.1}$$

where A and A_o denote the wave amplitude at either end wall, and T is the period of a natural mode of oscillation of the basin.

From Eq. (3.3.95) the coefficient $\bar{\alpha}$ can be expressed as

$$\bar{\alpha} = \sum_{i=1}^{n} \bar{\alpha}_i = \sum_{i=1}^{n} \frac{\pi}{Q_i} \tag{5.1.2}$$

where Q_i denote the "Q" factor defined in Section 3.3.3, associated

with the dissipative source S_i and n is the total number of dissipative sources. Five sources of dissipation which can affect wave oscillations in closed rectangular basins in laboratory have been investigated in Section 3.3.1. The associated Q_i factors have been computed in Appendix E, yielding from Eq. (5.1.2) the following expressions for the corresponding decay coefficients:

bottom laminar boundary friction:

$$\bar{\alpha}_b = \frac{\pi}{h}\sqrt{\frac{\nu}{2\sigma}}\ \frac{2kh}{\sinh\ 2kh} \tag{5.1.3}$$

wall laminar boundary friction:

$$\bar{\alpha}_w = \frac{\pi}{h}\sqrt{\frac{\nu}{2\sigma}}\ [\frac{2h}{b} + \frac{2kh}{\pi}\ (1 - \frac{2kh}{\sinh\ 2kh})] \tag{5.1.4}$$

surface laminar boundary friction:

$$\bar{\alpha}_s = \frac{\pi}{h}\sqrt{\frac{\nu}{2\sigma}}\ \frac{C\,kh}{\tanh\ kh} \tag{5.1.5}$$

dry friction from meniscus action:

$$\bar{\alpha}_c = \frac{32\bar{\kappa}\Gamma_e}{\pi\rho g\ A}\ \frac{1}{b}\ (1+\frac{\pi}{2}\ \frac{b}{L}) \tag{5.1.6}$$

residual surface tension dissipation:

$$\bar{\alpha}_{ob} = K_{ob}\ \frac{2\Gamma_e}{\rho g b^2} \tag{5.1.7}$$

In these expressions ν denotes the kinematic viscosity of the liquid, h is the still water depth, Γ_e is the surface tension of the liquid air interface, ρ is the fluid density, g is the acceleration of gravity, C is the surface contamination factor equal to 1 for a fully contaminated surface, and $\overline{\kappa}$ and K_{ob} are two constants. The frequency σ of the wave oscillations corresponds to a natural mode of oscillation of the basin defined by:

$$kL = n\pi \quad , \quad n = 1,2,... \tag{5.1.8}$$

where k denotes the wave number. It is noted that only the decay coefficient $\overline{\alpha_c}$ varies with amplitude. This characteristic makes it easy to recognize this dissipation source experimentally.

The purpose of the experiments was to check the validity of the analysis and to determine the values of the two unknown coefficients $\overline{\kappa}$ and K_{ob} related to surface tension dissipation. The study of wave damping was conducted in a lucite basin with a length L = 60.95 cm, divided into six different widths: b = 4 cm, 5 cm, 6.15 cm, 8 cm, 13.8 cm, and 23 cm. For each basin width the decay coefficient was measured for eight depths corresponding to a range of kh from 0.3 to 1. All measurements were performed for the first mode of oscillation (n = 1 in Eq. (5.1.8)).

Ordinary filtered tap water was used for all experiments. In order to eliminate the effects of dry friction from meniscus action, a commercial solution of Kodak Photo-Flo 200, which acts

as a wetting agent, was added to the water in a concentration of one part per thousand. (This concentration was found empirically by adding successive quantities of wetting agent in the basin until no further decrease of the attentuation coefficient was observed).

The experimental procedure consisted in filling the basin with filtered tap water at the desired depth and adding the solution of Photo-Flo. The basin was fixed rigidly to the top of the wave plate connected to the hydraulic system described in Chapter 4 and was left at rest for about an hour. Then the wave plate was activated with a sinusoidal motion of small amplitude at a period corresponding to the lowest mode of oscillation of the basin and was stopped after a few oscillations. The wave motion was measured using a wave gage mounted at one end of the basin and the data acquisition system described in Chapter 4. A typical decay curve is illustrated in Figure 5.1.1

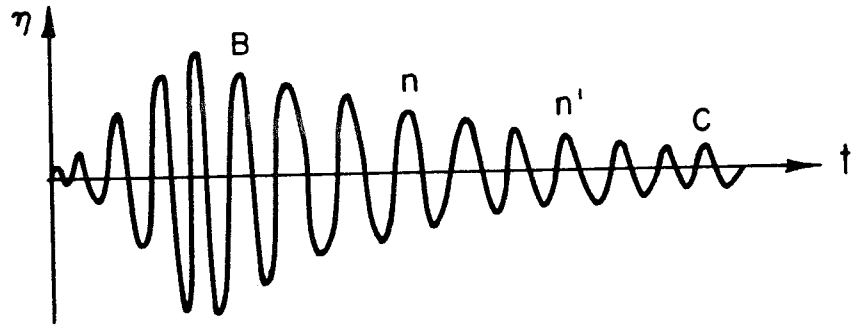

Figure 5.1.1 Typical decay curve.

Local decay coefficients $\bar{\alpha}_{n_1}$, associated with the amplitude A_{n_1}, could be computed from a least square fit of the logarithm of the expression:

$$\frac{A_n}{A_{n'}} = \exp[-\bar{\alpha}_{n_1}(n - n')] \tag{5.1.9}$$

where A_n and $A_{n'}$ denote the wave amplitudes at the n^{th} and n'^{th} oscillation, respectively, and the averaged amplitude A_{n_1} defined as:

$$A_{n_1} = \frac{1}{(n' - n+1)} \sum_{j=n}^{n'} A_j \tag{5.1.10}$$

The number n-n' was usually chosen between 4 and 10. The discrete variation of $\bar{\alpha}_{n_1}$ with A_{n_1} could then be obtained with this method. This allowed detection of the variation of the decay coefficient with amplitude between point B (three oscillations after the basin motion was stopped) and point C (corresponding to a wave amplitude approximately equal to $1/20^{th}$ of its value at point B).

One important problem is the determination of the permissible experimental maximum wave amplitude in order for the analytical expressions for the decay coefficients to apply. In principle, those results are applicable within the range of validity of Stokes second order theory such that the second term in the Stokes expansion remains much less than unity. In the case of a rectangular basin the expression given by Keulegan (1959) leads to:

$$\frac{A_k}{2} N_2 = \bar{\varepsilon} < O(1) \qquad (5.1.11)$$

where

$$N_2 = \frac{\cosh^2 kh(\cosh 2kh + 2)}{\sinh^2 kh \sinh 2kh}$$

Keulegan (1959) found experimentally that the relative error in the wave amplitude, using second order Stokes theory, was less than 5% if $\bar{\varepsilon}$ is chosen equal to 0.1. Table 5.1.1 gives the resulting maximum permissible wave amplitude as a function of the depth, based on this value of $\bar{\varepsilon}$, for the first mode of oscillation and a basin length equal to 60.95 cm.

Table 5.1.1 Maximum permissible wave amplitude compatible with Stokes second order theory as a function of the depth.

h(cm)	kh	A(cm)
20	1.03	6.0
16	0.82	3.8
12.5	0.64	1.9
10.5	0.54	1.4
9.0	0.46	1.0
8.0	0.41	0.7
7.0	0.36	0.4
6.0	0.31	0.3

The experiments were performed such that the wave amplitude at point B (in Figure 5.1.1) remained within the range indicated by Table 5.1.1.

5.1.2 Experimental Results

The experimental variation of the attenuation coefficient $\bar{\alpha}$ with the wave amplitude is plotted in Figure 5.1.2 for various widths and a constant value of $kh = 0.82$ in the presence of a wetting agent in a concentration of one part per thousand. It is noted that $\bar{\alpha}$ remains essentially constant with the amplitude for nearly all the widths investigated, indicating no effect of dry friction from meniscus action. For $b = 4$ cm $\bar{\alpha}$ varies only slightly with the amplitude A, probably resulting from some residual dry damping not completely eliminated by the action of the detergent. In the case of Figure 5.1.2 the maximum initial wave amplitude is approximately 20 mm. It can be mentioned that similar tests were conducted for small initial wave amplitudes equal to 3 mm; essentially no difference was noticed between the two sets of runs: in both cases the damping coefficient remained constant as A varied and were equal for given values of b and kh.

Figure 5.1.3 demonstrates the importance of the action of the wetting agent in reducing the damping coefficient. The two curves correspond to a 6 cm width and $kh = 0.83$. When the wetting agent is added to the water there is essentially no variation in $\bar{\alpha}$ with A. Conversely when no wetting agent is used, $\bar{\alpha}$ increases markedly as the wave amplitude decreases from 25 mm to 2 mm; the discrepancy between the two curves is attributed to the dissipation caused by the dry friction of the meniscus against the lucite wall in the absence of detergent. In the absence of a wetting agent

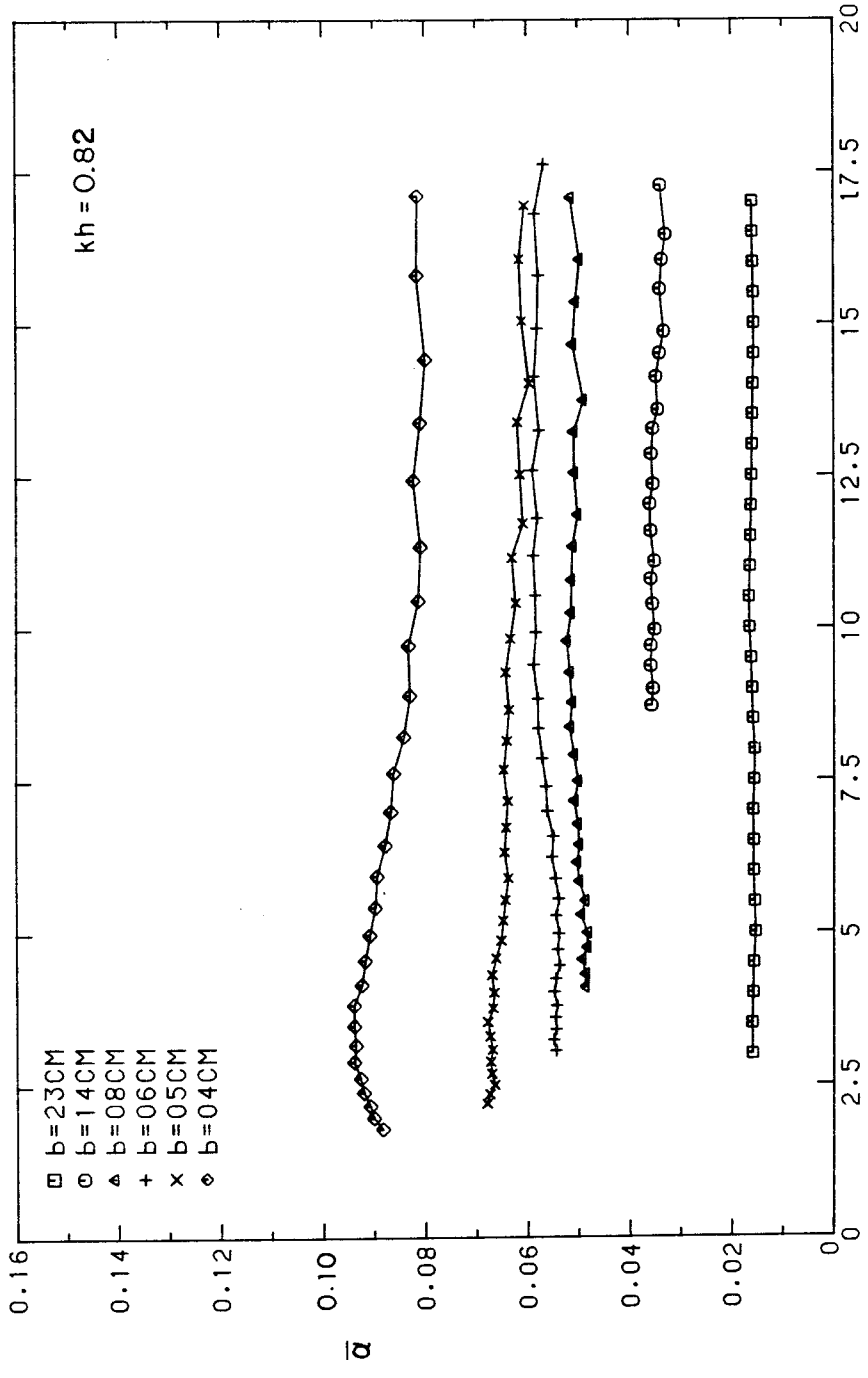

Fig. 5.1.2 Examples of variation of the decay coefficient with amplitude for various widths in the presence of a wetting agent; kh = 0.82.

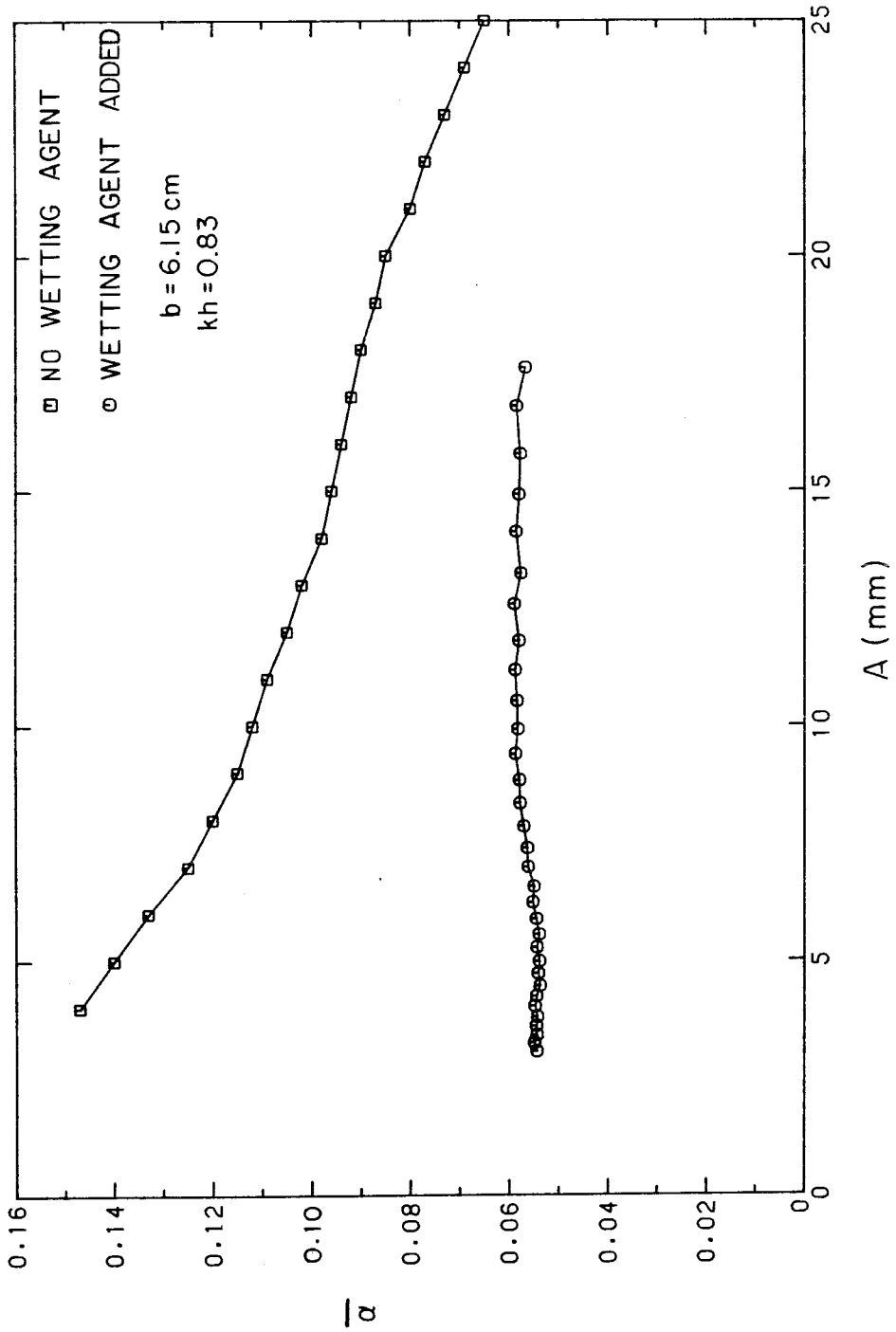

Fig. 5.1.3 Variation of the decay coefficient with wave amplitude with and without wetting agent; kh = 0.83, b = 6.15 cm.

it was noted during experiments that the liquid surface near the walls was rough and irregular. In contrast, when enough wetting agent was added to the water, the contact region appeared glassy and no roughness of the water surface was observed. Thus the vertical distance between the two curves can be set equal to the coefficient $\overline{\alpha}_c$ corresponding to dry friction. Using Eq. (5.1.6) and the experimental values of $\overline{\alpha}_c$ inferred from Figure 5.1.3, the coefficient $\overline{\kappa}$ appearing in Eq. (5.1.6) yields:

$$\overline{\kappa} = 0.35 \pm 0.04$$

This value is based on a surface tension Γ_e corresponding to an air-distilled water interface equal to 72 g/sec^2. It is of the same order of magnitude as that mentioned by Miles (1967, i.e., $\overline{\kappa} = 0.31$.)

The variation of $\overline{\alpha}$ with kh and with basin width b is presented in Figure 5.1.4. Each graph of Figure 5.1.4 corresponds to a given width. The dashed lines represent the theoretical variation of $\overline{\alpha}_b + \overline{\alpha}_w$ (bottom and wall friction) coefficient with kh derived from Eqs. (5.1.3) and (5.1.4). The solid lines represent the theoretical variation of $\overline{\alpha}_b + \overline{\alpha}_w + \overline{\alpha}_s$ (bottom, wall, and surface friction) coefficient with kh derived from Eqs. (5.1.3), (5.1.4), and (5.1.5). The symbols represent the experimental data. For this set of experiments wetting agent was added to the water in order to eliminate

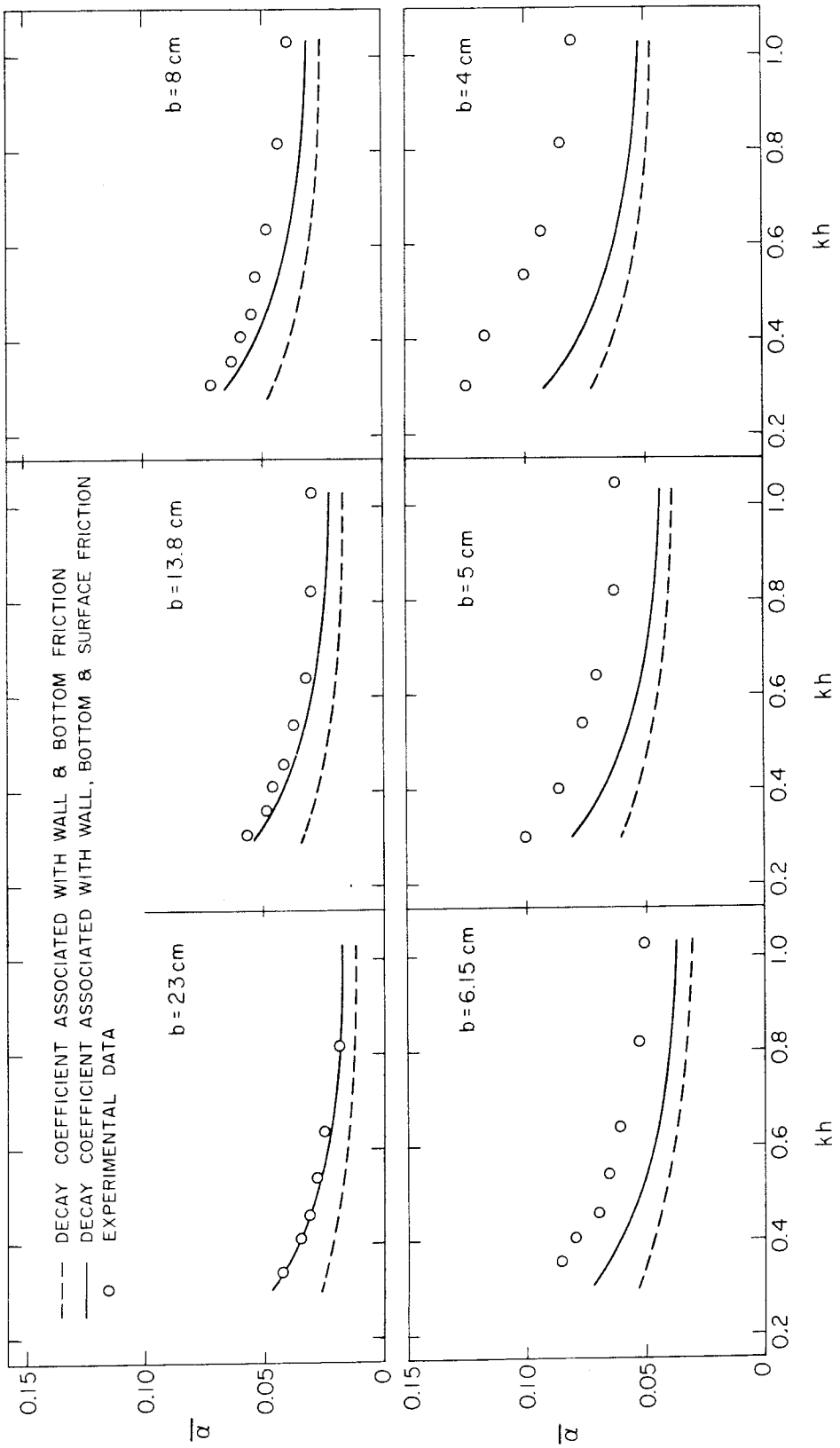

Fig. 5.1.4 Variation of the decay coefficient with kh for various widths in the presence of wetting agent.

the dissipation related to dry friction of the meniscus against the walls. For the largest width, b = 23 cm, the data agree well with the analysis if bottom, wall, and surface friction effects are taken into account; this indicates that surface friction must indeed be considered as a significant source of dissipation. In particular, in shallow water (kh = 0.3) the actual dissipation rate is 33% higher than predicted by bottom and wall friction only. As the width decreases, the measured dissipation rate becomes larger than that predicted by theory; the difference between experiments and theory increases as b decreases and for a basin width of 4 cm the dissipation rate is 40% larger than predicted by theory. It should be noted that the difference between the experimental decay coefficient $\overline{\alpha}$ and $\overline{\alpha}_b + \overline{\alpha}_w + \overline{\alpha}_s$ apparently remains independent of kh for a given width. The difference $\overline{\alpha} - (\overline{\alpha}_b + \overline{\alpha}_w + \overline{\alpha}_s)$ is shown as a function of b in Figure 5.1.5. (The vertical bars show the variation of this coefficient with kh for the indicated basin width). Even with the scatter of the data a definite trend can be observed. In particular the slope of the line (obtained by a visual best fit) joining the segments is -2 on the log-log scale indicating a variation of $\overline{\alpha} - (\overline{\alpha}_b + \overline{\alpha}_w + \overline{\alpha}_s)$ proportional to $1/b^2$.

Attributing this discrepancy to the surface tension effects reflected in the damping coefficient $\overline{\alpha}_{ob}$, the coefficient K_{ob} appearing in Eq. (5.1.7) is found by identifying the experimental curve of Figure 5.1.5 with Eq. (5.1.7) as:

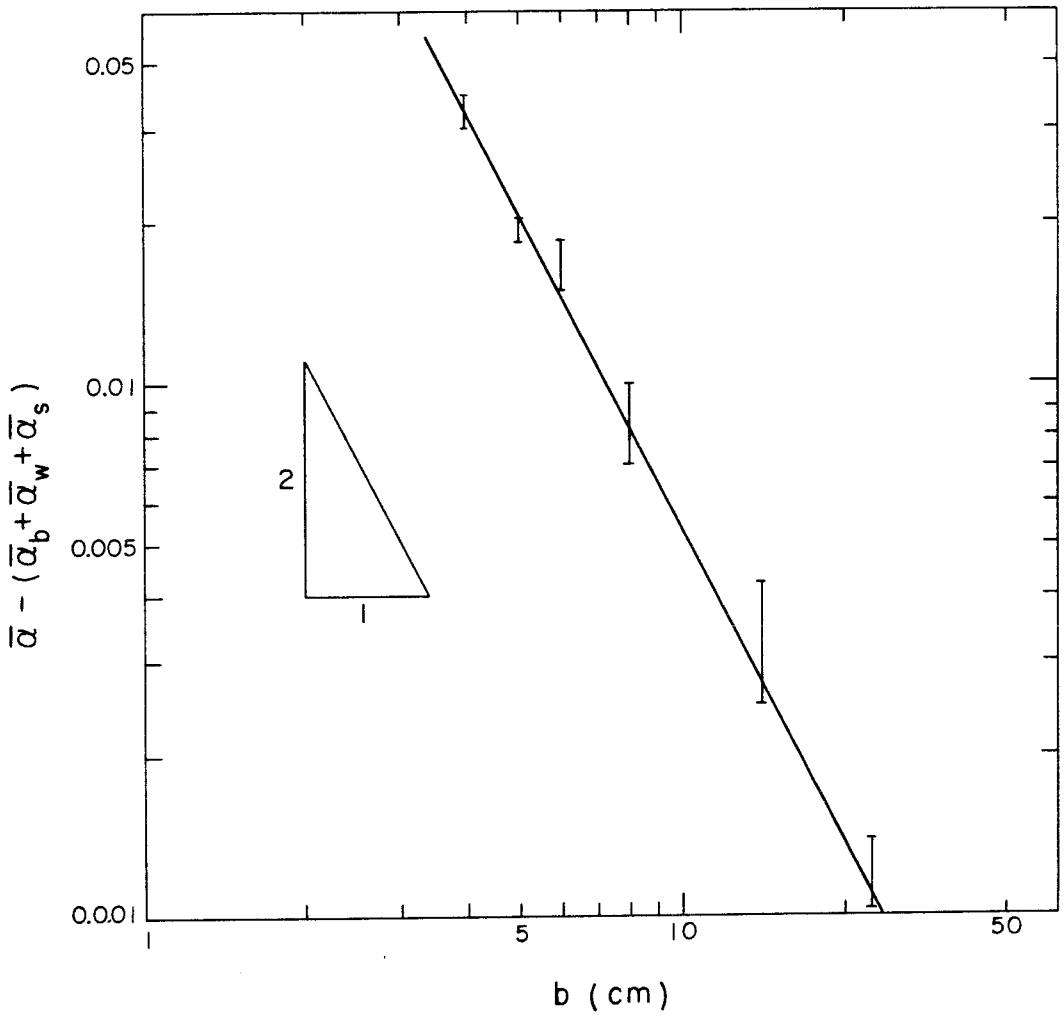

Fig. 5.1.5 Variation of the residual decay coefficient with width b.

$$K_{ob} = 3.3 \tag{5.1.12}$$

which gives

$$\bar{\alpha}_{ob} = 6.6 \frac{\Gamma_e}{\rho g b^2} \tag{5.1.13}$$

Keulegan (1959) found experimentally an expression for $\bar{\alpha}_{ob}$ based on dimensional analysis for similar basins as:

$$\bar{\alpha}_{ob} = 0.10 \frac{\Gamma_e T^2}{\rho b^3} \tag{5.1.14}$$

If the parameters from his experiments are substituted into Eq. (5.1.14) one obtains:

$$\bar{\alpha}_{ob} = 6.65 \frac{\Gamma_e}{\rho g b^2} \tag{5.1.15}$$

which compares favorably with Eq. (5.1.13). This tends to confirm that the mathematical form assumed in Section 3.1.1 to characterize the residual dissipative source related to surface tension and leading to the attenuation coefficient $\bar{\alpha}_{ob}$ (expressed in Eq. 5.1.7)) is correct, although an adequate explanation for the existence of this dissipative source appears to be lacking.

The results of this investigation also tend to show that with the experimental conditions described in this section, no other source of dissipation, apart from those reflected in the attenuation

coefficient $\bar{\alpha}_b, \bar{\alpha}_w, \bar{\alpha}_s, \bar{\alpha}_c$, and $\bar{\alpha}_{ob}$, appears significant.

For some other experimental conditions this conclusion should probably be modified. In particular, a critical Reynolds number beyond which the oscillatory flow inside the boundary layer becomes turbulent was stated by Jonsson (1978) as $u\delta_e/\nu = 563$, where u is the inviscid orbital velocity just outside the boundary layer, ν is the kinematic viscosity, and $\delta_e = (2\nu/\sigma)^{1/2}$ is the boundary layer thickness; this critical value can actually be reached for some laboratory conditions. Also the friction of the portion of the fluid above still water level against the walls induces some additional damping neglected in this study which may account for a significant fraction of the total energy dissipated when the ratio A/h is of order unity.

In order to appreciate the relative importance of the dissipation mechanisms discussed here, Table 5.1.2 gives the values of $\bar{\alpha}_b + \bar{\alpha}_w$, $\bar{\alpha}_s$, $\bar{\alpha}_c$, and $\bar{\alpha}_{ob}$ based on Eqs. (5.1.3) to (5.1.7) for three different widths and kh = 0.3. The values for the dry damping coefficient are based on a wave amplitude of 10 mm.

Table 5.1.2 Variation of the damping coefficients with various widths.

α \ b	23 cm	8 cm	4 cm
$\bar{\alpha}_b + \bar{\alpha}_w$	0.027	0.045	0.072
$\bar{\alpha}_s$	0.019	0.019	0.019
$\bar{\alpha}_c$	0.025	0.056	0.100
$\bar{\alpha}_{ob}$	0.000	0.008	0.03

Dry friction of the meniscus against the lucite walls appears to be the most important source of dissipation for the two smallest widths and thus cannot be neglected unless the lucite walls have been wetted due to the addition of detergent. Assuming this is the case, the combined effects of surface shear stress and surface tension, associated with the decay coefficients $\bar{\alpha}_s + \bar{\alpha}_{ob}$, account for about 40% of the total dissipation for the three widths; this clearly shows their importance in laboratory conditions. Surface tension dissipation associated with the coefficient $\bar{\alpha}_{ob}$ can be neglected for larger widths (say $b \geq 13$ cm); it accounts for 13% of the total dissipation when $b = 8$ cm and 33% when $b = 4$ cm, thus demonstrating its importance for small widths.

Two applications for the present experimental study follow from these results:

(i) In the experimental study presented in Section 5.2 on the transient excitation of a closed basin, two basin widths, $b = 12$ cm and $b = 23$ cm were used. Also, a wetting agent was added to the water for each experiment: Therefore, the only significant sources of dissipation to be considered are the bottom, walls, and surface friction which have been included in the formulation presented in Section 3.2.

(ii) In the experimental study presented in Sections 6.2, 6.3, and 6.4 on the transient wave induced oscillations in a rectangular harbor, the harbor widths used ranged from 4 cm to 15 cm and wetting agent was not always present. Therefore, it was found necessary in some cases, after an estimation of the dissipation related to surface tension effects, to correct the

experimental results for these effects using the method presented in Section 3.3.3. Those considerations will be discussed in more detail in Chapter 6.

5.2 The Closed Basin Excitation

5.2.1 Introduction

Experimental and theoretical results are presented in this section, which correspond to the wave dynamics resulting from the transient and steady state excitation of a closed rectangular basin. The only measured wave parameter was the wave height, therefore the discussion will be limited to this quantity.

The excitation motion chosen for the basin was a horizontal sinusoidal motion characterized by the amplitude d and the frequency σ. From the analysis performed in Section 3.2 the water surface elevation can be completely defined by six dimensionless parameters:

$$\frac{\eta/h}{d/L} = F\left(\frac{t\sqrt{gh}}{L}, \frac{x}{L}, \frac{d}{L}, \frac{h}{L}, \frac{\sigma L}{\sqrt{gh}}, \gamma_s\right) \tag{5.2.1}$$

where

$$\gamma_s = \frac{L}{h\sqrt{gh}} \left(\frac{\nu\sigma}{2}\right)^{1/2} \left(1 + C + \frac{2h}{b}\right) \tag{5.2.2}$$

The dissipation parameter γ_s includes only bottom, walls, and surface friction. Dissipation from surface tension is expected to remain small compared to boundary friction dissipation for the reason invoked in Section 5.1.2; it is therefore neglected here.

For a given time t and a given position x the nondimensionalized amplitude η/h, scaled by d/L, depends on four parameters: the nonlinear parameter d/L, which describes the relative excursion of the basin, the dispersion parameter h/L, the frequency parameter $\sigma L/\sqrt{gh}$ and the dissipation parameter γ_s. A more accurate measure of the dispersion is h/λ, where λ denotes the wave length associated with the frequency σ. Using the linear nondispersive theory, λ can be simply approximated as: $\lambda = 2\pi\sqrt{gh}/\sigma$ so that a relevant measure of dispersion effects is:

$$\frac{h}{\lambda} \simeq \frac{1}{2\pi} \frac{\sigma L}{\sqrt{gh}} \frac{h}{L} \tag{5.2.3}$$

If nonlinear effects are neglected, d/L does not appear any more as a variable in the function F and merely acts as a scaling parameter for η/h.

Some important results were derived from the linear dispersive and dissipative theory, presented in Section 3.2.2. In particular, the resonant frequencies (neglecting dissipation) are given by:

$$\frac{\sigma_o L}{\sqrt{gh}} = (2n+1)\pi\left[1 - \frac{1}{6}(2n+1)^2\pi^2\left(\frac{h}{L}\right)^2\right] \tag{5.2.4}$$

where n defines a particular free mode of oscillation of the basin.

The evolution of the wave amplitude with time at either end wall, for a continuous excitation at resonance, is given by:

$$\frac{\eta}{h} = 4 \frac{d}{L} \frac{(2n+1)\pi}{\gamma_s} \left(1 - \exp\left[- \frac{\gamma_s}{2n+1} \frac{t}{T}\right]\right) \tag{5.2.5}$$

so that, at steady state

$$\frac{\eta}{h} = 4 \frac{d}{L} \frac{(2n+1)\pi}{\gamma_s} \tag{5.2.6}$$

and during the initial stage of the excitation:

$$\frac{\eta}{h} = 4\pi \frac{d}{L} \frac{t}{T} \tag{5.2.7}$$

The characteristic time to reach steady state, or equivalently for the transients to be reduced to 5% of their original value is such that:

$$\frac{\sigma t}{2\pi} = \frac{(2n+1)\pi}{\gamma_s} \tag{5.2.8}$$

Finally, according to the linear theory, a node exists at all times at $x/L = 1/2$ for the excitation considered in this experimental study.

The range of validity of both the nonlinear and linear dispersive and dissipative theories has been found in Section 3.2.4 as:

$$\frac{h}{\lambda} \simeq \frac{\sigma}{2\pi} \sqrt{\frac{h}{g}} < 0.1 \tag{5.2.9}$$

In addition a Stokes parameter $\underline{U}_s$ was used to define the range of validity of the linear dispersive theory:

$$\underline{U}_s = \left(\frac{\eta^+ - \eta^-}{2h}\right)\left(\frac{2\pi\sqrt{gh}}{\sigma h}\right)^2 \qquad (5.2.10)$$

where η^+ and η^- denote the positive and negative extremes respectively at the end walls. Linear dispersive and dissipative theory applies only if:

$$\underline{U}_s \leq 0(10) \qquad (5.2.11)$$

Two rectangular lucite basins were used for the experiments; the first one was 60.95 cm long and 23 cm wide and the second one was 117.5 cm long and 12 cm wide. Both were fixed rigidly on top of the wave plate connected to the hydraulic system described in Chapter 4 and the wave motion was recorded with a wave gage clamped on top of the basin (and thus moving with the basin) and the data acquisition system described in Chapter 4. Wetting agent was added to the water for all experiments.

Section 5.2.2 deals with the basin initially at rest, continuously excited with a small displacement amplitude relative to the basin length. In Section 5.2.3 the results of the analysis presented in Section 3.2.3 on the nonlinear standing mode of oscillations are investigated experimentally. Section 5.2.4 deals with transient basin excitations of short duration but finite displacement amplitudes. Finally, a summary of the main results is presented in Section 5.2.5.

5.2.2 Transient and Steady States for a Continuous Excitation Near the First Two Resonant Modes

Figure 5.2.1a shows the variation at $x = L$ of both the steady state and maximum transient extrema corresponding to the linear-dispersive theory with the relative frequency of excitation σ/σ_o, where σ_o is obtained from Eq. (5.2.4) for the first resonant frequency, i.e., $n = 0$ in Eq. (5.2.4). The values of the dimensionless parameters are: $d/L = 0.0032$, $h/L = 0.098$, $\sigma_o L\sqrt{gh} = 3.0915$, $\gamma_s = 0.045$ for $\sigma/\sigma_o = 1$. The two curves are similar to the response of a damped linear oscillator near resonance; they are approximately symmetric about $\sigma = \sigma_o$ and the maximum transient and the steady state wave amplitudes $(\eta/h)_T$ and $(\eta/h)_S$ show small variation with σ/σ_o except within about 4% of the resonant frequency where they increase significantly. The transient response $(\eta/h)_T$ is always larger than $(\eta/h)_S$ except at resonance where the two become equal. (At resonance $(\eta/h)_S$ is given by Eq. (5.2.6)). The value of the Stokes parameter $\underline{U}_s$ computed from Eqs. (5.2.10) and (5.2.6), corresponding to the steady state conditions, is 360, implying the linear theory is not adequate at resonance. However, $(\eta/h)_S = 0.05$ away from resonance where $\underline{U}_s \simeq 40$, which is near the range of validity of the linear theory.

A few water surface time histories at one end wall obtained from the linear dispersive and dissipative theory are presented in Figure 5.2.1b (η/h versus $\sigma t/2\pi$ at $x = L$). They show a good symmetry about the mean water level. The amplitude of the oscillations grows linearly with time at first and is given by Eq. (5.2.7). After a few oscillations, however, the influence of either the forced frequency (which induces a beat pattern near $\sigma = \sigma_o$) or dissipation (at $\sigma = \sigma_o$) alters this linear growth. The

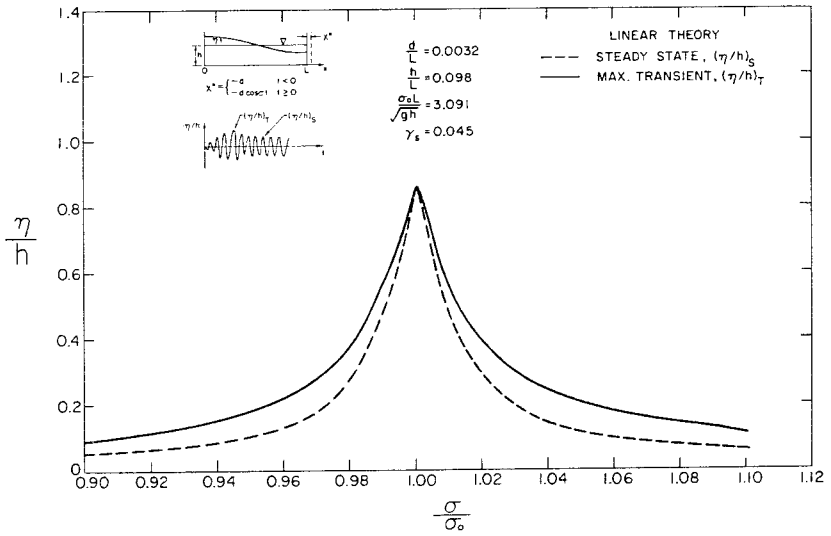

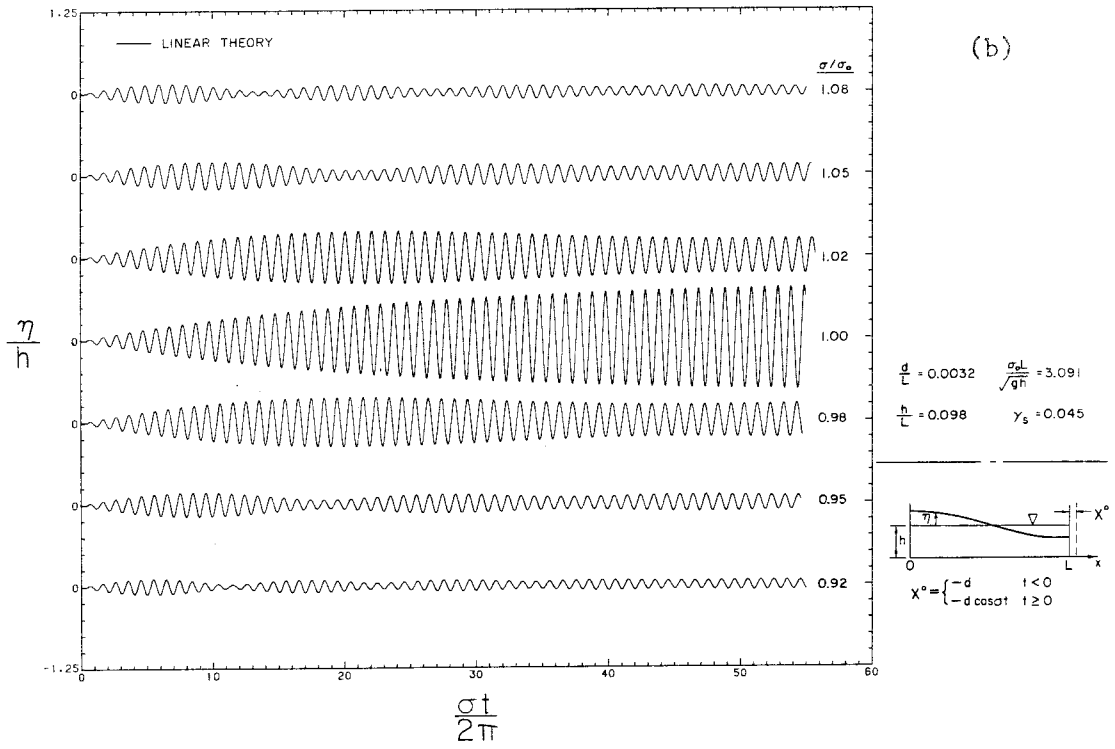

Fig. 5.2.1 (a) Variation of the relative wave extrema at x=L with frequency of excitation near the lowest resonant frequency (b) Time histories of free surface profiles at x=L; linear solution; d/L = 0.0032, h/L = 0.098 γ_s = 0.045.

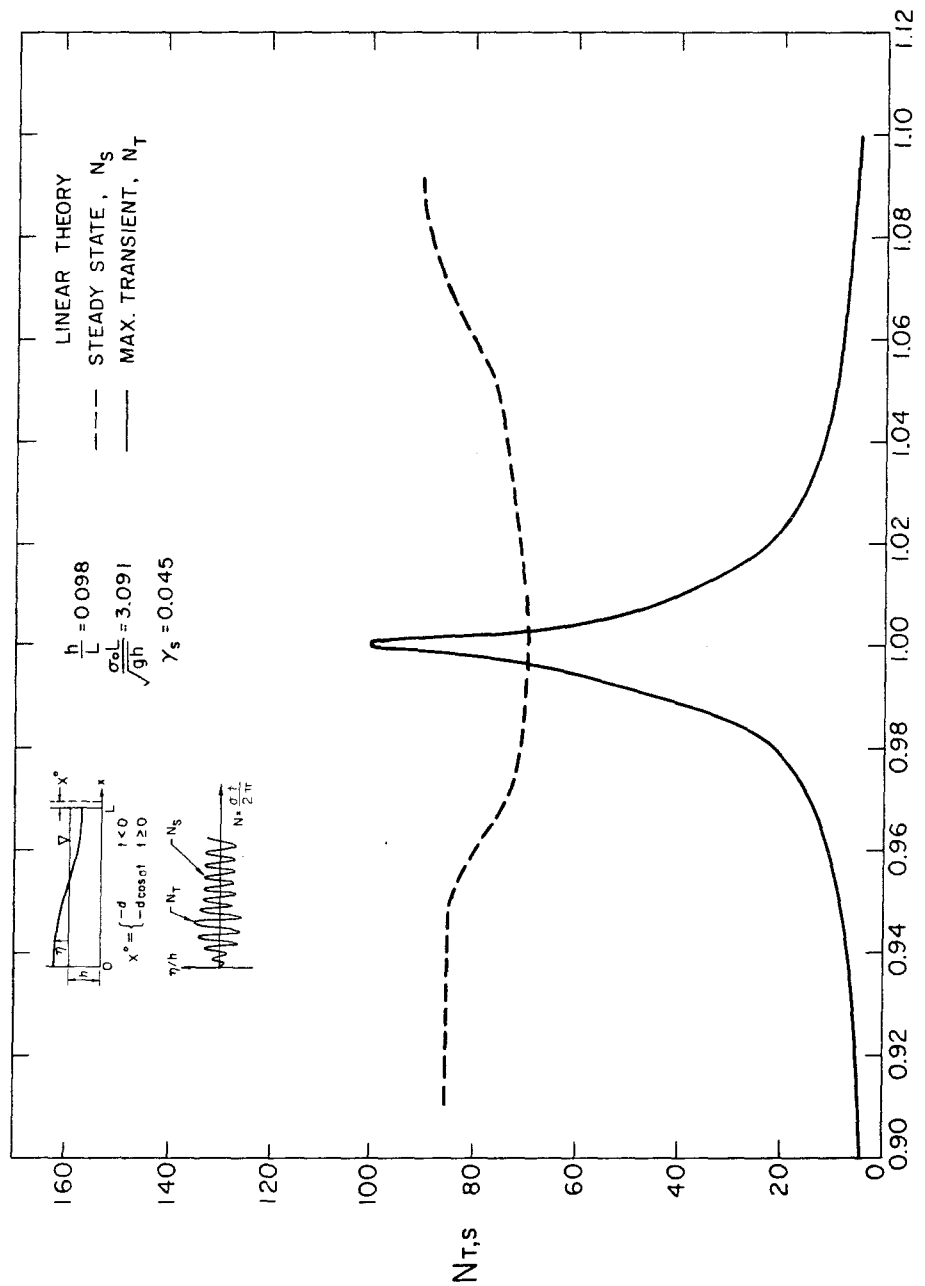

Fig. 5.2.2 Variation of the number of oscillations required to reach maximum transient and steady state conditions with frequency of excitation near the first resonant frequency; linear solution, h/L = 0.098, γ_s = 0.045.

beat pattern is created by the superposition of the free oscillation mode corresponding to $\sigma = \sigma_o$ and the forced oscillation imposed by the exciting frequency σ; this results in a beat half-period characterized by $\sigma_o/|\sigma - \sigma_o|$ oscillations; thus as $|\sigma - \sigma_o|/\sigma_o$ decreases, the period of the beats increases until it becomes theoretically infinite. With increasing time the beats diminish due to dissipation and steady state oscillations result.

Figure 5.2.2 shows the variation of the number N_T of oscillations required to achieve maximum transient wave amplitude $(\eta/h)_T$ with σ/σ_o and the corresponding variation of the number N_S of oscillations for full establishment of steady state. Steady state is, by definition, considered to have taken place at time t when the relative variation of all positive extrema along the wave record at x = L is less than 5% from time t onwards. The number N_T increases as $|\sigma - \sigma_o|/\sigma_o$ decreases, which can be related directly to the variation of the beat period with σ. Since the maximum transient amplitude occurs during the first beat for the linear case, N_T can be set approximately to $\sigma_o/2|\sigma - \sigma_o|$, i.e., a quarter period of a beat, as can be checked from Figure 5.2.2. The only exception is for the range of values of σ within 1% of σ_o for which N_T is primarily controlled by friction. The number N_S varies only slightly with σ/σ_o near resonance and is governed strictly by friction. Its value, at resonance, is given by Eq. (5.2.8), i.e., $N_S = 70$.

Since the nonlinear parameter d/L merely acts as a scaling parameter in the linear theory, Figures 5.2.1a and 5.2.1b can be derived for any other values of d/L by multiplying η/h by $(d/L)/0.0032$, and Figure

5.2.2 remains unchanged with scaling.

The experimental variation of the positive and negative extrema $(\eta/h)_T$ and $(\eta/h)_S$ with σ/σ_o at x = L are presented in Figure 5.2.3 for the same values of the dimensionless parameters as in Figure 5.2.1 and are compared to the nonlinear dispersive dissipative theory. Obvious differences can be noted between Figure 5.2.3 and Figure 5.2.1a, confirming the inadequacy of the linear model for these conditions near resonance. The response curves are no longer symmetric about $\sigma/\sigma_o = 1$ but bend toward the right and the maxima now occur at $\sigma/\sigma_o = 1.07$, where the response curves exhibit a large discontinuity (or jump). (The frequencies at which a discontinuity takes place in the response curves will be termed "bifurcation frequencies" in the remaining discussion.) This behavior is attributed to the effects of nonlinearities and can be related to the "hard spring" solution of the Duffing's equation (Stoker, 1950).

The oscillations are quite asymmetric about the still water level; the ratio of positive to negative water surface elevations becomes nearly eight for $\sigma/\sigma_o = 1.07$ during the transient stage of the oscillation. In contrast to the positive extrema, the negative extrema vary little with σ/σ_o and reach a minimum value of about -0.2. Another feature of the response which is different from the linear results is the existence of a secondary jump which takes place at $\sigma/\sigma_o = 0.97$. This feature seems to pertain only to the forced basin oscillations in the shallow water range. Experiments by Fultz (1962) on closed basin oscillations in the intermediate and the deep water range resulted in response curves with only one discontinuity. Therefore this feature must

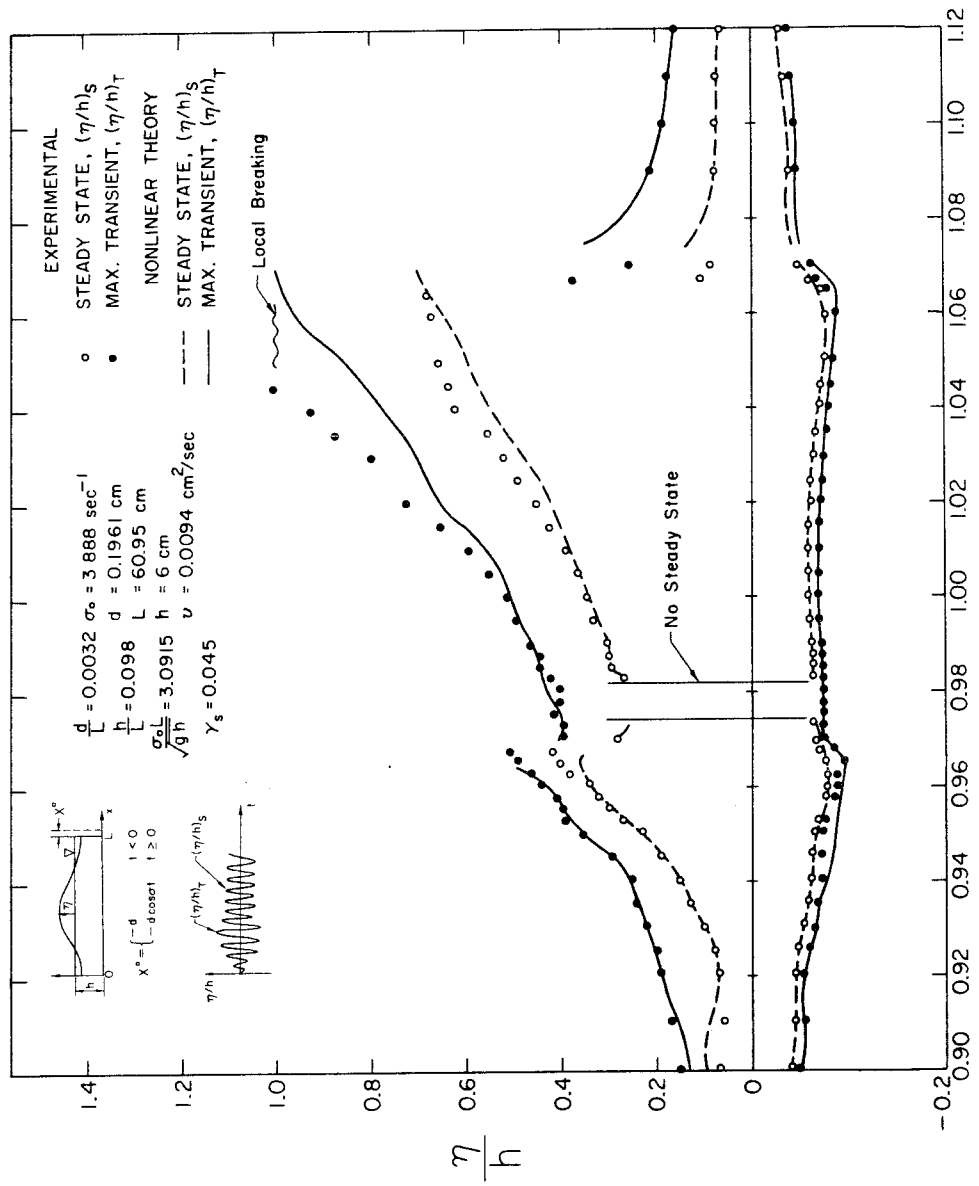

Fig. 5.2.3 Variation of relative wave extrema at x=L with frequency of excitation near the lowest resonant frequency; comparison between the nonlinear solution and experiments; d = 0.196 cm, L = 60.95 cm, h = 6 cm.

be attributed to the effect of small dispersion.

Steady state is achieved for all values of σ/σ_o except near the second bifurcation frequency where a beat pattern develops with period different from that which the linear theory predicts and diminishes at a much slower rate than predicted by the linear theory. This also constitutes a significant departure from the linear theory and will be examined in more detail shortly.

Positive maximum transient extrema $(\eta/h)_T$ remain larger than the positive steady state extrema $(\eta/h)_S$ and this difference increases markedly near $\sigma/\sigma_o = 1.07$. By contrast their negative counterparts follow almost the same curve.

The computed curves in Figure 5.2.3 were obtained from a large number of numerical wave records, each of about 100 oscillations, corresponding to a basin length discretization of 30 nodes. Hence, the computed response curves result from a lengthy computational process and were obtained only for the conditions of Figure 5.2.3. The comparison between the nonlinear theory and the experiments appears good. In particular, the location of the two discontinuities is correctly predicted. The only marked discrepancy appears for the values of η/h greater than 0.7 where the theory predicts lower values than the experiments do. Considering that the nonlinear dispersion theory is based on finite but small relative wave amplitudes, good agreement with experiments up to a value of η/h of about 0.7 is actually remarkable. For larger relative wave heights a more complete theory should be used such as the equations derived by Su and Gardner (1969) which apply to any wave situation with small dispersion but arbitrary relative wave height.

Several water surface time histories obtained from experiments are presented in Figure 5.2.4a showing the variation of the relative amplitude η/h at $x = L$ as a function of the normalized time, $\sigma t/2\pi$. Familiar beat patterns which diminish with time can be observed for each record, but the wave shapes are no longer sinusoidal; near the main bifurcation frequency they look like cnoidal waves ($\sigma/\sigma_o = 1.10$, 1.07, 1.01) and are indeed closely related to the nonlinear mode shapes of oscillations derived in Section 3.2.3 which will be discussed in Section 5.2.3. In the record corresponding to $\sigma/\sigma_o = 1.04$ the slope of the positive envelope of the oscillations remains constant for the first few oscillations as predicted by the linear theory, but then increases markedly before decreasing. This "hardening" behavior during the transient stage is caused by the nonlinearities and becomes actually more pronounced closer to the main bifurcation point. As σ decreases, a second oscillation appears at the trough of the main wave at $\sigma/\sigma_o = 1.01$. This oscillation grows in amplitude behind the main wave as σ is further decreased until it becomes equal in amplitude to the first wave for $\sigma/\sigma_o = 0.96$. Then the two waves tend to merge together ($\sigma/\sigma_o = 0.94$) until eventually a nearly sinusoidal wave appears ($\sigma/\sigma_o = 0.91$). The maximum transient extrema $(\eta/h)_T$ usually take place during the first beat except near the second bifurcation frequency. For $\sigma/\sigma_o = 0.96$, $(\eta/h)_T$ reaches its maximum value during the third beat at the 30th oscillation. This characteristic is typical near a secondary bifurcation frequency as will be seen for other cases. Thus, for a continuously excited basin in the resonant region, the steady state wave shape is very sensitive to the exciting frequency σ.

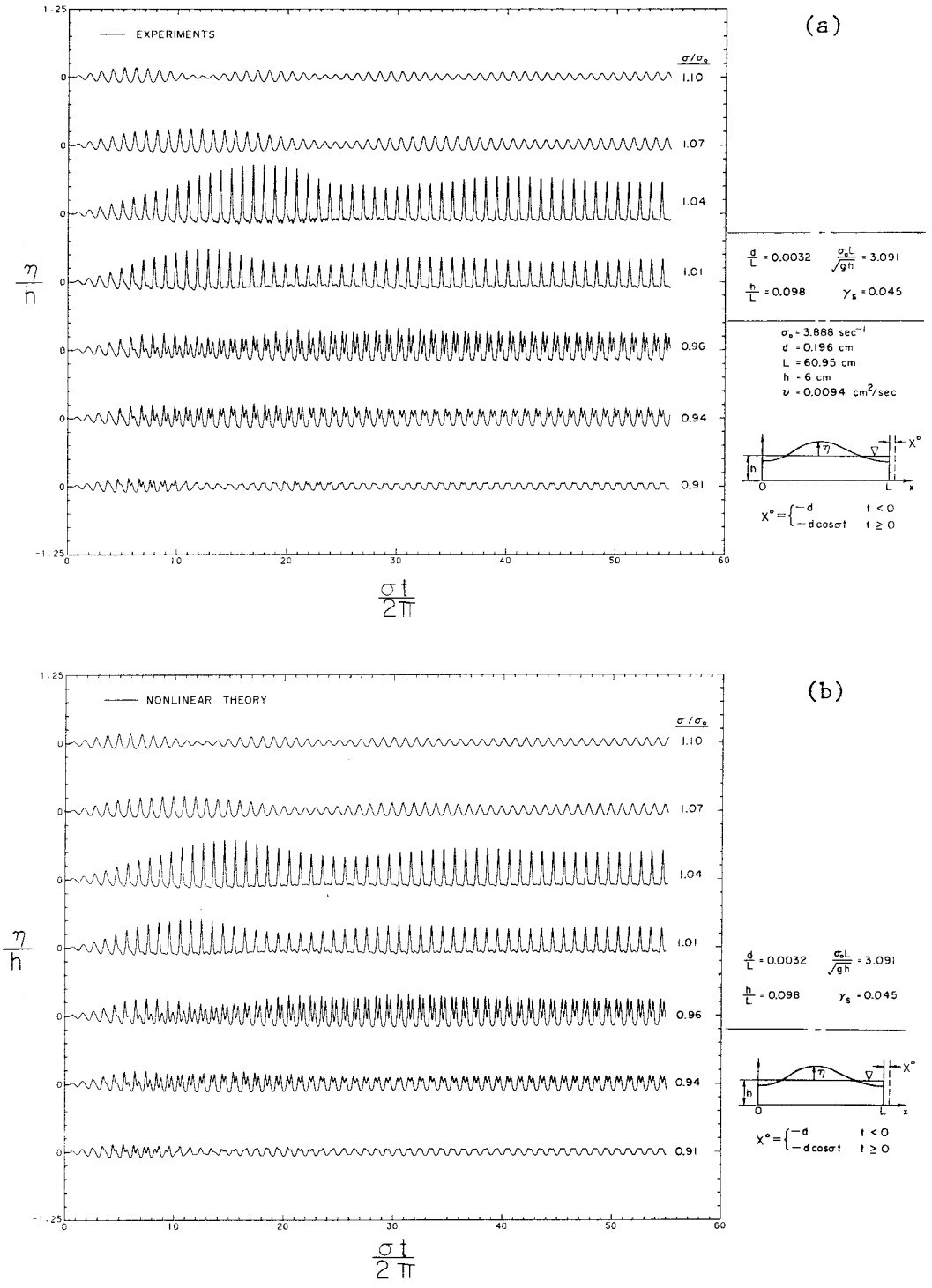

Fig. 5.2.4 Time histories of free surface profile at x=L near the lowest resonant frequency; (a) experiments, (b) nonlinear solution; d = 0.196 cm, L = 60.95 cm, h = 6 cm.

The corresponding computed wave records are presented in Figure 5.2.4b. They compare well with the experiments, confirming the validity of the analysis and of the numerical treatment. The only discrepancy is a small mismatch in the time of occurrence of the extrema for some records.

Additional experimental water surface time histories at $x = L$ are presented in Figure 5.2.5a. The upper curve corresponds to the same experimental conditions as those presented in Figure 5.2.4, with $\sigma/\sigma_o = 0.98$. Referring to Figure 5.2.3, this excitation frequency belongs to the frequency range for which no steady state could be obtained. Beats with a half period equal to 18 times the excitation period can be observed. They do not result from a linear process, since, from the linear theory, the half-period of a beat would contain 50 oscillations which is not the case here. Also, according to the linear theory, those beats should disappear after 70 oscillations because of dissipation. However, they are still visible in Figure 5.2.5a after 130 oscillations. Hence, these are truly nonlinear beats caused by the nonlinear interaction of the oscillation with itself which induces a secondary oscillation with a slightly different frequency from the excitation frequency σ. This nonlinear feature is even more apparent when the parameter d/L is increased from 0.0032 to 0.0048 (the lower record in Figure 5.2.5a); it is recalled that d/L is the ratio of the amplitude of the basin excitation to the basin length. The period of the beat is the same as in the previous case, but the maximum height of the secondary oscillation is bigger relative to the main oscillation. This feature results in a much more pronounced beat

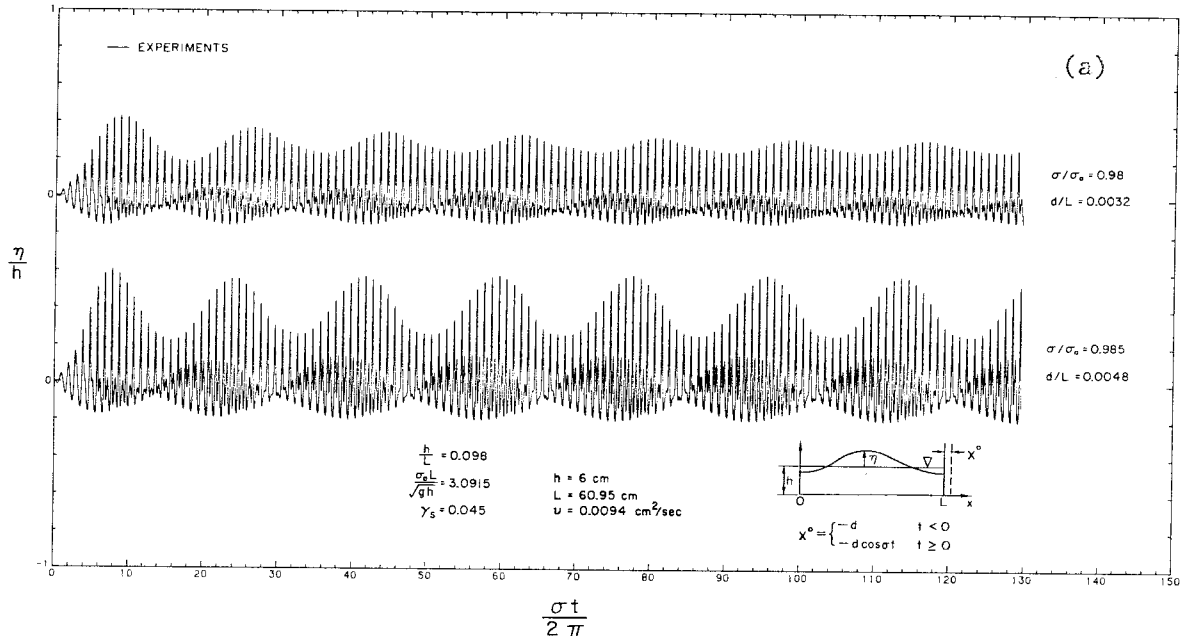

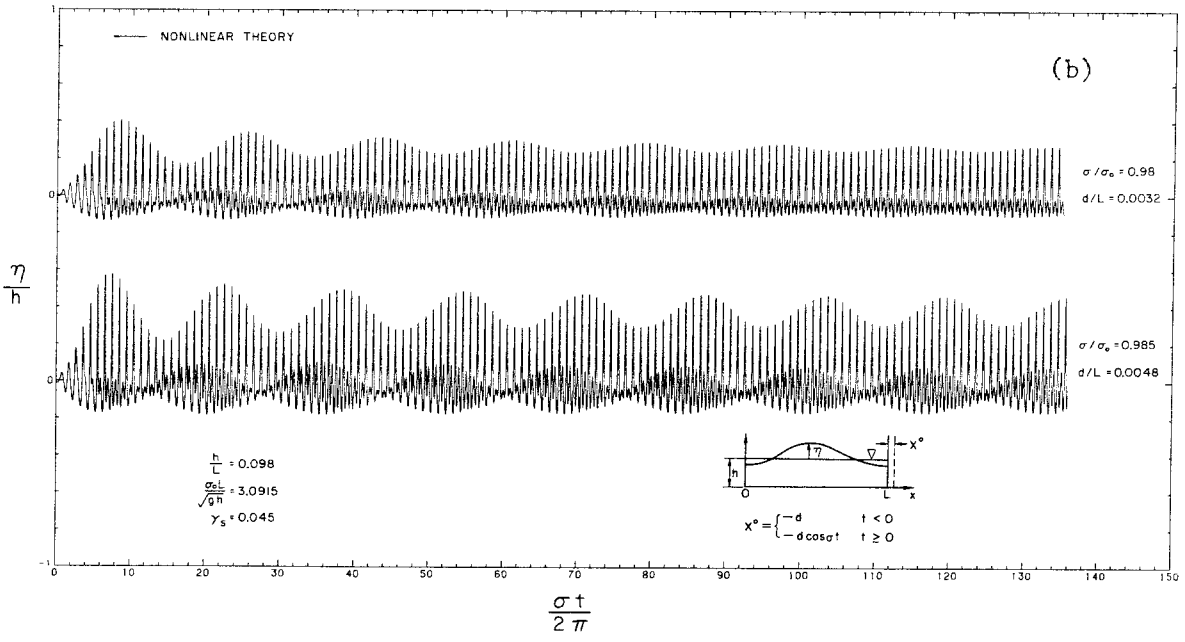

Fig. 5.2.5 Time histories of free surface profile at x=L near the lowest resonant frequency; (a) experiments, (b) nonlinear solution; L = 60.95 cm, h = 6 cm.

pattern. Also nonlinearities tend to act against dissipation in the sense that for larger ratio of d/L (0.0048) the beats appear to be attenuated more slowly.

Figure 5.2.5b shows the corresponding theoretical wave elevation time histories at x = L obtained from the nonlinear dispersive dissipative theory. The same pattern can be observed as in the experiments (Figure 5.2.5a) Although in both theoretical wave records shown the beats are damped faster than in the experiments. Also, for the computed wave record corresponding to d/L = 0.0048, the half period of the beats is only 16 times the exciting period compared to 18 times for the experiments. Those numerical computations show that it is indeed possible to produce these nonlinear beats without invoking the existence of cross waves along the width of the basin as a generation mechanism, since it is recalled that the equations used in the present computations only contain one spatial variable, i.e., the x coordinate.

The experimental and computed variation with σ/σ_o of the number of oscillations, N_T, for the motion to reach a maximum (the maximum transient amplitude) and the number of oscillations N_S required to reach steady state are presented in Figure 5.2.6 for the same values of the dimensionless parameters as in Figure 5.2.3. The experimental data show N_T remains small away from the bifurcation points, and a jump in the value of N_T occurs at the main bifurcation frequency, $\sigma/\sigma_o = 1.07$. Several discontinuities take place near the second bifurcation frequency, $\sigma/\sigma_o = 0.96$ and result from the fact that the maximum transient oscillations do not take place during the first beat but during the third beat for $0.955 < \sigma/\sigma_o < 0.965$ and during the second beat for

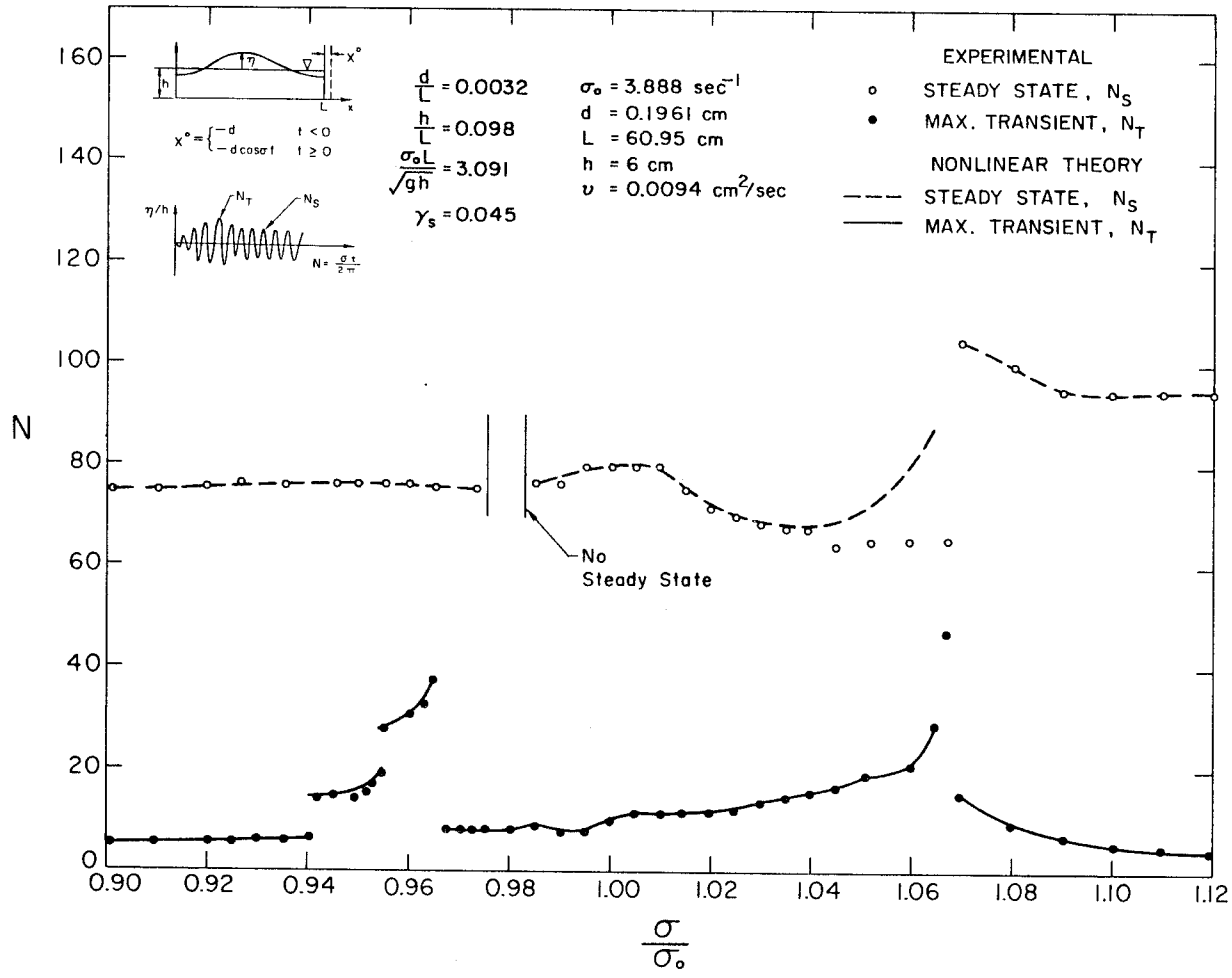

Fig. 5.2.6 Variation of the number of basin oscillations required to reach maximum transient and steady state conditions with the frequency of excitation near the lowest resonant frequency; comparison between experiment and nonlinear solution; d = 0.196 cm, L = 60.95 cm, h = 6 cm.

$0.945 < \sigma/\sigma_o < 0.955$. The computed variation of N_T with σ/σ_o agrees well with the experiments over the full range of the abscissa.

The variation of the quantity N_S with σ/σ_o determined experimentally remains relatively small except in the vicinity of the main bifurcation frequency, where N_S increases slightly as σ/σ_o decreases from 1.09 to 1.07 and then decreases sharply before increasing toward a constant value close to that predicted by the linear theory, i.e., $N_S = 70$. The corresponding values of N_S determined numerically agree well with the experiments except for the abscissal range of $1.04 < \sigma/\sigma_o < 1.06$, where the experimental values are smaller than the theory predicts. This difference may be caused by the local wave breaking due to extreme heights reached near the main bifurcation frequency; this accentuates energy dissipation which reduces the number of transient oscillations.

The evolution of spatial wave profiles at given times as determined from experiments is presented in Figure 5.2.7a for $\sigma/\sigma_o = 1.04$ during the interval following the maximum transient extremum, which occurs at time t_{in} such that $\sigma t_{in}/2\pi \simeq 15$. A single "hump-like" wave travels back and forth in the basin and looks like the moving wave profile resulting from the linear superposition of two cnoidal waves traveling in opposite directions. (This nonlinear mode shape was shown in Section 3.2.3). The computed profiles for corresponding times are presented in Figure 5.2.7b and generally appear similar to the experimental results. At the nondimensional time $\sigma(t - t_{in})/2\pi = 1$ as the wave reflects from the end wall, the theoretically determined wave height is about 15% lower than that determined experimentally.

The evolution of wave profiles measured experimentally is pre-

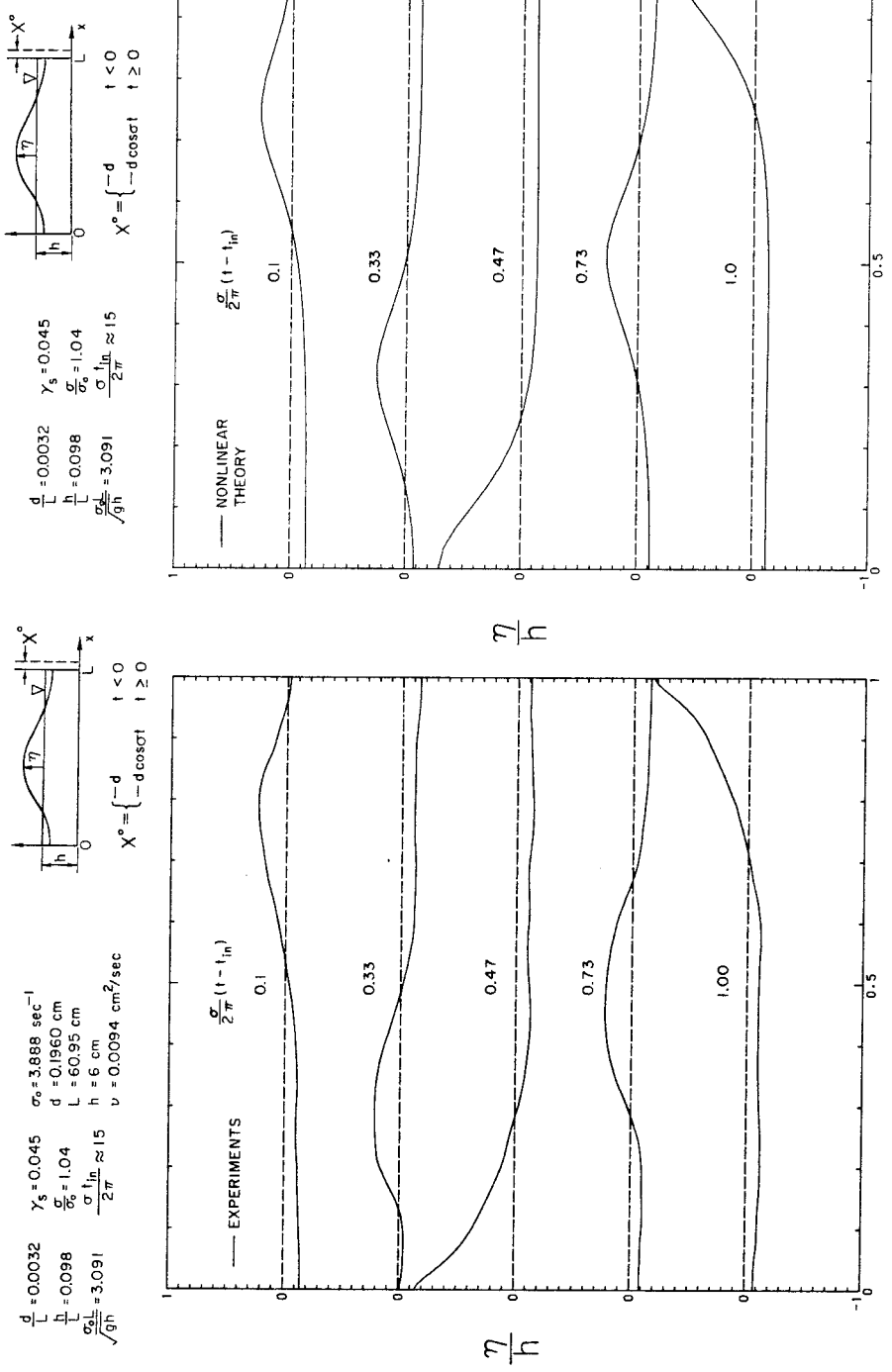

Fig. 5.2.7 Evolution with time of the wave profiles along the basin within one period; (a) experiments, (b) nonlinear solution; $\sigma/\sigma_o = 1.04$, d = 0.196 cm, L = 60.95 cm, h = 6 cm.

sented in Figure 5.2.8a for $\sigma/\sigma_o = 0.96$ (near the second bifurcation frequency) during the interval following the maximum transient extremum. That extremum occurs at time t_{in} such that $\sigma t_{in}/2\pi = 30$. Two waves clearly can be seen moving back and forth; the evolution of the main and the secondary waves are indicated by a solid arrow and a dashed arrow, respectively. It is noted that wave extrema occur not only at the end walls of the basin during the reflection process, but also when the two waves interact, e.g., at $\sigma(t - t_{in})/2\pi = 0.15$ and $\sigma(t - t_{in})/2\pi = 0.70$.

The corresponding wave profiles determined numerically and presented in Figure 5.2.8b show reasonably good agreement with the experiments with regard to both the wave shape and the wave height. (It is recalled that the experimental profiles were obtained photographically as described in Chapter 4, which introduces some irregularities in the profiles.) Thus, nonlinear effects and dispersive effects can introduce quite different profiles compared to a fully linear system near resonance. Also, no standing wave profile with a node at $x/L = 0.5$ is observed, but instead a moving wave pattern with one or more waves traveling back and forth in the basin occurs near resonance.

In order to study the effect of the nonlinear parameter d/L, the experimental variation of $(\eta/h)_S$ and $(\eta/h)_T$ with σ/σ_o has been determined by reducing d/L from 0.0032 to 0.0016 and letting the other parameters remain unchanged, and the results are shown in Figure 5.2.9. A few computed points also are presented in this figure; they agree reasonably well with the experiments. The shapes of both the transient and the steady state response curves are similar to those of Figure 5.2.3. The main resonant frequency is shifted to $\sigma/\sigma_o = 1.04$ and the

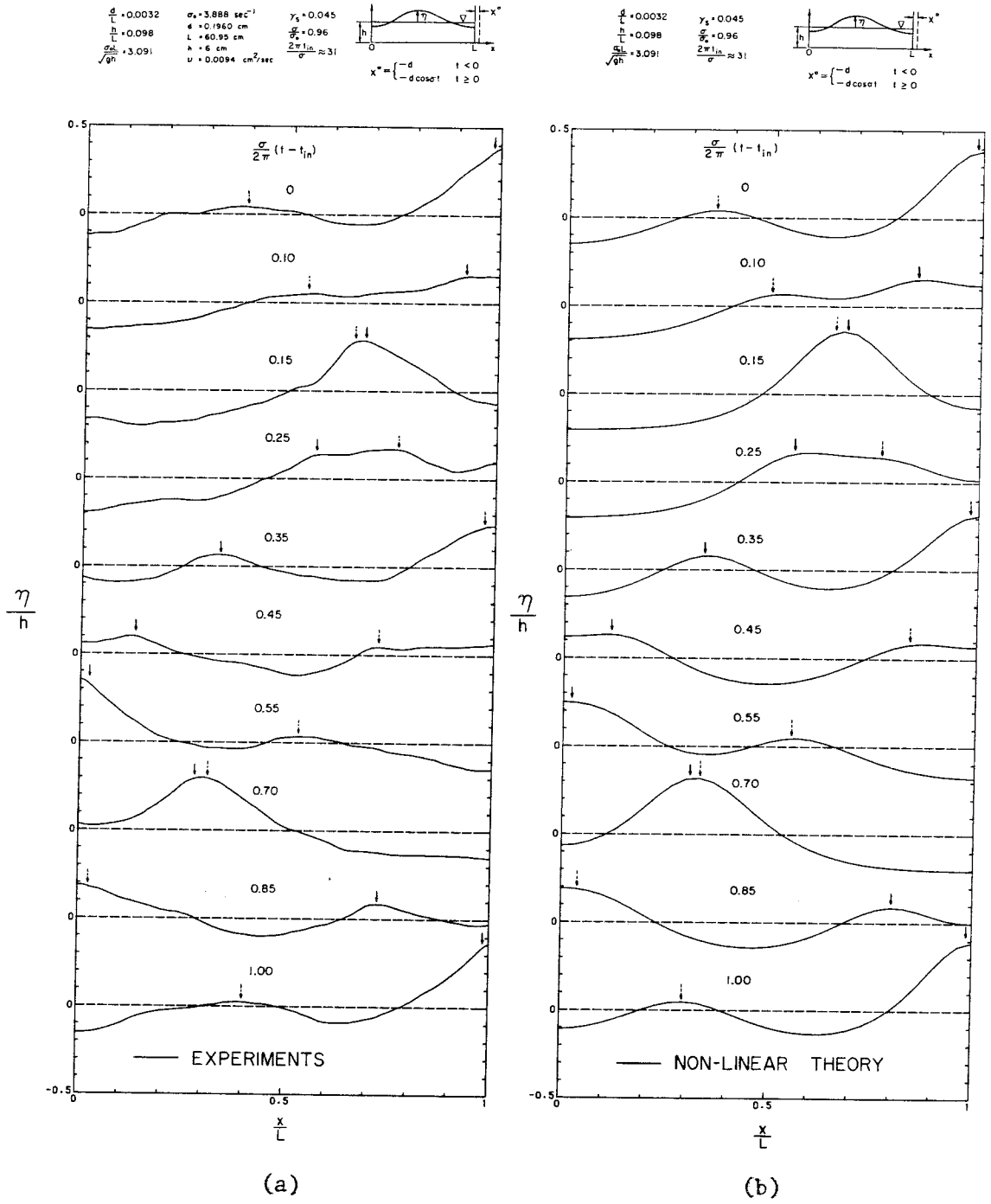

Fig. 5.2.8 Evolution with time of the wave profiles along the basin within one period; (a) experiments, (b) nonlinear solution; σ/σ_o = 0.96, d = 0.196 cm, L = 60.95 cm, h = 6 cm.

second bifurcation frequency is shifted to about $\sigma/\sigma_o = 0.95$, the latter exhibiting a very weak discontinuity. Steady state is achieved at all frequencies suggesting that the beats which were discussed previously depend directly on the magnitude of the nonlinearities as described by the parameter d/L. One would expect that as d/L is further decreased the response curves converge toward that described by the linear theory and presented in Figure 5.2.1.

Several experimental wave records of η/h versus the nondimensional time parameter $\sigma t/2\pi$ at $x = L$ are presented in Figure 5.2.10a and can be compared to the corresponding theoretical records shown in Figure 5.2.10b. There appears to be good agreement between the experiments and the theory, and the profiles are similar to those shown in Figures 5.2.4a and 5.2.4b for the case of a larger excitation, i.e., $d/L = 0.0032$. Thus, once nonlinear effects appear, they seem to induce a wave structure which is somewhat independent of d/L provided records are compared at similar frequencies relative to the position of the two bifurcation points. (This conclusion may be misleading: The dependence of the wave structure on the ratio d/L is weak compared to that of h/L; nevertheless it exists and further experiments and a simple analysis will demonstrate it later in this section.)

Figure 5.2.11 shows the experimentally determined variation with σ/σ_o of the number of oscillations N_T corresponding to the maximum transient amplitude and the number of oscillations N_S required to reach steady state. A few computed points are also presented on this figure; they agree reasonably well with the experiments. Again the

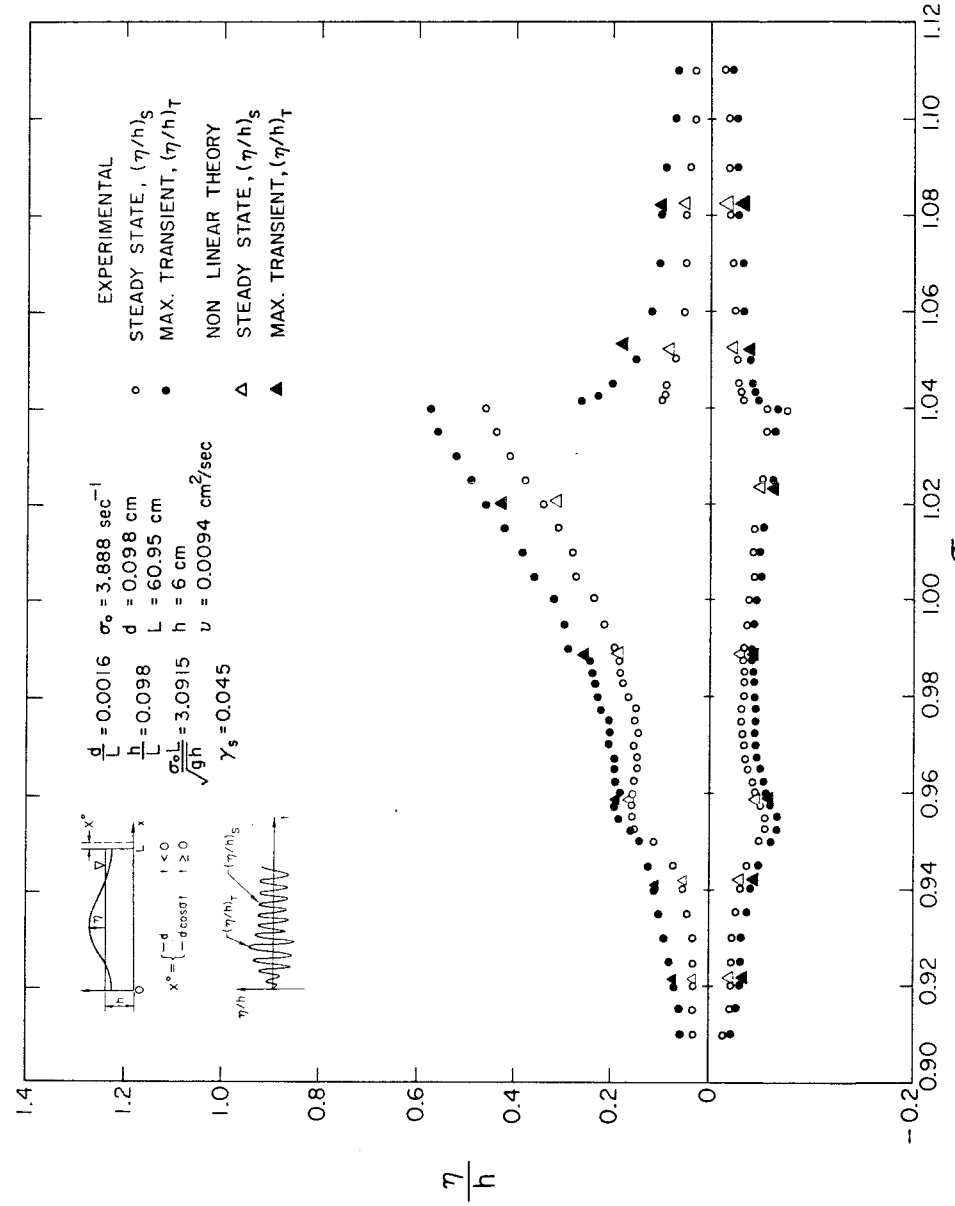

Fig. 5.2.9 Variation of relative wave extrema at x=L with frequency of excitation near the lowest resonant frequency, comparison between experiments and nonlinear solution; d = 0.098 cm, L = 60.95 cm, h = 6 cm.

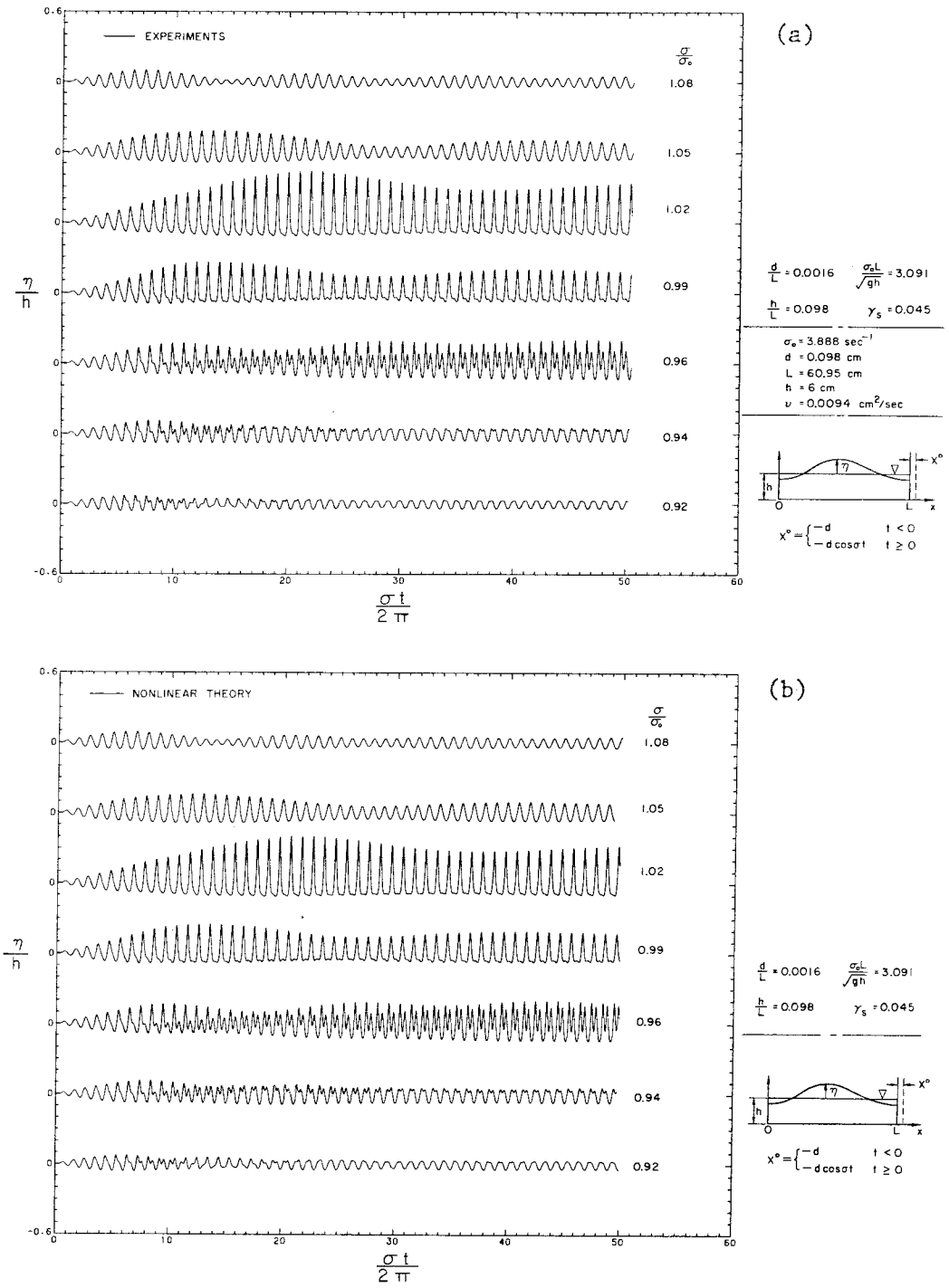

Fig. 5.2.10 Time histories of free surface profile at x=L near the lowest resonant frequency; (a) experiments, (b) nonlinear solution; d = 0.098 cm, L = 60.95 cm, h = 6 cm.

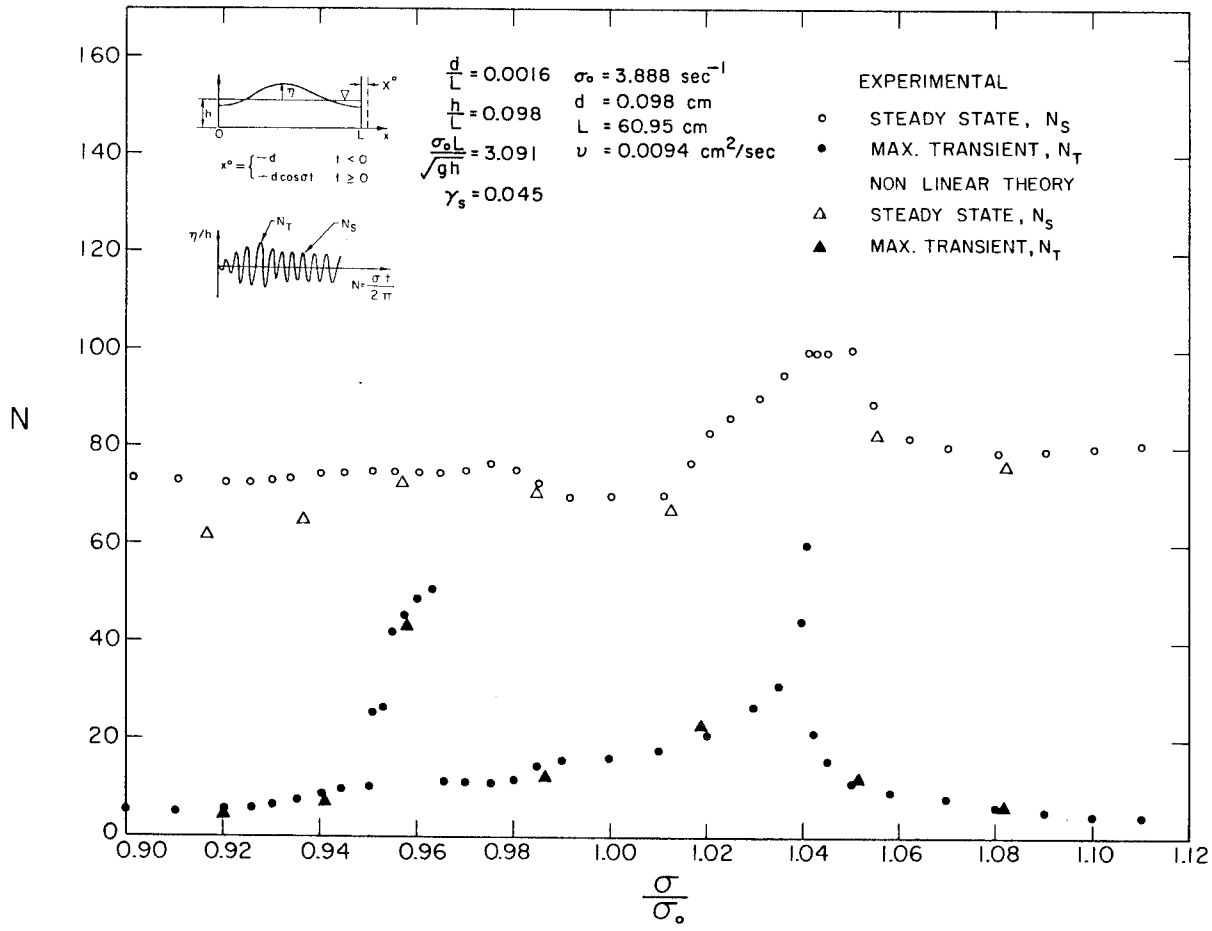

Fig. 5.2.11

Variation of the number of basin oscillations required to reach the maximum transient and steady state conditions with the frequency of excitation near the lowest resonant frequency, comparison between experiments and nonlinear theory; d = 0.098 cm, L = 60.95 cm, h = 6 cm.

curve appears very similar to those of Figure 5.2.6, and the only difference is that, since local breaking does not take place near the main bifurcation frequency for the example of Figure 5.2.11, an abrupt change of N_S is not observed near this frequency as in Figure 5.2.6.

The effect of the dispersion parameter is investigated by reducing h/L from 0.098 to 0.051 while keeping d/L the same as in Figure 5.2.3, i.e., 0.0032. The new linear resonant frequency σ_o is defined by $\sigma_o L/\sqrt{gh} = 3.128$ and the dissipation parameter is calculated from the experimental conditions at $\sigma = \sigma_o$ as $\gamma_s = 0.075$. For these conditions the experimental variation of $(\eta/h)_T$ and $(\eta/h)_S$ with σ/σ_o at $x/L = 1$ is presented in Figure 5.2.12. Also shown in Figure 5.2.12 are several computed points; a good agreement is obtained with the experiments. There are certain similarities with the results shown in Figure 5.2.3, but also differences can be observed. First, the main bifurcation frequency is shifted to a larger relative frequency (about $\sigma/\sigma_o = 1.085$) and the maximum positive value of $(\eta/h)_T$ measured at that normalized frequency is less than 0.8. The resulting response curves look, therefore, "flatter and more stretched" towards larger σ/σ_o compared to Figure 5.2.3. This feature can be related to the shape for small values of the dispersion parameter h/λ, of the amplitude frequency curves in Figure 3.2.4 which correspond to a nonlinear free mode of oscillation of the rectangular basin. As the relative frequency σ/σ_o decreases from $\sigma/\sigma_o = 1.08$, $(\eta/h)_S$ and $(\eta/h)_T$ do not decrease in a monotonic fashion suggesting the presence of secondary bifurcation frequencies with small "jumps." One of these can clearly

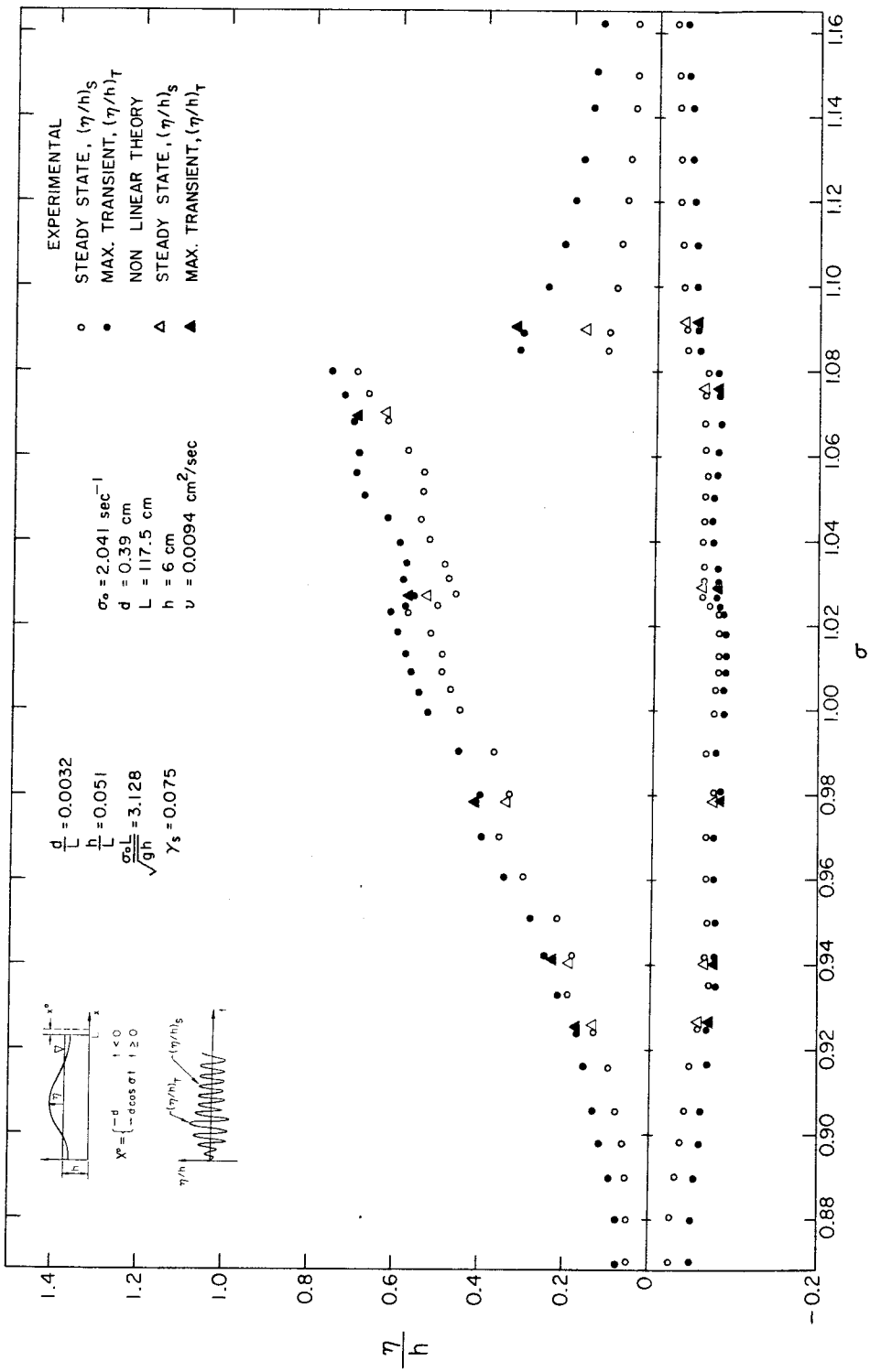

Fig. 5.2.12
Variation of relative amplitude η/h at x=L with frequency of excitation near the lowest resonant frequency, comparison between experiments and nonlinear theory; d = 0.39 cm, L = 117.5 cm, h = 6 cm.

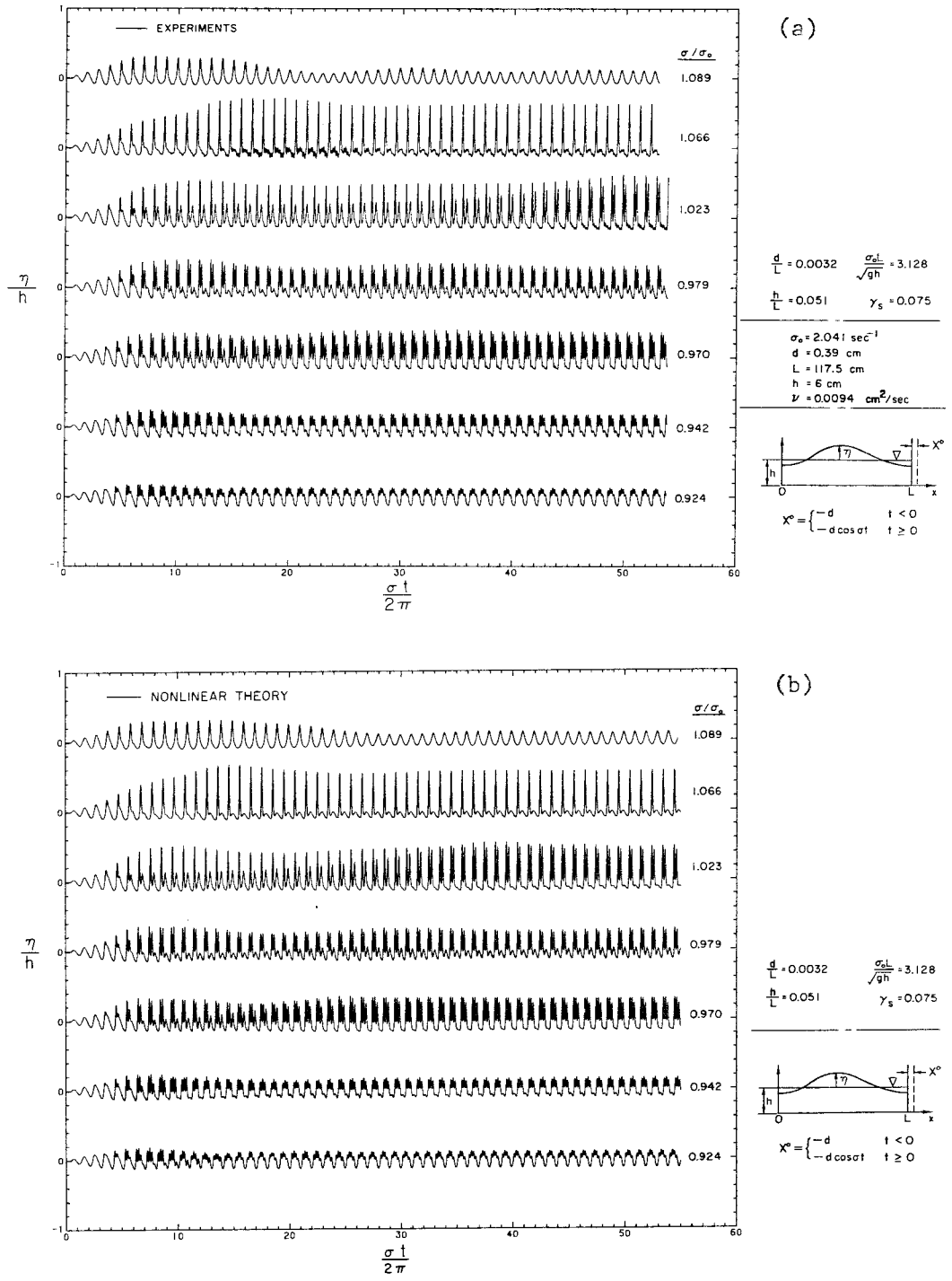

Fig. 5.2.13 Time histories of free surface profiles at x=L near the lowest resonant frequency; (a) experiments, (b) nonlinear solution; d = 0.39 cm, L = 117.5 cm, h = 6 cm.

be seen at $\sigma/\sigma_o = 1.025$, and another can possibly be detected at $\sigma/\sigma_o = 0.975$. The difference in amplitude between the results for the transient and the steady state remains small for all frequencies for these experiments. Finally, it should be noted that steady state conditions are reached for all frequencies.

Several experimental wave records at $x = L$ are presented in Figure 5.2.13a for various excitation frequencies along with corresponding theoretical records in Figure 5.2.13b. In both figures the variation of the relative wave amplitude η/h is presented as a function of normalized time $\sigma t/2\pi$. Considering Figure 5.2.13a first, the wave records appear similar to those of Figure 5.2.4 with a "cnoidal" shape for frequencies which are close to the main bifurcation frequency. As σ/σ_o decreases, a secondary wave develops and approaches the amplitude of the main wave at $\sigma/\sigma_o = 1.023$, this is nearer to the main bifurcation frequency than for the case shown in Figure 5.2.4 For smaller values of σ/σ_o a third wave develops ($\sigma/\sigma_o = 0.97$) and then a fourth wave ($\sigma/\sigma_o = 0.942$). Eventually the four waves merge together at $\sigma/\sigma_o = 0.924$ to form a "sinusoidal" profile. For the two wave records corresponding to $\sigma/\sigma_o = 1.023$ and $\sigma/\sigma_o = 0.97$, the maximum of the envelope of the waves does not occur during the first beat, but during the second beat, suggesting the existence of bifurcation frequencies near this frequency. (This is similar to what was observed from the results of the experiment with larger dispersion effects presented in Fig. 5.2.4.)

The computed wave records were evaluated with the basin length discretized into 41 nodes. The theoretical curves shown in Figure

5.2.13b appear to agree with the experimental observation of Figure 5.2.13a. Some differences are noted for $\sigma/\sigma_o = 1.066$, where the theory does not predict the higher frequency waves appearing in the trough of the main wave, and for $\sigma/\sigma_o = 1.023$ where the measured number of oscillations required to reach maximum transient state ($N_T = 50$) is longer than the computed one ($N_T = 40$).

It seems reasonable to infer from these results that if the dispersion parameter h/L is decreased further, the number of secondary oscillations in the wave records will increase accordingly. The Stokes number, defined by Eq. (5.2.10), is equal to 840 near the first bifurcation frequency for the case of Figure 5.2.13a and was equal to 360 for the case of Figure 5.2.4. This also suggests that the number of secondary oscillations which may emerge near resonance increases with the Stokes parameter; this will be discussed additionally in Section 5.2.4 which deals with transient excitations.

The experimental variation of the relative wave height $(\eta^+ - \eta^-)/h$ for steady state conditions with the relative frequency of excitation σ/σ_o is presented in Figure 5.2.14; the quantities η^+ and η^- denote the positive extremum and the negative extremum, respectively. (The value of the dimensionless parameters are $d/L = 0.00094$, $h/L = 0.034$, $\sigma_o L/\sqrt{gh} = 9.263$, and $\gamma_s = 0.19$ at $\sigma/\sigma_o = 1$.) The frequency σ_o is given by Eq. (5.2.4) with n = 1, i.e., it corresponds to the third resonant mode of oscillation. A true measure of the dispersion parameter is h/λ which from Eq. (5.2.3) is equal to 0.05. This is the same value as was used in the experiments which were presented in

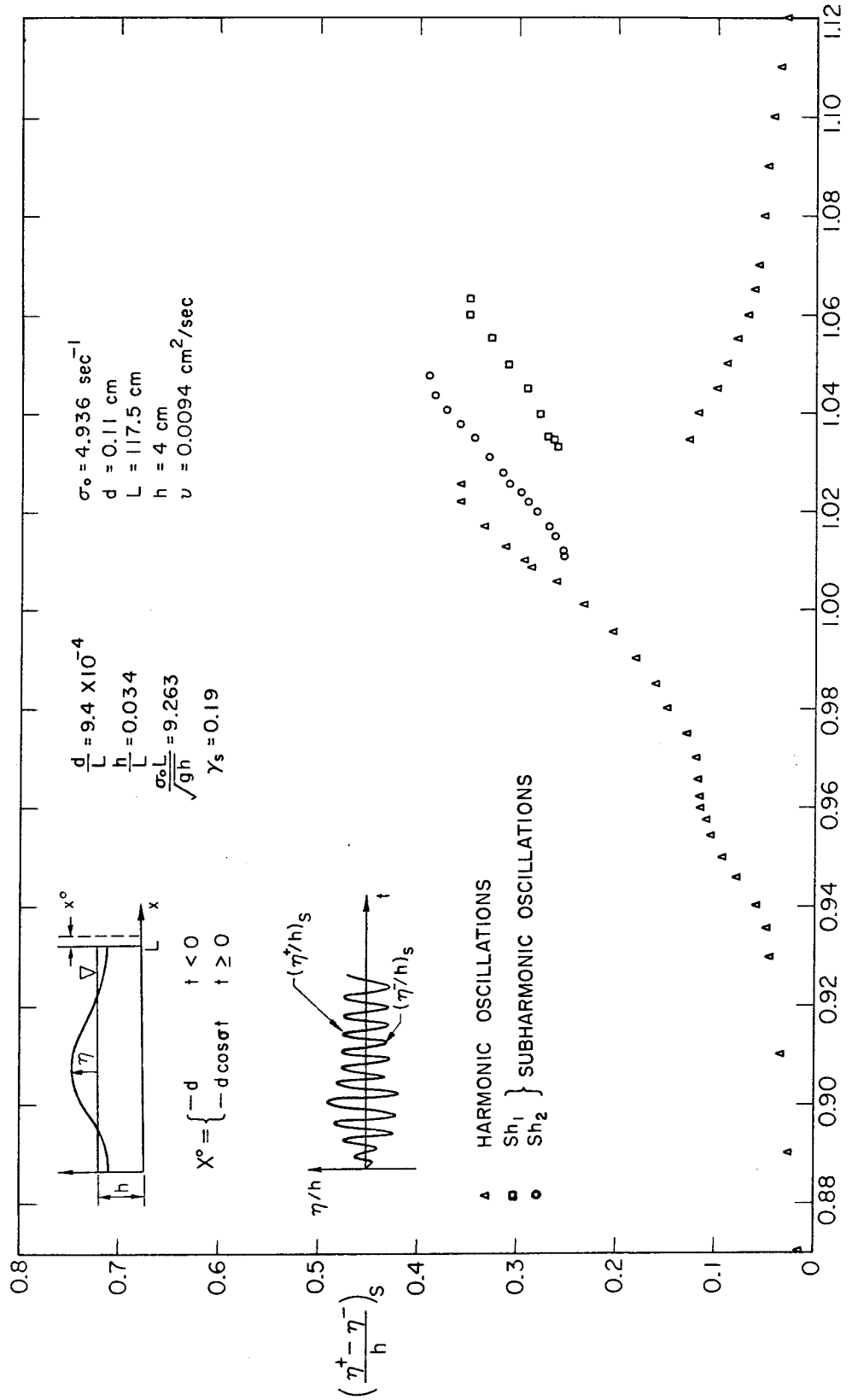

Fig. 5.2.14 Variation of the experimental relative wave height at x=L for steady state conditions with frequency of excitation near the third lowest resonant frequency; d = 0.11 cm, L = 117.5 cm, h = 4 cm.

Figures 5.2.4 and 5.2.5; hence, the effects of dispersion are the same also.

Figure 5.2.14 was obtained by first allowing the steady state oscillations to develop at a given frequency and then increasing or decreasing the frequency a small amount and letting the basic oscillations come to a new steady state value. The amplitude of oscillations of the basin was kept constant. The new feature which was obtained for these higher mode experiments is the existence of stable subharmonic oscillations which lie on branch curves denoted on Figure 5.2.14 as Sh1 and Sh2. For these branch curves the frequency of oscillation is one-third of the exciting frequency. In particular, for $1.035 < \sigma/\sigma_o < 1.05$ three stable states of oscillations can be obtained. It was found experimentally that once a steady state oscillation has been reached on a particular branch curve, and if the excitation frequency is changed until the frequency reaches the bifurcation frequency value, the response remains on that particular curve. If after the bifurcation point is reached the frequency is increased a small amount, the response suddenly changes until it corresponds to the branch curve beneath it. Thus, referring to Figure 5.2.14 starting at $\sigma/\sigma_o = 1.0$, if the excitation frequency is increased incrementally after first reaching steady state at the lower frequency, branch curves Sh2, Sh1, and the lower response at about $\sigma/\sigma_o = 1.06$ will be realized. (Conversely, with a decrease in frequency on a given branch curve, similar jumps can be seen, but in this case the jumps would lead to a branch curve with a larger response.)

It is possible by starting at rest and exciting the basin at a constant frequency and amplitude to reach steady state on any of the four branch curves shown in Figure 5.2.14. This was done experimentally and Figure 5.2.15 shows the evolution with time of selected wave records obtained at x = L. The period of the oscillation for the records corresponding to σ/σ_o = 1.042, 1.01, and 0.96 is equal to the period of the excitation. For σ/σ_o = 1.034 the steady state response lies on the Sh1 curve and for σ/σ_o = 1.02 the steady state response lies on the Sh2 curve. For the latter two records, the period of oscillation is three times the excitation period. As seen in Figure 5.2.15 the record corresponding to the steady state oscillations for σ/σ_o = 1.034 (Sh1 curve) consists of one dominant oscillation, while the Sh2 curve (σ/σ_o = 1.02) consists of two dominant oscillations.

An interesting feature of the wave record corresponding to σ/σ_o = 1.042 is the time it takes for the subharmonics to develop from rest; actually at least 150 oscillations are necessary. This may be related to the extremely narrow frequency bandwidth along which subharmonics of the Sh1 type can be generated, starting from rest, using a constant frequency of excitation. Also, subharmonics of the Sh2 type emerge sooner when σ/σ_o = 1.02 but it still takes some time to obtain them (at least 70 oscillations for fully developed state). This suggests that for transient problems those subharmonics may not have time to emerge. On the wave record corresponding to σ/σ_o = 0.96, a small secondary wave emerges. Its amplitude remains small because of the small value of d/L. As a comparison the nonlinear parameter corresponding

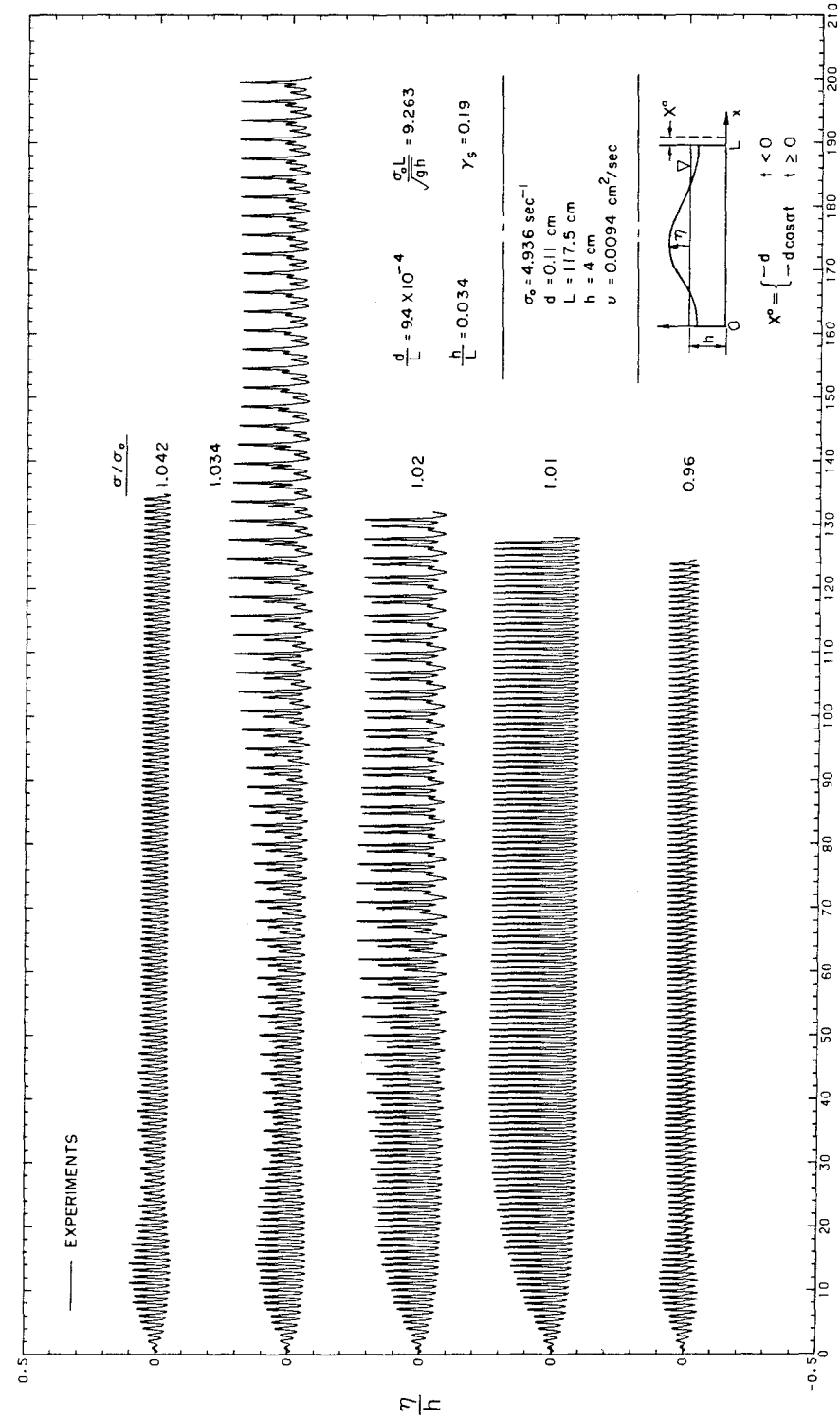

Fig. 5.2.15 Time histories of the free surface profile from experiments at x=L near the third lowest resonant frequency; d = 0.11 cm, L = 117.5 cm, h = 4 cm.

to Figure 5.2.9 is nearly twice as large for the same measure of dispersion.

5.2.3 Nonlinear Standing Modes; Comparison with the Analytical Solution

It has been shown in Section 3.2.3 (after Rogers and Mei, 1975) that the nonlinear free modes of oscillation could be represented as the sum of two cnoidal waves of the same amplitude and period propagating in opposite directions. The corresponding steady state variation of the wave amplitude with time at either end wall can be derived from Eq. (3.2.107) as:

$$\frac{\eta}{2H} = \left(\frac{d^t}{H} - \frac{h}{H}\right) + cn^2\left[2K\,\frac{\sigma t}{2\pi}\,|\,m\right] \qquad (5.2.12)$$

where η denotes the wave elevation at the back wall, h is the still water depth, d^t is the vertical distance between the bottom of the basin and the trough of the wave, cn is the cnoidal Jacobian elliptic integral of the first kind, m is the elliptic parameter, t is the time, σ is the circular frequency, and H is the cnoidal wave height.

It is seen from Eq. (5.2.12) that at the end walls the time history of the wave elevation is exactly equal to the time history of twice the wave elevation of a cnoidal wave moving in one direction and recorded at some location. In particular the total wave height at the end walls is given by:

$$\eta^+ - \eta^- = 2H$$

where η^+ and η^- represent the positive and negative wave elevation

at the end walls, respectively.

Some useful results obtained in Section 3.3.3 can be rewritten here for purposes of clarity for the subsequent discussion. The shape of the wave defined by Eq. (5.2.12) depends on only the Stokes parameter:

$$\frac{U}{s} = \frac{H\lambda^2}{h^3} \tag{5.2.13}$$

where the wave length λ is related to the basin length L by:

$$\lambda = \frac{2L}{n} \quad \text{and} \quad n = 1,2,\cdots \tag{5.2.14}$$

The relative frequency of the free modes of oscillation is a function of both H/h and h/λ, i.e.:

$$\frac{\sigma}{\sigma_o} = f(H/h, h/\lambda) \tag{5.2.15}$$

where σ_o denotes the frequencies of the free modes of oscillation computed from the linear dispersive theory. For a given value of h/λ, the relative frequency σ/σ_o depends only on the relative wave height H/h.

In this section the time history of the water surface variation at one end of the basin, determined experimentally, is compared to the computed shape given by Eq. (5.2.10), i.e., from the nonlinear standing mode theory presented in Section 3.2.3. It is noted that the nonlinear standing mode theory assumes a zero velocity at the end-walls of the basin. Therefore, one problem is the experimental generation of those nonlinear modes by a "correct" excitation.

Experimentally the rectangular basin was moved sinusoidally. It is noted for that motion only the modes corresponding to uneven values of the number n (Eq. 5.2.14) can be excited (see Section 3.2.2). The choice of the relative frequency σ/σ_o to excite a nonlinear mode can be determined with reference to Figure 5.2.16, which represents the nonlinear steady state response to a sinusoidal excitation. The amplitude-frequency curve for normal free modes of oscillation, which is defined by Eq. (5.2.15) is represented by the curve PE on Figure 5.2.16. The forced steady state response curve corresponding to a sinusoidal excitation is represented by the curve DCNBA on Figure 5.2.16. For a basin excited from rest with a constant frequency σ and a constant amplitude d , only the branches AB and DC can be obtained. However, the branch DC can be continued by starting the solution at some position in DC and by increasing the frequency σ while keeping the amplitude of the excitation the same until the branch point N is

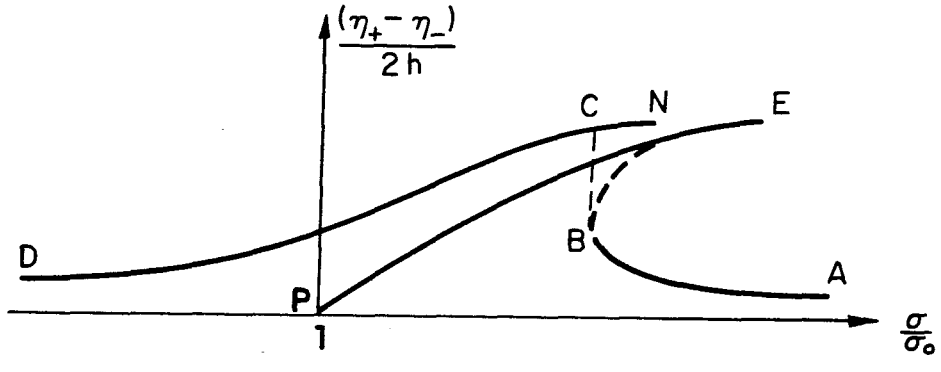

Figure 5.2.16 Definition sketch of a nonlinear steady state response curve to a sinusoidal excitation.

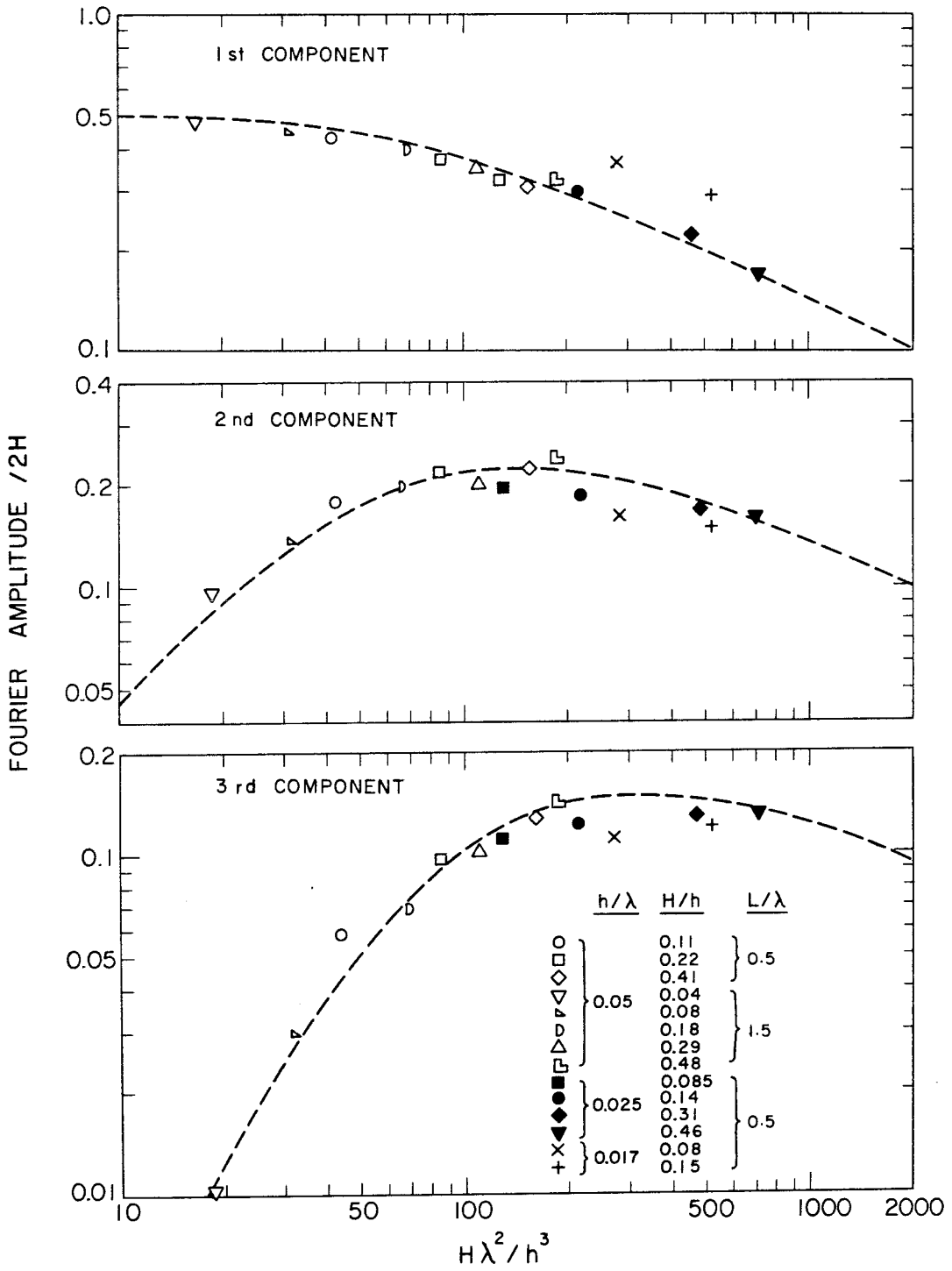

Fig. 5.2.17 Variation of the amplitude of the first three Fourier components of the wave recorded at x=L. Comparison between experiments and the nonlinear standing wave solution.

reached. If the point N lies on (or close to) the frequency amplitude curve PE the branch point N is reached. (If the frequency is further increased, then the solution falls on the lower branch curve BA.) If the point N lies on (or close to) the frequency amplitude curve PE the wave shape at the end walls should satisfy Eq. (5.2.12). The strategy consists then of varying the nonlinear parameter d/L for a given value of h/λ, each measurement being made at point N, in order to obtain several measurements along the curve PE. The periodic records can be compared with the theory through harmonic analysis and by a direct comparison of the wave shape during one period.

The results for the first three frequency components are presented in Figure 5.2.17 where the component amplitudes normalized by twice the cnoidal wave height, are plotted against $H\lambda^2/h^3$. The dashed curves represent the first three theoretical Fourier components of a cnoidal wave. Three experimental values of h/λ were chosen: $h/\lambda = 0.05, 0.025, 0.017$. For $h/\lambda = 0.05$ the first and third free modes were obtained whereas in the other case only the first mode was produced. Figure 5.2.17 shows good agreement between the theory and all the experiments corresponding to $h/\lambda = 0.05$; the agreement remains good when $h/\lambda = 0.025$ for the first component and becomes poorer for the other two components. With respect to the case with $h/\lambda = 0.017$, the experimental data appear to differ significantly from the theory.

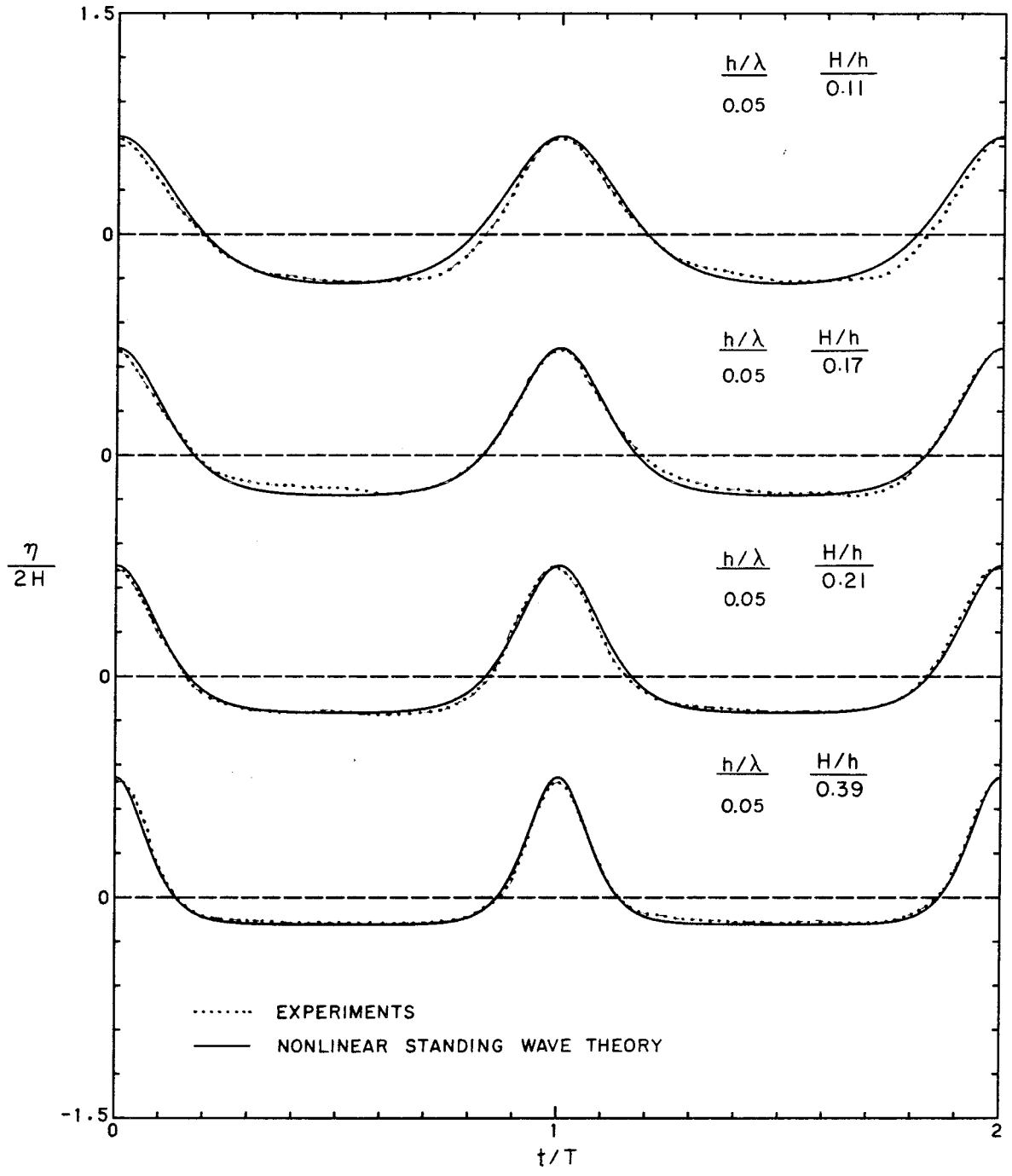

Fig. 5.2.18(a) Comparison of experimental wave records at x=L with the nonlinear analytical standing wave solution, $h/\lambda = 0.05$.

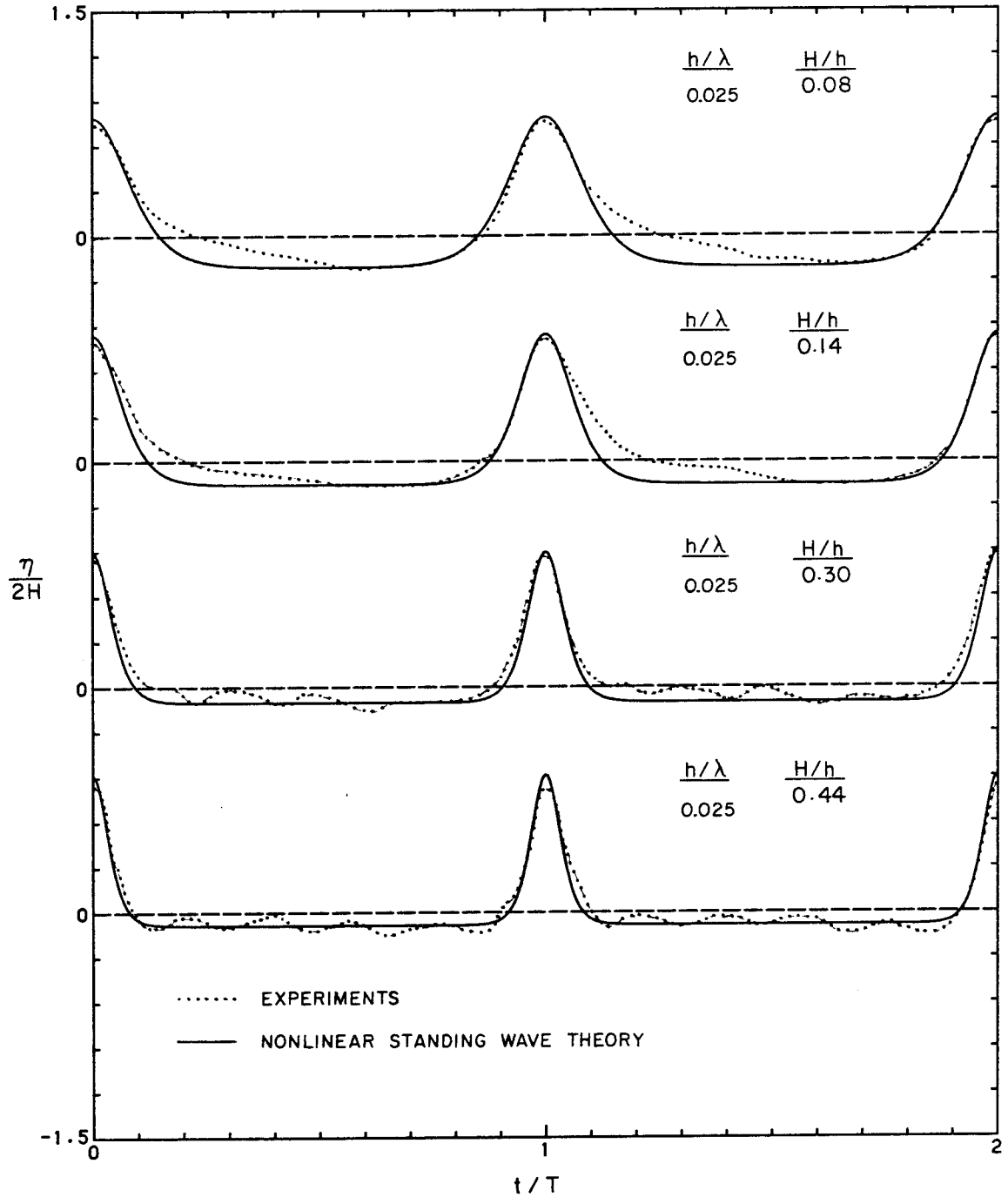

Fig. 5.2.18(b) Comparison of experimental wave records at x=L with the nonlinear analytical standing wave solution, $h/\lambda = 0.025$.

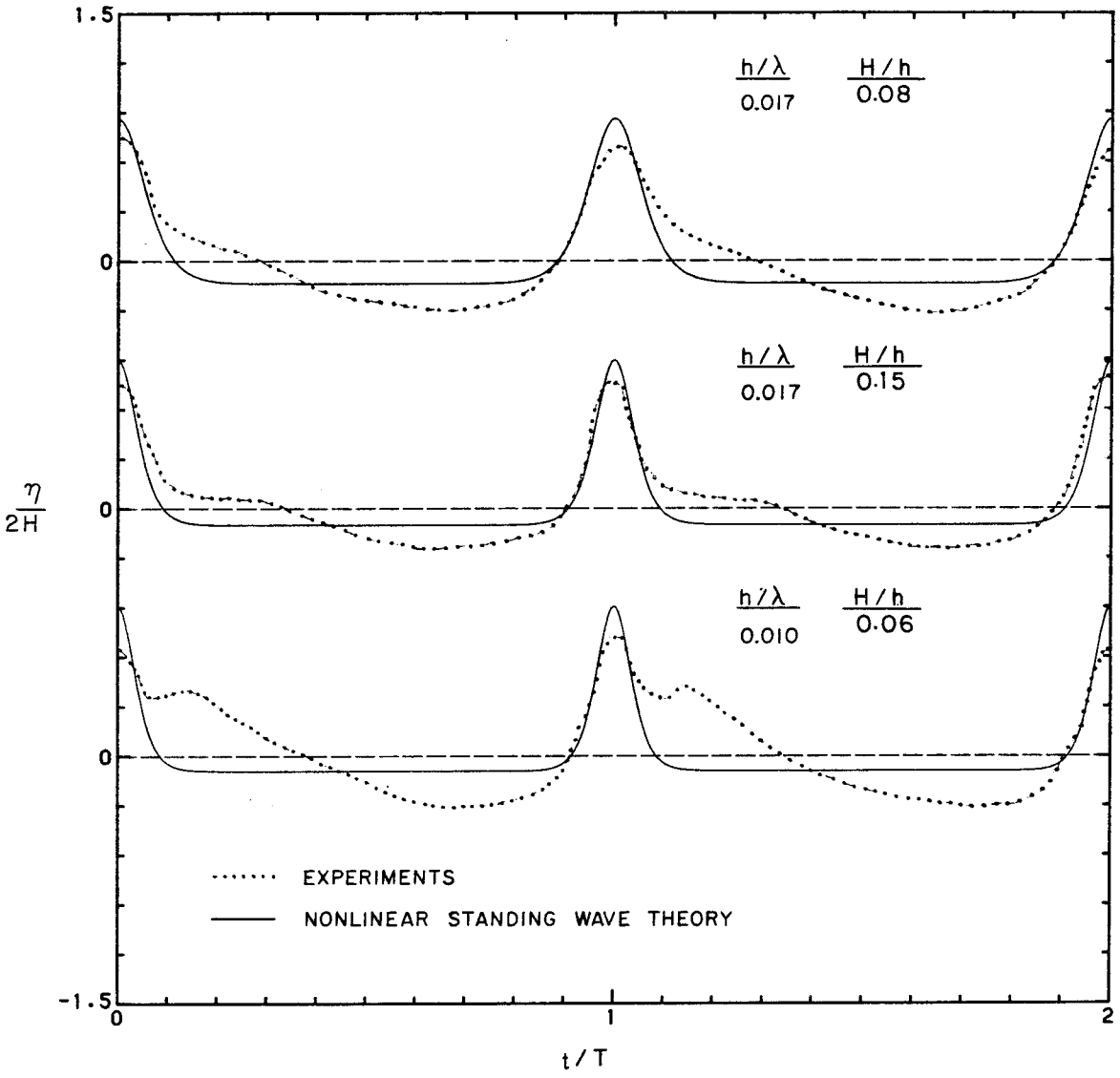

Fig. 5.2.18(c)

Comparison of experimental wave records at x=L with the nonlinear analytical standing wave solution, $h/\lambda = 0.017, 0.010$.

Some experimental wave records at $x = L$ are compared to the theory in Figures 5.2.18a, 5.2.18b, and 5.2.18c with the ordinates as $\eta/2H$ and the abscissa t/T. Four experimental values of h/λ are presented: $h/\lambda = 0.05, 0.025, 0.017, 0.010$. Again the quality of the agreement between experiment and the results of the nonlinear steady wave theory appears to depend more on the dispersion parameter h/λ than on the relative wave height H/h. In Figure 5.2.18a the experimental wave record corresponds to $h/\lambda = 0.05$; it is seen that the theoretical shape agrees quite well with the experiments. In Figure 5.2.18b all the experiments correspond to $h/\lambda = 0.025$; some discrepancies become apparent especially for smaller values of the relative wave height h/λ. As the dispersion parameter decreases further the agreement between theory and experiment becomes worse as shown on Figure 5.2.18c. In fact a secondary wave begins to emerge on the back of the main wave for $h/\lambda = 0.017$ and becomes well formed for $h/\lambda = 0.010$.

A conclusion related to these experiments is that a nonlinear cnoidal mode shape, although predicted by the theory, cannot be obtained for values h/λ smaller than approximately 0.025 by using a sinusoidal motion of the basin. Perhaps another form of excitation may generate these modes for small values of the dispersion parameter although the proper choice, if any, remains unclear.

These results at least explain the cnoidal-like shape of the wave records near the main bifurcation frequency described in Section 5.2.2. They also provide a partial verification of the analytical solution of the nonlinear standing mode problem in shallow water and this sheds some light on one possible wave

structure associated with long wave excitation in closed basins.

5.2.4 Transient Excitation

In Section 5.2.2 waves were induced in a closed rectangular basin by a small but continuous sinusoidal motion of the basin and nonlinearities were produced by the gradual build-up of the wave near a resonant frequency. The wave dynamics were investigated further by moving the basin with two periodic excursions and then leaving it at rest. This section presents the results of that investigation to further characterize the interaction effects of the nonlinearities, dispersion, and dissipation on the wave evolution for transient excitations.

It has been shown previously that for a basin which is continuously excited near resonance, the wave shape is very sensitive to the frequency of the basin motion. To verify whether or not this feature remains true for a transient excitation, five experiments were conducted, corresponding to the same excitation motion (two period excursion of the basin motion) but different frequencies. The resulting wave records of the relative wave amplitude η/h versus $\sigma t/2\pi$ at $x = L$ are presented in Figure 5.2.19. The dimensionless parameters for the experiment are: $d/L = 0.0094$, $h/L = 0.051$, $\sigma_o L/\sqrt{gh} = 3.128$, $\gamma_s = 0.075$, and the frequency range is: $0.77 < \sigma/\sigma_o < 1.43$. The same characteristics are observed for each curve: After several periods, the oscillations appear to divide into two or three waves. Thus, the shape of the waves which result from a transient excitation appears to be relatively insensitive to the frequency of the motion over a rather

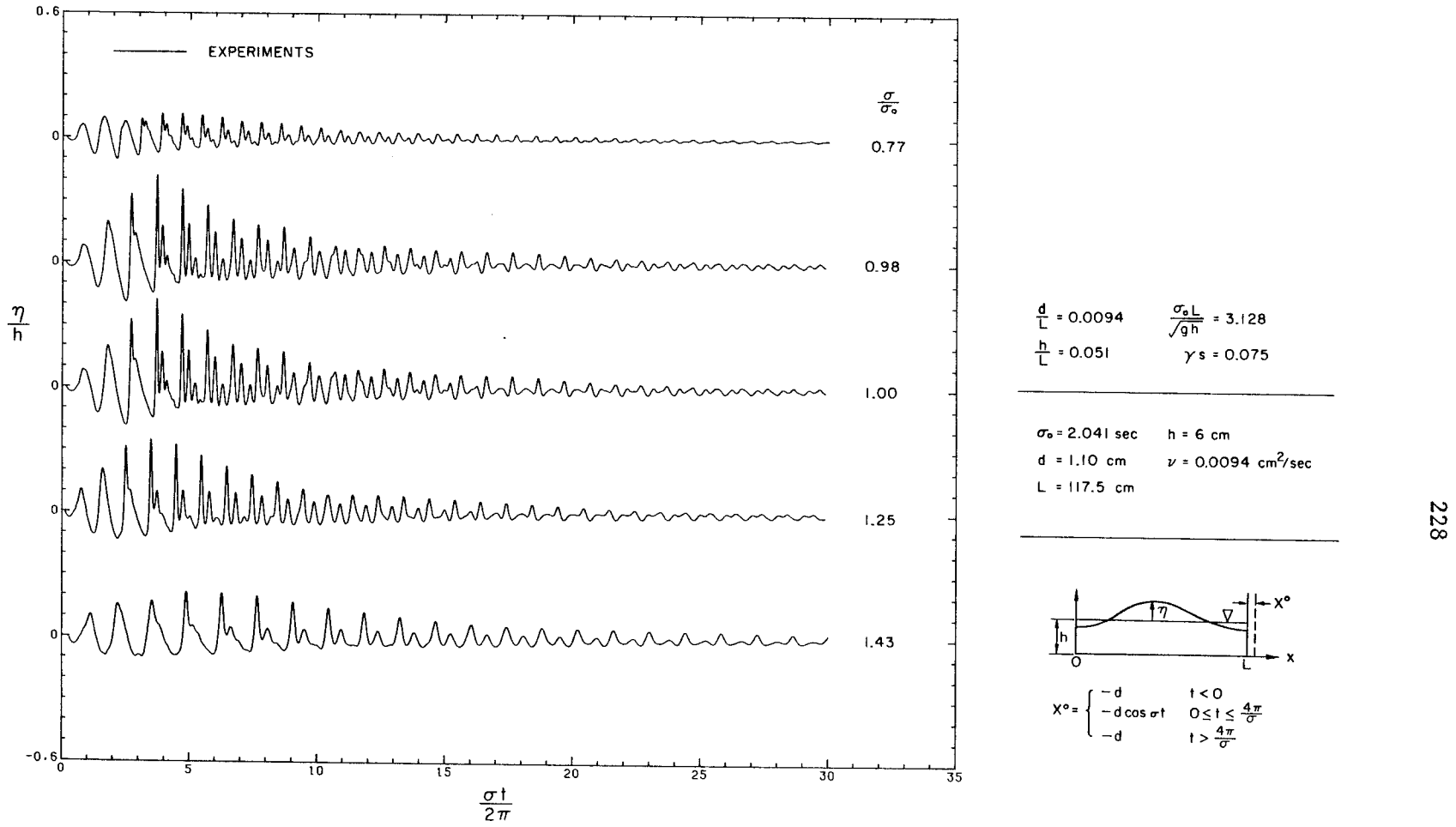

Fig. 5.2.19 Experimental time histories of free surface profile at x=L for various frequencies of excitations near the lowest resonant frequency resulting from a transient excitation, d = 1.10 cm, h = 6 cm, L = 117.5 cm.

wide range of frequencies. (The frequency σ_o given by Eq. (5.2.4) with $n = 0$ has been chosen for all the cases investigated next.)

Four series of experiments were conducted. For each set h/L was held fixed and the wave was recorded at x = L for three values of d/L = 0.0014, 0.0037, 0.0094. (Four values of h/L were considered: 0.098, 0.051, 0.034, and 0.021.) For all runs the excitation consisted of two cycles of oscillation. A characteristic Stokes parameter derived from Eq. (5.2.10) and based on the wave amplitude at the end of the excitation motion (Eq. 5.2.7) and the excitation frequency σ_o (Eq. 5.2.4) gives:

$$\underline{U}_s \simeq 102 \frac{d/L}{(h/L)^2} \tag{5.2.16}$$

Table 5.2.1 Values of Stokes parameter at the end of the excitation.

h/L \ d/L	0.0014	0.0017	0.0094
0.098	14	38	98
0.051	54	142	362
0.034	120	320	812
0.021	316	838	2162

From previous analysis one would expect the wave to depart from its linear behavior for $\underline{U}_s > 0(10)$ (see Eq. (5.2.11)).

The dissipation parameter γ_s which measures the effects of energy dissipation along the bottom, walls, and surface cannot be controlled experimentally for a given basin length. It is entirely determined by

the depth h; therefore, as the dispersion parameter is decreased γ_s increases accordingly. The only way to separate the effect of dissipation from dispersion is through numerical computations; this will be treated later.

For experiments where the normalized excitation parameter, d/L, varies, the relative wave elevation η/h has been normalized with respect to d/L as: $(\eta/h)/(d/L)$. The normalized experimental time wave histories of $(\eta/h)/(d/L)$ versus $\sigma t/2\pi$ at $x = L$ are presented in Figure 5.2.20a for the three amplitudes of basin motion shown in Table 5.2.1. The common dimensionless parameters are: $h/L = 0.098$, $\sigma_o L/\sqrt{gh} = 3.0915$, and $\gamma_s = 0.045$. For the smallest excitation ($d/L = 0.0014$) a damped sinusoidal wave shape is apparent. For $d/L = 0.0037$ a minor beat pattern appears and a small secondary wave emerges in the trough of the main wave a few periods after the basin motion has stopped. Finally, for $d/L = 0.0094$ a beat pattern becomes quite apparent and a secondary wave distinctly emerges.

The beats are due to the superposition of the forced mode causing the basin to oscillate at the frequency of excitation σ_o and the nonlinear free mode of oscillation, whose frequency varies with the wave height. As the wave decays the period of the beats becomes larger due to a gradual shift of frequency of the nonlinear mode toward σ_o.

It is interesting to note that the maximum wave height takes place for the three curves two cycles after the basin motion has stopped. Also, the maximum relative wave height during the fourth oscillation increases with increasing d/L. In Figure 5.2.20a the Stokes number associated with the upper curve is 14, which indicates the behavior of

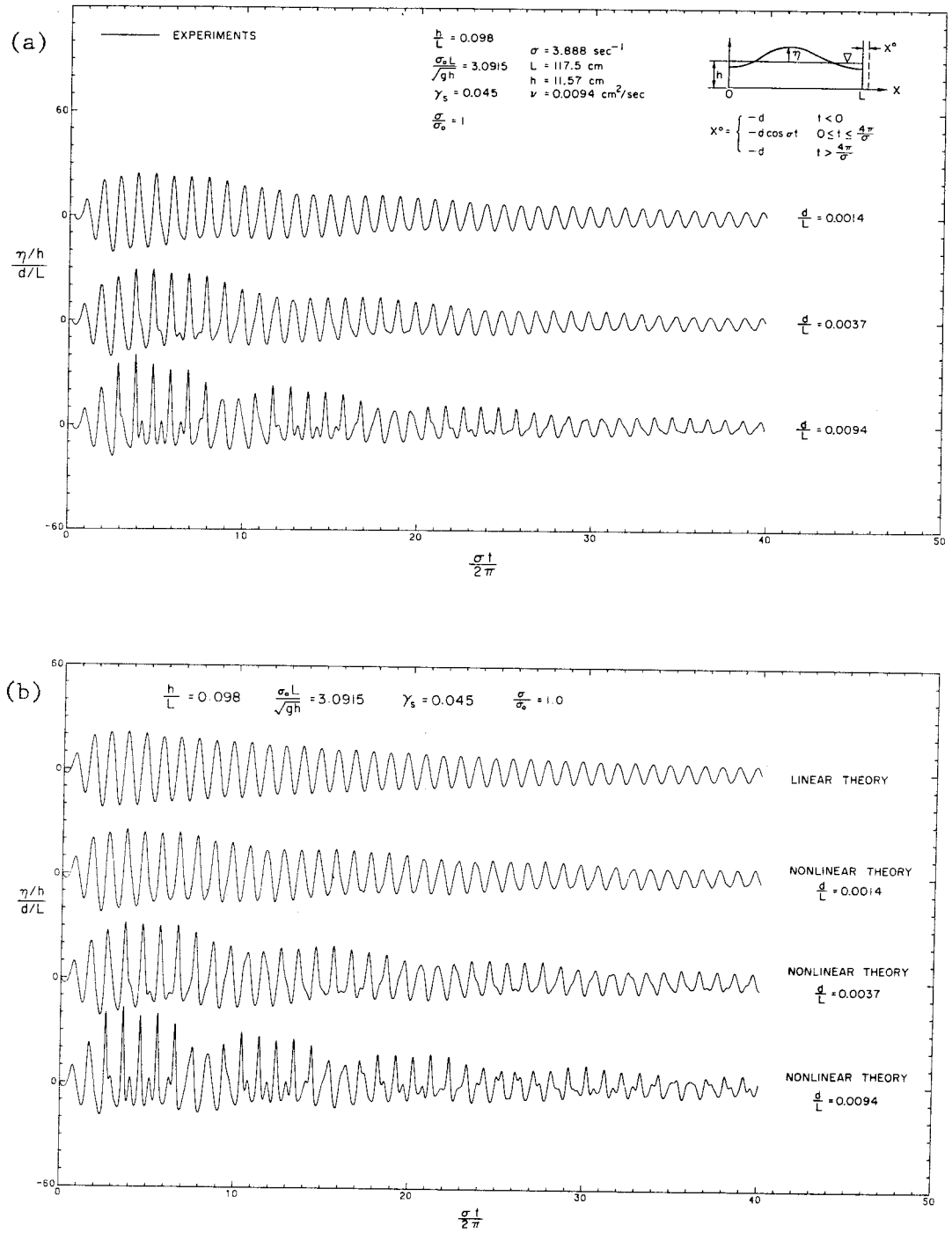

Fig. 5.2.20 Time histories of free surface profile at x=L for three excitation amplitudes resulting from a transient excitation; (a) experiments, (b) nonlinear theory; L = 117.5 cm, h = 11.57 cm.

the oscillations should be nearly linear. For the case of $d/L = 0.0037$ the Stokes number is 38, implying a departure from the linear behavior. Finally, for the lower record in Figure 5.2.20a, with a Stokes number equal to 98, the effect of nonlinearities appears significant.

The corresponding wave records obtained from the nonlinear dispersive theory are presented in Figure 5.2.20b; a theoretical record from the linear dispersive dissipative theory is included for reference. (The basin length was discretized into 31 nodes for the nonlinear numerical computations.) There is reasonably good agreement with the experimental results shown for Figure 5.2.20(a), although for $d/L = 0.0094$ the experimental record tends to decay at a faster rate than the corresponding computed one. This suggests that some additional source of dissipation may be created by the large waves resulting from a strong basin excitation, e.g., turbulent boundary friction. In order to check whether or not turbulent friction is responsible for this slightly larger experimental rate of damping, the Reynolds number associated with the boundary layer thickness, defined by Jonsson (1978) as $Re = u\sqrt{2/\nu\sigma}$ (see Section 5.1), can be computed for the lower record ($d/L = 0.0094$). The orbital velocity u can be estimated away from the end wall as $u \simeq 0.5(\eta^{+} - \eta^{-})\sqrt{g/h}$. The resulting Reynolds number, based on the wave elevation at the fourth oscillation is found as 356. The critical value given by Jonsson (1978) beyond which the oscillating flow inside the boundary layer becomes turbulent is 563. This tends to indicate that no additional dissipation caused by turbulent friction has taken place during this run.

A second set of experimental records is presented in Figure 5.2.21a with the dispersion parameter, h/L, decreased to 0.051, the dissipation parameter γ_s is increased to 0.075, and $\sigma_o L/\sqrt{gh} = 3.128$. It is noted in the upper record which corresponds to $\underline{U}_s = 54$ a secondary wave develops. This secondary wave emerges sooner and reaches a higher amplitude in the middle record which corresponds to $\underline{U}_s = 142$. Finally, three waves emerge in the record for which $\underline{U}_s = 362$. Nonlinear beats are no longer observed apparently because friction effects become important.

The corresponding wave records computed from the nonlinear dispersive-dissipative theory are presented in Figure 5.2.21b. (The basin length for this set was discretized into 41 modes for the numerical computations.) The same type of "breakdown" of the main oscillation as observed experimentally is seen in the three cases. However, the evolution of the wave with time for the largest excitation (i.e., d/L = 0.094) differs more from the experimental one than for the smaller ratios of d/L; in particular, the experimental wave decays faster than the computed one. The largest Reynolds number associated with the experimental run is about 130, which is less than the critical value given by Jonsson (1978), i.e., Re = 563. This suggests that no turbulent dissipation has taken place during that run. The reason such a discrepancy is observed for the rate of wave damping between the experimental wave record and the computed wave record remains unclear.

Figure 5.2.22a shows the results of experiments conducted to investigate the evolution of the wave system for the following

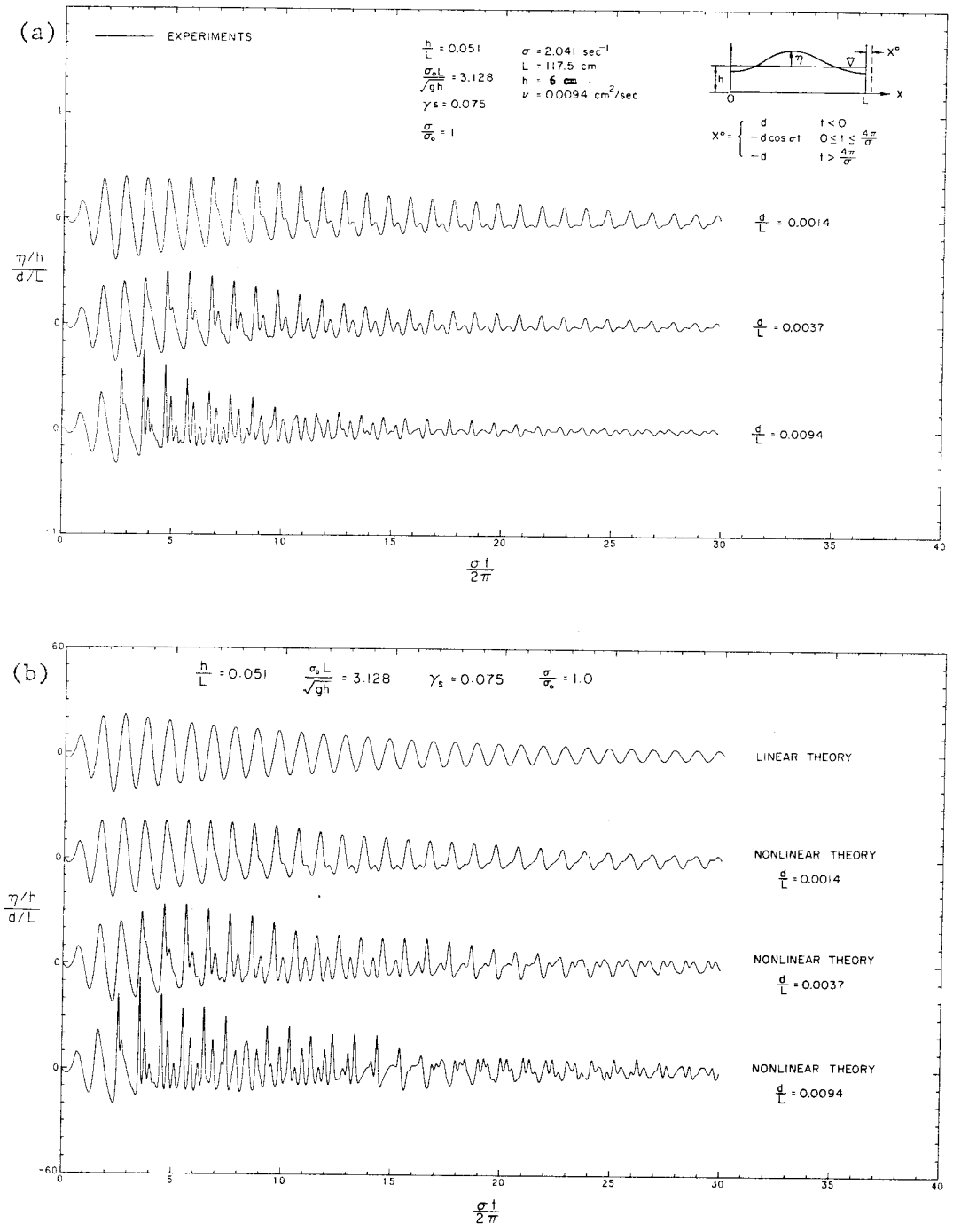

Fig. 5.2.21 Time histories of free surface profile at x=L for three amplitudes of excitation due to a transient excitation; (a) experiments, (b) nonlinear theory, L = 117.5 cm, h = 6 cm.

conditions: $h/L = 0.034$, $\gamma_s = 0.111$, and $\sigma_o L/\sqrt{gh} = 3.14$. A secondary wave tends to develop for the relative excitation of $d/L = 0.0014$ for which $\underline{U}_s = 120$, but friction appears to affect this evolution. The main wave separates into three secondary waves in the second record corresponding to $d/L = 0.0037$ and $\underline{U}_s = 320$. Finally, four or five waves emerge from the main wave in the lower record for which $d/L = 0.0094$ and $\underline{U}_s = 812$. Figure 5.2.22a shows that the division of the main oscillation into secondary waves occurs at smaller relative times as the nonlinear parameter d/L increases. For a small dispersion parameter, such as it is here, the nonlinear effects act first by steepening the wave. This process takes less time to develop for a large initial wave amplitude. Near the peaked wave front of the wave the water particles experience a large vertical acceleration and hence dispersion begins to act by creating the observed secondary oscillations.

Figure 5.2.22b shows the wave records obtained using the nonlinear dispersive theory for the same conditions as for the experiment of Figure 5.2.22a. (The basin length was divided into 51 nodes for the numerical computations.) The comparison with the experiments looks good for all three curves computed from the nonlinear theory; in particular, the rate of damping appears to be correctly predicted for the three curves. An interesting feature is that as the nonlinear parameter d/L increases the decay rate of the oscillation also increases, as can be observed in Figure 5.2.22b, although the dissipation parameter γ_s remains the same (i.e., $\gamma_s = 0.111$) for the three curves. By

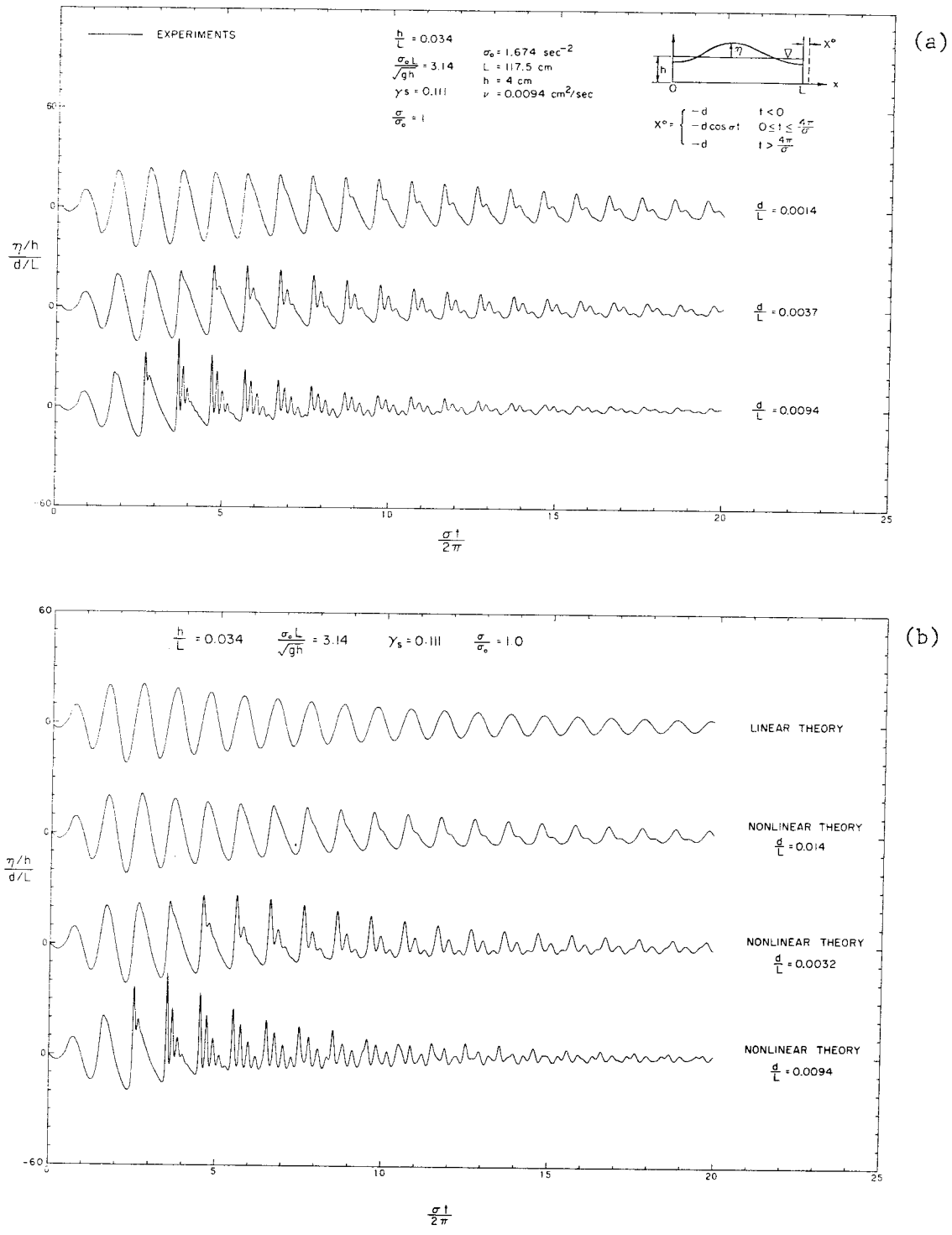

Fig. 5.2.22 Time histories of free surface profile at x=L for three amplitudes of excitation due to a transient excitation; (a) experiments, (b) nonlinear theory, L = 117.5 cm, h = 4 cm.

comparison the decay rates look similar for the three curves in Figure 5.2.20b corresponding to a larger dispersion parameter. This would tend to indicate that for a fixed dissipation coefficient γ_s the decay rate of the wave increases with $\underline{U}_s$.

Figure 5.2.23a shows the evolution with time of the experimental wave records for the following conditions: $h/L = 0.021$, $\sigma_o L/\sqrt{gh} = 3.14$ and $\gamma_s = 0.181$. For this case one would expect viscous dissipation to play a significant role since from the results of the linear theory (see Eq. (5.2.8)) the wave height should be reduced to 5% of its initial value after 15 oscillations. In fact, it is quite interesting to observe how it affects both nonlinearities and dispersion. In the record corresponding to $d/L = 0.0014$ and $\underline{U}_s = 316$ no secondary oscillations are observed; in fact damping begins almost immediately at the end of the excitation. However the shape of the waves changes with time with the front face steepening and the back face flattening, which characterize a growth of nonlinearities as the wave is damped. The same behavior is observed for the record such that $d/L = 0.0037$ and $\underline{U}_s = 838$. In addition, small secondary oscillations appear on the back face of the wave which, after some time, has the familiar triangular shape of a finite volume bore propagating in shallow water. For the record corresponding to $d/L = 0.0094$ and $\underline{U}_s = 2162$, the triangular shape develops more rapidly while more secondary oscillations with higher amplitude develop on the back face of the wave. Still the amplitude of those secondary waves remains much smaller than in the case of Figure 5.2.22a, implying that relatively larger friction effects must be present which negate the effects

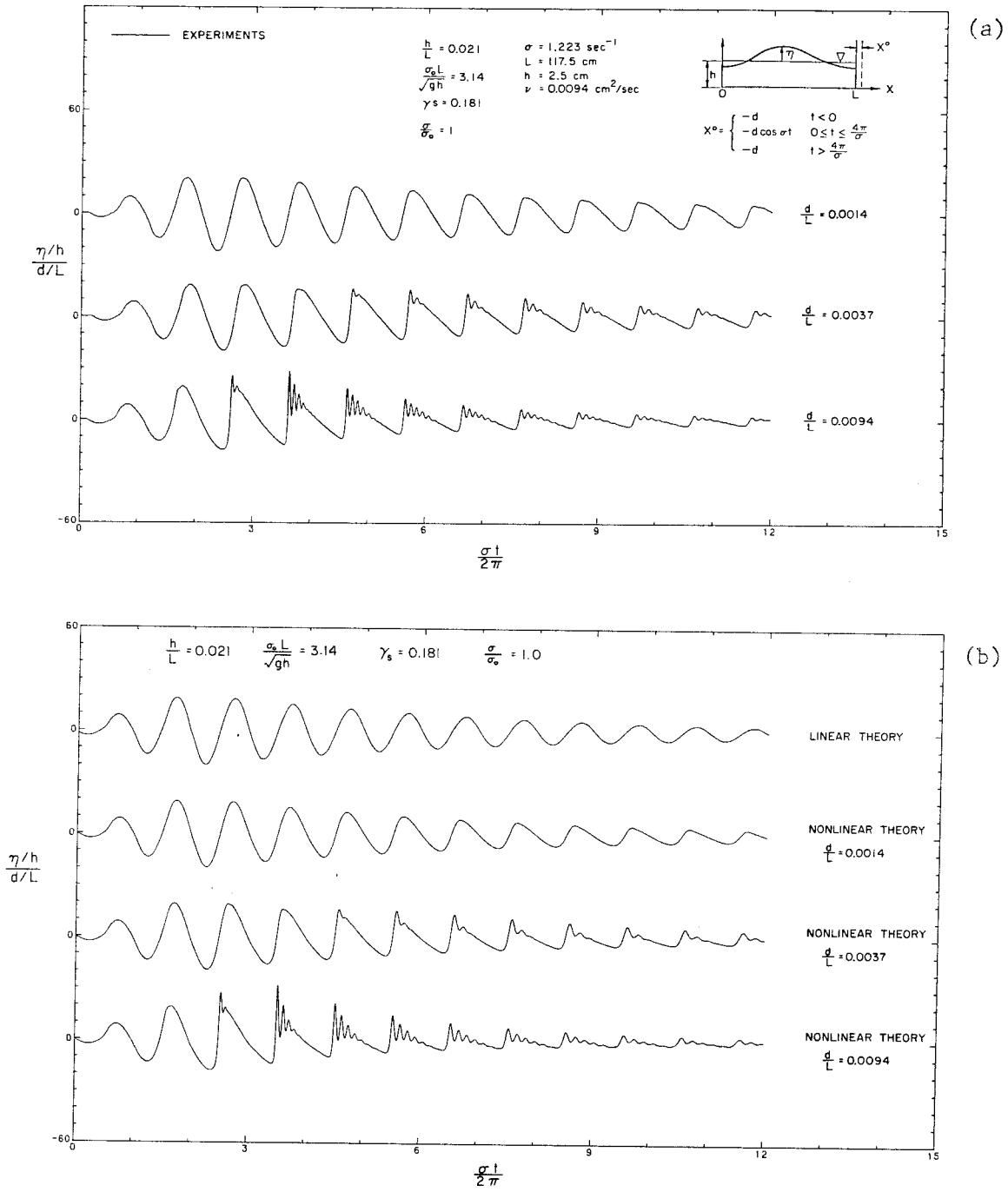

Fig. 5.2.23 Time histories of free surface profile at x=L for three amplitudes of excitation due to a transient excitation; (a) experiments, (b) nonlinear theory, L = 117.5 cm, h = 2.5 cm.

of dispersion.

The corresponding theoretical wave records are presented in Figure 5.2.23b. (The basin length was divided into 71 nodes in order to model the secondary oscillations properly.) These records appear to agree well with the experiments.

To assess the effect of friction on the dynamics of waves for the conditions of the experiments with initially small dispersion, theoretical wave records were evaluated for the same conditions as the results presented in Figure 5.2.23 except the dissipation parameter was decreased by a factor of four from $\gamma_s = 0.181$ to $\gamma_s = 0.045$. These results are presented in Figure 5.2.24. Significant differences can be observed between the corresponding theoretical records in Figures 5.2.23 and 5.2.24. For d/L = 0.0014 ($\underline{U}_s = 316$) nonlinearities cause the wave to steepen and act against viscous dissipation; this results in a very small decay rate over the twelve first oscillations. The dispersion effects begin to appear after the nonlinear effects cause the main wave to steepen and peak and then secondary waves emerge and grow. Thus, for a small oscillation, it takes time for the nonlinearities to grow and consequently for the effect of initially small dispersion to manifest itself. In the record corresponding to d/L = 0.0037 ($\underline{U}_s = 838$) the wave steepens faster and soon separates into four secondary waves of larger amplitude than those seen in the corresponding computed wave record in Figure 5.2.23. Finally, in the last record for which d/L = 0.0094 ($\underline{U}_s = 2162$) the wave begins to disperse almost immediately, separating into six or seven secondary oscillations. It is interesting to note how much

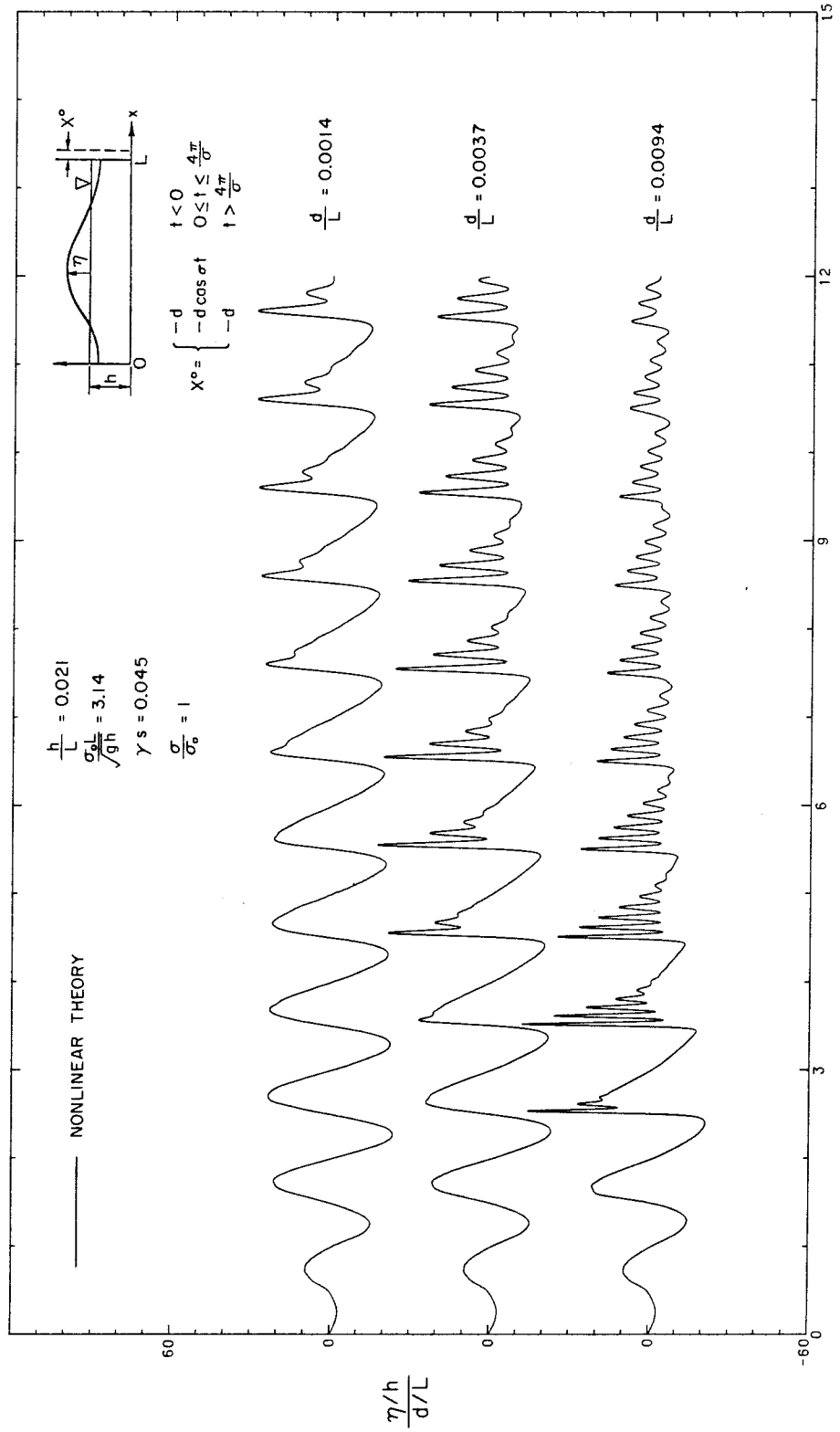

Fig. 5.2.24
Time histories of free surface profile at x=L for three amplitudes of excitation due to a transient excitation; nonlinear theory; h/L = 0.021, γ_s = 0.045.

faster the amplitude decreases for the larger values of the excitation parameter d/L, as noted earlier. So dissipation, in addition to damping the overall wave motions, also acts against dispersion by strongly damping the secondary oscillations which tend to develop on the back face of the wave. In addition, the larger the number of secondary waves (or, equivalently, the smaller the wave length of each secondary wave) the stronger the decay rate of the overall wave.

It can be checked from most of the transient wave records which have been presented (both from the results of experiments and from theory) that the main wave divides into a number of secondary oscillations, and this number appears to increase as the Stokes parameter increases. A physical interpretation of this can be given as follows. It is first recalled that the characteristic length associated with the Stokes number is defined as $2\pi\sqrt{gh}/\sigma$ where σ denotes the characteristic frequency of the basin excitation. On the other hand, the characteristic length ℓ which defines the Ursell number is a local length at a given location inside the basin and at a given time. A long unidirectional wave always tends to evolve in such a way as to satisfy a balance everywhere between nonlinear effects and frequency dispersion; thus the resulting Ursell number associated with the local wave form must approach the order of unity in the absence of dissipation. In the present situation in the initial stage of the wave evolution, e.g., at the end of the excitation period, the wave profile has a sinusoidal shape so that a characteristic wave length

can be chosen the same as that defining the Stokes number. Therefore, a characteristic Ursell number can be chosen as given by Eq. (5.2.16):

$$\underline{U}_r \simeq 102 \frac{(d/L)}{(h/L)^2} \tag{5.2.17}$$

in which (d/L) represents the nonlinearities associated with the wave height and $(h/L)^2$ the dispersion. After several oscillations the wave divides up into a number N_f of waves so that a new measure of a local wave length becomes L/N_f and the resulting measure of dispersion becomes $(hN_f/L)^2$. Assuming that the various wave heights remain of the same order of magnitude as the one at the end of the basin motion, the resulting Ursell number becomes:

$$\underline{U}_r \simeq 102 \frac{d/L}{(hN_f/L)^2} \tag{5.2.18}$$

Since this number must be of order unity, the variation of the number N_f can be derived from Eq. (5.2.18) as:

$$N_f \sim \frac{(d/L)^{1/2}}{(h/L)} \tag{5.2.19}$$

The variation of N_f with $[(d/L)^{1/2}/(h/L)]$ is presented in Figure 5.2.25 where the number of fissioned waves N_f has been obtained from the transient wave records. (Figure 5.2.23a is not considered because the effects of dissipation are too large for those wave records and invalidates the above derivation.) The linear trend tends to confirm the validity of the above reasoning. (The one data point which deviates from this line at an abscissa value of 1.75 probably

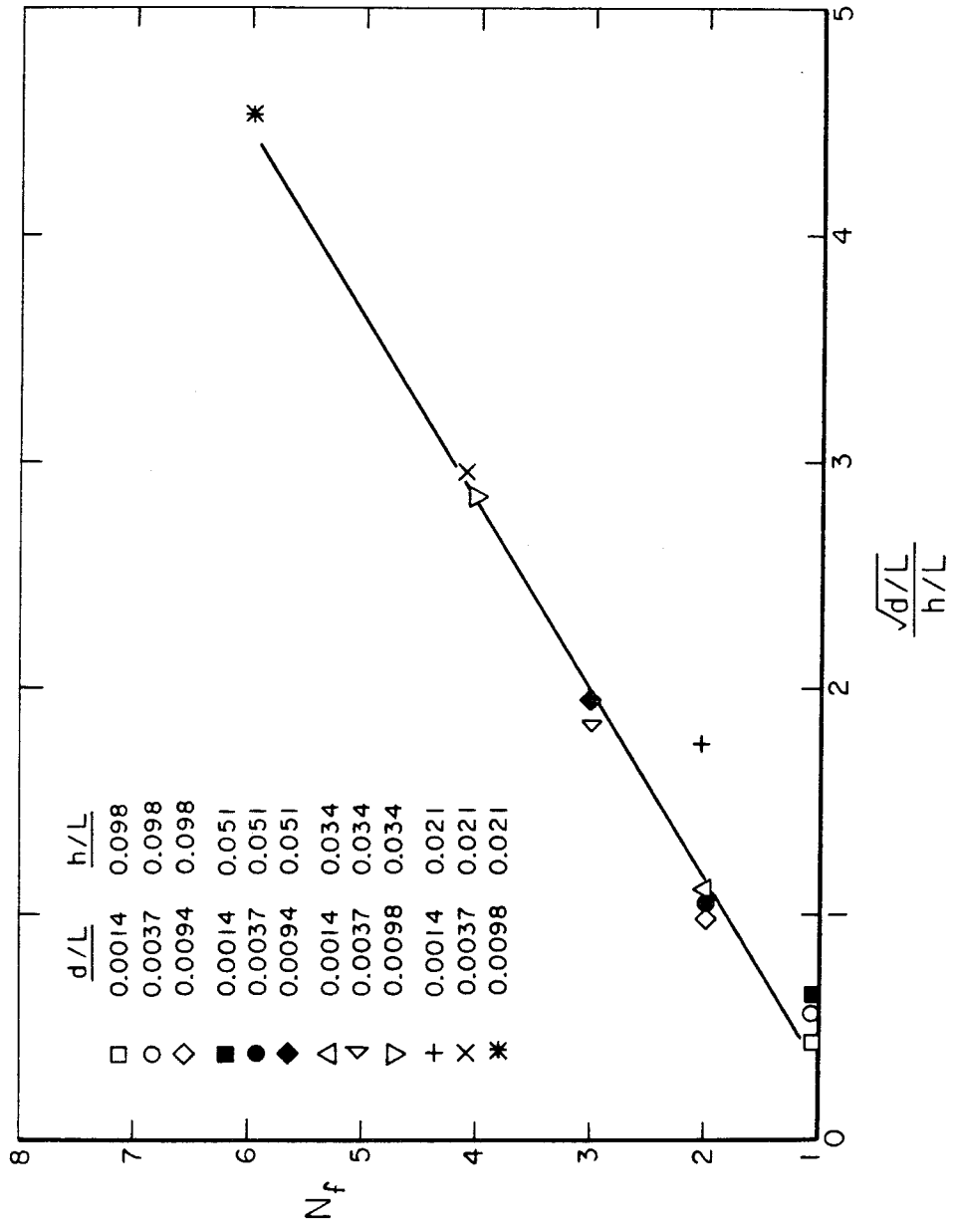

Fig. 5.2.25 Variation of the number N_f of fissioned waves which develop with time with $\sqrt{d/L}/(h/L)$.

comes about from the fact that the computation was stopped before the wave had enough time to completely separate out, and reach its final balanced state.) A visual best fit straight line relating N_f and $\sqrt{d/L}/(h/L)$ yields:

$$N_f = \begin{cases} 1 & \text{if } \dfrac{\sqrt{d/L}}{h/L} \leq 0.5 \\ 1.25 \dfrac{\sqrt{d/L}}{h/L} + 0.4 & \text{if } \dfrac{\sqrt{d/L}}{h/L} > 0.5 \end{cases} \tag{5.2.20}$$

Eq. (5.2.20) can be expressed more generally by using the Stokes number defined in Eq. (5.2.16):

$$N_f = \begin{cases} 1 & \text{if } \underline{U}_s \leq 25 \\ 0.125 \sqrt{\underline{U}_s} + 0.4 & \text{if } \underline{U}_s > 25 \end{cases} \tag{5.2.21}$$

The Stokes number defined in Eq. (5.2.10) constitutes an important parameter for the excitation problem in two respects. It first defines the range of validity of the linear dispersive theory. For example, if $\underline{U}_s \leq 0(10)$ it suffices to use the linear dispersive theory; if $\underline{U}_s \geq 0(10)$ nonlinear dispersive theory must be employed. Also in the latter case the standing wave pattern changes to a moving wave pattern where the concept of node becomes irrelevant. In addition, considering transient excitations, it has been possible to relate the number of waves emerging after several oscillations

to the Stokes parameter calculated at the end of the duration of the excitation, for the case where dissipation effects remain small. (If not, the prediction of the number of developing secondary oscillations given by Eq. (5.2.21) may become invalid because of the large damping rate of those secondary oscillations after they have emerged.)

One must use caution in applying Eq. (5.2.21) to the problem of a basin continuously excited near resonance. In this case the wave evolution is constrained by the motion of the basin and appears from the previous results to be very sensitive to the excitation frequency σ. Near the main bifurcation frequency a cnoidal-like wave develops; the establishment of normal modes of oscillations which have a well-defined structure is compatible with the basin motion (provided the dispersion parameter h/L is not too small). (Note that the Ursell number associated with the cnoidal wave is of order unity, if the proper length ℓ is chosen.) Away from the main bifurcation frequency, the cnoidal wave structure associated with a normal mode of oscillation is no longer compatible with the basin motion and the main oscillation separates into a number of secondary oscillations in a manner similar to that observed for the transient problem.

Table 5.2.2 gives the characteristic parameters, the number of waves computed from Eq. (5.2.21) and the maximum number of waves observed for the four sets of experiments from which steady state response curves are obtained. The value of $(\eta^+ - \eta^-)/2h$ for each set is chosen at the frequency corresponding to the largest number of emerging secondary waves.

Table 5.2.2 Comparison between calculated and observed values of N_f for steady state excitation

Figure No.	$\frac{\eta^+ - \eta^-}{2h}$	h/L	$\frac{\sigma_o L}{\sqrt{gh}}$	$\frac{U}{s}$	N_f calculated (Eq. 5.2.21)	N_f observed
5.2.4	0.4	0.098	π	170	2.01	2
5.2.10	0.2	0.098	π	85	1.6	2
5.2.13	0.4	0.051	π	623	3.52	3-4
5.2.15	0.1	0.034	3π	42	1.21	1

As seen from Table 5.2.2 the computed values of N_f results agree well with the observed ones, which tend to confirm the applicability of Eq. (5.2.21) to the estimation of the maximum number of waves which can develop in the case of a continuous excitation.

5.2.5 Summary

Several aspects of long wave oscillations in a closed rectangular basin have been investigated in Section 5.2. The results can be summarized as follows:

For a continuous excitation it has been found that, near resonance, a linear theory is inadequate to describe the wave evolution in the basin. Instead the nonlinear dispersive dissipative theory agreed well with the experiments for all the cases investigated. The wave shape, near resonance, is very sensitive to the frequency of the excitation; a cnoidal wave shape which can be predicted analytically develops near the main bifurcation frequency provided that the dispersion parameter is not too small. As the excitation frequency is

decreased the main wave divides up into a number of secondary oscillations as a result of the small dispersion.

For the transient excitation the importance of the Stokes number in defining the range of applicability of the linear theory and in estimating the number of secondary oscillations developing with time (if dissipation effects remain small) has been demonstrated. Some steady state features have been related with the transient results. It has been verified, in particular, that for the cases investigated the maximum number N_f of secondary waves emerging with time at resonance is also a function of the Stokes number. The applicability of these results to the harbor problem will be discussed in Chapter 6. A major difference with the basin problem is the usually much larger damping rate of the wave in harbor and bay situations. This may somewhat alter some of the present conclusions relevant to the basin oscillation problem.

(THIS PAGE IS BLANK, DUE TO ERROR IN PAGINATION)

CHAPTER 6

PRESENTATION AND DISCUSSION OF THE RESULTS FOR THE HARBOR

Experimental results on the oscillations of harbors induced by transient and continuous nonlinear long waves are presented in this chapter and compared to theoretical results.

Experimental considerations concerning the range of the experiments, the simulation of the open sea conditions, and the incident wave system are discussed in Section 6.1. An experimental investigation of leakage losses and entrance losses for a narrow rectangular harbor is presented in section 6.2. The relative importance of the various sources of dissipation which affect the response of a narrow rectangular harbor are also discussed in this section. In Section 6.3 the response of a narrow rectangular harbor with a flat bottom excited by a continuous train of periodic incident long waves is discussed. The transient excitation of a harbor with a finite number of incident waves is investigated in Section 6.4. Three harbor shapes were used for these experiments: a fully open narrow rectangular harbor with a flat bottom, a fully open narrow rectangular harbor with a linearly decreasing depth, and a fully open and a partially open harbor with a trapezoidal planform and constant depth.

6.1. Experimental Considerations

6.1.1 Range of the Experiments and the Simulation of the Open Sea Conditions

The long wave theory developed in Section 3.1 only applies if the ratio of depth to wavelength remains small compared to unity, i.e.,

$h/\lambda << 1$. To satisfy this condition in the laboratory, all the experiments presented in this chapter were performed in the shallow water range, with:

$$\frac{h}{\lambda} < 0.05 \tag{6.1.1}$$

The solution developed in Sections 3.3 and 3.4 treats the case of a harbor connected to the open sea where the incident waves after being reflected from the coastline propagate away without returning, and the radiated waves which emanate from the harbor entrance decay to zero at an infinite distance from the harbor and also do not return. However, in the laboratory the experiments must be conducted in a wave basin of finite size; thus, the reflected waves from the coastline and the radiated waves from the harbor mouth may be reflected from the wave plate and the side walls of the basin, violating the desired open sea condition. In previous investigations, e.g., Lee (1971), the open sea condition was simulated by performing the experiments in deep water and by absorbing the reflected and radiated waves with wave absorbers located along each side of the basin and a wave filter located in front of the wave paddle. In the present study this procedure proved undesirable for two reasons. First, all the experiments were performed in the shallow water range, which significantly alters the efficiency of wave absorbers such as those used by Lee (1971). Second, most of the incident waves were nonlinear, and they would have been altered significantly by filters located in front of the wave machine; thus, the shape of the waves at the coastline could not have been controlled.

For these reasons a wave filter was not used and an alternative method was chosen to satisfy the open sea condition experimentally. From

the analysis performed in Section 3.3 the number of oscillations required for the harbor to reach steady state for the case of periodic incident waves is usually less than eight. Taking this as a reference, the maximum wavelength of the incident waves such that eight oscillations can be realized in the harbor before the first incident wave reflected from the wave plate returns to the harbor, is given by:

$$\lambda = \frac{2L_b}{8} \tag{6.1.2}$$

where L_b denotes the distance between the wave plate and the coastline (about 7 meters for these experiments); thus:

$$\lambda \simeq 175 \text{ cm} \tag{6.1.3}$$

Therefore, with this wavelength the presence of the wave plate is not felt inside the harbor until the ninth oscillation; this provides enough time for adequate information on the characteristics of the harbor dynamics to be obtained. Combining Eq. (6.1.1) and (6.1.3) yields the maximum permissible depth as:

$$h = 9 \text{ cm} \tag{6.1.4}$$

In practice the experiments were performed in water depths between 4 cm and 10 cm, with incident wavelengths between 150 cm and 175 cm.

Even though efficient wave absorbers for long waves are difficult to construct in a limited area, to minimize the effects of reflection of the radiated wave from the side walls of the basin, wave absorbers composed of wire mesh screens were installed along each side wall. (See Chapter 4 for their characteristics). Using the analysis of Goda and Ippen (1963) the reflection coefficients of these absorbers for the experimental conditions which are typical of this study were estimated

to be between 30% and 60%. Although this is large, in reality only a small fraction of the radially spread radiated wave returns to the harbor mouth before the effects of reflection from the wave plate are felt; hence, the wave absorbers proved useful in further reducing the effects of the presence of the side walls. In fact, for all experiments conducted there was no evidence of disturbance of the wave oscillations inside the harbor caused by the proximity of the side walls.

6.1.2 The Incident Wave System

Weakly nonlinear incident long waves such as solitary and cnoidal waves were used for the experiments. Several experiments were performed to determine the characteristics of the generated waves in the present study. Three wave gages were installed in the basin at locations A, B, and C as shown in Figure 6.1.1; gage A was installed on the centerline of the basin, 180 cm downstream from the wave plate, gage B was placed on the centerline of the basin against the coastline with the harbor mouth closed, and gage C was placed against the coastline 150 cm apart from gage B, near the side wall wave absorbers.

One major concern in the present investigation is the effect of the lateral wave absorbers on the shape of the incident wave. As shown in Fig. 6.1.1 the guide walls used to prevent leakage around the sides of the wave generator extend 250 cm downstream from the wave plate. Beyond that distance the generated wave diffracts laterally. Considering that the ratio of the total basin width occupied by the absorbers to the length of the wave plate is more than 0.3, this may induce a significant change in the wave shape as the waves propagate toward the coastline.

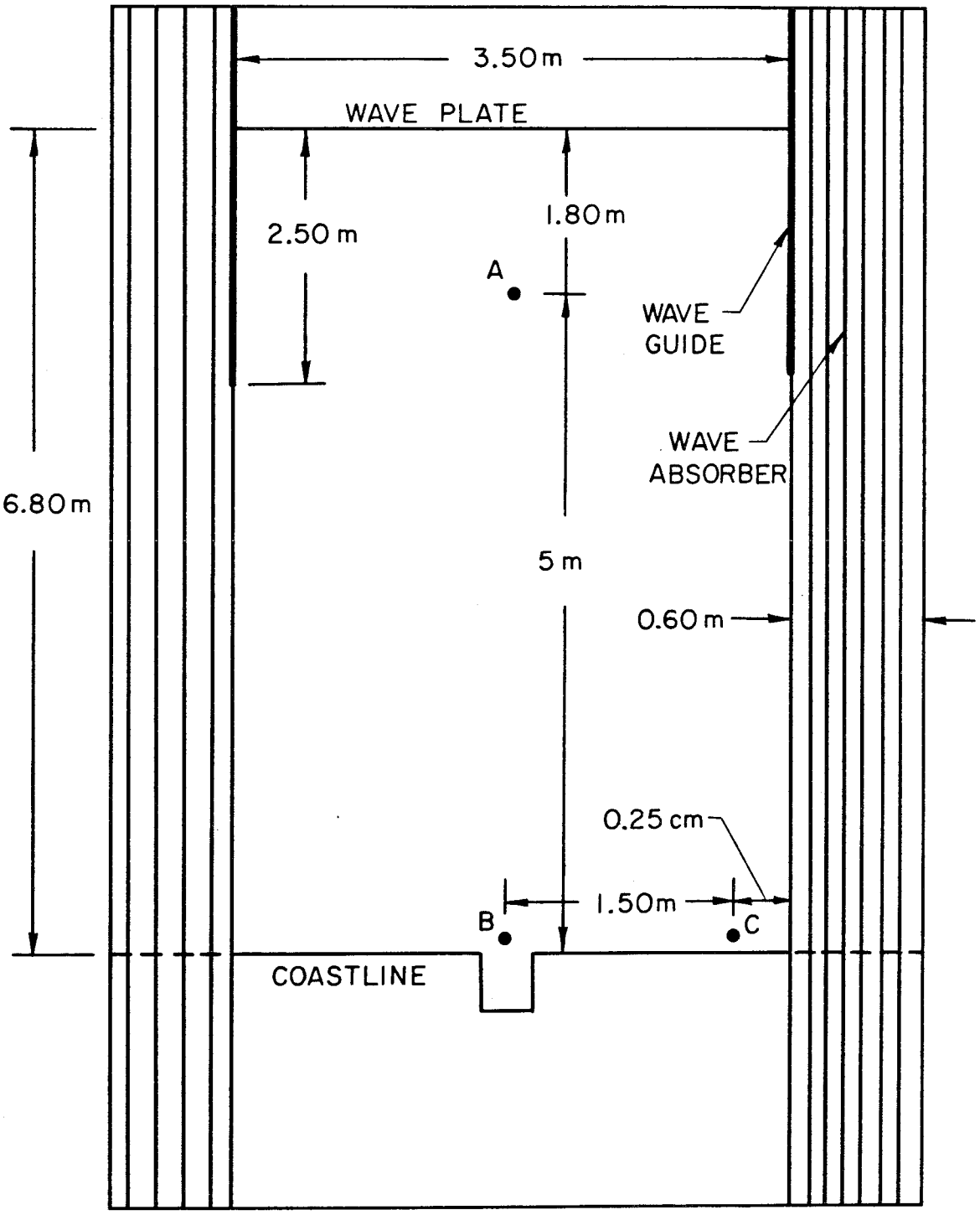

Fig. 6.1.1 Location of the wave gages in the basin used for the experimental study of the incident wave system.

Two series of experiments were performed by generating solitary waves using the method described by Goring (1978) with nominal wave height ratios, H/h, of 0.1 and 0.5. Each series consisted of two tests, one with movable vertical side walls extending parallel to the wave absorbers from the end of the existing fixed side walls to the coastline and the other without them. (These walls were constructed of 16 gage galvanized iron.)

Fig. 6.1.2 shows the water surface time histories at each location for a relative wave height of H/h = 0.1 and a depth h = 6 cm. (The corresponding stroke S_p of the wave machine is 3.6 cm and the time duration T of the plate motion is 2.27 sec.) The wave elevation η is normalized by the depth h at location A and by twice the depth at locations B and C to account for wave reflection at the latter locations.

Considering first the experiments with the side walls extending to the coastline, it is seen that the wave essentially retains its shape as it propagates from location A to locations B and C. The variation of the wave shape laterally is small, as can be judged by comparing the wave records at B and C. It is noted that the experimental wave height at location A is about 30% less than the value predicted by the theory. Part of that discrepancy may be due to leakage under the wave plate as it moves forward, despite the presence of the seals around the plate. This may explain the slightly negative mean value of the small oscillations trailing the main wave. This possibly indicates the existence of a small fluid velocity created by the static pressure difference between each side of the plate at the end of the plate motion. This pressure difference is at least equal to $S_p h/d_p$, where d_p denotes the

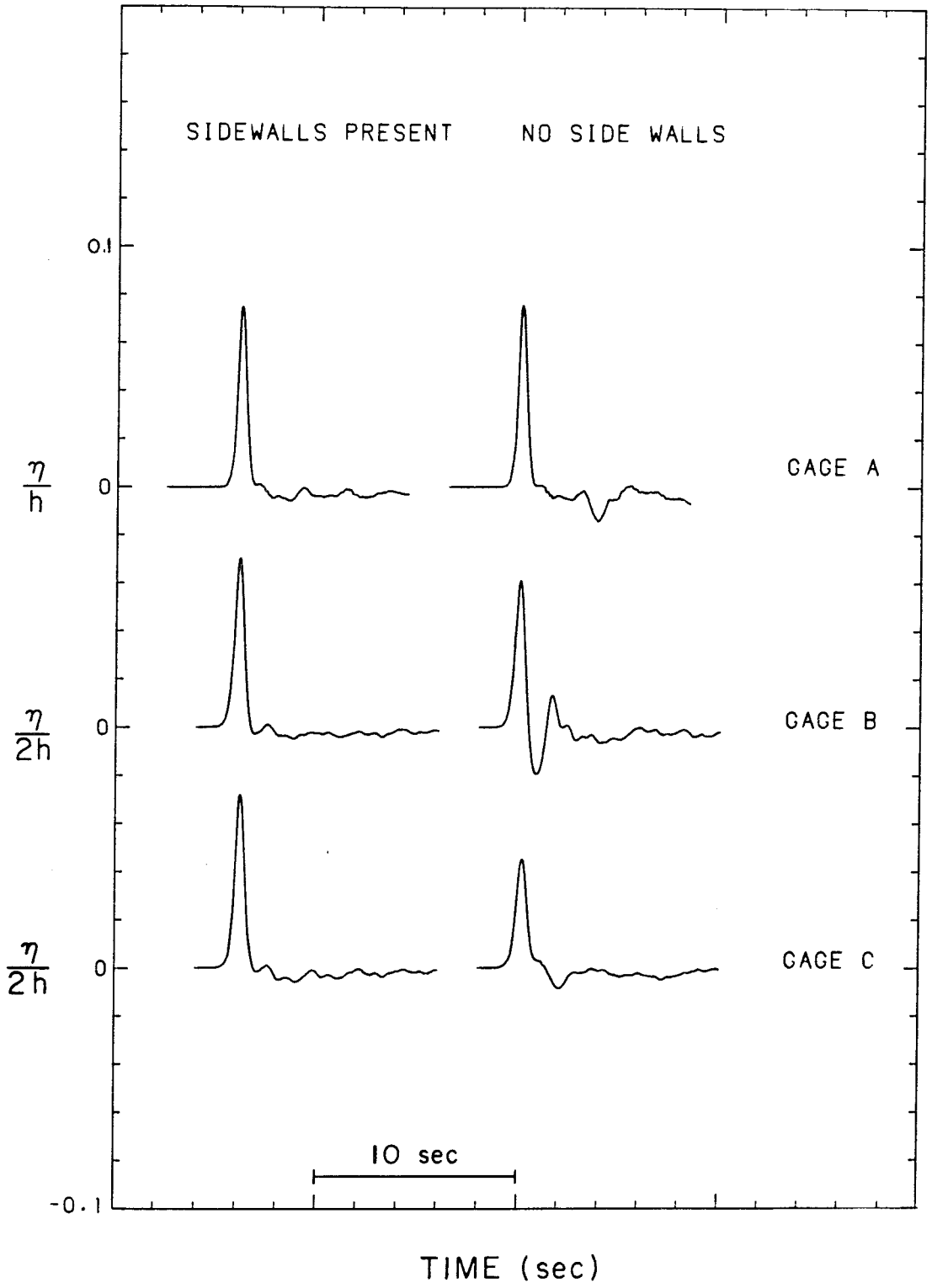

Fig. 6.1.2 Shape of solitary waves at locations A, B, and C for H/h = 0.1, h = 6 cm, S_p = 3.6 cm, T = 2.27s.

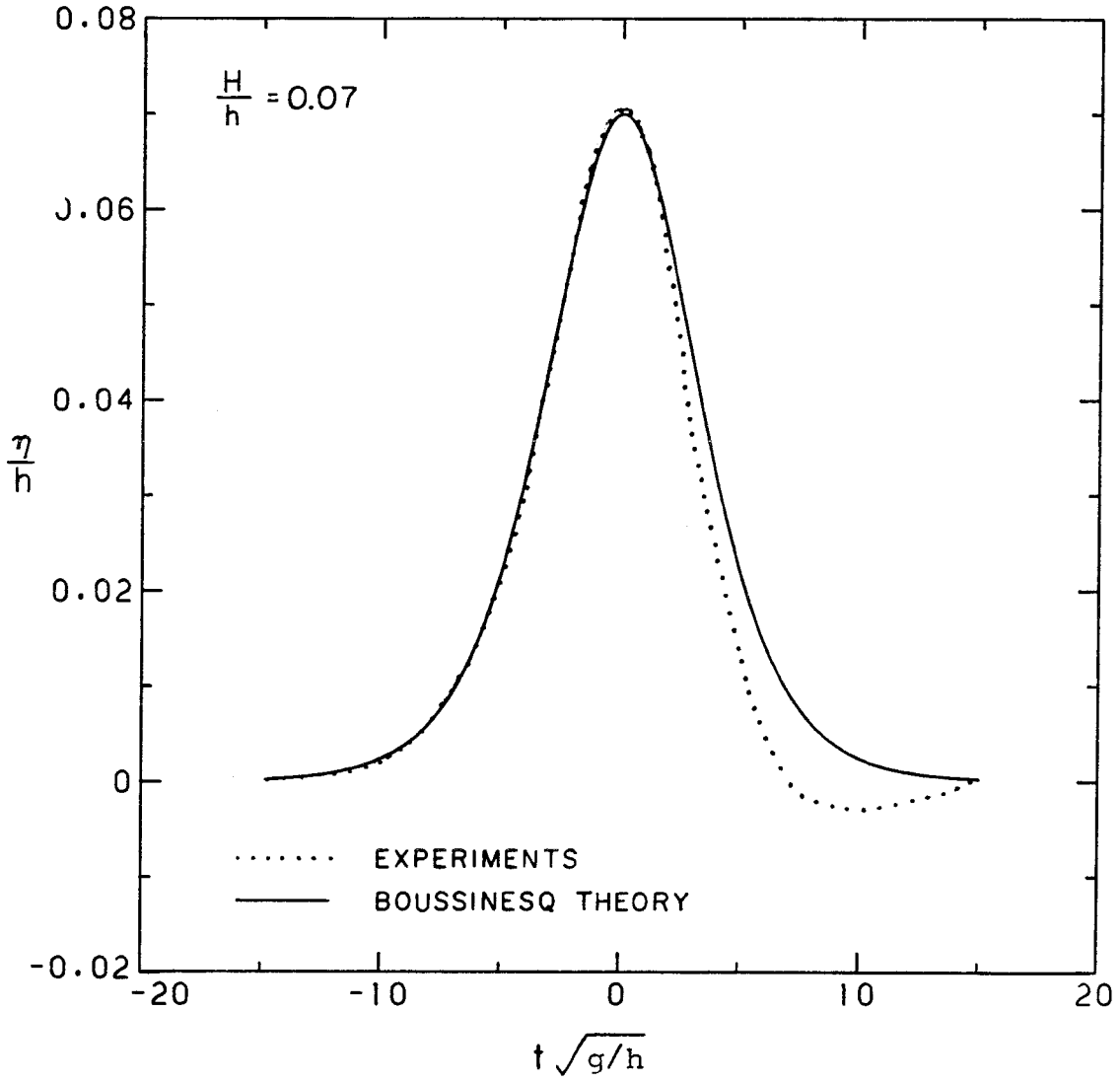

Fig. 6.1.3 Comparisons of the experimental shape of solitary wave measured at coastline on the centerline of the basin with Boussinesq theory (h = 6 cm, sidewalls in place).

distance between the wave plate and the basin wall behind it. In the present case d_p = 70 cm for the mean position of the piston so that the resulting value of $S_p h/d_p$ is not negligible. It is possible to further assess the importance of leakage effects by assuming that the mean negative level H_ℓ of the trailing wave is proportional to the static head difference $S_p h/d_p$. From the generation relationships developed by Goring (1978) S_p/h is proportional to $(H/h)^{1/2}$, and the ratio H_ℓ/H which measures the relative importance of the leakage effects is then proportional to:

$$\frac{H_\ell}{H} \sim \frac{h}{d_p} \frac{1}{\sqrt{H/h}} \tag{6.1.5}$$

Thus, the relative leakage effects increase with depth and with decreasing distance d_p, and for a given depth and d_p they decrease as H/h increases.

The shape of the incident-reflected wave at the coastline determined experimentally is compared with the solitary wave shape derived from the Boussinesq equations in Fig. 6.1.3. The front of the wave measured experimentally agrees well with the theoretical solution, but the back face does not, perhaps due to the leakage effects mentioned.

Considering next the case where the sidewalls are removed, in Fig. 6.1.2 it is seen that the shape of the wave changes markedly as it propagates toward the coastline. A secondary oscillation appears behind the main wave and its height approaches one-half of the height of the main wave at location B. The wave height of the leading wave at location C is about 60% of the height of the wave at location B and the shape is quite different. These features emphasize the two-dimensional character of the incident wave when the sidewalls are removed.

Fig. 6.1.4 shows similar water surface time histories for a relative height of H/h = 0.5, h = 5 cm. The stroke and duration of the wave machine motion are S_p = 8.2 cm, T = 1.0 sec. With the sidewalls in place the wave shape is about the same at the three locations. The wave height obtained experimentally at location A in Fig. 6.1.4 is still about 30% less than the value predicted by the theory (H/h = 0.5), but the negative water surface elevation observed in Fig. 6.1.2 behind the main wave has almost completely disappeared, which agrees with the trend predicted by Eq. (6.1.5). The shape of the wave at the coastline determined experimentally agrees well with the theory for the whole wave, as can be seen in Fig. 6.1.5. In the absence of the sidewalls a secondary oscillation appears at gage B in Fig. 6.1.4 due to the diffraction of the wave around the permanent sidewalls into the wave absorber region.

In summary, both diffraction into the lateral wave absorbers and leakage under the wave plate tend to change the shape of the solitary wave which is generated initially. As a result it appears difficult to predict its characteristics (shape and spectral energy content) as it reaches the coastline. Therefore, the solitary wave was not used to excite the harbor in this study.

Two series of experiments were performed with cnoidal waves, generating a group of five waves with nominal Stokes numbers, $H\lambda^2/h^3$, equal to 50 and 650. Each series consisted of three experiments and the waves were recorded at the same locations as were the solitary waves. In the first run, the cnoidal waves were generated using the plate motion as prescribed by Goring (1978), denoted herein as elliptic motion, with the "removable" sidewalls present. In the second run the waves were generated

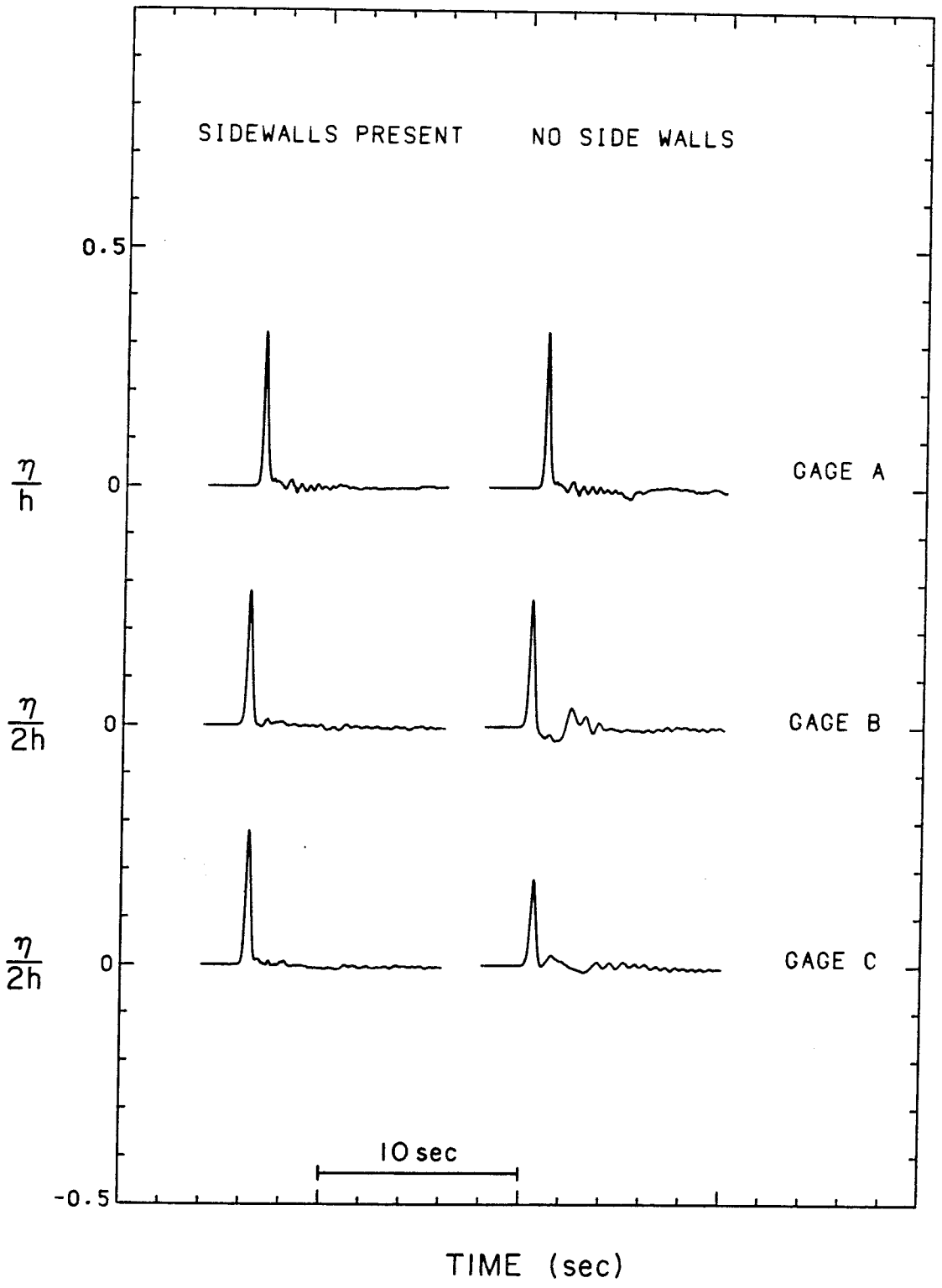

Fig. 6.1.4 Shape of solitary waves at locations A, B, C for H/h = 0.5, h = 5 cm, S_p = 8.2 cm, T = 1s.

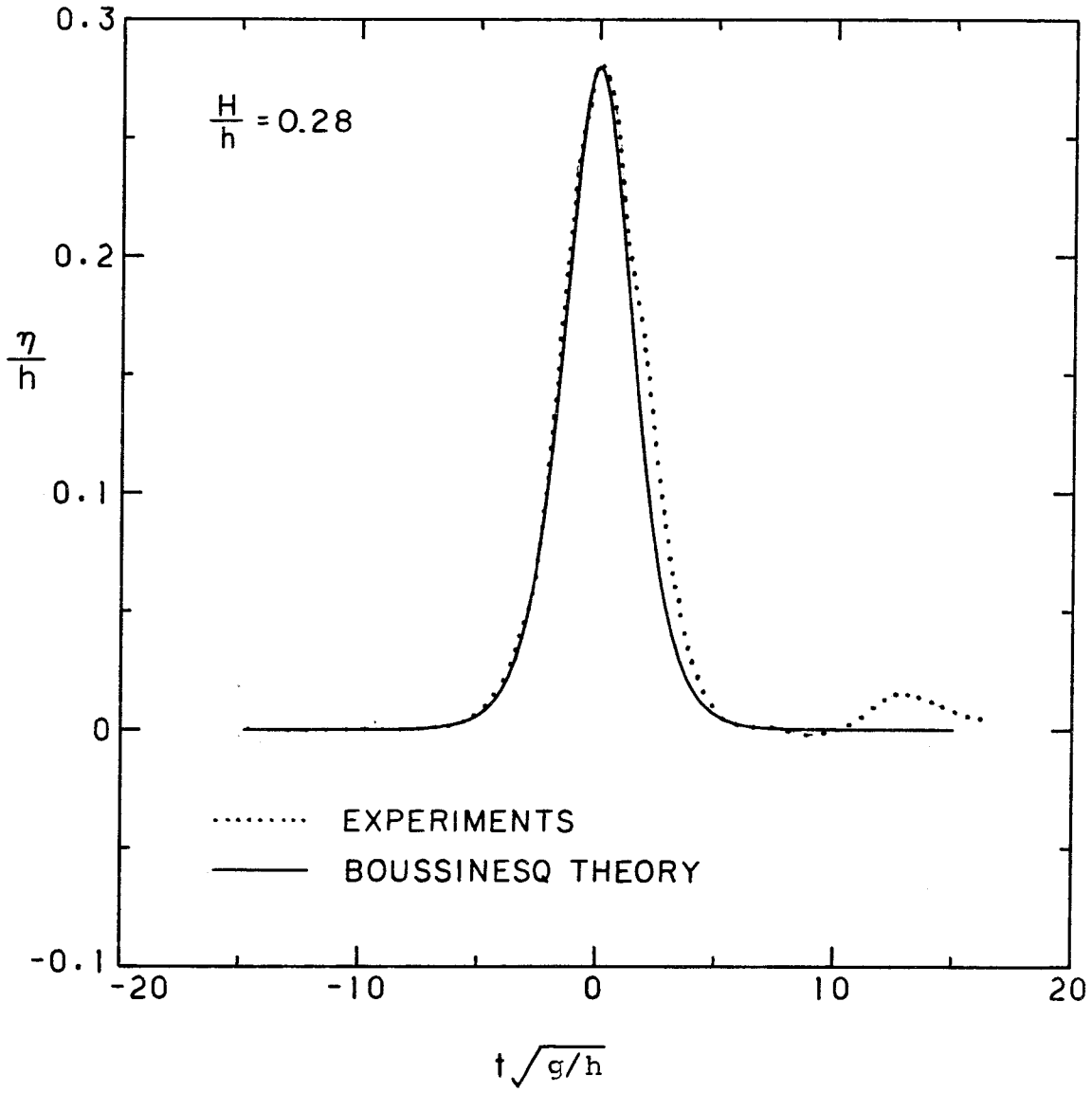

Fig. 6.1.5 Comparison of the experimental shape of a solitary wave measured at coastline on the centerline of the basin with the Boussinesq theory (h = 5 cm, sidewalls in place).

using the same elliptic plate motion without the "removable" walls. In the third run a sinusoidal plate motion was used with the same stroke and same period as in the other two cases but with sidewalls installed.

Figure 6.1.6 shows the water surface time history at each location for $H\lambda^2/h^3 = 50$, $H/h = 0.12$, $h = 6$ cm, $T = 1.613$ sec, and $S_p = 2.35$ cm. Considering first the elliptic plate motion, the experimental wave height at location A is about 25% less than that predicted by the wave generation relationships. At location C, when no sidewalls are present, it is significantly reduced by diffraction effects but the wave shape at location B seems to be only slightly altered by diffraction. The wave shape at the coastline on the centerline of the basin is compared with the wave shape from the cnoidal theory (see Section 3.2.3) in Fig. 6.1.7. With the sidewalls along the wave absorbers good agreement is obtained. When the sidewalls are removed a small secondary wave appears at the trough of the main oscillations but nevertheless the shape remains reasonably close to the theoretical one. As expected, when the waves are produced by a sinusoidal plate motion (Fig. 6.1.6) they do not retain their original shape as they propagate. As seen at locations B and C, secondary waves tend to form at the back of the main oscillations as the waves try to attain a permanent shape.

Similar results are observed in Fig. 6.1.8 for $H\lambda^2/h^3 = 650$, $H/h = 0.5$ $h = 6$ cm, $T = 2.51$ sec, $S_p = 5.8$ cm. In the presence of sidewalls the shape of the waves varies little between location A and B. It is noted that the relative wave height is equal to 0.33 at location A compared to 0.5 predicted by theory. Such a discrepancy, also found in the three other cases investigated previously, can possibly be explained by leakage

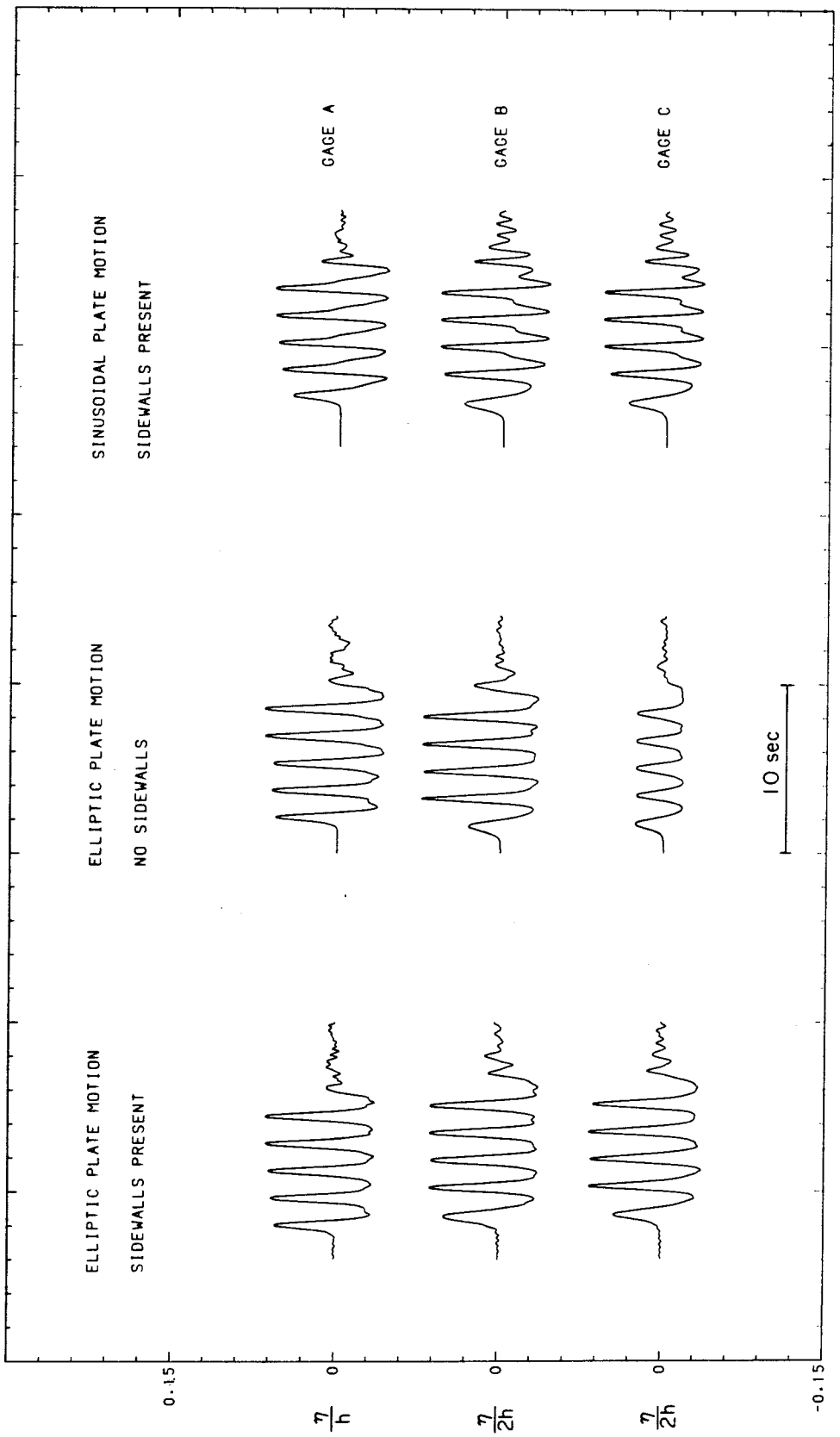

Fig. 6.1.6 Shape of the cnoidal waves at locations A, B, C for H/h = 0.12, h = 6 cm, S_p = 2.35 cm, T = 1.613 s.

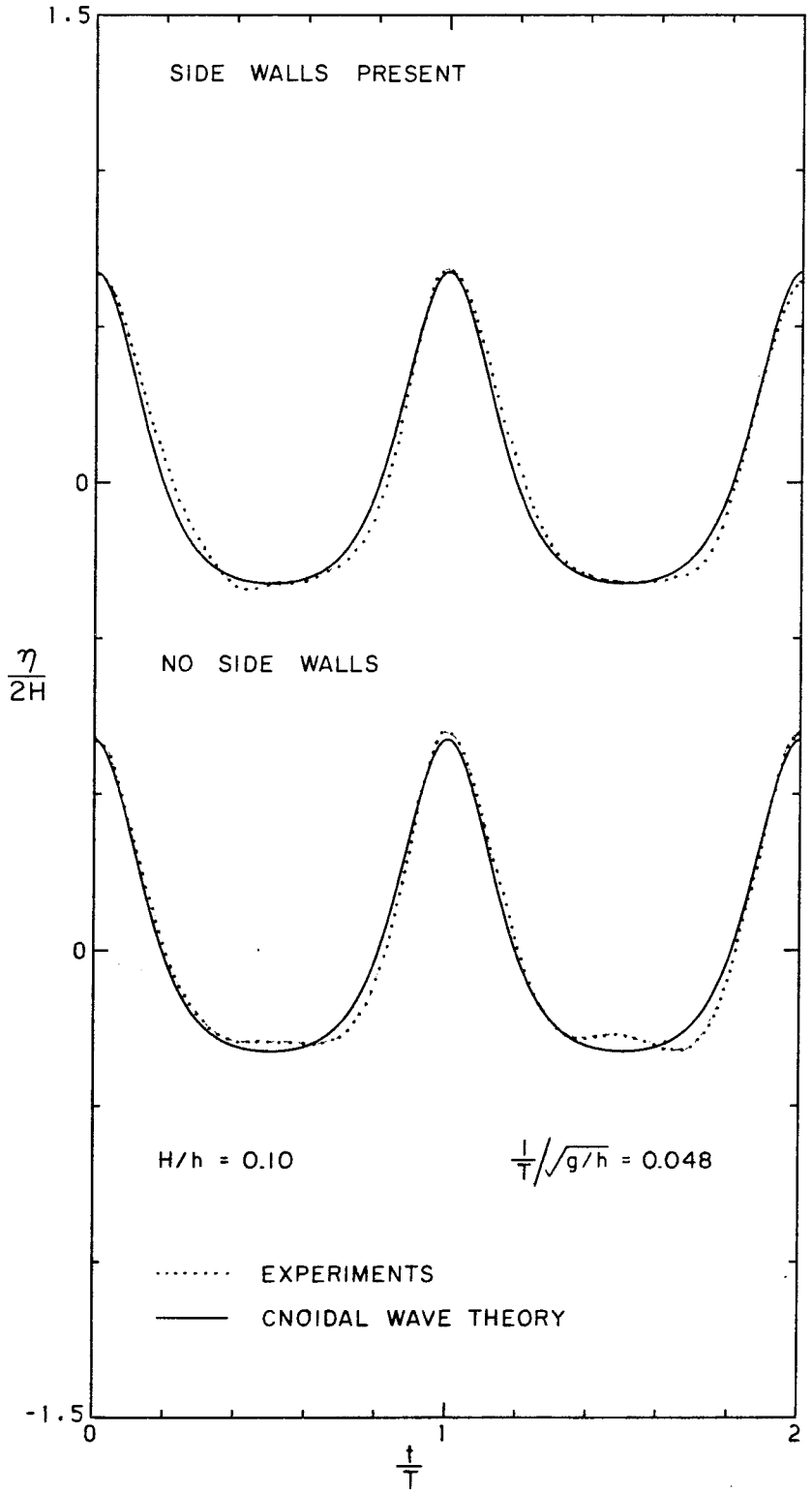

Fig. 6.1.7 Comparision of the experimental shape of cnoidal wave at coastline on the centerline of the basin with the cnoidal wave theory, with and without sidewalls, for h = 6 cm, T = 1.613 sec.

effects mentioned previously. As the wave propagates from location A to location B, its height is reduced further by 25%. Assuming a decay law for the wave height of the form:

$$\frac{A_o}{A} = \exp\left[-\bar{f}\,\frac{x}{h}\right] \tag{6.1.6}$$

the decay factor $\bar{f}$ is found as 0.0025 for this case. This value is fairly high but consistent with the experimental results of Goring (1978). In the absence of sidewalls the shape of the waves varies slightly between location A and location B. The wave shapes at the coastline on the centerline of the basin are compared with the cnoidal theory in Fig. 6.1.9. Theory and experiments agree reasonably well when the sidewalls are in place. In the absence of sidewalls the wave shape is no longer symmetric about the crest in this case. So diffraction does affect the cnoidal wave shape in some cases, but this effect is not as dramatic as for the solitary wave. One way to correct for the skewness of the incident wave is by extending the guide walls one or two meters further than in Fig. 6.1.1. This procedure was used for some of the experiments presented in Section 6.3, especially those corresponding to a large Stokes number, to obtain an incident wave shape which is more symmetric about the crest at the coastline.

In the case of a sinusoidal plate motion Fig. 6.1.8 shows that secondary waves form near the plate and the wave shape changes drastically as the waves propagates toward the coastline. This points out the importance of a properly generated wave motion to control the characteristics of the wave at the coastline.

The following conclusions are drawn from Figs. 6.1.6 through 6.1.9. A sinusoidal plate motion appears inadequate to generate a nonlinear

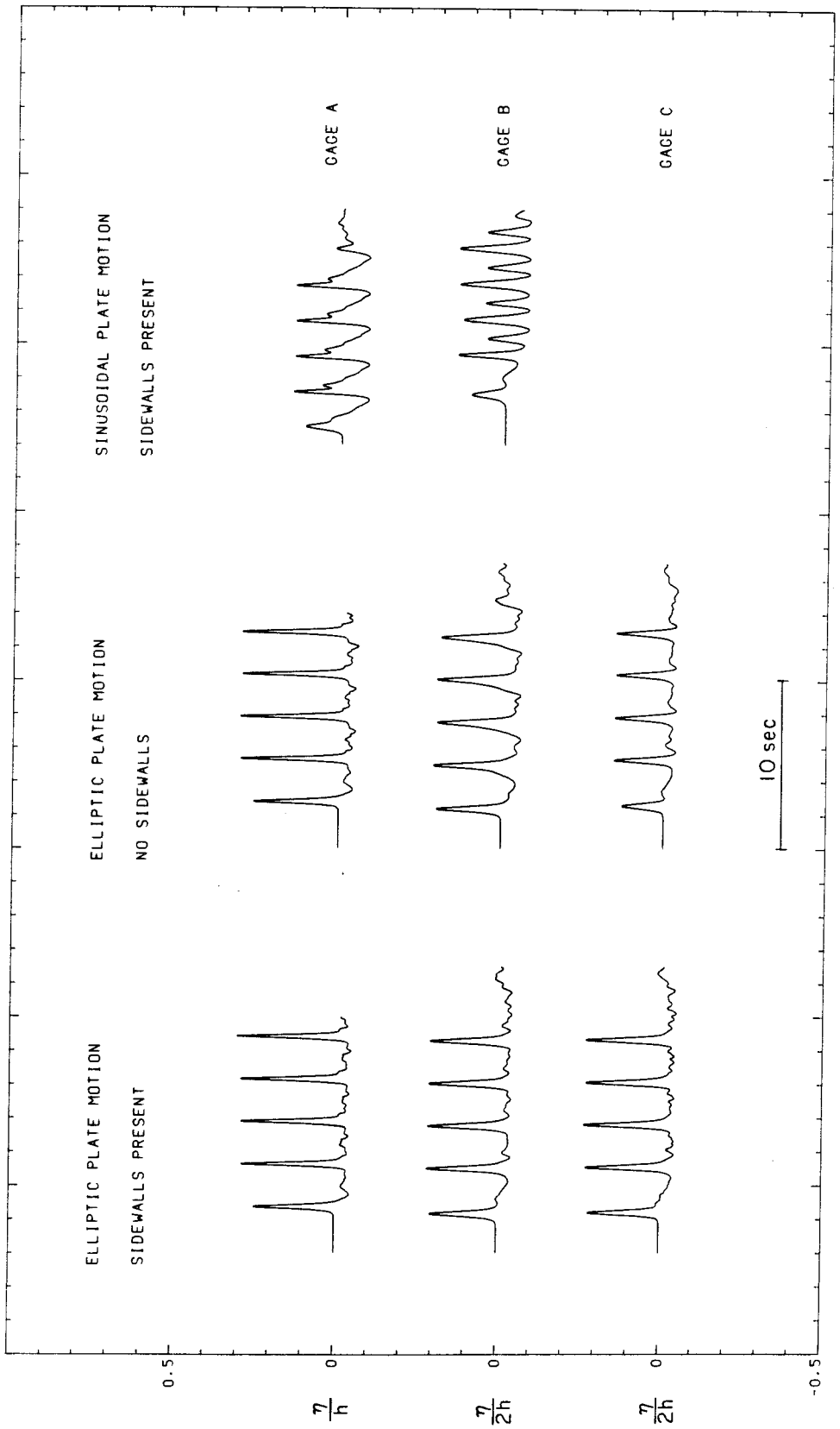

Fig. 6.1.8 Shape of cnoidal waves at locations A, B, C for H/h = 0.5, h = 6 cm, S_p = 5.8 cm, T = 2.51 s.

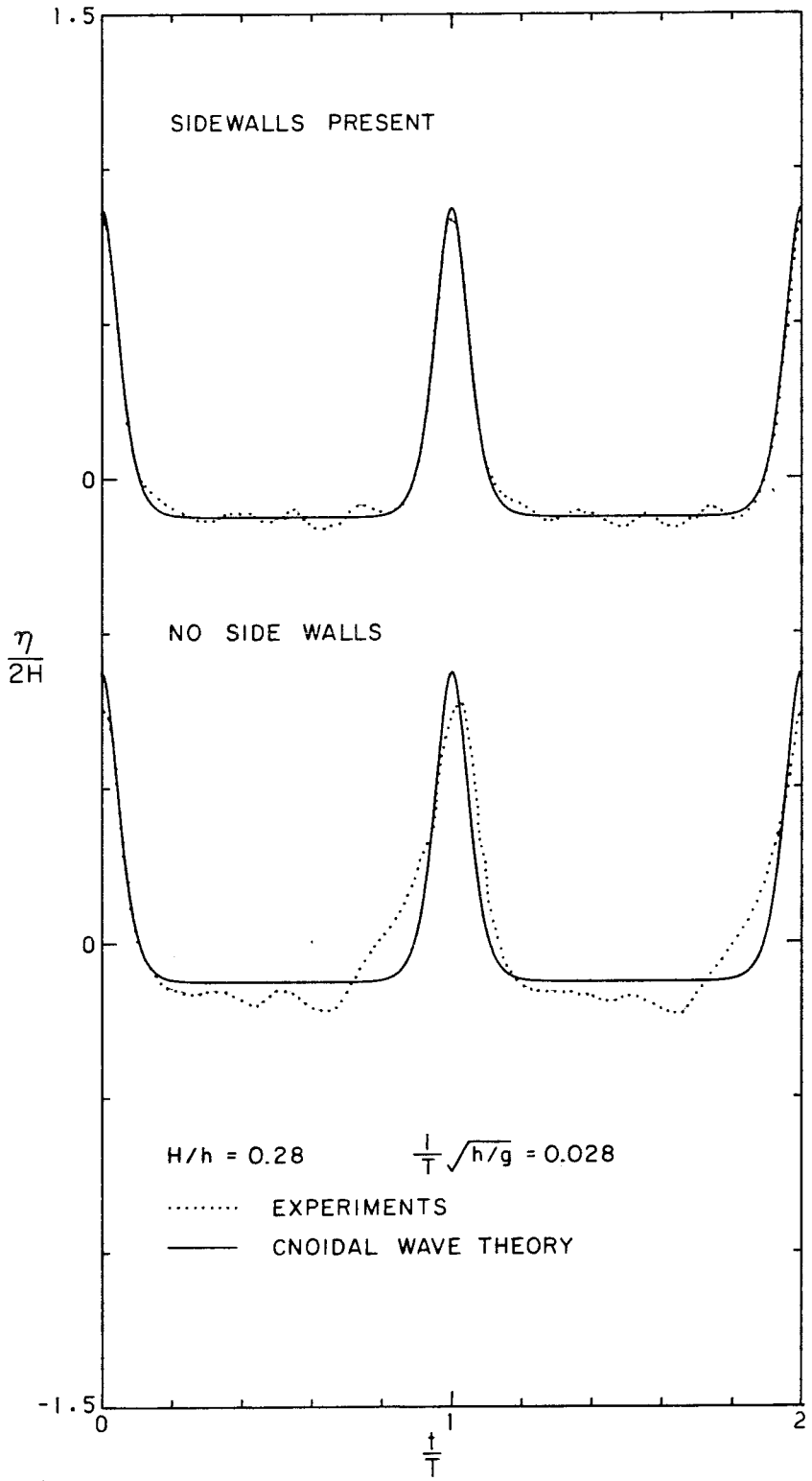

Fig. 6.1.9 Comparison of the shape of cnoidal waves at coastline on the centerline of the basin with the cnoidal wave theory, with and without sidewalls, h = 6 cm, T = 2.51 s.

periodic train of long waves. The resulting wave does not have a proper balance between nonlinearities and dispersion (the imbalance increases with the Stokes number), and, therefore, it changes as it propagates. Conversely, the proper elliptic motion of the plate generates a wave with a permanent form, so that the resulting shape at the coastline closely resembles that near the plate. The effects of diffraction through the wave absorbers remain fairly small for a cnoidal wave group so that the energy content and the shape of the waves near the coastline on the centerline of the basin can be controlled fairly well by the plate generation parameters. These cnoidal waves have the additional advantage of containing a dominant frequency which is convenient for the study of resonance in a harbor.

All the experimental results dealing with the harbor study which will be presented here were performed using cnoidal waves. In the case of the continuous excitation of the harbor (Section 6.3) a continuous train of cnoidal waves was generated. In the case of a transient excitation (Section 6.4) a small number of cnoidal waves was generated and then the wave plate was brought to rest.

6.2 Experiments on Leakage and Entrance Dissipation

A correct interpretation of the experimental results obtained in the laboratory for the problem of wave dynamics of a rectangular harbor requires a quantitative knowledge of the effect on the response of various dissipation mechanisms. The dissipation effects related to boundary friction and surface tension have already been presented and discussed in Section 5.1 in connection with the study of the water surface oscillations induced in a moving closed rectangular basin. Two

additional sources of dissipation have been investigated experimentally and are discussed in this section: the losses due to leakage under the boundaries of the model harbor and losses due to flow separation at the entrance. (The former is a loss which is generally peculiar to experimental facilities.)

6.2.1 Introduction

In the analysis presented in Section 3.3 the response of a narrow rectangular harbor to a plane harmonic incident wave was obtained analytically from a linear theory. Various sources of energy dissipation were included in a model, such as boundary friction, leakage underneath the walls and losses due to flow separation at the entrance. Two other undetermined parameters, namely the average gap thickness e underneath the walls and the entrance friction coefficient f_e, were included in the solution. An experimental method is presented in this section for evaluating these two parameters. It is based on the reduction near a resonant frequency of the wave elevation inside the harbor caused by dissipation.

Using the notations of Section 3.3 the expression for the wave amplitude A at the backwall is given by:

$$R = \left| \frac{\hat{\eta}_3(-L,0)}{A_I} \right| = |Y| \frac{a}{b} \left[\frac{1}{|\sin kL|} \right] + O(\varepsilon, \mu_t) \qquad (6.2.1)$$

where the normalized average velocity $|Y|$ at the harbor mouth is:

$$|Y| = \frac{\sigma|\hat{u}_3|}{kg\ A_I} = \frac{1}{[B^2 + (\chi_r + \chi_\mu + \chi_\varepsilon + \chi_f)^2]^{1/2}} \qquad (6.2.2)$$

and χ_r, χ_μ, χ_ε, χ_f represent the effects of radiation damping, viscous boundary friction, leakage losses, and entrance separation losses, respectively, and are defined by Eqs. (3.3.80) through (3.3.83); the quantity B is defined in Eq. (3.3.79). The gap e is contained in the term χ_ε and the entrance loss coefficient f_e is incorporated in the term χ_f. Usually each of these dissipation terms is of order less than unity so that the quantity $|Y|$ remains of order unity except for some values of L/λ for which $B = 0$. Then $|Y| = O(\frac{1}{\Sigma\chi_i})$ and resonant conditions are obtained in the harbor. For simplicity of notation the amplitude $|\hat{n}_3(-L,0)|$ of the wave elevation at the back wall and the amplitude $|\hat{u}_3|$ of the velocity at the harbor mouth will be denoted as A and U_e, respectively, in the subsequent discussion.

The variation of the amplification factor R with the dimensionless wave number kL is presented in Figure 6.2.1, from the linear theory, for a fully open harbor with an aspect ratio b/L equal to 0.2 in the absence of viscous dissipation (i.e., $X_\mu = X_\varepsilon = X_f = 0$). Resonance takes place for kL = 1.3, 4.2 and 7.15. Those values of kL are reasonably close to those corresponding to the limiting case where b/L = 0, which yields $kL = \frac{\pi}{2}, \frac{3\pi}{2}, \frac{5\pi}{2}$, respectively.

The method used to obtain the gap width e and/or the entrance friction coefficient f_e consists of obtaining the amplification factor R from experiments computed as the ratio of the first harmonic component of the steady state oscillation at the back wall to the first harmonic component of the steady state oscillation at the coastline on the centerline of the basin with closed harbor entrance. Equations (6.2.1) and (6.2.2) can then be solved for χ_ε or χ_f, assuming all other terms in the equation

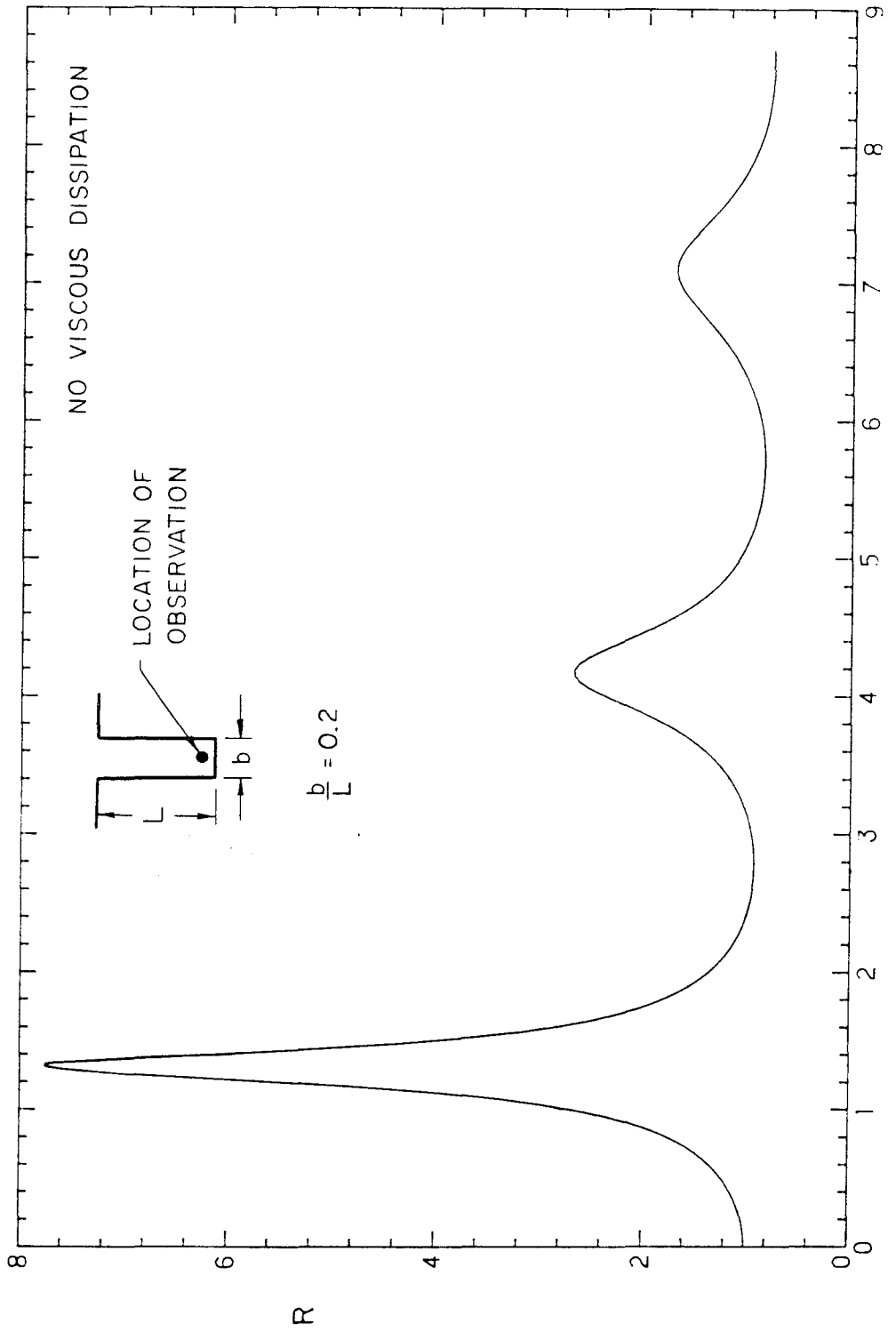

Fig. 6.2.1
Variation of the amplification factor with kL in the absence of viscous dissipation, case of a fully open rectangular harbor with b/L = 0.2.

are known. In order to achieve maximum accuracy it was important to conduct the experiments near a resonant frequency for the following reason. Equation (6.2.2) can be rewritten as:

$$|Y| = \frac{1}{(B^2 + \chi^2)^{1/2}} \tag{6.2.3}$$

where χ denotes the sum of the dissipative terms χ_i. Differentiating $|Y|$ with respect to χ yields:

$$\frac{d|Y|}{d\chi} = \frac{|\chi|}{(B^2 + \chi^2)^{3/2}} \tag{6.2.4}$$

The ratio $d|Y|/d\chi$ is a maximum for $B = 0$, that is, at resonance. Therefore, the sensitivity of the amplification factor to dissipation is the highest at (or near) resonance, thus the evaluation of dissipation is most accurate near resonance.

It is recalled that the derivation presented in Section 3.3 (and hence the method presented in this section) to evaluate the gap width and the entrance loss coefficients are determined from a linear theory which neglects convective nonlinearities in the equations of motion. It will be shown in Section 6.3 that such an assumption near resonance is completely invalid when the harbor length L becomes comparable to the incident wavelength λ. However, it is reasonable for ratios of L/λ about 0.25, i.e., near the first resonant mode. As an indication of the linear response of a narrow rectangular harbor near the first resonant mode, the transient response to an incident train of sinusoidal waves was computed at the back wall of a fully open rectangular harbor for the following conditions: $b/L = 0.2$, $h/\lambda = 0.05$, $\sigma L/\sqrt{gh} = 1.3$, $(A_1/h)_o = 0.05$;

no viscous effects were included in the calculations. The time history of the normalized wave elevation η/h, computed from the linear theory (Section 3.3) is plotted as a function of the dimensionless time $\sigma t/2\pi$ in Fig. 6.2.2 and compared to the curve obtained from the nonlinear dispersive theory (Section 3.4). (The curve for $\sigma L/\sqrt{gh} = 0$ corresponds to the incident wave system, i.e., L = 0.) The two curves shown for $\sigma L/\sqrt{gh} = 1.3$ agree well both in shape and in amplitude; the wave height computed from the nonlinear theory is slightly smaller than the one resulting from the linear theory, but this constitutes the only apparent discrepancy. In particular, very little harmonic distortion is noted with regard to the results of the nonlinear theory, although the relative wave height of the oscillations reaches 0.7. This comparison suggests that convective nonlinearities can reasonably be neglected at the first resonant mode for the case shown. This is an important aspect of the problem which will be discussed more fully later.

The experimental results concerning the effects of leakage under the harbor boundaries due to a gap and flow separation at the entrance are presented in the following two sections (6.2.2 and 6.2.3).

6.2.2 Leakage losses

Leakage losses arise in the laboratory from the presence of a small gap between the walls of a harbor model and the bottom of the wave basin. For the experiments dealing with the continuous excitation of a harbor, the walls were not sealed. (The reasons for this will become apparent when the results are presented in Section 6.3.) The purpose of the experiments presented in this section was to determine the average gap width, e, so that the leakage loss coefficient ε defined

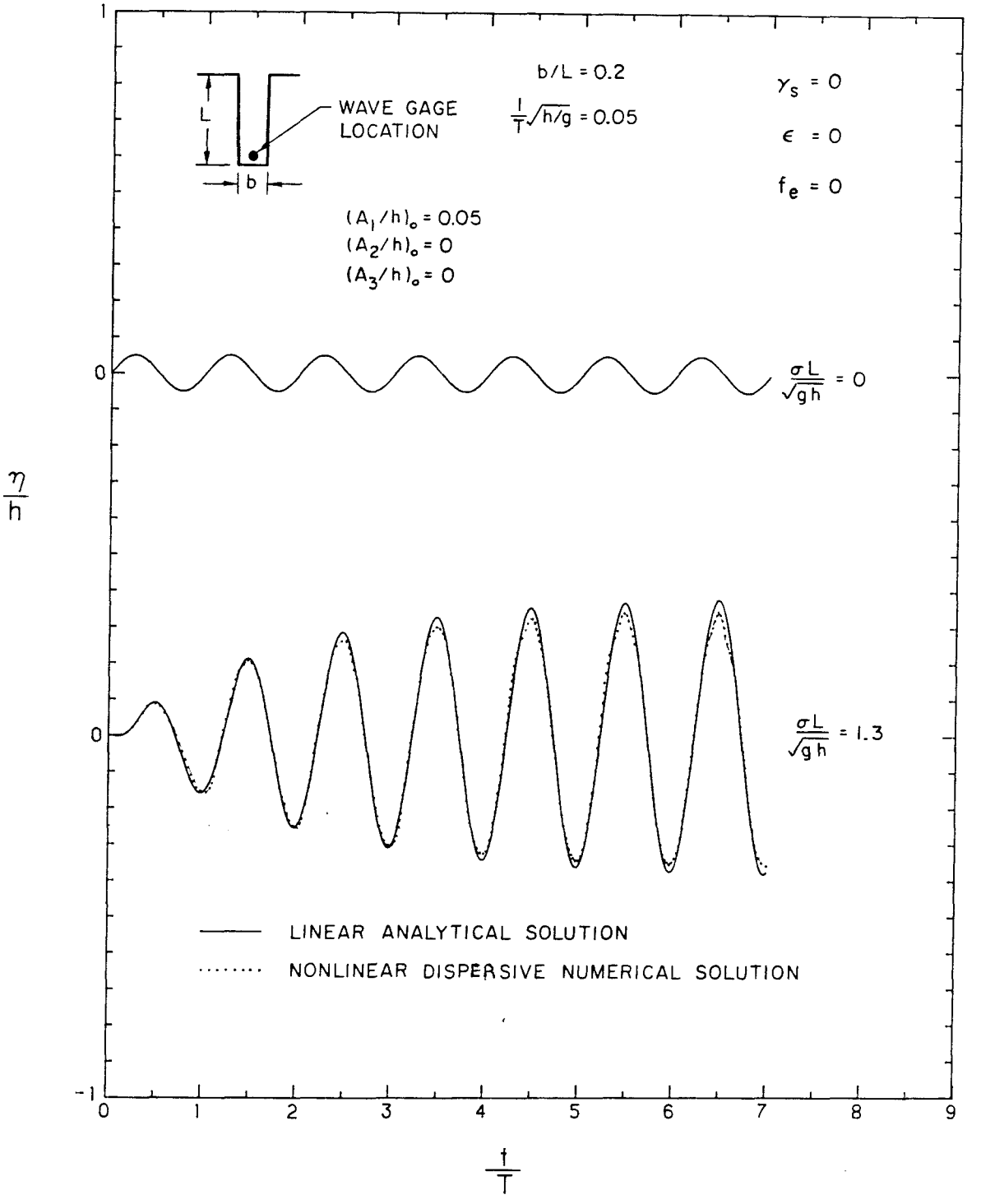

Fig. 6.2.2 Transient response of a fully open rectangular harbor with a sinusoidal excitation at the first resonant mode b/L = 0.2, comparison between linear theory and nonlinear theory.

by Eq. (3.3.40) could be defined. A fully open harbor was used for all the experiments; the width b and the length L were set to 8 cm and 40 cm, respectively for all experiments. The corners of the mouth were rounded with a 5 cm radius to minimize losses due to flow separation at the entrance. A finite element harmonic analysis (Lepelletier, 1978) was used to determine that the round corners used for the experiments did not appreciably modify the harbor response computed with sharp corners at the entrance.

Three series of experiments were performed using depths of 10 cm, 8 cm, and 6 cm. Each series consisted of five experiments which differed from one another by the height of the incident wave. Each experiment consisted of three runs: First the incident wave elevation was recorded at the coastline on the centerline of the basin with the harbor entrance closed. In the second run the entrance was opened and the wave was recorded at the back wall of the harbor without sealant between the walls and the wave basin bottom. In the last run the same measurement was taken after the harbor walls had been sealed to the basin bottom with mastic. The period of the incident waves was set such that $\sigma L/\sqrt{gh} = 1.3$, corresponding to resonant conditions for the first mode of oscillation of the harbor.

A convenient parameter which provides a measure of the energy contained in a periodic wave with period T is the equivalent relative wave amplitude $\sqrt{E_a}/h$ defined such that

$$E_a = \frac{2}{T}\int \eta^2 \, dt \qquad (6.2.5)$$

Parseval's identity yields:

$$E_a = \frac{A_o^2}{2} + \sum_{i=1}^{\infty} A_i^2 \qquad (6.2.6)$$

where A_i denotes the amplitude of i^{th} harmonic component. For a purely sinusoidal wave with zero mean value, $\sqrt{E_a}$ is just equal to the amplitude of the wave, i.e., A_1.

The steady state characteristics of the incident wave at the coastline (with the harbor entrance closed) within one period are given in Table 6.2.1 for the experiment conducted.

Table 6.2.1

Table 6.2.1 Steady state characteristics of the incident wave at the coastline

h (cm)	T (sec)	$h/\sqrt{gh}\ T$	$(\sqrt{E_a}/h)_I$	A_1/h	A_2/h	A_3/h
10	2.0	0.05	0.008	0.0079	0.000	0.000
			0.015	0.014	0.001	0.000
			0.026	0.025	0.003	0.000
			0.038	0.037	0.005	0.000
			0.051	0.05	0.006	0.000
8	2.29	0.04	0.012	0.012	0.001	0.000
			0.019	0.012	0.003	0.000
			0.03	0.03	0.001	0.002
			0.04	0.037	0.011	0.004
			0.07	0.064	0.026	0.016
6	2.64	0.03	0.02	0.018	0.006	0.002
			0.03	0.026	0.011	0.003
			0.045	0.038	0.022	0.005
			0.06	0.49	0.031	0.012
			0.08	0.06	0.043	0.02

It is seen from Table 6.2.1 that the relative importance of higher harmonics increases as $\sqrt{E_a}/h$ increases and as the depth decreases. This is in accordance with the cnoidal wave theory: for a cnoidal wave the relative importance of higher harmonics increases as the Stokes number increases.

The variation of the experimental amplification factor R (defined as the ratio of the steady state amplitude of the first harmonic component at the back wall to the steady state amplitude of the first harmonic component at the coastline (with the harbor entrance closed) with $(\sqrt{E_a}/h)_I$ is denoted by hollow circles in Fig. 6.2.3. It is seen that, for a small amplitude wave, i.e., a small abscissal value, R decreases as $(\sqrt{E_a}/h)_I$ decreases. This indicates the effect of a dissipation source which increases with decreasing wave amplitude. The only source of dissipation discussed herein which has this feature appears to be dry friction related to surface tension without a wetting agent. In order to correct the experimental data for this effect the procedure discussed in Section 3.2 can be applied here. The factor R_c associated with dry friction can be obtained from Eq. (E37) in Appendix E and Eq. (3.3.99) as:

$$\frac{1}{R_c} = \frac{8}{\pi} \frac{\bar{\kappa}}{\rho g A} \Gamma_e \frac{1}{b} \left(1 + \frac{\pi}{4} \frac{b}{L}\right) \tag{6.2.7}$$

where $\bar{\kappa} = 0.35$. The amplification factor R, corrected for this effect, is given by: $1/(1/R - 1/R_c)$, and the corrected data are denoted by the solid circles in Fig. 6.2.3. For reference the computed amplification factor affected by radiation and laminar boundary friction only is indicated by a dashed line in each portion of the figure.

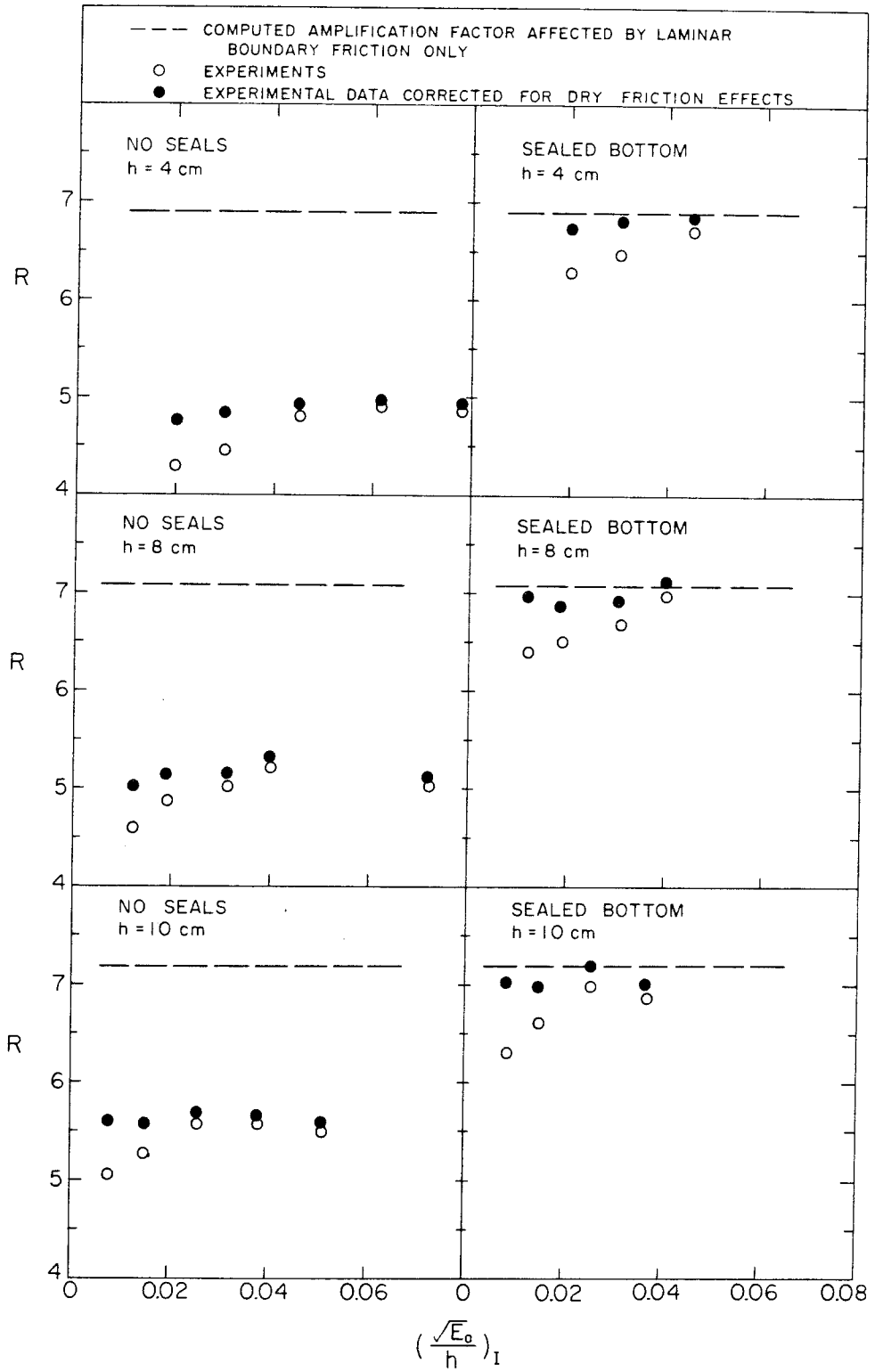

Fig. 6.2.3 Variation of the amplification factor R with $(\sqrt{E_a}/h)_I$, with and without the walls of the rectangular harbor sealed to the bottom.

It is seen that for a given depth, the corrected values for the amplification factor remain fairly constant. For larger amplitude incident waves the response decreases, perhaps indicating an influence of entrance dissipation. A substantial reduction in the amplification factor due to leakage can be observed for each depth. With seals, for h = 10 cm, R is about seven, which is close to the value predicted by the linear theory, i.e., R = 7.2; without seals the response decreases to about 5.5 for these conditions. For h = 8 cm the amplification factor reaches a value close to seven with the bottom sealed and about 5.2 without seals. Finally, for h = 6 cm, R decreases from 7.7 with seals to less than 5 without seals.

Two major conclusions can be drawn from these results:

(i) Leakage losses cannot be neglected in the present study and they must indeed be incorporated in the theoretical models to be compared with the experiments.

(ii) In the absence of leakage the experimental data closely follow the results predicted by a linear theory. This supports the hypothesis that at the first resonant mode for a narrow harbor nonlinear convective terms are negligible.

From the experimental values of R the dissipation term χ_ε can be computed from Eq. (6.2.2), where χ_f is set equal to zero. The gap width is derived from χ_ε using Eqs. (3.3.82) and (3.3.40). (The wall width t_e in these experiments was 1.2 cm.) Those calculations yield the following results:

e = 0.041 cm for h = 10 cm

e = 0.045 cm for h = 8 cm

e = 0.043 cm for h = 6 cm

These three values for e are in reasonable agreement, and, thus, the average width of the gap is taken to be:

$$e = 0.043 \text{ cm.}$$

The gap, although of the right order of magnitude, appears fairly large. This is possibly due to the approximation made in Appendix D which led to the linear analytical expression for the "leaky" boundary condition. In particular with this value of e, expressions derived in Appendix D show that the neglected quadratic losses caused by the gap are about 25% of the total leakage losses. However, even if the analytical expression used for the leakage loss does not represent exactly the true loss mechanism, it allows a sufficiently accurate quantitative estimate to be made of that dissipation source. Hence it will be used in subsequent sections when comparing linear and nonlinear theories with experiments.

6.2.3 Separation Losses at the Entrance

Separation losses at the harbor entrance arise from an abrupt change in the geometry of the harbor at the mouth which induces flow separation, jet formation, and turbulent dissipation of energy. Unlike the loss of energy due to leakage beneath the harbor walls which usually only applies to laboratory conditions, entrance losses occur in both laboratory and prototype harbors. It also turns out to be one of the most efficient means of dissipating energy; this will be discussed more fully in Section 6.2.4.

The difference in elevation between each side of the entrance is expressed as:

$$\Delta\eta = \frac{f_e}{2g} |u|u \qquad (6.2.8)$$

The entrance loss coefficient f_e is not well defined for an oscillatory flow, and the purpose of this section is to determine this coefficient experimentally for a periodic flow such as that induced by the oscillation of a harbor.

Dimensional analysis shows that the coefficient f_e for a symmetric entrance opening depends in general on the following dimensionless parameters:

$$f_e = f_e \left(\frac{a}{b}, \frac{b}{L}, \frac{aU_e}{\nu}, \frac{U_e}{a\sigma}, \frac{H}{h}, S_h\right)$$

The physical significance of each of these parameters can be briefly discussed as follows:

(i) The opening ratio a/b is equal to the ratio of the mouth width a to the harbor width b. For a unidirectional, steady, fully turbulent flow, an estimate of the coefficient f_e for a/b = 1 can be obtained from one dimensional engineering hydraulics (e.g., Streeter, 1971). Table 6.2.2 shows the entrance coefficient for an inward steady flow and an outward steady flow through the harbor mouth. For the cases where the unsteady effects can be neglected, the entrance coefficient can be estimated for the harbor oscillation problem (for the fully open entrance) by taking the average of the values corresponding to the outgoing and the ingoing flow through the mouth.

(ii) The width ratio b/L does not depend on the geometric characteristics of the entrance and therefore should not affect, in principle, the coefficient f_e. (However, some of the

experiments showed some dependence in some cases, as will be seen shortly.)

Table 6.2.2 The postulated loss coefficient for a/b = 1 for a fully turbulent, steady flow for sharp edges (see Streeter, 1971)

a/b	1.0
(ingoing flow)	0.5
(outgoing flow)	1.0

(iii) The coefficient $U_e/a\sigma$ is proportional to the number of times a fluid particle travels distance a in half a period and thus can be interpreted as an inverse Strouhal number which provides a measure of the unsteadiness of the flow. For large values of $U_e/a\sigma$ separation flow has enough time to establish fully and the influence of the periodicity in f_e can be neglected. Conversely for small values of $U_e/a\sigma$ one would expect f_e to be strongly influenced by the periodicity of the flow.

(iv) The Reynolds number aU_e/ν is expected to influence the entrance loss coefficient only for relatively small values. As an indication, the flow resistance through a circular orifice into a large tank is unaffected by viscosity for $aU_e/\nu > 1000$ (Rouse, 1946). This critical value of 1000 can be used as a guide to estimate the importance of viscous effects in the present problem. In particular, at resonance the velocity at the entrance is related to the wave amplitude at the backwall by:

$$U_e = \frac{b}{a}\frac{A}{h}\sqrt{gh}$$

so that the relative minimum wave amplitude at the backwall required to neglect viscous effect at the entrance is:

$$\frac{A}{h} = 1000\,\frac{\nu}{b\sqrt{gh}}$$

For the present experiments $\nu = 0.01$ cm^2/sec, h = 10 cm, b = 7 cm, this gives A/h = 0.01. Therefore the influence of viscosity on f_e can be expected to remain small in most cases.

(v) The relative height ratio at the backwall of the harbor conceivably may affect the friction coefficient f_e for large values, as will be seen later.

(vi) The shape factor S_h characterizes the local geometry of the harbor at the opening. The influence of the local shape of the harbor around the mouth on the friction coefficient f_e is expected to be fairly significant since the wave dissipation directly depends on the separation pattern of the flow at the entrance which in turn is induced by the local harbor geometry.

Several series of experiments were performed by changing the planform and entrance gap of the harbor as defined by a/b and b/L. For each harbor configuration ten experiments were performed varying the incident wave height. (For all the experiments a water depth of 10 cm and a wave period of 2 sec were used.) The harbor configurations for each set of experiments are given by Table 6.2.3. They were chosen to satisfy the resonant conditions (in the absence of viscous dissipation) at the first mode of oscillation of the harbor (B = 0 in Eq. (6.2.2)).

The quantity r_e in Table 6.2.3 denotes the radius of the corners at the mouth for the fully open harbor and the radius of the rounded edges of the breakwaters for the partially closed harbor.

Table 6.2.3 Harbor characteristics for each series of experiments

b/L (nominal)	a/b (nominal)	a (cm)	b (cm)	L (cm)	r_e (cm)
.2	1.0	8.0	8.0	41.0	5.0
.2	1.0	8.0	8.0	41.0	0.5
.2	0.8	6.4	7.5	38.5	0.3
.2	0.6	4.6	7.5	37.0	0.3
.2	0.4	3.0	7.5	36.0	0.3
.2	0.2	1.5	7.5	35.0	0.3
.4	1.0	14.0	14.0	35.0	0.5
.4	0.2	2.5	12.5	31.0	0.3
.4	0.1	1.25	12.5	31.0	0.3

The characteristics of the incident wave at the coastline on the centerline of the basin (with the harbor mouth closed) are presented in Table 6.2.4. It can be seen that the relative importance of higher harmonics remains small for all wave heights.

Each experiment consisted of two runs: first, the incident wave was recorded at the coastline (with the harbor closed). In the second run the wave elevation was recorded at the backwall of the harbor. A harmonic analysis of the steady state oscillations was performed for each record. (For this set of experiments steady state conditions were obtained after about four or five oscillations.) The amplification

factor R was defined as before as the ratio of the steady state amplitude of the first harmonic component at the backwall to the steady state amplitude of the first harmonic component at the coastline. (R was corrected for the effects of dry friction using the same procedure as in Section 6.2.2). Equations (6.2.1) and (6.2.2) could then be solved for the entrance coefficient f_e related to the parameter χ_f by Eq.(3.3.83). Since all the experiments on entrance losses were performed before the importance of leakage losses was realized, the term χ_ε had to be included in Eq. (6.2.2) for a correct determination of f_e.

Table 6.2.4 Characteristics of incident waves at the coastline

$(\sqrt{E_a}/h)_I$	A_1/h	A_2/h	A_3/h
0.029	0.0286	0.003	0.000
0.042	0.0415	0.005	0.002
0.055	0.0572	0.007	0.002
0.067	0.0659	0.011	0.004
0.090	0.0895	0.009	0.003
0.110	0.109	0.010	0.004
0.132	0.130	0.020	0.007
0.165	0.163	0.021	0.009
0.201	0.194	0.038	0.016
0.229	0.223	0.038	0.032

To appreciate the effects of entrance dissipation on resonance, the variation of the amplification factor R with $(\sqrt{E_a}/h)_I$ is presented in Fig. 6.2.4 for each harbor configuration. On each graph the dashed

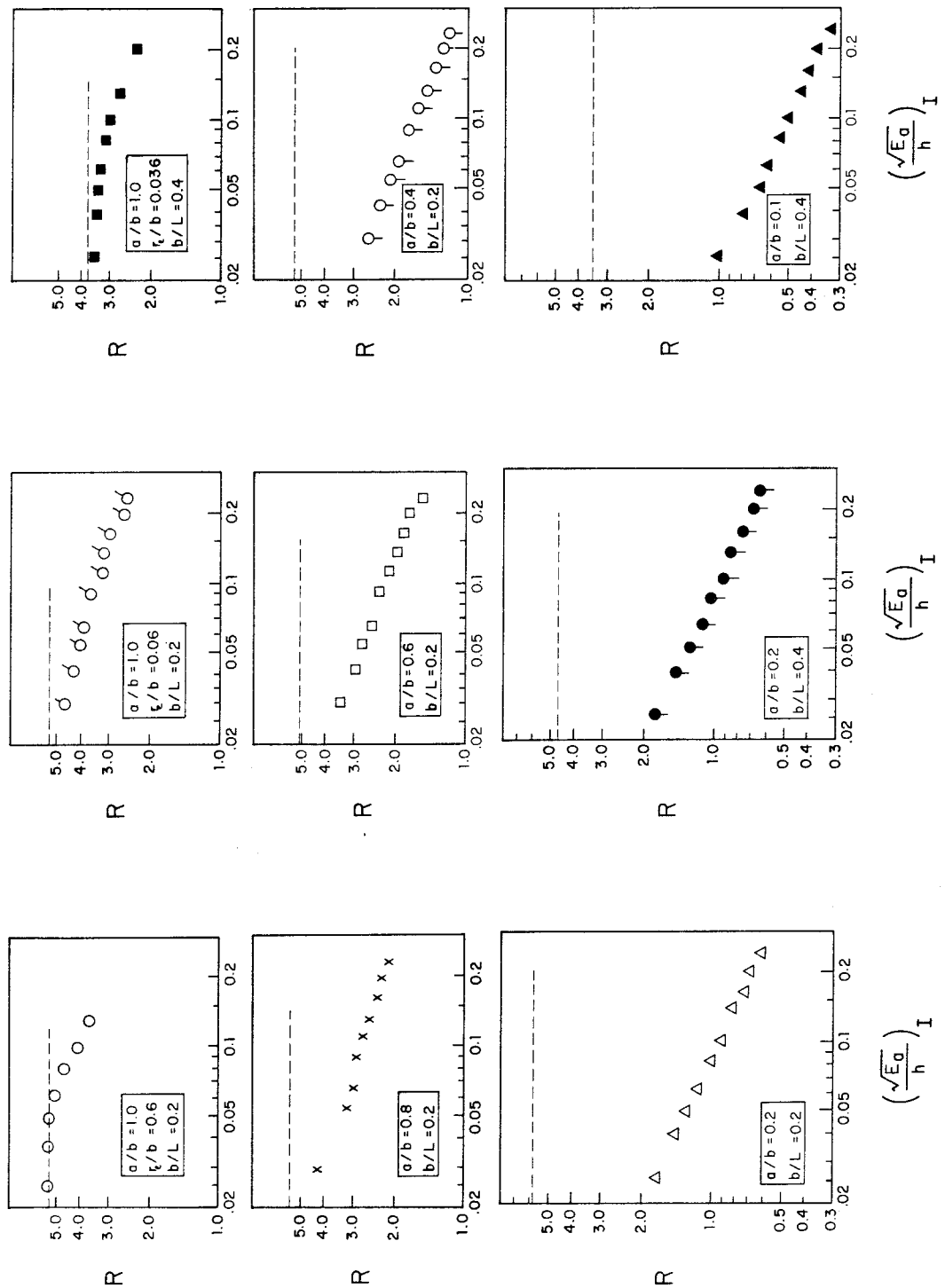

Fig. 6.2.4 Variation of the amplification factor R with $(\sqrt{E_a}/h)_I$ for various shapes of the rectangular harbor.

line indicates the values of the amplification factor which includes the effects of radiation, viscous boundary friction, and leakage losses. The symbols represent the experimental data. For the fully open harbor with large corner radii at the entrance ($r_e/b = 0.6$) the experiments coincide with the dashed line for small incident wave heights. This shows that entrance dissipation is apparently negligible for these cases. However, as $(\sqrt{E_a}/h)_I$ increases, R begins to decrease indicating that entrance dissipation begins to manifest itself for larger values of incident wave heights. For a fully open harbor with corners with small radii ($r_e/b = 0.06$) the response decreases with $(\sqrt{E_a}/h)_I$ for the full range of the abscissa, indicating that entrance dissipation affects all the measurements for these experiments.

For a partially closed harbor ($a/b < 1$) the difference between experimental values of R and values indicated by the dashed lines (for which no entrance losses are included) increases as the opening ratio a/b decreases for a fixed incident wave height; it also increases with $(\sqrt{E_a}/h)_I$ for a given opening ratio. Actually, resonance as defined here is suppressed for almost all wave heights for $a/b \leq 0.2$. An interesting feature, when entrance loss becomes significant, is the common slope, i.e., $-\frac{1}{2}$, for all experimental curves. This implies that R varies inversely as the square root of $(\sqrt{E_a}/h)_I$ when entrance loss becomes the dominant dissipative mechanism. (This feature will be explained simply later).

The variation of the entrance loss coefficient with the parameter $U_e/a\sigma$ derived from the experimental data of Fig. 6.2.3 is presented in Fig. 6.2.5 for the case of the fully open harbor. The velocity at the entrance was computed from the experimental amplification factor R,

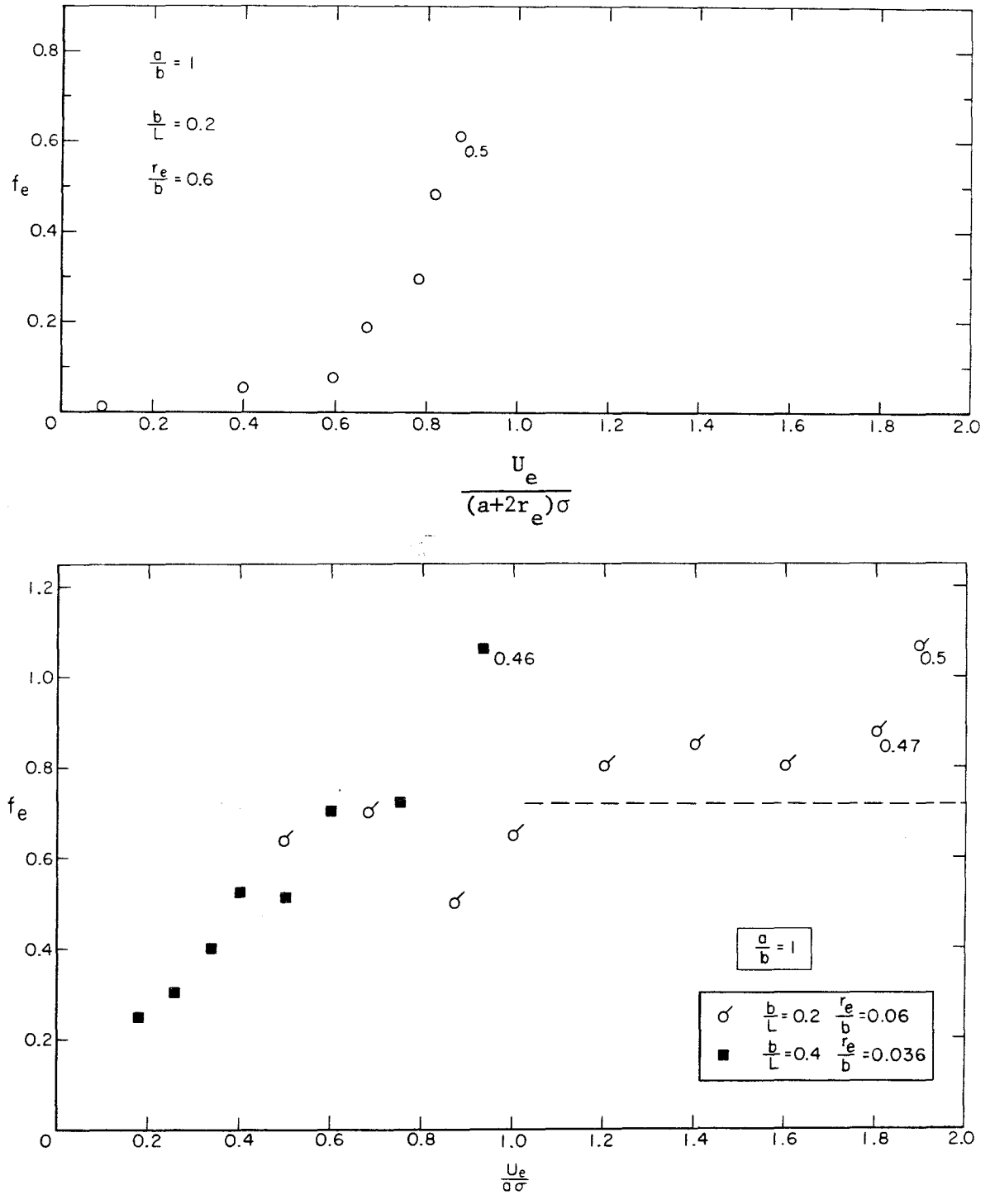

Fig. 6.2.5 Variation of f_e with $U_e/a\sigma$ for fully open harbor (the horizontal dashed line indicates the averaged steady state value).

using Eq. (6.2.1). Considering first the harbor with small corner radii ($r_e/b = 0.06$), the entrance loss coefficient f_e varies in a linear manner with $U_e/a\sigma$ and reaches a constant value equal to approximately 0.8 as $U_e/a\sigma$ becomes greater than 1. The data corresponding to $b/L = 0.2$ and $b/L = 0.4$ seem to agree fairly well with each other, which tends to indicate, as expected, that f_e is not a function of the aspect ratio b/L. The numbers next to the symbols in the upper and lower portions of Fig. 6.2.5 indicate values of the relative wave amplitude at the backwall greater than 0.45. For these extreme wave heights the coefficient f_e takes higher values, which indicate, in the absence of any additional source of dissipation, that f_e may become also a function of the wave amplitude in the harbor for some extreme conditions. Ignoring the points for which the relative wave amplitude is greater than 0.45, the shape of the curve can be interpreted from visual observation as follows. For values of the parameter $U_e/a\sigma$ less than unity, losses are induced by vortices at each corner of the entrance. If $U_e/a\sigma$ is further increased, flow separation becomes apparent and a well-formed jet in addition to the vortices is observed during the first half period when the flow is directed inwards in the harbor. The same jet pattern develops again during the second half period when the flow is directed outwards. Once flow separation is well formed, the entrance loss coefficient remains relatively constant as seen in Fig. 6.2.5.

For large radius corners at the entrance ($r_e/a = 0.6$) a relevant measure of the unsteady parameter is $U_e/(a+2r_e)\sigma$ where an effective width of the mouth is considered. It is seen from the lower part of Fig. 6.2.5 that f_e remains negligible for small values of the unsteady parameter and then f_e increases gradually. For all experiments $U_e/(a+2r_e)\sigma$ remains

less than unity and the only experimental evidence of energy dissipation which was observed was the formation of vortices without "clean cut" jet formation.

Figure 6.2.6 shows the variation of f_e with $U_e/a\sigma$ for partially closed harbors and two harbor planforms. For a/b = 0.8, f_e seems to increase linearly until $U_e/a\sigma = 1.3$ and then remains constant, i.e., $f_e = 1.10$. For a/b = 0.6, the experimental variation of f_e with $U_e/a\sigma$ remains small. It is noted that the unsteady parameter $U_e/a\sigma$ is greater than unity for all values of $U_e/a\sigma$. For a/b = 0.4, the range of variation of f_e with $U_e/a\sigma$ is rather large (between 1.10 and 1.30), but no definite trend can be observed.

For a/b = 0.2, the experimental data corresponding to b/L = 0.4 are definitely distinct from those corresponding to b/L = 0.2 even if this difference remains relatively small. Part of this discrepancy possibly may be attributed to the small physical scale of the present model harbor. For b/L = 0.2, the distance between the edge of the breakwater and the sidewalls of the harbor is only 2.5 cm whereas it is about 5 cm for b/L = 0.4.

From these experimental results, two regimes seem to take place, at least for the fully open harbor. In the first regime, corresponding to $U_e/a\sigma < 1$, full flow separation does not have time to take place within half a wave period and dissipation is induced by vortex formation at the corners of the entrance, and f_e seems to grow linearly with $U_e/a\sigma$. In the second regime, corresponding to $U_e/a\sigma \geq 1$, the flow appears to separate from the boundary and a jet forms. (These conclusions are based on direct observation.) The data indicate the influence of the periodicity of the flow does not seem as important for this region and f_e remains constant as $U_e/a\sigma$ increases.

For the partially closed harbor, only limited data are available

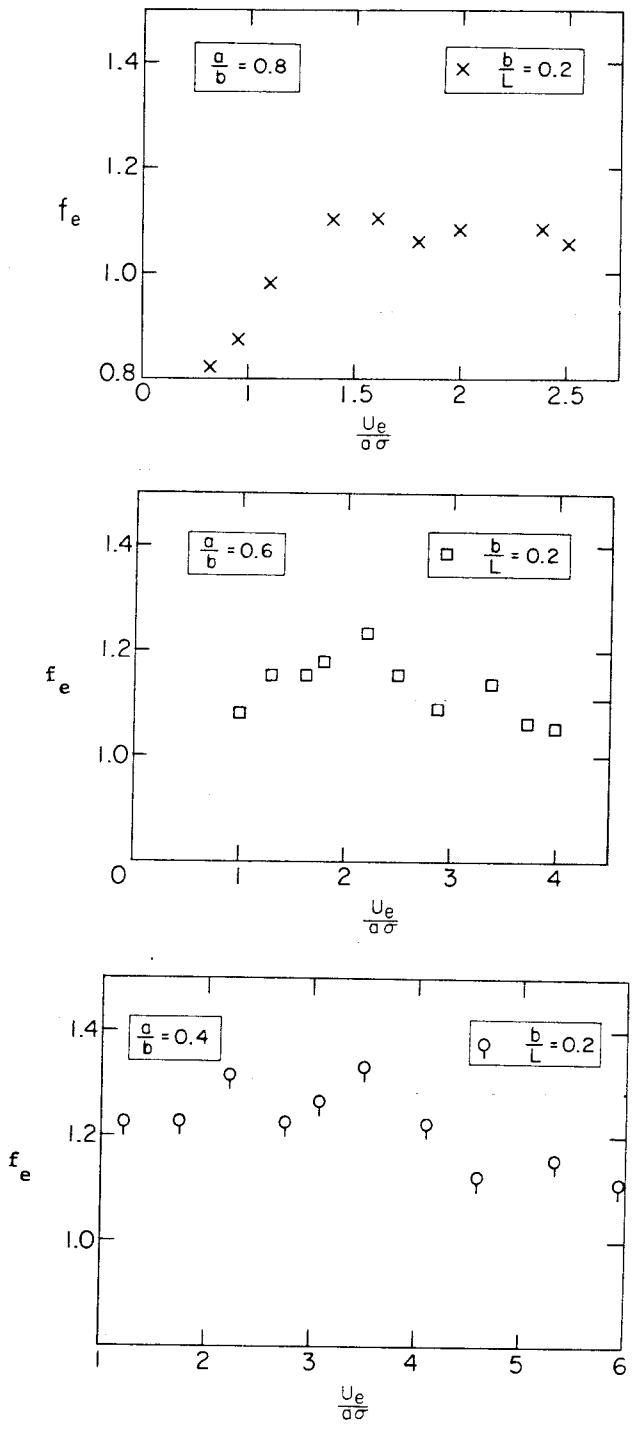

Fig. 6.2.6 (a) Variation of f_e with $U_e/a\sigma$ for a partially closed harbor; a/b = 0.8, 0.6, 0.4

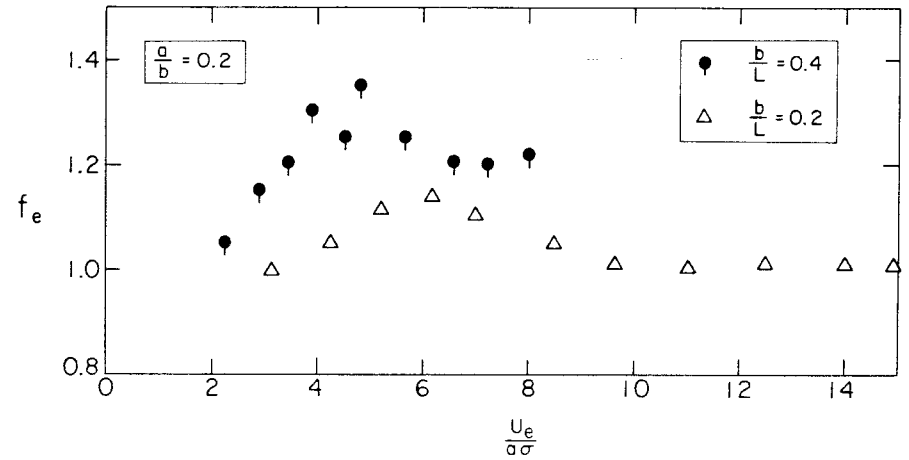

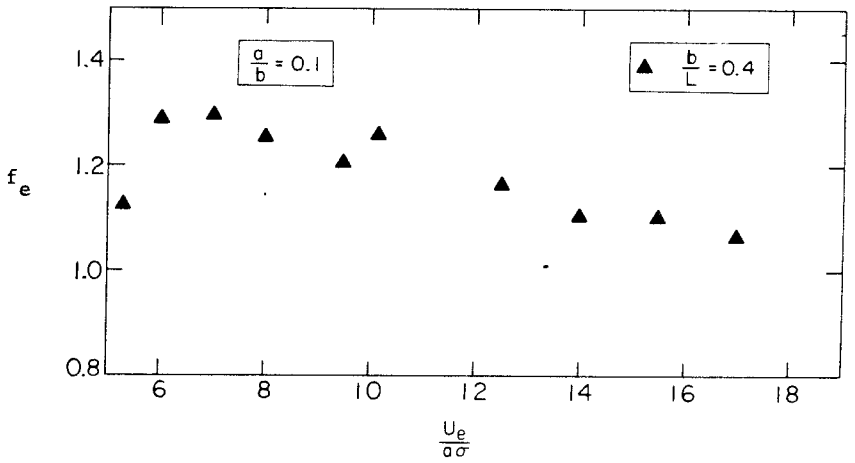

Fig. 6.2.6 (b) Variation of f_e with $U_e/a\sigma$ for a partially closed harbor; a/b = 0.2, 0.1

which support this conclusion, since most of the data correspond to values of $U_e/a\sigma$ greater than one. It was not possible to operate in the region $U_e/a\sigma < 1$ for $a/b \leq 0.6$ because on the one hand the resulting wave amplitude to be measured would have been very small and therefore the measurements somewhat inaccurate, and on the other hand the effects of viscosity (the Reynolds number) on the entrance loss coefficient f_e would probably begin to be important. It should be mentioned, the jet flow was observed for all cases of the partially closed harbor for $U_e/a\sigma > 1$.

The range of variation of the Reynolds number for each harbor configuration is indicated in Table 6.2.5. For all cases investigated $U_e a/\nu$ remains larger than 10^3 which suggests that viscosity has little effect on the entrance loss coefficient for the present experiments. According to Ingard and Ising (1967) the viscous contribution to orifice resistance for an accoustical wave becomes unimportant for flow velocities much greater than $(8\sigma\nu)^{1/2}$. This condition is always fulfilled in the present experiments.

Table 6.2.5 Range of variation of the Reynolds number $U_e a/\nu$ for each harbor configuration

a/b	b/L	$U_e a/\nu$ (min)	$U_e a/\nu$ (max)
0.8	0.2	8500	35000
0.6	0.2	7000	28000
0.4	0.2	5000	20000
0.2	0.2	2200	11000
0.2	0.4	4600	15000
0.1	0.4	11000	57000

With the results of Figures 6.2.5 and 6.2.6 in mind a simplified representation of the variation of f_e with $U_e/a\sigma$ is postulated.

The corresponding equations are:

(i) For fully open harbor with small corners radii:

$$f_e = \begin{cases} 0.8 \quad U_e/a\sigma & \text{if} \quad U_e/a\sigma < 1 \\ 0.8 & \text{if} \quad U_e/a\sigma \geq 1 \end{cases} \tag{6.2.9}$$

(ii) For partially closed harbor: $(a/b \leq 0.8)$

$$f_e = \begin{cases} 1.15 \quad U_e/a\sigma & \text{if} \quad U_e/a\sigma < 1 \\ 1.15 & \text{if} \quad U_e/a\sigma \geq 1 \end{cases} \tag{6.2.10}$$

Two remarks can be made here. First, for a partially closed harbor the dependence of f_e on the opening ratio a/b is dropped in Eq. (6.2.10). The validity of this simplification for the harbor oscillations will be investigated shortly. Second, in all experiments on entrance dissipation the parameter $U_e/a\sigma$ was varied leaving σ approximately constant because of experimental constraints (see Sec 6.1). Whether or not the same conclusions would be obtained if $U_e/a\sigma$ was changed by varying σ but leaving U_e constant, although this is postulated here, remains to be proved experimentally.

In order to check whether or not Eqs. (6.2.9) and (6.2.10) provide a reasonable description of the experimental results the amplification factor has been computed by solving Eq. (6.2.1) using Eqs. (6.2.9) and (6.2.10) for each case, which is defined by the incident-reflected wave amplitude at the coastline and by the harbor geometry. The variation of the computed values of the amplification factor, R, with those obtained

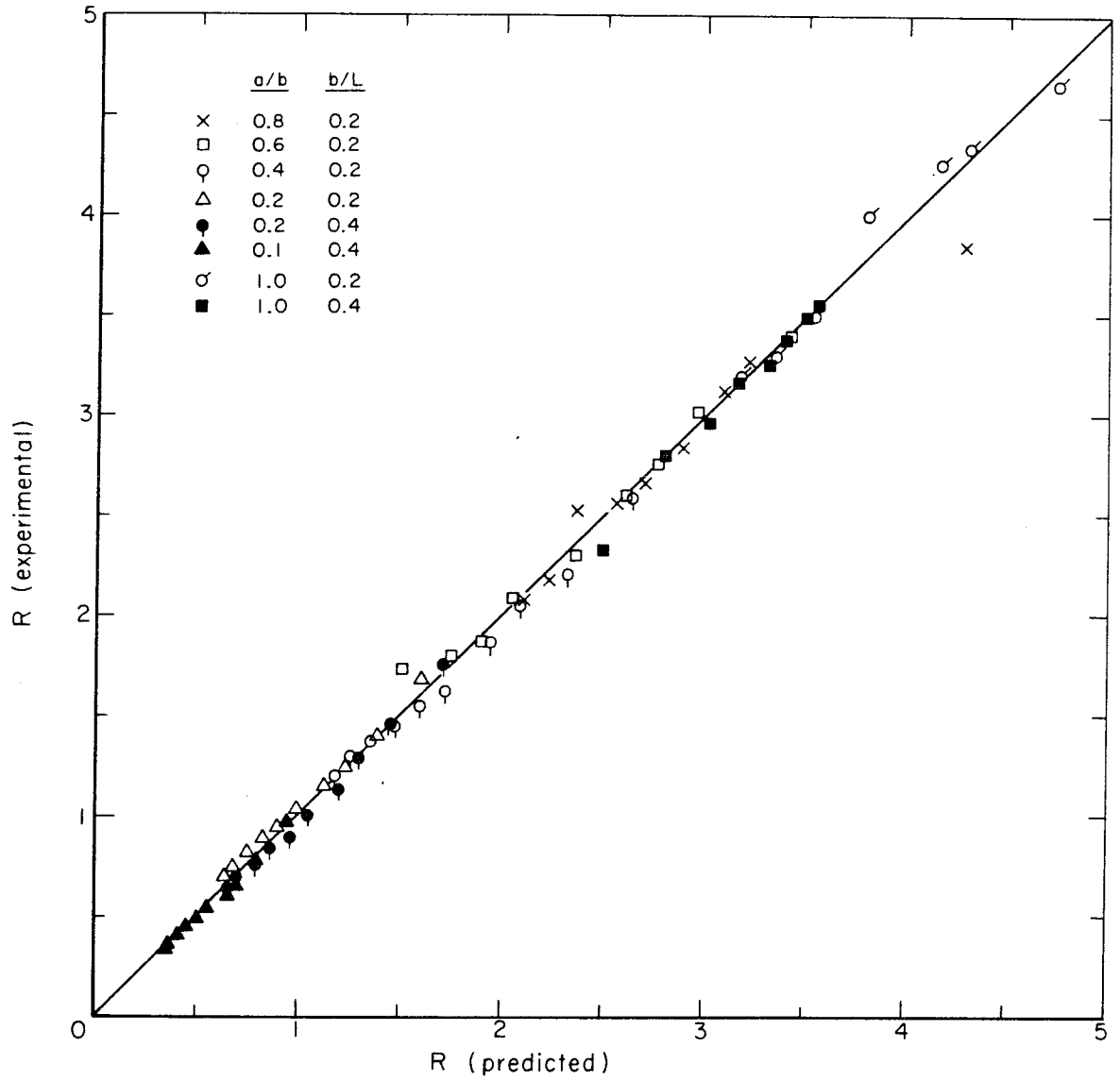

Fig. 6.2.7 Comparison between predicted and experimental values of the amplification factor near the first resonant mode.

experimentally is presented in Fig. 6.2.7. It is seen that almost all points lie close to the line which represents perfect agreement between the predicted and experimental values of R. The effects of entrance dissipation further can be characterized considering a situation where the most important dissipation source is entrance friction. That is, it is assumed momentarily that the dissipation parameters, χ_r, χ_μ, and χ_ε can be neglected in Eq. (6.2.2) when compared to χ_f and $B \simeq 0$. Therefore Eq. (6.2.2) becomes:

$$|Y| = \frac{1}{\chi_f} \tag{6.2.11}$$

Substituting the expression (3.3.83) for χ_f yields, from Eq. (6.2.11), the following expression for $|Y|$.

$$|Y| = \left(\frac{6\pi}{8}\right)^{1/2} \frac{1}{\sqrt{f_e}} \frac{1}{\sqrt{A_I/h}} \tag{6.2.12}$$

Using Eq. (6.2.1) and taking $kL = \pi/2$, the amplification factor at the backwall becomes:

$$R = \left(\frac{6\pi}{8}\right)^{1/2} \frac{a}{b} \frac{1}{\sqrt{f_e}} \frac{1}{\sqrt{A_I/h}} \tag{6.2.13}$$

Several comments can be drawn from Eq. (6.2.13) for the case where entrance separation plays a significant role. The amplification factor R decreases linearly with a/b, which clearly demonstrates the irrelevancy of the harbor paradox which predicts a contrary behavior. R varies also like the inverse of the square root of the incident wave amplitude. (Of course, there is a limit to the applicability of Eq. (6.2.13) as A_I/h decreases.) This feature can be verified for all curves on Fig. 6.2.4

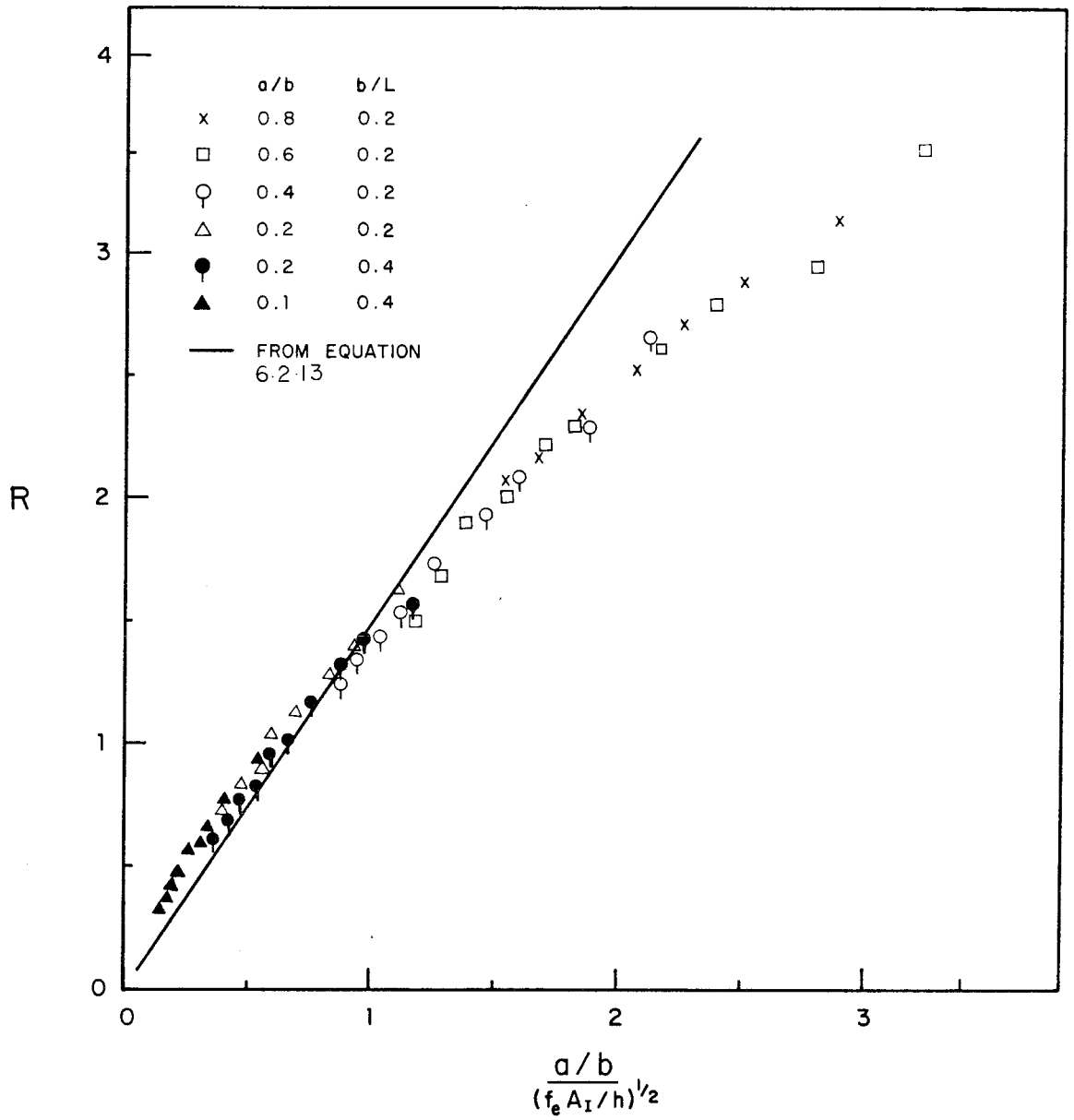

Fig. 6.2.8 Variation of the amplification factor with $(a/b)/(f_e A_I/h)^{1/2}$.

for $a/b \leq 0.8$. Also R varies like $1/\sqrt{f_e}$; hence, there is a small dependence on R of the friction factor for conditions of large entrance dissipation.

The dimensionless ratio $(a/b)/(f_e A_I/h)^{1/2}$ appears to be an important parameter in describing the relative importance of entrance dissipation. In order to quantify this, the experimental amplification factor of the first mode has been plotted versus this parameter in Fig. 6.2.8 for partially closed harbors ($a/b \leq 0.8$). The curve represents Eq. (6.2.13) with $f_e = 1.15$. It is seen that agreement between the data and the curve defined by a constant entrance loss parameter remains reasonable for abscissa values less than about unity. This corresponds to the regime where entrance dissipation dominates the other dissipation sources. For abscissa values greater than unity, disagreement becomes significant indicating the other dissipative sources can no longer be neglected in determining the amplification factor.

The generation of higher harmonics due to the quadratic nature of the entrance loss expression was investigated by comparing the second and third harmonic components of the wave elevation at the backwall to the same components corresponding to the incident wave. No difference within the range of accuracy of the measurement could be found for all experimental cases. It is thus concluded that within the present experimental range the generation of higher harmonics from entrance dissipation can be neglected.

In summary, this aspect of the investigation has pointed out the degree of variability of the entrance friction coefficient for a periodic flow. For values of the parameter $U_e/a\sigma$ greater than unity, the

coefficient f_e can be considered constant. For $U_e/a\sigma$ less than unity f_e appears to be a linear function of $U_e/a\sigma$. The results of entrance losses can, in principle, be applied to any harbor shape with an abrupt change of geometry at some location. A narrow rectangular shape was used only as a convenient means for determining this coefficient f_e. The results of the study will be applied in subsequent sections.

6.2.4 The Relative Importance of the Various Dissipation Sources in a Narrow Rectangular Harbor for Laboratory Conditions

Various losses which could affect and reduce the response of a harbor to incident waves in laboratory situations have been presented in the previous section. These include: boundary friction, surface tension dissipation (Section 5.1), leakage losses (Section 6.2.2), and separation losses at the entrance (Section 6.2.3).

The purpose of the section is to evaluate, from the physical considerations discussed in Section 3.3.3, the relative importance of those various sources in reducing resonance in the case of a narrow rectangular harbor, i.e., corresponding to a ratio b/L less than 0.4. Restricting the present discussion to shallow water waves, the amplification factor R, as affected by the various dissipative mechanism near a resonant frequency, can be estimated from the results of Section 3.3.3 as:

$$R = \frac{1}{\sum_i 1/R_i} \tag{6.2.14}$$

where R_i denotes the amplification factor associated with a particular dissipative source, i.e., the amplification factor which would prevail if only that dissipative source alone were present. It is recalled

that the ratio $1/R_i$ can be used to measure the effectiveness of source S_i in dissipating energy in the harbor. The expression for the amplification factor associated with each source of dissipation can be derived as follows from the Q_i factor computed in Appendix E and from the relation in (3.3.99) between R_i and Q_i:

(i) Radiation damping

$$\frac{1}{R_r} = (2n+1)\,\frac{\pi}{4}\,\frac{b}{L} \tag{6.2.15}$$

where b and L denote the harbor width and length, respectively, n is the mode number corresponding to resonant conditions such that in shallow water:

$$\frac{\sigma L}{\sqrt{gh}} \simeq (2n+1)\,\frac{\pi}{2}$$

where h is the depth and σ is the frequency of the incident harmonic wave system. (It is recalled that when $b/L \to 0$, $1/R_r$ does not depend on a/b.)

(ii) Laminar boundary friction

$$\frac{1}{R_\mu} = (2n+1)\,\frac{\pi}{4}\,\mu_t \tag{6.2.16}$$

where the boundary friction parameter is given by:

$$\mu_t = \frac{1}{h}\left(\frac{\nu}{2\sigma}\right)^{1/2}\left[1 + C + \frac{2h}{b}\right]$$

where ν is the fluid kinematic viscosity and C is the surface contamination factor equal to unity in the present study. The three terms in the parentheses account for the bottom, surface, and wall friction, respectively.

(iii) Leakage loss

$$\frac{1}{R_\varepsilon} = \varepsilon(1 + \frac{L}{b}) \tag{6.2.17}$$

where the leakage parameter ε is given by:

$$\varepsilon = \frac{e^3}{12\nu t_e} \sqrt{g/h}$$

where g is the acceleration of gravity, t_e the thickness of the harbor walls, and e the gap width between the walls. In the present study t_e = 1.2 cm and e ≃ 0.043 cm.

(iv) Separation loss at the entrance

$$\frac{1}{R_f} = K_f R \tag{6.2.18}$$

where K_f is defined by:

$$K_f = \frac{4}{3\pi} f_e (\frac{A_I}{h}) (\frac{b}{a})^2$$

where a is the mouth width of the harbor, (A_I/h) denotes the wave amplitude at the coastline on the centerline of the basin with the entrance closed, and R is the overall amplification factor. The entrance loss coefficient, f_e, is given by Eqs. (6.2.9) and (6.2.10). It is noted that R_f is a function of the overall amplification factor R due to the nonlinear nature of the entrance separation loss.

(v) Surface tension dissipation related to dry friction

$$\frac{1}{R_c} = \frac{\pi}{4} (2n+1) \frac{11.2\Gamma_e}{\pi^2 \rho g b A_I} (1 + \frac{\pi}{4} \frac{b}{L}) \frac{1}{R} \tag{6.2.19}$$

where Γ_e denotes the air-distilled water surface tension ($\simeq$ 72 g/sec^2). It is noted that $1/R_c$ depends on R because of the nonlinear nature of this friction source, but unlike entrance dissipation which increases as R increases, dry friction dissipation decreases as R increases.

(vi) Residual surface tension dissipation

$$\frac{1}{R_{ob}} = \frac{\pi}{4}(2n+1)\frac{2}{\pi}\frac{3.3}{\rho g b^2}\Gamma_e \tag{6.2.20}$$

It is recalled that Eq. (6.2.14) remains quantitatively reasonable only for values of the resulting amplification factor R greater than, say two, for reasons discussed in Section 3.3. If this condition is not met, the value of the amplification factor, R, given by Eq. (6.2.14) is usually smaller than the maximum value which is shifted toward a smaller frequency, and should be considered qualitatively only. On the other hand, it appears to give the right value of R at the frequency such that $\sigma L/\sqrt{gh} \simeq (2n+1)\frac{\pi}{2}$, even in cases of strong dissipation.

To compute the amplification factor related to a nonlinear dissipative form such as the effect of separation at the harbor entrance and dry friction, it is necessary to know the overall amplification factor R. It is anticipated at this point that dry friction effects do not appreciably affect the overall amplification factor R. Therefore R can be determined in the following way:

Equation (6.2.14) is rewritten as:

$$\frac{1}{R} = \sum_i \left(\frac{1}{R_i}\right)_\ell + \sum_j \left(\frac{1}{R_j}\right)_{n\ell} \tag{6.2.21}$$

where $(R_i)_\ell$ refers to any amplification factor associated with a linear dissipative source, i.e., such that the mean power dissipated by the

source is proportional to the square of the wave amplitude and $(R_j)_{n\ell}$ denotes any amplification factor associated with a quadratic dissipative source, so that the mean power dissipated by this source is proportional to the third power of the wave amplitude. For instance, entrance separation and rough turbulent boundary friction are quadratic dissipative sources. All amplification factors associated with quadratic dissipation can be written in the form:

$$(\frac{1}{R_j})_{n\ell} = K_j R \tag{6.2.22}$$

where K_j is a fixed linear coefficient specific to the dissipation mechanism, so that Eq. (6.2.21) becomes:

$$\frac{1}{R} = \sum_i (\frac{1}{R_i}) + (\sum_j K_j)\ R \tag{6.2.23}$$

The resulting overall amplification factor at resonance is found by simply solving Eq. (6.2.23) algebraically for R.

In the present case the only quadratic dissipative source is entrance separation. The coefficient K_f contains the entrance loss parameter f_e which may vary with $U_e/a\sigma$ as seen in Section 6.2.3. In order to account for this variation the following iterative procedure is recommended. First an estimate for f_e is made. Equation (6.2.23) is solved for R and the velocity at the entrance U_e is computed from R as

$$U_e = \frac{A_I}{h} \sqrt{gh}\, \frac{b}{a}\, R$$

The value $U_e/a\sigma$ follows and the coefficient f_e is then determined from Eqs. (6.2.9) or (6.2.10). Usually this process needs to be repeated one more time for a correct determination of R. Once the

overall amplification R has been computed, the amplification factor associated with each quadratic dissipative source is obtained from Eq. (6.2.22).

This simplified method can be used to estimate the relative importance of the various dissipative sources. As an example, the following four cases are considered for the rectangular harbor:

(i) First resonant mode, fully open harbor

(ii) First resonant mode, partially closed harbor.

(iii) Second resonant mode, fully open harbor.

(iv) Second resonant mode, partially closed harbor.

The values of the inverse amplification factor corresponding to each dissipative source is shown in Fig. 6.2.9 for each of the four cases. The physical parameters from which the $1/R_i$ were computed are also indicated in that figure; they correspond to typical laboratory conditions in the present study. It is recalled from Section 3.3.3 that $(1/R_i)/(1/R_j)$ is the ratio of the mean power dissipated by the source S_i to the mean power dissipated by the source S_j. Therefore, $1/R_i$ is a measure of the energy dissipated by the source S_i.

It is seen that for all four cases radiation and entrance dissipation are the two most important damping sources; for the partially closed harbor entrance separation becomes the most important dissipative source. The magnitude of the dissipation due to leakage is next in importance. For the first resonant mode, dissipation induced by leakage is about one-fourth that due to radiation; nevertheless it is not negligible. For the second mode the relative importance of leakage grows slightly when compared to radiation. The effect of laminar boundary friction

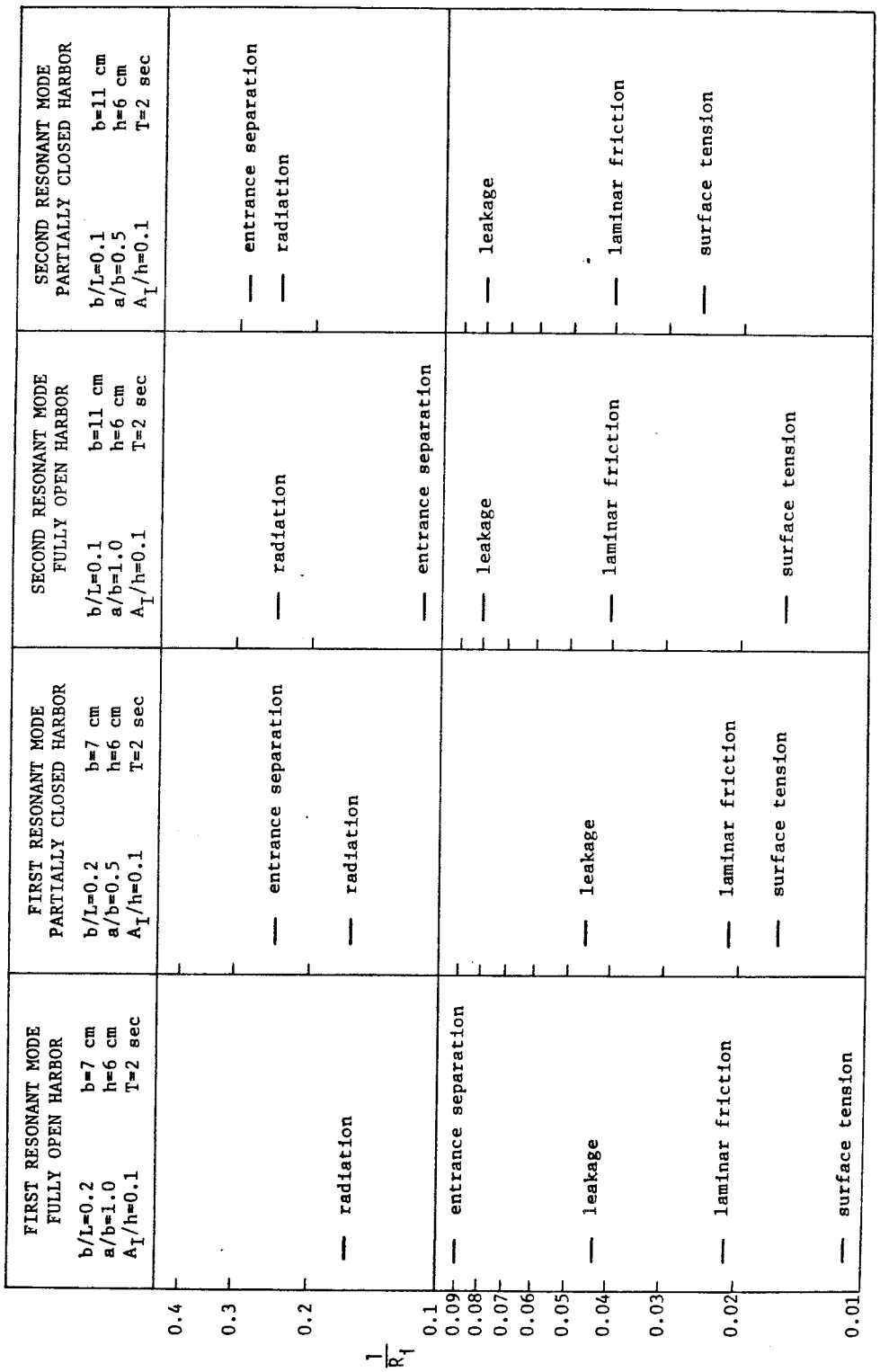

Fig. 6.2.9 The relative importance of the various sources of dissipation near resonance for four different situations, in laboratory conditions.

is fourth in importance, dissipating about one-ninth that due to radiation for the first mode oscillation and about one-fifth for the second mode. The relative importance of leakage and laminar friction grows for the second mode when compared to the effects of entrance separation for the fully open harbor. Surface tension (which on Fig. 6.2.9 includes both dry friction and the residual dissipation source related to surface tension) is of least importance, but as mentioned in Section 5.1 the ratio of the power dissipated by surface tension cannot be neglected when compared to that dissipated by laminar friction. It is about one-half the power dissipated by viscous boundary friction for three out of the four cases investigated. It is recalled that dry friction is mainly responsible for surface tension dissipation and that one way to drastically reduce it is to add a wetting agent.

In experimental conditions of Fig. 6.2.9 the wave amplitude chosen at the coastline, $A_I/h = 0.1$, is fairly large. The effect of entrance dissipation decreases markedly for smaller incident wave amplitudes. For example, for the fully open harbor case, at the first resonant mode a relative wave amplitude at the coastline equal to 0.05 induces a loss due to entrance effects equivalent to that of leakage.

6.2.5 Summary

In summary, the effects of entrance separation, leakage, and laminar friction when combined, usually induce more dissipation than the inviscid effect of radiation. Therefore, to correctly predict the maximum amplification factor near resonance it is crucial to include these three effects in the analysis. Surface tension can be safely neglected only if a wetting agent is added to the water in the wave basin.

Otherwise it can introduce a relatively important dissipation, especially for small wave amplitudes, e.g., less than 0.5 cm. It is emphasized at this point that the simplified analysis of Section 6.2.4 provides a method of determining the relative importance of the various dissipative sources, and can yield only an estimate of the resulting overall amplification factor. In particular the effects of nonlinear convective effects were neglected. This assumption, as will be seen in Section 6.3. is reasonable at the first resonant mode but it becomes incorrect at the second mode.

A last remark concerns the total damping associated with oscillation induced in a closed rectangular basin compared to the damping connected with wave induced oscillation in a rectangular harbor. In the study of the motions in a rectangular basin discussed in Chapter 5 the important dissipative sources were laminar friction at the boundaries and dissipative effects related to surface tension. However, for the cases of Fig. 6.2.9 those sources account for less than 7% of the total dissipation in the harbor. Therefore, one can expect that the growth of nonlinearities observed in the closed rectangular basin will also be seen in the harbor, but to a lesser extent because of the comparatively much stronger dissipation effects.

6.3 The Excitation of a Narrow Rectangular Harbor by a Continuous Train of Periodic Long Waves

6.3.1 Introduction

Experimental and theoretical results are presented in this section for the finite amplitude waves which are produced in a narrow rectangular harbor with a constant depth by a continuous train of periodic long waves incident upon the entrance. The basic features

of harbor oscillations associated with nonlinearities, frequency dispersion, and dissipation will be discussed in some detail.

From the analysis of Section 3.4, for a given incident wave shape, the transient and steady state characteristics of the oscillations at a given location inside the rectangular harbor can be defined by the following dimensionless parameters:

$$\frac{\eta/h}{H/h} = F\left(\frac{t\sqrt{gh}}{\ell}, \frac{H}{h}, \frac{h}{\ell}, \frac{L}{\ell}, \frac{a}{b}, \frac{b}{L}, \gamma_s, \varepsilon, f_e\right) \qquad (6.3.1)$$

where t is the time, g is the acceleration of gravity, h is the still water depth, a, b, L are the entrance width, the width, and the length of the rectangular harbor, respectively. H denotes the characteristic wave height and ℓ a characteristic wave length of the incident wave system, γ_s is the laminar boundary friction coefficient, ε is the leakage coefficient, and f_e is the entrance loss coefficient. The length ℓ, for the discussion presented next, is chosen as $T\sqrt{gh}$, where T is the period of the incident waves ($\sigma = 2\pi/T$) so that $L/\ell \sim \sigma L/\sqrt{gh}$.

A useful method for investigating these effects consists of obtaining the response of the harbor from the variation of the steady state wave characteristics inside the harbor with the length ratio L/ℓ by keeping the relative shape of the harbor, b/L, the same. The reason the steady state investigation is important is mainly because, given a periodic incident wave, steady state conditions are reached in the harbor within a few oscillations. Therefore an understanding of steady state features yields a good insight into the transient harbor oscillation problem.

It is recalled (Section 6.1) that steady state conditions were obtained experimentally after exciting the harbor from at-rest conditions

before the effects of the finite size of the wave basin were felt in the harbor. In the present study, as mentioned previously, the incident waves are a series of approximately identical cnoidal waves which have certain nonlinear features associated with them. Therefore, the characteristic horizontal length ℓ associated with these waves cannot be varied without also changing their spectral energy content. Consequently, for all cases presented, the ratio L/ℓ was changed by varying the harbor length L and simultaneously changing the entrance width and the harbor width accordingly.

For these experiments since the walls of the harbor were adjusted during the tests some leakage losses were noted. The results were corrected for these effects.

For purposes of terminology in the following discussion the solution obtained using the fully dispersive linear analysis described in Section 3.3 will be termed the linear analytical solution, and the solution obtained using the finite element analysis described in Section 3.4 is denoted as the numerical solution. In the latter it will be indicated for each case if nonlinear and/or dispersive features are incorporated. For both solutions the inclusion of dissipative effects will be indicated by the values of the loss parameters: γ_s, ε and f_e.

It became apparent during the initial stages of the experimental investigation that the nonlinear features which develop in the harbor are strongly related to the mode which is excited. Therefore, the following presentation is divided into two parts. In Section 6.3.2 the harbor response near the lowest resonant mode is discussed, and in Section 6.3.3 the harbor response near the second resonant mode is treated.

6.3.2 The Harbor Response Near the First Resonant Mode

Four sets of response curves were obtained near the first resonant mode of a narrow rectangular harbor. The characteristics of the incident wave and the harbor are given for each case in Table 6.3.1. In Table 6.3.1 $(A_1/h)_o$, $(A_2/h)_o$, $(A_3/h)_o$ denote the relative amplitude of the first three Fourier components of the incident cnoidal waves, measured on the center line of the basin at the coastline with harbor entrance closed. The period of the plate motion is denoted by T or, equivalently, the period of the first harmonic component of the incident wave system; a, b, L are the entrance width, the harbor width, and the length of the rectangular harbor, respectively. The equivalent relative wave amplitude $(\sqrt{E_a}/h)_o$ at the coastline is defined using Eq. (6.2.6). As seen from Table 6.3.1, the first harmonic amplitude dominates the others and lies in the shallow water range for all cases, as indicated by the values of the parameters $(\sqrt{h/g})/T$ which are all less than 0.05. However, the amplitude of higher harmonics cannot be neglected when compared to that of the first component. Therefore, even considering only the linear theory, those higher harmonics (such that the n^{th} harmonic has a period T_n equal to T/n) may appreciably modify the waves in the harbor by exciting higher modes of oscillation of the harbor in addition to the lowest which is excited by the first harmonic of the wave.

As the basis of comparison with later results, the response of a rectangular harbor to sinusoidal waves from a linear theory is presented in Fig. 6.3.1 for two cases: $b/L = 0.2$, $a/b = 1.0$ and $b/L = 0.2$, $a/b = 0.5$. The theory used is inviscid and the ordinate represents the amplification factor at the backwall and the abscissa is the dimensionless

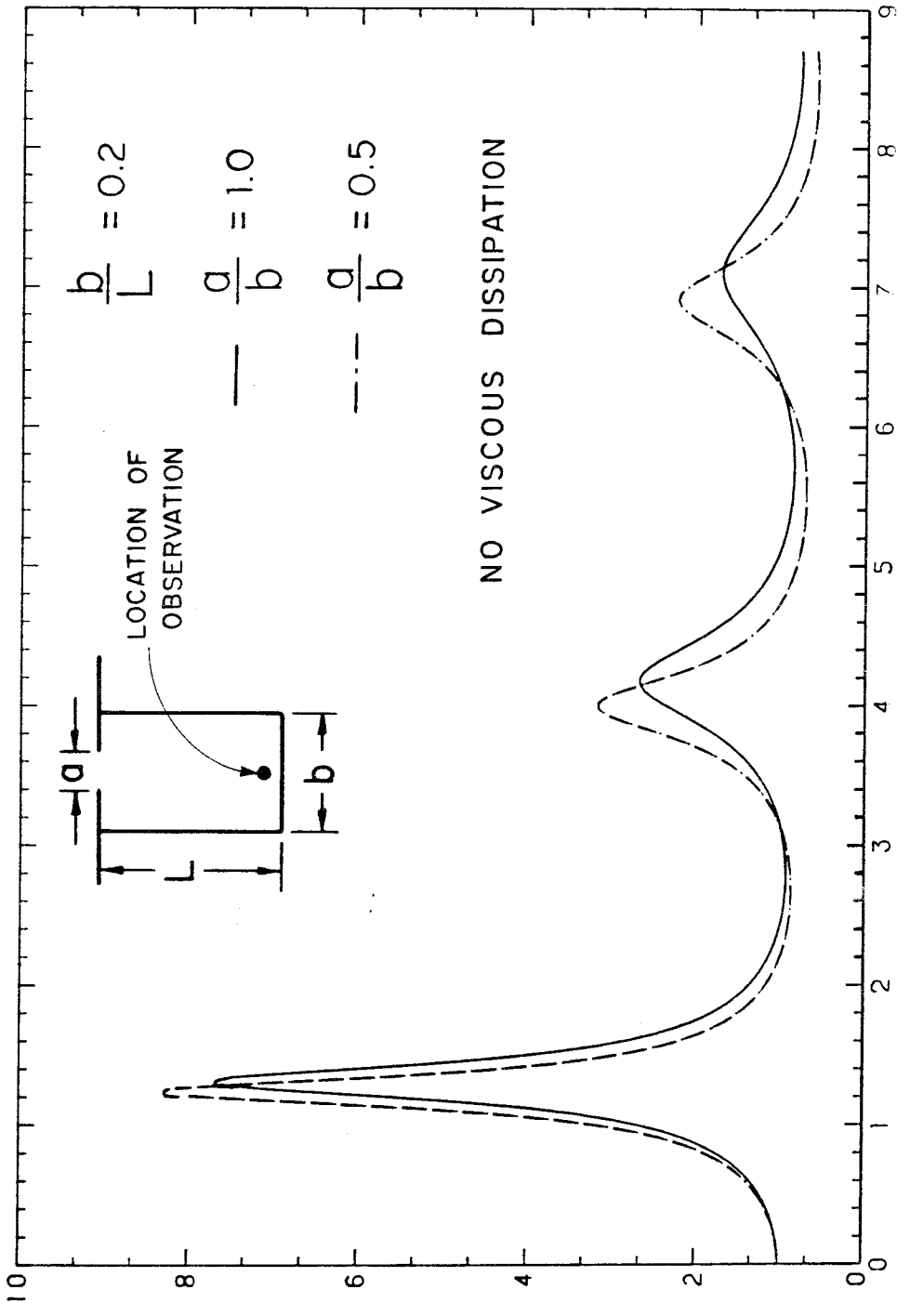

Fig. 6.3.1 Variation of the amplification factor R with kL for a rectangular harbor for inviscid conditions, b/L = 0.2, a/b = 1.0 and b/L = 0.2, a/b = 0.5.

wave number kL, where the wave number k is related to the wave frequency σ by the usual linear dispersion relationship:

$$\sigma^2 = kg \tanh kh \qquad (6.3.1)$$

Table 6.3.1 Experimental conditions for the experiments performed near the first resonant mode

	h (cm)	T (sec)	$\frac{1}{T}\sqrt{\frac{h}{g}}$	$(\sqrt{E_a}/h)_o$	$(\frac{A_1}{h})_o$	$(\frac{A_2}{h})_o$	$(\frac{A_3}{h})_o$	$\frac{b}{L}$	$\frac{a}{b}$
Case 1a	6.0	2.170	0.036	0.05	0.046	0.017	0.005	0.2	1.0
Case 1b	6.0	1.90	0.041	0.13	0.116	0.051	0.020	0.2	1.0
Case 1c	4.0	2.87	0.022	0.104	0.082	0.047	0.036	0.2	1.0
Case 1d	6.0	1.90	0.041	0.15	0.136	0.052	0.017	0.2	0.5

It should be noted that the higher harmonic components in the experimental incident cnoidal wave are not in the shallow water range. Therefore, if the harbor response is considered a linear process the full dispersion relationship (Eq. 6.3.1) must be used to relate σ_n (where σ_n denotes the frequency of the n^{th} harmonic component) to k. This is one reason a fully dispersive linear analysis was presented in Section 3.3.

Figure 6.3.1 shows a sharp peak at the first resonant mode (kL = 1.3). The two other peaks correspond to the excitation of the second and third modes, respectively. In reality, viscous dissipation reduces this amplification. Table 6.3.2 gives the values of γ_s, ε, and f_e for each case to be considered, along with the resulting amplification factor for the first mode estimated from the simplified analysis presented in Section 6.2.4 and the relative harbor opening a/b.

Table 6.3.2 Effects of viscous friction on the amplification factor at the first resonant mode

	γ_s*	ε	f_e	R	a/b
Case 1a	0.15	0.0075	0.7	3.5	1.0
Case 1b	0.15	0.0075	0.8	3.0	1.0
Case 1c	0.22	0.0092	0.8	3.0	1.0
Case 1d	0.15	0.0075	1.15	1.6	0.5

* $\gamma_s = 2\pi\mu_{bs}$

It is noted in Table 6.3.2 that for the fully open harbor cases the maximum amplification is reduced to about one-half its inviscid value. In addition, when the harbor is partially closed (a/b = 0.5), the amplification factor is further reduced by half and resonance is nearly nonexistent. Each case can be defined approximately by three characteristics: the incident wave amplitude (moderate or large), dispersion (moderate or small) and dissipation (moderate for a fully open harbor, and large for a partially closed one). More precisely the range over which each denomination applies is indicated in Table 6.3.3 below.

Table 6.3.3 Definition of experimental range of non-linearities, dispersion and dissipation.

	Large	Moderate	Small
$(\sqrt{E_a}/h)_o$	0.10 - 0.16	0.05 - 0.06	
$(\frac{1}{T}\sqrt{h/g})$		0.035 - 0.05	0.020 - 0.025
R	1.5 - 1.7	2.5 - 3.5	

The results are presented separately for each case, such that one characteristic is changed at a time, the other two remaining the same.

6.3.2.1 Case 1a: Moderate Amplitude, Moderate Dispersion, Fully Open Harbor

The variation of the positive and negative steady state wave extrema with $\sigma L/\sqrt{gh}$ as obtained experimentally at the backwall of the harbor is presented in the upper graph of Fig. 6.3.2 and is compared with the linear analytical solution and the nonlinear-dispersive solution. It should be mentioned at this point that the numerical results necessitated a different finite element mesh configuration for each harbor length; this process proved time consuming, and consequently only a few numerical runs were performed for comparison with experiments for each case. The values of the dissipation parameters γ_s, ε, f_e vary with $\sigma L/\sqrt{gh}$. They are indicated in Fig. 6.3.2 (and for all subsequent figures where response curves are presented) for the value of $\sigma L/\sqrt{gh}$ corresponding to resonant conditions. The parameters γ_s and ε can be computed simply for each harbor length, but the entrance loss coefficient f_e may depend on the local inverse Strouhal number computed at the harbor mouth which is not known a priori. However, for simplicity, this coefficient was set constant for all harbor lengths for a given response curve, and was chosen from the simplified analysis presented in Section 6.2.4.

In the response curve shown in the upper part of the figure 6.3.2 agreement between the experimental results and those from the linear theory appears reasonably good. The first peak at an abscissal value of $\sigma L/\sqrt{gh} = 0.6$ corresponds to the lowest resonant mode for the second harmonic component; the main peak at $\sigma L/\sqrt{gh} = 1.3$ is the

(a)

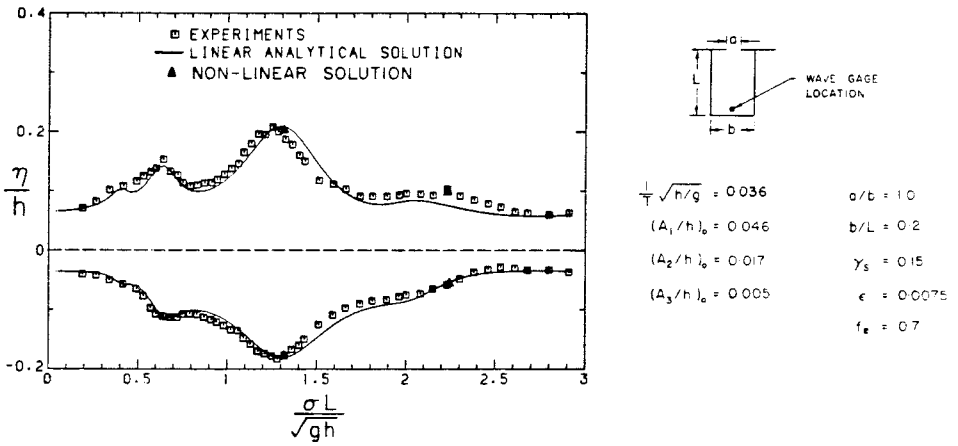

(b)

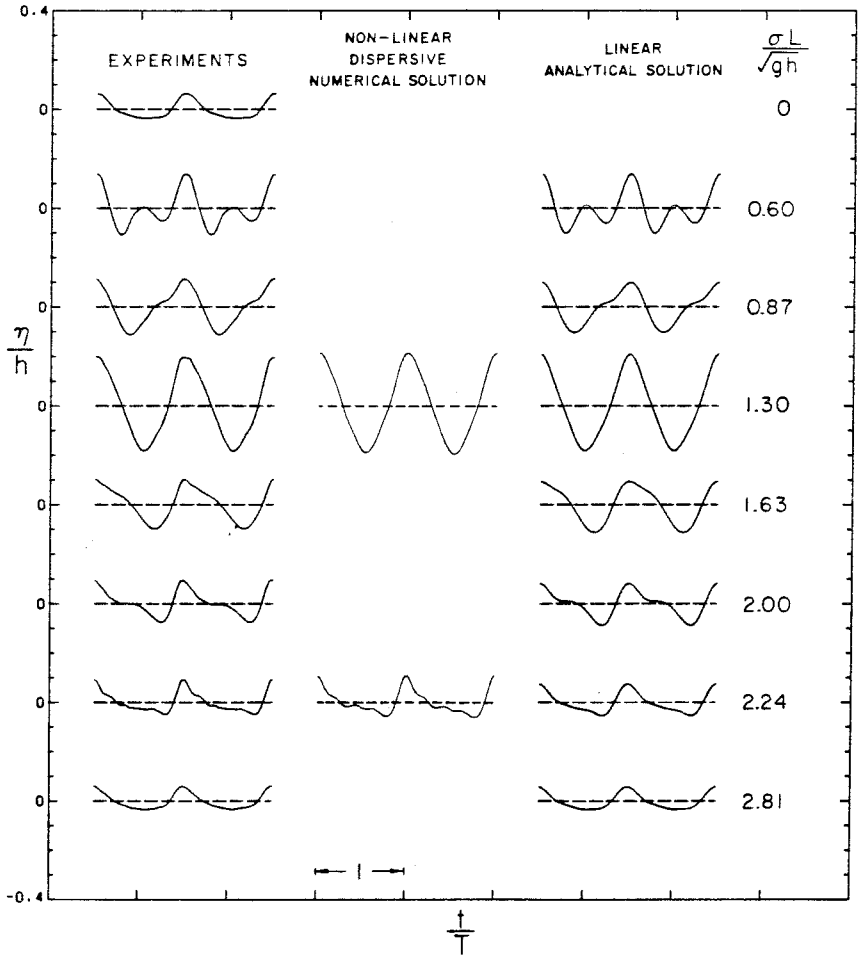

Fig. 6.3.2 (a) Variation of the steady state wave extrema with $\sigma L/\sqrt{gh}$, at the backwall, (b) steady state wave records at the backwall for several values of $\sigma L/\sqrt{gh}$; comparison between experiments, linear and nonlinear solutions; Case 1a, h = 6 cm, T = 2.17 s.

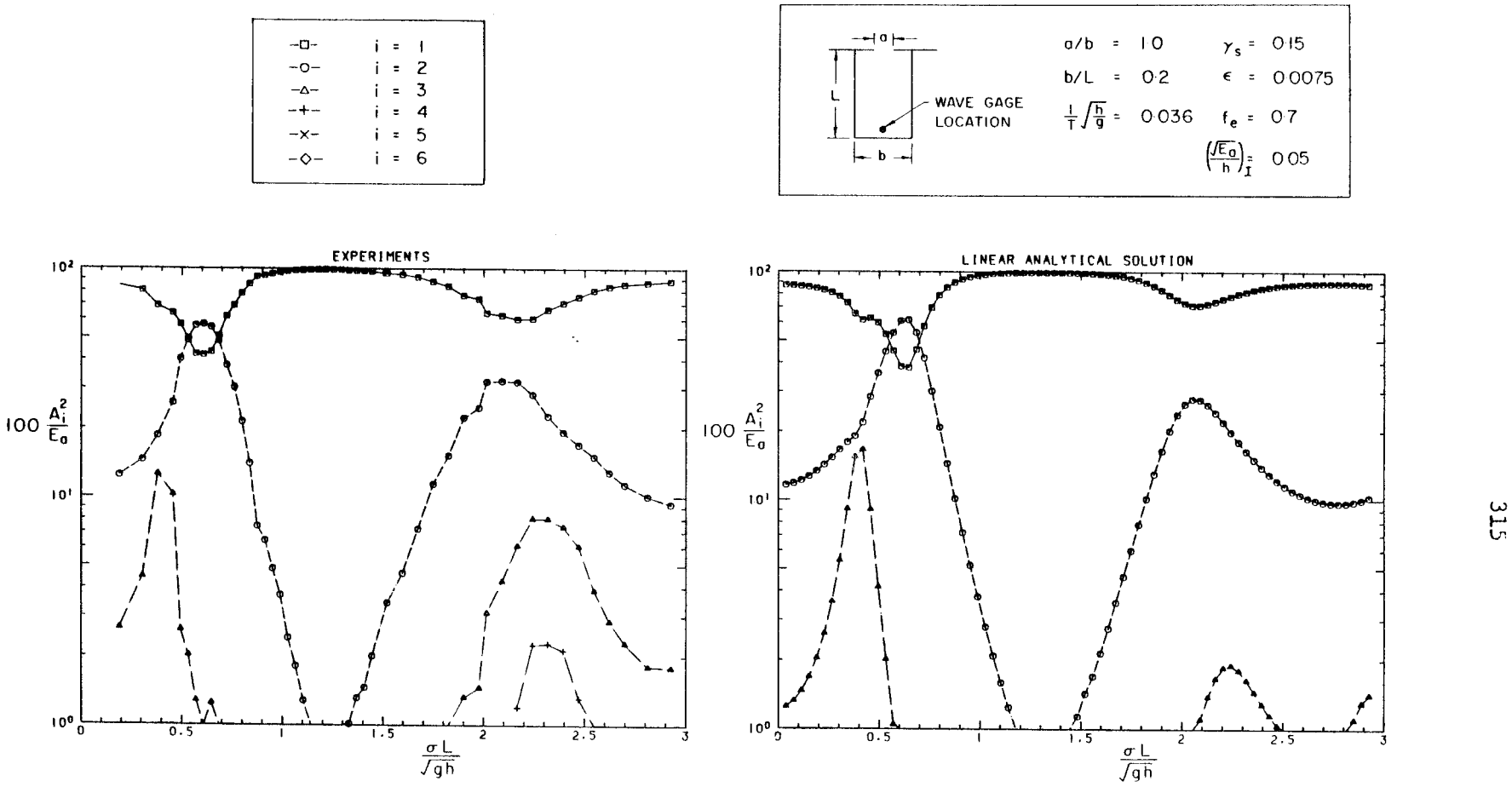

Fig. 6.3.3
Variation of percentage of wave energy with $\sigma L/\sqrt{gh}$ for the first six Fourier components, at the backwall, comparison between experiments, linear and nonlinear solution, Case 1a; h = 6 cm, T = 2.17 s.

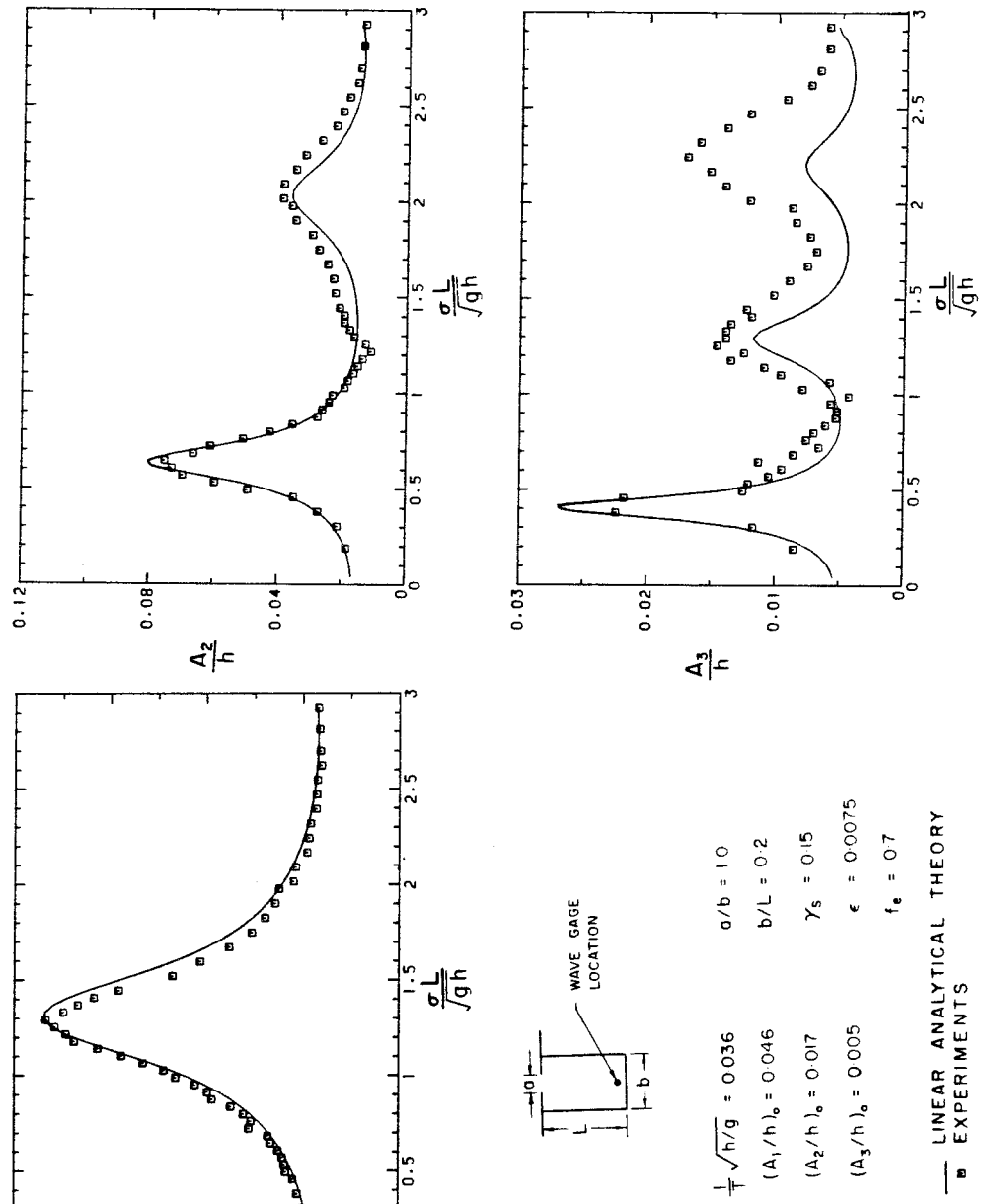

Fig. 6.3.4
Variation of the relative wave amplitude with $\sigma L/\sqrt{gh}$ for the first three Fourier components, at the backwall, comparison between experiments, linear and nonlinear solution, Case 1a; h = 6 cm, T = 2.17 s.

response at the first resonant mode for the first harmonic component; the third extremum at $\sigma L/\sqrt{gh} = 2.05$ corresponds to the second resonant mode for the second harmonic component. It is near this third peak that the experimental results disagree somewhat with the results of the linear theory.

In the lower portion of Figure 6.3.2 several steady state wave records obtained at the backwall are presented. The upper curve at $\sigma L/\sqrt{gh} = 0$ represents the steady state waveform at the coastline with closed harbor mouth, i.e., L =0. For the harbor lengths presented (or for the other values of $\sigma L/\sqrt{gh}$) the agreement of the waves obtained in the experiments and from both theories is good.

Nonlinear effects from these experiments can be evaluated further by presenting the results in two complementary ways. In the first, at the backwall and for each value of $\sigma L/\sqrt{gh}$, the percentage of wave energy contained in each harmonic component is computed, i.e., $100\ A_i^2/E_a$, where A_i denotes the amplitude of the i^{th} Fourier component, and E_a is given as before by:

$$E_a = \frac{A_o^2}{2} + \sum_{n=1}^{\infty} A_n^2$$

In the second approach the relative wave amplitude A_i/h (i = 1,2,3) versus $\sigma L/\sqrt{gh}$ is obtained for the first three Fourier components at the backwall. A comparison between linear theory and experiments for each of these two methods leads to fairly good understanding of the manner in which nonlinearities affect wave induced oscillations in this simply shaped harbor.

The experimental variation of the percentage of wave energy with $\sigma L/\sqrt{gh}$ is presented in Fig. 6.3.3 for the first six Fourier components and is compared with the linear analytical solution; (such curves are termed energy percentage curves for simplicity in the following discussions). The experiments appear to agree well with the linear theory for nearly all values of $\sigma L/\sqrt{gh}$ investigated. The major difference between the experiments and the theory is for $\sigma L/\sqrt{gh} = 2.2$ where the third harmonic is somewhat larger than what the linear theory predicts. The variation of the relative amplitude A_i/h, for $i = 1,2,3$, with $\sigma L/\sqrt{gh}$ is presented in Figure 6.3.4. The comparison between linear theory and experiments is good for the first and second harmonics. It is noted that the experimental amplification curve appears quite smooth, i.e., there are no spurious peaks which could relate to reflections inside the wave basin. This tends to confirm the validity of the present experimental approach in simulating the open sea conditions. Some discrepancy between experiments and linear theory arises for the third harmonic component around $\sigma L/\sqrt{gh} = 2.2$ in which the experiments indicate higher amplitudes. Since for this experimental value the amplitude of the first two harmonic components agree well with the linear theory, the discrepancy may be due to some form of nonlinear resonance phenomenon which manifests itself by producing higher harmonics with small interaction with the first two lowest harmonic components.

6.3.2.2 Case 1b: Large Amplitude, Moderate Dispersion, Fully Open Harbor

In this example, dispersion and dissipation effects are kept approximately the same as in case 1a, but nonlinear effects are

larger. The first harmonic component of the incident wave has more than doubled and the relative importance of the higher components has increased.

The upper portion of Fig. 6.3.5 shows the variation of the relative steady state wave extrema, η/h, with $\sigma L/\sqrt{gh}$. Again, the linear analytical solution agrees well with the experiments except around $\sigma L/\sqrt{gh} = 2.2$, where the positive wave elevation exhibits a peak 30% higher than what the linear theory predicts. It should be noted the location of this peak does not correspond to the resonant conditions by the second harmonic, i.e., $\sigma L/\sqrt{gh} \simeq 2$. The nonlinear dispersive solution agrees quite well with the experiments for the four points investigated which include $\sigma L/\sqrt{gh} = 2.2$.

Considering the steady state wave records shown in the lower portion of Fig. 6.3.5, the correspondence of the wave shapes between linear analytical theory and experiments remains good for $\sigma L/\sqrt{gh} < 1.5$. In particular, both the wave height and the wave shape are correctly predicted by the linear theory at the first resonant mode for both the first harmonic component ($\sigma L/\sqrt{gh} = 1.3$) and the second harmonic component ($\sigma L/\sqrt{gh} = 0.6$). This agreement for the highest peak appears indeed remarkable when one considers the large relative wave height, i.e., $H/h = 0.8$, reached by the oscillations at the backwall for $\sigma L/\sqrt{gh} = 1.3$. However, as the harbor length is increased, some secondary oscillations appear behind the main oscillation and the front of the wave steepens; this experimental feature exists also for the wave record computed from the nonlinear dispersive theory, but it is not observed in the results of the linear theory. Away from resonance, at $\sigma L/\sqrt{gh} = 2.84$, the wave shape at the backwall becomes similar to the incident wave

(a)

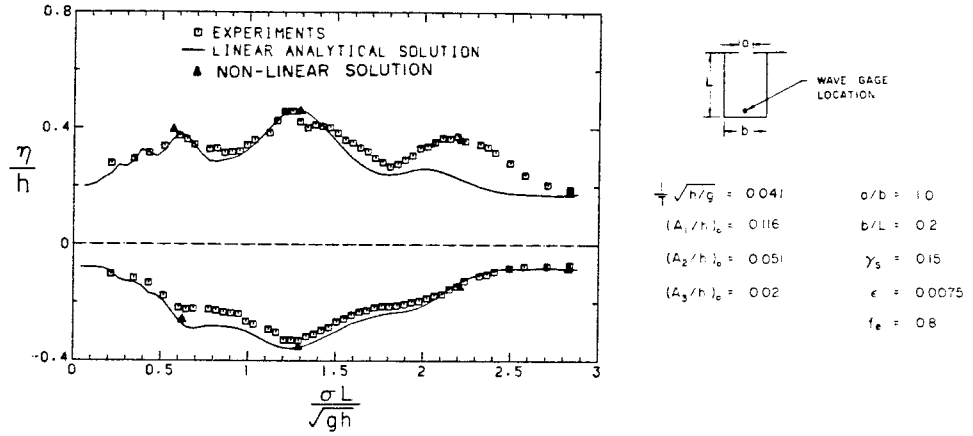

(b)

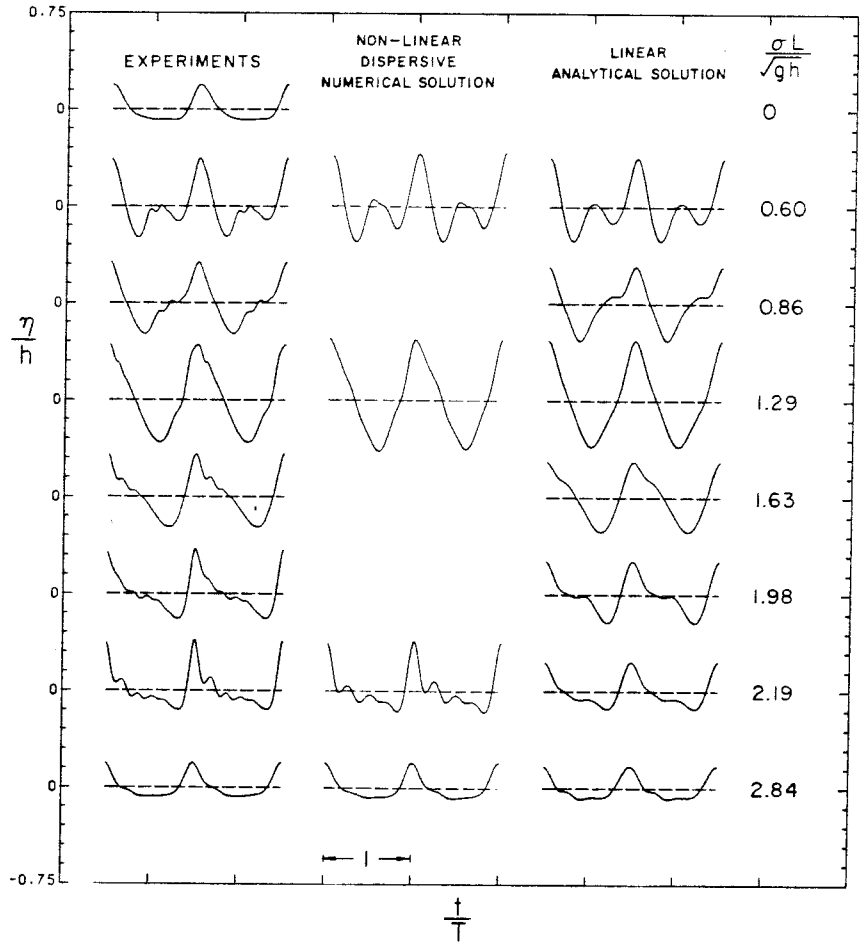

Fig. 6.3.5 (a) Variation of the steady state wave extrema with $\sigma L/\sqrt{gh}$, at the backwall, (b) steady state wave records at the backwall for several values of $\sigma L/\sqrt{gh}$; comparison between experiments, linear and nonlinear solution, Case 1b; h = 6 cm, T = 1.9 s.

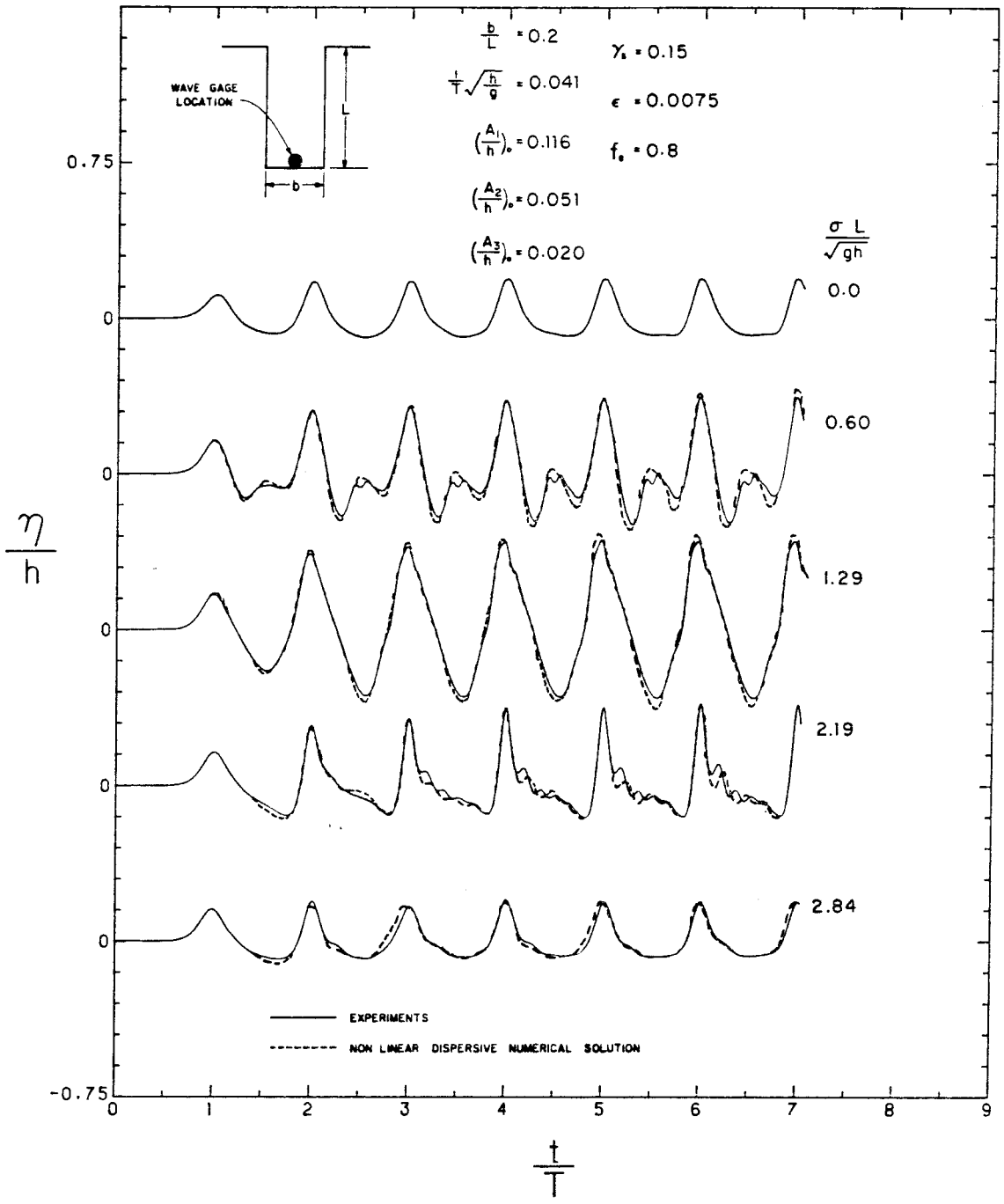

Fig. 6.3.6 Transient wave records at the backwall for several values of $\sigma L/\sqrt{gh}$ around the first resonant mode. Comparison between experiments and nonlinear theory. Case 1b; h = 6 cm, T = 1.9 s.

shape, and agreement between linear solution, nonlinear solution, and experiments is again good.

Before pursuing the discussion of steady state wave oscillations, it is of interest to evaluate the importance of transient effects for the experimental conditions of Fig. 6.3.5. The experimental water surface time histories of η/h are presented in Fig. 6.3.6 for several of the values of $\sigma L/\sqrt{gh}$ shown in Figure 6.3.5 and are compared to the nonlinear dispersive numerical solution. (No special attention was given to the exact time origin during the experiments; therefore, the wave records have been arbitrarily aligned on the first extremum of the oscillations.) First, good agreement is observed between the experiments and the nonlinear dispersive theory for all records. Although for $\sigma L/\sqrt{gh} = 2.19$, the phase and the amplitude of the secondary oscillations do not align exactly, the features are qualitatively similar. It is interesting how rapidly steady state oscillations are realized in contrast to the experiments in the closed basin (see for example Figure 5.2.4). This is probably due to the higher dissipation rate for this harbor situation compared to the closed basin. Also, the maximum transient wave height does not overshoot the steady state features. Therefore, for the case of Fig. 6.3.6. transient effects appear small.

Returning to the considerations of the steady state oscillations, for the example of Fig. 6.3.5 the percentage energy curves in Fig. 6.3.7 show the same anomaly (although much more pronounced) as mentioned earlier between experiments and linear theory in the region of $\sigma L/\sqrt{gh} > 1.5$. While for short lengths ($\sigma L/\sqrt{gh} < 1.5$) the experimental results follow the predictions of the linear theory, for larger harbor

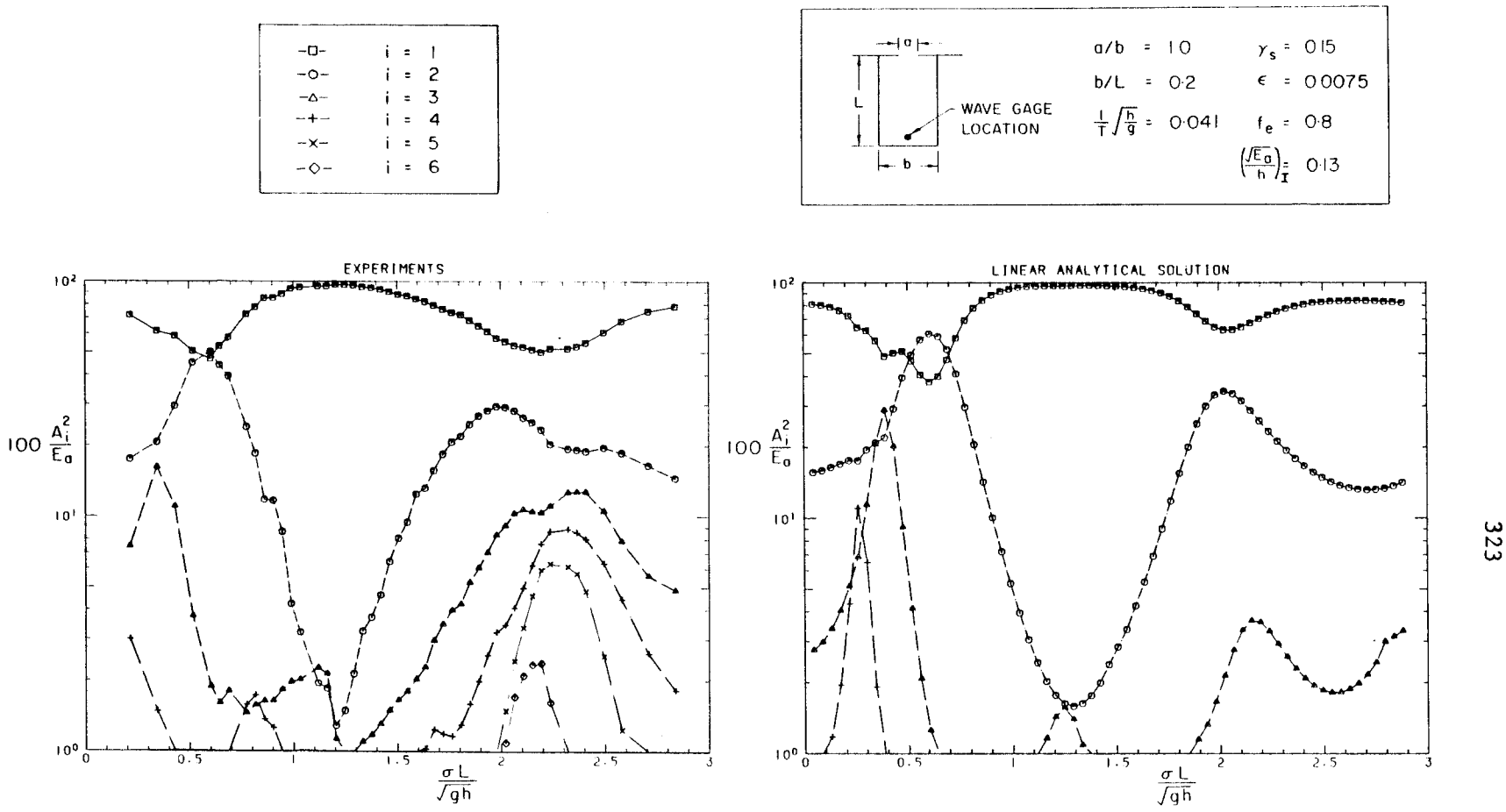

Fig. 6.3.7
Variation of percentage of wave energy with $\sigma L/\sqrt{gh}$ for the first six Fourier components, at the backwall, comparison between experiments, linear and nonlinear solution, Case 1b; h = 6 cm, T = 1.9 s.

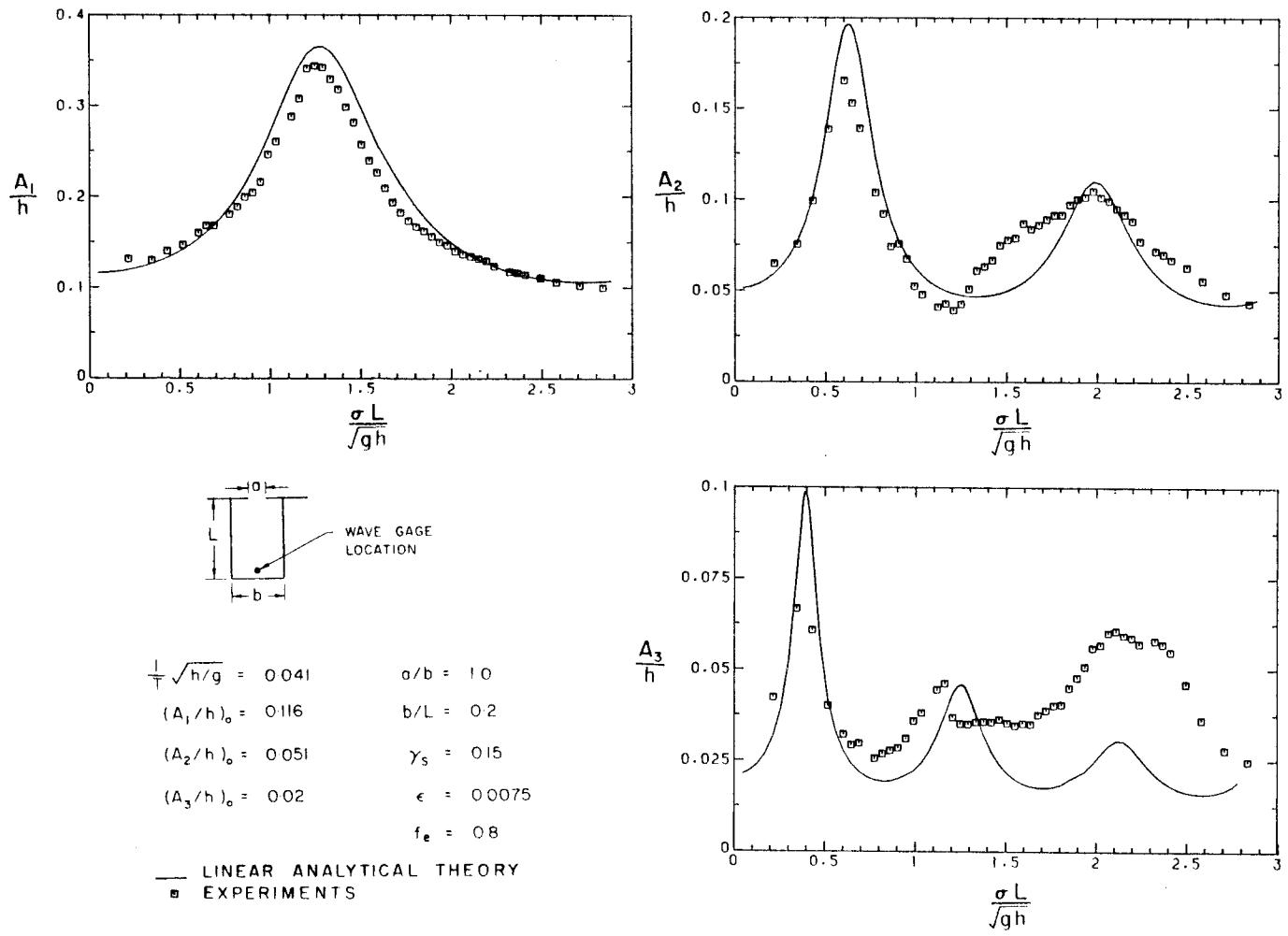

Fig. 6.3.8 Variation of the relative wave amplitude with $\sigma L/\sqrt{gh}$ for the first three Fourier components, at the backwall, comparison between experiments, linear and nonlinear solution, Case 1b; h = 6 cm, T = 1.9 s.

lengths higher harmonics are generated and grow in relative importance until at $\sigma L/\sqrt{gh} = 2.4$, where the third, fourth and fifth harmonic components contain about 25% of the total wave energy compared to 3% for the linear theory. The response curves for the first three Fourier components are presented in Fig. 6.3.8. An interesting feature of these curves is the reasonably good agreement between the linear theory and the experiments for the first two harmonics for the full range of harbor lengths investigated. In contrast, the third harmonic component exhibits much larger values from experiments than predicted from the linear theory for $\sigma L/\sqrt{gh} > 1.5$ and reaches a maximum disagreement at $\sigma L/\sqrt{gh} = 2.2$.

It appears, from Figs. 6.3.7 and 6.3.8, that effect of nonlinearities is most important at $\sigma L/\sqrt{gh} = 2.2$, and the relative importance of this mode increases with increasing incident wave height. It is produced by a nonlinear resonant process which generates or enhances higher harmonics while leaving the amplitude of the first two harmonic components reasonably intact. In other words, for this nonlinear resonant mode little energy is transferred from the lower to the higher harmonic components.

The question of whether or not these nonlinear resonant conditions are triggered or enhanced by the presence of higher harmonics in the incident wave can only be answered numerically by computing the harbor response to a sinusoidal incident wave at $\sigma L/\sqrt{gh} = 2.2$. The variation of the normalized wave elevation $\eta/(A_1)_o$ with t/T is presented in Fig. 6.3.9 for three relative incident wave amplitudes $(A_1/h)_o$ equal to 0.03, 0.07, and 0.15, for a length ratio $\sigma L/\sqrt{gh} = 2.2$, an aspect ratio b/L = 0.2, and a relative period $\sqrt{h/g}/\ T = 0.04$. No viscous dissipation is included in the computations. The importance of the transient phase of the

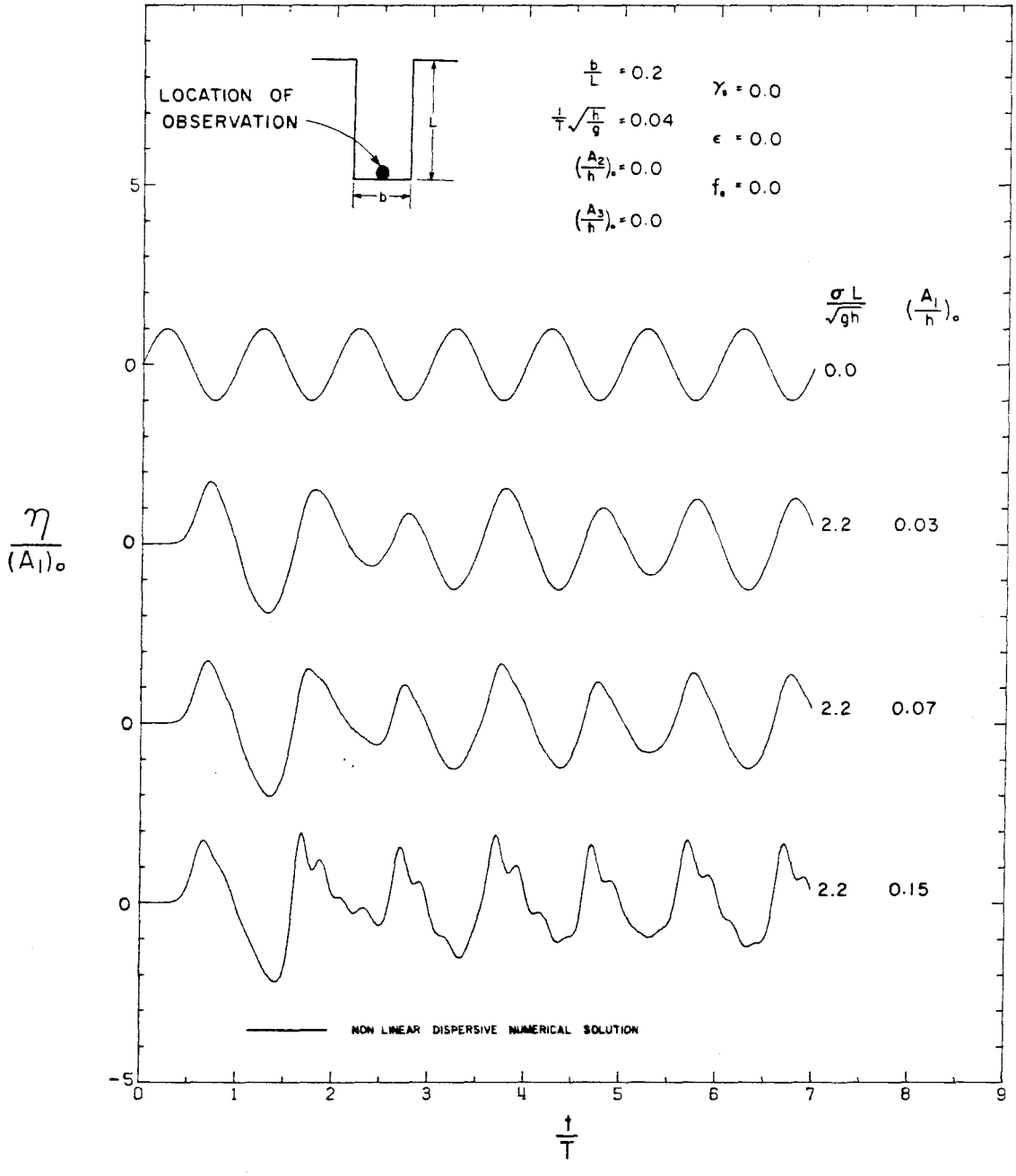

Fig. 6.3.9
Computed transient wave records at the backwall for sinusoidal excitations with various amplitudes, b/L = 0.2, $\sigma L/\sqrt{gh}$ = 2.2, $1/T\sqrt{h/g}$ = 0.04.

oscillation can be appreciated for this case, for which the negative wave elevation at the end of the first oscillation reaches twice the incident-reflected wave amplitude at the coastline. When steady state conditions are achieved (which, for the case of Fig. 6.3.9 does not occur until at least the seventh oscillation) the relative trough elevation keeps a fairly constant value equal to -1.25 for the three incident waves, but the relative crest elevation increases from 1.25 for $(A_1/h)_o = 0.03$ to 1.70 for $(A_1/h)_o = 0.15$. In addition, higher harmonics are generated for the largest incident wave, similar to what is observed in Fig. 6.3.5. Therefore, nonlinear resonant conditions obtained in the case of Fig. 6.3.5 need not be triggered by the presence of higher harmonics in the incident wave. They result directly from the magnitude of the incident wave height.

6.3.2.3 Case 1c: Large Amplitude, Small Dispersion, Fully Open Harbor

The experimental conditions are approximately the same as in case 1b except that the depth to wavelength parameter $\sqrt{h/g}/T$ has been decreased from 0.041 to 0.022. Hence, the dispersion effects become smaller. The resulting Stokes parameter associated with the incident waves is increased and, consequently, the relative importance of higher harmonics in the incident wave is larger.

The variation of positive and negative steady state wave extrema with $\sigma L/\sqrt{gh}$ is presented in the upper portion of Fig. 6.3.10. Good agreement can be seen between the experimental results and those from the linear theory for nearly all values of $\sigma L/\sqrt{gh}$ investigated. The only slight discrepancy occurs around $\sigma L/\sqrt{gh} = 2.6$, where the positive wave extremum obtained from the experiments is larger than what the

(a)

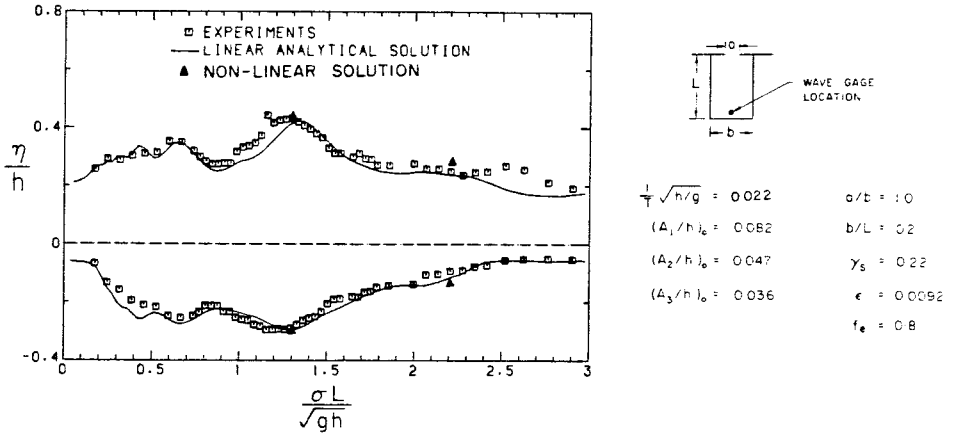

(b)

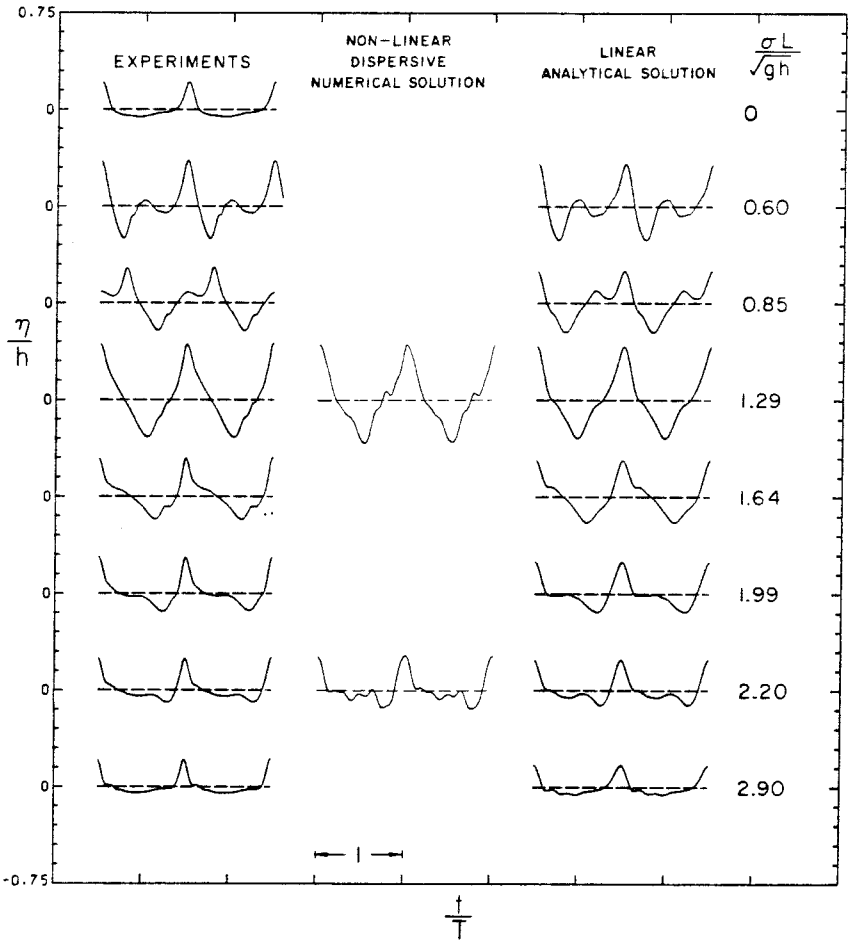

Fig. 6.3.10 (a) Variation of the steady state wave extrema with $\sigma L/\sqrt{gh}$ at the backwall, (b) steady state wave records at the backwall for several values of $\sigma L\sqrt{gh}$; comparison between experiments, linear and nonlinear solutions, Case 1c; h = 4 cm, T = 2.87 s.

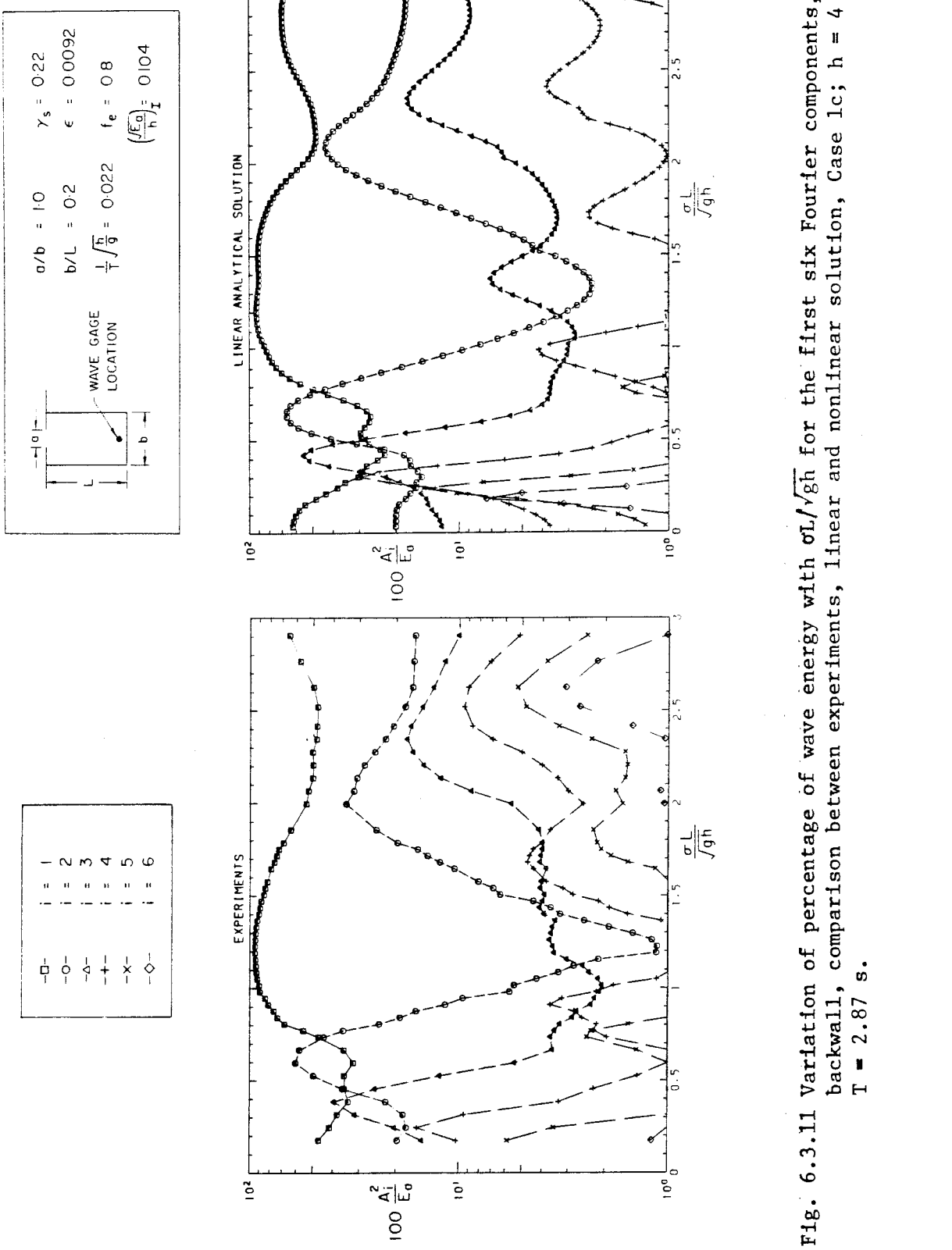

Fig. 6.3.11 Variation of percentage of wave energy with $\sigma L/\sqrt{gh}$ for the first six Fourier components, at the backwall, comparison between experiments, linear and nonlinear solution, Case 1c; h = 4 cm, T = 2.87 s.

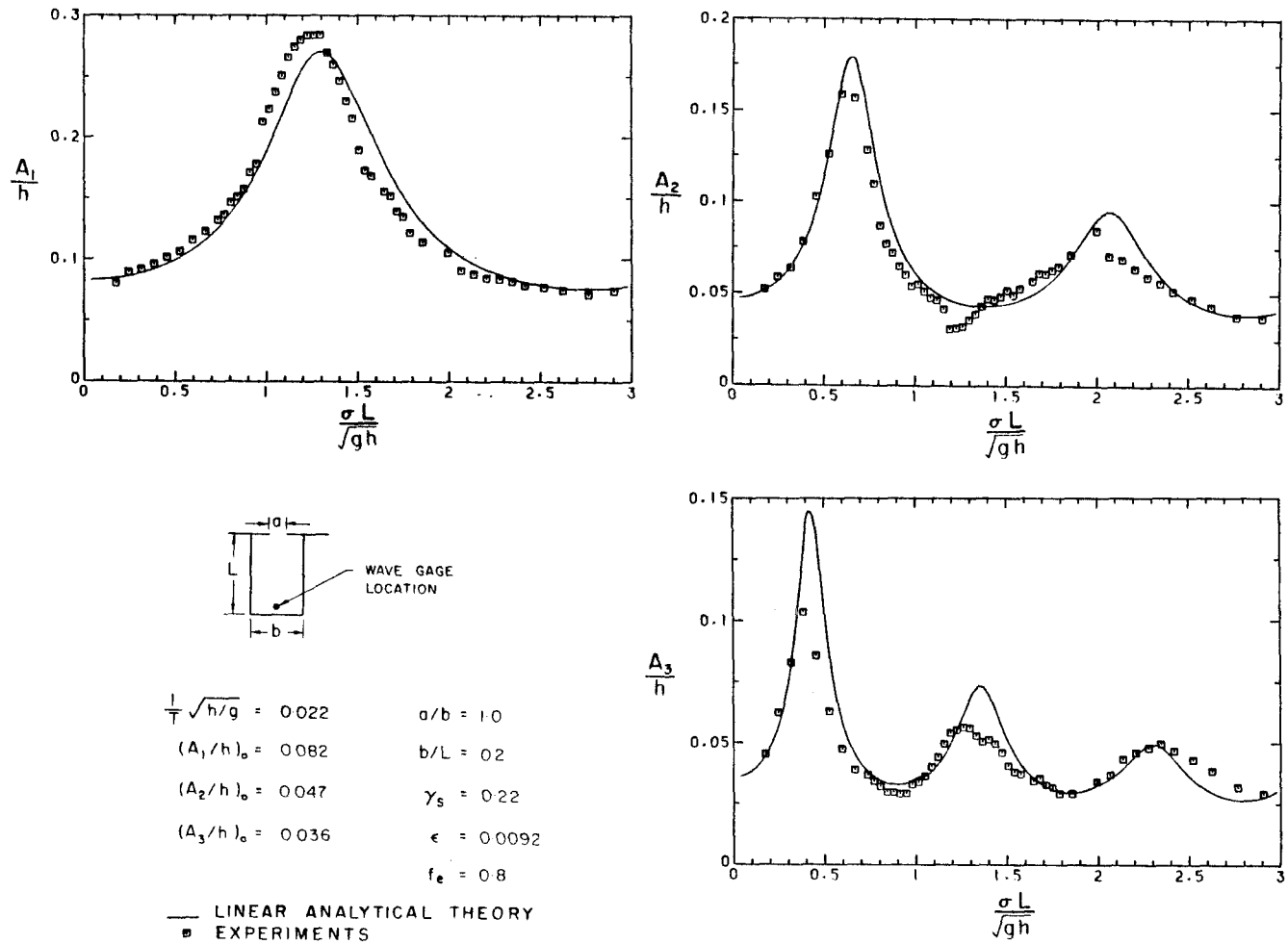

Fig. 6.3.12 Variation of the relative wave amplitude with $\sigma L/\sqrt{gh}$ for the first three Fourier components, at the backwall, comparison between experiments, linear and nonlinear solution, Case 1c; h = 4 cm, T = 2.87 cm.

linear theory predicts. Selected portions of the steady state wave records (experimental and theoretical) are presented in the lower portion of Fig. 6.3.10 for several values of $\sigma L/\sqrt{gh}$. For all curves, agreement between linear theory and experiments appears good. In particular the secondary oscillations which evolved in case 2b for $\sigma L/\sqrt{gh} > 1.5$ are hardly observed for these conditions. (The nonlinear numerical solution also compares reasonably well for the two values of $\sigma L/\sqrt{gh}$ investigated.) For $\sigma L/\sqrt{gh} = 2.2$, the numerical solution exhibits several secondary oscillations of higher frequency than in case 1b, but with smaller amplitudes.

Turning to the percentage energy curves in Fig. 6.3.11, the importance of higher harmonics can be appreciated by considering the rather complicated pattern in the experimental and the theoretical results. The correspondence between the linear theory and the experiments is quite good except around $\sigma L/\sqrt{gh} = 2.2$ where higher harmonics, not predicted by the linear theory, emerge. The percentage of wave energy contained in the fourth, fifth, and sixth components reached 15% for the experiments, compared to 2% for the linear results. The response curves for the first three harmonic components are presented in Fig. 6.3.12. It is noted the experiments agree well with the linear theory for all three components over the full range of $\sigma L/\sqrt{gh}$ which was investigated.

It appears then, that smaller dispersion induces some nonlinear resonance interaction which is shifted towards somewhat larger values of $\sigma L/\sqrt{gh}$ and which is characterized by the generation of higher frequency secondary oscillations of rather small amplitude. These results are consistent with those obtained in the investigation of the

oscillations in a closed basin for which it was found that, near resonance, the frequency of secondary oscillations increases with smaller dispersion. It was also found that high frequency secondary oscillations are very sensitive to dissipation. In the present case, the dissipation effects are considerably more important than in the closed basin problem; therefore, the higher harmonics produced by nonlinear resonant effects are strongly reduced by dissipation. This consideration, compounded by the higher viscous dissipation rate in the case 1c compared to case 1b (see Table 6.3.2), probably explains the better agreement between experiments and linear theory in case 1c than in case 1b. This example illustrates the effectiveness of dissipation in offsetting the effects of nonlinearities, i.e., the generation of nonlinear resonant conditions not predicted by the linear theory.

6.3.2.4 Case 1d: Large Amplitude, Moderate Dispersion, Partially Open Harbor

The experimental conditions are approximately the same as in case 1b, except that the harbor mouth is partially closed to half its width ($a/b = 0.5$). The purpose of this section is to investigate the effects of the rather strong dissipation at or near resonance which is introduced by the partially closed entrance.

The upper part of Fig. 6.3.13 shows the variation of the steady state wave extrema with $\sigma L/\sqrt{gh}$. The positive experimental curve shows a rather interesting feature. The second peak induced by the nonlinear resonant mode ($\sigma L/\sqrt{gh} = 2.2$) becomes as large as the peak induced by the linear resonant conditions for the first harmonic computed near $\sigma L/\sqrt{gh} = 1.3$. This can be explained in the following way: The dissipative effects of entrance separation, which increase with the velocity at the mouth, are

(a)

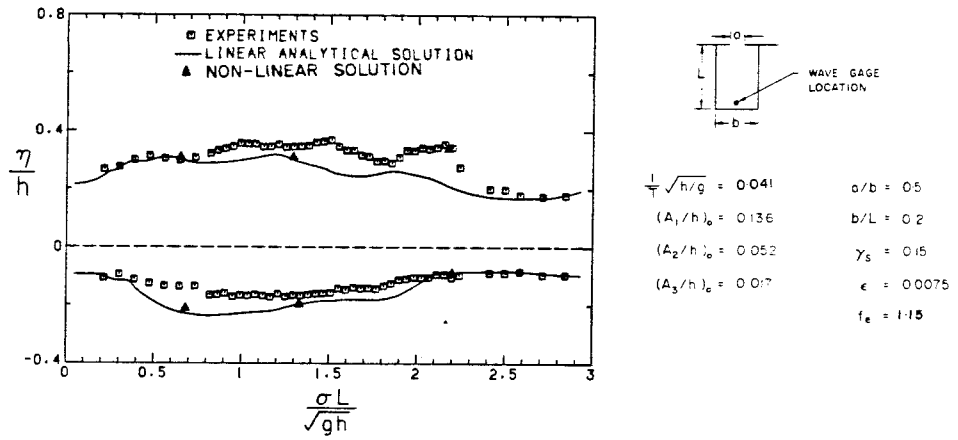

(b)

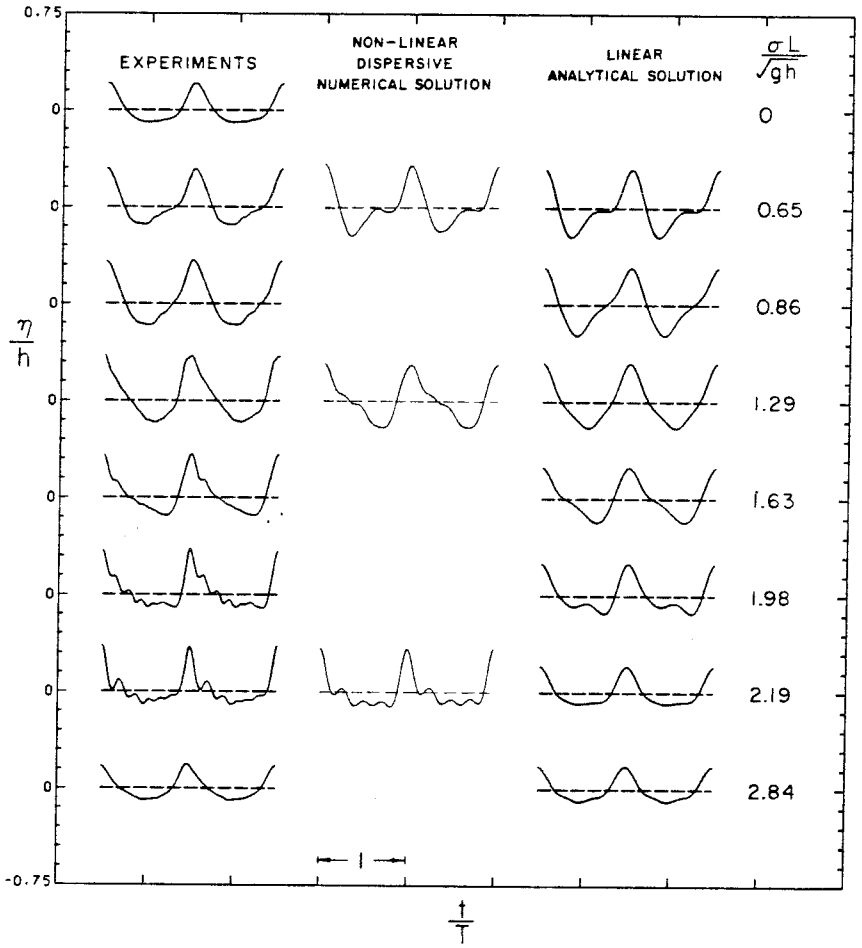

Fig. 6.3.13

(a) Variation of the steady state wave extrema with $\sigma L/\sqrt{gh}$, at the backwall, (b) steady state wave records at the backwall for several values of $\sigma L/\sqrt{gh}$; comparison between experiments, linear and nonlinear solution, Case 1d; h = 6 cm, T = 1.9 s.

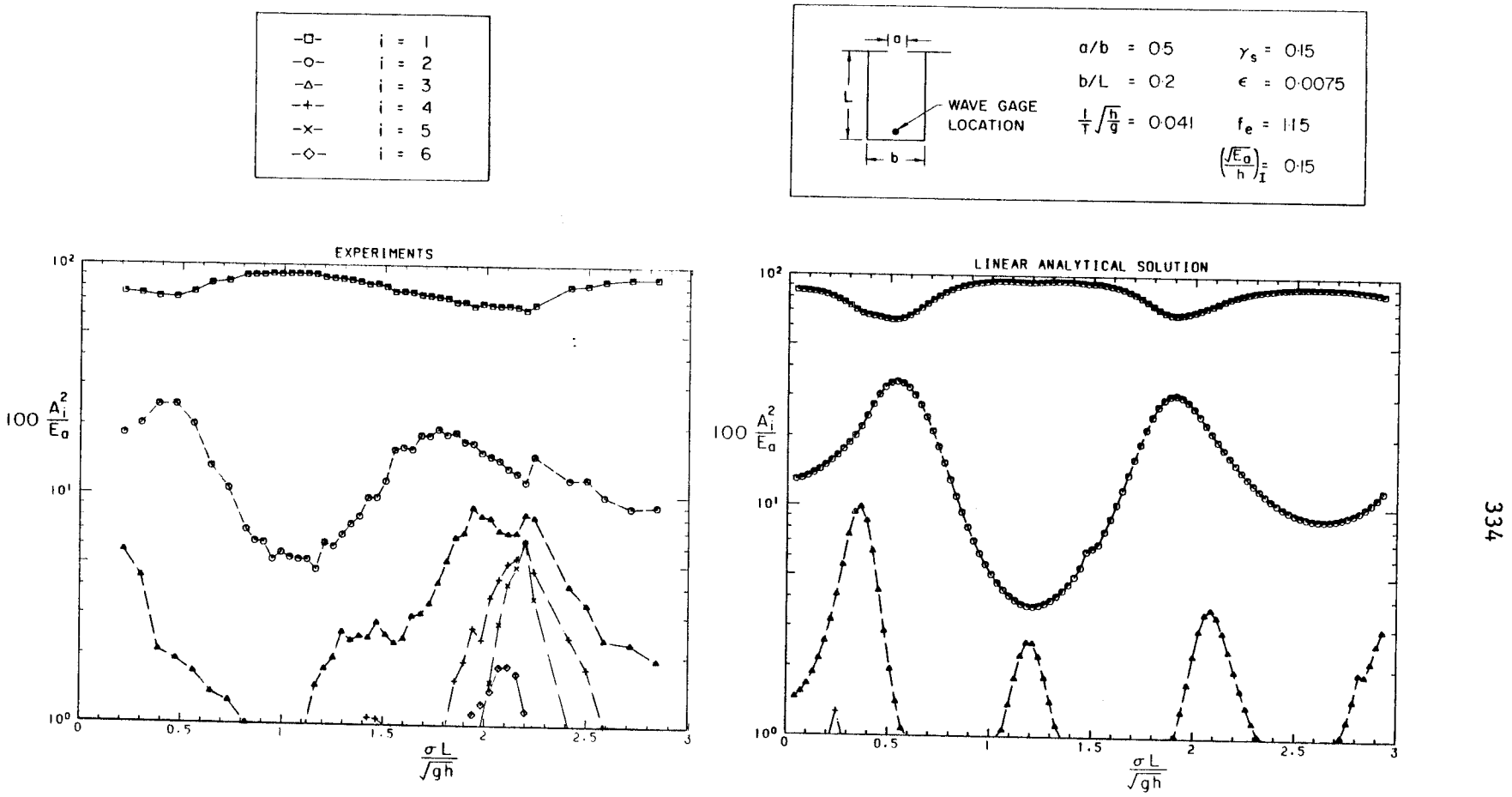

Fig. 6.3.14

Variation of percentage of wave energy with $\sigma L/\sqrt{gh}$ for the first six Fourier components, at the backwall, comparison between experiments, linear and nonlinear solution, Case 1d; h = 6 cm, T = 1.9 s.

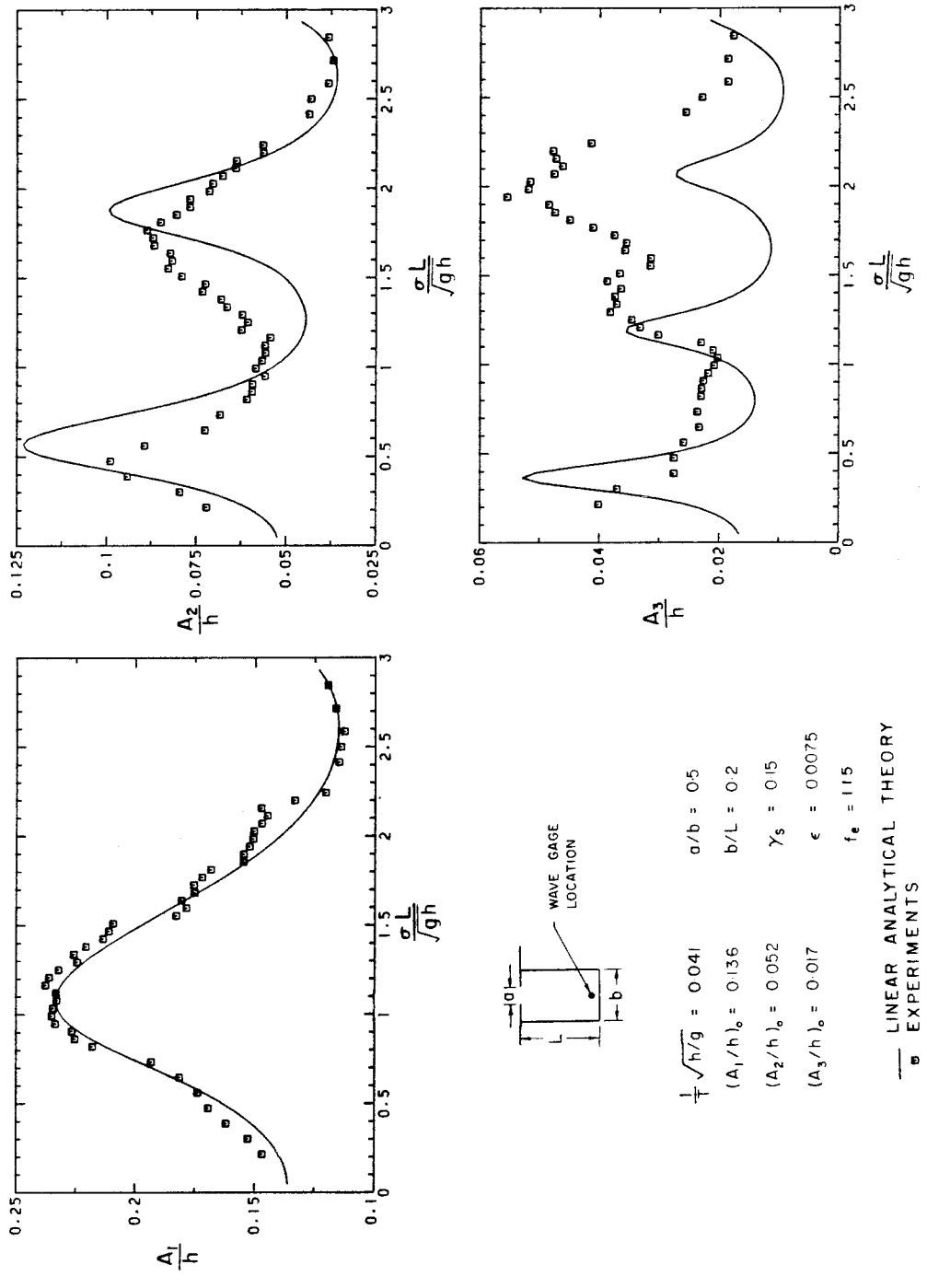

Fig. 6.3.15 Variation of the relative wave amplitude with $\sigma L/\sqrt{gh}$ for the first three Fourier components, comparison between experiments, linear and nonlinear solution, Case 1d; h = 6 cm, T = 1.9 s.

most severe for $\sigma L/\sqrt{gh} = 1.3$, where a node exists near the entrance. In contrast, near $\sigma L/\sqrt{gh} = 2.2$, where nonlinear resonance occurs, the velocity at the mouth becomes smaller since, from the linear theory, a node no longer exists near that location. Therefore, entrance separation does not affect substantially the development of the nonlinear resonant features at $\sigma L/\sqrt{gh} = 2.2$.

The agreement of the experiments with the linear theory is rather poor around $\sigma L/\sqrt{gh} = 2.2$, as expected, but it is also rather poor for smaller values of $\sigma L/\sqrt{gh}$, where the positive extrema are underpredicted and the negative extrema are overpredicted. The nonlinear theory agrees well with the experiments for $\sigma L/\sqrt{gh} = 2.2$, but shows the same tendency as the linear solution for $\sigma L/\sqrt{gh} = 0.6$. The reason for this discrepancy is not clear. Examples of several steady state wave records are presented in the lower portion of Fig. 6.3.13. For $\sigma L/\sqrt{gh} > 1.3$, the growth of secondary oscillations is observed again and good agreement is obtained between the experimental results and the results of the nonlinear theory for $\sigma L/\sqrt{gh} = 2.2$.

The energy percentage curves in Fig. 6.3.14 and the amplitude response curves in Fig. 6.3.15 follow the same trend as for case 1b: entrance separation reduces the maximum amplification factor for the first harmonic component down to about 1.7 ($= A_i/A_o$) at resonance, but does not prevent the development of higher harmonics near $\sigma L/\sqrt{gh} = 2.2$. Actually, the amplitudes of the third harmonic component for this harbor length are both equal to about 0.055 for case 1d and 1b. This shows that nonlinear resonance develops as fully in case 1d as in case 1b.

To demonstrate the capability of the numerical program in modeling separation loss at the entrance of the harbor, four experiments were

performed by exciting the harbor continuously with different opening ratios a/b. The fixed dimensionless parameters are $(H/h)_{inc} = 0.1$, $b/L = 0.2$, $\sqrt{h/g}/T = 0.05$, $\sigma L/\sqrt{gh} = 1.2$, $\gamma_s = 0.113$, and $\varepsilon = 0.006$, corresponding to T = 2.0 sec and h = 10 cm. The opening ratios a/b were set equal to 1.0, 0.8, 0.4, 0.2. For this set of experiments the harbor was not sealed to the floor of the basin; consequently, the leakage loss parameter ε has a non-zero value. The entrance friction factor f_e is determined from the simplified analysis of Section 6.2.4 as 0.8 for the fully open cases, 1.15 for the other cases. Figure 6.3.16 shows the variation of the relative wave surface displacement η/h at the backwall with dimensionless time t/T for the four opening ratios. It is seen that the numerical solution agrees reasonably well with the experiments although it predicts a slightly larger amplification for a/b = 1., 0.8, and 0.4 by about 15%. The efficiency of the breakwater in reducing resonance for small values of a/b can be appreciated by considering the higher curve and the lower curve in Fig. 6.3.16; the former corresponds to a/b = 1 and the latter to a/b = 0.2. For the partially closed harbor resonance is completely suppressed compared to the example of the fully open harbor where the wave height at the backwall is more than three times the incident wave height.

In prototype situations the depth to wavelength ratio $\sqrt{h/g}/T$ is smaller than in laboratory, typically by one order of magnitude. In order to investigate the effects of very small dispersion on the first resonant mode, numerical experiments were performed using a sinusoidal incident wave with $b/L = 0.2$, $\sigma L/\sqrt{gh} = 1.3$, $(A_1/h)_o = 0.05$, and no viscous

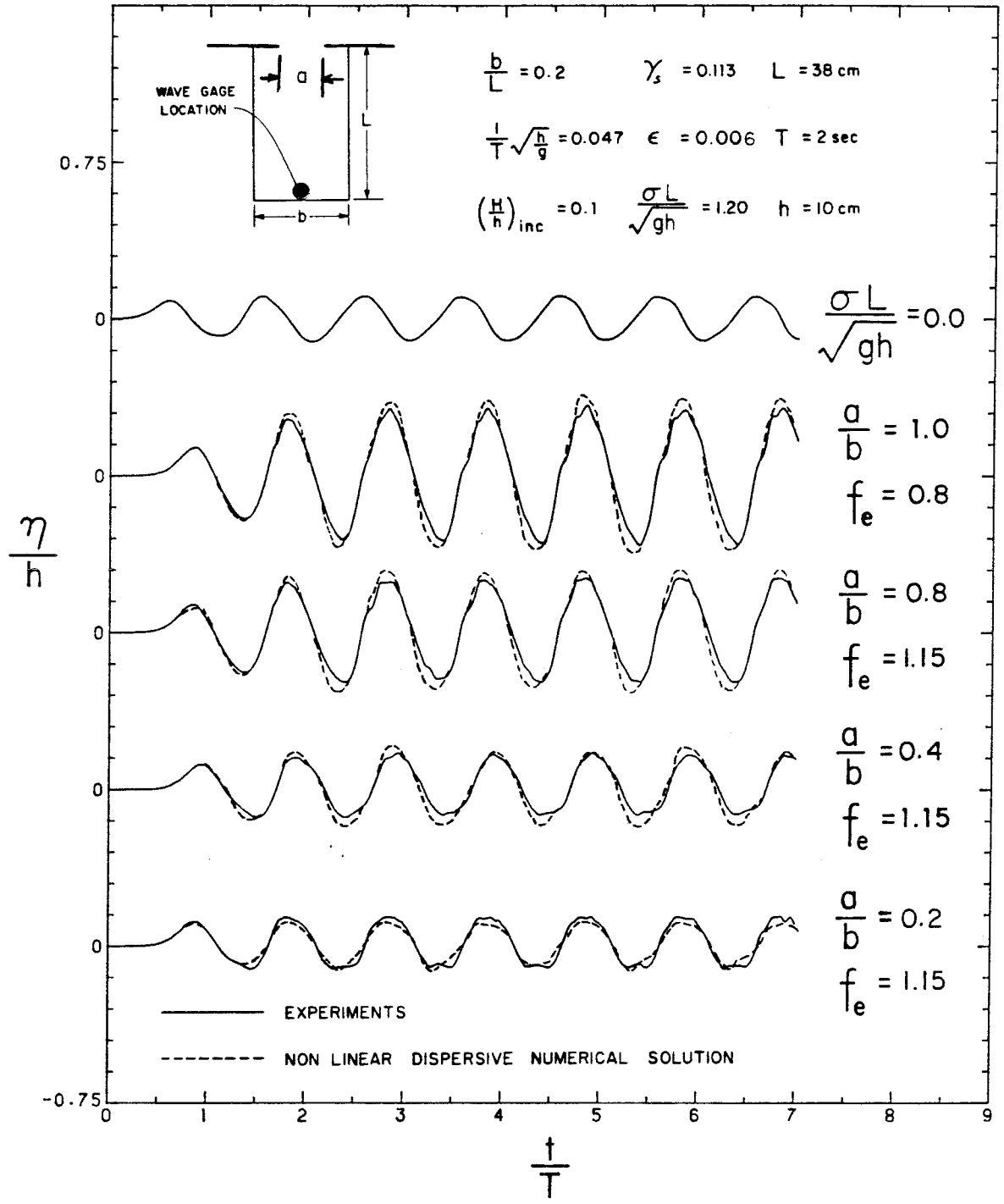

Fig. 6.3.16 Transient wave records at the backwall for various opening ratios a/b near the first resonant mode, comparison between experiment and nonlinear solution, L = 38 cm, T = 2 sec, h = 10 cm.

dissipation. The time history of the relative water surface elevation, η/h, at the backwall is presented in Fig. 6.3.17 for three values of $\sqrt{h/g}/T$: 0.03, 0.009, and 0.003. The three waves evolve with time in a similar manner and retain their shape which is approximately sinusoidal even when the relative wave height at the backwall reaches 0.8. Therefore, the effects of nonlinearities with small dispersion can also be neglected for these conditions.

6.3.3 The Harbor Response Near the Second Resonant Mode

Five sets of response waves were obtained near the second resonant mode for a rectangular harbor where for this mode the harbor essentially appears longer relative to the incident wavelength. The characteristics of the incident wave and of the harbor for each case are given in Table 6.3.4.

Table 6.3.4 Experimental conditions for the experiments performed near the second resonant mode

	h (cm)	T (sec)	$\frac{1}{T}\sqrt{\frac{h}{g}}$	$(\frac{\sqrt{E_a}}{h})_o$	$(\frac{A_1}{h})_o$	$(\frac{A_2}{h})_o$	$(\frac{A_3}{h})_o$	$\frac{b}{L}$	$\frac{a}{b}$
Case 2a	7.5	1.81	0.048	0.06	0.058	0.004	0.002	0.1	1.0
Case 2b	7.5	1.81	0.048	0.117	0.114	0.026	0.010	0.1	1.0
Case 2c	4.0	2.36	0.027	0.127	0.11	0.055	0.026	0.1	1.0
Case 2d	7.45	1.805	0.049	0.11	0.104	0.018	0.006	0.1	0.5
Case 2e	7.5	1.78	0.048	0.16	0.151	0.06	0.02	0.1	1.0

Cases 2a, 2b, 2c, and 2d correspond approximately to the same experimental conditions as cases 1a, 1b, 1c, and 1d, respectively, except that the width ratio b/L is now reduced to 0.1 to decrease radiation damping at

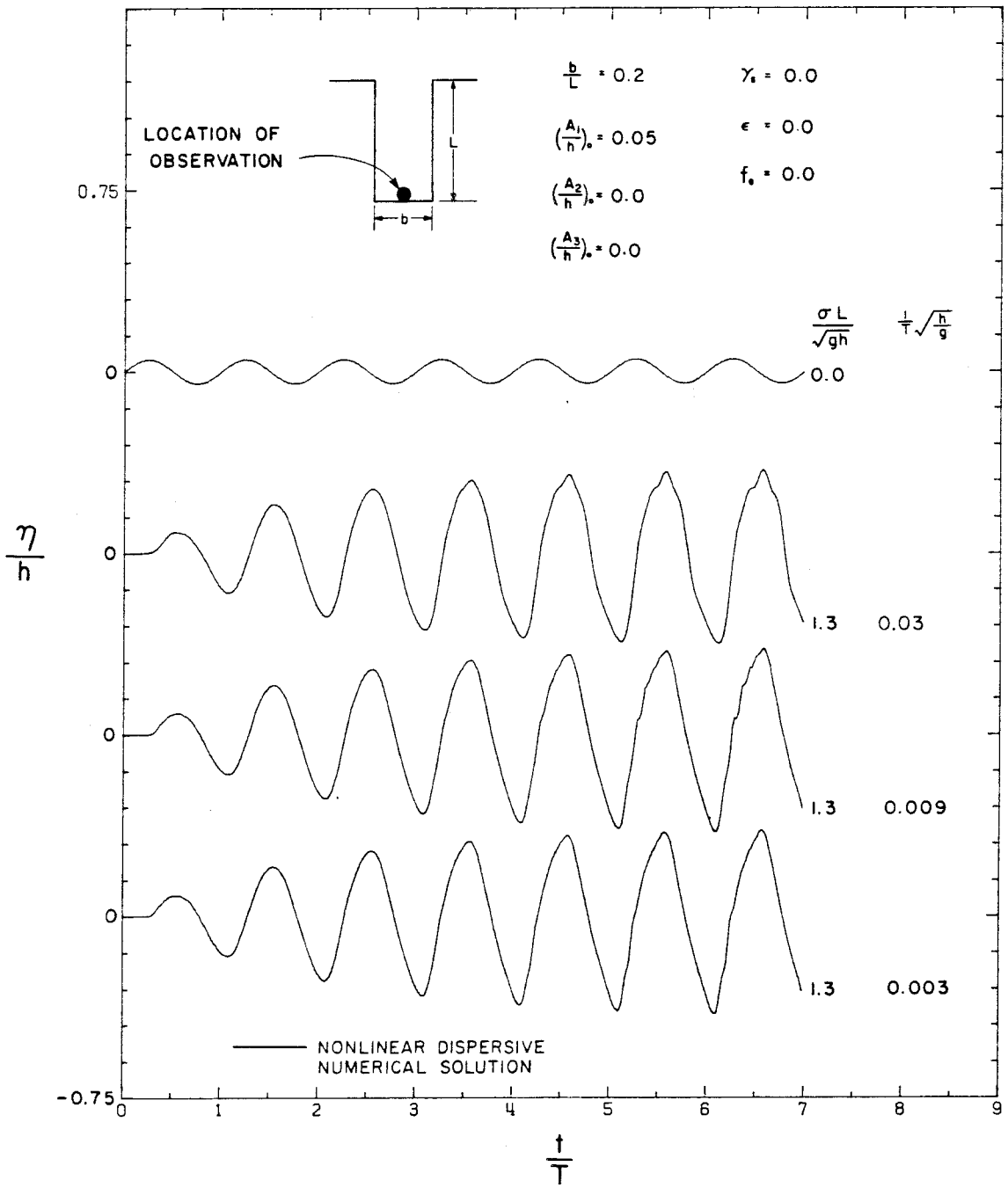

Fig. 6.3.17 Computed transient wave records at the backwall for sinusoidal excitations for various values of $1/T\sqrt{h/g}$, no viscous dissipation, b/L = 0.2, $(A_1/h)_o$ = 0.05, $\sigma L/\sqrt{gh}$ = 1.3.

the second resonant mode. Case 2e corresponds to the same experimental conditions as case 2b, except that the incident wave height is larger.

This section deals with the excitation of the second mode of the harbor by the first harmonic component of the incident cnoidal wave system. As a basis of comparison with subsequent results the variation from the linear theory of the amplification factor at the backwall with the normalized wave number kL is presented in Fig. 6.3.18 for b/L = 0.1 and for a/b = 1.0 and a/b = 0.5, in the absence of viscous dissipation. The three maxima in Fig. 6.3.18 correspond to the second (kL ≃ 4.3), third (kL ≃ 7.5), and fourth (kL ≃ 10.5) resonant modes. The peak which is associated with the second resonant mode appears fairly sharp, but actually viscous dissipation tends to modify this by reducing the amplification. Table 6.3.5 gives the values of the various dissipation parameters: ε, γ_s, and f_e for each case and the estimated amplification factors at the second resonant mode (kL = 4.3) based on the simplified analysis of Section 6.2.4.

Table 6.3.5 Effects of viscous friction on the amplification factor at the second resonant mode

	γ_s**	ε	f_e	a/b	R
Case 2a	0.11	0.0067	0.10	1.0	3.0
Case 2b	0.11	0.0067	0.5	1.0	2.4
Case 2c	0.19	0.0092	0.4	1.0	2.3
Case 2d	0.11	0.0067	1.0	0.5	1.7
Case 2e	0.11	0.0067	0.0	1.0	3.0

**$\gamma_s = 2\pi\mu_{bs}$

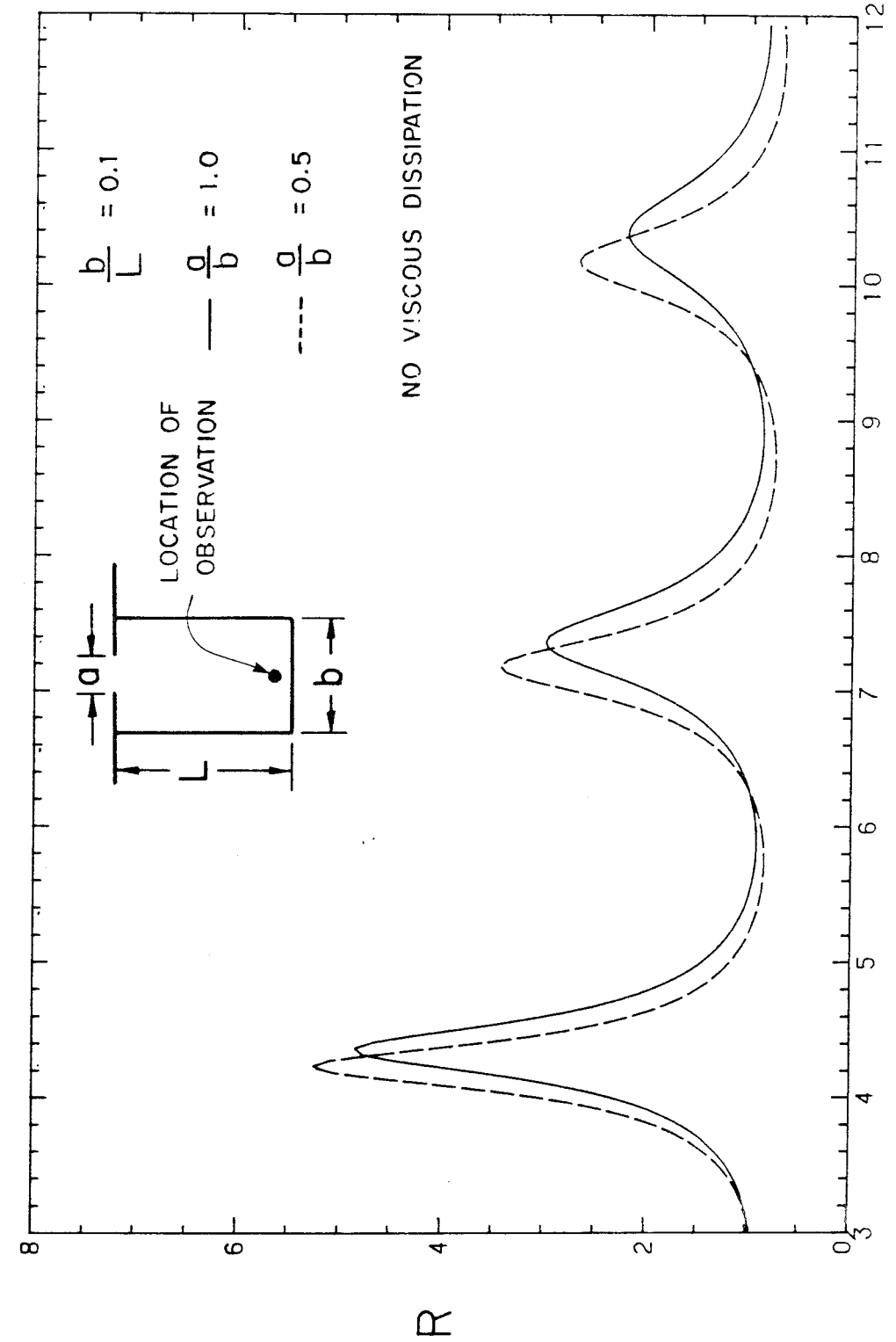

Fig. 6.3.18 Variation of the amplification factor with kL for a rectangular harbor for inviscid conditions; b/L = 0.1, a/b = 1.0 and b/L = 0.1, a/b = 0.5.

From Table 6.3.5 it is seen that viscous dissipation reduces the response at the second mode substantially and therefore must be included in the various numerical models for a meaningful comparison with the experiments. The experimental and theoretical results for each case are presented next.

6.3.3.1 Case 2a: Moderate Amplitude, Moderate Dispersion, Fully Open Harbor

The variation of the positive and negative steady state wave extrema with $\sigma L/\sqrt{gh}$ is presented in the upper part of Fig. 6.3.19. Although the experimental conditions are similar to Case 1a, the agreement between the linear theory and the experiments is not as good as in the case of Fig. 6.3.2. In particular, the experimental positive extremum is less than what the theory predicts for $\sigma L/\sqrt{gh} = 4.3$, and a secondary peak seems to emerge for $\sigma L/\sqrt{gh} = 5.0$. The wave extrema computed from the nonlinear theory compare well with the experiments.

An extracted portion of the steady state wave records for several values of $\sigma L/\sqrt{gh}$ is presented in the lower graph of Fig. 6.3.19. The front face of the oscillations steepens more than the linear theory predicts from $\sigma L/\sqrt{gh} = 3.50$ to 4.96, and small secondary oscillations appear on the back face of the main oscillation at $\sigma L/\sqrt{gh} = 4.96$. The numerical nonlinear solutions agree well with the experiments and agree better than the results of the linear theory.

The corresponding energy percentage curves are shown in Fig. 6.3.20. In contrast to the results of the linear theory, the experimental results show that the growth of the first harmonic component near resonance is accompanied by the simultaneous growth of higher harmonics. These higher

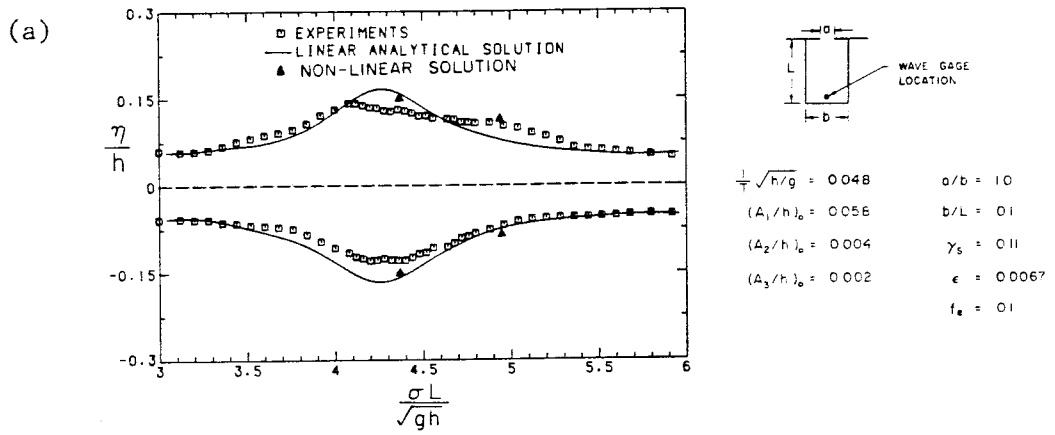

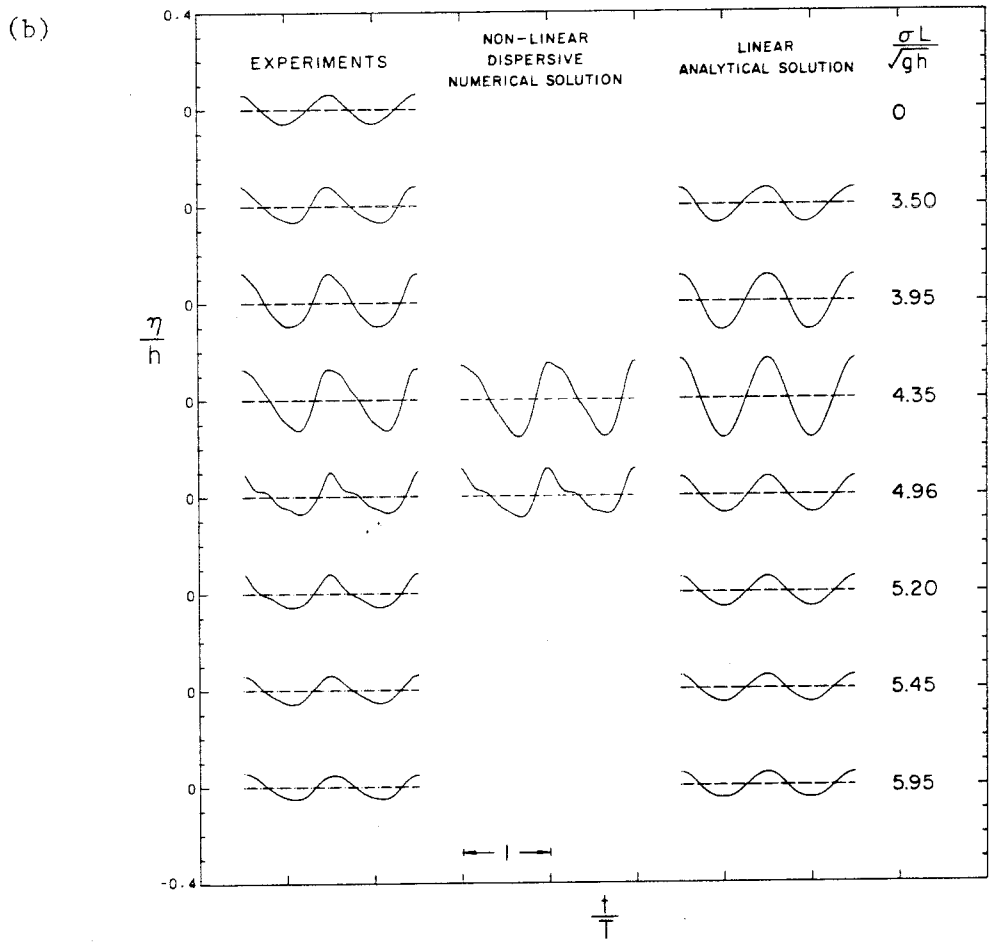

Fig. 6.3.19 (a) Variation of the steady state wave extrema with $\sigma L/\sqrt{gh}$, at the backwall, (b) steady state wave records at the backwall for several values of $\sigma L/\sqrt{gh}$; comparison between experiments, linear and nonlinear solution, Case 2a; h = 7.5cm, T = 1.81 s.

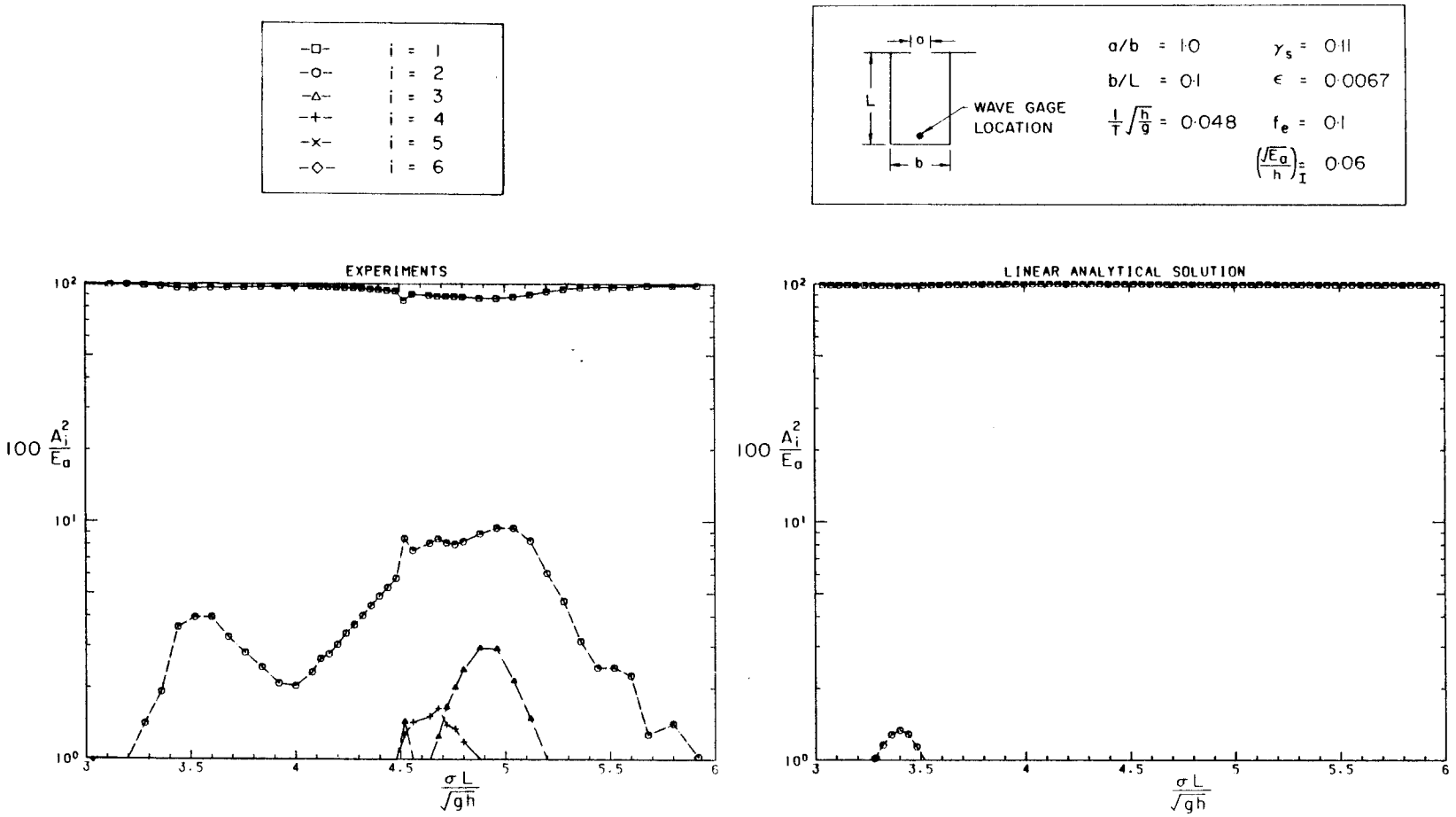

Fig. 6.3.20 Variation of percentage of wave energy with $\sigma L/\sqrt{gh}$ for the first six Fourier components, at the backwall, comparison between experiments, linear and nonlinear solution, Case 2a; h = 7.5 cm, T = 1.81 s.

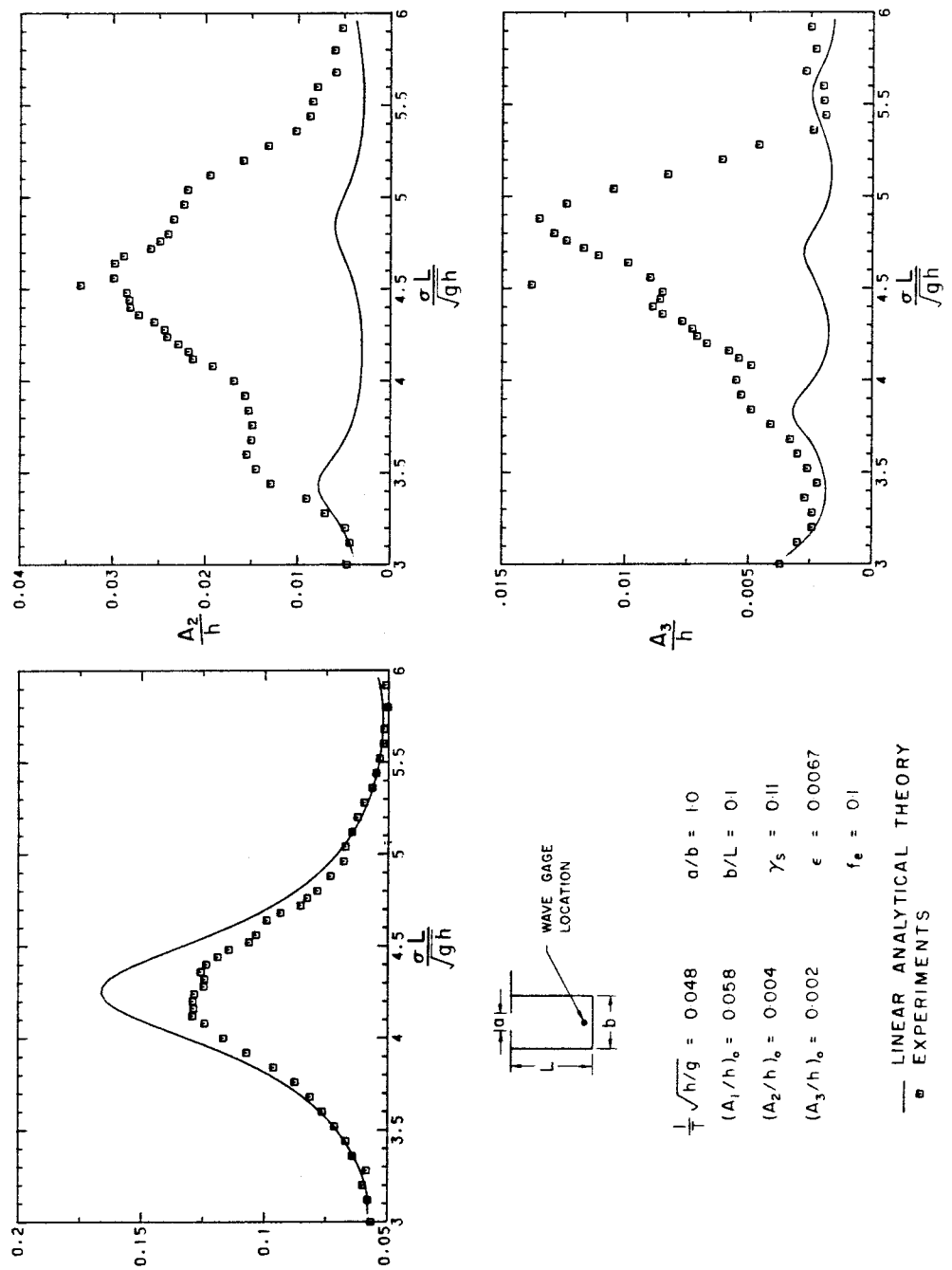

Fig. 6.3.21 Variation of the relative wave amplitude with $\sigma L/\sqrt{gh}$ for the first three Fourier components, comparison between experiments, linear and nonlinear solution, Case 2a; h = 7.5 cm, T = 1.81 s.

harmonics continue to grow as the harbor length is increased, until at about $\sigma L/\sqrt{gh} = 5.0$ where their relative importance culminates. The amplitude response curves for the first three Fourier components are presented in Fig. 6.3.21. The ratio of the wave amplitude predicted by the linear theory to the experimental wave amplitude at $\sigma L/\sqrt{gh} = 4.4$ is about 1.3, whereas the amplitude for the second and third harmonic components obtained experimentally at $\sigma L/\sqrt{gh} = 4.4$ is much larger than linear theory predicts. Therefore, it can be concluded that for the second resonant mode a transfer of energy takes place from the lowest to the higher frequency components, resulting in a "nonlinear inviscid damping" of the lowest harmonic at resonance. This new feature did not appear to exist for the first resonant mode. As $\sigma L/\sqrt{gh}$ is increased further, the amplification of the second and third harmonic components grows also, until a maximum is reached at about $\sigma L/\sqrt{gh} = 5.0$. For this value, the amplification of the first harmonic is well predicted by the linear theory, but complete disagreement between experimental and linear curves can be observed for the second and third harmonics. This suggests the existence of a second nonlinear resonant mode around $\sigma L/\sqrt{gh} = 5.0$ which is characterized by the production of harmonics, similar to those obtained in Section 6.3.2.1 for the first mode.

6.3.3.2 Case 2b: Large Amplitude, Moderate Dispersion, Fully Open Harbor

The experimental conditions are the same as for case 2a, except that the incident wave height is now twice as large. The upper portion of Fig. 6.3.22 shows the variation of the steady state wave extrema with $\sigma L/\sqrt{gh}$. The difference between the experimental results and the linear theory appears greater than that shown for case 2a in

(a)

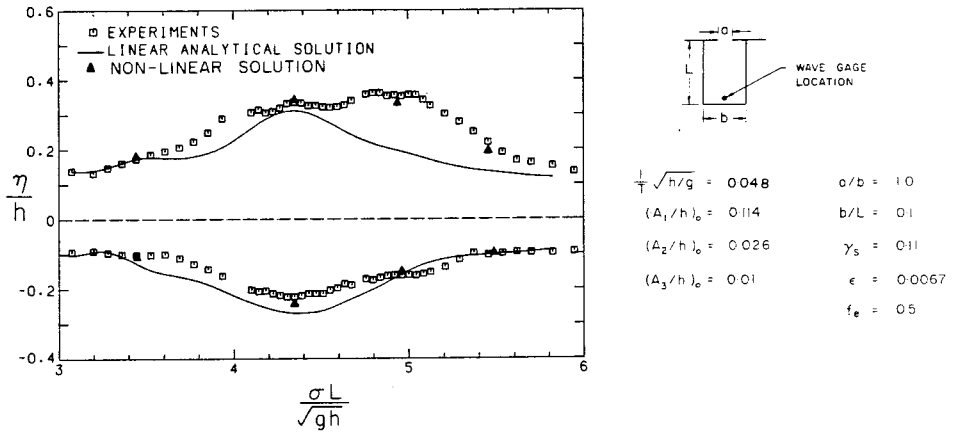

(b)

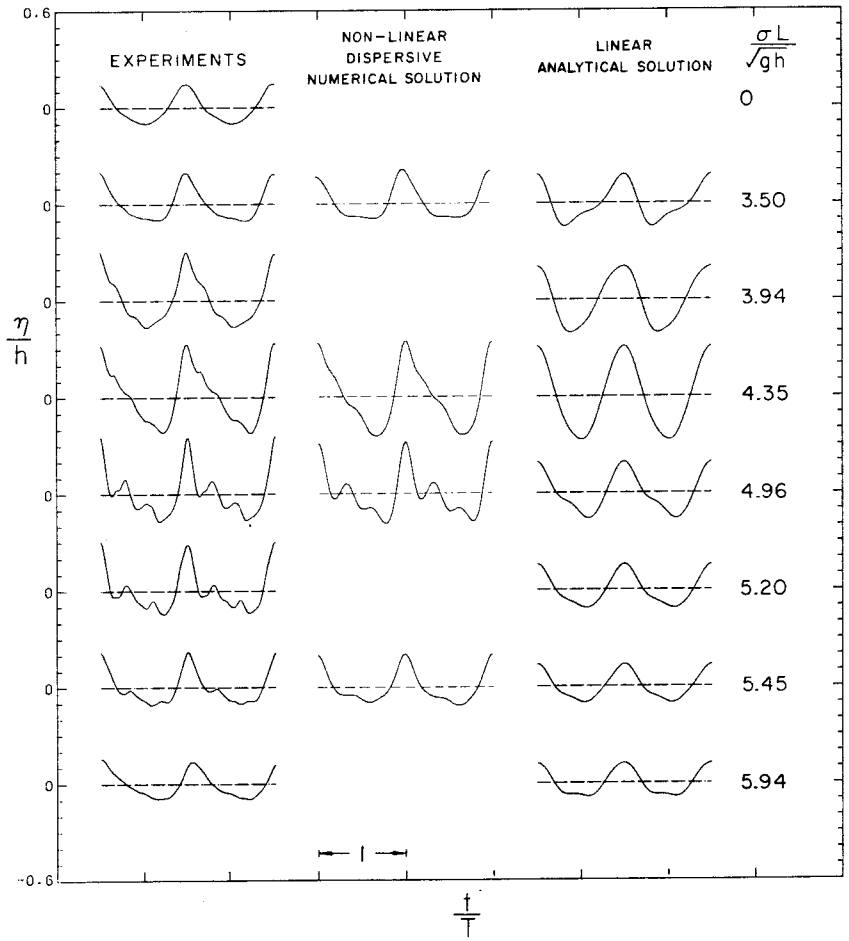

Fig. 6.3.22 (a) Variation of the steady state extrema with $\sigma L/\sqrt{gh}$, at the backwall, (b) steady state wave records at the backwall for several values of $\sigma L/\sqrt{gh}$; comparison between experiments, linear and nonlinear solution, Case 2b; h = 7.5 cm, T = 1.81 s.

Figure 6.3.19. In particular, the positive peak is shifted from $\sigma L/\sqrt{gh} = 4.4$ to about $\sigma L/\sqrt{gh} = 5.0$. The skewness of the positive extremum curve is also quite apparent. For $\sigma L/\sqrt{gh} = 5.0$, the ratio of positive to negative extrema reaches 2.5 compared to 1.1 for the linear theory. Thus, the general shape of response curves for the steady state bears a certain resemblance to the results obtained for the closed rectangular basin. It is noted that the agreement between the nonlinear dispersive solution to the experiments is good.

Several wave records are presented in the lower portion of Fig. 6.3.22 for steady state conditions. The experimental results and the linear theory differ significantly and in contrast, the nonlinear theory agrees reasonably well with experiments for the four curves which were obtained numerically. For $\sigma L/\sqrt{gh} = 3.50$, a slight extremum takes place on the linear curve on Fig. 6.3.22, which indicates the excitation of the third resonant mode by the second harmonic component of the incident wave. However, the wave shape described by the linear theory and shown below, characterized by a distorted front face, does not agree with either the experiments or the nonlinear theory. This means that the harbor cannot be considered for this case as a linear transducer for the incident wave. Thus, the effects of higher frequency components in the incident wave cannot be simply linearly superimposed; they become directly related to the over-all nonlinear behavior of the wave inside the harbor. As $\sigma L/\sqrt{gh}$ increases, so does the wave height and the front face of the wave steepens and secondary oscillations appear and grow in amplitude. At $\sigma L/\sqrt{gh} = 5.2$ the secondary oscillations attain a height about one-third of the main oscillation. It should be noted,

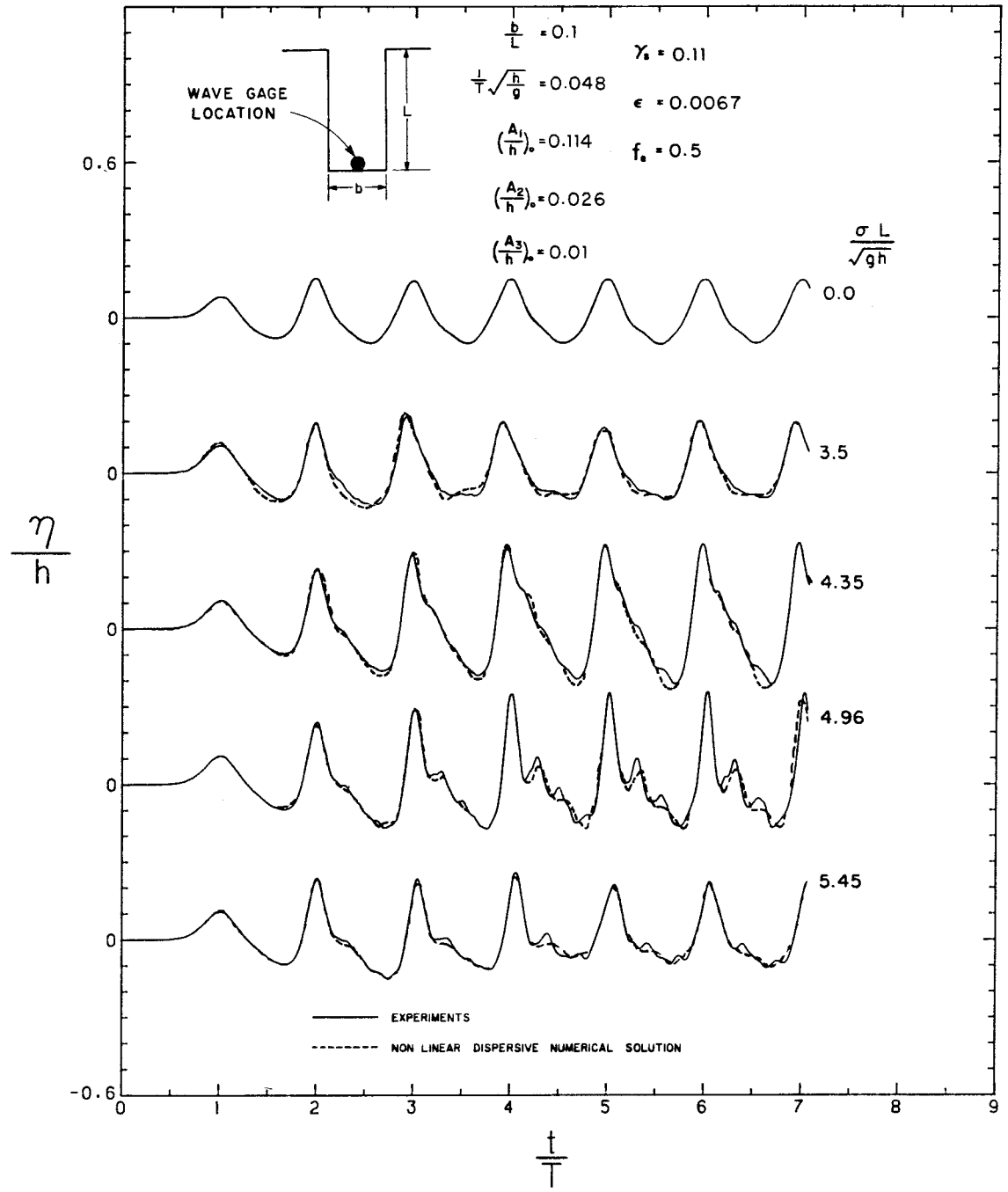

Fig. 6.3.23 Transient wave records at the backwall for several values of $\sigma L/\sqrt{gh}$ near the second resonant mode, Case 2b; h = 7.5 cm, T = 1.81 s.

for these experiments, the nonlinear resonant processes inside the harbor are quite similar to features observed in the closed basin; in particular, the main oscillation at resonance divides into several secondary oscillations as a result of the attempt of the wave to balance nonlinear and dispersive effects. However, these oscillations remain smaller than what was observed for the closed rectangular basin, probably because of the strong damping (viscid and inviscid) for the harbor which limits their development. For $\sigma L/\sqrt{gh} = 5.94$, which corresponds to a nonresonant condition, the wave shape at the backwall is again similar to the incident wave.

To estimate the transient effects near the second resonant mode, the time history of the relative wave elevation η/h at the backwall is presented in Fig. 6.3.23 for several values of $\sigma L/\sqrt{gh}$ and is compared with the experiments. Again, the nonlinear solution agrees well with the experiments for all cases. It is seen that nonlinear effects become fully developed after four oscillations, and steady state conditions occur within five oscillations for all examples. Thus, the transient effects remain small for these conditions.

The steady state energy percentage curves on Fig. 6.3.24 clearly show the generation of higher harmonics which accompanies the nonlinear resonant process. For $\sigma L/\sqrt{gh} = 5.2$, the second, third, and fourth harmonic components contain about 50% of the wave energy, compared to only 7% predicted by the linear theory. It can be observed from Fig. 6.3.24 that only higher harmonics up to the fourth are generated by this nonlinear resonant process. The amplitude response curves for the first three harmonic components are shown in Fig. 6.3.25. The

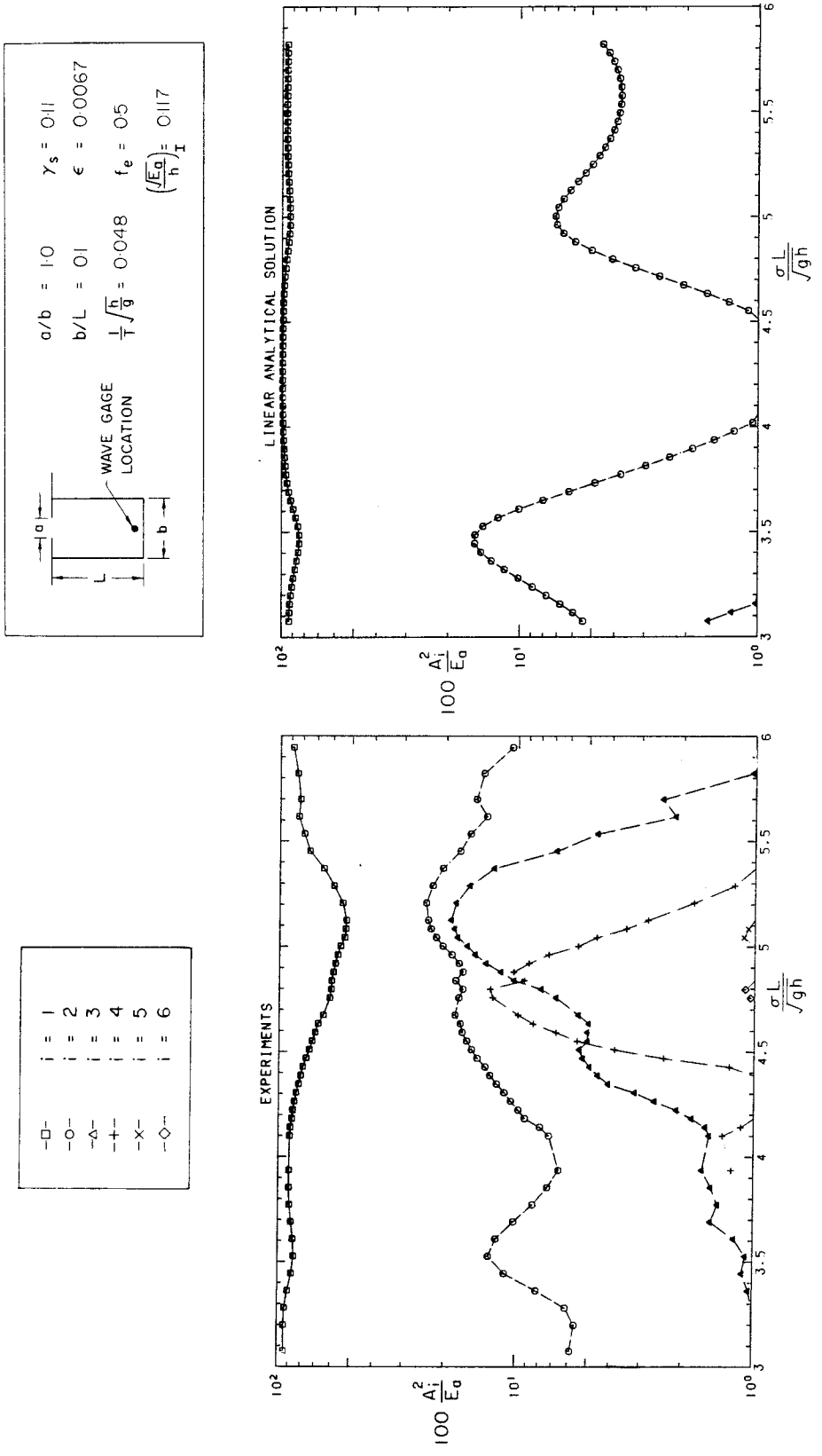

Fig. 6.3.24 Variation of percentage of wave energy with $\sigma L/\sqrt{gh}$ for the first six Fourier components, at the backwall, comparison between experiments, linear and nonlinear solution, Case 2b; h = 7.5 cm, T = 1.81 s.

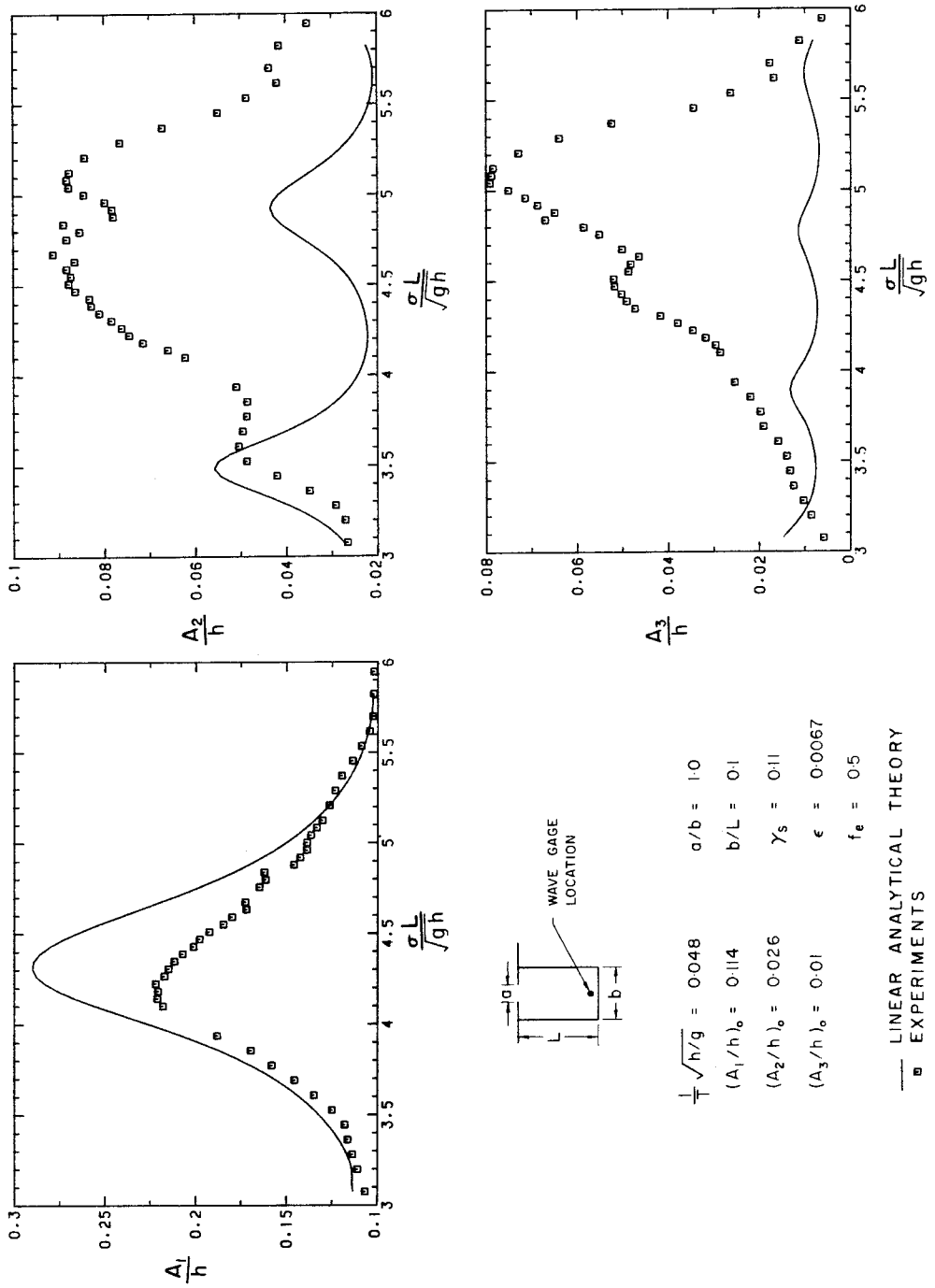

Fig. 6.3.25 Variation of the relative wave amplitude with $\sigma L/\sqrt{gh}$ for the first three Fourier components, comparison between experiments, linear and nonlinear solution, Case 2b; h = 7.5 cm, T = 1.81 s.

nonlinear process of energy transfer from the lowest to higher harmonic components is clearly seen for $\sigma L/\sqrt{gh} = 4.4$ where the ratio of maximum amplitude computed from the linear theory to the corresponding experimental amplitude reaches 1.4 for the lowest harmonic. The response curves for the second and third harmonic component obtained experimentally is significantly different from that which is predicted by the linear theory. This indicates that they result from the nonlinear interaction of the main oscillation triggered by the second resonant mode.

6.3.3.3 Case 2c: Large Amplitude, Small Dispersion, Fully Open Harbor

The experimental conditions are similar to those of case 2b, except that the depth parameter $\sqrt{g/h}/\ T$ is decreased from 0.048 to 0.027. As a consequence, the amount of energy in the higher harmonics in the incident wave is larger.

The variation of the relative positive and negative steady state wave extrema with $\sigma L/\sqrt{gh}$ for this case is presented in Fig. 6.3.26. The second harmonic component in the incident wave has an amplitude equal to half that of the first harmonic component, and this explains the presence of these rather well defined peaks on the linear response curve. The peak at $\sigma L/\sqrt{gh} = 3.80$ corresponds to the amplification of the second harmonic at the third resonant mode, the main peak at $\sigma L/\sqrt{gh} = 4.3$ corresponds to the amplification of the first harmonic at the second resonant mode, and finally, the peak at $\sigma L/\sqrt{gh} = 5.2$ corresponds to the amplification of the second harmonic component at the fourth resonant mode. Relatively large differences between the response curve predicted from the linear theory and that determined from experiments can be observed, and the shape of the experimental response

(a)

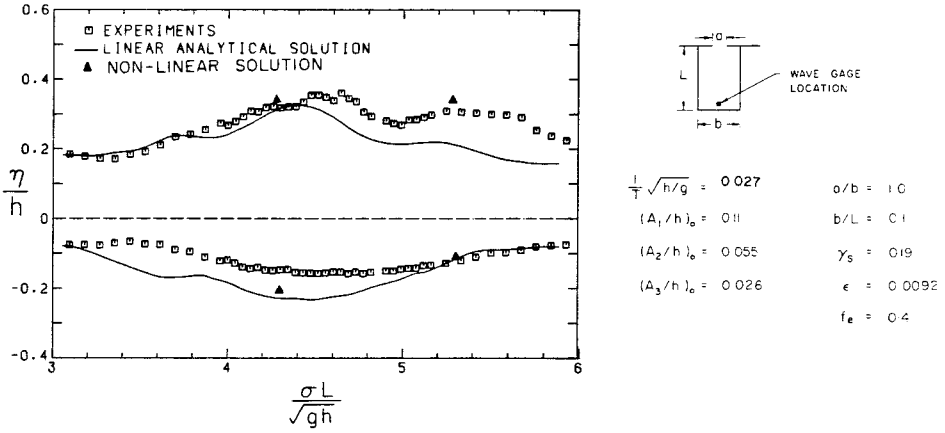

(b)

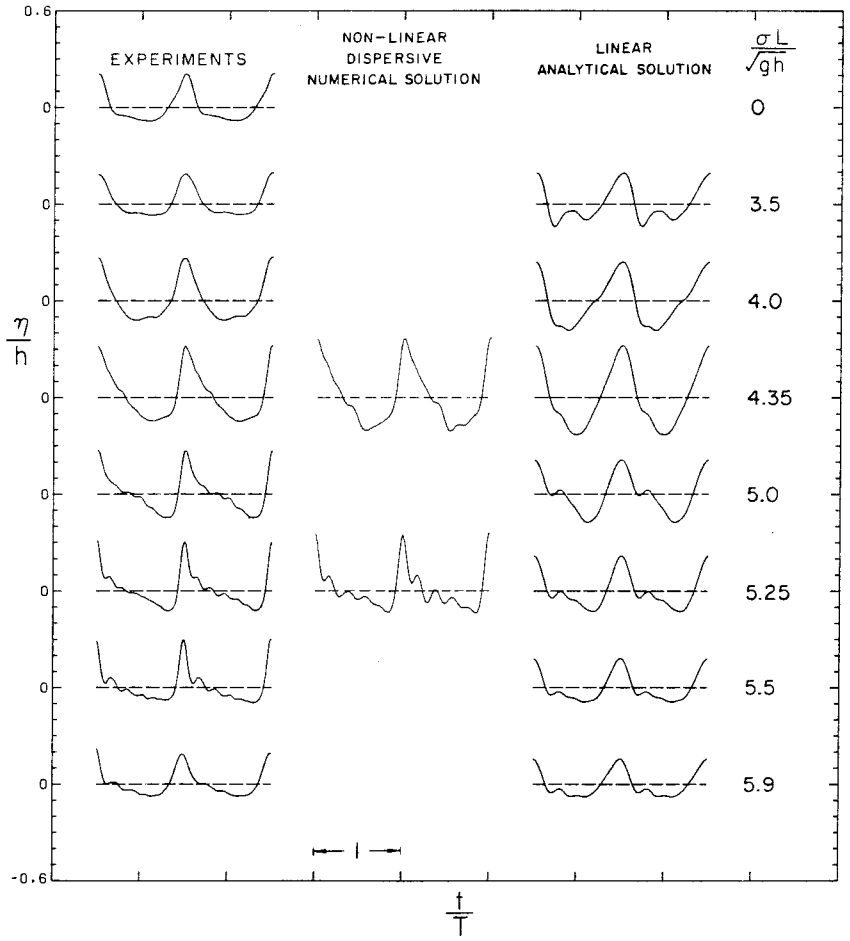

Fig. 6.3.26 (a) Variation of the steady state wave extrema with $\sigma L/\sqrt{gh}$ at the backwall, (b) steady state wave records at the backwall for several values of $\sigma L/\sqrt{gh}$; comparison between experiments, linear and nonlinear solution, Case 2c; h = 4 cm, T = 2.36 s.

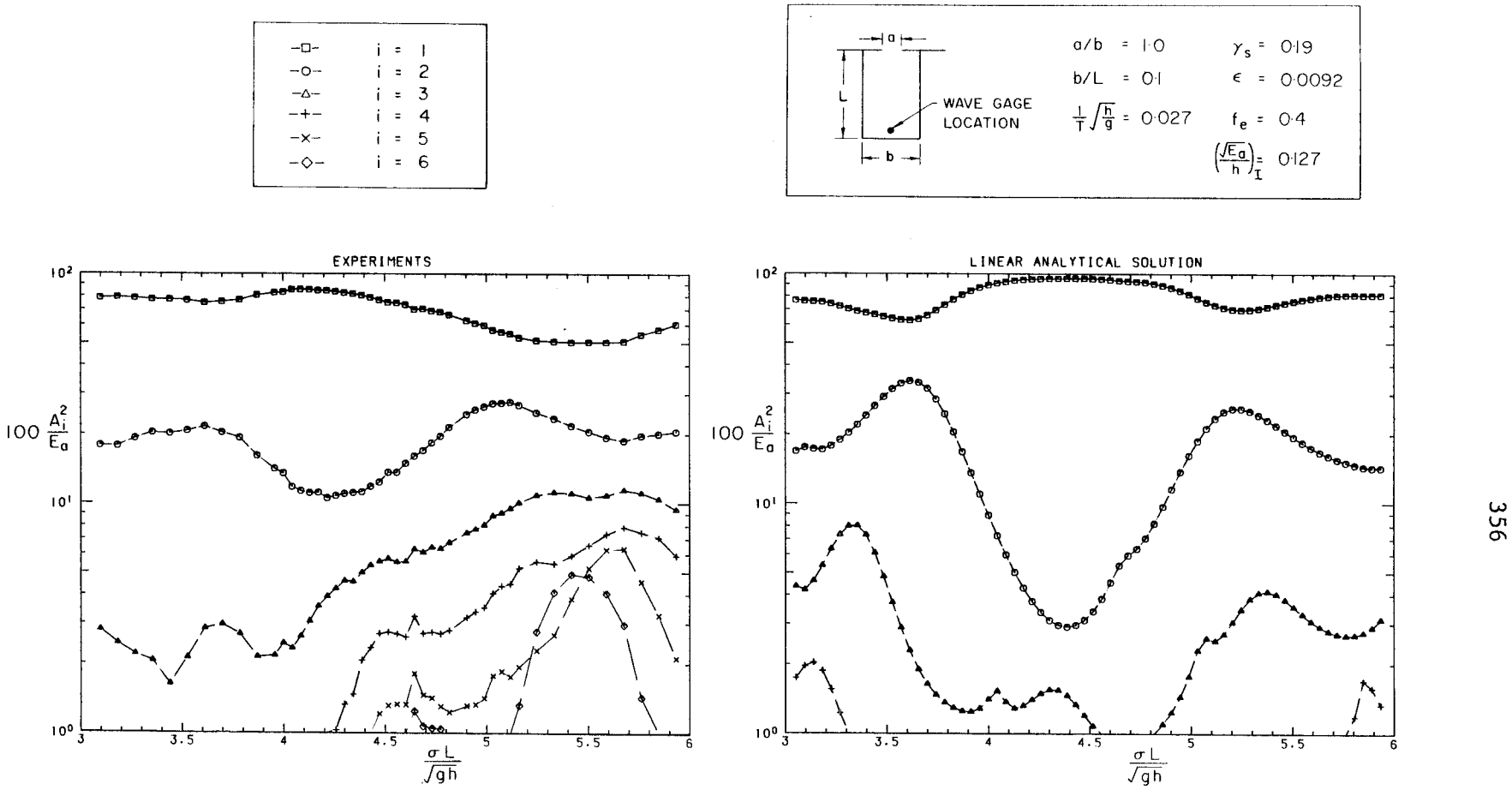

Fig. 6.3.27 Variation of percentage of wave energy with $\sigma L/\sqrt{gh}$ for the first six Fourier components at the backwall, comparison between experiments, linear and nonlinear solution, Case 2c; h = 4 cm, T = 2.36 s.

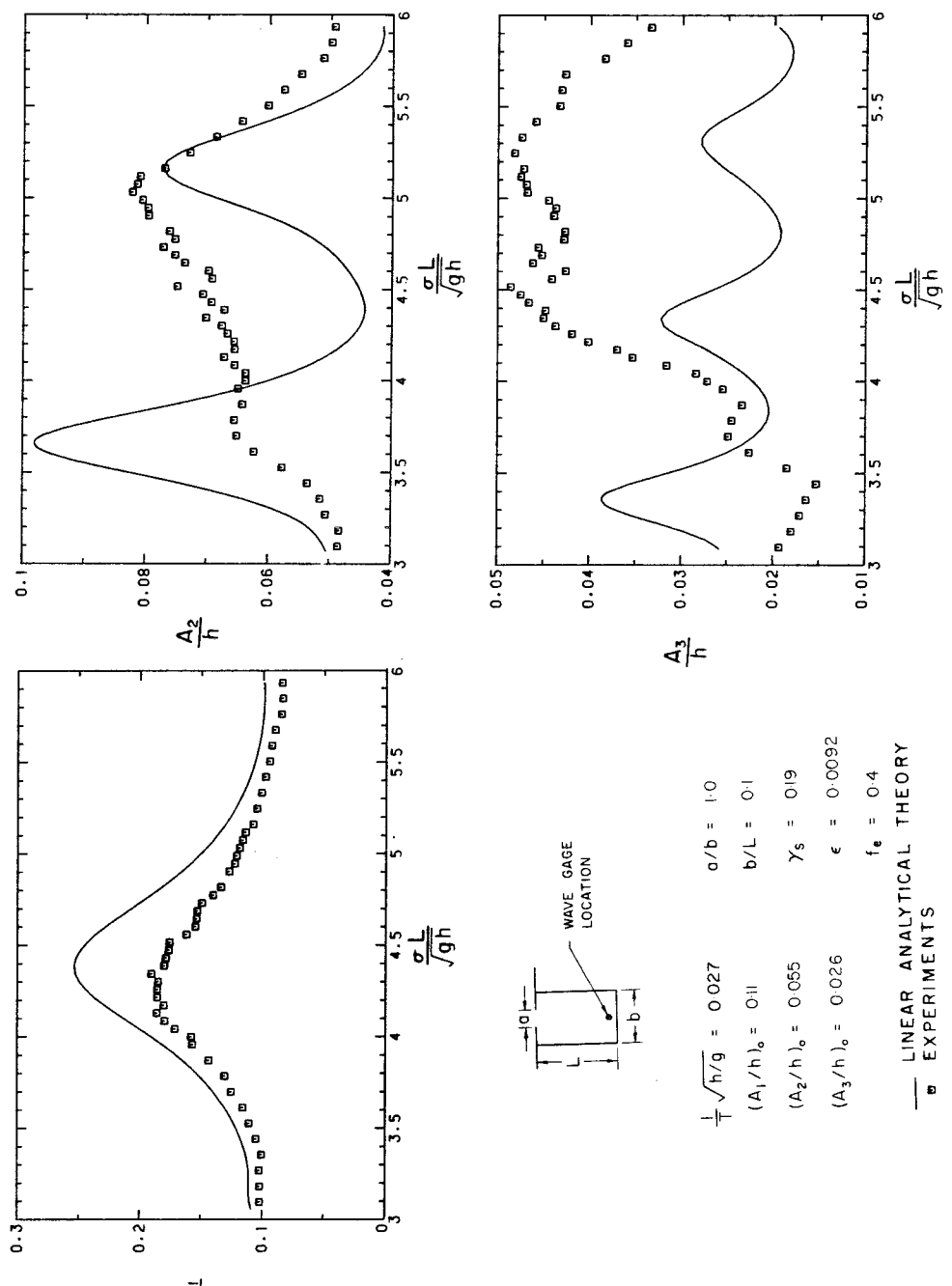

Fig. 6.3.28 Variation of the relative wave amplitude with $\sigma L/\sqrt{gh}$ for the first three Fourier components, comparison between experiments, linear and nonlinear solution, Case 2c; h = 4 cm, T = 2.36 s.

curve is somewhat different from that in Fig. 6.3.22. Two distinct experimental extrema now occur in the experimental curve at $\sigma L/\sqrt{gh} = 4.5$ and $\sigma L/\sqrt{gh} = 5.4$, respectively. The occurrence of the second experimental peak and the third linear peak at about the same value of $\sigma L/\sqrt{gh}$, i.e., around 5.2, is believed to be coincidental, since the experimental wave behavior is not believed to be governed by linear theory for $\sigma L/\sqrt{gh} = 5.2$, but rather emanates from the characteristics of the nonlinear resonant oscillations.

Several steady state wave records are presented in the lower part of Fig. 6.3.26. For $\sigma L/\sqrt{gh} > 4.3$, secondary oscillations appear on the back face of the main wave but with small amplitudes. Nevertheless, the number of oscillations is larger than for case 2b, e.g., for $\sigma L/\sqrt{gh} = 5.25$ four secondary oscillations are clearly seen. The same features are obtained on the corresponding nonlinear wave record, although secondary oscillations have somewhat larger amplitudes. These observations are consistent with the results of the oscillation of a closed rectangular basin which showed a larger number of secondary oscillations for smaller values of the dispersion parameter. For $\sigma L/\sqrt{gh} > 4.3$, the nonlinear resonant conditions which develop are mainly characterized by the presence of higher harmonic components. The frequency of these harmonics increases as the effects of dispersion decrease, and they tend to be damped more efficiently by dissipation. Consequently the secondary peak observed in upper graph of Fig. 6.3.26 may not be fully developed because of dissipation effects.

In the energy percentage curves shown in Fig. 6.2.27, the effects of small dispersion in generating higher frequency components is clearly

demonstrated. In particular for $\sigma L/\sqrt{gh} = 5.6$, the fifth and sixth components contain 10% of the total energy, whereas in case 2b those components were negligible. The amplitude response curves in Fig. 6.2.28 exhibit similar features to case 2b. The same nonlinear damping is observed for the first harmonic. The ratio of maximum amplitude computed from the linear theory to the corresponding experimental amplitude reaches 1.35. Higher harmonics grow until a certain point ($\sigma L/\sqrt{gh} = 5.5$) and then stop rapidly, as can be seen from the response of third harmonic in Fig. 6.3.28.

To investigate further the effects of small dispersion on the second resonant mode, numerical experiments using the nonlinear dispersion solution were performed with a sinusoidal input wave for: $b/L = 0.1$, $\sigma L/\sqrt{gh} = 4.95$, $(A_1/h)_o = 0.1$, and no viscous dissipation. The computations were made for three "depth-to-wavelength" parameter values ($\sqrt{h/g}/T$) which correspond more to prototype conditions: 0.03, 0.009, and 0.003. The time history of the variation of the water surface elevation η/h at the backwall is presented in Fig. 6.3.29 for these conditions. For the three curves the steady state wave height is about twice that corresponding to $\sigma L/\sqrt{gh} = 0$ (compared to about unity for the linear theory). The nonlinear resonant oscillations are characterized by a steep front face and secondary oscillations on the back face. Finally, the number of secondary oscillations tends to increase for smaller dispersions but their amplitude tends to decrease in the same time.

6.3.3.4 Case 2d: Large Amplitude, Small Dispersion, Partially Closed Harbor

The effects of entrance dissipation on nonlinear resonant interactions near the second resonant mode were investigated by reducing

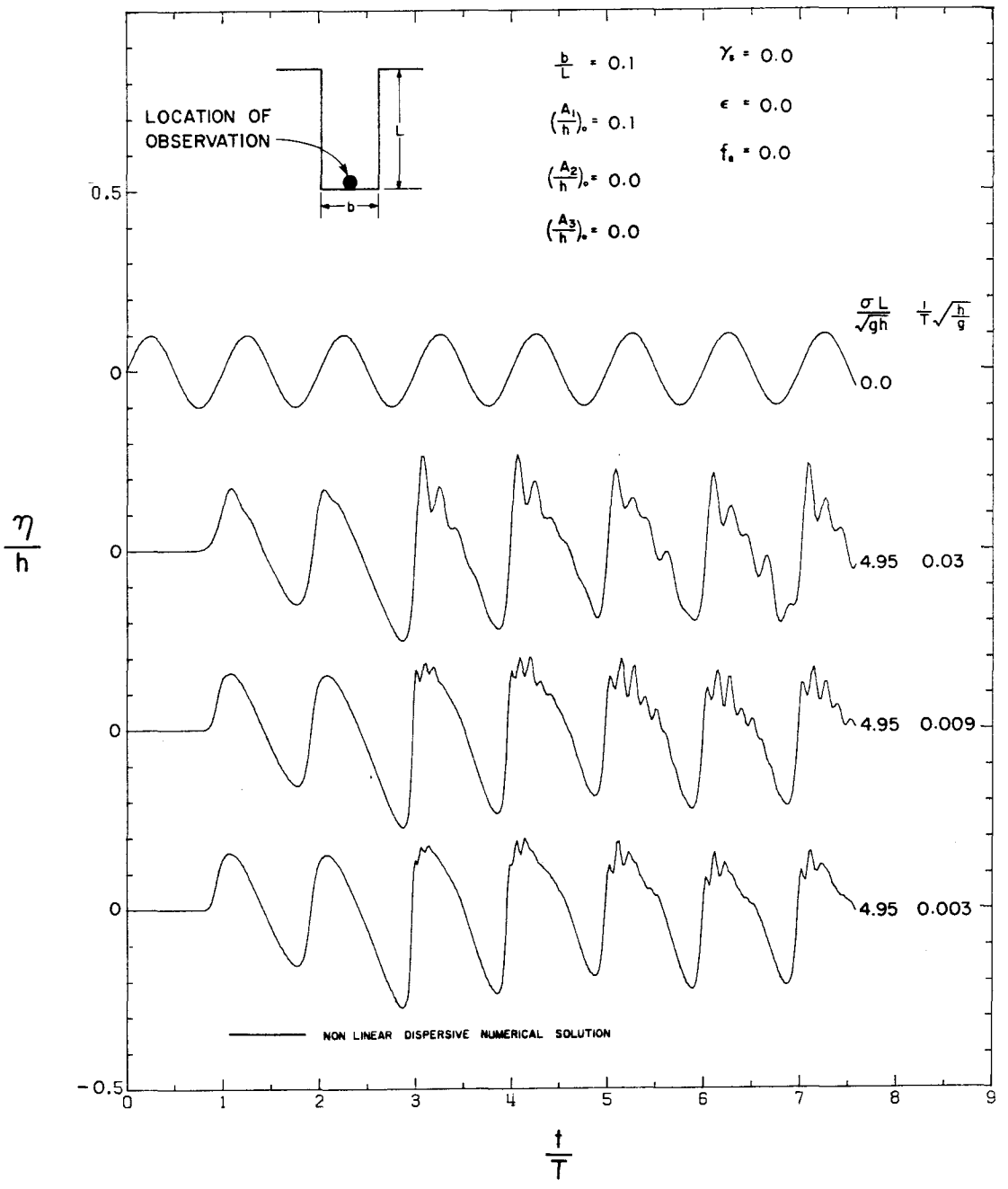

Fig. 6.3.29 Computed transient records at the backwall for sinusoidal excitations, for various values of $1/T\sqrt{h/g}$. No viscous dissipation b/L = 0.1, $(A_1/h)_o$ = 0.1, $\sigma L/\sqrt{gh}$ = 4.95.

the harbor entrance to half the fully open width. Figure 6.3.30 shows the variation of the relative steady state extrema with $\sigma L/\sqrt{gh}$. It is noted resonance is almost completely suppressed near $\sigma L/\sqrt{gh} = 4.4$ and in the experiments a distinct peak results from the nonlinear resonant process at $\sigma L/\sqrt{gh} = 5.00$.

Selected segments of some steady state wave records are presented in the lower portion of Fig. 6.3.30 for various values of $\sigma L/\sqrt{gh}$ obtained experimentally and from the nonlinear and linear theories. The wave shapes from the linear theory are in better agreement with the experiments than in the other cases, which shows that nonlinear features have been reduced by the energy dissipation introduced by the partially closed entrance. Some secondary oscillations appear behind the main wave in the wave record obtained experimentally. This feature is not predicted by the nonlinear theory, although the wave height is correctly predicted.

The energy percentage curves are shown in Fig. 6.3.31. The generation of higher harmonics around $\sigma L/\sqrt{gh} = 5.0$ is relatively less important than for case 2b. In the latter case the third and fourth harmonic components contain a maximum of about 35% of the total wave energy, compared to 12% for case 2d. The amplitude response curves for the first three harmonic components presented in Fig. 6.3.32 show similar effects as observed for the fully open case; however, the features are somewhat attenuated by entrance dissipation.

6.3.3.5 Case 2e: Large Amplitude, Moderate Dispersion, Fully Open Harbor

In previous cases data were obtained at only one location: the backwall of the harbor. In this section in addition to

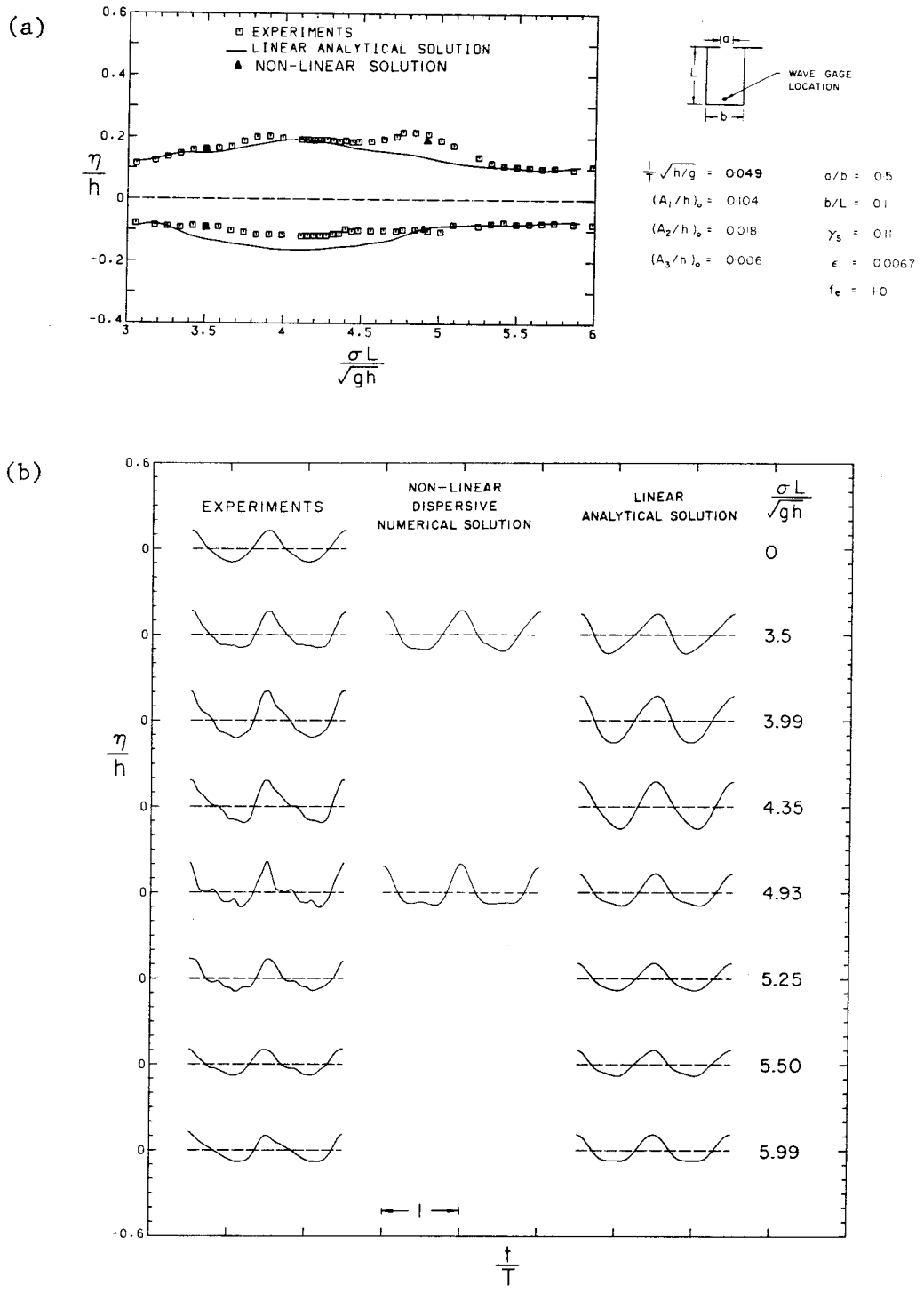

Fig. 6.3.30 (a) Variation of the steady state wave extrema with $\sigma L/\sqrt{gh}$ at the backwall, (b) steady state wave records at the backwall for several values of $\sigma L/\sqrt{gh}$; comparison between experiments, linear and nonlinear solution, Case 2d; h = 7.45 cm, T = 1.805 s.

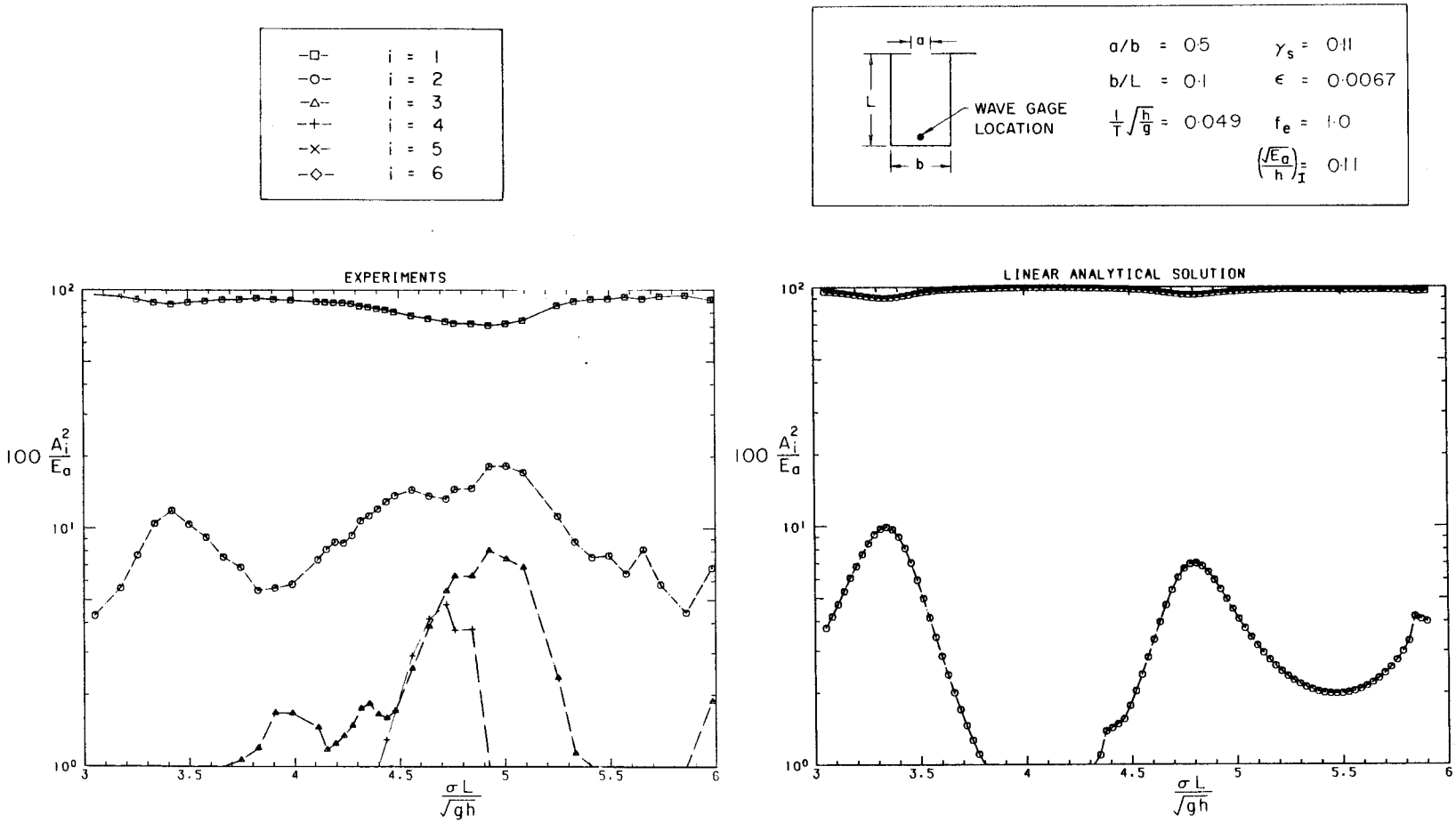

Fig. 6.3.31 Variation of percentage of wave energy with $\sigma L/\sqrt{gh}$ for the first six Fourier components, at the backwall, comparison between experiments, linear and nonlinear solution, Case 2d; h = 7.45 cm, T = 1.805 s.

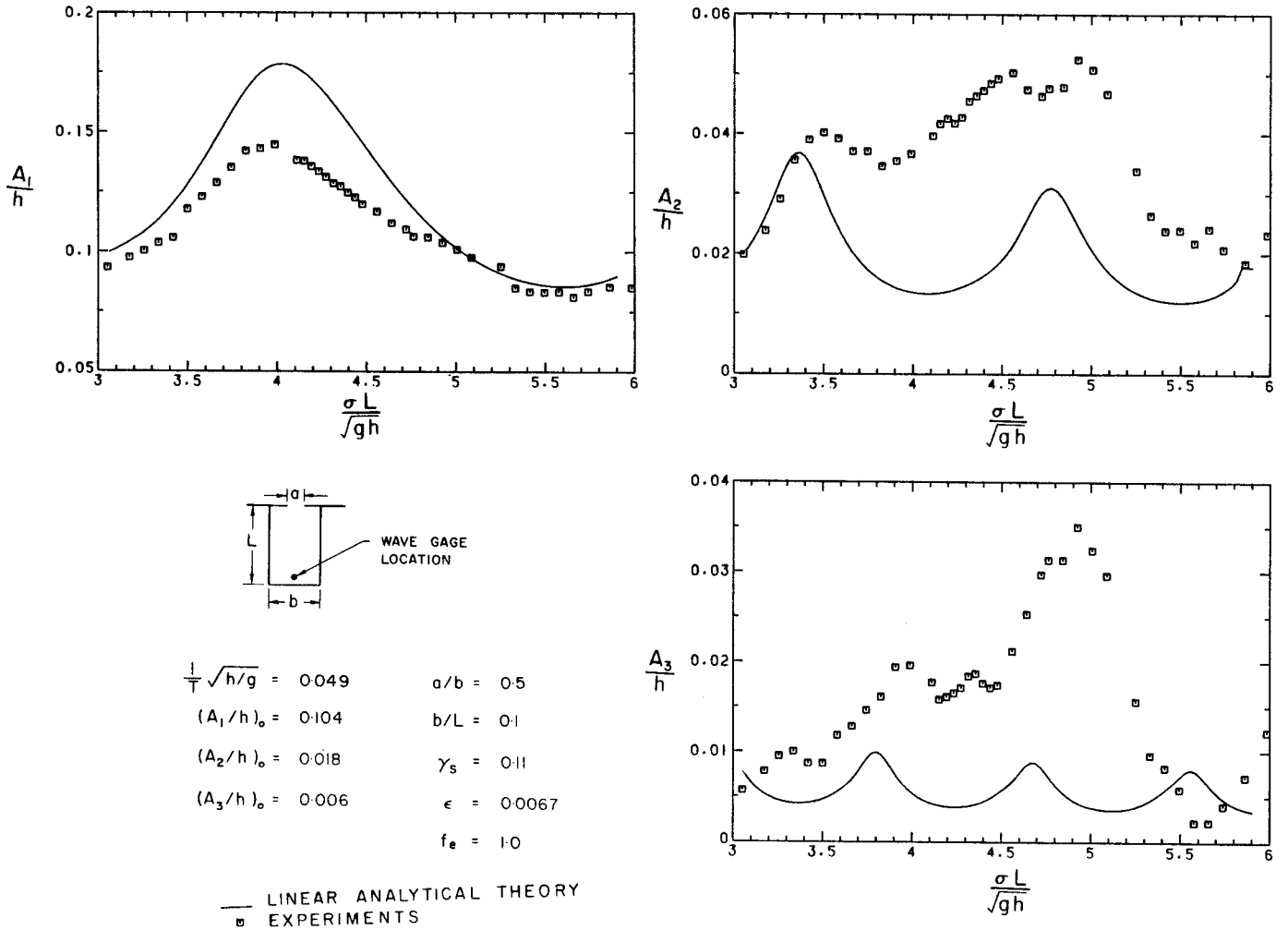

Fig. 6.3.32 Variation of the relative wave amplitude with $\sigma L/\sqrt{gh}$ for the first three Fourier components, comparison between experiments, linear and nonlinear solution, Case 2d; h = 7.45 cm, T = 1.805 s.

obtaining the variations of the water surface elevation with time at a given location, the variation with distance was also evaluated at different elapsed times. The experimental profiles were compared to both the linear analytical solution and the nonlinear dispersive solution. To clearly characterize the nonlinear behavior of the wave inside the harbor for the second resonant mode, a fairly large incident wave was used as input, i.e., $(\sqrt{E_a}/h)_o = 0.16$ and the small radius corners at the entrances used for all other cases ($r_e = 0.5$ cm) were replaced by the large radius corners ($r_e = 5$ cm) to minimize entrance dissipation.

First the response curves obtained experimentally and from the linear theory are presented in Fig. 6.3.33 similar to the other cases investigated. The same nonlinear features seen before, although somewhat enhanced here, are observed. It is seen that the negative extremum measured experimentally is relatively independent of $\sigma L/\sqrt{gh}$. The response associated with the experiments is a maximum for $\sigma L/\sqrt{gh} = 5.0$ and the corresponding ratio of the positive extremum over the negative extremum reaches three. The discrepancy between experiments and linear theory is obvious especially when the positive wave extrema are compared at resonance. Good agreement is obtained between experiments and nonlinear results even for $\sigma L/\sqrt{gh} = 5.0$ where the experimental relative wave height reaches 0.8.

The experimental steady state wave records presented in the lower part of Fig. 6.3.33 do not agree at all with the results of the linear theory. In contrast, the experiments agree quite well with the nonlinear dispersive theory. For $\sigma L/\sqrt{gh} > 4.3$ secondary oscillations appear and the main wave divides into three separate waves.

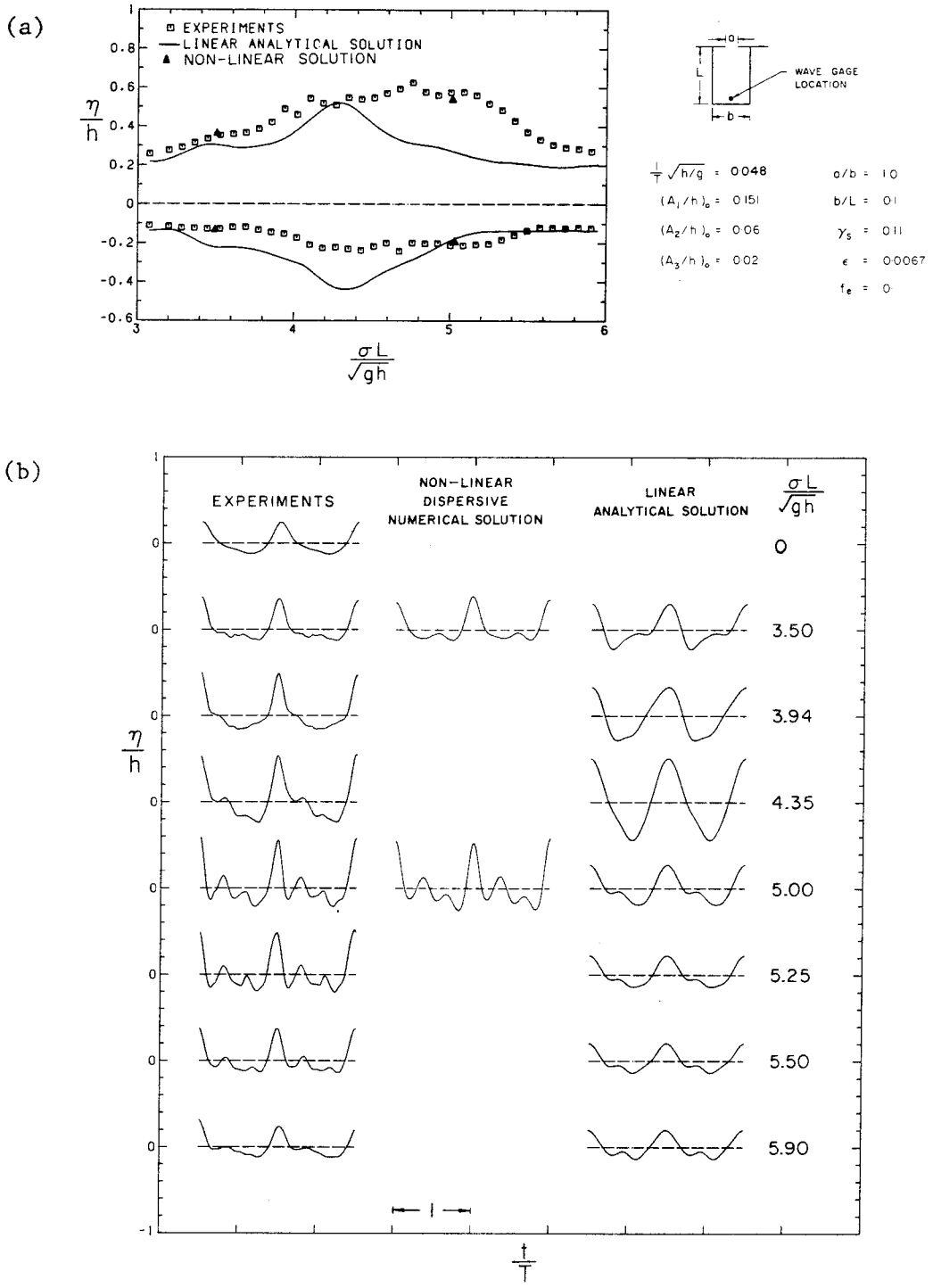

Fig. 6.3.33 (a) Variation of the steady state wave extrema with $\sigma L/\sqrt{gh}$ at the backwall, (b) steady state wave records at the backwall for several values of $\sigma L/\sqrt{gh}$; comparison between experiments, linear and nonlinear solution, Case 2e; h = 7.5 cm, T = 1.78 s.

The photographic method used to obtain experimental wave profile (variation of the water surface elevation with distance) inside the closed rectangular basin turned out to be unsuitable for the harbor because of physical constraints. Instead, steady state wave profiles were obtained experimentally by using the following procedure: A series of transient Eulerian wave gage records were taken at sixty equally spaced locations inside the harbor. For each of these sixty runs the same incident wave was generated and the wave was recorded at a given location inside the harbor. Then the wave gage was moved to the next location and the process was repeated. For each run the wave was recorded by a second gage, located at a fixed position just outside the harbor in order to provide the same time origin for all records. This method proved accurate because of the high degree of repeatability of the hydraulically driven wave generation system, and due to the analogue-to-digital data acquisition system used in this study.

The experimental steady state wave profiles for twelve different times within one wave period are presented in Fig. 6.3.34. These were measured along the centerline of the harbor and the profiles are compared with the linear analytical solution and the nonlinear dispersive numerical solution. The positions $x/L = -1$ and $x/L = 0$ correspond to the backwall and the mouth, respectively. The wave elevation in millimeters is plotted as the ordinate. (It is recalled that $h = 7.45$ cm for this case).

The experiments and the nonlinear theory agree fairly well for all times. The linear theory produces a completely different pattern which resembles a standing wave pattern. No nodes are seen with the linear theory because the incident wave used as input in the calculation is

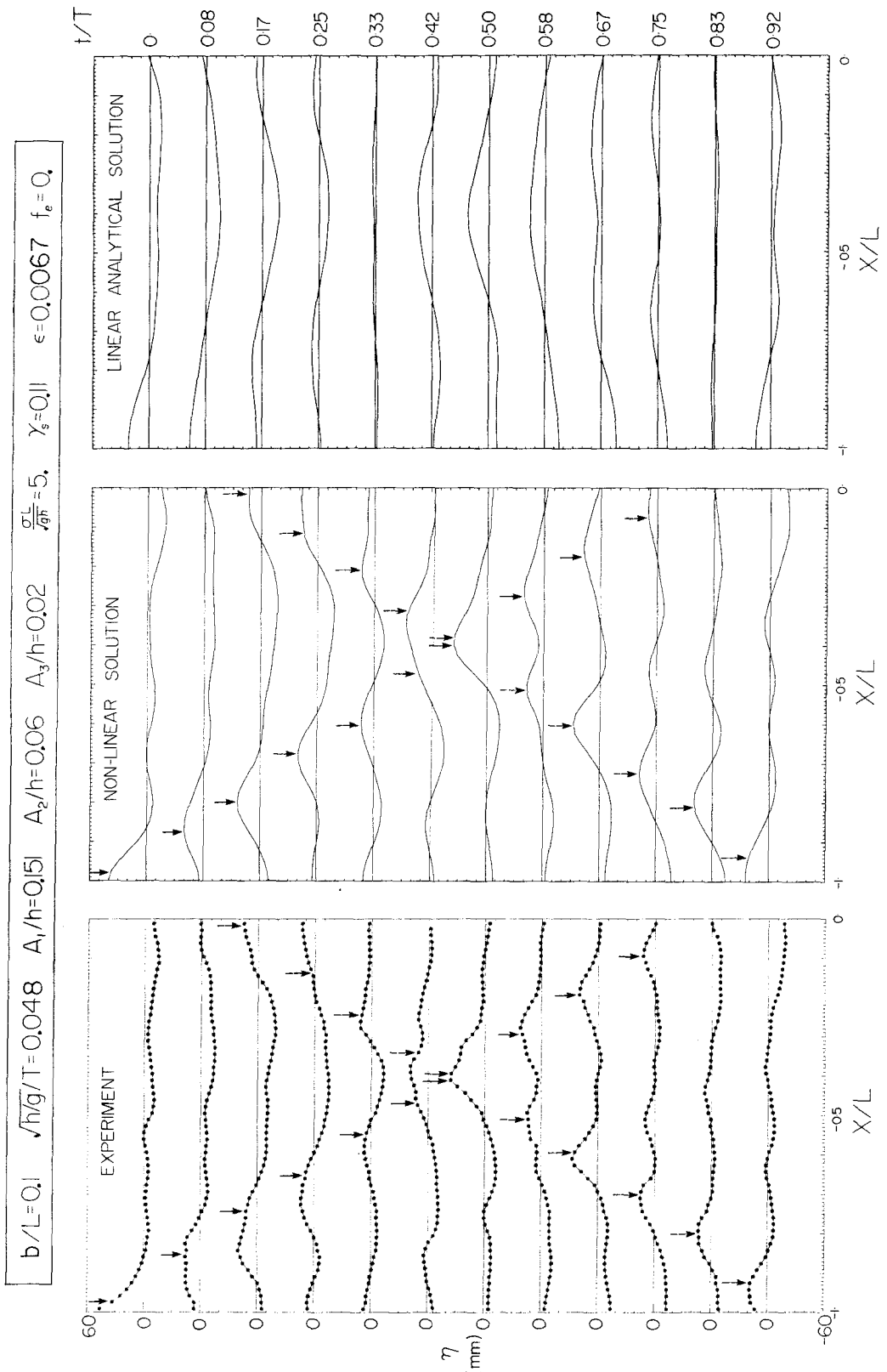

Fig. 6.3.34 Evolution of steady state wave profiles with time inside the harbor, Case 2e; h = 7.5 cm, T = 1.78 s, L = 120 cm, comparison between experiments, linear and nonlinear solutions.

not symmetric about the mean water level consequently the intersection of the wave elevation with the mean water level oscillates about the positions $x/L = -0.33$ and $x/L = 0.0$. One important feature associated with the experimental profiles is the moving wave pattern characterized mainly by two "hump-like" waves indicated by the full line and the hatched arrows in Fig. 6.3.34, which travel in and out of the harbor. Secondary travelling oscillations complicate that pattern further, and are mainly responsible for additional local extrema such as the one observed at $x/L = -0.6$ for $t/T = 0.67$. The similarity between this wave pattern and those obtained with the closed basin is obvious (see Fig. 5.2.8).

If dispersion effects are decreased one would expect to obtain more secondary local extrema along the harbor. If they are further reduced, viscous dissipation is expected to damp out the secondary oscillations and triangular shaped waves travelling in and out of the harbor should be obtained.

6.3.4 Summary

The nonlinear resonant oscillations of a narrow rectangular harbor have been investigated experimentally and theoretically and discussed in Section 6.3. The main results can be summarized as follows.

For short bays, such that $\sigma L/\sqrt{gh} < 0.6$, nonlinear convective effects do not appear and can be reasonably neglected even when the wave height of the oscillations is of order unity. In this range the harbor acts as a linear transducer which sees the incident wave as a signal composed of various frequencies, but does not perceive the nonlinear nature of this wave. In fact the harbor length L is too small for the nonlinear effects to have space enough to develop.

As the bay length increases relative to the incident wavelength, some nonlinear features of the bay response begin to appear. Nonlinear resonant conditions, not predicted by the linear theory, may be triggered inside the harbor for a sufficiently large incident wave amplitude, and higher harmonics are generated which increase this wave height.

For even longer bays, such that the second mode resonant conditions are met, the importance of nonlinearities is apparent. At the second resonant mode the ratio L/ℓ is about 0.75 and the wave has enough space (and time) to resonate in a nonlinear manner, similar to that observed for the closed basin. These nonlinear features are somewhat attenuated because of dissipation, but nevertheless they cannot be neglected.

6.4 The Transient Excitation of a Harbor

Section 6.3 was specialized to a narrow rectangular harbor with constant depth, excited by a continuous train of nonlinear incident waves. The main purpose was to analyze in detail the interactive effects of finite wave amplitude, dispersion, and dissipation on the wave dynamics inside the harbor for this geometrically simple shape.

In this section the investigation is extended to wave oscillations in harbors induced by a transient train of incident cnoidal waves for a fully open rectangular harbor with a constant depth, a fully open rectangular harbor with a linearly varying depth, and a fully open and partially open harbor with a trapezoidal planform and a constant depth.

For each case investigated the experiments are compared to the results of the nonlinear dispersive numerical model; the linear solution is also presented for most of the results. All the experimental wave records were taken at the backwall of the harbor.

6.4.1 A Narrow Rectangular Harbor with a Constant Depth

In a first series of experiments two cnoidal incident waves were generated with the primary purpose of investigating the growth and decay of the oscillations in the harbor when the period T (associated with the frequency σ) of the cnoidal incident wave matched one of the natural periods of oscillations of the harbor. For this series the bottom of the harbor was sealed to the basin floor and the corners of the entrance were rounded to minimize leakage and entrance dissipation, respectively.

The variation of the relative water surface displacement η/h with dimensionless time t/T at the backwall is presented in Fig. 6.4.1 for three incident relative wave heights: $(H/h)_{inc} = 0.05$, 0.10, and 0.17, where H denotes the incident wave height before it reaches the harbor or, equivalently, one-half the wave height at the coastline with closed harbor entrance (assuming the reflection process at the coastline is linear). The other dimensionless parameters are $b/L = 0.2$, $\sqrt{h/g}/T = 0.047$, $\sigma L/\sqrt{gh} = 1.3$, $\gamma_s = 0.13$, $\varepsilon = 0.0$, $f_e = 0.0$ corresponding to the physical parameters L = 35 cm, T = 1.92 sec, h = 8 cm. The value of the frequency parameter $\sigma L/\sqrt{gh}$ corresponds to resonant conditions for the first mode of oscillation of the harbor. In each graph the full line represents the experiments, the line composed of short dashes represents the nonlinear numerical solution and the line of long dashes corresponds to the linear solution. The upper curve in each graph is the incident wave record at the coastline with the harbor entrance closed. In the case of Fig. 6.4.1 the linear curves were obtained from the analytical solution of Section 3.3.

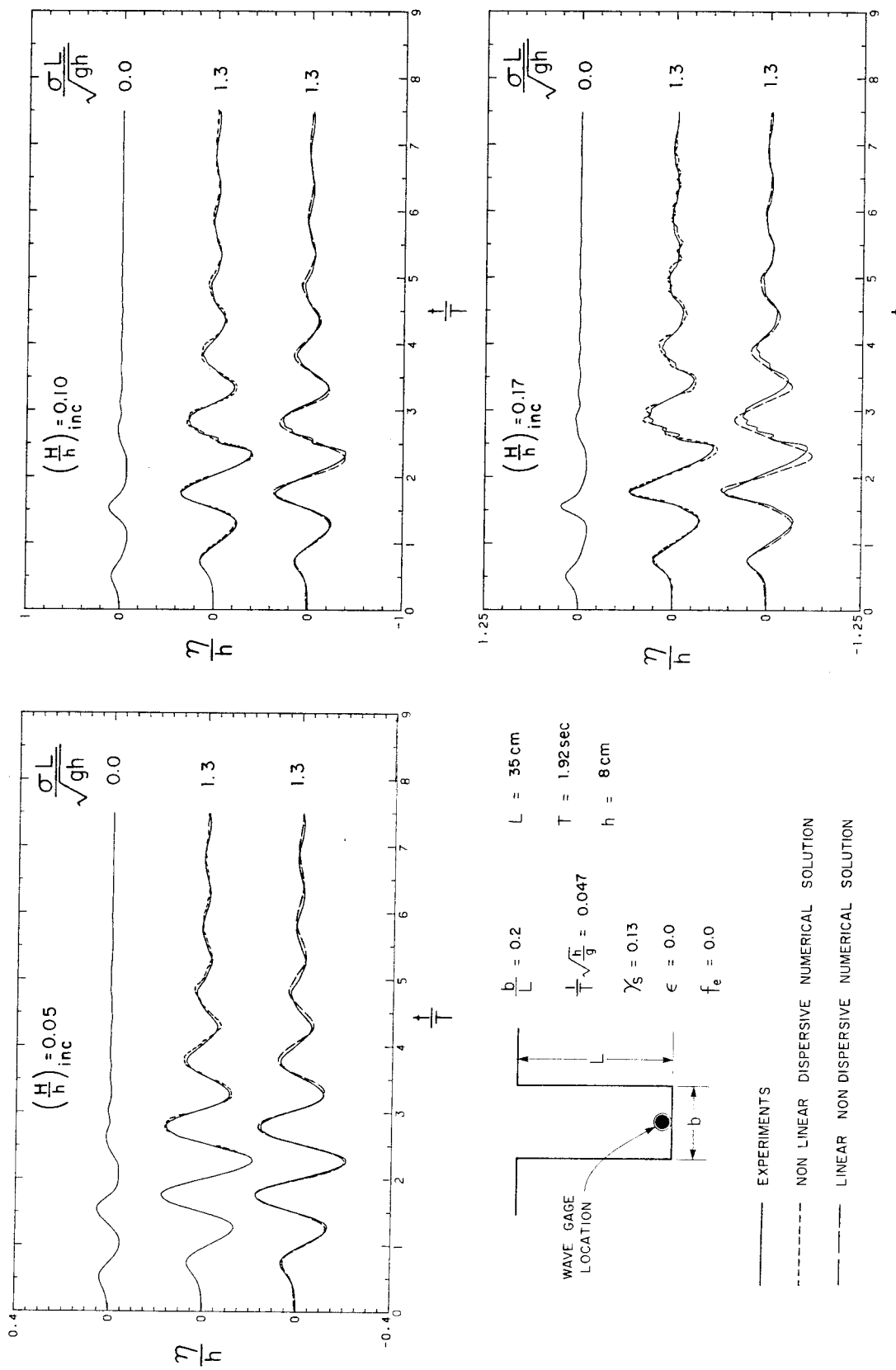

Fig. 6.4.1 Transient wave records at the backwall for a fully open harbor for three incident wave heights. Comparison between experiments, linear and nonlinear solutions. L = 35 cm, T = 1.92 s, h = 8 cm.

For the smallest incident wave, $(H/h)_{inc} = 0.05$, both linear and nonlinear theories agree well with the experiments. Resonance develops over a relatively short time, and the height of the second oscillation reaches 3.5 times the incident wave height at the coastline. Therefore, in prototype situations resonance conditions can indeed lead to a substantial amplification of the transient incident waves even if the number of waves is small (e.g. less than three). The decay rate of the harbor oscillations after the excitation phase is rather large: the wave motion has almost disappeared inside the harbor within five oscillations. Good agreement between experiments and linear and nonlinear theories is again obtained for $(H/h)_{inc} = 0.10$. For the largest incident wave $(H/h)_{inc} = 0.17$ only a slight discrepancy is observed between experiments and linear theory. In particular small secondary oscillations appear on the front face of the third wave. These oscillations are reproduced by a nonlinear solution which agrees well with the experiments. Such a good agreement appears indeed remarkable if one considers the wave height reached at the backwall during the second oscillation is 1.4 times the depth! The decay rate of the wave is well predicted by both theories. These results confirm the conclusion of Section 6.3: for a harbor with a short length relative to the incident wave length convective nonlinearities can be neglected and it is sufficient to use a linear formulation.

Similar results are presented in Fig. 6.4.2. The incident wave characteristics are the same as for Fig. 6.4.1 and the dimensionless parameters are $b/L = 0.1$, $\sqrt{h/g}/T = 0.047$, $\sigma L/\sqrt{gh} = 4.5$, $\gamma_s = 0.13$, $\varepsilon = 0$, $f_e = 0.0$, with the physical parameters $L = 121$ cm, $T = 1.92$ sec, $h = 8$ cm. The value of the frequency parameter $\sigma L/\sqrt{gh}$ corresponds to

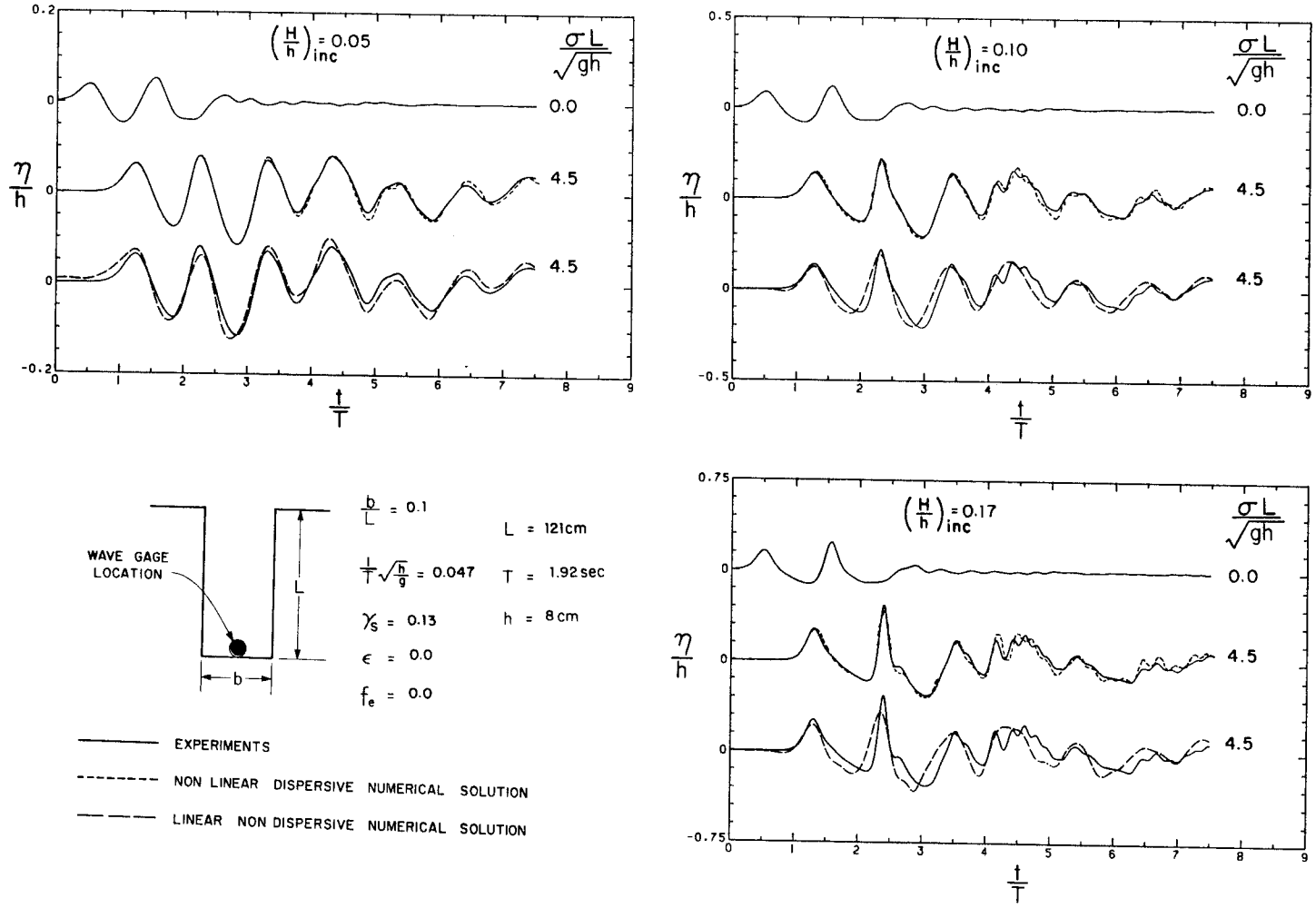

Fig. 6.4.2

Transient wave records at the backwall for a fully open harbor for three incident wave heights, comparison between experiments, linear and nonlinear solutions. L = 121 cm, T = 1.92 s, h = 8 cm.

resonant conditions for the second mode of oscillations of the harbor. For a relative incident wave height of $(H/h)_{inc} = 0.05$ linear theory agrees fairly well with the experiments and the agreement is even better between the nonlinear solution and the experiments. For $(H/h)_{inc} = 0.1$ there is some difference between the experiments and the linear solution. In particular secondary oscillations not predicted by the linear solution appear on the fourth experimental wave oscillations; however, the differences are indeed small. The oscillations are predicted by the nonlinear theory which also shows a good overall agreement with the experiments. Finally, for $(H/h)_{inc} = 0.17$ the difference between the recorded wave and the record computed from the linear theory becomes relatively large. The detailed features of the oscillations (in particular the second oscillation) emanating from the nonlinear interactions are not reproduced by the linear results. In contrast, the local experimental wave forms are in nearly perfect agreement with the nonlinear theory. It is seen from this last part of Fig. 6.4.2 that nonlinear effects cause the oscillations to peak and dispersion effects appear to become important and cause the main oscillations to separate into secondary waves.

Thus, if the second mode is excited nonlinear effects tend to modify the shape of the wave; in particular, a larger difference is found between experiments and linear theory in the case of Fig. 6.4.2, where the second mode of the harbor is excited, than in the case of Fig. 6.4.1 where the first mode is excited. These results are consistent with those obtained in Section 6.3 for the case of a continuous excitation.

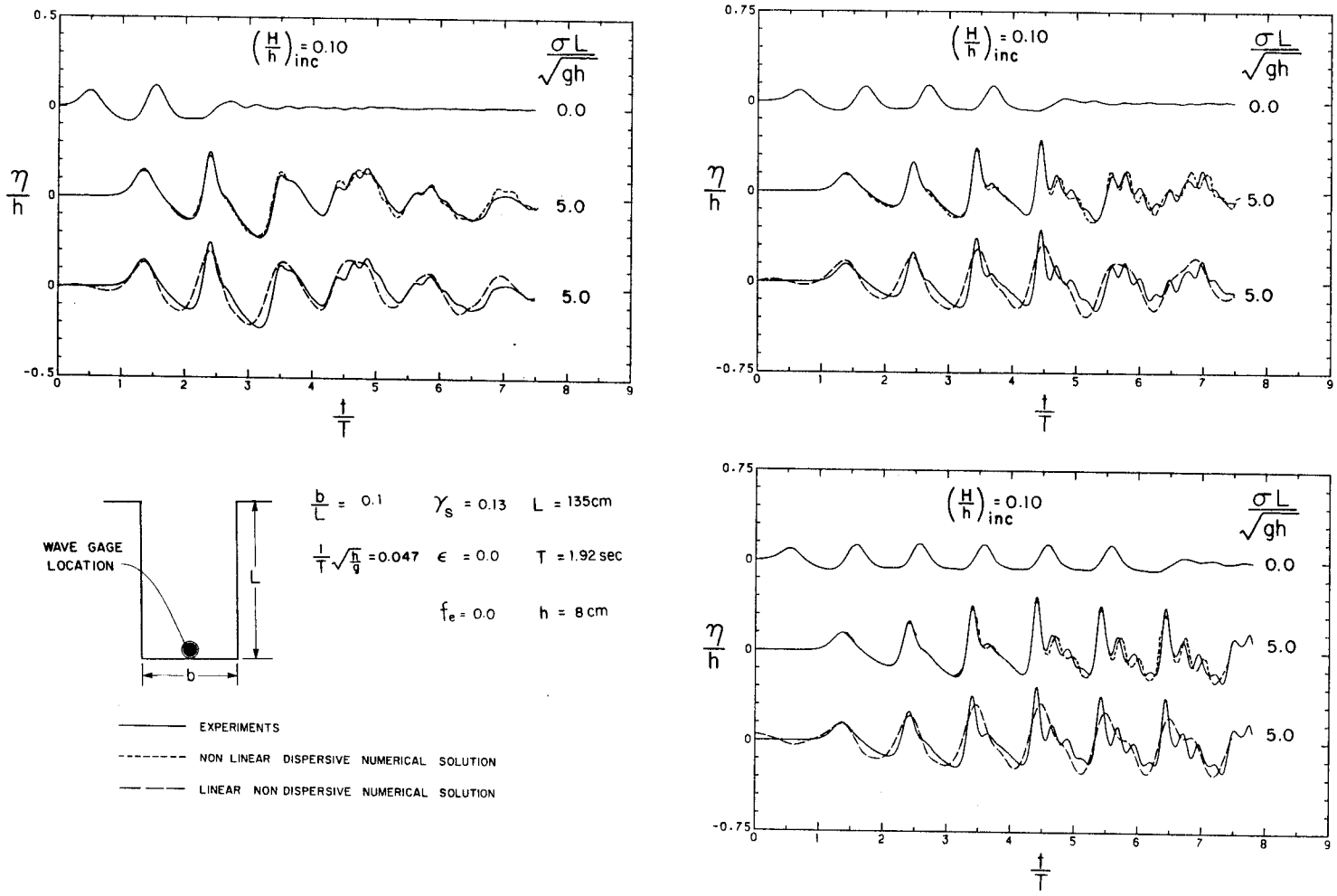

Fig. 6.4.3 Transient wave records at the backwall for a fully open harbor for incident waves of different durations, comparison between experiments, linear and nonlinear solutions, L = 135 cm, T = 1.92 s, h = 8 cm.

Attention is focused next on the number of incident waves required to obtain fully developed nonlinear features when the second mode of the harbor is excited.

It was seen in Fig. 6.4.2 that when the incident wave consists of only two oscillations, some nonlinear effects modify the shape of the wave, but the overall agreement between the linear theory and experiments remains reasonable. The variation of the relative water surface displacement η/h with dimensionless time t/T is presented in Fig. 6.4.3 for three incident waves, consisting of two, four and six oscillations respectively, with the same relative wave height $(H/h)_{inc} = 0.1$. The other dimensionless parameters for the experiments are: $b/L = 0.1$, $\sqrt{h/g}/T = 0.047$, $\sigma L/\sqrt{gh} = 5.0$, $\gamma_s = 0.13$, $\varepsilon = 0.0$, and $f_e = 0.0$, corresponding to L = 135 cm, T = 1.92 sec, and h = 8 cm. When the harbor is excited by two incident waves, some nonlinear features can be observed, but the overall response appears to follow a linear theory reasonably well. In the case of four oscillations of the incident wave the shape of the wave at the backwall begins to differ markedly from the linear solution. During the fourth oscillation it separates out into three waves as a result of dispersion acting against nonlinearities. Finally, when the incident wave consists of six oscillations nonlinear features emerge at about the third oscillation and become fully developed during the fifth oscillation. It is noted that for the three cases the nonlinear dispersive solution agrees well with the experiments with regard to both the shape of the wave and the height. Thus, it takes some time for nonlinearities to develop. For excitations of a short duration, it should be noted the wave can be damped out before nonlinearities can establish themselves.

6.4.2 A Narrow Rectangular Harbor with a Linearly Varying Depth

Three experiments were performed with a fully open narrow rectangular harbor with a linearly varying depth. The slope was made out of an anodized aluminum plate with supports beneath it and it was sealed onto the harbor walls with tape. The experiments differed from each other by the height of the incident wave: $H/h = 0.05, 0.1, 0.17$. The other wave parameters and the harbor dimension remained the same except for the factor f_e. (It is important to note that this case was used to demonstrate the capabilities of the numerical program and was not intended to investigate variable depth harbors.)

The fixed dimensionless parameters are: $b/L = 0.1$, $h_1/h = 0.5$, $\sqrt{h/g}\ T = 0.047$, $\sigma L/\sqrt{gh} = 3.69$, $\gamma_s = 0.12$, $\varepsilon = 0.0$, where h_1 denotes the still water depth at the backwall of the harbor. The corresponding physical parameters are $h = 8$ cm, $L = 100$ cm, and $T = 1.92$ sec. The harbor length was determined such that it corresponds to the resonant conditions for the second mode of oscillations of the harbor in a linear sense, i.e., the resonant frequencies were determined using the linear harmonic numerical program used by Lepelletier (1978). Since small radii were used at the mouth for these experiments ($r_e = 0.5$ cm), the entrance separation coefficient is not zero and is obtained from the analysis of Section 6.2.4 and Eq 6.2.9 (assuming constant depth) as $f_e = 0.2$, 0.4, 0.6, respectively.

The variation of the relative water surface displacement η/h with the dimensionless time t/T at the backwall is presented in Fig. 6.4.4 for each case. Two incident waves were generated for $(H/h)_{inc} = 0.05$ and 0.1 while only one was generated for $H/h = 0.17$, in order to prevent breaking from occurring inside the harbor during the second oscillation.

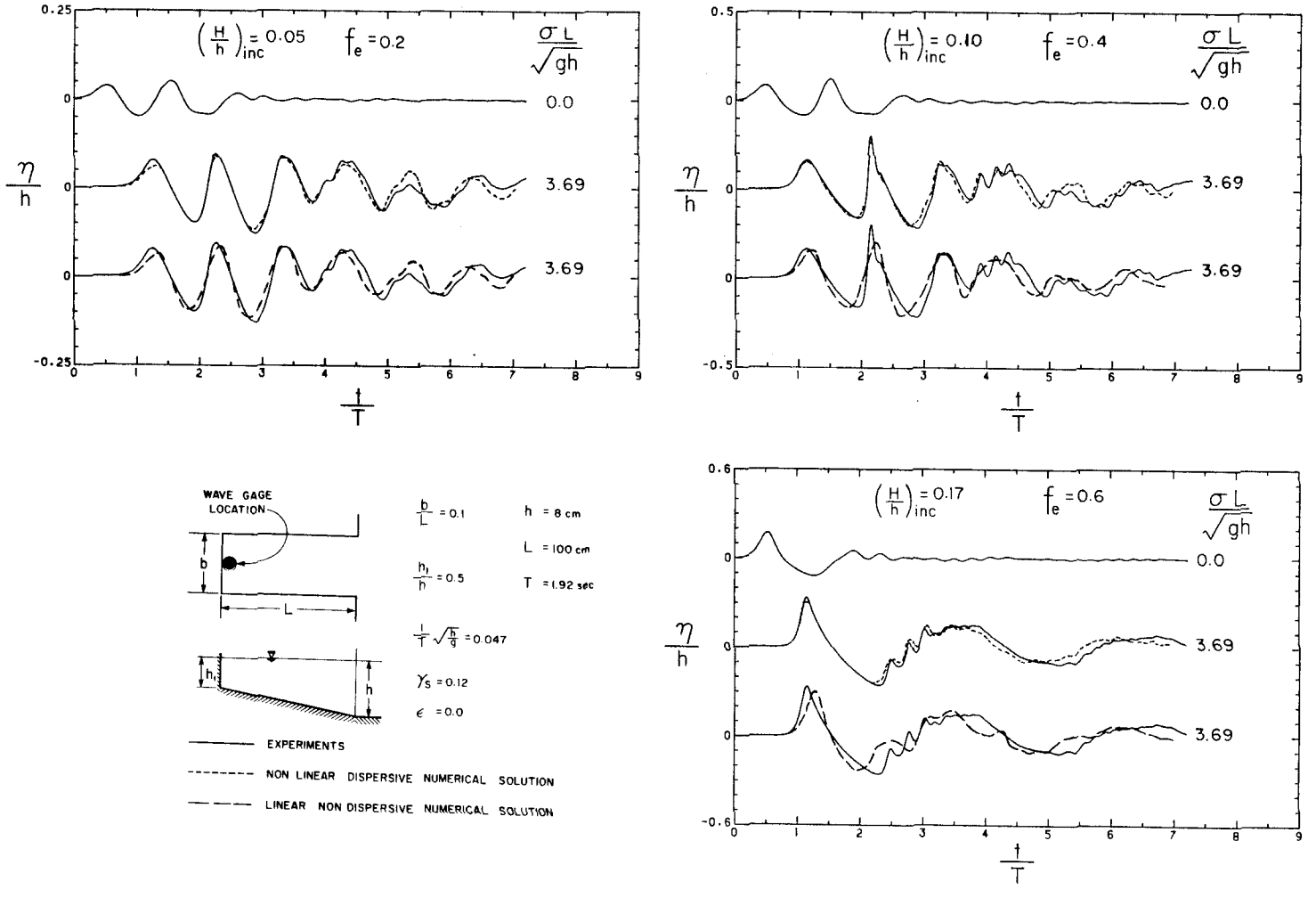

Fig. 6.4.4 Transient wave records at the backwall for a fully open harbor with linearly varying slope. Comparison between experiments, linear and nonlinear solutions, L = 100 cm, T = 1.92 s, h = 8 cm, h_1 = 4 cm.

Since some quadratic dissipation must be included in the solution, the linear analytical solution developed in Section 3.3 cannot be used for transients, instead the linear curves in Fig. 6.4.4 are produced by the linear nondispersive numerical solution. For $(H/h)_{inc} = 0.05$ both linear and nonlinear solutions agree reasonably well with the experiments. (Some local discrepancy occurs with the nonlinear solution during the fifth oscillation, which is not understood.) For $(H/h)_{inc} = 0.1$ the nonlinear features begin to clearly appear. The front face of the second oscillation at the backwall is quite steep and secondary oscillations develop during the fourth oscillation. A comparison with the graph in Fig. 6.4.2 corresponding to the same incident wave amplitude shows that nonlinear effects develop more for the linear varying depth, as would be expected. The agreement between the nonlinear solution and the experiments appear quite satisfactory (except for the fifth oscillation). Finally, for $(H/h)_{inc} = 0.17$ a phase shift appears clearly for the first maxima between the experimental results and the results of the linear theory, showing that the wave celerity, as the first incident wave propagates on the slope, is greater than what the linear theory predicts. The secondary oscillations appearing on the front face of the second wave are nicely reproduced by the nonlinear solution. It is noted that, in this last case, the lowest mode of the harbor becomes excited also by the incident wave, as evidenced by the long period oscillations, with a dimensionless period of about 2.5 which develops after the first oscillation.

In summary, for this variable depth harbor, the nonlinear theory agrees generally well with the experiment; however, the overall features of the linear solution are not too different from the experiments. This

is probably because, in this case, the ratio of the harbor length to the incident wave length is only 0.6; nonlinear-dispersive effects which begin to develop on the slope do not have time enough to develop fully before the wave reaches the backwall of the harbor. Actually, this situation is probably typical of most tsunamis, where the wave length is usually much larger than the length of the bay or harbor so that even if the bottom slopes, nonlinear and dispersive effects may not have space (or time) enough to develop.

6.4.3 A Trapezoidal Harbor with a Constant Depth

In addition to the dynamic effect of resonance the wave height in a harbor also can be increased significantly by concentrating its energy through geometric focusing. In particular, Green's law indicates that the height H of a linear nondispersive wave propagating in a constant depth but decreasing width channel is given by:

$$\frac{H}{H_o} = \left(\frac{b_o}{b}\right)^{1/2}$$

In the case of a natural bay with a trapezoidal shape, the resulting concentration of energy is at the bay head and may result in a very large wave height with devastative effects. To explore this effect three experiments were performed with a fully open harbor with constant depth for relative wave heights: $(H/h)_{inc}$ = 0.05, 0.10 and 0.17. The characteristics of the harbor are given by L = 122 cm, the entrance width b = 20 cm, the backwall width b_1 = 4 cm, the incident wave period T = 1.92 sec, and the water depth h = 8 cm. The values of the corresponding dimensionless parameters are $\frac{1}{T}\sqrt{h/g}$ = 0.047, $\sigma L/\sqrt{gh}$ = 4.51,

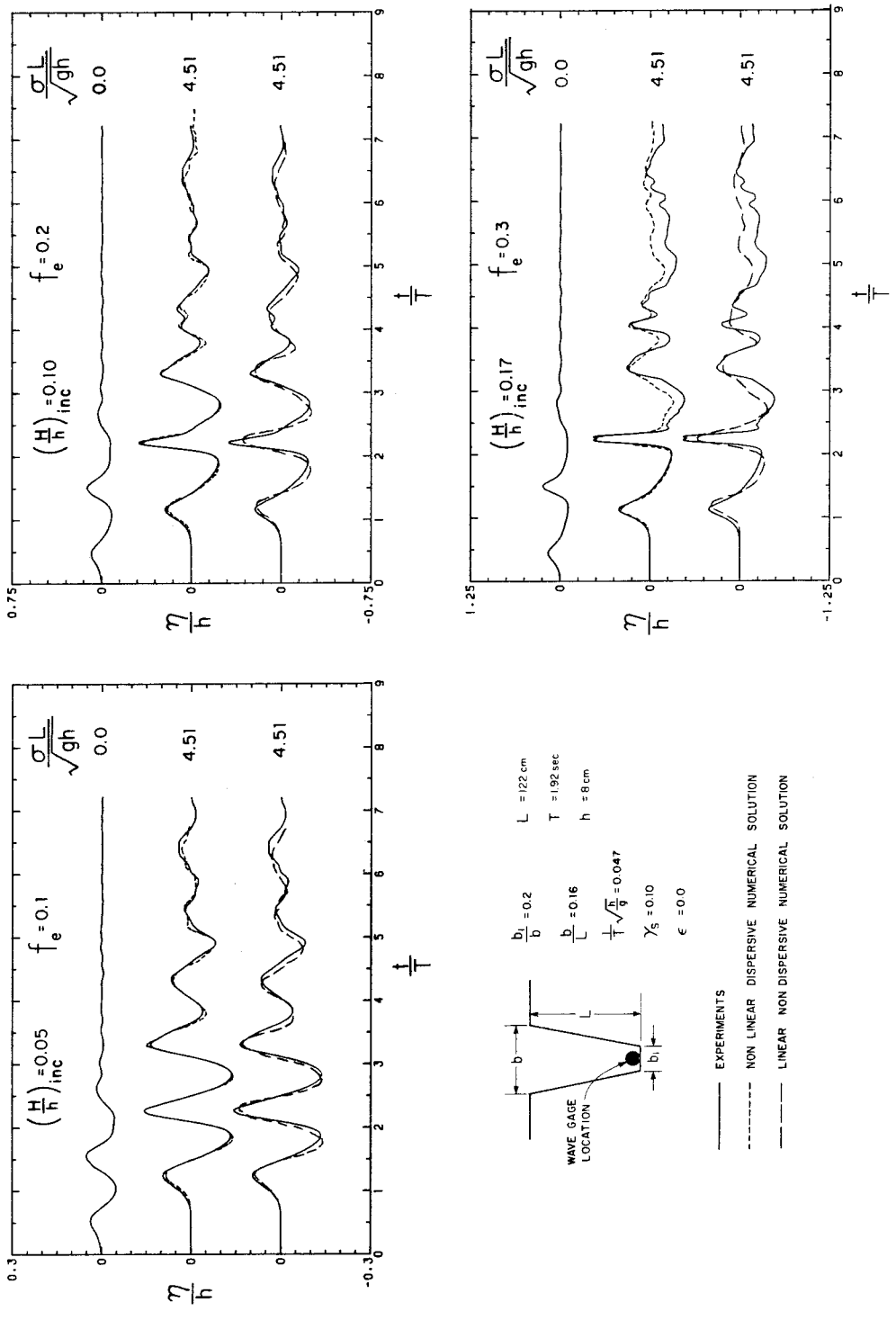

Fig. 6.4.5 Transient wave records at the backwall for a fully open trapezoidal harbor, comparison between experiments, linear and nonlinear solutions, L = 122 cm, T = 1.92 s, h = 8 cm, b = 20 cm, b_1 = 4 cm.

γ_s = 0.10 and ε = 0.0. The entrance loss coefficient f_e based on the incident wave height is 0.1, 0.2, 0.3, respectively, for the three relative wave heights. Figure 6.4.5 shows the variation of the relative water surface displacement at the backwall η/h, with t/T. For $(H/h)_{inc}$ = 0.05 and 0.10 the agreement between the experiments and both linear and nonlinear theories is fairly good although the nonlinear results agree better. For $(H/h)_{inc}$ = 0.17 the first two oscillations are correctly predicted by the nonlinear theory. The shape of the second oscillation is particularly interesting and differs from everything encountered so far. It consists of a very peaked and impulsive type wave; such a wave shape would have quite an impact on coastal sited structures due to the amount of energy concentrated over a relatively short time. It is noted the positive wave height at the backwall is quite large (η/h = 0.8). In comparison, the linear theory predicts a somewhat smaller wave although certain gross features of the wave system are retained. As mentioned, considering the effects of such a wave it is probably important in this case to use the nonlinear theory to more correctly predict the exact wave shape. After the second oscillation, however, a marked discrepancy is noted between theories and experiments for the negative part of the wave records. It is believed that problems of experimental data reduction may be responsible for this. In the case of the largest wave height, the wave record was taken in two steps, following a procedure described in Chapter 4. It is quite possible that an error was introduced when reducing the data related to the negative part of the wave record causing some vertical shift in the data. This explanation seems to be supported by the fact that, apart from the shift, the shape of the oscillations agree well between experiments and nonlinear theory.

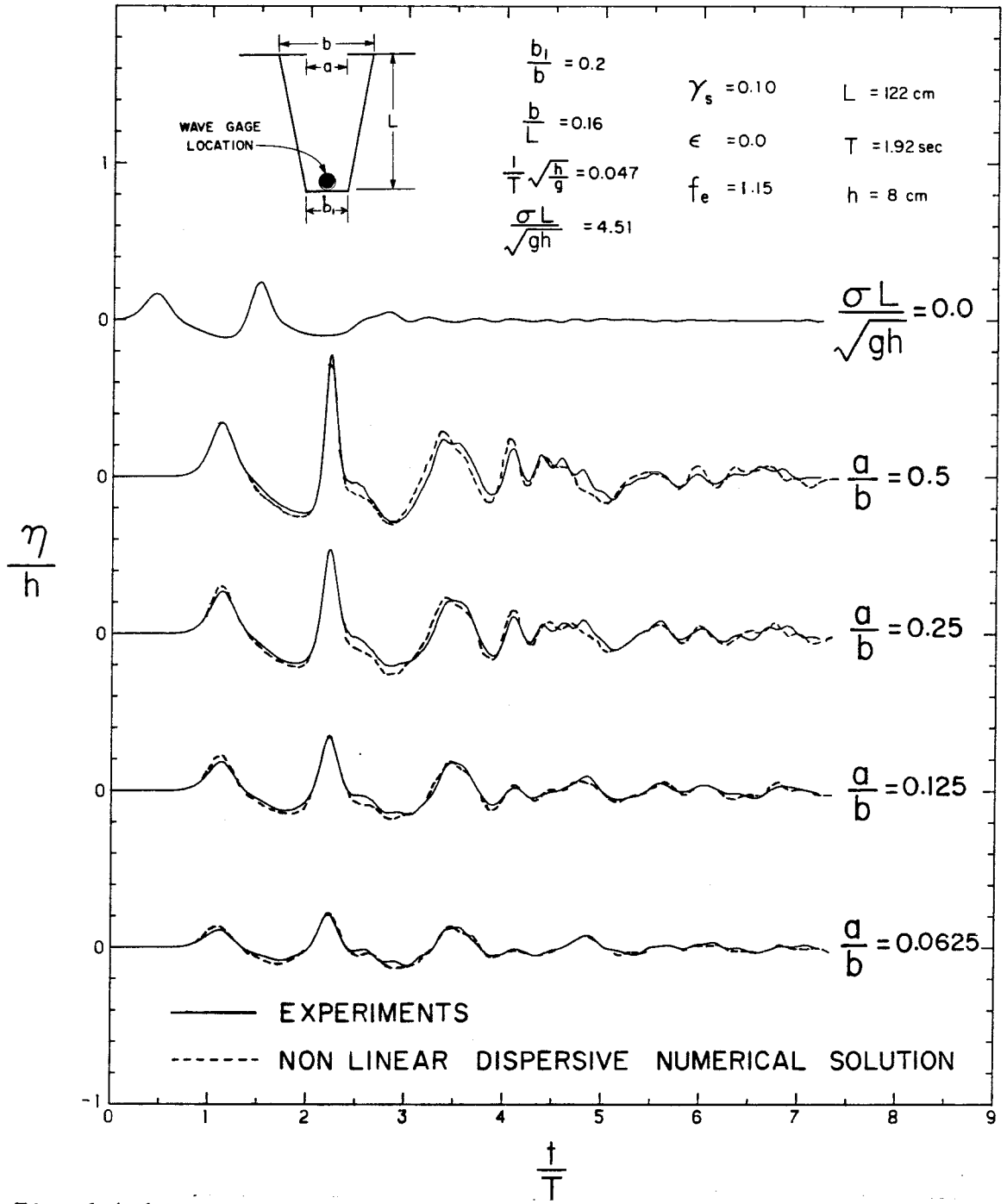

Fig. 6.4.6 Transient wave records at the backwall for a trapezoidal harbor with partially closed entrance, comparison between experiments and nonlinear solutions, L = 122 cm, T = 1.92 s, h = 8 cm, b = 20 cm, b_1 = 4 cm.

The efficiency of a breakwater at the mouth to reduce those dramatic amplification effects is investigated next by considering the incident waves which correspond to $(H/h)_{inc} = 0.17$ in Fig. 6.4.5, and the same harbor characteristics as previously described except that the harbor entrance is partially closed. The variation of the relative water surface displacement η/h with t/T at the backwall is presented in Fig. 6.4.6 for opening ratios: $a/b = 0.5$, 0.25, 0.125, and 0.0625, respectively. The entrance loss coefficient, f_e, is set equal to 1.15 for the four cases. It is noted first that the nonlinear dispersive numerical solution agrees well with the experiments for all four cases. This agreement demonstrates decisively the capability of the present numerical solution in modeling the interaction effect of nonlinearities, dispersion and entrance dissipation. The curves of Fig. 6.4.6 also show that the breakwater becomes markedly efficient only for opening ratios less or equal to 0.125. For values greater than this, the wave oscillations are not markedly reduced for this harbor configuration. Therefore, in practice, the resulting length of the breakwater required to protect a trapezoidal bay efficiently may be rather substantial. (More attention will be given to this feature in the discussions of Chapter 7.)

6.4.4 Summary

In summary, the transient study has shown that if the incident waves are limited to a small number of oscillations, the overall behavior of the wave dynamics in the harbor for the harbor configurations investigated and for resonant excitation conditions remains reasonably close to that predicted by the linear theory. In particular the effects of linear resonance and geometric focusing can significantly enhance

the wave height inside the harbor or bay even for a short duration of the excitation. It appears that nonlinear effects and dispersion effects change the wave form locally by inducing wave peaking and the formation of small secondary oscillations, but they do not modify the overall wave structure predicted by the linear theory. However, in cases where a precise knowledge of the wave profile is desired a nonlinear solution must be used. In fact, it is difficult to estimate the degree of agreement between the results of linear and nonlinear theories based only on one Eulerian measurement. Probably a better appreciation of the discrepancy would be obtained from comparing wave profiles along the harbor as was done in Fig. 6.3.34. This figure showed that a moderate discrepancy between experiments and theory for the Eulerian wave records at the backwall could occur for completely different spatial wave patterns inside the harbor.

CHAPTER 7

APPLICATION OF THE RESULTS TO PROTOTYPE SITUATIONS

In Chapters 5 and 6 the discussion of the dynamics of waves in closed basins and harbors in general was restricted to laboratory conditions. Most of the conclusions inferred with regard to those investigations would be expected to be valid in prototype harbors with similar geometric characteristics. However, in this regard some important differences with respect to the dissipation and the importance of nonlinearities in the prototype compared to the laboratory case must be given attention. These two aspects will be considered in Section 7.1 and 7.2, respectively. The numerical method developed in Section 3.4 has been applied to the response of Ofunato Bay (Japan) to the tsunami of 16 May 1968 and this is treated in Section 7.3. Finally general considerations for prototype harbors with arbitrary planform and variable depth are presented in Section 7.4.

7.1 The Various Sources of Dissipation in the Prototype

Several sources of dissipation are considered in the harbor response study presented in Chapter 6. These include the effects of: laminar boundary friction, leakage underneath the harbor walls, surface tension, separation losses at constrictions and energy radiation to the open sea. The second and third apply specifically to laboratory conditions. Attention will be given in this section to the effects of energy dissipation on the response of a prototype harbor. The effect of turbulent friction at the boundary will be considered here compared to laminar friction which was incorporated in the laboratory arrangement

discussed in Chapter 6. In addition to the boundary friction dissipation, radiation damping and the separation loss at the entrance are discussed; these later two have been treated previously. Two other forms of dissipation are presented here which pertain primarily to prototype situations. The first deals with partially absorbing lateral boundaries, i.e., the effect of imperfect reflections from the harbor boundaries. The second is a possible way of limiting the effects of resonance and it is associated with the construction of submerged breakwaters to add to the interior dissipation. These will be discussed individually herein. To obtain some quantitative estimates the harbor planform is assumed to be rectangular with a small width to length ratio, and the effectiveness of each dissipative source S_i is measured by computing the factor R_i which is associated with it.

(i) Radiation Damping

The amplification factor related to radiation damping has been derived in Section 6.2.4 as:

$$\frac{1}{R_r} = (2n+1)\,\frac{\pi}{4}\,\frac{b}{L} \tag{7.1.1}$$

where b and L denote the width and the length, respectively, of the harbor and n refers to a particular natural mode of oscillation of the harbor.

(ii) Separation Loss at the Entrance

The amplification factor R_f related to the loss of energy due to flow separation at the entrance of the harbor has also been derived on Section 6.2.4 as:

$$\frac{1}{R_r} = K_f\, R \tag{7.1.2}$$

where R denotes the overall amplification factor at the backwall resulting from all sources of dissipation and K_f is defined by:

$$K_f = \frac{4}{3\pi} f_e \left(\frac{A_I}{h}\right) \left(\frac{b}{a}\right)^2 \tag{7.1.3}$$

where f_e is the separation loss coefficient, $\left(\frac{A_I}{h}\right)$ is the relative wave amplitude of the incident-reflected wave at the coastline, i.e., twice the incident wave amplitude, a is the mouth width.

(iii) Turbulent Boundary Friction

The factor Q_τ corresponding to turbulent boundary friction has been computed in Appendix E. The expression for R_τ follows, using Eq. (3.3.99) as:

$$\frac{1}{R_\tau} = K_\tau R \tag{7.1.4}$$

where
$$K_\tau = (2n+1) \frac{\pi}{4} \left(\frac{16}{9} \frac{1}{\pi^3}\right) C_e \sqrt{\frac{g}{h}} \left(\frac{A_I}{h}\right) T \tag{7.1.5}$$

where g is the acceleration of gravity, T is the period of the wave motion and C_e is the boundary friction coefficient. In general, the coefficient C_e depends both on a local Reynolds number and the relative roughness of the bottom. For a rough turbulent flow (which is likely to be the case for most prototype situations), it is only a function of the relative roughness a_δ/k_r (according to Jonsson, 1978) where a_δ denotes the water particle excursion outside the boundary layer and k_r is the Nikuradse roughness parameter. In most prototype tsunami situations $a_\delta/k_r > 1000$ which gives from Jonsson's diagram, $C_e < 0.01$. In the subsequent consideration C_e is chosen somewhat less than this as:

$$C_e = 5 \times 10^{-3}.$$

(iv) Partially Absorbing Lateral Boundaries

Imperfect reflection at a lateral boundary, e.g., a beach, is characterized by a reflection coefficient $\bar{r}$ defined as the ratio of the reflected wave to the incident wave which is less than unity. It was shown, in Appendix C, that the resulting factor $Q_{\bar{r}}$ is the same as that corresponding to the loss associated with leakage in the model with the parameter ε replaced by $\left(\frac{1 - \bar{r}}{1 + \bar{r}}\right)$. Assuming that only the bay head is partially reflective the factor $R_{\bar{r}}$ can be derived from Eq. (6.2.17), taking L/b = 0, as:

$$\frac{1}{R_{\bar{r}}} = \frac{1 - \bar{r}}{1 + \bar{r}} \tag{7.1.6}$$

It should be realized that dissipation at the boundaries of a harbor can be related to different mechanisms. The effectiveness of this process in mitigating resonance can be characterized by a reflection coefficient $\bar{r}$ only in an approximate way, since this form of dissipation may result from complex wave interactions which cannot be described simply. For example, this imperfect reflection may be associated with wave runup on the sloping boundary which is highly nonlinear and may be accompanied by a change in the wave shape during the reflection process. Nevertheless, if from the runup mechanism it is possible to define a reflection coefficient, Eq. (7.1.6) is useful in estimating as a first approximation of this effect on the overall magnitude of the response of a harbor or bay. As an example it will be assumed in the following discussion that the reflection coefficient is 90%.

(v) Submerged Breakwaters

As mentioned earlier one plausible way to increase interior harbor dissipation may be to increase the roughness of the bottom of a harbor by constructing a series of submerged breakwaters perpendicular to the direction of wave propagation. Neglecting other wave effects which may be important in certain aspects of the problem it is interesting to estimate the effect of such structures on reducing the effect of resonance. It should be noted that this discussion is presented here only to suggest there may be other types of dissipation which can be introduced (if feasible from an engineering viewpoint) to reduce the effects of long waves in a harbor. If a submerged breakwater is considered, the mean power dissipated by a single breakwater can be given as:

$$W_{\tau s} = h_b \, b \, \frac{1}{T} \int_0^T \frac{1}{2} \rho \, C_s \, u^2 |u| \, dt \qquad (7.1.7)$$

where h_b denotes the height of the submerging breakwater, b is the width of the bay, u is the wave particle velocity along the bay, T is the characteristic wave period and C_s is the drag coefficient of order unity. If a series of such breakwaters are built and spaced a distance x_b apart, the calculations show that the resulting quantity $W_{\tau s}$ is given by Eq. (7.1.7) with the boundary friction coefficient replaced by an effective skin friction coefficient C_{es} such that:

$$C_{es} = C_s \frac{h_b}{x_b} \qquad (7.1.8)$$

In the following discussion C_s is chosen equal to unity.

The relative importance of the five dissipative sources mentioned can be estimated using the simplified method presented in Section 6.2.4 for the following four cases:

(i) First resonant mode, fully open harbor

(ii) First resonant mode, partially closed harbor

(iii) Second resonant mode, fully open harbor

(iv) Second resonant mode, partially closed harbor.

The value of the inverse amplification factor corresponding to each dissipative source is shown in Fig. 7.1.1 for each of the four cases. The prototype parameters from which the parameters $1/R_i$ were computed are indicated in the figure; they correspond to typical prototype conditions with a fairly large incident tsunami.

Comparison between Fig. 7.1.1 and Fig. 6.2.9 indicates an overall rate of energy dissipation in the harbor which is larger in the prototype than in a laboratory model, at least for the conditions of Figs. 7.1.1 and 6.2.9. (It is recalled that the total rate of energy dissipation is proportional to the sum of the inverse of the amplification factors related to each source.) This difference is mainly due to the presence, in prototype, of one additional highly dissipative source, namely the postulated use of submerged breakwaters. Turbulent boundary friction and partial reflection at the bay head are of least importance as dissipation mechanisms for the first resonant mode and for the conditions of Fig. 7.1.1. At the second mode they dissipate more energy than entrance separation only for a fully open harbor.

For the conditions of Fig. 7.1.1 submerged breakwaters for three out of four cases appear even more efficient than separation losses at

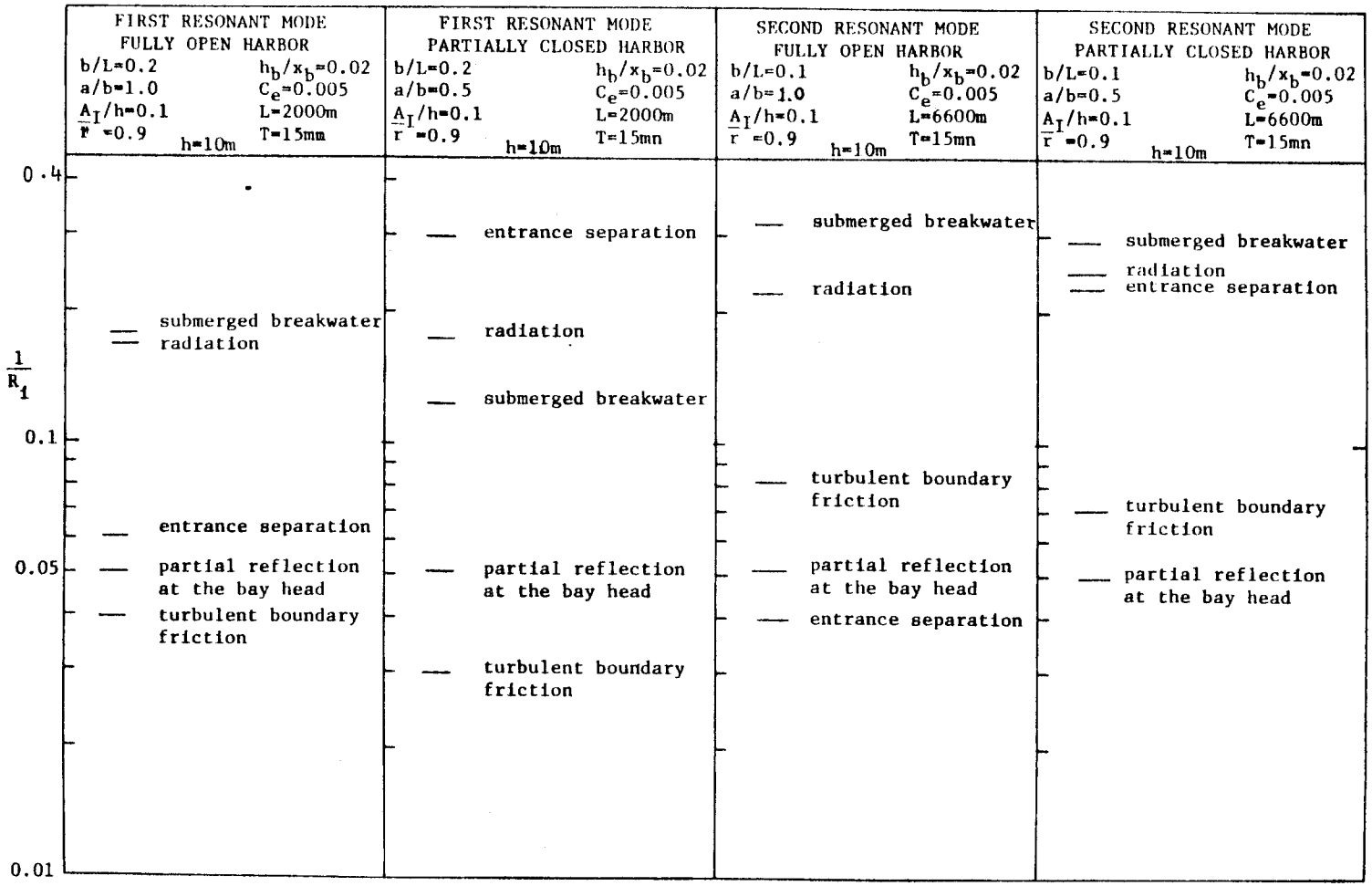

Fig. 7.1.1 The relative importance of the various sources of dissipation near resonance for four different situations, in prototype conditions.

the entrance. This suggests their potential usefulness. They could conceivably be used for bays which may not be completely protected by breakwaters at the bay entrance. In particular it was seen that a trapezoidal bay required a very small opening ratio to be effectively protected from tsunamis. An alternative would be to allow a wider entrance and to build submerged breakwaters regularly spaced from the mouth to the head of the bay.

7.2 Manifestation of Nonlinear Oscillations in Prototype: Case of Long and Narrow Bays

This discussion is limited to long narrow bays with constant depth so that the wave motion inside the bay remains essentially one-dimensional. The extension to more general harbor shapes will be discussed in Section 7.4.

Results from Chapter 5 have shown that some of the nonlinear features associated with wave oscillations in closed narrow basins can be conveniently characterized by the Stokes parameter equal to:

$$\underline{U}_s = \frac{H}{h^3} (T\sqrt{gh})^2 \qquad (7.2.1)$$

where H denotes half the wave height at the end walls, h is the still water depth and T is the period of the oscillation motion. It was found (Section 5.2.4) that in the absence of strong dissipation and for $\underline{U}_s > 0(10)$ the main oscillation usually decomposed into a number of secondary oscillations proportional to $\sqrt{\underline{U}_s}$. This feature constituted one of the most important manifestations of the interaction of nonlinearities with frequency dispersion. Also, when the front face of the wave steepened nonlinearities tended to transform a standing wave pattern into a moving wave pattern inside the closed basin.

From the results of Chapter 6 two situations must be considered when the effect of nonlinearities must be estimated in a long narrow harbor. Each of these two cases is presented next.

7.2.1 Case of a Harbor Length Much Smaller Than the Incident Wave Length

For a small harbor length to wave length ratio, i.e., $L/\lambda < 0.25$, convective nonlinearities do not have space enough to develop so that linear theory can be used for the complete range of relative wave height, H/h, and depth to wave length, h/λ. The harbor does not perceive the nonlinear nature of the incident wave and tends to act as a linear transducer. As a result the significance of the Stokes number in characterizing the importance of the nonlinear effects becomes irrelevant in this case.

7.2.2 Case of a Harbor Length of the Same Order as the Incident Wave Length

When the harbor length becomes of comparable magnitude to the incident wave length (i.e., $L/\lambda > 0.25$) convective nonlinearities have enough space to be realized. The resulting nonlinear characteristics induced near resonance by the buildup of wave energy in the harbor were found to be qualitatively similar to those which developed in the closed basin. However, these effects are reduced somewhat because of the comparatively stronger effects of dissipation in the harbor. In prototype situations the dispersion parameter, which can be measured by $(h/T\sqrt{gh})^2$ is typically smaller by two orders of magnitude than in laboratory conditions. Two conclusions regarding prototype situations can be drawn from this. First, the Stokes parameter $\underline{U}_S$ is likely to be much greater than 10 (which is the upper limit at which the wave

oscillations can be considered as linear). Therefore, if resonant conditions develop, the resulting wave interactions will tend to be governed by a nonlinear theory. Second, the large number of emerging secondary oscillations, which is an increasing function of the parameter $\underline{U}_s$, becomes at the same time very much affected by dissipation (this was seen in Chapters 5 and 6); in particular the transient experiments with the closed basin in Section 5.2.4, showed that for the same value of the dissipation coefficient γ_s the damping effects on the secondary oscillation increased with the number of these oscillations. Therefore, in the prototype secondary oscillations may not be observed at all, and resonant conditions are likely to be characterized by a steepening of the front face of the oscillations and the evolution with time of the advancing wave towards a shape which has a triangular finite bore-like profile somewhat smoothed by damping effects.

Based on the results of Fig. 6.3.29 dispersion can be neglected and a nonlinear nondispersive theory can be used if:

$$\underline{U}_s \geq 0(10^4)$$

An important question not addressed so far is the time required for nonlinearities to develop in the harbor (or basin) near resonant conditions. Physically, at resonance, the wave system can be considered as traveling back and forth between the end and the entrance of the harbor or bay. One way to estimate the time required for the nonlinearities to develop is to compute the corresponding propagation distance for a wave traveling in one direction only required for the effects of nonlinearities to become important. Goring (1978) computed

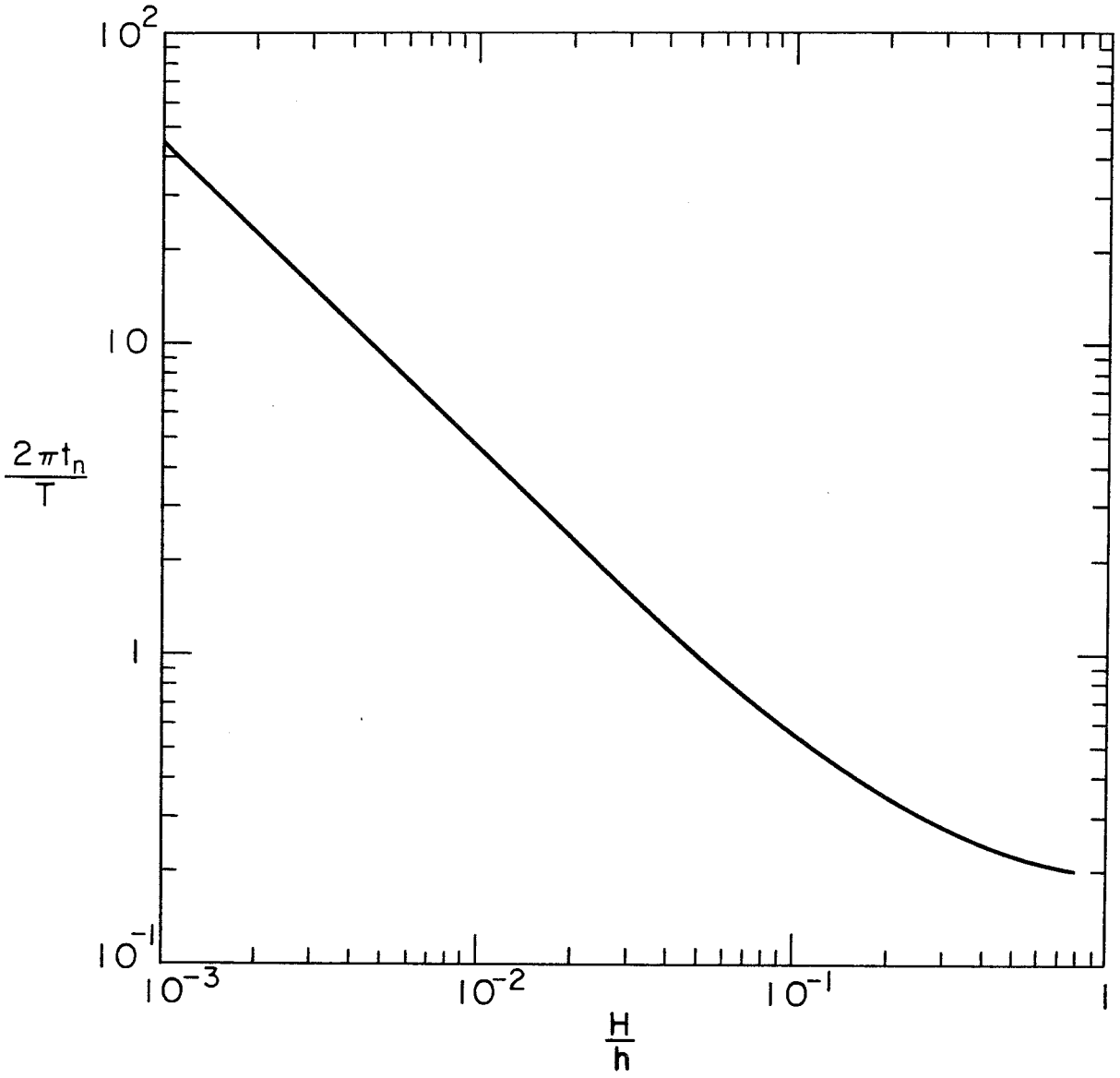

Fig. 7.2.1 Theoretical variation of the time t_n required for nonlinear effects to become important near resonance, with relative wave height (adapted from Goring, 1978).

such a distance x_n for a wave with a hump-like shape defined by a characteristic frequency Ω and its relative height H/h. The distance x_n was determined such that a local Ursell number associated with the front face of the wave differed by 10% between the values computed from the linear nondispersive theory and the nonlinear nondispersive theory. These results can be directly applied to the present problem by assuming $\sigma = \Omega$. The variation of $2\pi t_n/T$ with H/h is presented in Fig. 7.2.1 where t_n indicates the time after which nonlinear effects cannot be neglected for a wave trapped in the harbor at resonance. From this graph it is seen that for all harbor experiments presented in Chapter 6, nonlinear effects must be considered after the first oscillation. It is important to emphasize at this point that the degree to which nonlinear effects affect harbor oscillations remains fairly small in most cases, as seen from the results obtained in Chapter 6. For engineering purposes these effects may possibly be ignored; their appreciation depends on the application being considered.

7.3 The Response of Ofunato Bay to the Tsunami of 16 May 1968

As an example of the application of this research to a prototype harbor, the numerical scheme presented in Section 3.4 is used to determine the effect of tsunamis in Ofunato Bay located in Japan along the northeast coast of Honshu Island, Iwate Prefecture. The feature which makes this bay of particular interest is that a breakwater was constructed there in 1967 to reduce the effect of tsunamis. It is useful to use the analysis developed in this study to investigate its effectiveness.

A map of this bay (extracted from the Bulletin of the Earthquake Research Institute, Tokyo Imperial University, 1934) is presented in Fig. 7.3.1. Ofunato Bay is 1.7 km wide at the mouth and has a length of about 7.7 km. Its bathymetry is rather complicated, as shown on Fig. 7.3.1, with a water depth varying from 50 meters at the mouth to less than 10 meters at the bay head.

On May 16, 1968 an earthquake of magnitude 7.8 (the Tokachi-Oki earthquake) occurred off the Pacific coast of northeast Japan and a tsunami was generated and reached the coast. Actual wave records were obtained at Nagasaki and Ofunato located near the bay mouth and the bay head, respectively (see locations on Fig. 7.3.2). A breakwater had been constructed after the Chilean tsunami of 1960 and had been completed in 1967. It has a width opening of 200 m and its location across the bay is indicated in Fig. 7.3.2 by the letters I and J.

Ito (1970) performed a series of numerical calculations to examine the efficiency of the newly constructed breakwater in dissipating the wave energy of the incoming tsunami and protecting the town of Ofunato. These computations were performed with a finite difference model based on the linearized long wave equations except for across from the breakwater opening where a quadratic form for the head loss was incorporated in the equations of motion. In his calculations the outer sea was replaced by a long channel slightly wider than the bay mouth. To reconstruct the incident wave Ito obtained the transfer function of the bay at Nagasaki from his numerical scheme and divided each of the first 30 Fourier components of the wave record at Nagasaki by the magnitude of the transfer function at each corresponding frequency. In the present study, the same incident wave as determined by Ito was used as input for the numerical calculations.

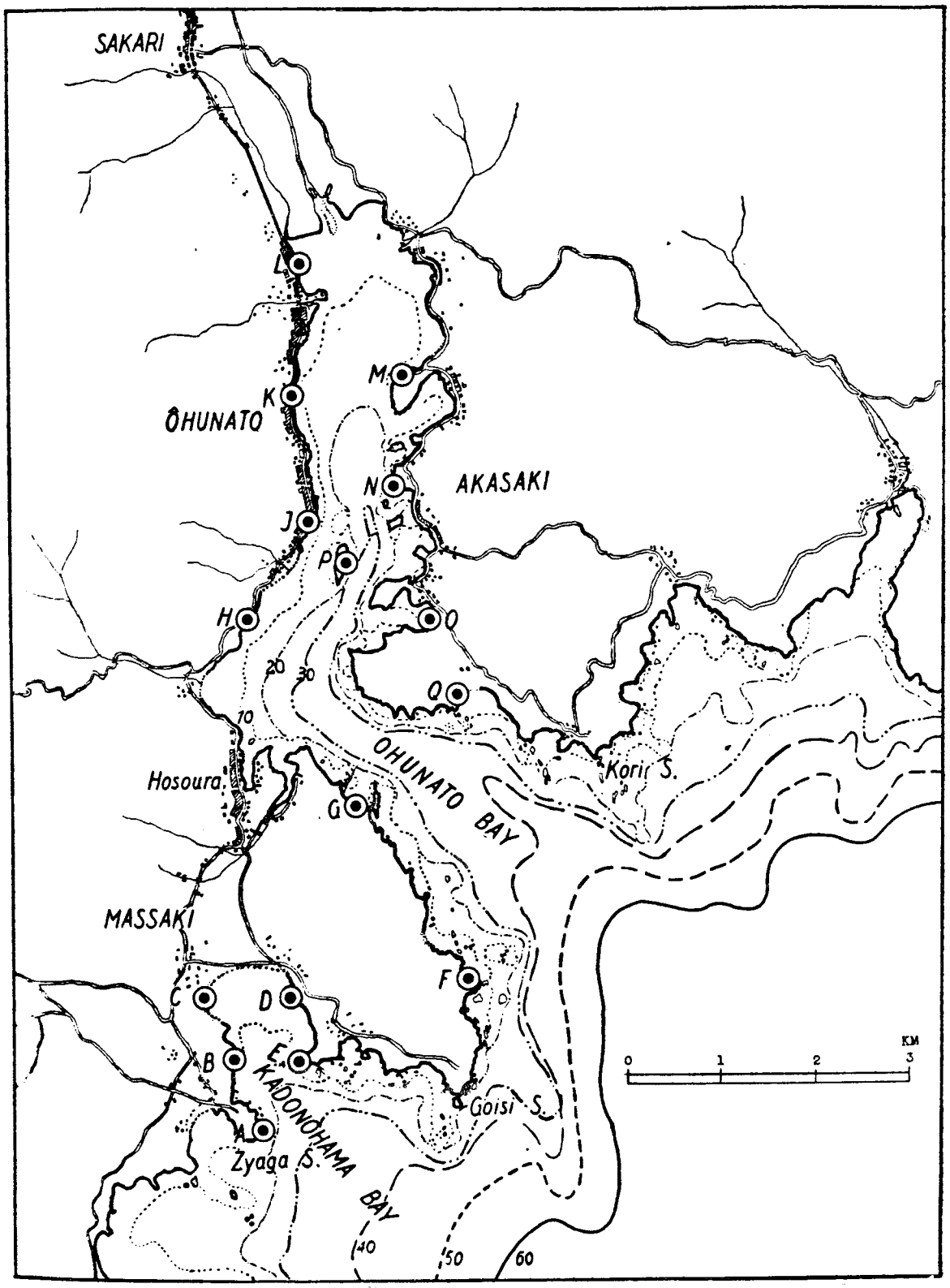

Fig. 7.3.1 Map of Ofunato Bay (from the Bulletin of the Earthquake Research Institute, Tokyo Imperial University, 1934).

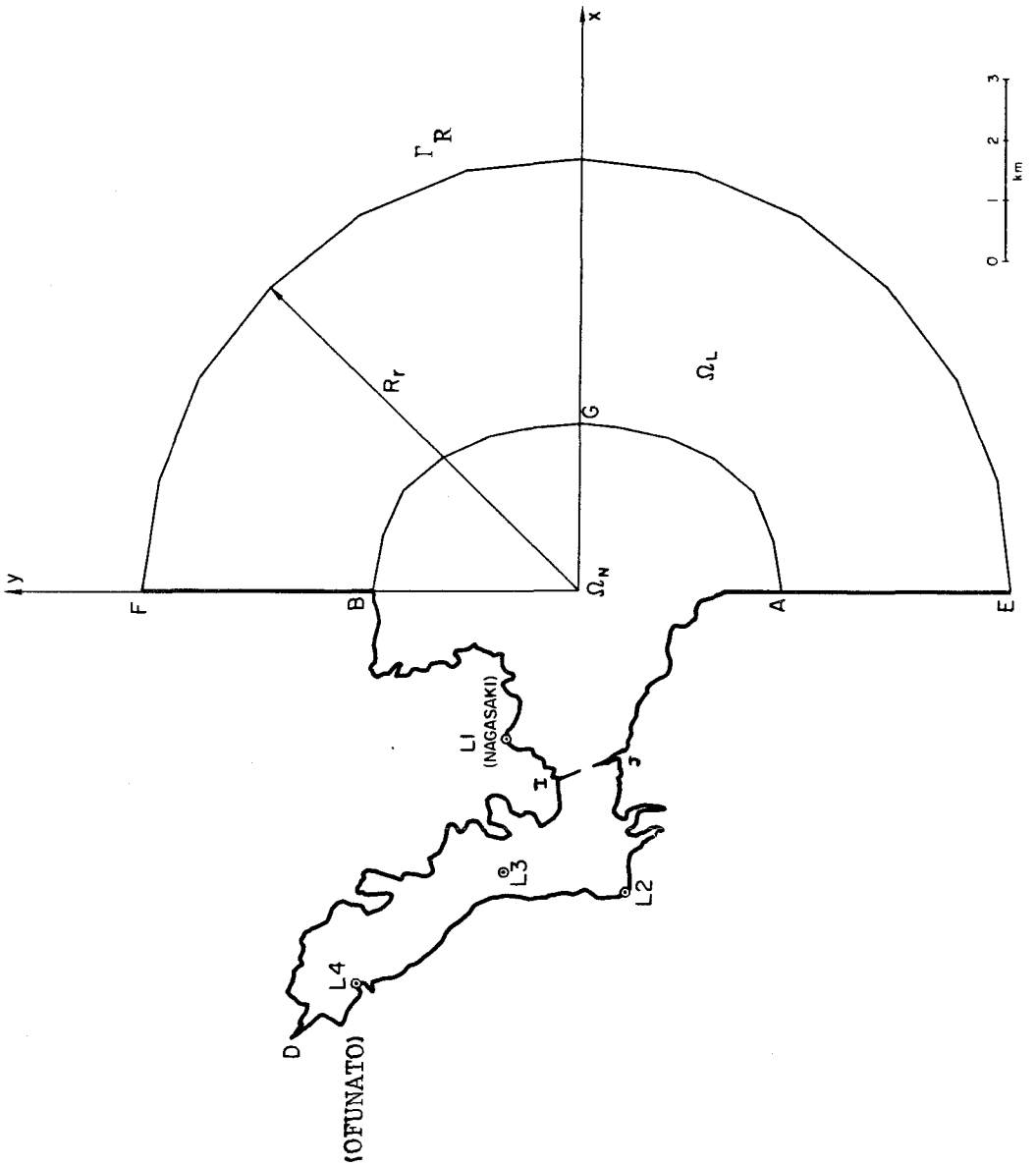

Fig. 7.3.2 Representation of the bay region and the outer region for the numerical calculations.

For the calculations presented in this study the bay region and the outside region were represented as shown in Fig. 7.3.2. Beyond points A and B the coastline was taken to be straight. The bay region is delineated by the curve ADBG with depths obtained from Fig. 7.3.1. (The water depth was set to a minimum of 10 meters along the lateral boundaries.) The exterior region is delineated by the curve EAGBF and the semicircle Γ_R with a depth assumed constant and equal to 50 m. The plane incident wave used was the same as determined by Ito (1970). The incident wave has a dominant period of about 15-20 min. and hence, the characteristic wave length can be computed as:

$$\lambda \approx \sqrt{gh}\, T = 20 \text{ km}$$

The ratio of the mouth width (without breakwater) to the wave length is about 0.1. Therefore, from the analysis of Section 3.4 the radiated wave is correctly transmitted through the radiative boundary Γ_R with the present numerical scheme:

$$R_r/\lambda \approx 0.6$$

This gives: $R_r \approx 12$ km.

The finite element grid corresponding to R_r = 11 km is presented in Fig. 7.3.3 without breakwater. To check how much error would be introduced in the time records inside the harbor if R_r was reduced, computations were also carried with the mesh presented in Fig. 7.3.4 which corresponds to R_r = 7 km. The numerical wave records obtained with these two mesh configurations, using linear nondispersive theory with no viscous dissipation, are compared in Fig. 7.3.5 at four different locations, L1 (Nagasaki), L2, L3, and L4 (Ofunato) indicated in

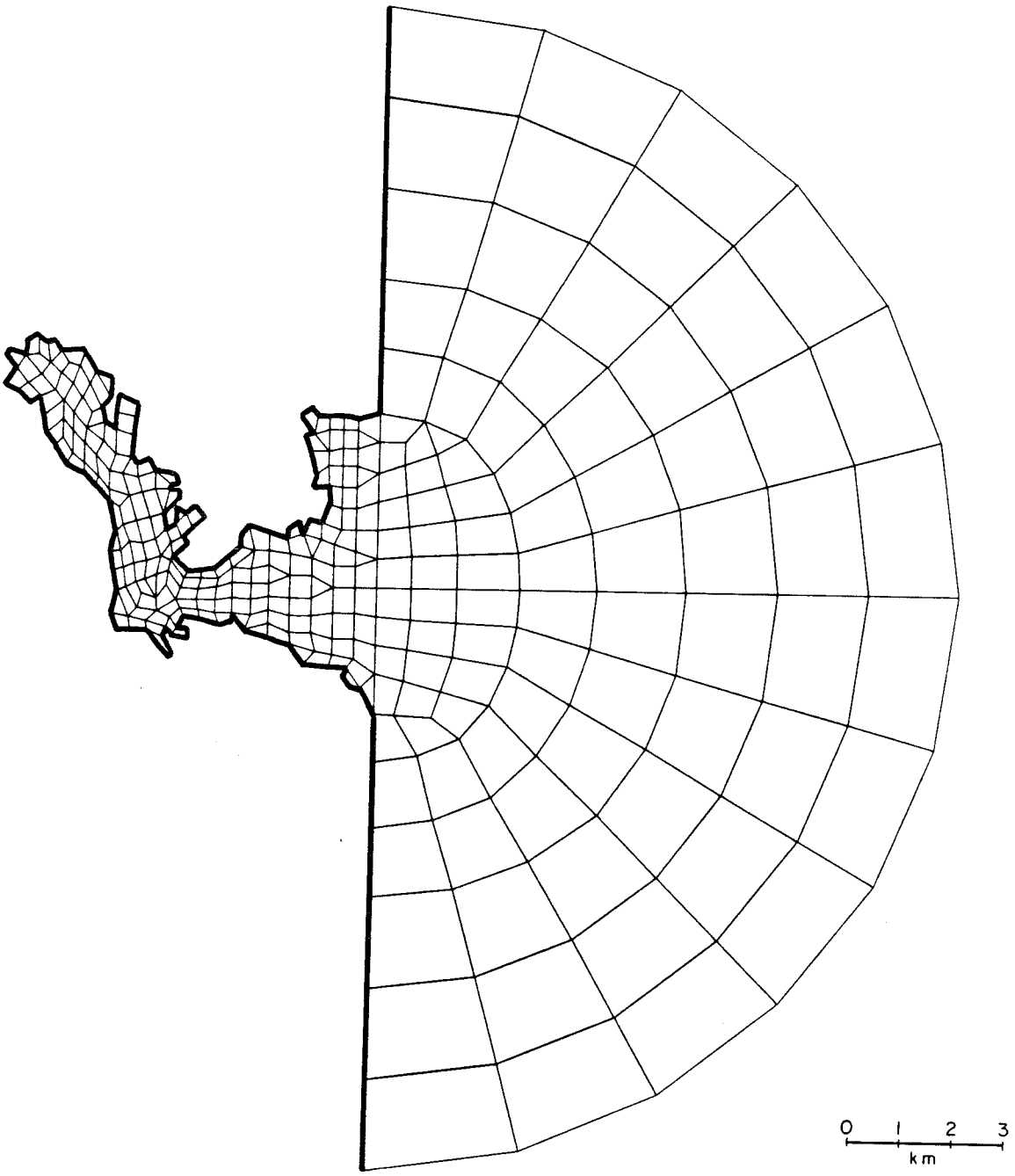

Fig. 7.3.3 Finite element grid without breakwater, R_r = 11km.

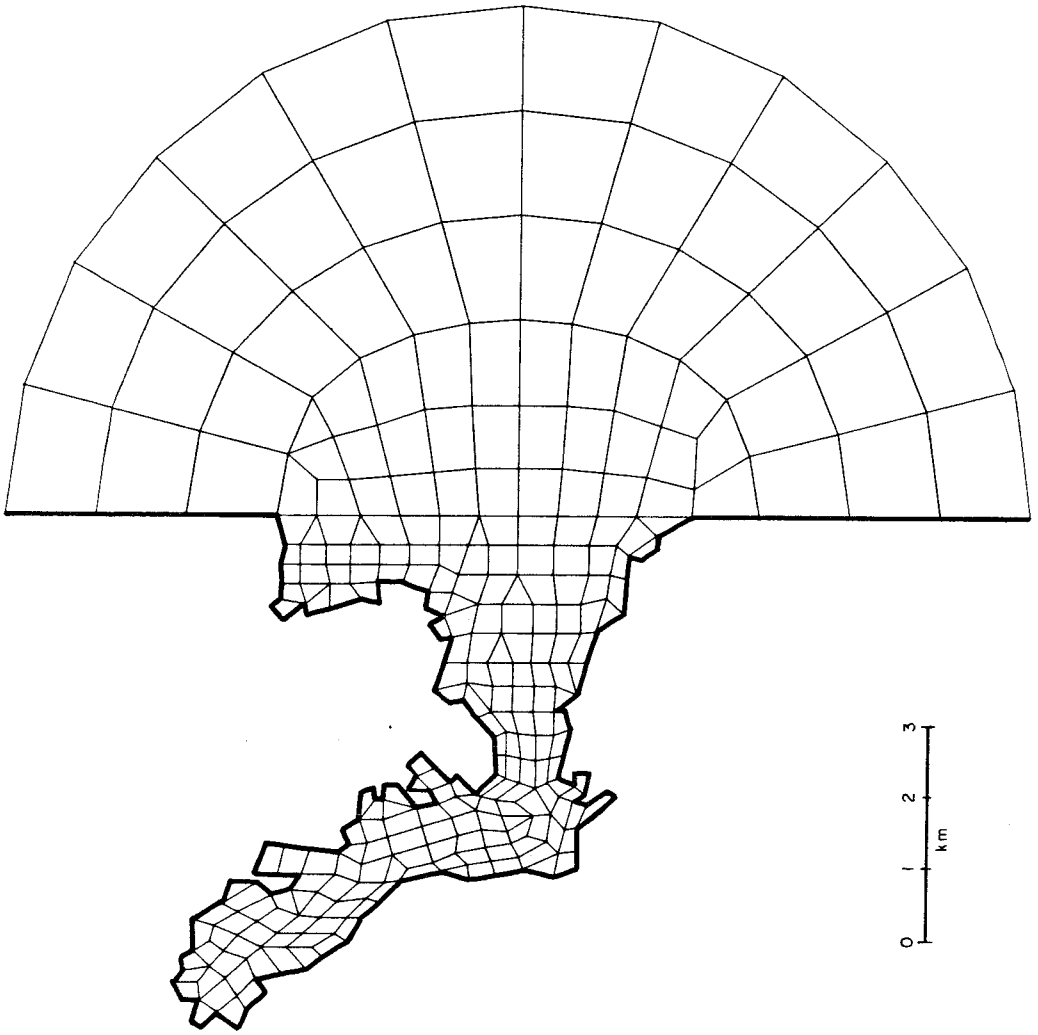

Fig. 7.3.4 Finite element grid without breakwater, R_r = 7 km.

Fig. 7.3.2. Surprisingly, virtually no difference is noted between the two sets of results. This indicates that, in practice, the radiative boundary can be located at a smaller distance from the mouth than the analysis indicates which results in increased computational efficiency. This probably introduces an error in the radiative wave pattern in region Ω_L but this error does not appear to propagate back into the interior region, at least for the incident wave shown in Fig. 7.3.5.

The nonlinear effects were investigated by comparing the results of the linear nondispersive theory to those of the nonlinear dispersive theory and the results are presented in Fig. 7.3.6. In this case where the ratio of the bay length to wavelength is about 0.25 the linear theory agrees well with the nonlinear theory. From the results of Chapter 6, with such a small ratio, nonlinear effects do not have space to develop and the linear theory should apply. This is confirmed by the results in Fig. 7.3.6.

The effects of the breakwater on the tsunami were finally investigated. The finite element mesh with the breakwater in place is shown in Fig. 7.3.7 and the results of the computations with and without the breakwater are shown in Fig. 7.3.8 at each of the four locations. Fairly small differences are noted between the two sets of results except at Ofunato where the peak amplitudes are reduced a maximum of 40% by the breakwater. When the breakwater is in place little amplification is obtained between Nagasaki and Ofunato which agrees with Ito's results. However, Ito's results predict at Ofunato wave amplitudes without breakwater which are twice as large as those resulting from the presence of the breakwater (compared to only a maximum of 40% difference in

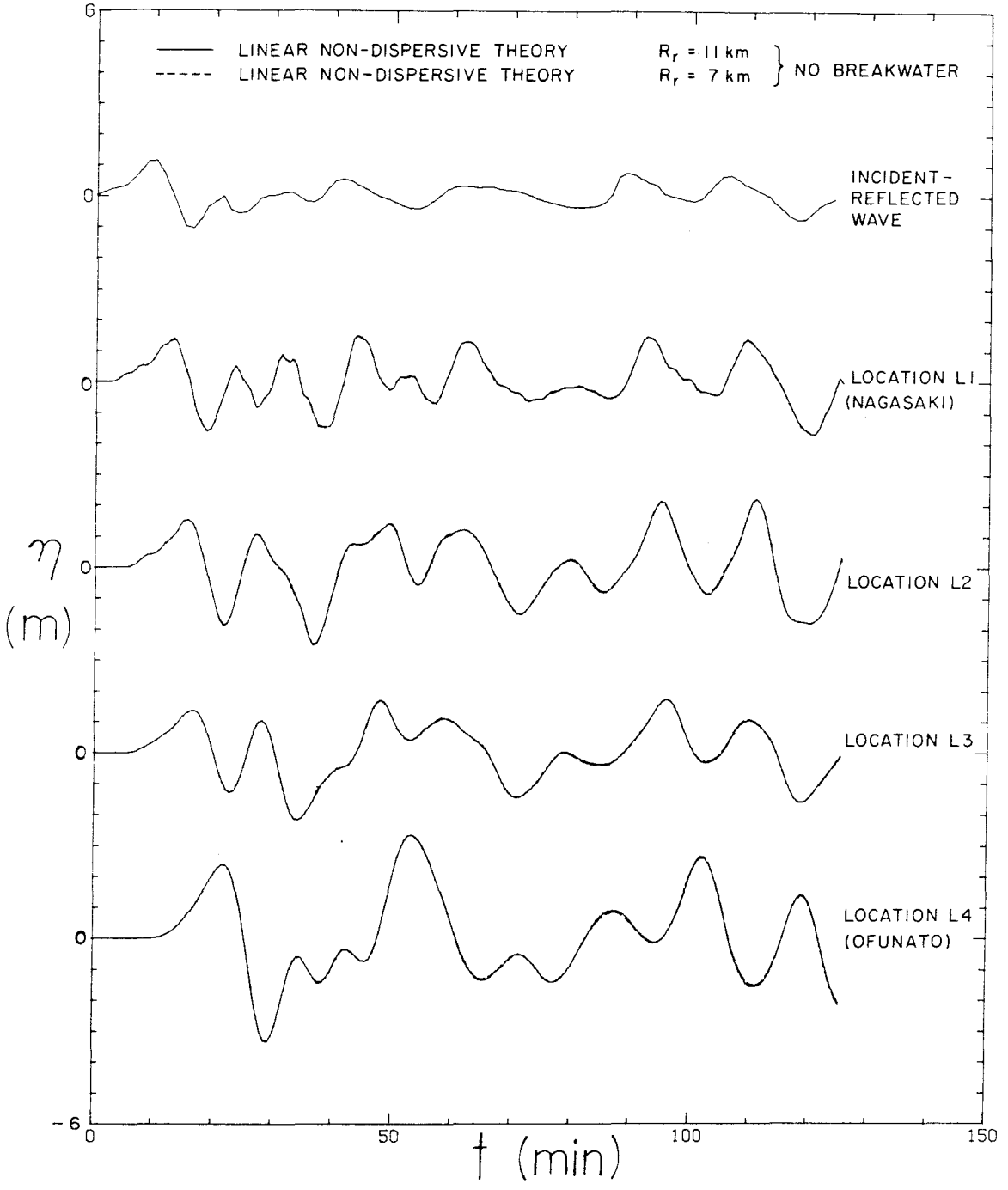

Fig. 7.3.5 Computed wave records at four locations inside the Ofunato Bay from the linear nondispersive theory. Comparison of the results for R_r = 7 km and R_r = 11 km.

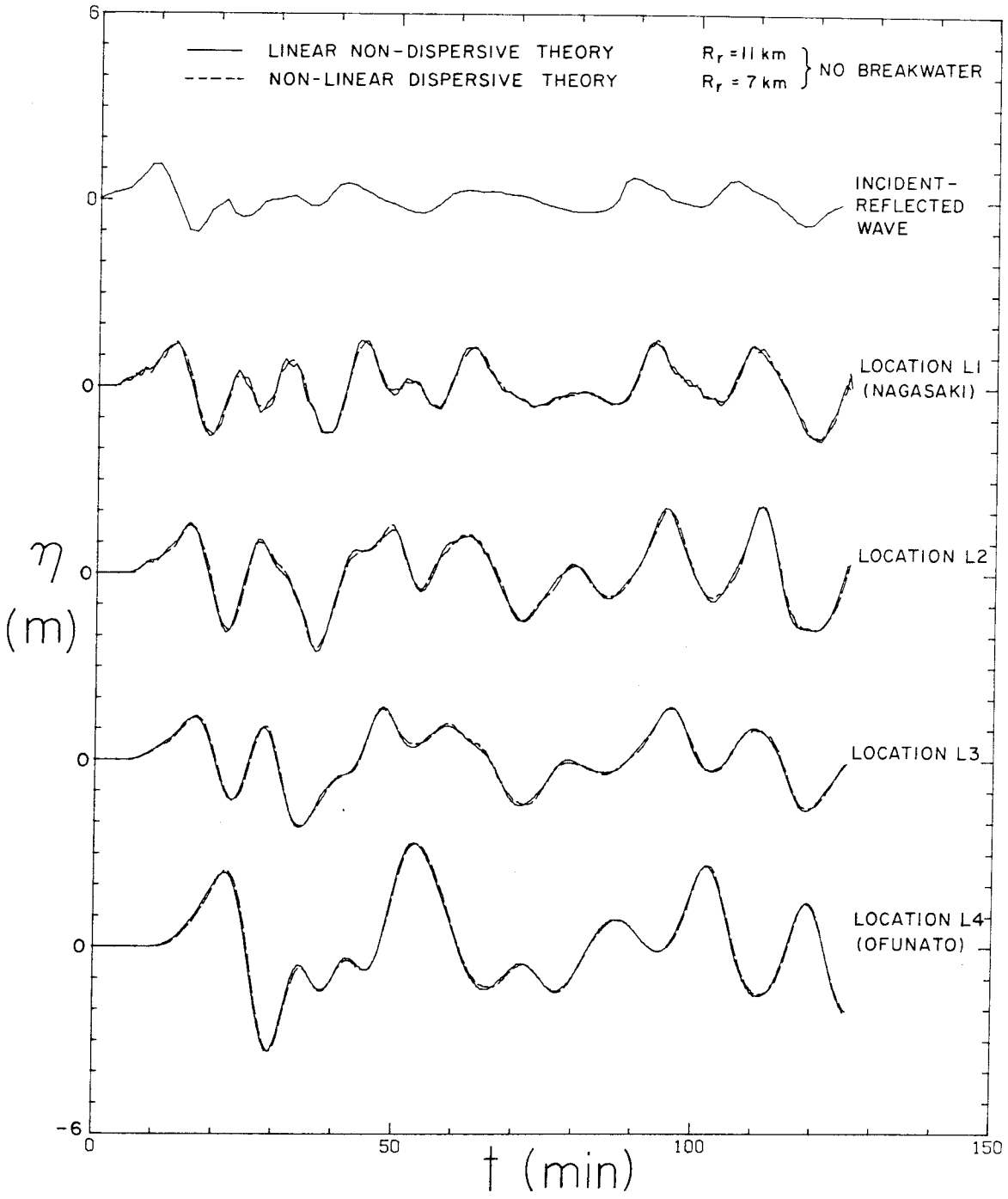

Fig. 7.3.6 Computed wave records at four locations inside the Ofunato Bay. Comparison between the nonlinear dispersive solution and the linear nondispersive solution.

the peak values with the present results). Such a discrepancy possibly can be explained by the fact that open sea conditions are not simulated in Ito's model, therefore the characteristics of the wave response inside the harbor may be affected by this. Also the wave records computed from this present study exhibit larger amplitudes by more than 50% of the measured wave records presented in Ito's paper. This is probably because the transfer function at Nagasaki used for the determination of the incident wave would have been different if computed with the present model. Therefore, a quantitative comparison between the present computation and the measured wave records at Ofunato would be meaningful only if the incident wave was computed from the transfer function derived with the present finite element model.

It is difficult from the wave records in Fig. 7.3.8 to derive any quantitative reliable information on the steady state response characteristics of the Ofunato Bay with and without breakwater because of the short time duration of these records. Nevertheless certain features of the response can be seen in Fig. 7.3.9(a) which represent the normalized energy density spectra for the two computed wave records at Ofunato with and without breakwater, which are shown in Fig. 7.3.8. The spectra are normalized by the mean square of the amplitude for the case without breakwater so that the area under the curve for the case without breakwater is unity. Two peaks are apparent on each spectrum. The peak corresponding to the 40 min period is almost wiped out by the action of the breakwater while that corresponding to the 17 min period remains largely unaffected. Two computed response curves of the bay at Ofunato are presented in Fig. 7.3.9(b). They were obtained by taking the ratio of the square

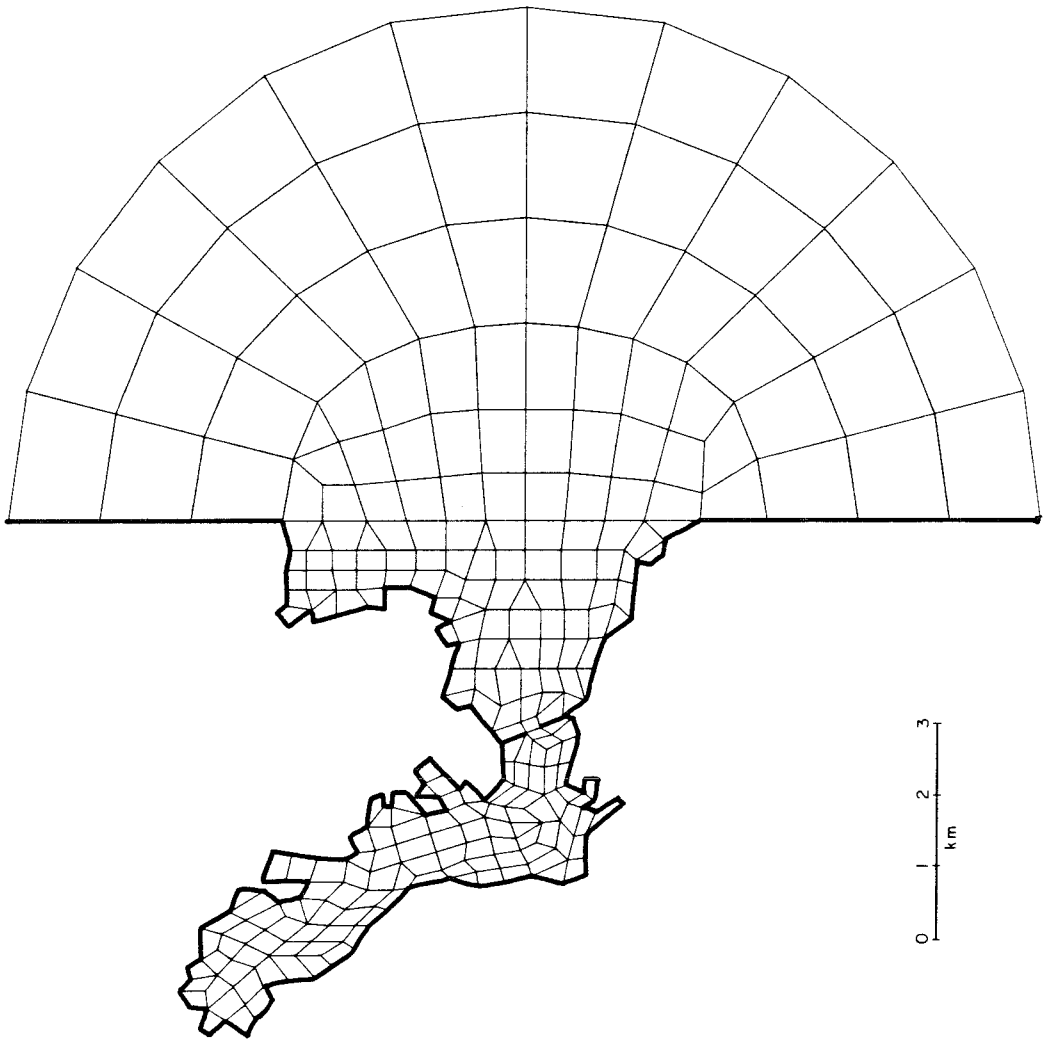

Fig. 7.3.7 Finite element grid with breakwater.

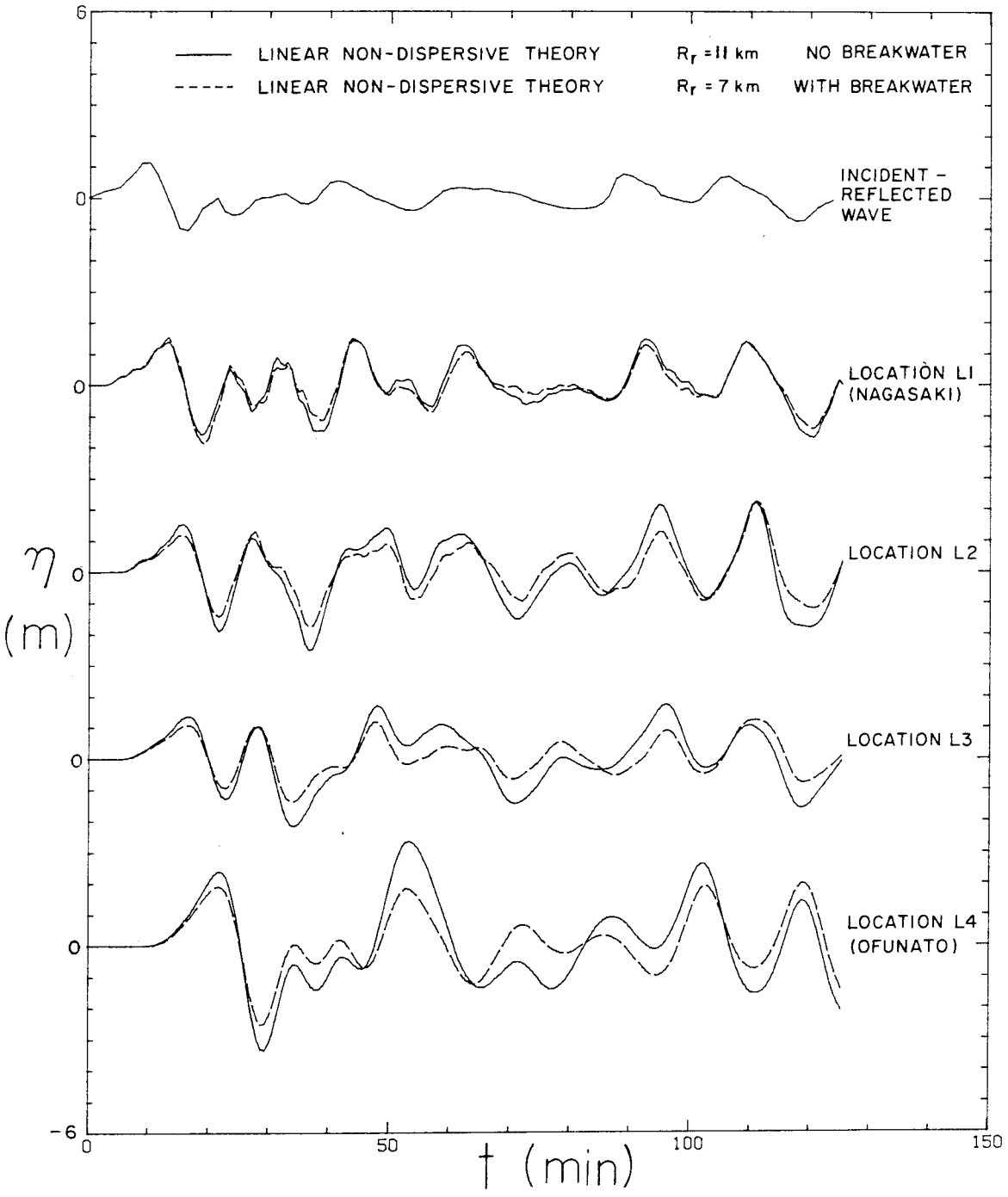

Fig. 7.3.8 Computed wave records at four locations inside the Ofunato Bay from the linear nondispersive solution, with and without breakwater.

root of energy density at Ofunato to that of the incident-reflected wave. The two peaks on each curve correspond to the lowest resonant modes of Ofunato Bay. It is apparent from Fig. 7.3.9(b) that the lowest mode has about a 40 min period while the second mode has about a 15 min period. The breakwater is most efficient in reducing the bay response at the lowest mode by a factor of about 2.5 but it does not affect significantly the amplitude of the second mode. These features agree with the field data presented by Horikawa and Nishimura (1970).

The reason why the breakwater is efficient at the lowest mode and inefficient at the second mode can be understood by considering the values of the length parameter $\sigma L/\sqrt{gh}$, where L denotes the distance between the bay head and the breakwater, h is the average depth of the bay between the bay head and the breakwater and σ is the circular frequency associated with the incident wave. At the first mode $\sigma L/\sqrt{gh} \simeq 1.2$ (based on L = 6500 m and h = 20 m) which from the results of Section 3.3 indicates the existence of a node around the breakwater location; therefore the amplitude of the wave velocity is maximum at that location and this, in turn , maximizes the efficiency of the breakwater in dissipating energy. At the second mode, $\sigma L/\sqrt{gh} \approx 3.2$, which indicates the existence of an antinode at the breakwater location; the wave velocity is therefore small near that location and the breakwater is inefficient in dissipating energy.

7.4 General Considerations for Prototype Harbors with Arbitrary Planforms and Variable Depths

Most of the present investigation has been limited to long and narrow harbors with constant depth. However, the results obtained for this rather restrictive geometry can reasonably be extended to fully

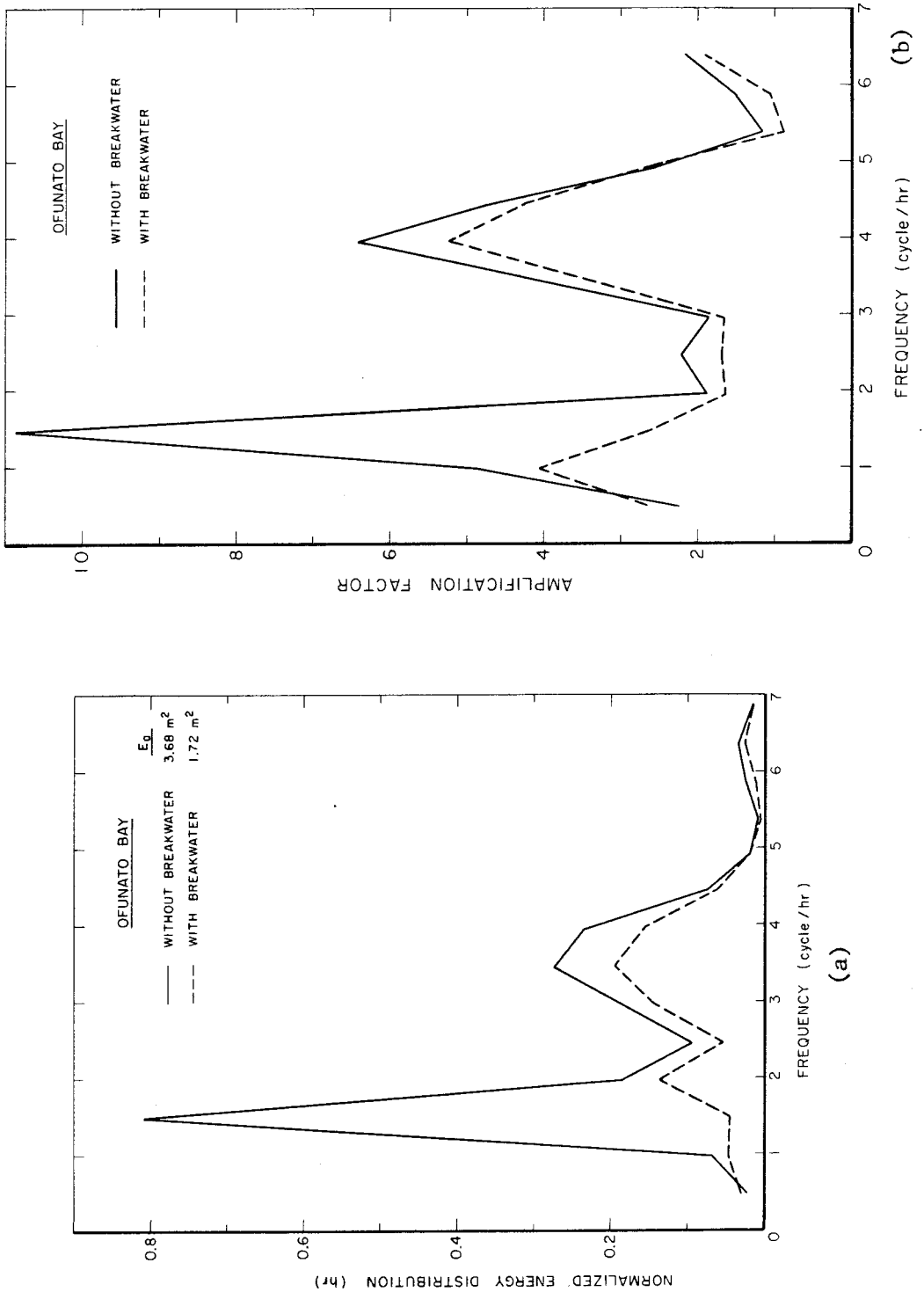

Fig. 7.3.9 (a) Computed normalized energy density spectra at Ofunato, (b) Response curves at Ofunato from the computed transient wave records.

three-dimensional harbor shapes as follows, in the case where no significant runup takes place at the lateral boundaries.

(i) If $L/\lambda < 0(1)$ where L denotes a characteristic length for the harbor or bay, nonlinear effects are expected to remain small or negligible. The Helmholtz mode, which is the most susceptible to be excited by the long period tsunamis, falls generally in that category.

(ii) If $L/\lambda \geq 0(1)$, nonlinear theory should, in general, be used if the Stokes number defined by Eq. (7.2.1) is much larger than ten. The manifestation of nonlinear effects cannot be described in general terms and must depend on the bathymetric conditions as well as the specific shape of each particular harbor. A study of nonlinear effects in each case can be carried out using the nonlinear program presented in Section 3.3 which proved adequate for the harbor situations investigated in this study.

If significant runup takes place at the lateral boundaries, the conclusions stated above do not hold anymore. Since the runup is a nonlinear process in itself it can induce a different overall wave pattern inside the harbor or bay and the characteristics of the subsequent wave oscillations may be drastically modified in some cases.

CHAPTER 8

CONCLUSIONS AND RECOMMENDATIONS FOR FUTURE STUDIES

8.1 Conclusions

The major objective of this study has been to investigate, experimentally and theoretically, the response of an arbitrary shaped harbor (or bay) with variable depth to transient nonlinear incident long waves, resulting in possible nonlinear oscillations. First, in Chapter 5 the wave dynamics of a closed rectangular basin were investigated in the shallow water wave range. Some of the dissipative and nonlinear effects which applied to oscillations in the basin could also be applied to the waves induced in harbors. Thus, this preliminary study helped clarify several features pertaining to harbor oscillations. The results from the second part of the investigation dealing with the continuous and transient excitations of a harbor were presented in Chapter 6. A detailed study of the nonlinear and dispersive effects and dissipative effects has been conducted for a long and narrow rectangular harbor with constant depth for the case of a continuous excitation. This study has been extended to other harbor shapes for the case of a transient excitation. The results of this investigation have been applied to prototype situations and this is discussed in Chapter 7. In particular the general theory has been used to compute the response of Ofunato Bay to the tsunami resulting from the Tokachi-Oki earthquake of May 16, 1968.

For convenience, the major conclusions drawn from this study are arranged in the order in which the results have been presented in Chapters 5,6, and 7.

Energy Dissipation in Standing Waves in a Closed Rectangular Basin

1. The major sources of energy dissipation for waves induced in a closed rectangular basin in the laboratory are bottom, wall and surface viscous laminar friction, and dissipation associated with surface tension effects.

2. For a narrow basin ($b < 8$ cm) and for a basin not wetted by the liquid inside it (e.g., lucite and distilled water) the most significant source of dissipation is dry friction of the meniscus against the wall.

Rectangular Closed Basin Excitation in the Shallow Water Wave Range

3. For a continuously excited basin and for shallow water waves the linear theory becomes inadequate at resonance. The nonlinear-dispersive-dissipative solution developed in Section 3.2.1 shows good agreement with the experiments for all cases investigated in this study.

4. The wave shape, for a continuously excited basin near resonance is very sensitive to the frequency of excitation; a cnoidal wave shape which can be predicted analytically develops near the main bifurcation frequency, provided the dispersion parameter is not too small and a "hump-like" wave travels to and fro between the basin walls. For small dispersion as the excitation frequency is decreased the main wave divides into a number of secondary oscillations.

5. The nonlinear standing wave solution presented in Section 3.2.3 agrees reasonably well with the experiments if the dispersion parameter h/λ is not larger than about 0.03; no cnoidal wave profile could be obtained experimentally for smaller values of h/λ.

6. For the transient excitation of a closed rectangular basin the importance of the Stokes number in defining the range of applicability of the linear theory and in predicting some of the waves features which develop with time (e.g., the number of secondary oscillations) has been demonstrated. The Stokes number also has been found useful in the case of the waves generated by a continuous basin excitation.

The Generation and Propagation of Long Waves of Permanent Shape in the Wave Basin

7. All the waves generated experimentally had a wave height of 25% to 30% smaller than predicted by the generation relationships. Some of this discrepancy may be attributed to leakage between the wave plate and the bottom and guide walls of the wave basin.

8. If the guide walls are extended for the whole basin length and if leakage effects are minimized, the solitary wave profile obtained at the coastline agrees reasonably well with that obtained from the theory of Boussinesq. However, the diffraction of a solitary wave into the wave absorbers along the sides of the basin alters the solitary wave shape significantly.

9. The shape of cnoidal waves at the coastline agrees reasonably well with the cnoidal wave theory. The effect of diffraction

of the waves due to the wave absorbers mounted along the walls of the basin somewhat modifies the experimental profiles but not as much as for solitary waves.

Effect of Dissipation in a Long and Narrow Rectangular Harbor

10. Leakage losses, caused by the presence of a small gap underneath the walls for a harbor just sitting on the basin floor have been found to be significant.

11. Flow separation at the entrance of the harbor is very efficient in dissipating wave energy and thus in reducing the effects of resonance in the harbor. This source of dissipation increases for smaller relative openings, a/b, and for larger relative incident wave heights, H/h.

12. Experiments indicate that the head loss coefficient f_e varies linearly with the parameter $U_e/a\sigma$ if $U_e/a\sigma < 1$. If $U_e/a\sigma \geq 1$, this coefficient remains approximately constant; for this range good comparison between the theory and the experiments has been obtained if f_e is taken equal to 0.8 for a fully open harbor and 1.15 for a partially closed entrance ($a/b \leq 0.8$).

13. Among the four sources of dissipation investigated experimentally, entrance dissipation appears to be the most efficient in reducing the effect of resonance. Leakage comes next, followed by viscous laminar friction and surface tension.

The Excitation of a Narrow Rectangular Harbor by a Continuous Train of Periodic Long Waves

14. For the first resonant mode, for which $L/\lambda < 0.25$, nonlinearities can be neglected even for large relative wave amplitudes inside the harbor. It appears that a linear dissipative theory is sufficient to describe the wave evolution in the harbor for this condition.

15. For a ratio of the harbor length to the wave length, L/λ larger than 0.25, a nonlinear-dispersive-dissipative theory generally must be used at or near resonance. Secondary resonant peaks not predicted by the linear theory have been obtained using the nonlinear solution developed in Section 3.4 and confirmed experimentally. Near the second resonant mode the main oscillation separates into several secondary oscillations and the number of these increases as the dispersion parameter decreases.

Transient Excitation of Harbors

16. For the three shapes investigated (a narrow rectangular harbor with a constant depth, a narrow rectangular harbor with a linearly decreasing depth and a trapezoidal harbor with a constant depth) nonlinear effects have been found to remain negligible near the first mode and small near the second mode. They tend to affect the wave shape locally but the overall wave pattern appears to be predicted reasonably well by a linear theory.

17. The effect of the converging sidewalls on the wave for the trapezoidal harbor is significant. This can be mitigated by a

breakwater only for very small opening ratios, e.g., $a/b < 0.125$, for the harbor with the trapezoidal shape which was investigated here.

18. For almost all the cases investigated in the harbor studies good agreement has been found between the numerical solution developed in Section 3.4 and the experiments. This suggests that this solution could be used with some confidence in prototype situations if the corresponding dissipation sources can be accurately evaluated.

Application to Prototype Situations

19. Some additional sources of dissipation have been investigated analytically as a means to reduce further the effects of resonance in prototype harbors or bays. It has been found that submerged breakwaters (if feasible from an engineering point of view) yield a degree of efficiency comparable to the usual breakwaters at a harbor entrance in dissipating wave energy.

20. The response of Ofunato Bay to the tsunami caused by the Tokachi-Oki earthquake of May 16, 1968 has been obtained numerically. The numerical solution has shown that the nonlinear convective effects must have remained very small in the Ofunato Bay for this tsunami. It has also shown that the breakwater constructed across the Ofunato Bay operates selectively, in the sense that it is efficient in dissipating wave energy at a period corresponding to the fundamental resonant mode of the bay but it

does not reduce resonant effects corresponding to the second natural mode of oscillation.

8.2 Recommendations for Future Studies

The numerical model on transient harbor oscillations presented in this study allows us to handle fairly general situations. However, some uncertainties remain and some important aspects related to harbor and bay oscillations need further investigation:

1. The present experimental investigation should be extended to more general harbor geometries and compared to the present model to carefully investigate under which conditions a simple linear analytical model can be used to describe the harbor oscillation for these geometries.

2. It has been realized that flow separation at a sudden contraction and expansion constitutes a particularly efficient means of dissipating wave energy in harbors and bays in some situations. However, some doubt still remains on the value of the head loss coefficient f_e for a wider range of parameters than those investigated in this study. Experiments which investigate this loss directly without working from the harbor response "backwards" are suggested.

3. An important effect not considered in this study is the run-up and run-down of waves on the sloping boundaries around the bay or harbor. More work is needed to understand the nature of this process. Then it may be possible, in a subsequent step, to

couple the run-up process to the numerical program developed in this study in order to treat the total problem of the interaction between wave oscillations inside the harbor and the run-up along the boundaries.

4. Of interest to seismologists and geophysicists is the knowledge of the deep-water signature of the tsunami which would hopefully lead to a better knowledge of the tectonic generation mechanism. However, most of the tide gages are placed in bays or harbors where the oscillations induced by tsunamis are very much affected by the local response characteristics. Once the importance of the factors affecting the wave oscillations (e.g., nonlinearities, dispersion, dissipation) have been evaluated, using, for instance, the present numerical program, a strategy should be investigated to determine the signature of the incident wave outside the bay, from tide gage records inside. This constitutes what can be termed the "inverse harbor problem." It is relatively simple when the oscillations in the harbor are governed by the linear inviscid theory. It becomes much more involved when the effects of convective nonlinearities or nonlinear viscous dissipation (e.g., due to the effect of breakwaters) become significant.

5. It has been assumed throughout this study that the outer region has a constant depth. However, in prototype situations it usually has a variable depth. In addition there may be an

interaction between the continental shelf and the harbor or bay which should be investigated. Neither of these would introduce an unusual complication to the present numerical treatment of the harbor problem.

(THIS PAGE IS BLANK, DUE TO ERROR IN PAGINATION)

LIST OF REFERENCES

Abramowitz, M. and Stegun, I.A. (1972), "Handbook of Mathematical Functions," Dover Publications Inc., New York.

Bathe, K.J. and Wilson, E. L. (1976), "Numerical Methods in Finite Element Analysis," Prentice-Hall Inc., New Jersey.

Brigham, O.E. (1974), "The Fast Fourier Transform," Prentice-Hall Inc., New Jersey.

Carrier, G.F. and Shaw, R.I. (1969), "Response of Narrow Mouthed Harbors to Tsunamis," Proc. International Symposium on Tsunamis, IUGG, Oct. 1969.

Chen, H.S. and Mei, C.C. (1974), "Oscillations and Wave Forces in an Offshore Harbor," Report 190, R.M. Parsons Laboratory for Water Resources and Hydraulics, MIT, 1974.

Chen, M., Divoky, D. and Hwang, L.S. (1978), "Application of the Three Dimensional Boussinesq Type Equations to Tsunamis Modeling," Proc. of the Symposium on Tsumanis, Ensenada, Mexico, Manuscript Report Series No. 48, Department of Fisheries and the Environment, Ottowa, Canada.

Chester, W. (1968), "Resonant Oscillations of Water Waves I. Theory," Proceedings, Royal Society of London, Vol. 308, pp. 5-22.

Chester, W. and Bones, J.A. (1967), "Resonant Oscillations of Water Waves II. Experiment," Proceedings, Royal Society of London, Vol. 306. pp. 23-30.

Chwang, A.T. and Wu, T.Y. (1976), "Cylindrical Solitary Waves," Proc. IUTAM Symposium on Water Waves in Water of Varying Depth, Comberra, Australia.

Cole, J.D. (1969), Perturbation Methods in Applied Mathematics," Ed. Blaisdel.

Fultz, D. (1962), "An Experimental Note on Finite Amplitude Standing Gravity Waves," Journal of Fluid Mechanics, Vol. 13.

Goring, D.G. (1978), "Tsunamis - The Propagation of Long Waves Onto a Shelf," W.M. Keck Laboratories of Hydraulics and Water Resources, Report No. KH-R-38, California Institute of Technology, Pasadena, California.

Hammack, J.L. (1972), "Tsunamis - A Model of Their Generation and Propagation," W.M. Keck Laboratory of Hydraulics and Water Resources, Report No. KH-R-28, California Institute of Technology, Pasadena, California.

Horikawa, K. and Nishimura, H. (1970), "On the Function of Tsunami Breakwaters," Coastal Engineering in Japan, Vol. 13, 1970.

Houston, J. R. (1978), "Interaction of Tsunamis With the Hawaiian Islands Calculated by a Finite-element Numerical Model," Journal of Physical Oceanography, 8-1: 93-101.

Houston, J. R. and Butler, H. L. (1979), "A Numerical Model for Tsunami Inundation," Technical Report HL-79-2, U.S. Army Engineer Waterways Experiment Station, CE Vicksburg, Mississippi.

Houston, J.R. and Garcia, A.W. (1978), "Type 16 Flood Insurance Study: Tsunami Prediction for the West Coast of the Continental United States," Technical Report H-78-26, U.S. Army Engineers Waterways Experiment Station, CE. Vicksburg, Mississippi.

Hughes, T.J.R., Pister, K.S. and Taylor, R.L. (1978), "Implicit Explicit Finite Elements in Nonlinear Transient Analysis," Proc. Fenomech '78 Stuttgart West Germany, August 30-September 1, 1978.

Hwang, L. S. (1979), "Tsunamis," Proceedings of the National Science Foundation Workshop, Organized and Edited by Hwang, L. S. and Lee, Y. K.

Hwang, L. S., and Tuck, E. O. (1970), "On the Oscillation of Harbors of Arbitrary Shape," Journal of Fluid Mechanics, 1970, Vol. 2, pp. 447-464.

Ingard, V. and Ising, H. (1967), Journal of Acoustical Society of America Vol. 2, pp. 6-17 (1967).

Ippen, A. T., Editor (1966), Estuary and Coastline Hydrodynamics, McGraw-Hill Book Company, New York.

Ippen, A. T. and Raichlen, F. (1962), "Wave Induced Oscillations in Harbors: the Problem of Coupling of Highly Reflective Basins," Report No. 69, Hydrodynamics Laboratory, Massachusetts Institute of Technology, May 1962.

Ippen, A. T. and Goda, Y. (1963), "Wave Induced Oscillations in Harbors: the Solution of a Rectangular Harbor Connected to the Open Sea," Report No. 59, Hydrodynamics Laboratory, Massachusetts Institute of Technology, 1963.

Ito, Y. (1970), "On the Effect of Tsunamis-Breakwater," Coastal Engineering in Japan, Vol. 13, 1970.

Jonsson, I. G. (1978), "A New Approach to Rough Turbulent Boundary Layers," Series paper 17, Institute of Hydrodynamics and Hydraulics Engineering, Technical University of Denmark.

Kamphuis, J.W. (May 1975), "Friction Factor Under Oscillatory Waves," Journal of the Waterways Harbors and Coastal Engineering Division, WW2.

Kawahara, M., Takeuchi, N., and Yoshida, T. (1978), "Two Step Explicit Finite Element Model for Tsunami Wave Propagation Analysis," International Journal for Numerical Methods in Engineering, Vol. 12, pp. 331-351.

Keulegan, G. H. (1948), "Gradual Damping of Solitary Waves," United States Department of Commerce, National Bureau of Standards, Research Paper RP 1895, Vol. 40, pp. 487-498.

Keulegan, G. H. (1959), "Energy Dissipation in Standing Waves in Rectangular Basins," Journal of Fluid Mechanics, Vol. 8, p. 33.

Korteweg, D. J. and de Vries, G. (1895), "On the Change of Form of Long Waves Advancing in a Rectangular Canal, and On a New Type of Long Stationary Wave," London, Edinburgh and Dublin Philosophical Magazine, Series 5, Vol. 39, pp. 422-443.

Lamb, H. (1932), "Hydrodynamics," Sixth Edition, Cambridge University Press.

Lee, J. J. (1971), "Wave-Induced Oscillations in Harbors of Arbitrary Geometry," Journal of Fluid Mechanics, 1971, Vol. 45, pp. 375-394.

Lee, J. J. and Raichlen, F. (1972), "Oscillations in Harbors with Connected Basins," Proc. A.S.C.E. JWWH, 98: WW3, August 1972.

Leendertse, J. J. (1967), "Aspects of a Computational Model for Long-Period Water Wave Propagation," Memo, RM-529U-PR, Rand Corp, Santa Monica, California, 1967.

Lepelletier, T. G. (1978), "Response of Harbors to Transient Waves: A Progress Report," Technology Memo, 78-S W. M. Keck Laboratory of Hydraulics and Water Resources, California Institute of Technology, March 1978.

Lin, C. C. (1957), "Motion in the Boundary Layer With a Rapidly Oscillating External Flow," Proc. 9th International Congress Applied Mechanics, Brussels, Vol. 14, p. 155.

Mei, C. C., Liu, P. and Ippen, A. T. (1974), "Quadratic Loss and Scattering of Long Waves," Proc. A.S.C.E. Journal of Waterways, Harbors, and Coastal Engineering Division, 100: WW3, August 1974.

Miles, J. W. and Munk, W. H. (1961), "Harbor Paradox," Proc. A.S.C.E. Journal of Waterways, Harbors Division, Vol. 87, pp. 111-180.

Miles, J. W. (1967), "Surface Wave Damping in Closed Basins," Proc. Royal Society, A 297.

Miles, J. W. (1974), "Harbor Seiching," Annual Review of Fluid Mechanics, Vol. 6, 1974.

Miles, J. W. and Lee, Y. K. (1975), "Helmotz Resonance of Harbors," Journal of Fluid Mechanics, 1975, Vol. 67, pp. 445-464.

Mungall, J. C. H. and Reid, R. O. (1978), "A Radiation Boundary Condition for Radically Spreading Non-Dispersive Gravity Waves," Technical Report Ref. 78-2-T, Texas A & M Research Foundation.

Newmark, N. M. (1959), "A Method of Computation for Structural Dynamics," Journal of the Engineering Mechanics Division A.S.C.E. pp. 67-94.

Olsen, K. and Hwang, L. S. (1971), "Oscillations in a Bay of Arbitrary Shape and Variable Depth," Journal of Geophysical Research, Vol. 76, pp. 5048-5064, 1971.

Raichlen, F. (1965), "Wave-Induced Oscillations of Small Moored Vessels," Report kH-R-10, W. M. Keck Laboratory of Hydraulics and Water Resources, California Institute of Technology.

Raichlen, F. (1966), "Estuary and Coastline Hydrodynamics," Edited by Ippen, A. T., McGraw-Hill.

Raichlen, F. (1976), "Coastal Wave Hydrodynamics -- Theory and Engineering Applications," Lecture Notes for Summer courses 1.69s at MIT; Course Organizer: C. C. Mei, Ralph M. Parsons Laboratory for Water Resources and Hydrodynamics - Department of Civil Engineering, Massachusetts Institute of Technology, Cambridge, Massachusetts.

Rogers, S. R. and Mei, C. C. (1975), "A Note on Nonlinear Standing Waves in Shallow Waters," (unpublished paper).

Rogers, S. R. and Mei, C. C. (1978), "Nonlinear Resonant excitation of a Long and Narrow Bay," Journal of Fluid Mechanics, 88: 1, 1978.

Rouse, H. (1946), "Elementary Mechanics of Fluids," New York, Wiley.

Schlichting, H. (1960), "Boundary Layer Theory," Fourth Edition, McGraw-Hill Publications.

Stoker, J. J. (1950), "Non Linear Vibrations," New York, Interscience.

Streeter, V. L. (1971), "Fluid Mechanics," McGraw-Hill, Fifth Edition.

Su, C. H. and Gardner, C. S. (1969), "Korteweg-de Vries Equations and Generalizations III. Derivation of Korteweg-de Vries Equation and Burgers Equation," Journal of Mathematical Physics, Vol. 10, pp. 536-539.

Ünlüata, Ü. and Mei, C. C. (1975), "Effects of Entrance Loss on Harbor Oscillations," Proc. ASCE Journal of Waterways, Harbors, and Coastal Engineering Division, 101: WW2, May 1975.

Ursell, F. (1953), "The Long Wave Paradox in the Theory of Gravity Waves," Proc. Cambridge Philosophical Society, Vol. 49, pp. 685-694.

Van Dorn, W. G. (1965), "Tsunamis," Advances in Hydroscience, Vol. 2.

Van Dorn, W. G. (1966), "Boundary Dissipation of Oscillatory Waves," Journal of Fluid Mechanics, Vol. 24, Part 4, pp. 769-779.

Verhagen, J. H. G. and Wijngaarden, L. (1956), "Non-Linear Oscillations of Fluid in a Container," Journal of Fluid Mechanics, Vol. 22, Part 6, pp. 737-754.

Wilson, B. W. (1972), "Seiches," Advances in Hydroscience, Academy Press, New York, Vol. 8.

Whitham, G. B. (1974), "Linear and Nonlinear Waves," A. Wiley-Interscience Publication.

Wu, T. Y. (1979), "Tsunamis," Proc. of the National Science Foundation Workshop, Organized and Edited by Hwang, L. S. and Lu, Y. K.

(THIS PAGE IS BLANK, DUE TO ERROR IN PAGINATION)

LIST OF SYMBOLS

A	Wave amplitude
A_c	Characteristic acceleration of the basin motion
A_I	Wave amplitude of incident-reflected wave system
a	Mouth width
a_δ	Water particle excursion outside the boundary layer
b	Harbor (basin) width
b_1	Harbor width at backwall for trapezoidal harbor
C	Wave celerity
C_e	Turbulent boundary friction factor
C_{es}	Effective skin friction coefficient for submerged breakwater
C_o	Linear wave celerity (linear dispersive theory)
C_s	Drag coefficient for a submerged breakwater
C	Surface contamination factor
E	Complete elliptic integral of the second kind
E_n	Mean wave energy in harbor (basin)
$\sqrt{E_a}$	Equivalent wave amplitude for a periodic wave containing several harmonies
$\overline{f}$	Decay coefficient
f_e	Entrance friction coefficient
g	Acceleration due to gravity
H	Wave height
H_ℓ	Mean negative wave height of the trailing wave
h	Still water depth
h_b	Height of submerged breakwater
h_o	Characteristic still water depth

h_1	Still water depth at backwall of the harbor for a linearly decreasing depth
i	Imaginary number $\sqrt{-1}$
K	Complete elliptic integral of the first kind
K_{ob}	Constant related to residual surface tension dissipation
k	Wave number
k_r	Nikuradse roughness parameter
L	Basin length or characteristic harbor length
ℓ	Characteristic length of a wave
m	Elliptic parameter
N_f	Number of emerging secondary waves
N_i, N_j	Shape functions
N_S	Number of oscillations required to reach steady state
N_T	Number of oscillations required to achieve maximum transient oscillations
p	Static pressure
p_d	Dynamic pressure
Q	"Q" factor
Q_c	"Q" factor associated with dry damping of meniscus against the wall
Q_f	"Q" factor associated with separation losses
Q_{ob}	"Q" factor associated with residual surface tension dissipation
Q_r	"Q" factor associated with partial reflection
Q_μ	"Q" factor associated with laminar boundary friction
Q_ε	"Q" factor associated with leakage losses
Q_r	"Q" factor associated with radiation damping
Q_τ	"Q" factor associated with turbulent boundary friction
$Q_{\tau s}$	"Q" factor associated with dissipation from submerged breakwater

R	Overall amplification factor (The subscript notation for the amplification factor related to a particular source is the same as that used for the corresponding Q factor)
R_r	Distance of radiation boundary from the harbor mouth
r	$(x^2 + y^2)^{\frac{1}{2}}$
$\bar{r}$	Reflection coefficient
r_e	Radius of curvature of the corners at the harbor entrance
S_i	Particular source of dissipation
S_h	Shape factor of the entrance
S_p	Stroke of wave plate motion
s	complex variable
T	Wave period
t	Time
t_e	Width of the harbor walls
t_n	Time required for non-linearities to become important
U_e	Amplitude of velocity at the mouth
U_i	Amplitude of the component of the velocity in x_i direction
$\underline{U}_r$	Ursell number
$\underline{U}_s$	Stokes number
u	Same as u_1
u_g	Horizontal component of leakage velocity in the gap underneath the wall
u_i	Velocity component in x_i direction (i = 1,2)
u_i^{ℓ}	Velocity component in x_i direction (i = 1,2) inside boundary layer
$\overline{u_i}$	Average velocity component in x_i direction (i = 1,2)
u_n	Outward normal velocity
V_i^o	Translational velocity component of frame of reference in x_i direction (i = 1,2)

v	Same as u_2
W	Overall energy dissipated in one period (The subscript notation for the energy dissipated by a particular source is the same as that used for the corresponding Q factor)
w	Velocity component in vertical direction
w_g	Vertical component of velocity in the gap underneath the wall
X_1°	Basin motion in the x_1° direction
x_b	Distance between two submerged breakwaters
x_n	Distance required for nonlinear effects to become important
x_1 (or x)	Co-ordinate distance in the first horizontal direction
x_2 (or y)	Co-ordinate distance in the second horizontal direction
x_1°	Co-ordinate distance in the first horizontal direction in a Newtonian frame of reference
x_2°	Co-ordinate distance in the second horizontal horizontal direction in a Newtonian frame of reference
z	Co-ordinate distance in vertical direction
z°	Co-ordinate distance in vertical direction in a Newtonian frame of reference
z_+	$t + x$ variable
z_-	$t - x$ variable.
α	Nonlinear parameter
$\bar{\alpha}$	Decay coefficient
α_c	Correction factor for kinetic energy
β	Dispersion parameter
β_*, γ_*	Numerical parameters
Γ_e	Surface tension
γ	Dissipation parameter
γ_s	Dissipation parameter for a sinusoidal motion
δ	Frequency parameter
δ_e	Boundary layer thickness

ε	Leakage parameter
$\bar{\varepsilon}$	Small number compared to unity
ε_e	Equivalent leakage parameter
ζ	Distance from the boundary in direction normal to boundary
η	Wave elevation
η_I	Wave elevation of the incident reflected wave system
η_s	Wave elevation of the radiated wave system
κ	Nondimensionalized wave number
$\bar{\kappa}$	Coefficient of Coulomb frictional force
λ	Wavelength for a periodic wave
λ_*	Penalty parameter in finite element solution
μ_{bs}	Laminar boundary friction factor associated with bottom and surface friction
μ_t	Laminar boundary friction factor associated with bottom, side walls and surface friction
μ_t'	Laminar boundary friction factor associated with bottom, side walls, end walls and surface friction
ν	Kinematic viscosity
ξ_1	Distance in first direction parallel to boundary
ξ_2	Distance in second direction parallel to boundary
$\bar{\xi}$	Wave plate displacement
π	The constant 3.14159
ρ	Fluid density
σ	Characteristic frequency of the forcing motion
σ_o	Resonant frequency for the linear, slightly dispersive model
τ	Boundary shear stress
Φ	Potential function
$\bar{\Phi}$	Averaged potential function over the depth

Φ_I	**Potential function for the incident-reflected wave system**
ϕ	Shape function
χ_r	Dissipation parameter associated with radiation damping
χ_f	Dissipation parameter associated with separation losses
χ_ε	Dissipation parameter associated with leakage losses
χ_μ	Dissipation parameter associated with laminar boundary friction
Ω	Characteristic frequency of a wave with a hump-like shape
ψ	**Potential function for the radiated wave**

SPECIAL SYMBOLS

$\lvert\cdot\rvert$	Modulus or absolute value
$\bar{\cdot}$	Averaged value
$\lVert\ \rVert$	Amplitude of harmonic function
$\underset{\sim}{\nabla}$	Gradient operator
$\sim$	Proportional to
$\approx$, $\simeq$	Approximately equal to
$\frac{\partial(\ \ )}{\partial(\ \ )}$	Partial derivative
$O(-)$	Order of magnitude of quantity between brackets
i,j,k	Integer indices
(.,.)	Scalar product

APPENDIX A

THE UNSTEADY BOUNDARY LAYER EQUATIONS AND SOLUTION

Consider a slightly viscous three-dimensional flow near a flat solid surface. The coordinate system is shown in Figure A1.

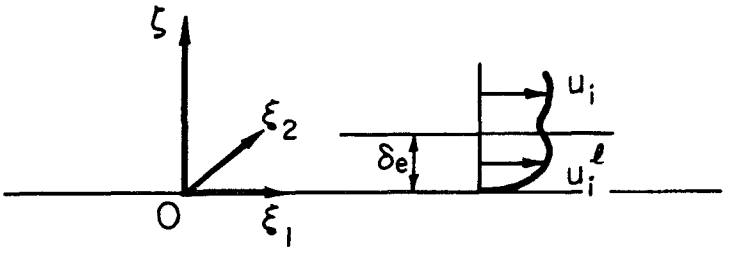

Fig. A1 Definition sketch for the local coordinate system of the boundary layer equations.

ζ denotes the coordinate in the direction normal to the boundary, ξ_1 and ξ_2 are the coordinates in the plane normal to the ζ direction, $\delta_e(\xi_1,\xi_2)$ is the boundary layer thickness, $u_i(\xi_1,\xi_2,\delta_e,t)$ is the velocity component in the direction ξ_i (i=1,2) just outside the boundary layer and $u_i^{\ell}(\xi_1,\xi_2,\zeta,t)$ is the velocity component in the direction ξ_i inside the boundary layer. The unsteady laminar boundary layer equations are given by Schlichting (1960) as:

$$\frac{\partial u_i^{\ell}}{\partial t} + u_j^{\ell}\frac{\partial u_i^{\ell}}{\partial \xi_j} + w^{\ell}\frac{\partial u_i^{\ell}}{\partial \zeta} = -\frac{1}{\rho}\frac{\partial p}{\partial \xi_i} + \nu\frac{\partial^2 u_i^{\ell}}{\partial \zeta^2} \qquad i=1,2 \qquad (A.1)$$

where p is the pressure impressed in the boundary layer by the external flow, w^{ℓ} the velocity component in the ζ direction, ν the kinematic viscosity and ρ the fluid density. Just outside the boundary layer the

momentum equations in the direction parallel to the boundary are:

$$\frac{\partial u_i}{\partial t} + u_j \frac{\partial u_i}{\partial \xi_j} + w \frac{\partial u_i}{\partial \zeta} = - \frac{1}{\rho} \frac{\partial p}{\partial \xi_i} \qquad i=1,2 \qquad (A.2)$$

Neglecting convective terms and subtracting Eq. A.2 from Eq. A.1 yields the linearized boundary layer equations in unsteady flow:

$$\frac{\partial (u_i^{\ell} - u_i)}{\partial t} = \nu \frac{\partial^2 u_i^{\ell}}{\partial \zeta^2} \qquad i=1,2 \qquad (A.3)$$

u_i^{ℓ} is a function of ξ_1, ξ_2, ζ whereas u_i only depends on ξ_1 and ξ_2.

Equivalently Eq. (A.3) can be written as:

$$\frac{\partial (u_i - u_i^{\ell})}{\partial t} = \nu \frac{\partial^2 (u_i - u_i^{\ell})}{\partial \zeta^2} \qquad (A.4)$$

with the boundary conditions:

$$u_i - u_i^{\ell} = u_i \qquad \zeta = 0 \qquad (A.5)$$

$$u_i - u_i^{\ell} = 0 \qquad \zeta = \infty \qquad (A.6)$$

Eq. (A.5) expresses the zero slip condition at the boundary. Eq. (A.6) is justified by performing a formal matching procedure between the exterior and the boundary layer regions, valid as long as δ_e remains small compared to a characteristic horizontal length.

Equation (A.4) is solved using the Laplace transform technique. Define:

$$f_i(\xi_1, \xi_2, \zeta, t) = u_i - u_i^{\ell} \qquad (A.7)$$

The Laplace transform of f is defined as:

$$\tilde{f}_i(\xi_1,\xi_2,\zeta,s) = \int_o^\infty e^{-st} f_i(\xi_1,\xi_2,\zeta,t)\, dt \tag{A.8}$$

Assume the following initial condition:

$$f_i = 0 \qquad t = 0 \tag{A.9}$$

Multiplying both sides of Eq. (A.4) by e^{-st}, integrating with respect to t and using Eq. (A.9) yields a differential equation for $\tilde{f}_i$:

$$\nu \frac{\partial^2 \tilde{f}_i}{\partial \zeta^2} - s\, \tilde{f}_i = 0 \tag{A.10}$$

with the boundary conditions:

$$\tilde{f}_i = 0 \qquad \zeta = \infty \tag{A.11}$$

$$\tilde{f}_i = \int_o^\infty u_i\, e^{-st}\, dt \qquad \zeta = 0 \tag{A.12}$$

The solution for $\tilde{f}_i$ is:

$$\tilde{f}_i = \exp\left[-\sqrt{\frac{s}{\nu}}\,\zeta\right] \int_o^\infty u_i\, e^{-st}\, dt \tag{A.13}$$

f_i is obtained from the inversion integral for the Laplace transform:

$$f_i(\xi_1,\xi_2,\zeta,t) = \frac{1}{2\pi i} \int_{Br} e^{st}\, \tilde{f}_i(\xi_1,\xi_2,\xi,s)\, ds \tag{A.14}$$

where $\int_{Br}$ is the Bromwich contour defined as:

$$\int_{Br} = \lim_{\Gamma \to \infty} \int_{\mu - i\Gamma}^{\mu + i\Gamma} \tag{A.15}$$

where μ is a positive constant. Of special interest is the expression for the shear stress τ_i in the ξ_i direction at the wall, defined as:

$$\frac{\tau_i}{\rho} = \nu \frac{\partial u_i^{\ell}}{\partial \zeta} \qquad \zeta = 0 \tag{A.16}$$

The expression for $\frac{\partial u_i^{\ell}}{\partial \zeta}$ at $\zeta = 0$ can be derived from Eq. (A.13) and one integration by parts (assuming the fluid motion starts from rest at t=0) as:

$$\frac{\partial u_i^{\ell}}{\partial \zeta} = -\frac{\partial f_i}{\partial \zeta} = \frac{1}{2\pi i} \int_{Br} \frac{e^{st}}{\sqrt{s\nu}} \int_o^{\infty} \frac{\partial u_i}{\partial t} e^{-st}\, dt\, ds \qquad \zeta = 0 \tag{A.17}$$

Using the following relations:

$$\sqrt{\frac{1}{s\nu}} \quad \supset \quad \sqrt{\frac{1}{\pi \nu t}}$$

$$\tilde{g}(s)\, \tilde{h}(s) \quad \supset \quad \int_o^{\infty} h(t')g(t-t')dt'$$

where the sign $\supset$ denotes the correspondence between a function and its Laplace transform, a final expression for $\frac{\partial u_i^{\ell}}{\partial \zeta}$ is obtained at $\zeta = 0$ as:

$$\frac{\partial u_i^{\ell}}{\partial \zeta} = \sqrt{\frac{1}{\pi \nu}} \int_o^{\infty} \frac{1}{\sqrt{t'}} \frac{\partial u_i(t-t')}{\partial t} dt' \qquad \zeta = 0 \tag{A.18}$$

The laminar shear stress component τ_i at the boundary is given by:

$$\frac{\tau_i}{\rho} = \nu \frac{\partial u_i^{\ell}}{\partial \zeta} = \sqrt{\frac{\nu}{\pi}} \int_o^{\infty} \frac{1}{\sqrt{t'}} \frac{\partial u_i(t-t')}{\partial t} dt' \qquad \zeta = 0 \tag{A.19}$$

Specializing to a sinusoidal flow defined by

$$u_i = U_i \cos \sigma t \quad , \tag{A.20}$$

Equation (A.19) becomes:

$$\frac{\tau_i}{\rho} = \sqrt{\nu\sigma}\, U_i \cos\left(\sigma t + \frac{\pi}{4}\right) \qquad \zeta = 0 \tag{A.21}$$

The energy dissipated in one period per unit area is computed as:

$$W = \int_0^T \tau_k u_k dt = \frac{\rho}{2}\sqrt{\frac{\nu\sigma}{2}}\,(U_1^2 + U_2^2)T \qquad \zeta = 0 \tag{A.22}$$

The same value for W is achieved from an expression for $\frac{\tau_i}{\rho}$ at $\zeta = 0$ given by

$$\frac{\tau_i}{\rho} = \sqrt{\frac{\nu\sigma}{2}}\, U_i \cos\sigma t = \sqrt{\frac{\nu\sigma}{2}}\, u_i \tag{A.23}$$

Equation (A.23) can then be considered equivalent to Eq. (A.21); its big advantage lies in the fact that the shear stress at the boundary is simply related to the velocity component u_i, which brings considerable simplification for the numerical treatment of Equation (3.1.35).

APPENDIX B

DERIVATION OF THE EXPLICIT FORM OF THE LINEAR SOLUTION OF THE CLOSED BASIN EXCITATION PROBLEM

The expression for the wave amplitude $\eta(x,t)$ has been derived in integral form in Eq. (3.2.56) of Section (3.2.2) and is rewritten for clarity:

$$\eta(x,t) = -\frac{1}{2\pi i}\int_{B_r} \frac{s}{s^2+\delta^2} \frac{\sinh\kappa_o(x-\frac{1}{2})}{\kappa_o \cosh(\frac{\kappa_o}{2})} [\exp(st) + (-1)^{m+1}\exp(s(t-\frac{m\pi}{\delta}))]ds \tag{B.1}$$

with
$$\kappa_o = \frac{s^{1/2}(s+\gamma_s)^{1/2}}{\sqrt{\frac{\beta}{3}}(s+i\sqrt{\frac{3}{\beta}})^{1/2}(s-i\sqrt{\frac{3}{\beta}})^{1/2}} \tag{B.2}$$

The notations are the same as in Subsection (3.2.2): β, γ_s, δ are fixed parameters, i is the imaginary number $\sqrt{-1}$, m is an integer and B_r denotes the Bromwich contour. In order to render the function $\kappa_o(s)$ analytical almost everywhere in the s plane, branch cuts must be defined along with the range of variation of the various angles associated with them. With the choice indicated on Fig. B1 it can be checked that $\kappa_o(s)$ is single valued and analytical everywhere in this plane, except along the branch cuts indicated by hatched lines. The problem is to find an explicit expression for $\eta(x,t)$ in a series form. Two cases must be considered according to the sign of $(t - \frac{m\pi}{\delta})$.

(i) <u>First case</u>: $t > \frac{m\pi}{\delta}$

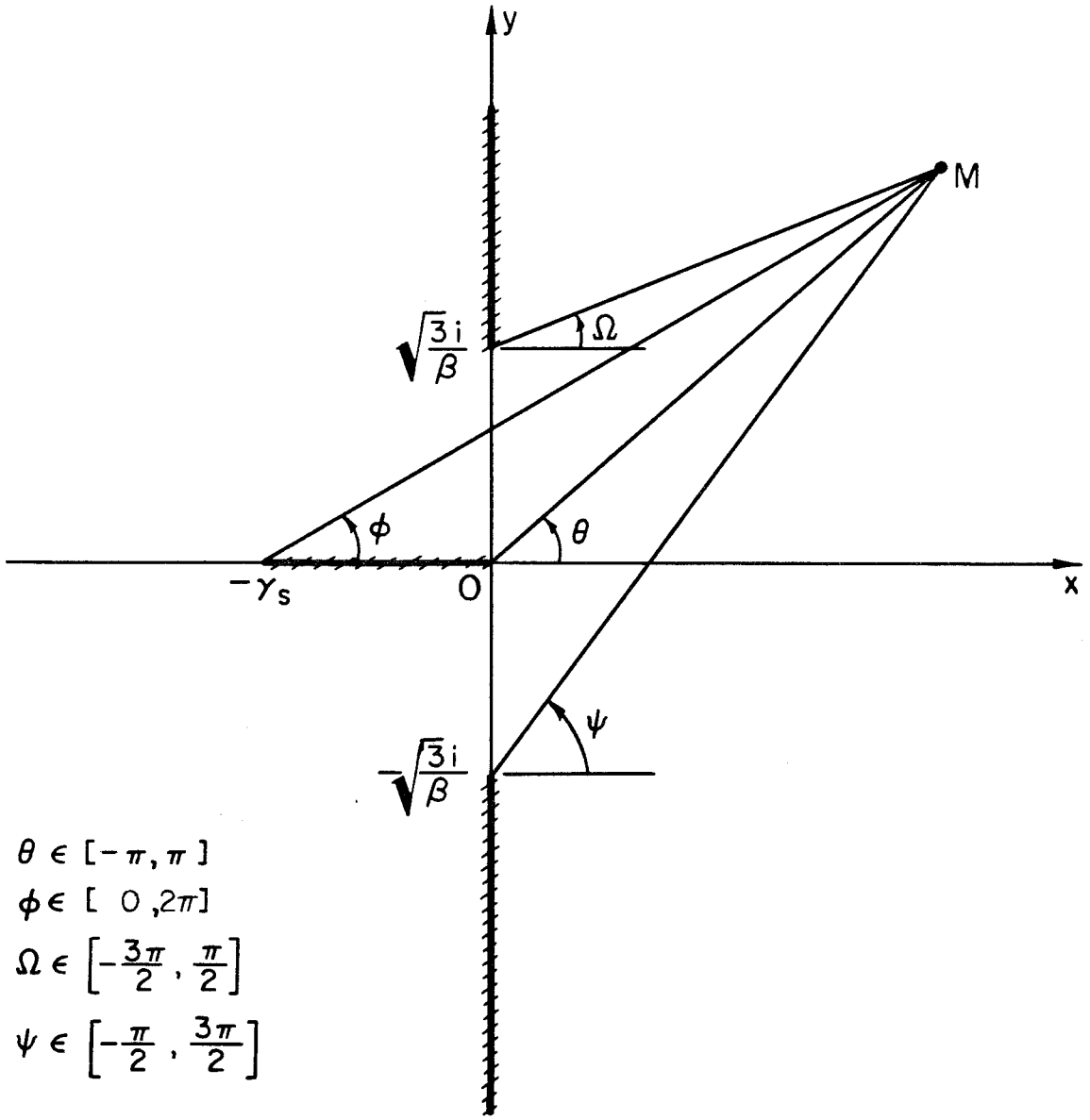

Fig. B1 Location of the branch cuts (hatched lines) and range of variation of the various angles associated with them.

Defining G(s) as the integrand under the integral sign in Eq. (B.1) the Residue theorem is applied inside the integral contour $C_{1\Gamma}$ indicated on Fig. B2 , and the following equation is obtained:

$$\int_{\mu-i\Gamma}^{\mu+i\Gamma} G(s)ds + \int_{C_{1\Gamma}} G(s)ds + \int_{\sum B_{ri}} G(s)ds + \int_{\sum C_{ri}} G(s)ds$$

$$= 2\pi i \left(\sum_{n} \text{Res } G(s=s_n) \right) \qquad \text{(B.3)}$$

where $C_{1\Gamma}$ denotes the path on the big circle with radius Γ, $\sum B_{ri}$ is the path along all the branch cuts, $\sum_{C_{ri}}$ the path along all the small circles of radius r_i around the branch points, and s_n a singular point inside the contour. After calculations it turns out that the sum of the integrals along the branch cuts and each integral around a branch point tend to zero as r_i tends to zero. Also $\int_{C_{1\Gamma}} G(s)ds \to 0$ as $\Gamma \to \infty$, therefore an explicit expression for $\eta(x,t)$ is given as:

$$\eta(x,t) = -\sum_{n} \text{Res } G(s=s_n) \qquad \text{(B.4)}$$

An examination of G(s) shows that three removable singularities exist as $s=0, +i\delta, -i\delta$: the residue of G(s) at those points is therefore zero. The only isolated singularities of G(s) are given by:

$$\cosh \frac{K_o}{2} = 0 \iff i \frac{K_o}{2} = (2n+1) \frac{\pi}{2} \qquad n=0,\pm1,\pm2 \qquad \text{(B.5)}$$

Neglecting terms of order $0(\gamma^2)$ the solution of Eq. (B.5) is:

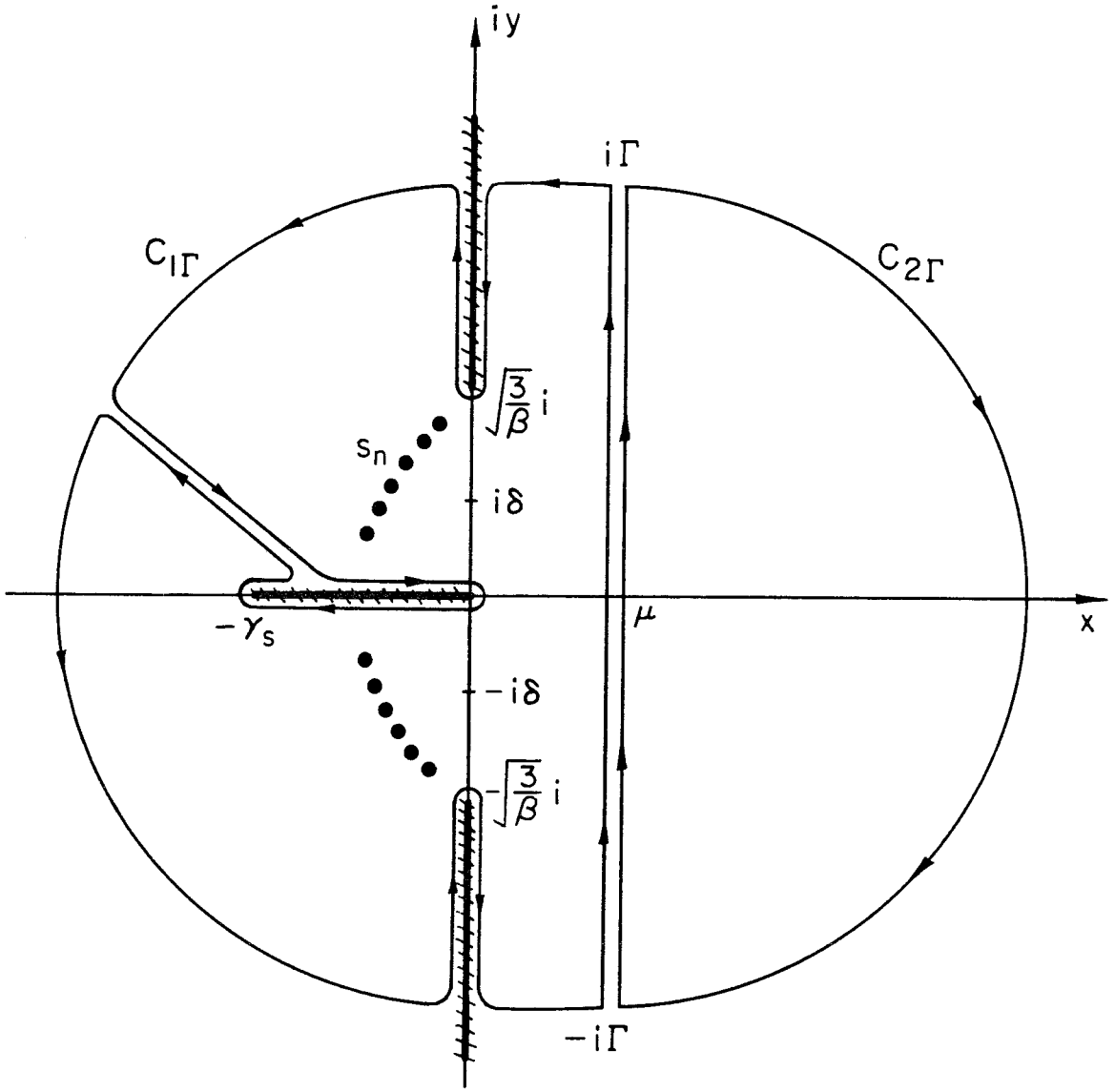

Fig. B2 Definition sketch for the integral contours $C_{1\Gamma}$ and $C_{2\Gamma}$ (the hatched lines represent the branch cuts and the dots indicate the position of the poles).

$$s_n = \begin{cases} \dfrac{-\gamma_s - i2a_n(1+\frac{\beta}{3}a_n^2)^{1/2}}{2(1+\frac{\beta}{3}a_n^2)} & \text{if } n \geq 0 \\ \dfrac{-\gamma_s + i2a_n(1+\frac{\beta}{3}a_n^2)^{1/2}}{2(1+\frac{\beta}{3}a_n^2)} & \text{if } n < 0 \end{cases} \tag{B.6}$$

with $a_n = (2n+1)\pi$.

The residue of G(s) at $s=s_n$ can then be computed. The result is:

$$\text{Res } G(s=s_n) = (-1)^n \sin[a_n(x-\tfrac{1}{2})]\, f_n'\, e^{s_n t} \tag{B.7}$$

with
$$f_n' = f_n[1+(-1)^{m+1}\exp(-m\pi\tfrac{s_n}{\delta})] \tag{B.8}$$

$$f_n = \frac{4\,s_n}{(s_n^2+\delta^2)} \cdot \frac{1+\frac{\beta}{3}s_n^2}{[2s_n+\gamma_s(1-\frac{\beta}{3}s_n^2)]} \tag{B.9}$$

It can be noticed that Res $G(s=s_n)$ is conjugate of Res $G(s=s_{-n-1})$, n=0,1,2..., so that

$$\sum_{n=-\infty}^{\infty} \text{Res } G(s=s_n) = 2\sum_{n=0}^{\infty} \text{Re}\{\text{Res } G(s=s_{-n-1})\} \tag{B.10}$$

The complete solution follows directly from Eqs. (B.4), (b.7) and (B.10).

Second case: $t \leq \frac{m\pi}{\delta}$

The integrand G(s) must be separated into two functions:

$$G(s) = G_1(s) + G_2(s) \text{ where:} \tag{B.11}$$

$$G_1(s) = \frac{s}{s^2+\delta^2} \frac{\sinh \kappa_o (x-\frac{1}{2})}{\kappa_o \cosh (\frac{\kappa_o}{2})} e^{st} \tag{B.12}$$

$$G_2(s) = \frac{s}{s^2+\delta^2} \frac{\sinh \kappa_o (x-\frac{1}{2})}{\kappa_o \cosh (\frac{\kappa_o}{2})} (-1)^{m+1} \exp[s(t-\frac{m\pi}{\delta})] \tag{B.13}$$

so that:

$$\eta(x,t) = -\frac{1}{2\pi i}\int_{B_r} G_1(s)ds - \frac{1}{2\pi i}\int_{B_r} G_2(s)ds \tag{B.14}$$

Applying the Residue theory inside the integral contour $C_{2\Gamma}$ indicated in Fig. B2 the following equation is obtained:

$$\int_{B_r} G_2(s)ds + \int_{C_{2\Gamma}} G_2(s)ds = -2\pi i \sum \text{Res} G_2(s=s_n) \tag{B.15}$$

No singularities exist inside this contour. Furthermore,

$$\int_{C_{2\Gamma}} G_2(s)ds \to 0 \text{ as } \Gamma \to \infty \tag{B.16}$$

Therefore, the value of the second integral in Eq. (B.14) is zero. For the first integral of Eq. (B.14) the same contour $C_{1\Gamma}$ as in the case where $t > \frac{m\pi}{\delta}$ is considered. In addition to the singularities already found, two poles are located as $s=\pm i\delta$. It is assumed that $\delta < \sqrt{3/\beta}$ so that the poles do not lie on a branch cut.

The residues of $G_1(s)$ at $s=\pm i\delta$ are obtained as:

$$\text{Res } G_1(s=\pm i\delta) = \frac{1}{2} \frac{\sin \kappa (x-\frac{1}{2})}{\kappa \cos \frac{\kappa}{2}} e^{\pm i\delta t} \tag{B.17}$$

where κ is defined as:

$$\kappa = \frac{\delta(1 \mp i\frac{\gamma_s}{2\delta})}{(1-\frac{1}{3}\beta\delta^2)^{1/2}} \tag{B.18}$$

where it is understood that $\gamma_s << 1$.

The expression for the Residue of $G_1(s)$ at $s=s_n$ is the same as before except that in Eq. (B.7) f_n' must be replaced by f_n. The solution $\eta(x,t)$ for this case is then:

$$\eta(x,t) = -2\sum_{n=1}^{\infty} \mathrm{Re}\{\mathrm{Res}\ G_1(s=s_n)\} - 2\mathrm{Re}\{\mathrm{Res}\ G_1(s=\pm i\delta)\} \qquad \text{(B.19)}$$

This completes the derivation of the explicit solution for the linear basin excitation problem.

(THIS PAGE IS BLANK, DUE TO ERROR IN PAGINATION)

APPENDIX C

EQUIVALENT LEAKAGE LOSS COEFFICIENT ASSOCIATED WITH A PARTIALLY REFLECTIVE BOUNDARY

Consider a linear harmonic plane wave in shallow water which is normally incident to a beach or any wave absorber located at x = 0. The wave system can be decomposed into an incident wave $\eta_1(x,t)$ and a reflected wave $\eta_2(x,t)$ such that:

$$\eta_1 = A_1 \sin(\sigma t - kx) \tag{C.1}$$

$$\eta_2 = A_2 \sin(\sigma t + kx) \tag{C.2}$$

where the wave number k is related to the frequency σ by:

$$k = \frac{\sigma}{\sqrt{gh}} \tag{C.3}$$

where h and g denote the depth and the acceleration of gravity, respectively. The effectiveness of the absorbing boundary is measured by the reflection coefficient $\bar{r}$ defined as the ratio of the reflected wave amplitude A_2 to the incident wave amplitude A_1.

In order to estimate the effectiveness of this source of dissipation in reducing resonance in harbors, an equivalent leakage velocity u_n is sought in the form:

$$u_n = \varepsilon_e \sqrt{\frac{g}{h}} (\eta_1 + \eta_2) \tag{C.4}$$

where ε_e is an equivalent leakage coefficient to be determined.

The wave energy by unit width dissipated in one period by partial reflection is equal to:

$$W_{\bar{r}} = \int_{-h}^{0}\int_{0}^{T} u_1 p_{d_1}\, dtdz - \int_{-h}^{0}\int_{0}^{T} u_2 p_{d_2}\, dtdz \qquad (C.5)$$

where, in shallow water the dynamic pressure p_d and the horizontal velocity u are given, respectively, by:

$$p_d = \rho g \eta \quad , \quad u = \eta\sqrt{g/h} \qquad (C.6)$$

Substituting Eq. (C.6) into Eq. (C.5) one obtains:

$$W_{\bar{r}} = \rho g \sqrt{gh}\, \frac{A_1^2 - A_2^2}{2} T = \rho g \sqrt{gh}\, \frac{A_1^2}{2} (1 - \bar{r}^2)\, T \qquad (C.7)$$

The wave energy by unit width dissipated in one period by leakage is:

$$W_\varepsilon = \int_{-h}^{0}\int_{0}^{T} u_n (p_{d_1} + p_{d_2})\, dt\, dz \qquad (C.8)$$

or, using Eq. (C.4),

$$W_\varepsilon = \rho g \sqrt{gh}\, \varepsilon_e \frac{(A_1 + A_2)^2}{2} T = \rho g \sqrt{gh}\, \varepsilon_e \frac{A_1^2}{2} (1 + \bar{r})^2\, T \qquad (C.9)$$

Equating expressions (C.7) and (C.9), the equivalent leakage velocity is found as:

$$\varepsilon_e = \frac{1 - \bar{r}}{1 + \bar{r}} \qquad (C.10)$$

This result is used in Chapter 7 to compare the effectiveness of the various sources of dissipation in prototype harbors, including dissipation related to partial reflection.

(THIS PAGE IS BLANK, DUE TO ERROR IN PAGINATION)

APPENDIX D

DERIVATION OF THE BOUNDARY CONDITION AT A WALL WITH A SMALL GAP BETWEEN THE WALL AND THE BOTTOM

The problem is illustrated by the definition sketch of Fig. D1. A small gap, e, exists underneath a vertical wall with t_e separating a region where wave action takes place from a quiescent semi-infinite region. The presence of the wave in region A creates a pressure difference between A and B, inducing a flow underneath the wall. Three steps are successively considered in this development: the computation of the velocity profile in the gap, the relation between the pressure difference between A and B and the wave parameters, and the derivation of an equivalent leakage velocity to be used as a boundary condition at the walls.

(i) Computation of the velocity profile in the gap

The velocity vector consists of the horizontal velocity component $u_g(x_n,z,t)$ and the vertical velocity component $w_g(x_n,z,t)$, where x_n refers to the normal horizontal outward direction to the wall. Assuming the flow is unidirectional ($w_g \equiv 0$), the continuity equation and the momentum equation in the z direction yield:

$$u_g(x_n,z,t) = u_g(z,t) \tag{D.1}$$

$$p(x_n,z,t) = p(x_n,t) \tag{D.2}$$

where p is the static pressure.

The momentum equation in the x_n direction yields:

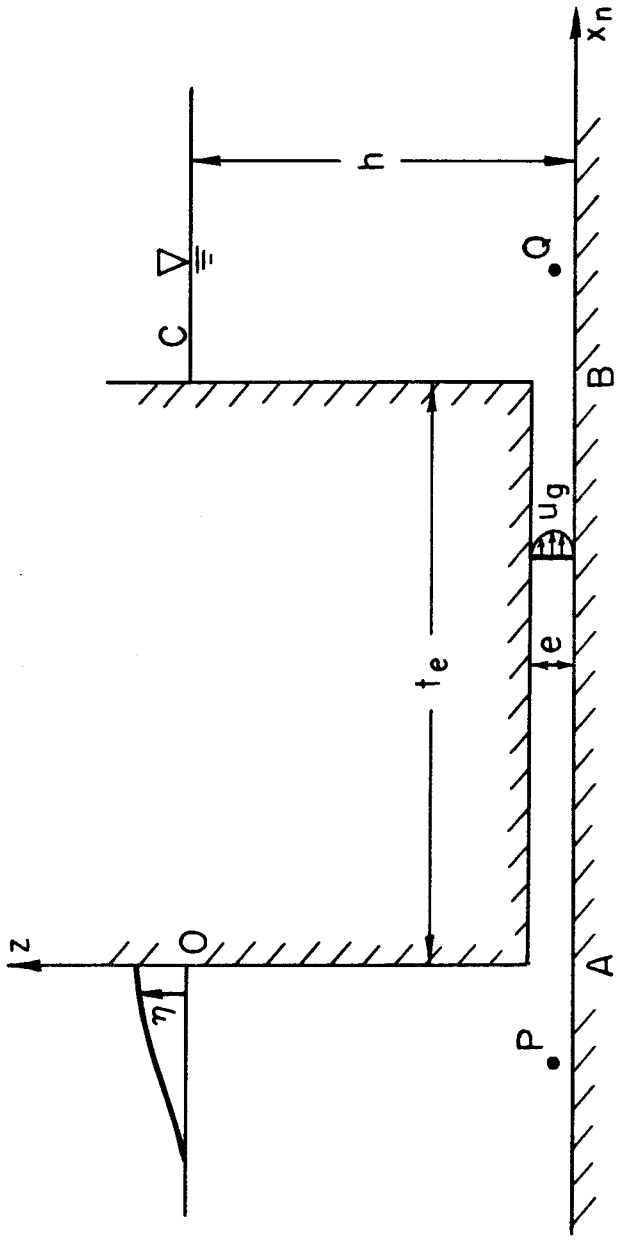

Fig. D1 Definition sketch for the laminar leakage underneath a wall.

$$\frac{\partial u_g}{\partial t} = -\frac{1}{\rho}\frac{\partial p}{\partial x_n} + \nu \frac{\partial^2 u_g}{\partial z^2} \tag{D.3}$$

where ρ and ν are the density and the kinematic viscosity of the fluid, respectively. The order of magnitude of the unsteady term can be compared to that of the viscous term in the following:

$$0\left(\frac{\partial u_g/\partial t}{\partial^2 u_g/\partial z^2}\right) = \frac{e^2}{\nu T} \tag{D.4}$$

where T refers to the typical period of the motion in typical laboratory conditions $e \leq .3\text{mm}$, $T \sim 1$ sec and $\nu = 10^{-2}\text{cm}^2/\text{sec}$ so that

$$\frac{e^2}{\nu T} < .05 \tag{D.5}$$

The unsteady term can consequently be neglected and the momentum equation becomes:

$$\frac{\partial p}{\partial x_n} = \rho\nu \frac{\partial^2 u_g}{\partial z^2} \tag{D.6}$$

The boundary conditions are:

$$u_g(-h) = u_g(-h+e) = 0 \tag{D.7}$$

Since $\frac{\partial p}{\partial x_n}$ does not depend on z, Eq. (D.6) can be integrated readily:

$$u_g(z,t) = \frac{1}{\nu\rho}\frac{1}{2}(z+h)(z+h-e)\frac{\partial p}{\partial x_n} \tag{D.8}$$

The mean velocity is obtained as:

$$\overline{u_g}(t) \equiv \frac{1}{e}\int_{-h}^{-h+e} u_g dz = -\frac{1}{\nu\rho}\frac{e^2}{12}\frac{\partial p}{\partial x_n} \tag{D.9}$$

From Eq. (D.9), $\frac{\partial p}{\partial x_n}$ does not depend on x, therefore:

$$\frac{\partial p}{\partial x_n} = \frac{p_B - p_A}{t_e} \tag{D.10}$$

where p_B and p_A denote the pressure at B and A.

(ii) Relation between the pressure difference between O and B and the wave parameters

The Bernouilli equation can be applied between the points P and A, A and B, B and C:

$$\frac{p_P}{\rho g} = \alpha_c \frac{\bar{u}_g^2}{2g} + \frac{p_A}{\rho g} \tag{D.11}$$

where α_c is a correction factor for the kinetic energy ($\alpha_c = 0(1)$)

$$\frac{\alpha_c \bar{u}_g^2}{2g} + \frac{p_A}{\rho g} = \frac{p_B}{\rho g} + \frac{\alpha_c \bar{u}_g^2}{2g} + \frac{E_g}{\rho g} \tag{D.12}$$

$$\frac{p_B}{\alpha_c \rho g} + \frac{\alpha_c \bar{u}_g^2}{2g} = h + \frac{\alpha_c \bar{u}_g^2}{2g} \tag{D.13}$$

where E_g is the head loss due to laminar friction along the gap. The pressure p_p can be derived from the inviscid irrotational wave theory as:

$$\frac{p_P}{\rho g} = \frac{\eta}{\cosh kh} + h \tag{D.14}$$

where η is the wave elevation at A and k is the wave number.

Combining Eqs. (D.11) to (D.14) the following is obtained:

$$\frac{\eta}{\cosh kh} = \alpha_c \frac{\bar{u}_g^2}{2g} + \frac{E_g}{\rho g} \tag{D.15}$$

or, using Eq. (D.9), (D.10) and (D.12):

$$\frac{\eta}{\cosh kh} = \alpha_c \frac{\bar{u}_g^2}{2g} + \bar{u}_g \frac{12\nu t_e}{ge^2} \tag{D.16}$$

Eq. (D.16) can be written in the form:

$$X = \varepsilon_o(1 - \alpha_c X^2) \tag{D.17}$$

where
$$\varepsilon_o = \frac{e^2}{12\nu t_e} \left(\frac{g\eta}{2\cosh kh} \right)^{1/2} \tag{D.18}$$

$$X = \frac{\bar{u}_g}{\sqrt{\frac{2g\eta}{\cosh kh}}} \tag{D.19}$$

The solution of Eq. (D.17) is:

$$X = \varepsilon_o + 0(\varepsilon_o^2) \tag{D.20}$$

Typical values corresponding to the experimental conditions are $e = .3$ mm, $\eta = 10$ mm, $\nu = 0.01$ cm^2/sec, $t_e = 1$ cm, $kh \ll 1$ so that $\varepsilon_o \leq .1$.

Thus, neglecting the quadratic velocity term induces a relative error less than 10%. Therefore, as a reasonable approximation, the leakage velocity is considered as a linear function of the wave amplitude at the wall, such that:

$$\bar{u}_g = \frac{e^2 g}{12\nu t_e} \frac{\eta}{\cosh kh} \tag{D.21}$$

(iii) Derivation of the boundary condition at the wall

The expressions for the horizontal components of the velocity vector and the dynamic pressure are assumed to be of the form:

$$u_n(x_1,x_2,z,t) = \mathrm{Re}\left\{ \hat{u}_n(x_1,x_2) \quad \frac{\cosh k(z+h)}{\cosh kh} \, e^{-i\sigma t} \right\}$$

$$p_d(x_1,x_2,z,t) = \mathrm{Re}\left\{ \rho g \hat{\eta} \, \frac{\cosh k(z+h)}{\cosh kh} \, e^{-i\sigma t} \right\} \tag{D.22}$$

$$\eta(x_1,x_2,t) = \mathrm{Re}\left\{ \hat{\eta}(x_1,x_2) \, e^{-i\sigma t} \right\}$$

where u_n denotes the outward normal component of the horizontal velocity vector at the wall.

The idea consists of deriving an expression for $\hat{u}_n$ such that the energy flux caused by the "equivalent" leakage velocity u_n is equal to the energy flux caused by the actual leakage. $\hat{u}_n$ is thus determined by the equation:

$$\int_0^T \int_{-h}^{o} u_n p_d \, dz dt = e \int_0^T \bar{u}_g P_d \, dt \qquad z = -h \tag{D.23}$$

After calculations $\hat{u}_n$ is found as:

$$\hat{u}_n = \frac{e^3}{3\nu t_e} \frac{gk}{2kh + \sinh 2kh} \hat{\eta} \tag{D.24}$$

Eq. (D.24) expresses the boundary condition to be used in case of a leakage through a small gap at the bottom.

(THIS PAGE IS BLANK, DUE TO ERROR IN PAGINATION)

APPENDIX E

COMPUTATION OF THE Q FACTORS CORRESPONDING TO VARIOUS SOURCES OF DISSIPATION IN A NARROW RECTANGULAR HARBOR AND IN A RECTANGULAR BASIN

E.1 Case of a Narrow Rectangular Harbor

A definition sketch for the coordinate system and the notation are the same as presented in Section 3.3.2. Combining Eqs. (3.3.20) to (3.3.23), (3.3.33), (3.3.34) and (3.3.35) and the relations (3.3.87) and (3.3.88) corresponding to the resonant condition for a narrow rectangular harbor induced oscillations leads to the resonant mode shapes defined by:

$$u(x,z,t) = \begin{cases} \mathrm{Re}\left\{ i \dfrac{Agk}{\sigma} \dfrac{\cosh k(z+h)}{\cosh kh} \sin k(x+L)\ e^{-i\sigma t} \right\}, & x < 0 \\ \mathrm{Re}\left\{ i \dfrac{b}{a} \dfrac{Agk}{\sigma} \dfrac{\cosh k(z+h)}{\cosh kh} \sin kL\ e^{-i\sigma t} \right\}, & x = 0 \end{cases} \tag{E.1}$$

where the expression for u at the harbor entrance is derived from continuity considerations

$$w(x,z,t) = \mathrm{Re}\left\{ -i \frac{Agk}{\sigma} \frac{\sinh k(z+h)}{\cosh kh} \cos k(x+L)\ e^{-i\sigma t} \right\} \tag{E.2}$$

$$p_d(x,z,t) = \mathrm{Re}\left\{ \rho g A \cos k(x+L) \frac{\cosh k(z+h)}{\cosh kh} e^{-i\sigma t} \right\} \tag{E.3}$$

$$\eta(x,t) = \mathrm{Re}\left\{ A \cos k(x+L)\ e^{-i\sigma t} \right\} \tag{E.4}$$

$$kL = (n+1)\frac{\pi}{2} \qquad n=0,1,2... \tag{E.5}$$

$$\sigma^2 = kg \tanh kh \tag{E.6}$$

The total mean energy in the harbor is given by (Ippen, 1966):

$$E_n = \frac{1}{4}\rho g\, A^2 Lb \tag{E.7}$$

At this point each source of dissipation must be considered individually:

(i) Loss due to separation at the entrance

A consistent head loss equation can be written as:

$$\frac{\Delta p_{d(0,z,t)}}{\rho g} = \frac{1}{2g} f_e |u(0,z,t)|\, u(0,z,t) \frac{\cosh kh}{\cosh k(h+z)} \tag{E.8}$$

where Δp is the pressure difference across x=0.

In order to check the consistency of Eq. (E.8), Eqs. (E.1) and (E.3) can be substituted into Eq. (E.8) to give:

$$\Delta\eta(0,t) = \frac{1}{2g} f_e |u(0,0,t)|\, u(0,0,t) \tag{E.9}$$

No dependence in z appears for $\Delta\eta(0,t)$ as expected. Furthermore, the expression for the wave amplitude discontinuity is the same as for shallow water waves with the horizontal component of the velocity evaluated at the surface.

The mean power dissipated by flow separation at the entrance is given by:

$$\frac{dW_f}{dt} = \frac{a}{T}\int_o^T\int_{-h}^o \Delta p_d(0,z,t)\ u(0,z,t)dz\ dt \qquad (E.10)$$

The Q_f factor is defined as:

$$\frac{1}{Q_f} \equiv \frac{1}{\sigma E_n}\frac{dW_f}{dt}$$

After some algebraic manipulations Q_f is found as:

$$\frac{1}{Q_f} = \left(\frac{4}{\pi}\frac{1}{(2n+1)}\frac{b}{a}\right)\left(\frac{f_e}{2}\frac{8}{3\pi}\frac{k}{\sigma}\frac{b}{a}\frac{Agk}{\sigma}\right)\left(\frac{1}{2}+\frac{kh}{\sinh 2kh}\right) \qquad (E.11)$$

The quantity Q_f can also be expressed as:

$$\frac{1}{Q_f} = \frac{4}{\pi}\frac{1}{2n+1}\frac{b}{a}\chi_f\left(\frac{1}{2}+\frac{kh}{\sinh 2kh}\right)$$

where χ_f is defined by Eq. (3.3.83), by noting that the quantity $\overline{\hat{u}_3(0,y)}$ appearing in Eq. (3.3.78), from its definition becomes equal in the present case to $\frac{b}{a}\frac{Akg}{\sigma}$.

(ii) Laminar Boundary Friction

The mean power dissipated in the harbor is given by (see Appendix A):

$$\frac{dW_\mu}{dt} = \frac{1}{T}\int_o^T \rho\left(\frac{\nu\sigma}{2}\right)^{1/2}\iint_s (\hat{u}^2+\hat{w}^2)ds\ dt \qquad (E.14)$$

where s is the total surface wetted by the fluid. The Q_μ factor is defined as:

$$\frac{1}{Q_\mu} \equiv \frac{1}{\sigma E_n} \frac{dW_\mu}{dt} \tag{E.15}$$

After calculations Q_μ is found as:

$$\frac{1}{Q_\mu} = \frac{1}{h}\sqrt{\frac{\nu}{2\sigma}}\left[\frac{2h}{b} + \frac{2kh}{\sinh 2kh} + C\,\frac{kh}{\tanh kh} + \frac{kh}{\pi}\left(1 - \frac{2kh}{\sinh 2kh}\right)\right] \tag{E.16}$$

The terms between brackets result from side walls, bottom, surface and backwall friction respectively.

The parameter Q_μ can be written also as:

$$\frac{1}{Q_\mu} = \frac{4}{\pi}\,\frac{1}{2n+1}\,\frac{b}{a}\,\chi_\mu\left(\frac{1}{2} + \frac{kh}{\sinh 2kh}\right) \tag{E.17}$$

where χ_μ is given by Eq. (3.3.81) and μ_t is given by Eq. (3.3.37) except for the friction term at the backwall which was not considered when Eq. (3.3.37) was derived. A heuristic way to account for this term would consist in replacing the expression for μ_t in Eq. (3.3.81) by:

$$\mu_t' = \frac{1}{h}\left(\frac{\nu}{2\sigma}\right)^{1/2}\left(\frac{2\sinh 2kh}{2kh+\sinh 2kh}\right)\left[\frac{2kh}{\sinh 2kh} + \frac{C\,kh}{\tanh kh} + \frac{2h}{b} + \frac{kh}{\pi}\left(1 - \frac{2kh}{\sinh 2kh}\right)\right] \tag{E.18}$$

However, in practice, the correction term can be neglected when compared with the other friction terms either in the case of a narrow basin ($kb \ll 1$) or in shallow water which corresponds to the range of the present harbor experiments.

(iii) Leakage Losses

The mean power dissipated in the harbor in one period is given by:

$$\frac{dW_\varepsilon}{dt} = \frac{1}{T}\int_o^T e\left\{ b\bar{u}_g(t)\ \ p(-L,-h,t) + 2\int_{-L}^{o} \bar{u}_g(t)\ p(x,-h,t)dx \right\} dt \quad (E.19)$$

where $\bar{u}_g$ is the fluid velocity underneath the gap in the outward normal direction to the boundary; from the results of Appendix D $\bar{u}_g$ is related to P_d by:

$$\bar{u}_g(t) = \frac{1}{\nu\rho}\frac{e^2}{12t_e} P_d(x,-h,t) \quad (E.20)$$

where e and t_e denote the gap and the wall thicknesses. The Q_ε factor is defined as:

$$\frac{1}{Q_\varepsilon} \equiv \frac{1}{\sigma E_n}\frac{dW_\varepsilon}{dt} \quad (E.21)$$

After calculations Q_ε is found as:

$$\frac{1}{Q_\varepsilon} = \frac{4}{\pi}\frac{1}{(2n+1)}\frac{e^3}{12t_e\nu}\left(1+\frac{L}{b}\right)\left(\frac{kg}{\tanh kh}\right)^{1/2}\frac{1}{\cosh^2 kh} \quad (E.22)$$

Equation (E.21) can be written as:

$$\frac{1}{Q_\varepsilon} = \frac{4}{\pi}\frac{1}{(2n+1)}\frac{b}{a}\chi_\varepsilon\left(\frac{1}{2}+\frac{kh}{\sinh 2kh}\right) \quad (E.23)$$

where χ_ε is defined by Eq. (3.3.82).

(iv) Radiation Damping

The mean power lost by radiation is given by:

$$\frac{dW_r}{dt} = \frac{a}{T}\int_0^T \int_{-h}^{o} Pd_r(0,z,t)\ u(0,z,t)dz\ dt \qquad (E.24)$$

where Pd_r is the pressure associated with the radiated wave and given by:

$$Pd_r(x,z,t) = \rho g\ \eta_r \frac{\cosh\ k(z+h)}{\cosh\ kh} \qquad (E.25)$$

The expression for the radiated wave amplitude η_r at the harbor entrance can be derived from Eq. (3.3.73) as:

$$\eta_r(0,t) = Re\{\frac{\sigma}{2g}\ \hat{u}(0,0)\ a[1 + \frac{2i}{\pi}\ \ell n(0.1987\ ka)]\ e^{-i\sigma t}\} \qquad (E.26)$$

where $\hat{u}(0,0) = i\ \frac{b}{a}\frac{Agk}{\sigma}$ (E.27)

The Q_r factor is defined as:

$$\frac{1}{Q_r} \equiv \frac{1}{\sigma E_n}\frac{dW_r}{dt} \qquad (E.28)$$

After calculations Q_r is found as:

$$\frac{1}{Q_r} = \frac{4}{\pi}\frac{1}{(2n+1)}\frac{b}{a}\chi_r\ (\frac{1}{2} + \frac{kh}{\sinh\ 2kh}) \qquad (E.29)$$

where χ_r is defined by Eq. (3.3.80).

(v) Rough Turbulent Boundary Friction

This type of friction is likely to occur in actual harbors and it is of interest to compute the associated Q factor in order to estimate its wave attenuating effect as compared with the other sources of dissipation.

For simplification purposes the analysis is restricted to bottom friction in shallow water. The turbulent shear stress for oscillating flows is usually considered in the form:

$$\tau = \frac{1}{2}\rho C_e |u| u \tag{E.30}$$

where C_e denotes the average boundary friction factor. Experiments by Kamphuis (1975) showed that C_e depends on both a Reynolds number and a relative roughness parameter and its usual range lies between 10^{-3} and 10^{-1}. The mean power dissipated in the harbor is given by:

$$\frac{dW_\tau}{dt} = \frac{b}{T}\int_0^T\int_{-L}^{0} \tau\, u\, dx\, dt \tag{E.31}$$

Q_τ is defined as:

$$\frac{1}{Q_\tau} \equiv \frac{dW_\tau/dt}{\sigma E_n} \tag{E.32}$$

After calculation Q_τ is found as:

$$\frac{1}{Q_\tau} = \frac{16}{9\pi^3} C_e \sqrt{\frac{g}{h}}\, \frac{A}{h}\, T \tag{E.33}$$

(vi) Dry friction from meniscus action

The vertical force per unit length on the fluid at the liquid-lucite-air interface is given by Eq. (3.3.3) as:

$$F = -\bar{\kappa}\, \Gamma_e \frac{d\eta/dt}{|d\eta/dt|} \tag{E.34}$$

where Γ_e denotes the surface tension at the air-liquid interface and $\bar{\kappa}$ a constant. The resulting mean power dissipated in the harbor is given by:

$$\frac{dW_c}{dt} = \frac{1}{T}\int_o^T \left[bF \frac{d\eta}{dt} + 2\int_o^L F \frac{d\eta}{dt}\, dx \right] dt \tag{E.35}$$

Q_c is defined as:

$$\frac{1}{Q_c} \equiv \frac{dW_c/dt}{\sigma E_n} \tag{E.36}$$

After calculation Q_c is found as:

$$\frac{1}{Q_c} = \frac{32\bar{\kappa}\Gamma_e}{\pi^2 \rho g A} \frac{1}{b}\left(1 + \frac{\pi}{4}\frac{b}{L}\right) \tag{E.37}$$

(vii) Residual surface tension dissipation

It has been conjectured in Section 3.3.1 that there exists a dissipative source related to surface tension but independent of dry friction from meniscus action. It has been assumed that it could be expressed mathematically by a vertical force applied on the water surface at equi-distance between the walls, as:

$$F \sim \frac{\Gamma_e \eta}{b} \tag{E.38}$$

Assuming further a slight phase shift between F and η, the resulting mean power dissipated in the harbor can be expressed by:

$$\frac{dW_{ob}}{dt} = \frac{1}{T}\int_0^T\int_0^L F\,\frac{d\eta}{dt}\,dxdt \tag{E.39}$$

which gives:

$$\frac{dW_{ob}}{dt} = K_{ob}\,\Gamma_e A^2\,\frac{L}{b} \tag{E.40}$$

where K_{ob} is a constant to be found from experiments. Q_{ob} is defined as:

$$\frac{1}{Q_{ob}} \equiv \frac{dW_{ob}/dt}{\sigma E_n} \tag{E.41}$$

After calculations, Q_{ob} is given by:

$$\frac{1}{Q_{ob}} = \frac{2}{\pi}\,\frac{1}{b^2}\,\frac{K_{ob}\Gamma_e}{\rho g} \tag{E.42}$$

E.2 Case of a Closed Rectangular Basin

The mode shapes are the same as for the narrow rectangular harbor except that the resonant values of kL are given by:

$$kL = (2n+1)\pi \qquad n=0,1,2... \tag{E.43}$$

for a rigid basin excited back and forth.

Five sources of dissipation must be considered in this case: laminar bottom friction, laminar wall friction, laminar surface friction, dry friction from meniscus action, residual dissipation from surface tension.

After calculations, it turns out that the expression for the Q_μ factor associated with the laminar boundary friction forces is the same as in the case of the harbor except that friction is exerted in the basin case on two end walls, not only one. Thus the Q_μ factor is given by:

$$\frac{1}{Q_\mu} = \frac{1}{h}\sqrt{\frac{\nu}{2\sigma}}\left[\frac{2h}{b} + \frac{2kh}{\sinh 2kh} + C\frac{kh}{\tanh kh} + \frac{2kh}{\pi}\left(1 - \frac{2kh}{\sinh 2kh}\right)\right] \qquad (E.44)$$

The Q_c factor associated with dry friction from meniscus actions can be derived similarly from the harbor results by noticing that friction is exerted on the end walls, not only one:

$$Q_c = \frac{32\bar{\kappa}\Gamma e}{\pi^2 \rho g A}\frac{1}{b}\left(1 + \frac{\pi}{2}\frac{b}{L}\right) \qquad (E.45)$$

The expression for the Q_{ob} factor corresponding to the residual source of dissipation associated with surface tension is identical to the expression found in the case of the harbor and is therefore given by Eq. (E.42).

One important application of these results is the possibility of uncoupling the experimental investigation of dissipation caused by laminar boundary friction and surface tension from the investigation of the other sources of dissipation present in the harbor. One can just conduct this investigation in a closed rectangular basin since there exists almost a one to one correspondence between the Q_i factors corresponding to those sources for the harbor, and for the closed basin. Indeed, these considerations are applied in Section 5.1 in the experimental study of boundary friction and surface tension dissipation.

APPENDIX F

F1. DERIVATION OF A TIME DEPENDENT RADIATIVE BOUNDARY CONDITION FOR RADIALLY SPREADING LINEAR NONDISPERSIVE WAVES

This derivation is based on the approach taken by Mungall and Reid (1978). Consider the fluid domain bounded on the left by a straight coastline indented by a harbor (see Fig. F1).

In Region Ω_L (delineated by AGC, Γ_R, BA, CD in Fig. F1, the wave system characterized by the potential wave function Φ consists of two parts: the incident-reflected wave, Φ_I, and the radiated wave ψ . Region Ω_L is assumed to be located sufficiently far away from the harbor entrance so that the nonlinearities in the radiated wave due to harbor oscillations become negligible. The potential function associated with the radiated wave satisfies the linear nondispersive wave equation:

$$\nabla^2\psi = \frac{1}{gh}\frac{\partial^2\psi}{\partial t^2} \tag{F.1}$$

where h is the still water depth (assumed uniform throughout the fluid domain) and g is the acceleration of gravity. Since the coastline is perfectly reflective ψ must satisfy the following boundary condition:

$$\frac{\partial\psi}{\partial x} = 0 \quad \text{on AB,CD} \tag{F.2}$$

A general solution of Eq. (F.1) satisfying Eq. (F.2) can be found in polar coordinates as:

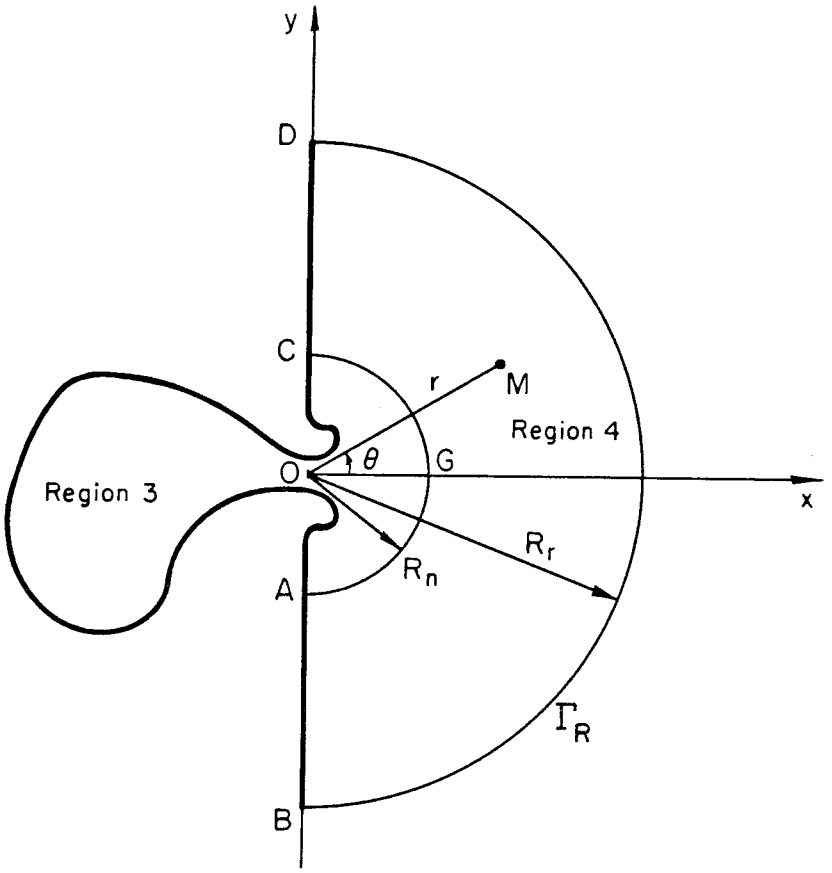

Fig. F1 Definition sketch for radiated wave away from the harbor.

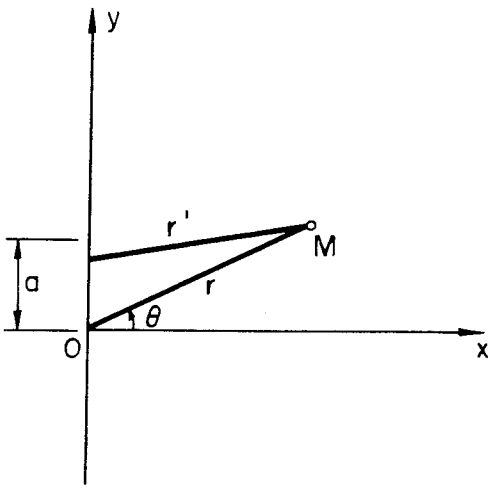

Fig. F2 Definition sketch for a straight coastline all the way to the harbor entrance.

$$\psi(r,\theta,t) = \mathrm{Re}\sum_{n=0}^{\infty}\int_{o}^{\infty}\psi_n(k)H_n^1(kr)\, e^{-i\sigma t}\cos n\theta\, dk \qquad (F.3)$$

where H_n^1 denotes the Hankel function of the first kind, of n^{th} order, $\sigma = k\sqrt{gh}$ and $\psi_n(k)$ are functions of k depending on the geometry of the radiative disturbance. In principle, any Bessel function would be suitable but only the Hankel function H_n^1 satisfies the requirement that waves originating from the harbor entrance are outgoing.

The next step is to evaluate $\frac{\partial\psi}{\partial r}$ at a large distance from the origin. From Eq. (F.3):

$$\frac{\partial\psi}{\partial r} = \mathrm{Re}\sum_{n=0}^{\infty}\int_{o}^{\infty}k\psi_n(k)\,\frac{d[H_n^1(kr)]}{d(kr)}\, e^{-i\sigma t}\cos n\theta\, dk \qquad (F.4)$$

for large values of $z = kr$ (Abramowitz and Stegun (1972), p. 364) the Hankel function H_n^1 becomes:

$$H_n^1(z) = \sqrt{\frac{2}{\pi z}}\left[\frac{1 + i(4n^2-1)}{8z} - \frac{(4n^2-1)(4n^2-9)}{2(8z)^2} + iO(z^{-3})\right]e^{i(z-(2n+1)\pi/4)} \qquad (F.5)$$

and,

$$\frac{dH_n^1(z)}{dz} = \sqrt{\frac{2}{\pi z}}\left[i - \frac{(4n^2+3)}{8z} - i\,\frac{(4n-1)(4n+15)}{2(8z)^2} + O(z^{-3})\right]e^{i(z-(2n+1)\pi/4)} \qquad (F.6)$$

A relationship between $H_n^1(z)$ and $\frac{dH_n^1(z)}{dz}$ of the following form is investigated:

$$H_n^1(z)\left[i + \frac{A}{z} + i\,\frac{B}{z^2} + O(z^{-3})\right] = \frac{dH_n^1(z)}{dz} \qquad (F.7)$$

The unknown coefficients A and B can be evaluated by identification using Eqs. (F.5) and (F.6):

$$A = -\frac{1}{2} \quad , \qquad B = -\frac{(4n^2-1)}{8} \tag{F.8}$$

If the approximation is made that

$$\frac{dH_n^1(z)}{dz} = [i - \frac{1}{2z}]\ H_n^1(z) \tag{F.9}$$

Then, Eq. (F.4) becomes:

$$\frac{\partial\psi}{\partial r} = \mathrm{Re}\sum_{n=0}^{\infty}\int_0^{\infty}\psi_n(k)\ H_n^1(kr)(ik - \frac{1}{2r})\ e^{-i\sigma t}\ \mathrm{cosn}\theta\ dk \tag{F.10}$$

Or:

$$\frac{\partial\psi}{\partial r} = -\frac{1}{\sqrt{gh}}\frac{\partial\psi}{\partial t} - \frac{1}{2r}\psi \tag{F.11}$$

Eq. (F.11) is the time dependent boundary condition for a radially spreading wave far away from the source region. This condition is incorporated in the numerical scheme presented in Section 3.4 to force the radiated wave to be transmitted according to Eq. (F.11) through a radiative boundary which is a semicircle located at some distance from the harbor mouth. (It is noted a perfectly reflective boundary would correspond to $\frac{\partial\psi}{\partial r} = 0$). Actually Eq. (F.11) is exactly satisfied mathematically only for an infinite distance from the mouth. Therefore its use in the numerical scheme at some finite distance r induces reflection of a small percentage of the radiated wave energy back towards the harbor mouth. The amount of reflection depends on the distance r at which the radiative boundary is placed and an estimate of this will be made presently. Eq. (F.11) can also be written as:

$$\frac{d}{dt}\,(r^{1/2}\psi) = 0 \quad \text{on} \quad \frac{dr}{dt} = \sqrt{gh} \tag{F.12}$$

In other words, the quantity $(r^{1/2}\psi)$ is conserved along an outward-directed characteristic. One obvious question is: how close to the source can the radiation condition (F.11) be used within a few percent error? As the approximation made in Eq. (F.9) shows, it depends both on the size of the source and the characteristic wave length, reflected in the importance of the neglected terms $0(n^2/k^2r^2)$ or rather $0(\psi_n n^2/k^2r^2)$. For a point source $\psi_n = 0$ for $n \geq 1$, and thus the minimum distance from the mouth beyond which Eq. (F.11) applies reasonably well only depends on the wave length. However, if the source has a finite size, this distance is increased due to the presence of the term $\psi_n n^2$ which grows with the source size.

To get an estimate of the minimum radius R_r for which the radiation condition (F.11) can be used within a few percent error, consider the simplified case of a straight coastline all the way to the harbor entrance (Fig. F2). Assume, in addition, that the radiated wave satisfies the linear nondispersive wave equation even near the harbor mouth. The solution for ψ is expressed in the harmonic case as (Lamb, 1932, Art. 305):

$$\psi = \int_o^a \frac{\partial \psi}{\partial n}\, H_o^1\,(kr')d\eta \tag{F.13}$$

where a is the mouth width and r' the distance between a field point M(x,y) and a source point $(0,\eta)$ located along the entrance:

$$r' = (x^2+(y-\eta)^2)^{1/2} \tag{F.14}$$

For a small value of a/r, where r is the distance between M and the origin, r' is given by:

$$r' = r\left(1 - \frac{\eta\sin\theta}{r} + O\left(\frac{a^2}{r^2}\right)\right) \tag{F.15}$$

Restricting the analysis to small values of ka a Taylor expansion of $H_o^1(kr')$ around $r' = r$ yields:

$$H_o^1(kr') = H_o^1(kr) - k\eta\sin\theta \frac{dH_o^1(kr)}{d(kr)} + \frac{k^2\eta^2}{2} O\left(\frac{d^2H_o^1(kr)}{d(kr)^2}\right) \tag{F.16}$$

Assume that $\frac{\partial\psi}{\partial n}$ can be approximated by a constant value $\overline{\frac{\partial\psi}{\partial n}}$ along the mouth. The expression for ψ becomes:

$$\frac{\psi(r,\theta)}{a\,\overline{\frac{\partial\psi}{\partial n}}} = H_o^1(kr) + \frac{(ka)}{2}\sin\theta\, H_1^1(kr) + \frac{(ka)^2}{6} O\left(\frac{d^2H_o^1(kr)}{d(kr)^2}\right) \tag{F.17}$$

For large values of $z = kr$

$$\frac{d\,H_n^1(z)}{dz} \sim \left(i - \frac{1}{2z} - \frac{i(4n^2-1)}{8z^2}\right) H_n^1(z) \tag{F.18}$$

$$H_n^1(z) \sim \sqrt{\frac{2}{\pi z}} \exp\left[i\left(z - \frac{n\pi}{2} - \frac{\pi}{4}\right)\right] \tag{F.19}$$

Differentiating Eq. (F.17) with respect to r and using Eq. (F.18) and (F.19) it is found that $\frac{\partial\psi(r,\theta)}{\partial r}$ can be approximated by:

$$\frac{\partial\psi(r,\theta)}{\partial r} = ik\ \psi(r,\theta) - \frac{1}{2r}\ \psi(r,\theta) \tag{F.20}$$

with a relative error:

$$Er\% = Max\left(\frac{1}{8(kr)^2}\ ,\ \frac{ka}{4(kr)^2}\ ,\ O[\frac{(ka)^2}{6}]\right) \tag{F.21}$$

Eq. (F.20) corresponds to the radiation condition (F.11) for the harmonic case for large values of r. The relative error in Eq. (F.21) can also be interpreted as a reflection coefficient for the radiated wave at the radiative boundary.

For values of ka less than 0.5, Eq. (F.20) is verified within a few percent according to Eq. (F.21) if the radiative boundary is located at a distance from the origin equal to 0.6λ where λ denotes the wave length. As ka increases, the value of kr should be increased accordingly to keep the relative error small as seen from the second term of Eq. (F.21). If ka is larger than 0.5, Eq. (F.21) becomes inadequate to estimate the relative error and new terms should be considered in the Taylor expression of Eq. (F.16). But the trend for larger values of ka can be inferred from Eq. (F.21): As ka increases, kr must also increase for a given relative error, until eventually it reaches a value for which the radiative condition is no longer economical to use because of the large region to discretize outside the harbor.

As a concluding remark it can be noticed that the region from which the radiated wave propagates need not be centered at the origin as long

as the order of magnitude of the product kd (where d denotes the distance between the origin and the center of the source) remains smaller than unity.

F2. ESTIMATION OF THE RADIATED WAVE HEIGHT OUTSIDE A NARROW MOUTHED HARBOR

The potential function of a linear wave radiated from the entrance of a harbor is expressed by Eq. (F.13). Specializing to the case of a narrow mouth, i.e., ka << 1, Eq. (F.13) can be approximated by:

$$\psi(x,y) \simeq a \frac{\partial \psi}{\partial n} \left| H_0^1(kr) \right| + O(ka) \tag{F.22}$$

where r denotes the distance between the field point and the center of the mouth. $\partial\psi/\partial n$ represents the flow velocity associated with the radiated wave at the entrance and is estimated by

$$\frac{\partial \psi}{\partial n} \simeq A \frac{\sqrt{gh}}{h} \tag{F.23}$$

where A denotes a typical wave amplitude inside the harbor. Since the magnitude of A depends on and is usually of the same order as the amplitude A_I of the incident-reflected wave system, expression (F.23) can also be approximated by:

$$\frac{\partial \psi}{\partial n} \simeq A_I \frac{\sqrt{gh}}{h} \tag{F.24}$$

The potential function ψ is related to the amplitude A_s of the radiated wave by:

$$\psi \simeq \frac{g}{\sigma} A_s \tag{F.25}$$

Substituting Eqs. (F.25) and (F.24) into Eq. (F.22) yields:

$$A_s \frac{g}{\sigma} \simeq \frac{aA_I\sqrt{gh}}{h} \left|H_o^1(kr)\right|$$

Noting that $\sigma = k\sqrt{gh}$ in shallow water the following relationship follows:

$$\frac{A_s}{A_I} \simeq (ka)\ H_o^1(kr) \tag{F.26}$$

Eq. (F.26) provides an order of magnitude for the radiated wave relative to the incident-reflected wave system. If for a given distance r, $O[ka\ H_o^1(kr)] < O(1)$, nonlinear interaction between the radiated and the incident wave system can be neglected beyond that distance. This result is used in the analytical formulation presented in Section 3.4.